GRADUATE SCHOOL
LIFE SCIENCE MUNICH

Dissertation at the
Graduate School of Life Sciences Munich,
Faculty of Biology,
Ludwig Maximilian's University, Munich,
for obtaining the degree of Dr. rer. nat.

Known and novel members of the endolysosomal transportome/channelome as candidates to rescue lysosomal storage diseases (LSDs)

Einar Kleinhans Krogsaeter

from **Longva, Norway**

2021

This dissertation was prepared
under the mentorship of Prof. Dr. Dr. Christian Grimm
at the Walther-Straub Institute of Pharmacology and Toxicology
at the Ludwig-Maximilians-Universität München

Primary examiner: Prof. Dr. Dr. Christian Grimm
Second examiner: Prof. Dr. Christof Osman

Thesis advisory committee members
Prof. Dr. Dr. Christian Grimm
Prof. Dr. Angelika Vollmar
Prof. Dr. Christof Osman (starting Jan 2019)
Dr. Eric Lambie (Aug 2017-Jan 2019)

Date of submission: 30/08/2021

Date of disputation: 22/02/2022

STATUTORY DECLARATION AND STATEMENT

Statutory Declaration

I hereby solemnly and sincerely declare that the dissertation presented herein was solely constructed by myself, Einar Kleinhans Krogsaeter, registered at Einsteinstraße 13 for the period of employment under supervision of Prof. Dr. Dr. Christian Grimm, independently and by permitted means only.

München, 24/08/2021 Einar Kleinhans Krogsaeter

Statement

I hereby declare that the following dissertation has not previously to its current submission been presented to any other examination boards, nor has the author, Einar Kleinhans Krogsaeter, been previously involved in any other doctoral examination without success.

München, 24/08/2021 Einar Kleinhans Krogsaeter

TABLE OF CONTENTS

1. List of Abbreviations

14-3-3	14-3-3 protein	LY	Lysosome
AAV9	Adeno-associated virus 9	MCOLN1	Mucolipin 1 (gene symbol)
AD	Alzheimer's Disease	MCOLN2	Mucolipin 2 (gene symbol)
ALG2	Alpha-1,3/1,6-mannosyltransferase	MCOLN3	Muculipin 3 (gene symbol
AMP	Adenosine Monophosphate	MERS-CoV	Middle East Respiratory Syndrome-Coronavirus
AMPK	AMP-activated protein kinase	MLIV	Mucolipidosis type IV
ATP	Adenosine Triphosphate	MPR	Mannose-6-phosphate receptor
Aβ	β-amyloid	MTOC	Microtubule organizing-center
BACE1	β-secretase	mTOR	Mechanistic target of rapamycin
cADPR	Cyclic ADP ribose	mTORC1	Mechanistic target of rapamycin, complex 1
CaM	Calmodulin	MVB	Multivesicular body
CaMKKβ	Calcium/calmodulin-dependent protein kinase kinase	NAADP	Nicotinic acid adenine dinucleotide phosphate
Cas9	CRISPR-associated protein 9	NAADP-BP	NAADP-binding protein
CCL2	CC-chemokine ligand 2	NAG	N-acetyl-beta-D-glucosaminidase
Ch	Cholesterol	NCL	Neuronal Ceroid Lipofuscinosis
CICR	Calcium-induced calcium release	Ned19	NAADP antagonist
CLN2/TPP1	Tripeptidyl Peptidase 1	NPA	Niemann-Pick A
CLN3	Ceroid Lipofuscinosis, Neuronal, 3	NPC1	Niemann-Pick C1
CLN3	Ceroid Lipofuscinosis, Neuronal, 5	PCR	Polymerase chain reaction
CLN7	Ceroid Lipofuscinosis, Neuronal, 7	PD	Parkinson's Disease
CRISPR	Clustered Regularly Interspaced Short Palindromic Repeats	PI(3,5)P2	Phosphatidylinositol 3,5-bisphosphate
CTL	Cytotoxic T-lymphocytes	PI(4,5)P2	Phosphatidylinositol 4,5-bisphosphate
CTx	Cholera toxin	PI3P	Phosphatidylinositol 3-phosphate
DFCP1	Double FYVE-containing protein	PM	Plasma membrane
DMD	Duchenne muscular dystrophy	PSEN1	Presenilin 1
DT40	B-lymphocyte cell line	Rab11	Ras-related protein Rab-11A
DYN	Dynamin	Rab4	Ras-related protein Rab-4A
EE	Early endosome	Rab5	Ras-related protein Rab-5A
EEA1	Early Endosomal Antigen 1	Rab7	Ras-related protein Rab-7A
EGF	Epidermal growth factor	RE	Recycling endosome
EM	Electron microscopy	RT-qPCR	Reverse transcriptase quantitative PCR
ERT	Enzyme-replacement therapy	RyR	Ryanodine Receptor
FDA	U.S. Food and Drug Administration	SARS-CoV-2	Severe Acute Respiratory Syndrome-Coronavirus 2
FIP2	FH protein interacting protein FIP2	shRNA	Short hairpin RNA
FYVE	Fab1, YOTB, Vac 1, EEA1-aassociated	SLC	Solute Carrier
GATE-16	Golgi-associated ATPase Enhancer of 16kDa	SM	Sphinigomyelin
Gb	Globoside	SNAP	Soluble NSF attachment protein
Gb3	Globotriasylceramide	SNARE	SNAP Receptor
GDI	Guanine nucleotide dissociation inhibitor	STx	Shiga toxin
GEF	Guanine nucleotide exchange factor	SYT7	Synaptotagmin 7
GFP	Green fluorescent protein	TFEB	Transcription Factor EB
GM1	GM1 Gangliosidosis	Tfn	Transferrin
GTP	Guanosine Triphosphate	TfR	Transferrin receptor
GWAS	Genome-wide association study	TGN	Trans-Golgi network
HZ	Heterozygous	TM	Transmembrane
IIS	Second domain, subunit number	TPC	Two-pore channel
IP3	Inositol triphosphate	TPC1	Two-pore channel 1
IP3R	IP3 Receptor	TPC2	Two-pore channel 2
iPSC	Induced pluripotent stem cell	TPCN1	Two-pore channel 1 (gene symbol)
JNCL	Juvenile Neuronal Ceroid Lipofuscinosis/Batten disease	TPCN2	Two-pore channel 2 (gene symbol)
JPT2	Jupiter microtubule associated homolog 2	TRPML1	Mucolipin 1
KO	Knock-out	TRPML2	Mucolipin 2
LBPA	Lysobisphosphatidic acid	TRPML3	Mucolipin 3
LDL	Low density lipoprotein	ULK1	Unc-51 like autophagy activating kinase 1
LE	Late endosome	Va	Varitint-Waddler allele
LPS	Lipopolysaccharide	VaJ	Varitint-Waddler allele, mild variant
LRRK2	Leucine-rich repeat kinase 2	VPS34	Phosphatidylinositol 3-kinase VPS34
LSD	Lysosomal storage disease	VSD	Voltage-sensing domaini
LSM12	LSM12 Homolog	WIPI2	WD-repeat domain phosphoinositide-interacting protein
LTP	Long-term potentiation	WT	Wild-type

2. LIST OF PUBLICATIONS

The thesis is based on the following manuscripts, referred to in-text by their roman numerals (I-IV):

I. **Selective agonist of TRPML2 reveals direct role in chemokine release from innate immune cells**
Eva Plesch*, Cheng-Chang Chen*, Elisabeth Butz*, Anna Scotto Rosato, **Einar K. Krogsaeter**, Hua Yinan, Karin Bartel, Marco Keller, Dina Robaa, Daniel Teupser, Lesca M. Holdt, Angelika M. Vollmar, Wolfgang Sippl, Rosa Puertollano, Diego Medina, Martin Biel, Christian Wahl-Schott, Franz Bracher, & Christian Grimm
eLIFE. 2018;7:e39720. **these authors contributed equally to this work*

II. **Agonist-mediated switching of ion selectivity in TPC2 differentially promotes lysosomal function**
Susanne Gerndt*, Cheng-Chang Chen*, Yu-Kai Chao*, Yu Yuan*, Sandra Burgstaller, Anna Scotto Rosato, **Einar K. Krogsaeter**, Nicole Urban, Katharina Jacob, Ong Nam Phuong Nguyen, Meghan T. Miller, Marco Keller, Angelika M. Vollmar, Thomas Gudermann, Susanna Zierler, Johann Schredelseker, Michael Schaefer, Martin Biel, Roland Malli, Christian Wahl-Schott, Franz Bracher, Sandip Patel, & Christian Grimm.
eLIFE. 2020;9:e54712. **these authors contributed equally to this work*

III. **TRPML2 is an osmo/mechanosensitive cation channel in endolysosomal organelles**
Cheng-Chang Chen*, **Einar K. Krogsaeter***, Elisabeth S. Butz, Yanfen Li, Rosa Puertollano, Christian Wahl-Schott, Martin Biel, & Christian Grimm.
Science Advances. 2020;6:eabb5064. **these authors contributed equally to this work*

IV. **Human genome diversity data reveal that L564P is the predominant TPC2 variant and a prerequisite for the blond hair associated M484L gain-of-function effect**
Julia Böck*, **Einar K. Krogsaeter***, Marcel Passon, Yu-Kai Chao, Sapna Sharma, Harald Grallert, Annette Peters, & Christian Grimm
PLOS Genetics. 2021;17(1):e1009236 **these authors contributed equally to this work*

V. **Repurposing of tamoxifen ameliorates CLN3 and CLN7 disease phenotype**
Chiara Soldati*, Irene Lopez-Fabuel*, Luca G. Wanderlingh, Marina G. Macia, Jlenia Monfregola, Alessanddra Esposito, Gennaro Napolitano, Marta Guevara-Ferrer, Anna Scotto Rosato, **Einar K. Krogsaeter**, Dominik Paquet, Christian Grimm, Sandro Montefusco, Thomas Braulke, Stephan Storch, Sara E. Mole, Maria Antonietta De Matteis, Andrea Ballabio, Julio Lopes-Sampaio, Tristan McKay, Ludger Johannes, Juan P. Bolanos, & Diego L. Medina.
EMBO Molecular Medicine. 2021;e13742. **these authors contributed equally to this work*

Furthermore, a manuscript in preparation for submission is attached addendum, not covered by the doctoral assessment as stated in §17 of the "Prüfungs- und Studienordnung der Ludwig-Maximilians-Universität München für den Promotionsstudiengang Life Science Munich (2019)":

VI. **Targeting TPC2 rescues lysosomal storage in mucolipidosis type IV, Niemann-Pick type C1 and Batten disease**
Einar K. Krogsaeter*, **Anna Scotto Rosato***, Carla Abrahamian, Dawid Jaslan, Julia Böck, Chiara Soldati, Barbara Spix, Amanda Wyatt, Daniela Borchert, Marcel Passon, Marc Stieglitz, Guido Hermey, Sandra Markmann, Doris Gruber-Schoffnegger, Susan Cotman, Ulrich Boehm, Thorsten Marquardt, Christian Wahl-Schott, Martin Biel, Elena Polishchuk, Diego Medina, Dominik Paquet, & Christian Grimm.
Manuscript in preparation. **these authors contributed equally to this work*

3. SHORT SUMMARY OF MANUSCRIPTS

I. **Selective agonist of TRPML2 reveals direct role in chemokine release from innate immune cells**
Eva Plesch*, Cheng-Chang Chen*, Elisabeth Butz*, (…), **Einar K. Krogsaeter**, (…), & Christian Grimm
eLIFE. 2018;7:e39720. **these authors contributed equally to this work*

The intracellular TRPML2 ion channel likely represents one of the least characterized known intracellular ion channels, as do the consequences of its activity remain enigmatic. While some previous efforts implicated TRPML2 activity to regulate trafficking of recycling endosomes (RE) and modulate immune-cell recruitment, the lack of pharmacological tools to activate the ion channels has rendered scientists reliant on slower genetic methods to investigate the channel function. Resultantly, the consequences of genetic TRPML2 modulation have not been directly linked to TRPML2 activity, as overexpression, mutation, or silencing of genes often brings about long-term adaptations to the cellular manipulations.

In this publication, we developed a selective TRPML2 agonist (ML2-SA1) that acts only on the TRPML2 isoform, but not the TRPML1 nor TRPML3 counterparts. This development allowed us to address the acute consequences of modulating TRPML2 activity, without interference of TRPML1 and TRPML3. Resultantly, we could localize the activity of TRPML2 on early and recycling endosomes. Furthermore, based on docking studies, mutagenesis and validation by calcium imaging and endolysosomal patch-clamp, we identified the binding site of ML2-SA1, selectively abolishing ML2-SA1 activity upon mutating the binding pocket. Using ML2-SA1, we demonstrate that acute TRPML2 activation results in early and recycling endocytic trafficking of transferrin. Finally, we show that LPS-stimulated macrophages utilize TRPML2 to accelerate the release of chemokines, which can be further accelerated by stimulating the macrophages with ML2-SA1.

Declaration of contribution: For this manuscript, I contributed by assessing the subcellular localization of TRPML2, isolating bone marrow-derived macrophages that were used in patch-clamp and functional assays, performing docking analyses to identify ML2-SA1 binding sites (not shown in the article), mutating amino acids interacting with ML2-SA1 based on docking studies, and validating these interactions by calcium imaging. I furthermore performed immunocytochemistry of CCL2 to assess trafficking of the chemokine, but due to unspecific labelling also observed in CCL2 knockout cells, this data was not used in the article.

Declaration: I agree that the reported contributions are correctly listed.

_____
Supervisor: Christian Grimm

II. Agonist-mediated switching of ion selectivity in TPC2 differentially promotes lysosomal function

Susanne Gerndt*, Cheng-Chang Chen*, Yu-Kai Chao*, Yu Yuan*, (…), **Einar K. Krogsaeter**, (…), & Christian Grimm.

eLIFE. 2020;9:e54712. **these authors contributed equally to this work*

The two-pore channels have been a contentious topic in ion channel biology for the last decade, with two opposing bases claiming that they are either NAADP-activated calcium channels or $PI(3,5)P_2$-activated sodium channels. The lack of pharmacological modulators selectively activating the channels have rendered the membrane impermeant, endogenous agonists NAADP and $PI(3,5)P_2$ the only available tools to characterize the channels. Adding another layer of complexity to the debate, it appears that NAADP requires a co-factor to activate the channel, rendering isolated lysosomes irresponsive to the otherwise highly potent TPC activator. The membrane impermeant nature of NAADP and $PI(3,5)P_2$ furthermore occludes possibilities of assessing TPC function in cellular assays, necessitating genetic manipulation or non-selective channel blockers to investigate the channel's impact on cell biology.

In this publication, we developed two classes of membrane-permeable TPC2-selective agonists. On one hand, the TPC2-A1-N class compounds rendered the channel highly calcium-permeable akin to the NAADP-activated channel. The agonists resultantly quickly mobilized a global calcium wave, halting endosomal movement and alkalinizing endosomes. The TPC2-A1-P class compounds contrarily rendered the channel principally sodium-permeable akin to the $PI(3,5)P_2$-activated channel. The very localized calcium efflux evoked by TPC2-A1-P had completely different effects on cell biology than its TPC2-A1-N counterpart, seemingly mobilizing endosomes and resulting in lysosomal exocytosis.

Declaration of contribution: For this manuscript, I contributed by isolating primary macrophage cells (alveolar macrophages) for endolysosomal patch-clamp analysis and analysing putative agonist binding sites using docking. I next mutated the identified putative agonist-interacting residues to abolish their activity, which was later validated by endolysosomal patch-clamp and calcium imaging experiments. I furthermore generated the dominant-negative TPC2 construct which was used to assess TPC2 function in regulating endosomal motility and endosomal acidification. Finally, I performed a series of high-resolution confocal calcium imaging experiments in WT and KO human fibroblasts using the TPC2 agonists ± electroporated TPC2, which were not included in the paper.

Declaration: I agree that the reported contributions are correctly listed.

_____

Supervisor: Christian Grimm

III. TRPML2 is an osmo/mechanosensitive cation channel in endolysosomal organelles
Cheng-Chang Chen*, **Einar K. Krogsaeter***, (…), & Christian Grimm.
Science Advances. 2020;6:eabb5064. **these authors contributed equally to this work*

Having previously characterized how acute TRPML2 activation can accelerate chemokine release, the mechanistic principles governing such acceleration remained enigmatic. Calcium fluxes are widely appreciated to facilitate endosomal trafficking, and ionic fluxes are understood to relieve membrane tension and permit endosomal tubulation and vesicular fusion/fission events, yet the existence of a mechanosensitive ion channel directly responding to stressors manifesting during endosomal trafficking has only been speculated about. Similar ion channels have previously been described on the plasma-membrane, but in these cases their involvement has either been proven to be indirect, or their mechanic regulation is not completely understood.

In this publication, we describe TRPML2 to constitute an osmo/mechanosensitive cation channel present on endosomes, and demonstrate the mechanisms underlying TRPML2 mechanosensitivity. Specifically, we illustrate that membrane stretch leads to TRPML2 activation, and membrane curvature inhibits channel activity. The TRPML2 counterparts TRPML1 and TRPML3 on the other hand do not respond to mechanic stimuli. Reasoning that membrane stretch can exert its effects on TRPML2 through the membrane-bound endogenous agonist $PI(3,5)P_2$, we mutated the TRPML2-unique residue L314 in the $PI(3,5)P_2$ binding pocket to its TRPML1/TRPML3 counterpart arginine. Upon doing so, we found that TRPML2 does no longer respond to mechanic stimuli. On one hand, this finding illustrates why TRPML2 is mechanosensitive, on the other the finding justifies why TRPML1 and TRPML3 are not. Consistent with high TRPML2 expression in fast recycling endosomes, we finally demonstrated that TRPML2 present on fast-recycling endosomes accelerates cargo (transferrin) recycling, while the mechano-insensitive TRPML2 shows comparatively slower recycling rates within the fast-recycling time-frame. Taken together, this publication shows that the mechanosensitive TRPML2 channel senses membrane stretch through its phospholipid binding pocket, activating the channel and accelerating endosomal trafficking.

Declaration of contribution: For this manuscript, I contributed by generating the TRPML2-mutant plasmids used in the study based on bioinformatic alignments of TRPML channels across isoforms and species, generating TRPML2 homology models, performing docking analysis of $PI(3,5)P_2$ against wild-type and L314R mutant TRPML2 homology models, and performing live-cell and fixed-cell transferrin trafficking assays to assess the functional relevance of TRPML2 mechanosensitivity. I also isolated primary cells used in this study (bone marrow-derived and alveolar macrophages), performed immunocytochemistry to assess TRPML2 localization in bone-marrow derived macrophages, and performed high-resolution calcium imaging to assess TRPML2 activity in smaller vs larger vesicles (the latter not being included in the publication).

Declaration: I agree that the reported contributions are correctly listed.

Supervisor: Christian Grimm	Shared first author: Cheng-Chang Chen

IV. Human genome diversity data reveal that L564P is the predominant TPC2 variant and a prerequisite for the blond hair associated M484L gain-of-function effect

Julia Böck*, **Einar K. Krogsaeter***, (…), & Christian Grimm

PLOS Genetics. 2021;17(1):e1009236 **these authors contributed equally to this work*

When developing TPC2 agonists to treat disease phenotypes, it is important to understand how TPC2 can act differently in various populations. Indeed, it is widely appreciated within the field of pharmacogenomics that distinct populations can respond variably to pharmacological interventions due to simple genetic differences of the drug targets or the drug-metabolizing enzymes. A recent article described how two prevalent TPC2 polymorphisms result in its gain-of-function: While the $TPCN2^{M484L}$ mutation results in pore dilation and increased conductivity, the $TPCN2^{G734E}$ mutation desensitizes the channel to mTORC1-dependent inhibition. These two different mutations conferring increased channel conductivity cause the same measurable outcome: An increased prevalence of blond hair colour. Perhaps more importantly however, these mutations dictate how responsive a treated individual would be to TPC2 agonists. As Paracelsus once stated: "All things are poison and nothing is without poison. Solely the dose determines that a thing is not a poison". Characterizing such gain-of-function polymorphisms could therefore be crucial in informing what would constitute an effective or toxic dose of a compound in a given population.

We built upon the previous publication describing gain-of-function polymorphisms of TPC2, and characterized all of the frequently occurring TPC2 polymorphisms. Compared to the other endolysosomal cation channels, TPC2 appears a highly polymorphic gene. The $TPCN2^{L564P}$ substitution is a dramatic example of this, occurring in nearly all sequenced Caucasians, and more than half of all sequenced native Africans and Asians. Only in the native American population, the wild-type $TPCN2^{L564}$ allele predominates. We demonstrate that this major polymorphic allele is a prerequisite for the gain-of-function exerted by the $TPCN2^{M484L}$ polymorphism. Furthermore, we map the distribution of the newly described polymorphisms, and functionally assess their impact on channel function. We find two other prevalent polymorphisms, $TPCN2^{K376R}$ and $TPCN2^{G387D}$, to confer mild increases in channel conductivity when stimulated with $PI(3,5)P_2$, highlighting the spectrum of TPC2 activity. We finally perform a GWAS meta-analysis to assess linkage between TPC2 polymorphisms and phenotypes, finding the mutations to predominantly impact hair colour, risks for developing type 2 diabetes, and the bone mineral density.

Declaration of contribution: For this manuscript, I contributed by data-mining sequencing datasets in different populations, and performing calculations relating to the obtained results. I furthermore sequenced fibroblasts and generated mutant TPC2 plasmids for electrophysiological characterization, and performed the meta-analysis of GWAS datasets to assess phenotypes linked to TPC2 polymorphisms.

Declaration: I agree that the reported contributions are correctly listed.

Supervisor: Christian Grimm

Shared first author: Julia Böck

V. Repurposing of tamoxifen ameliorates CLN3 and CLN7 disease phenotype
Chiara Soldati*, Irene Lopez-Fabula*, (…), **Einar K. Krogsaeter**, (…), & Diego L. Medina.
EMBO Molecular Medicine. Accepted. **these authors contributed equally to this work*

Batten disease, also known as childhood dementia or juvenile neuronal ceroid lipofuscinosis (JNCL), is a lysosomal storage disease caused by mutations in the lysosomal transmembrane protein CLN3. JNCL disease is marked by blindness manifesting around the age of 5, followed by delayed development, progressive neurodegeneration and dementia, and later often fatal seizures. The affected children rarely survive beyond the age of 20 years. Similar presentations occur upon mutations in CLN7, which encodes another lysosomal membrane SLC transporter. Critically, the neuronal ceroid lipofuscinoses (NCLs) currently lack treatment options. While enzyme replacement therapies have been pioneered for CLN2 disease (caused by defects in the soluble lysosomal protein TPP1), similar strategies are unavailable for JNCL, partially due to the transmembrane protein defects (complicating protein supplementation), partially due to the systemic disease phenotypes observed. Resultantly, recent scientific ventures have focused on restoring function to dysfunctional cellular pathways, such as autophagy, lipid/toxin trafficking, and organellar degradation. The hope is that small molecules correcting such defects can globally restore the normal physiology of the affected individuals, and represent therapeutic alternatives for these currently uncurable diseases.

In this work cell-based phenotypic screening was performed to identify new assays to investigate JNCL disease, alongside screening FDA-approved drugs for potential rescue effects in JNCL disease. An assay for staining Gb3 globosides in JNCL disease was developed using fluorescently labelled shigatoxin, and upon employing this it was found that the FDA-approved compound tamoxifen rescues Gb3 accumulation in NCL-affected cells. Upon its administration, tamoxifen activates the lysosomal biogenesis regulator TFEB, likely leading to lysosomal clearance of accumulated storage material, including Gb3 globosides and subunit C of the mitochondrial ATPase. Administration of tamoxifen to NCL-affected mice furthermore corrected motor defects in the animals, outlining that this FDA-approved compound could be repurposed to treat CLN3 and CLN7 disease.

Declaration of contribution: For this manuscript, I contributed by generating three novel iPSC models for juvenile neuronal ceroid lipofuscinosis, namely CLN3$^{\Delta Ex4\text{-}7}$, CLN3^{R405W}, and CLN3^{D416G}. Following extensive quality control, I differentiated these cells into cortical neurons, and supplied them for assessing storage pathology during the revision process of this publication.

Declaration: I agree that the reported contributions are correctly listed.

_____
Supervisor: Christian Grimm

VI. Targeting TPC2 rescues lysosomal storage in mucolipidosis type IV, Niemann-Pick type C1 and Batten disease

Einar K. Krogsaeter*, **Anna Scotto Rosato***, (…), & Christian Grimm.

Manuscript in preparation. **these authors contributed equally to this work*

The lysosomal storage diseases (LSDs) comprise a group of more than 50 inherited rare metabolic disorders, of which several affect children. Their name hails from accumulation of storage materials within the lysosomes, caused by either impaired trafficking within the cell, dysfunctional degradation of cargo, or defective expulsion of waste material by exocytosis. To date, treatment options for lysosomal storage diseases are in high demand. Resultantly, mucolipidosis type IV (MLIV) is a highly interesting LSD. Similar to LSDs like Niemann-Pick type C1 (NPC1) and Batten disease (JNCL; CLN3), MLIV causes childhood neurodegeneration, motor defects, and early-onset neurodegeneration. Unlike NPC1 and CLN3 however, TRPML1 is a druggable ion channel, with several agonists described to date. TRPML1 activity enhances several processes that appear impaired in LSDs such as autophagy and lysosomal exocytosis. Indeed, activation of TRPML1 has been shown capable to rescue MLIV, NPC1 and Fabry disease phenotypes, underscoring the benefit of lysosomal cation channels. Unfortunately, LSDs often exhibit impaired or absent TRPML1 activity. Thus, we focused on the ion channel TPC2. TPC2 is similarly to TRPML1 localized on lysosomal membranes, facilitates endolysosomal trafficking, and its activation boosts autophagy and results in lysosomal exocytosis. We hypothesized that TPC2 activation can rescue MLIV by compensating for lacking TRPML1 activity, and ameliorate NPC1 and Batten disease phenotypes, diseases where TRPML1 activity appears impaired.

During our studies, we developed cell-based assays to assess LSD pathology in patient fibroblasts, finding them to represent a good model for MLIV and NPC1. Batten disease fibroblasts were healthier in comparison, but upon cell-cycle arrest, these fibroblasts also developed storage defects. We found that TPC2 supplementation and/or activation largely restored normal physiology, rescuing trafficking defects, alleviated autophagic blockade, cleared accumulating cholesterol and storage material, and improved the cellular ultrastructure. While fibroblasts are a useful tool to assess disease mechanisms, our approach is highly dependent on TPC2 expression in relevant cell-types. Generating a reporter-mouse expressing GFP under control of the TPC2 promoter, we assessed TPC2 expression throughout the central nervous system. We found TPC2 to be expressed in neurons, astrocytes, and microglia, both in the disease-relevant hippocampus and cerebellum. Having determined TPC2 to be present in the right cell-types, we generated new iPSC-based models for MLIV and Batten disease with isogenic controls. The novel LSD models were differentiated into neurons, and neuronal pathology assessed. MLIV and Batten disease neurons suffered from lysosomal alkalinization, and MLIV neurons exhibited cathepsin B hyperactivity, endolysosomal expansion, and ultrastructural defects. Treatment with the TPC2 agonists restored almost all the investigated disease phenotypes, highlighting the potential for TPC2 activation to restore function in lysosomal storage diseases in the primary affected cell types.

Declaration of contribution: For this manuscript, Dr. Scotto Rosato and I collaborated in performing cell-based assays in patient fibroblasts, including the lactosylceramide trafficking assay, filipin staining for cholesterol, and rescue assays including compound treatment and drug target overexpression. I furthermore isolated organs, sliced, stained, and analyzed reporter mouse samples to assess TPC2 expression, and performed RT-qPCR to assess channel expression in human brain samples. I designed the strategy for gene-editing the novel CLN3 LSD iPSCs and carried out the gene-editing and quality control for all iPSCs. I differentiated these cells into cortical neurons, and assessed disease pathology including cathepsin B activity, assessing the size of the endolysosomal compartment by lysotracker staining, and measuring the lysosomal pH. I prepared samples for electron microscopy (but did not perform the electron microscopy myself) and performed the blinded analyses of these.

Declaration: I agree that the reported contributions are correctly listed.

Supervisor: Christian Grimm

Shared first author: Anna Scotto Rosato

4. ABSTRACT

The project presented herein addresses our limited understanding of organellar pharmacology. Specifically, the work was conceived to elucidate the biological relevance of the endolysosomal cation channels (mucolipins/TRPMLs and two-pore channels/TPCs) using novel, selective pharmacological modulators. On one hand, we developed a first-in-field selective TRPML2 agonist, ML2-SA1, which activates the TRPML2 ion channel on early endosomes, recycling endosomes, and lysosomes. We demonstrate how TRPML2 accelerates endosomal traffic, enhancing chemokine secretion and macrophage chemoattraction. TRPML2 activity is particularly important in the rapidly recycling pathway, where it mediates cargo transit directly from sorting endosomes to the plasma membrane. This function is largely conferred by its unqiue activation by membrane stretching, a feature we have shown to rely on a single amino acid in the TRPML2 phosphoinositide binding-pocket (L314). Mutation of L314 into its TRPML1/TRPML3 counterpart (L314R) abrogates TRPML2 osmosensitivity, and impedes the rapidly recycling pathway. These findings provide biological and structural information about TRPML2 function, laying the foundation for future endeavors modulating immune cell response and inflammation through the immune cell-restricted, druggable ion channel.

Our primary motivation for investigating the endolysosomal ion channels is development of new treatments for diseases currently lacking therapies. The lysosomal storage diseases (LSDs) represent one such family of diseases, where endolysosomal protein defects result in lysosomal dysfunction and (often) neurodegeneration. Mucolipidosis type IV (MLIV) is caused by dysfunction of the lysosomal TRPML1 ion channel, causing blindness and early-onset neurodegeneration. Aiming to treat LSDs such as MLIV, we investigated the related lysosomal ion channel TPC2. We characterized various TPC2 polymorphisms that increase its activity, and developed agonists for TPC2 that either facilitate high Ca^{2+} fluxes arresting endosomal motility or Na^{+} fluxes facilitating lysosomal exocytosis and enhancing autophagy. We used CRISPR/Cas9 to develop new induced pluripotent stem cell (iPSC) models for Neuronal Ceroid Lipofuscinosis (colloquially termed "childhood dementia") and MLIV, differentiating these into cortical neurons. We used the diseased human neurons to investigate treatments for LSDs, finding the autophagic enhancer tamoxifen and the two-pore channel 2 agonist TPC2-A1-P to counteract LSD phenotypes. TPC2-A1-P restored excessive lysosomal proteolysis, storage defects, and trafficking abnormalities in human MLIV neurons and patient fibroblasts. Similarly, TPC2-A1-P ameliorated LSD phenotypes in Niemann-Pick Disease type C1 fibroblasts (NPC1, also known as childhood Alzheimer's Disease), another LSD marked by impaired activity of lysosomal cation channels. We finally performed a proof-of-concept *in vivo* investigation, treating MLIV mice with TPC2-A1-P. While DMSO-treated MLIV mice exhibited gliosis of the cerebellum and hippocampus, TPC2-A1-P-injected mouse brains featured much fewer glial cells, akin to the wild-type controls. These findings demonstrate that pharmacological modulation of the endolysosomal system can restore physiology in a variety of lysosomal storage diseases *in vitro* and *in vivo*.

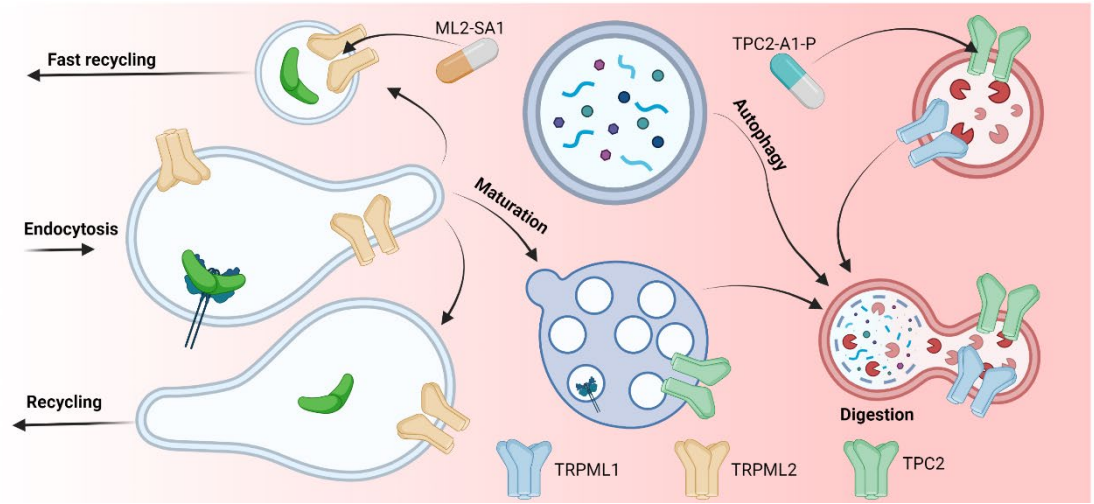

5. Introduction

5.1 The Endolysosomal System

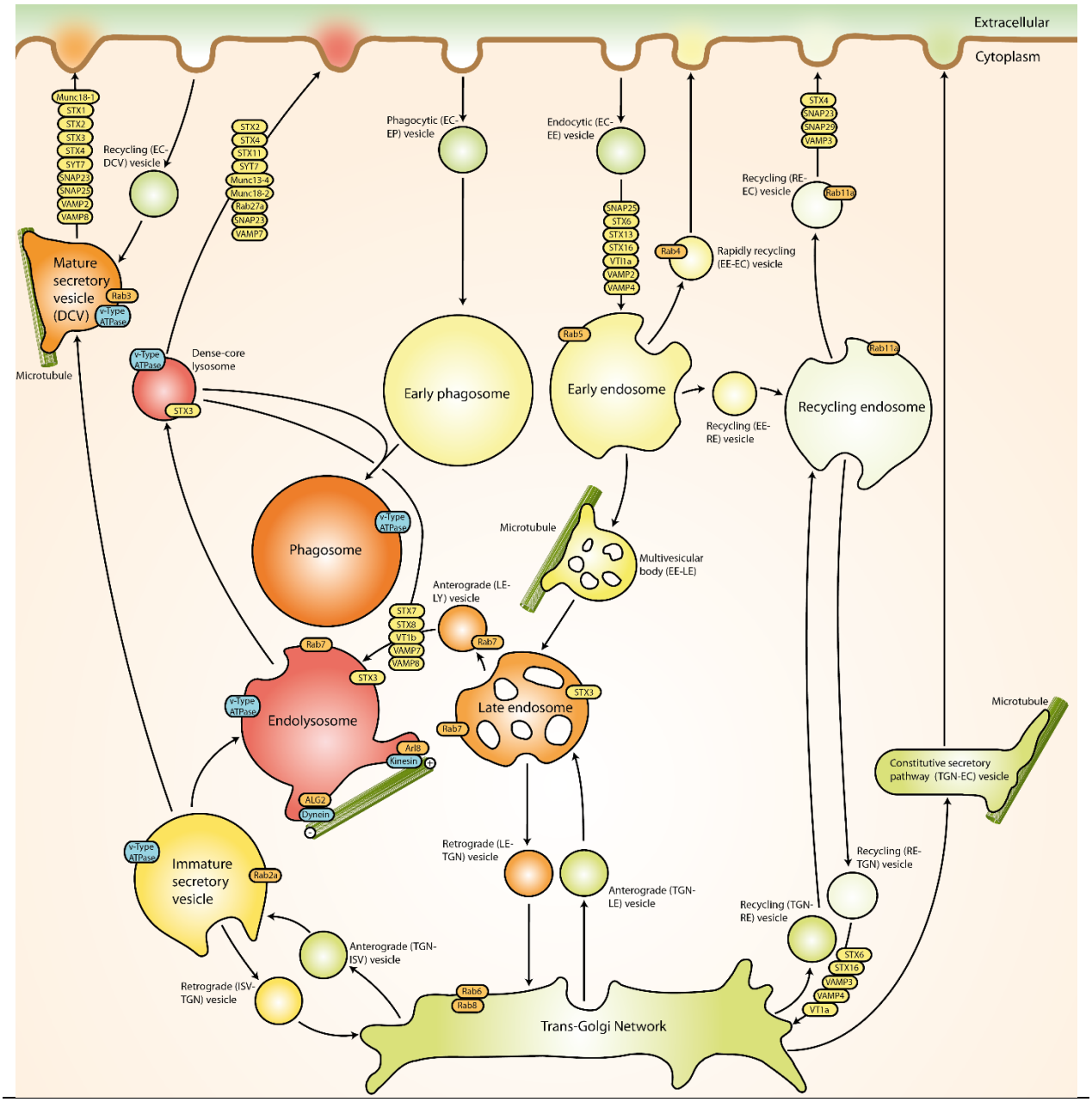

Figure 1: The endolysosomal system and its trafficking routes
The organelles and trafficking routes of the endosomal system are shown, as are some of their characteristic membrane markers, the small GTPases of the Rab family (orange). SNARE proteins involved in the trafficking steps are depicted (yellow), as are key players regulating organellar acidity (v-type ATPase) and mobility (kinesin for anterograde movement, dynein for retrograde movement) (blue).

The endolysosomal system comprises a diverse group of different larger organelles and smaller vesicles. Some vesicles are more static, such as the sorting endosome, a larger organized early endosome (EE). In the sorting endosome, cargo is sorted and packed into smaller intermediate compartments, which shuttle cargo to other compartments such as the recycling endosome (RE), or directly to the plasma membrane (PM). The EE itself may also mature, acidifying and forming

multivesicular bodies (MVB). Over time, the MVB develops into a late endosome (LE), at the boundary between the endosomal system and the degradative lysosomes. The LE can deliver its cargo either to the trans-Golgi network (TGN) or pass it on to lysosomes (LY) for degradation. The LY can either undergo exocytosis to recycle degraded material, expel pathogens, or repair the plasma membrane, or it can fuse with other intracellular organelles such as phagosomes or autophagosomes. These organelles contain endocytosed or intracellular material destined for degradation, respectively[1]. These organelles conveniently express distinct markers allowing their identification, with the markers often conferring characteristic traits to the respective compartment (Figure 1).

5.1.1 The Early Endosome

The early endosomes (EE; also known as sorting endosomes) are the point of entry for internalised, extracellular cargo. Upon endocytosis, vesicles release their luminal Ca^{2+} and Cl^-, and slowly start to accumulate K^+ and H^+ while trafficking to the EE[2]. This is in part mediated by the endolysosomal cation channel TRPML3, which facilitates cation fluxes upon endocytosis[3–5]. The compartment takes a tubulovesicular form, which through numerous sorting proteins coordinates vesicular trafficking and decides the fate of its contents. The classical EE marker and GTPase, Rab5, is in its active GTP-bound form situated on the plasma membrane (PM), endocytic vesicles, and the EE. Here, the active Rab5 orchestrates early endosomal fusion events, recruiting the cytosolic membrane fusion machinery through the scaffolding protein Rabaptin-5, which in turn recruits among others Rabex5, a Rab5-specific guanine nucleotide exchange factor (GEF). Thus, Rab5 initiates a positive feedback loop, recruiting more Rab5 protein alongside effector proteins for membrane fusion, such as early endosome autoantigen 1 (EEA1). The focal recruitment of EEA1 leads to endosomal docking, which in turn permits membrane fusion. Over time, Rab5 slowly hydrolyses its bound GTP, thereby limiting its own activity. In its GDP-bound state, Rab5 dissociates from the membrane, binding a guanine dissociation inhibitor (GDI) instead[6]. The EE can either sort its cargo for direct recycling to the plasma membrane via $Rab4^+$ fast recycling vesicles, indirect recycling through the $Rab7^+$ recycling endosome (RE) or keep its cargo while the endosome matures towards the $Rab7^+$ late endosomal (LE) lineage. Within a few minutes, the EE becomes unavailable for internalised cargo delivery as it matures[7]. Endosomal maturation is marked by a dramatic remodelling of the endosomal lipids, proteins, and luminal ions. The PM-associated lipid $PI(4,5)P_2$ is being replaced by PI(3)P and $PI(3,5)P_2$, Rab5 is shed and replaced by the LE-associated Rab7[8], and the vesicular proton pump (v-type ATPase) drives luminal acidification from 6.2 in the EE to 5.5 in the LE[1]. These compositional changes carry substantial implications for the downstream function of the endosomal compartment.

5.1.2 The Recycling Endosome

Compared to the peripheral early endosomes, the recycling endosome (RE) sits deeper in the cells. Frequently, the RE takes a highly reticulated form, consisting of an extensive network of tubules. In some cell-types this network branches out from the microtubule organizing centre (MTOC)[9], while in other cell-types it is dispersed throughout the cell[10]. The RE serves important functions in coordinating which PM-destined proteins are returned where, often in a site-directed manner. The perhaps most obvious relevance of the RE is reflected in polarized cells, where the protein compositions of the apical and basolateral membranes can largely differ, requiring the RE to direct specific proteins for recycling to their respective membranes[11,12]. While many players coordinating these complex recycling processes remain uncharacterized, some crucial recycling mediators have been revealed. One of the most characteristic proteins of the recycling endosome is the GTPase Rab11. Beyond associating with the RE, Rab11 also appears directly involved in cellular recycling processes. Alike Rab5, Rab11 exists in two states: It exists either on endosomal membranes in its GTP-bound active state, or in the cytosol in its GDP-bound form. When associating with endosomal membranes, Rab11 recruits membrane trafficking machinery (e.g. FIP2 and myosin Vb), facilitating plasma membrane recycling[13–15]. Furthermore, it also appears that Rab11 associates with recycled cargo, thereby implicating it in sorting processes[16]. Such cargo includes presenilin 1 (PSEN1), a key driver for familial early-onset Alzheimer's Disease (AD)[17], and the β-secretase (BACE1), another AD-implicated protein. BACE1 forms the catalytic subunit of the γ-secretase, a plasma membrane-resident protease exporting and cleaving β-amyloid (Aβ). In Alzheimer's disease, Aβ accumulates and forms extracellular plaques. Loss of Rab11 activity prevents the plasma membrane localization of BACE1 and secretion of the plaque-

forming Aβ[18]. While the functions of Rab11 reflects the varied roles of the RE, they also reveal that targeting endosomal trafficking pathways could have a modifying effect on the progression of such diseases.

5.1.3 The Late Endosome

Maturation of the early endosome sees the EE-associated Rab5 being replaced by the late-endosome (LE)-associated Rab7[8,19]. During this time, the endosome undergoes dramatic changes, most strikingly marked by the formation of intraluminal vesicles. For this reason, late endosomes are often referred to as multivesicular bodies (MVB)[20,21]. The formation of luminal vesicles is largely governed by the LE lipid LBPA, which creates limiting membrane invaginations that bud off into the LE lumen[22]. These LBPA-rich intraluminal vesicles can again fuse with the limiting membrane, releasing their contents. Normally, the formation of intraluminal vesicles represents a mechanism for sorting cargo for lysosomal degradation[21,23]. However, upon infection, this process is hijacked by viruses and toxins, permitting their endosomal escape before reaching the degradative lysosomes[24–26]. Alternatively, intraluminal vesicles can also be released by exocytosis, being released into the extracellular space as exosomes[27]. These exosomes can fulfil a variety of roles, including antigen presentation and target cell killing, extracellular matrix remodelling, and transferring nutrients and signalling molecules between cells[27,28]. Similarly to how viruses can hijack intraluminal vesicles to escape the endosomal system and enter the cytosol, viruses can also enter intraluminal vesicles to exit the cells through the exosome secretion pathway[21].

The late endosome furthermore importantly orchestrates the cargo exchange between the Golgi apparatus and the endolysosomal system, with the mannose-6-phosphate receptor (MPR) for example clustering acid hydrolases in the Golgi for collection and delivery to the LE. Upon reaching the LE, the acidic luminal pH causes the MPR to dissociate from its cargo. The MPR is subsequently recycled to the Golgi apparatus, while the dissociated acid hydrolases are trafficked onwards from the LE into lysosomes[29,30]. The retromer, which shuttles contents from the LE to the Golgi apparatus, has come under scrutiny as mutations in its constituent CLN3 and CLN5 proteins can cause the childhood neurodegenerative disease neuronal ceroid lipofuscinosis (NCL). CLN3 and CLN5 proteins together scaffold the characteristic LE marker Rab7 with the retromer, thereby facilitating cargo traffic between the LE and the Golgi apparatus. Loss of either CLN3 or CLN5 abrogates such traffic, preventing delivery of lysosomal proteins and enzymes, and results in the severe lysosomal storage disease NCL[31–34]. Taken together, defects in LE function can lead to a variety of disorders ranging from infectious diseases to neurodegeneration, warranting identification of druggable targets and novel therapies to slow disease progression.

5.1.4 The Lysosome

The lysosome was discovered by Christian de Duve *et al*. in 1955 as a membrane-bound structure containing various acid hydrolases[35]. It soon became obvious that the initially discovered lysosomes comprise a wide variety of acidic organelles with distinct functions: While some lysosomes could be seen to contain cytoplasmic contents (termed autophagic vacuoles), others sported an electron-dense interior (termed cytosomes)[36]. The initial observations of lysosomal heterogeneity have recently gained traction as individual lysosomes can be scrutinized by endolysosomal patch-clamp to assess channel and transporter activity[37], metabolomics to assess metabolite content[38], or nanoprobes to detect their ionic composition[39–43]. Based on such investigations, estimates have been made that around five distinct lysosomal functional clusters exist, each with distinct functional roles[38]. On one hand, the cell can engulf extracellular particles by phagocytosis to kill invading microbes or clear extracellular debris, delivering the particles to the phagolysosome for degradation[38,44]. Other lysosomes are filled with protons and chloride, rendering them highly acidic and degradative. Decreases in the luminal chloride concentration, as is seen in certain lysosomal storage diseases (LSDs), concomitantly alkalinizes the luminal pH and reduces the lysosomal degradative capacity[41,43]. The lysosomal sub-groups can themselves transition into other lysosomal types, with Zhu *et al*. noting a branch point where lysosomes either transition into lysosomes that degrade autophagic cargo, the autolysosomes, or endolysosomes which degrade endocytosed material delivered through the endosomal system[38].

While altered lysosomal function contributes to widespread disorders such as Alzheimer's disease[45–47], Parkinson's disease[45,48–50], and various cancers[51–55], the lysosomal storage diseases (LSDs) likely constitute the most obvious link between lysosomal dysfunction and disease[56]. The LSDs comprise roughly 50 inherited metabolic disorders, of which several are caused by mutations in lysosomal enzymes and membrane proteins. As the name suggests, the dysfunction of these lysosomal proteins result in the lysosomal accumulation of products, which ultimately causes lysosomal dysfunction and impairs cellular viability. For example, mutations in the proteolytic enzymes cathepsin D and F cause the neurodegenerative disorder neuronal ceroid lipofuscinosis[57,58], mutations in the lipid-metabolizing β-galactosidase causes GM1 gangliosidosis marked by ataxia and parkinsonism[59], and mutations in the lysosomal cation channel TRPML1 leads to the similarly neurodegenerative disorder mucolipidosis type IV (MLIV)[60–62]. LSDs are not limited to the central nervous system however, with the heart and liver also frequently being affected. Tragically, only palliative therapy is available for most of the LSDs, although substrate reduction and enzyme replacement therapies have been pioneered for a few disorders[56,63]. It is however feasible that small-molecule modulators of lysosomal function can ameliorate a wide range of LSDs due to their shared aetiologies. For example, cellular processes such as lysosomal trafficking, exocytosis, and autophagy appear common denominators across a variety of LSDs[56,62,64–69], raising hope that small molecule-mediated activation of such processes can prove effective therapies. Resultantly, the intracellular ion channels have been increasingly investigated, mediating the aforementioned processes. The discovery of small molecule endolysosomal ion channel modulators has proven effective in boosting endolysosomal transport and autophagy[61,70,79,71–78], setting the stage for further applications in LSDs.

5.2 The Endolysosomal Channelome

Historically, new drugs were discovered following their application in disease. Traditional remedies such as heterogeneous plant extracts were progressively purified to isolate the active ingredients responsible for the observed effects. Towards the end of the 20th century and later spurred on by the sequencing of the human genome[80], this paradigm largely shifted towards a more molecular approach. Instead of identifying the active drugs in already existing remedies, dysregulated disease pathways were identified alongside implicated, druggable proteins[81]. This approach renders the endolysosomal cation channels highly relevant, being both physiologically important and, when lacking or impaired, drivers of disease pathology. Furthermore, ligand-gated and voltage-gated ion channels appear viable drug targets, comprising 13% of all identified drug targets[82]. Additionally, their residency on endosomal membranes suggests that channel modulation could selectively ameliorate aberrant endosomal disease processes. The last decade brought about the identification of new endosomal channel modulators[55,61,71,74,75,83–85], which will prove of paramount importance when modifying dysregulated endosomal pathways.

5.2.1 The Mucolipins

The mucolipins (TRPMLs) comprise a family of intracellular transient receptor potential (TRP) channels, of which there are three isoforms in mammals[78,86]. While the strictly lysosomal isoform TRPML1 is ubiquitously expressed in human tissues[60], the EE/RE/LY-resident TRPML2 and EE/LY-resident TRPML3 isoforms appear restrictively expressed in immunogenic tissues, with some exceptions[87]. The TRPML family members are at negative membrane potentials activated by the endolysosomal phosphoinositide $PI(3,5)P_2$, permeating fluxes of calcium and sodium from the endolysosomal lumen into the cytosol[37,88–90]. On one hand, such fluxes allow remodelling of the luminal ionic content (e.g. exchanging cations for protons to facilitate endosomal acidification[91]), on the other hand lysosomal calcium release facilitates signalling and endosomal trafficking events. Evidently, the appropriate function of TRPML channels is crucial in such processes, as their loss or aberrant activation can lead to detrimental outcomes[62,79,92].

5.2.1.1 TRPML1 and Lysosomal Homeostasis

The lysosomal ion channel TRPML1 forms the most extensively characterized link between endolysosomal ion channel dysfunction and disease. Mutations in this protein cause mucolipidosis type IV (MLIV), a debilitating disease marked by infantile-onset visual impairment, motor dysfunction, and neurodegeneration. Following the identification of the gene underlying MLIV in the early 2000's[60,93–95], its encoded protein was demonstrated to constitute a lysosomal inwardly rectifying cation channel[96–99]. Since its discovery, the TRPML1 ion channel has been implicated in a number of crucial processes maintaining lysosomal homeostasis. The consequences of TRPML1-mediated calcium release unquestionably represent the best characterized signalling pathways of the ion channel.

On one hand, TRPML1 is situated at a crossroad regulating autophagy and nutrient availability. TRPML1-mediated calcium release directly activates transcription factor EB (TFEB), the master regulator of lysosomal biogenesis[100–102]. Under resting conditions, TFEB is phosphorylated by the mechanistic target of rapamycin complex 1 (mTORC1), facilitating its association with the 14-3-3 protein (14-3-3) and retention in the cytosol and on lysosomal membranes[103]. In this state TFEB is rendered inactive, unable to associate with its regulated genes to facilitate their transcription[101,102]. TRPML1-mediated calcium release however activates the calcium-sensitive phosphatase calcineurin, dephosphorylating TFEB. Subsequently, TFEB dissociates from 14-3-3 and is released from lysosomal membranes, permitting its nuclear translocation and transcription of genes implicated

in lysosomal biogenesis[72,104]. Beyond its role in autophagy through facilitating lysosomal biogenesis, Scotto-Rosato *et al.* elegantly demonstrated how TRPML1-mediated calcium signals can facilitate autophagic biogenesis. Calcium released by TRPML1 activates both the calcium/calmodulin-dependent protein kinase kinase (CaMKKβ) and AMP-activated protein kinase (AMPK). CaMKKβ/AMPK first activate the ULK1 complex, in turn activating the VPS34-complex to initiate phagophore formation. ULK1 and VPS34 elevate the phosphoinositide PI_3P levels, recruiting the phagophore-resident double FYVE-containing protein (DFCP1) and WD-repeat domain phosphoinositide-interacting (WIPI2) proteins[77]. Conversely, TRPML1-mediated calcium release can also activate mTORC1 via the calcium sensor calmodulin (CaM)[105], yet it remains unexplored whether TRPML1-mediated mTORC1 activation also affects TFEB phosphorylation. Instead, Sun *et al.* suggest this pathway of TRPML1-mediated mTORC1 activation to crucially re-activate mTORC1 after autophagy, preventing cell death due to mTORC1 inactivation[106]. mTORC1, in turn, can phosphorylate and inactivate TRPML1 and shut down autophagic progression[107]. Evidently, TRPML1 appears poised in the centre of both positive and negative feedback loops regulating autophagic progression[78,79,108].

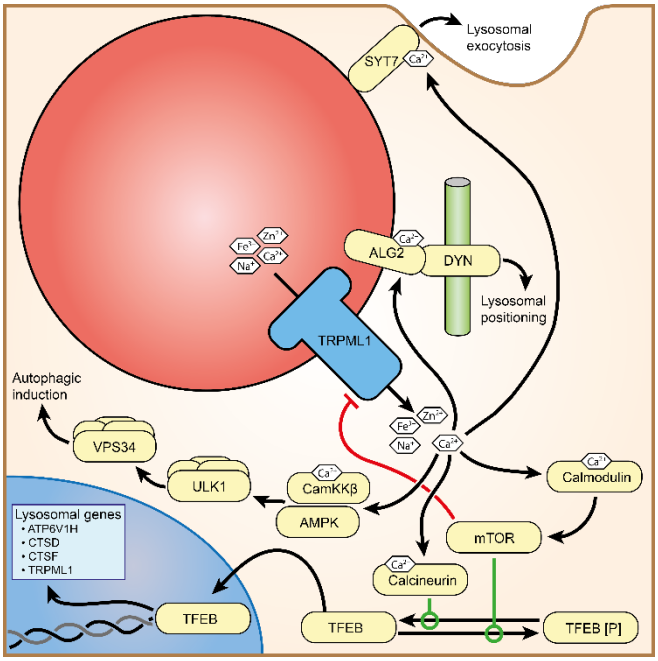

Figure 2: TRPML1-regulated pathways
TRPML1-mediated lysosomal calcium efflux appears crucially involved in numerous pathways required for cellular and lysosomal homeostasis. On one hand, released calcium initiates autophagy through stimulating CaMKKβ and AMPK, or enhances autophagy upon activating TFEB, triggering its nuclear translocation. Following autophagy, TRPML1-mediated mTOR reactivation through calmodulin shuts down the autophagic pathways. TRPML1 can also facilitate lysosomal exocytosis to support membrane repair or expulsion of lysosomal contents via the calcium-sensitive SYT7 or regulate lysosomal positioning upon recruiting the calcium-sensor ALG-2 and its associated motor proteins.

TRPML1 furthermore appears crucially involved in regulating lysosomal exocytosis[84,109,110] and positioning[111]. LaPlante *et al.* first noted that TRPML1-deficient fibroblasts possess several perinuclear lysosomes, unlike the scattered lysosomes observed in healthy fibroblasts. Transfection of TRPML1 however caused relocation of these lysosomes towards peripheral regions, suggesting that TRPML1 might be involved in anterograde lysosomal movement (from the nucleus towards the periphery). Suspecting that the perinuclear retention of lysosomes might affect their expulsion, the authors assessed lysosomal exocytosis in TRPML1-deficient cells. Strikingly, TRPML1-deficient cells stimulated with the calcium ionophore ionomycin released less of the lysosomal enzyme N-acetyl-beta-D-glucosaminidase (NAG). Furthermore, ionomycin-induced translocation of lysosomal membrane proteins to the plasma membrane appeared impeded[109]. Evidently, TRPML1 seemed necessary to facilitate lysosomal exocytosis. Since then, other groups have supported these findings. TFEB-mediated lysosomal exocytosis (and release of lysosomal contents) strictly depends on TRPML1 and calcium release[110]. The implications of TRPML1 in regulating exocytosis are vast. On one hand, the impaired gastric acid secretion observed in mucolipidosis type IV (MLIV)[112], a disease marked by TRPML1 dysfunction, has been attributed to dysfunctional exocytosis of parietal cell tubulovesicles[113]. In macrophages, ingestion of large particles triggers production of the endogenous TRPML1 agonist $PI(3,5)P_2$. TRPML1 activation subsequently causes calcium release, which in turn activates the SNARE-binding synaptotagmin 7 (SYT7) to facilitate membrane fusion and lysosomal exocytosis[84]. In an iPSC-derived neuronal model of Parkinson's disease (PD), TRPML1 activation and lysosomal exocytosis appear sufficient to reduce the accumulation of cytotoxic α-synuclein[114]. Dysfunctional lysosomal

exocytosis can also lead to muscle dystrophy. Sarcolemmal injuries are normally repaired upon lysosomal exocytosis in skeletal muscle cells, mediated by TRPML1 and calcium-sensing proteins. When TRPML1 is lost however, sarcolemmal membrane repair is impaired, and the skeletal muscle degenerates. Conversely, genetic TRPML1 supplementation is sufficient to correct muscle dystrophy, enhancing lysosomal exocytosis[115]. Recently, novel TRPML1 agonists were found to ameliorate muscle degeneration in a mouse model of Duchenne muscular dystrophy (DMD)[116], underscoring the physiological relevance of TRPML1 function and its regulation of lysosomal exocytosis.

Beyond its importance in lysosomal exocytosis, TRPML1 also regulates lysosomal positioning. Using pharmacological modulators, Li *et al*. found TRPML1 activation to facilitate retrograde trafficking of lysosomes (periphery to perinucleus), alike what is observed upon starvation. Genetic overexpression of TRPML1 led to similar observations, suggesting its direct involvement in lysosomal motility. TRPML1-mediated calcium release had previously been shown to recruit the calcium sensor Alpha-1,3/1,6-mannosyltransferase (ALG2)[117], which in turn recruits dynein motor proteins to facilitate retrograde lysosomal movement or lysosomal tubulation[111]. While these results contrast findings of perinuclear lysosome accumulation in TRPML1-deficient cells, it should be noted that the short-term effects observed by Li *et al*. upon pharmacological modulators likely differ from the long-term adaptations taking place in the case of LaPlante *et al*., investigating chronically TRPML1-deficient cells[109]. Taken together, it appears unquestionable that lysosomal calcium released from TRPML1 drastically impacts lysosomal movement and expulsion (Figure 2)[78,79].

5.2.1.2 TRPML2 and Immune Surveillance

TRPML2 likely represents the least investigated TRPML ion channel to date. TRPML2 was first discovered by Di Palma *et al*. while attempting to identify causative alleles underlying the TRPML3-associated varitint-waddler phenotype (see section 6.2.1.3). By means of a positional cloning strategy, the authors isolated transcripts for both TRPML2 and TRPML3, noting their similarities to TRPML1[3]. Unlike TRPML1, TRPML2 is mainly found in early endosomes (EE), recycling endosomes (RE), and lysosomes (LY)[74,118–123]. The channel constitutes a non-selective cation channel, partially inhibited by luminal protons (low pH)[121,124]. The implications of TRPML2 in immune cells was first noted by Song *et al*., observing high TRPML2 expression in the B-lymphocyte cell line DT40[118], and later supported by Samie *et al*. who highlighted its particularly high expression in the thymus and spleen[87]. Intriguingly, the latter found TRPML2 expression to be intricately linked to TRPML1 expression, observing reduced TRPML2 expression in TRPML1 KO mice in tissues otherwise rich in TRPML2. This finding was attributed to TRPML1-dependent calcium release likely inducing TRPML2 transcription[87]. Of note,

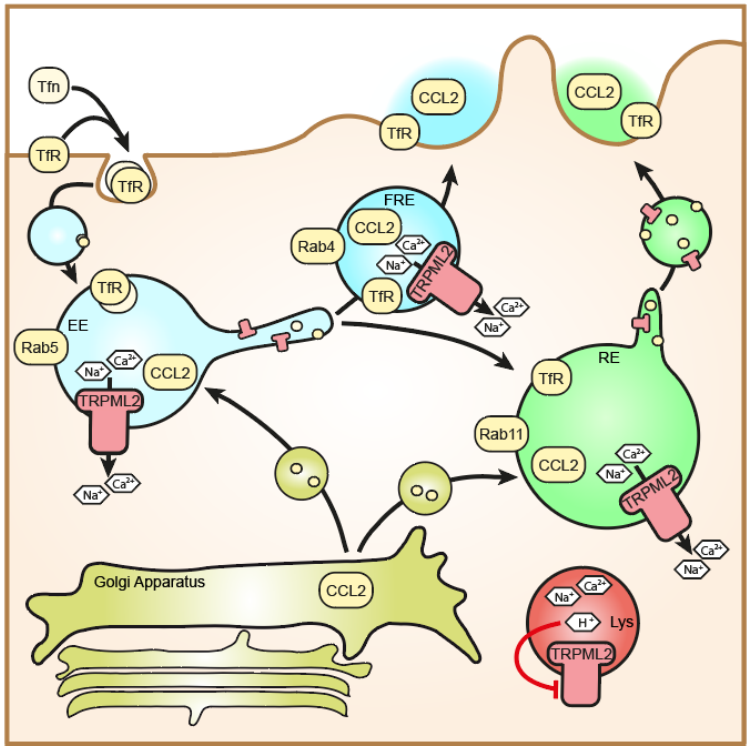

Figure 3: TRPML2-mediated trafficking
TRPML2 is particularly involved in trafficking through the early and recycling endosomal compartments (EE/RE). Transferrin (Tfn) and its receptor (TfR) are recycled through TRPML2^{+} endosomes and fast recycling endosomes (FRE). The chemokine CCL2 is likely also released through similar pathways upon macrophage activation. In lysosomes, TRPML2 is likely inactive, due to the high luminal content of protons.

calcium release is a crucial component of lipopolysaccharide (LPS)-induced gene expression in stimulated macrophages[125]. Accordingly, LPS appears a potent inducer of macrophage TRPML2 expression. Upon stimulation, the newly produced TRPML2 rapidly migrates to transferrin receptor $(TfR)^+$ structures[122], likely corresponding to early and recycling endosomes[126]. Here, TRPML2 appears to serve an important role in secreting pro-inflammatory chemokines, such as the macrophage chemoattractant protein CCL2. Accordingly, macrophage recruitment is markedly reduced in TRPML2 knock-out mice[122], while pharmacological TRPML2 activation enhances macrophage chemoattraction[74]. Thus, TRPML2 appears to fulfil the role of an inducible mediator of intracellular trafficking pathways, accommodating the need for a rapid response to infectious stimuli (Figure 3)[127].

5.2.1.3 TRPML3 and Endolysosomal Cation Channel Activation

TRPML3 was first identified by Di Palma *et al*. in an effort to identify the causative allele underlying the murine, dominant varitint-waddler (Va) phenotype[3]. In its homozygous most severe form, the Va locus causes deafness, a nearly entirely white coat colour, and reduced viability. Heterozygous Va carriers, or carriers of the variant Va^J locus, exhibit a milder phenotype, marked by residual hearing and coat colour dilution and variegation, with vestibular function and viability remaining normal[3,128–132]. The varitint-waddler mouse, which carries a constitutively activating TRPML3 mutation (A419P)[3], exhibits prenatal cochlear melanocyte death, followed by postnatal cochlear hair cell degeneration, secondary to unchecked calcium influx and cytosolic calcium overload[4]. The finding that TRPML3 can be activated by proline substitutions in its fifth transmembrane domain (TM5) would prove tremendously important in investigating channel function and gating. First of all, the realization that a helix-breaking proline insertion is sufficient to render the channel constitutively active has supported later structural investigations into TRPML3 channel conduction[4]. Hirschi *et al*. and Zhou *et al*. recently outlined the gating mechanism of TRPML3 based on cryo-EM investigations, finding TM6 movement to be crucial for ion conduction. Upon channel gating by its endogenous agonist $PI(3,5)P_2$, the intimately coupled TM5 and TM6 pore-lining helices swerve outwards, opening the otherwise narrow pore region[133,134]. The helix-breaking proline insertion likely carries similar consequences on the pore-lining helices, rendering the channel constitutively active. Secondly, the discovery that helix-induced links render TRPML3 constitutively active provided means of investigating TRPML activity in the absence of known channel modulators, spurring research extrapolating these findings to TRPML1[98] and TRPML2[121]. Finally, the discovery supported ventures to develop TRPML activators, leading to the identification of drugs binding and activating TRPMLs[70]. These drug scaffolds were developed to provide more selective mucolipin activators, facilitating development of the mucolipin agonists ML-SA1[71] and MK6-83[61], the TRPML2-selective ML2-SA1[74], and TRPML3-selective EVP21[74].

Functionally, TRPML3 appears to regulate membrane trafficking, where its knockdown causes intracellular transferrin and EGF accumulation, and overexpression decreases transferrin and EGF accumulation[5]. The authors' speculations that TRPML3 is preventing endocytosis were however refuted by Martina, Lelouvier and Puertollano (2009), who assessed EGF internalization in TRPML3-transfected cells. The authors found no difference between wild-type and TRPML3 overexpressing cells, indicating that the observed changes in EGF accumulation must be due to other factors than endocytosis. Instead, the authors found TRPML3 to prevent lysosomal delivery of EGFR, with the channel likely promoting other trafficking pathways instead[135]. Beyond trafficking, TRPML3 also regulates autophagic progression. Overexpressed TRPML3 highly localizes to autophagosomes, with its overexpression increases the number of autophagosomes[5,77,135]. The channel itself interacts with the autophagy inducer GATE-16, particularly during autophagic induction. Functionally, the authors speculated that TRPML3 could provide the calcium required for autophagosome biogenesis and its involved membrane fusion events[136,137]. It also appears that the presence of TRPML3 on autophagosomes prevents cargo degradation, with EGF (as previously mentioned) and ubiquitinylated proteins accumulating in $TRPML3^+$ endosomal compartments. Potentially, this appears a consequence of the observed endosomal pH elevation upon TRPML3 expression, as the endosomal pH increases by 1-2 units upon TRPML3 overexpression[135]. Effects on endolysosomal pH have however, until now, not been verified with in endogenous expression systems with appropriate knock-out controls. The intricacies of TRPML3-mediated regulation of endocytosis and autophagy are still being disentangled, but the channel certainly appears a crucial mediator in these processes.

5.2.2 The Two-Pore Channels

The two-pore channels (TPCs) comprise a family of intracellular voltage-gated ion channels (VIC), consisting of two to three isoforms in mammals, of which humans encode two functional transcripts (TPC1 and TPC2)[86,138–140]. TPC activity was first observed in plants, where Hedrich and Neher used patch-clamp to characterize calcium-induced currents on sugar beet vacuoles[141]. Ishibashi, Suzuki, and Imai would later clone the homologous TPC1 transcript from rat kidney cells, noting its similarity to voltage-gated sodium and calcium channels, besides encoding two sets of pore helices[138,142]. The connection between the enigmatic vacuolar calcium channel and the TPC1 gene was drawn by Peiter *et al*. a few years later, who overexpressed TPC1 and noted the currents associated with it[143]. The field of mammalian TPC research saw its dawn in 2009, as three groups described the TPC channels to constitute the elusive Ca^{2+}-mobilizing NAADP receptors[144–147]. Soon after, descriptions would follow claiming the channels to instead be activated by the endosomal phosphoinositide $PI(3,5)P_2$, alike the mucolipins, facilitating sodium release[147–149]. Furthermore, it was discovered that ATP and mTORC1 completely block TPC activity, indicating that the channels inactivate in nutrient-rich environments[148]. The contentious debate of whether TPCs are $PI(3,5)P_2$-activated sodium channels or NAADP-activated calcium channels continued for nearly a decade, largely due to the seemingly indirect binding mode of NAADP at the TPCs[150,151]. First in 2021, two direct NAADP receptors were identified, scaffolding NAADP and binding TPCs to facilitate calcium release[152–155]. Simultaneously, it was shown that TPC2 could be gated by two distinct means depending on the agonist, facilitating calcium- or sodium-dominant ion fluxes that result in distinct consequences[75,156]. It is now appreciated that the TPCs constitute highly context-dependent signalling mediators, either triggering global calcium-release and downstream signalling pathways upon NAADP binding, or releasing much smaller amounts of calcium locally upon $PI(3,5)P_2$ binding and favouring other signalling pathways.

5.2.2.1 The voltage-sensitive two-pore channel TPC1

The mammalian TPC1 channel was first described by Ishibashi, Suzuki, and Imai in 2000, being cloned from rat kidney cells. At the time, the authors noted its similarity to voltage-gated sodium and calcium channels, a parallel which would only become more relevant in the years to come[138]. The next few years largely focused on the role of TPCs in plants, until the 2009 breakthrough in mammalian TPC biology came. In 2009, Braliou *et al*. described how TPC1 expression mediates the NAADP response upon its microinjection through a whole-cell calcium imaging approach, and used shRNAs against TPC1 or pore-dead TPC1 overexpression ($TPC1^{L273P}$) to abrogate NAADP-induced calcium signals[145]. TPCs would subsequently garner substantial research interest, and descriptions soon followed about how TPC1 constitutes a voltage-dependent endosomal ion channel[157,158], regulated by the luminal pH[158], calcium[159,160], and cytosolic ATP/mTORC1[148]. The voltage-dependent activity of TPC1 was rationalized by She *et al*. in 2018, who described the second-domain transmembrane helix (IIS4) voltage-sensing domain (VSD) to confer voltage sensitivity. Using cryo-EM, the authors showed how membrane hyperpolarization causes an arginine (R540) to slide into the gating-charge transfer centre, where R540 halts and forces the pore shut[161]. A similar mechanism for voltage-dependence does in contrast not occur in TPC2, which encodes an isoleucine at the equivalent position. When mutated into an arginine however (I551R), the substitution renders TPC2 voltage-sensitive[162].

Functionally, Cang *et al*. reasoned that the high voltage-dependent activity of TPC1 can drive endosomal acidification through releasing cations, allowing the v-type ATPase to more efficiently pump in protons[158]. Pitt *et al*. complemented these findings through single-channel recordings, showing cytosolic calcium and NAADP to activate the channel, but also demonstrating proton permeability – The latter finding complicating interpretations of TPC1 function on endosomal acidification[159]. Indeed, both findings might hold true, as Cang *et al*. investigated the channel under $PI(3,5)P_2$-stimulated conditions[158], and Pitt *et al*. used NAADP to activate the channel[159]. Indeed, double TPC knockout lysosomes alkalinize upon starvation compared to wild-type controls (but not during basal/fed conditions)[149], supporting speculations that TPC1 can drive endosomal acidification. While single-TPC knockout cells do not show any change in the endolysosomal pH under basal conditions[163], similar investigations upon starvation are lacking. Beyond regulating endosomal acidification, endosomal transport also appears crucially regulated by TPC1, with the plasma membrane (PM)-to-Golgi trafficking of cholera toxin (CTx) being mediated by TPC1[163,164]. Accordingly,

genetic ablation of TPC1 impairs bacterial toxin trafficking and prevents toxin-induced cell death[164]. Similarly, TPC1 is required for the endosomal transport and infectivity of Ebola virus[165] and Middle East Respiratory Syndrome-Coronavirus (MERS-CoV)[62,166,167]. This function is likely mediated by the channel releasing cations that promote endosomal fusion. Indeed, the channel itself associates with numerous SNAP receptor (SNARE) proteins and Rab GTPases that mediate endosomal traffic[151,164,168], although an interacting, calcium-dependent SNARE protein has not yet been identified. The field of TPC-mediated endosomal trafficking however remains a young one, and hopefully the intricacies of these trafficking events will be revealed soon.

5.2.2.2 Physiology and Pathophysiology of the Controversial TPC2

Mammalian cells utilize three principal second messengers for intracellular calcium release: Inositol triphosphate (IP3), cyclic ADP ribose (cADPR), and nicotinic acid-adenine dinucleotide phosphate (NAADP). The mechanisms underlying IP3- and cADPR-mediated calcium signalling preceded the discovery of NAADP and its receptor, with the IP3 receptor (IP3R) being discovered in 1988[169], and the cADPR receptor better known as the ryanodine receptor (RyR) being discovered in 1991[170]. Both IP3R and RyR are situated on the endoplasmic reticulum (ER), propagating global calcium signals when stimulated. NAADP on the other hand liberates calcium from acidic stores[171–173], which in turn triggers calcium-induced calcium release (CICR) via the calcium-sensitive RyR and IP3R[174]. Calcraft *et al*. and Zong *et al*. later discovered TPC2 to constitute the lysosomal NAADP receptor, a lysosome-resident ion channel[144,146]. Upon generating a *Tpcn2* knock-out mouse, the authors showed that the NAADP-dependent calcium oscillations previously described in pancreatic β-cells[175,176] were absent in cells from animals lacking TPC2[144]. A few years later however, Wang *et al*. used the endolysosomal patch-clamp technique to assess NAADP-responsive currents acting on TPC2 *in situ*, reporting that "surprisingly, no measurable NAADP-activated whole-endolysosomal current was seen". Instead, Wang *et al*. reported TPC2 to constitute a sodium-permeable channel activated by $PI(3,5)P_2$, speculating that the released sodium could act in a fusogenic manner to promote membrane trafficking[148]. Initial suspicions that the difficulties measuring NAADP-evoked currents on lysosomal preparates could arise from an indirect binding of NAADP to the channels[150,177] were confirmed in 2021, as three groups independently characterized JPT2[152,153] and LSM12[154] to constitute accessory NAADP binding proteins (NAADP-BP), TPC2-interacting proteins required for NAADP-induced calcium release. Curiously, neither of these proteins had been previously identified to interact with either TPC protein[151,168,178], raising the possibility that the NAADP:NAADP-BP:TPC complex forms transiently in the presence of NAADP. Such a mode of action would explain why NAADP responsiveness is not seen on isolated lysosomal membranes, as the NAADP-BP would be lost during the isolation process. $PI(3,5)P_2$ sensitivity on the other hand appears an intrinsic property of the channel, not lost upon endolysosomal isolation[148,149,162,179]. Resultantly, the following years would see TPC2 function being explored either on the side of NAADP-mediated calcium release, or focusing on the preferential sodium release accompanying $PI(3,5)P_2$ activation.

TPC2 in the brain has primarily been recognized by virtue of its implications in NAADP signalling. Pandey *et al*. first discovered that neuronal glutamatergic signalling depends on NAADP[180]. This discovery would put TPC2 into the context of neuronal excitatory signal transduction, with glutamate marking the principal excitatory neurotransmitter in the central nervous system. These findings were later confirmed by Foster *et al*., showing that glutamate signals through NAADP and TPCs to release calcium from acidic stores, triggering CICR and promoting long-term potentiation (LTP)[181]. Beyond its roles in synaptic transmission, TPCs also appear to have a role in glutamate-induced autophagy of glial cells. Here, glutamate triggers an increase in the number of autophagosomes, which is prevented upon addition of the NAADP antagonist Ned19, overexpression of dominant negative TPC2 ($TPC2^{L265P}$), or knock-down of TPC2[182,183]. Garcia-Rua *et al*. similarly observed that TPC2 in cardiomyocytes is upregulated during energy depletion to accommodate to starvation conditions and accelerate the autophagic flux[184]. Other groups have countered this claim, arguing that NAADP-induced TPC2 activation alkalinizes the lysosomal pH, preventing autophagosome/lysosome fusion and arresting autophagy[185–188]. Evidently, the topic of TPC2 involvement in autophagy is contentious and the debate is far from settled, but it should be appreciated that the channel activity appears highly context-dependent, which could underlie the seemingly contradicting results.

The function of TPC2 in endolysosomal transport appears of particular interest, as the channel directly interacts with numerous SNARE proteins[151,168,178,189]. The SNAP Receptors (SNAREs) represent a large protein family forming crucial mediators of regulated membrane fusion[190]. The interaction between SNAREs and the calcium-permeable TPC2 is largely more than coincidental, as calcium release triggers SNAREs to facilitate membrane fusion. Accordingly, TPC2 knock-out mice exhibit endosomal trafficking defects, marked by an endosomal accumulation of cholesterol, EGF, and LDL[178]. Similarly, TPC2 is indispensable for viral trafficking through the endosomal compartments, with its blockade resulting in endosomal accumulation and reduced infectivity of Ebola virus[165], Middle East Respiratory Syndrome-Coronavirus (MERS-CoV)[166,167], and Severe Acute Respiratory Syndrome-Coronavirus 2 (SARS-CoV-2)[62,191,192]. Beyond endosomal trafficking, TPC2 mediates endolysosomal exocytosis, regulating the release of cytolytic granules from cytotoxic T-lymphocytes (CTLs)[193,194], glucagon secretion from pancreatic α-cells[195], and of insulin from pancreatic β-cells[176,196,197], although the latter is contested by other groups[148,198]. Here, the signalling context again probably governs the differing outcomes: Gerndt *et al*. recently demonstrated that TPC2 stimulation with a $PI(3,5)P_2$-mimetic agonist facilitates lysosomal exocytosis, while NAADP-mimicry rather arrests endosomal movement, with no effect on exocytosis[75]. It therefore appears critical to discriminate between $PI(3,5)P_2$- and NAADP-like modes of action when addressing the functional relevance of TPC2 in different signalling pathways.

Beyond its aforementioned implications in neuronal and glial physiology, TPC2 has come under scrutiny in the field of neurodegenerative diseases. Hockey *et al*. first reasoned that due to previous reports of aberrant endolysosomal morphology in Parkinson's disease (PD)[50], endolysosomal ion channels regulating such processes could underlie the observed pathology[199]. Using fibroblasts isolated from healthy and PD donors, the authors found that PD fibroblasts show an expansion of the lysosomal compartment. Treatment of the cells with the NAADP antagonist Ned19, or genetic knock-down of TPC2, ameliorated this lysosomal expansion[199]. Similarly, overexpression of dominant-negative TPC2 or NAADP antagonism prevents the autophagic induction mediated by the PD-associated LRRK2[200,201], indicating that TPC2 might be a driving factor in PD pathology. Several open questions however remain to this topic, perhaps most importantly, how the situation would look in neural cells. While fibroblasts certainly appear a relevant cell-model for investigating PD[202], it goes without saying that similar investigations in disease-relevant neural cells would be tremendously interesting. In particular, the effect of TPC2 on PD-associated α-synuclein aggregation and inclusion bodies – Lewy bodies – would prove vital in determining its effect on the principal PD hallmarks.

5.3 The Lysosomal Storage Diseases

The lysosomal storage diseases (LSDs) comprise a group of over 70 inherited metabolic disorders characterized by lysosomal dysfunction, often (but not always) caused defective lysosomal proteins. While fortunately being rare, their clinical outcome is severe and typically manifest in childhood, thus significantly impacting the quality of life of the affected children and relatives. The LSDs largely have a progressive neurodegenerative phenotype, leading to loss of independence and necessity of care as the disease develops. While significant advancements have been made to develop new therapies, particularly through enzyme replacement therapy (ERT), effective small-molecule treatment strategies remain elusive[56,65]. While proving more indirect means of treating disease than correcting the defective gene or replacing a missing enzyme, small molecule treatments could hopefully ameliorate systemic disease phenotypes and prove valuable stand-alone therapies or support gene/enzyme replacement therapies. Therapeutic efforts aimed at tackling Niemann Pick Disease type C1 (NPC1) illustrate this: AAV9-based gene delivery has recently been shown to deliver functional NPC1 genes to both the brain and visceral organs, both upon intracerebral and intracardiac injection[203–206]. Intriguingly, intracerebral NPC1 delivery shifted the humane end-points from neurological dysfunction towards peripheral organ failure[205]. The authors furthermore speculated that incomplete transduction could leave untransduced neurons vulnerable, and this partial neurodegeneration proving sufficient to trigger neuroinflammation and gliosis[205]. It therefore appears feasible that a combination of gene/enzyme replacement and small molecules restoring function to disease pathways will prove the optimal treatment.

5.3.1 Mucolipidosis Type IV

Mucolipidosis type IV (MLIV) was first described by Berman *et al*. at the Hadassah University in Jerusalem, Israel. Berman *et al*. described in 1974 a new systemic storage disease, presented by an infant of European Jewish origin. The mother herself noticed that her child developed bilateral corneal cloudiness at the age of six weeks. At 2.5 months of age, the child was examined at an outpatient clinic: Both corneas were indeed opaque, but beyond this, no abnormalities were apparent, and neurological function appeared normal. At eight months of age however, mild motor retardation was observed for the first time. Biopsies revealed an accumulation of cytoplasmic granules and large fat droplets in hepatocytes. By electron microscopy, the authors found abnormal lysosomal organelles and heterogeneous cytoplasmic inclusion bodies. Kupffer cells appeared as vacuolated foam cells, some vacuoles filled with fibrillogranular material or lamellar structures. Lamellar inclusion bodies were also observed in conjunctival epithelial cells and perinuclear regions of skin fibroblasts. Based on the congenital corneal clouding and the cells containing multilamellar inclusion bodies and vacuoles filled with fibrillogranular material, the authors termed the disease mucolipidoses type IV. Still, the authors pointed out, the disease does differ from other forms of mucolipidosis – Mucolipidosis type I (now termed sialidosis) manifests as a neurodegenerative disease already in infanthood, mucolipidosis type II causes psychomotor retardation early in life, and mucolipidosis type III is comparatively milder, with corneal opacities first manifesting around three years of age[209]. The typical progression of MLIV is summarized in Figure 4.

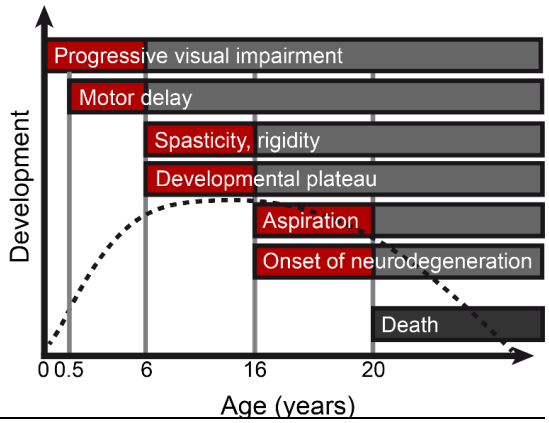

Figure 4: Progression of Mucolipidosis type IV

This figure is based on data presented by the indicated articles[94,207,208]. Onset is marked by red boxes, and continued disturbances by grey boxes. The dashed line displays delayed development until 6 years of age, reaching a plateau at the level of a 1-year-old.

5.3.2 Neuronal Ceroid Lipofuscinoses

The neuronal ceroid lipofuscinoses (NCLs) comprise a group of hereditary, progressive neurodegenerative diseases, of which most manifest in infancy or childhood[211,212]. The first case of NCL was described in 1826 by the Norwegian physician Stengel, who observed "highly notable illnesses" in four siblings that appear particularly interesting "physiologically and pathophysiologically"[213]. Batten (1903)[214], Vogt (1905)[215], and Spielmeyer (1905)[216] noted a similar disorder a century later, characterized by cerebral degeneration accompanied by blindness. This form would later be known as juvenile-onset NCL, or Batten's disease[217]. The following years, similar descriptions of late-infantile onset[218,219] and adult onset[220] forms of the disease surfaced, the latter adult-onset form not encompassing vision loss. Half a century later, a infantile onset disease variant was described[221,222]. Clearly, the NCLs encompassed a heterogeneous group of diseases which could manifest at any point of life[217]. The reasons for this heterogeneity would later be partially revealed by the Human Genome Mapping Project and its associated technologies, leading to the discovery of the (to date) 13 genes leading to different forms of NCL disease[223,224].

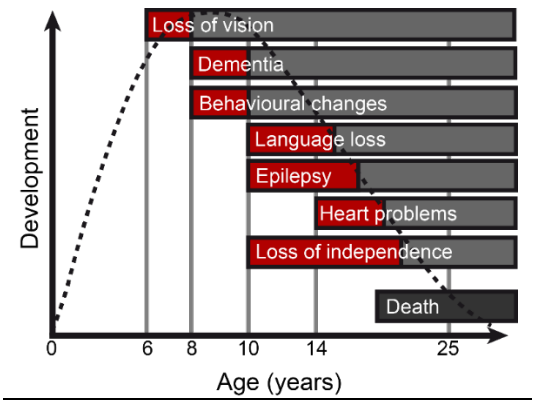

Figure 5: Progression of Juvenile NCL
The figure is based on data presented by the NCL Stiftung[210]. Onset is marked by red boxes, continued symptoms by grey boxes. The dashed line displays how children normally develop until 8 years of age, then deteriorate as symptoms start to manifest.

The most common form of NCL is caused by defects in the CLN3 gene, and underlies the classic juvenile NCL (JNCL) disease marked by progressive dementia and blindness (Figure 5)[226]. JNCL manifests between the age of 5 and 10 years, where affected children lose their vision. In the second to third decade, dementia and seizures ensue, with heart problems occurring following 14 years of age (Fig. CLN3-P)[210,226–230]. The cause of death varies, but appears to most prevalently result from epilepsy, infection, or congestive heart failure[229]. Nonetheless, the heterogeneity of JNCL disease itself should be stressed. Recently, an Iraqi man was described who experienced visual loss from the age of 12, and motor problems starting around the age of 30. The man was later found to homozygously carry the $CLN3^{R405W}$ mutation[231], which has previously been linked to development of blindness and retinitis pigmentosa[232,233]. This is not an isolated case associated with a single mutation, as another similar case has also been reported for a man carrying two missense mutations ($CLN3^{H315Q.fs*67/\Delta A349.L350}$)[234].

5.3.3 Niemann Pick C1 Disease

First described by Niemann in 1914[235] and later by Pick in 1926[236], essential lipoid histiocytosis (later termed Niemann-Pick disease) has been recognized for nearly a decade[237]. While initially being confused with the similar Gaucher's disease, Niemann-Pick disease showed prominent phosphatide storage in the spleen, contrasting the kerasin storage normally observed in Gaucher's disease[237,238]. Niemann-Pick Disease was later separated into four subgroups based on the age of onset, clinical presentation, and the level of sphingomyelin storage.[225,239] For example, Niemann-Pick Disease Type A (NPA) causes severe deterioration of the central nervous system (CNS), alongside visceral and cerebral sphingomyelin storage. Niemann Pick Disease Type C (NPC) on the other hand causes sub-acute nervous system involvement, with a comparatively moderate course and a less pronounced degree of visceral storage pathology[225,240]. Importantly, NPA shows decreased sphingomyelinase activity, contrasting NPC1 where sphingomyelinase activity is normal[225,241].

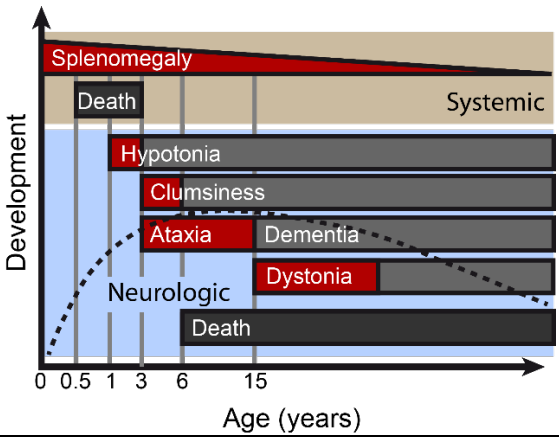

Figure 6: Progression of NPC1
The figure is based on data presented by Vanier *et al.*[225]. Onset is marked by red boxes, continued disturbances by grey boxes. The dashed line simplifies the developmental course, showing slowed development before deterioration as symptoms manifest.

Despite the stratification into four families, the clinical presentation of NPC1 is heterogeneous. The age of onset ranges from the perinatal period until adulthood, and the lifespan can vary between a few days until beyond 60 years of age. Most commonly, NPC1 presents as a progressive and fatal neurological disease. If present, systemic phenotypes precede the neurological disease. The systemic disease predominantly manifests as hepatosplenomegaly and problems with swallowing, while the neurological disorders typically include cerebellar ataxia, dysarthria, dysphagia, and progressive dementia, and occasionally seizures (Figure 6)[225].

5.3.4 The Molecular Basis of Lysosomal Storage Diseases

As the name suggests, lysosomal storage diseases result in the aberrant accumulation of lysosomal storage material. In some cases, the basis for such storage accumulation is rather direct: NPA for example is caused by an enzymatic defect of acid sphingomyelinase, which catalyses the break-down of sphingomyelin to ceramide. Resultantly, sphingomyelin accumulates, directly blocking the lysosomal ion channel TRPML1 and its associated downstream pathways[71]. Similar manifestations can be observed in NPC1 disease, which is caused by loss-of-function mutations in the lysosomal cholesterol exporter NPC1[242,243]. Despite the acid sphingomyelinase activity being preserved in NPC1 cells, the accumulating cholesterol is accompanied by sphingomyelin storage[244], which blocks TRPML1 and downstream pathways[71]. How impaired cholesterol transport can lead to sphingomyelin storage remains enigmatic. One theory is that cholesterol accumulation can lead to downstream trafficking defects, and mislocalisation of sphingolipids from the Golgi apparatus to lysosomes, as evidenced by impaired trafficking of lactosylceramide in NPC1 cells[71,245]. Another possibility is that accumulating cholesterol interacts with sphingomyelin[246], which in turn could alter its availability to acid sphingomyelinase and extend its lifetime. In either case, the concomitant primary storage of cholesterol and secondary storage of sphingomyelin appears a prime driver for pathology in NPC1, leading to downstream blockade of TRPML1 and its maintenance of lysosomal homeostasis[71]. Furthermore, the aberrant lysosomal recruitment of the nutrient-sensing mTOR complex to membrane cholesterol rafts also likely contributes to autophagic defects observed in NPC1[247]. In MLIV, which is caused by defects in the lysosomal cation channel TRPML1, the connections between protein dysfunction and storage pathology are more elusive. It is clear that TRPML1 acts as a driver for lysosomal biogenesis[77,100,102,110], acidification[248], trafficking[111,117], autophagy[47,73,104,249–252], degradation[253,254], and lipid handling[61,255–257], suggesting that impaired channel activity would directly and diversely detriment lysosomal function. It appears that lysosomal Ca^{2+} efflux is a crucial component, for example recruiting Ca^{2+}-sensitive adapter proteins for lysosomal movement[111,117], or inducing autophagy upon Ca^{2+}-dependent activation of calcineurin and TFEB[72] and the calcium-sensitive kinase CaMKKβ[77]. Furthermore, the efflux of cations (as mediated by e.g. TRPML1) has been suggested to support lysosomal acidification by enhancing the lysosomal proton pump (v-type ATPase), essentially exchanging luminal cations (Na^+, Ca^{2+}) for protons[91] (Figure 7).

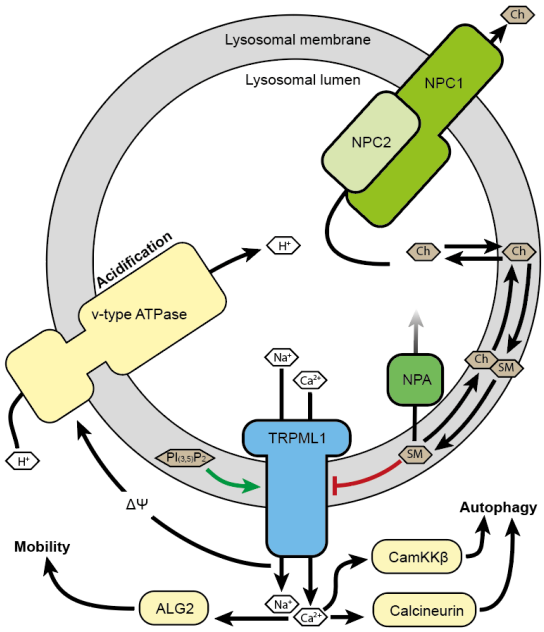

Figure 7: Molecular pathology in LSDs
Key drivers of lysosomal storage disease pathology are highlighted in the diagram. In NPC disease (NPC1 or NPC2), the lysosomal cholesterol (Ch) efflux machinery is dysfunctional, leading to Ch and sphingomyelin (SM) storage. In NPA, SM degradation is impaired. SM blocks TRPML1, the channel impaired in MLIV disease. Loss of TRPML1 disrupts its downstream signalling pathways, such as enhancement of the v-type ATPase and lysosomal acidification, ALG2 recruitment of the lysosomal motility machinery, and autophagic induction through the calcineurin and CamKIIβ.

6. AIMS OF THE THESIS

Aim 1: Develop and characterize endolysosomal channel modulators
We developed a selective agonist for TRPML2 (ML2-SA1) and identified its binding-site. We applied this compound to characterize the role of TRPML2 signalling in macrophages, demonstrating the channel to accelerate endosomal trafficking and secretion of the chemokine CCL2 (**Manuscript I**)[74]. We furthermore developed two classes of selective agonists for TPC2 mimicking its endogenous ligands $PI(3,5)P_2$ (TPC2-A1-P) and NAADP (TPC2-A1-N), and identified the binding site of TPC2-A1-P (**Manuscript II**)[75,156].

Aim 2: Identify cellular roles of mucolipins, TPCs, and CLN3
Having discovered TRPML2 to mediate chemokine secretion (**Manuscript I**)[74], we elaborated upon the mechanism underlying these effects. We found TRPML2 to uniquely sense membrane tension, unlike its TRPML1 and TRPML3 counterparts. This function appeared conferred by the phosphoinositide-binding pocket, resulting in channel activation upon membrane stretch. Loss of this sensitivity impaired endosomal trafficking, suggesting TRPML2 mechanosensitivity to be intricately linked to intracellular cargo transport (**Manuscript III**)[123,258]. We furthermore applied the novel TPC2 agonists to demonstrate how TPC2-A1-P and its smaller calcium release mediates lysosomal exocytosis, while the global calcium signals induced by TPC2-A1-N arrest lysosomal motility and cause luminal alkalinization (**Manuscript II**)[75]. We also demonstrate how CLN3 deficiency results in the accumulation of globosides (Gb), which can be stained for using fluorophore-labelled shigatoxin (**Manuscript V**)[259]. We finally generate new iPSC-based models lacking TRPML1 and CLN3 activity. We find neurons lacking TRPML1 to exhibit increased cathepsin B activity, while neurons lacking CLN3 exhibit decreased cathepsin B activity. We also observe an autophagic blockade in TRPML1- and CLN3-deficient cells, as well as lysosomal alkalinization (**Manuscript VI**).

Aim 3: Identify the role of endolysosomal channels in health and disease
Using our novel pharmacological tools, we demonstrate TRPML2 to be important for macrophage recruitment in response to noxious stimuli, rendering channel modulation potentially beneficial in immunological and infectious diseases (**Manuscript I**)[74]. Similarly, we identify how TPC2 agonists can prove beneficial in restoring lysosomal traffic through stimulating lysosomal exocytosis, which would likely prove beneficial in lysosomal storage diseases (LSDs) (**Manuscript II**)[75]. We however stress that caution should be taken upon TPC2 activation, as TPC2 polymorphisms altering channel function are widespread. Resultantly, TPC2-activating compounds would likely necessitate dose adjustment based on ancestry and/or genotype (**Manuscript IV**)[260].

Aim 4: Assess the efficacy of endolysosomal channel modulators in LSDs
Aiming to treat neurodegeneration upon intrinsically targeting neurons, activation of the macrophage/microglia-restricted TRPML2 channel would likely not prove efficient in neuron-based assays (**Manuscript I**)[74]. Therefore, we rather focused on the novel TPC2 agonist TPC2-A1-P identified in **Manuscript II** to restore function in lysosomal storage diseases due to its efficacy in promoting lysosomal exocytosis[75]. Unlike TRPML2, we found TPC2 to be expressed in a variety of central nervous system cell types. We found TPC2 activation to correct storage, autophagy, and trafficking defects in various patient fibroblasts. We next developed iPSC-based models for the lysosomal storage diseases mucolipidosis type IV and juvenile ceroid lipofuscinosis, and differentiated these into cortical neurons. We thereby found TPC2 activation to reduce the lysosomal cathepsin accumulation observed in MLIV neurons, reduce the pathogenic endosomal compartment expansion, and ameliorate ultrastructural abnormalities in the endolysosomal system (**Manuscript VI**).

7. Discussion

The material presented herein lays the foundation for pharmacological studies and interventions tackling endolysosomal dysfunction, with particular focus on disorders of endolysosomal trafficking and degradative pathways. Such disorders would most predominantly comprise the lysosomal storage diseases (LSDs), but the potential extent of the interventions go far beyond this. Cancers[51,52,55,261,262], infectious diseases[152,165–167,192,263–265], neurodegenerative[45–47,49,114,199] disorders and metabolic diseases[158,178,195,196] have all been shown to be affected by endolysosomal channel modulation, highlighting the possible impact endolysosomal cation channel modulation might have.

A major objective in developing new therapies is ensuring high potency at the target receptor, without interfering with unrelated biological pathways. Off-target effects can cause side effects and associated toxicity, which of course is undesirable for the patient. Initial descriptions of TRPML agonists featured compounds that activated all TRPML isoforms (TRPML1-TRPML3), of which each has distinct roles[61,70,71]. In effect, this would mean that a treatment with ML-SA1, aiming to activate TRPML1 to rescue lysosomal storage disease phenotypes[71], also would activate the counterparts TRPML2 and TRPML3, thereby activating the immune response[122]. Similarly, a therapy activating TRPML2 to boost the immune response would likely impact TRPML1 in different cell-types. We therefore developed a new TRPML2 agonist, ML2-SA1, which showed high on-target activity with negligible activity at its counterparts TRPML1 and TRPML3. Using molecular docking supported by mutagenesis, calcium imaging and endolysosomal patch-clamp, we showed that TRPML2-specific residues supported activation with ML2-SA1, with the mutation of these residues to the TRPML1/TRPML3 counterparts abolishing ML2-SA1 activity. Having developed a selective TRPML2 agonist, we demonstrated that the compound enhanced chemokine release from wild-type, but not TRPML2$^{-/-}$ macrophages. These findings marked the first description of a selective TRPML2 agonist, and highlighted how acute TRPML2 activation facilitates chemokine release[74].

While only unspecific agonists were available to investigate the function of TRPML channels, the TPC channels for long lacked membrane-permeable pharmacological tools to study their function. While the endogenous TPC agonists PI(3,5)P_2 and NAADP were to some extent successfully employed to investigate the channels' role[144,148,159,193,266], most studies relied on genetic perturbations to assess the physiological relevance of the TPCs[163,178,267,268]. The disagreements whether PI(3,5)P_2 or NAADP represented the endogenous TPC ligand did not help either, spurred on by difficulties recording NAADP-induced TPC currents from isolated lysosomes[144,148,269]. The discovery of membrane-permeable TPC agonists facilitating either PI(3,5)P_2- or NAADP-like ion fluxes should hopefully resolve this debate, indicating that the channel responds to either ligand. Upon performing a high-throughput screen for agonists activating TPC2, two distinct agonists were discovered: TPC2-A1-P and TPC2-A1-N. While TPC2-A1-P activated TPC2 with a high sodium > calcium permeability and resulted in lysosomal exocytosis, TPC2-A1-N facilitated higher calcium permeability, resulting in lysosomal alkalinization and arresting endolysosomal movement. Strikingly, the relative permeabilities mimicked those induced by PI(3,5)P_2 (for TPC2-A1-P) and NAADP (for TPC2-A1-N), suggesting that the agonists facilitated two different gating mechanisms. While providing new membrane-permeable tools for pharmacological investigations of TPC2, these findings also resolved a decade-long debate of how the TPC channels are activated[75,156].

Having developed novel agonists to acutely regulate endolysosomal ion channel function, we set out to investigate cellular processes regulated by the channels. Sun *et al*. previously described how TRPML2 is acutely upregulated in macrophages stimulated with lipopolysaccharide (LPS), and how this genetic upregulation is associated with chemokine release[122]. A few years later, we described how acute channel activation increases chemokine secretion from macrophages alongside descriptions of the first specific TRPML2 agonist[74], but still the mechanistic question was left unanswered. How does TRPML2 activity accelerate the release of chemokines? During electrophysiological measurements of TRPML2 activity, we discovered the channel to be activated by membrane stretch: Application of

hypotonic solutions leading to organellar swelling rapidly increased channel currents, while hypertonic solutions conversely blocked the channel. Measurements where we altered the patch pipette pressure confirmed our initial observations that TRPML2 could be mechanosensitive, leading us to investigate its related TRPML1 and TRPML3 counterparts. Intriguingly, neither TPRML1 nor TRPML3 responded to mechanic stimuli, despite their very similar architecture to TRPML2. Therefore, we hoped and reasoned, the TRPML2 mechanosensitivity might be governed by simple differences in the primary amino acid sequences. Considering that we were dealing with channel activation upon changes to the membrane tension, we further investigated the membrane-interacting, phosphoinositide binding domain of TPRML2. The endogenous ligand of TRPML2 is $PI(3,5)P_2$, thus we reasoned that changes in membrane curvature could affect the recruitment of $PI(3,5)P_2$, leading to channel activation. Upon comparing the TRPML phosphoinositide binding pockets, we found that one of the phosphoinositide-interacting arginines in TRPML1 and TPRML3 was substituted for a hydrophobic leucine in TRPML2. Marking the principal difference between the TRPML2 and TRPML1/3 $PI(3,5)P_2$ binding site, we mutated this leucine into an arginine (L314R), finding its mechanosensitivity to be abolished. This finding would prove the first identification of a single residue conferring direct mechanosensitivity to a TRP channel. We next assessed the functional relevance of this on endolysosomal trafficking using a transferrin trafficking assay. While the wild-type TRPML2 rapidly shuttled transferrin through the endolysosomal system, transferrin trafficking was much more delayed in cells encoding the mechanosensitive $TRPML2^{L314R}$ variant. Thus, we could demonstrate that the accelerated cargo trafficking mediated by TRPML2 relies on its mechanosensitivity[123,258].

Before employing the novel TPC modulator TPC2-A1-P for assessing rescue of lysosomal storage diseases, we observed a dramatic extent of polymorphisms in the human TPC2 gene. Such polymorphisms had already been described to confer increased conductivity through the channel pore ($TPC2^{M484L}$), or alleviate inhibition by the endogenous regulator mTORC1 ($TPC2^{G734E}$)[179], raising the possibility that the responsiveness to TPC2-based therapies might depend on an individual's TPC2 genotype. While mapping the different high-frequency TPC2 polymorphisms, we noticed three striking findings: Firstly, the wild-type TPC2 genotype nearly never occurred, being present primarily in native south Americans. Instead, we noticed that the $TPC2^{L564P}$ substitution predominated on a global scale, present in virtually all sequenced Caucasians, and more than 50% of all sequenced Asians, Africans, and Oceanians. Secondly, we noticed that additional polymorphisms nearly exclusively took place on the $TPC2^{L564P}$ background. This appeared of functional relevance, as the gain-of-function $TPC2^{M484L}$ mutation had no effect on the wild-type background, only conferring increased conductivity when present alongside $TPC2^{L564P}$. Our third major finding was that besides the previously characterized $TPC2^{M484L}$ and $TPC2^{G734E}$ genotypes, a set of other polymorphisms also occurred at a high frequency. The $TPC2^{K376R}$ showed roughly 30% prevalence in Europeans and Asians, while the $TPC2^{G387D}$ mutation occurs in roughly 20% of all sequenced Asians. Both of these mutations moderately increased the currents through TPC2, albeit not as dramatically as the $TPC2^{M484L}$ mutation[260]. These findings highlight that TPC2 activity is highly variable depending on the TPC2 genotype, and that treatments targeting TPC2 should be adjusted depending on the patient's genotype.

Having developed TPC2 agonists and mapped TPC2 responsiveness in various populations, we set out to apply the TPC2 agonists in lysosomal storage diseases (LSDs). We first assessed LSD pathology in patient fibroblasts, observing lipid trafficking defects in LSDs such as Niemann Pick type A (NPA), Niemann Pick type C1 (NPC1), and mucolipidosis type IV (MLIV). Supplementation of TPC2 alongside the TPC2 agonist was able to restore trafficking defects in NPC1 and MLIV cells, but not in NPA cells. We reasoned this might be due to NPC1 and MLIV encoding transmembrane proteins involved in membrane trafficking, while NPA is caused by an enzymatic defect (acid sphingomyelinase). TPC2 blockade on the other hand worsened the lipid trafficking defects, indicative that channel activation appears a feasible therapeutic strategy. Furthermore, we found TPC2 activation to reduce storage deficits in NPC1 and MLIV cells, marked by correction of cellular ultrastructure and a reduction in the lysosomal cholesterol content. Aiming to assess the potential of TPC2-mediated rescue in the most severely affected cells, we used CRISPR/Cas9 to generate new iPSC models[270,271] for MLIV and CLN3 Batten's disease/juvenile ceroid lipofuscinosis (JNCL). We next differentiated the iPSCs into cortical neurons[270] and assessed LSD pathology. While lipid trafficking and cholesterol assays proved not applicable to neurons, we confirmed previous reports of increased cathepsin activity in MLIV[253] and

decreased cathepsin activity in CLN3[34]. We also observed extensive endosomal expansion, and lysosomal alkalinization in MLIV and CLN3 neurons. We could furthermore see an accumulation of fingerprint inclusion bodies in the MLIV cells. Upon treating the cells with TPC2-A1-P, we reduced the cathepsin activity, reversed the endosomal expansion, and cleared fingerprint inclusion bodies from the cells, highlighting its potential to restore lysosomal homeostasis in LSDs.

8. BIBLIOGRAPHY

1. Scott, C. C., Vacca, F. & Gruenberg, J. Endosome maturation, transport and functions. *Semin. Cell Dev. Biol.* **31**, 2–10 (2014).

2. Scott, C. C. & Gruenberg, J. Ion flux and the function of endosomes and lysosomes: pH is just the start. *BioEssays* **33**, 103–110 (2010).

3. Di Palma, F. *et al.* Mutations in Mcoln3 associated with deafness and pigmentation defects in varitint-waddler (Va) mice. *Proc. Natl. Acad. Sci. U. S. A.* **99**, 14994–14999 (2002).

4. Grimm, C. *et al.* A helix-breaking mutation in TRPML3 leads to constitutive activity underlying deafness in the varitint-waddler mouse. *Proc. Natl. Acad. Sci. U. S. A.* **104**, 19583–19588 (2007).

5. Kim, H. J., Soyombo, A. A., Tjon-Kon-Sang, S., So, I. & Muallem, S. The Ca2+ channel TRPML3 regulates membrane trafficking and autophagy. *Traffic* **10**, 1157–1167 (2009).

6. Woodman, P. G. Biogenesis of the sorting endosome: The role of Rab5. *Traffic* **1**, 695–701 (2000).

7. Dunn, K. W. & Maxfield, F. R. Delivery of ligands from sorting endosomes to late endosomes occurs by maturation of sorting endosomes. *J. Cell Biol.* **117**, 301–310 (1992).

8. Rink, J., Ghigo, E., Kalaidzidis, Y. & Zerial, M. Rab conversion as a mechanism of progression from early to late endosomes. *Cell* **122**, 735–749 (2005).

9. Lin, S. X., Gundersen, G. G. & Maxfield, F. R. Export from pericentriolar endocytic recycling compartment to cell surface depends on stable, detyrosinated (Glu) microtubules and kinesin. *Mol. Biol. Cell* **13**, 96–109 (2002).

10. Hopkins, C. R., Gibson, A., Shipman, M. & Miller, K. Movement of internalized ligand-receptor complexes along a continuous endosomal reticulum. *Nature* **346**, 335–339 (1990).

11. Goldenring, J. R. Recycling endosomes. *Curr. Opin. Cell Biol.* **35**, 117–122 (2015).

12. Maxfield, F. R. & McGraw, T. E. Endocytic recycling. *Nat. Rev. Mol. Cell Biol.* **5**, 121–132 (2004).

13. Lindsay, A. J. & McCaffrey, M. W. Rab11-FIP2 functions in transferrin recycling and associates with endosomal membranes via its COOH-terminal domain. *J. Biol. Chem.* **277**, 27193–27199 (2002).

14. Hales, C. M., Vaerman, J. P. & Goldenring, J. R. Rab11 family interacting protein 2 associates with myosin Vb and regulates plasma membrane recycling. *J. Biol. Chem.* **277**, 50415–50421 (2002).

15. Lapierre, L. A. & Goldenring, J. R. Interactions of myosin Vb with Rab11 family members and cargoes traversing the plasma membrane recycling system. *Methods Enzymol.* **403**, 715–723 (2005).

16. Kelly, E. E., Horgan, C. P. & McCaffrey, M. W. Rab11 proteins in health and disease. *Biochem. Soc. Trans.* **40**, 1360–1367 (2012).

17. Dumanchin, C. *et al.* Presenilins interact with Rab11, a small GTPase involved in the regulation of vesicular transport. *Hum. Mol. Genet.* **8**, 1263–1269 (1999).

18. Udayar, V. *et al.* A Paired RNAi and RabGAP overexpression screen identifies Rab11 as a regulator of β-amyloid production. *Cell Rep.* **5**, 1536–1551 (2013).

19. Stoorvogel, W., Strous, G. J., Geute, H. J., Oorschot, V. & Schwartzt, A. L. Late Endosomes Derive from Early Endosomes by Maturation. *Cell* **65**, 417–427 (1991).

20. Palade, G. E. A Small Particulate Component of the Cytoplasm. *J. Biophys. Biochem. Cytol.* **1**, 59–68 (1955).

21. Piper, R. C. & Katzmann, D. J. Biogenesis and Function of Multivesicular Bodies. *Annu. Rev. Cell Dev. Biol.* **23**, 519–547 (2007).

22. Matsuo, H. *et al.* Role of LBPA and Alix in Multivesicular Liposome Formation and Endosome Organization. *Science* **303**, 531–534 (2004).

23. MacDodnald, C. *et al.* A Family of Tetraspans Organizes Cargo for Sorting into Multivesicular Bodies. *Dev. Cell* **33**, 328–342 (2015).

24. Abrami, L., Lindsay, M., Parton, R. G., Leppla, S. H. & Goot, F. G. Van Der. Membrane insertion of anthrax protective antigen and cytoplasmic delivery of lethal factor occur at different stages of the endocytic pathway. *J. Cell Biol.* **166**, 645–651 (2004).

25. Le Blanc, I. *et al.* Endosome-to-cytosol transport of viral nucleocapsids. *Nat. Cell Biol.* **7**, 653–664 (2005).

26. Robert, M., Russell, G., Nickerson, D. P. & Odorizzi, G. Molecular mechanisms of late endosome morphology , identity and sorting. *Curr. Opin. Cell Biol.* **18**, 422–428 (2006).

27. Heijnen, B. H. F. G., Schiel, A. E., Fijnheer, R., Geuze, H. J. & Sixma, J. J. Activated Platelets Release Two Types of Membrane Vesicles: Microvesicles by Surface Shedding and Exosomes Derived from Exocytosis of Multivesicular Bodies and alpha-Granules. *Blood* **94**, 3791–3799 (1999).

28. Pegtel, D. M. & Gould, S. J. Exosomes. *Annu. Rev. Biochem.* **88**, 487–514 (2019).

29. Ghosh, P., Dahms, N. M. & Kornfeld, S. Mannose 6-Phosphate Receptors: New Twists in the Tale. *Nat. Mol. Cell Biol.* **4**, 202–212 (2003).

30. Braulke, T. & Bonifacino, J. S. Sorting of lysosomal proteins. *Biochim. Biophys. Acta* **1793**, 605–614 (2009).

31. Mamo, A., Jules, F., Dumaresq-Doiron, K., Costantino, S. & Lefrancois, S. The Role of Ceroid Lipofuscinosis Neuronal Protein 5 (CLN5) in Endosomal Sorting. *Mol. Cell. Biol.* **32**, 1855–1866 (2012).

32. Yasa, S. *et al.* CLN3 regulates endosomal function by modulating Rab7A–effector interactions. *J. Cell Sci.* **133**, jcs234047 (2020).

33. Fossale, E. *et al.* Membrane trafficking and mitochondrial abnormalities precede subunit c deposition in a cerebellar cell model of juvenile neuronal ceroid lipofuscinosis. *BMC Neurosci.* **5**, 57 (2004).

34. Metcalf, D. J., Calvi, A. A., Seaman, M. N. J., Mitchison, H. M. & Cutler, D. F. Loss of the batten disease gene CLN3 prevents exit from the TGN of the mannose 6-phosphate receptor. *Traffic* **9**, 1905–1914 (2008).

35. de Duve, C., Pressman, B. C., Gianetto, R., Wattiaux, R. & Appelmans, F. Tissue Fractionation Studies. *Biochem. J.* **60**, 604–617 (1955).

36. de Duve, C. & Wattiaux, R. Functions of Lysosomes. *Annu. Rev. Physiol.* **28**, 435–492 (1966).

37. Chen, C.-C. *et al.* Patch-clamp technique to characterize ion channels in enlarged individual endolysosomes. *Nat. Protoc.* **12**, 1639–1658 (2017).

38. Zhu, H. *et al.* Metabolic profiling of single enlarged lysosomes. *Nat. Methods* **18**, 788–798 (2021).

39. Modi, S. *et al.* A DNA nanomachine that maps spatial and temporal pH changes inside living cells. *Nat. Nanotechnol.* **4**, 325–330 (2009).

40. Narayanaswamy, N. *et al.* A pH-correctable, DNA-based fluorescent reporter for organellar calcium. *Nat. Methods* **16**, 95–102 (2019).

41. Leung, K. H., Chakraborty, K., Saminathan, A. & Krishnan, Y. A DNA nanomachine chemically resolves lysosomes in live cells. *Nat. Nanotechnol.* **14**, 176–183 (2019).

42. Saminathan, A. *et al.* A DNA-based voltmeter for organelles. *Nat. Nanotechnol.* **16**, 96–103 (2021).

43. Chakraborty, K., Leung, K. H. & Krishnan, Y. High lumenal chloride in the lysosome is critical for lysosome function. *Elife* **6**, e28862 (2017).

44. Fairn, G. D. & Grinstein, S. How nascent phagosomes mature to become phagolysosomes. *Trends Immunol.* **33**, 397–405 (2012).

45. Lloyd-Evans, E. Acidic Ca2+ Stores in Neurodegeneration. *Messenger* **5**, 37–55 (2016).

46. Lee, J.-H. *et al.* Presenilin 1 Maintains Lysosomal Ca2+ Homeostasis via TRPML1 by Regulating vATPase-Mediated Lysosome Acidification. *Cell Rep.* **12**, 1430–1444 (2015).

47. Zhang, L. *et al.* TRPML1 Participates in the Progression of Alzheimer's Disease by Regulating the PPARγ/AMPK/Mtor Signalling Pathway. *Cell. Physiol. Biochem.* **43**, 2446–2456 (2017).

48. van Veen, S. *et al.* ATP13A2 deficiency disrupts lysosomal polyamine export. *Nature* **578**, 419–424 (2020).

49. Kilpatrick, B. S. Connecting Ca2+ and Lysosomes to Parkinson Disease. *Messenger* **5**, 76–86 (2017).

50. Tofaris, G. K. Lysosome-dependent pathways as a unifying theme in Parkinson's disease. *Mov. Disord.* **27**, 1364–1369 (2012).

51. D'Amore, A. *et al.* Loss of two-pore channel 2 (TPC2) expression increases the metastatic traits of melanoma cells by a mechanism involving the hippo signalling pathway and store-operated calcium entry. *Cancers (Basel).* **12**, 1–18 (2020).

52. Grimm, C., Bartel, K., Vollmar, A. M. & Biel, M. Endolysosomal cation channels and cancer—a link with great potential. *Pharmaceuticals* **11**, 4 (2018).

53. Xu, M. & Dong, X. P. Endolysosomal TRPMLs in cancer. *Biomolecules* **11**, 65 (2021).

54. Jha, A., Ahuja, M., Patel, S., Brailoiu, E. & Muallem, S. Convergent regulation of the lysosomal two-pore channel-2 by Mg2+, NAADP, PI(3,5)P2 and multiple protein kinases. *EMBO J.* **33**, 501–511 (2014).

55. Müller, M. *et al.* Gene editing and synthetically accessible inhibitors reveal role for TPC2 in HCC cell proliferation and tumor growth. *Cell Chem. Biol.* **28**, 1–13 (2021).

56. Platt, F. M., D'Azzo, A., Davidson, B. L., Neufeld, E. F. & Tifft, C. J. Lysosomal storage diseases. *Nat. Rev. Dis. Prim.* **4**, 27 (2018).

57. Shacka, J. J. & Roth, K. A. Cathepsin D Deficiency and NCL/Batten Disease: There's More to Death than Apoptosis. *Autophagy* **3**, 474–476 (2007).

58. Smith, K. R. *et al.* Cathepsin F mutations cause Type B Kufs disease, an adult-onset neuronal ceroid lipofuscinosis. *Hum. Mol. Genet.* **22**, 1417–1423 (2013).

59. Brunetti-Pierri, N. & Scaglia, F. GM1 gangliosidosis: Review of clinical, molecular, and therapeutic aspects. *Mol. Genet. Metab.* **94**, 391–396 (2008).

60. Sun, M. *et al.* Mucolipidosis type IV is caused by mutations in a gene encoding a novel transient receptor potential channel. *Hum. Mol. Genet.* **9**, 2471–2478 (2000).

61. Chen, C.-C. *et al.* A small molecule restores function to TRPML1 mutant isoforms responsible for mucolipidosis type IV. *Nat. Commun.* **5**, 4681–4691 (2014).

62. Grimm, C., Butz, E., Chen, C. C., Wahl-schott, C. & Biel, M. From mucolipidosis type IV to Ebola: TRPML and two-pore channels at the crossroads of endo-lysosomal trafficking and disease. *Cell Calcium* **67**, 148–155 (2017).

63. Platt, F. M. Emptying the stores: Lysosomal diseases and therapeutic strategies. *Nat. Rev. Drug Discov.* **17**, 133–150 (2018).

64. Bonam, S. R., Wang, F. & Muller, S. Lysosomes as a therapeutic target. *Nat. Rev. Drug Discov.* **18**, 923–948 (2019).

65. Sun, A. Lysosomal storage disease overview. *Ann. Transl. Med.* **6**, 476 (2018).

66. Schreij, A. M. A., Fon, E. A. & McPherson, P. S. Endocytic membrane trafficking and neurodegenerative disease. *Cell. Mol. Life Sci.* **73**, 1529–1545 (2016).

67. Parenti, G., Medina, D. L. & Ballabio, A. The rapidly evolving view of lysosomal storage diseases. *EMBO Mol. Med.* **13**, e12836 (2021).

68. Samie, M. A. & Xu, H. Lysosomal exocytosis and lipid storage disorders. *J. Lipid Res.* **55**, 995–1009 (2014).

69. Feng, X. & Yang, J. Lysosomal Calcium in Neurodegeneration. *Messenger* **5**, 56–66 (2016).

70. Grimm, C. *et al.* Small Molecule Activators of TRPML3. *Chem. Biol.* **17**, 135–148 (2010).

71. Shen, D. *et al.* Lipid Storage Disorders Block Lysosomal Trafficking By Inhibiting TRP Channel and Calcium Release. *Nat. Commun.* **3**, 731–751 (2012).

72. Medina, D. L. *et al.* Lysosomal calcium signalling regulates autophagy through calcineurin and TFEB. *Nat. Cell Biol* **17**, 288–299 (2015).

73. Medina, D. L. & Ballabio, A. Lysosomal calcium regulates autophagy. *Autophagy* **11**, 970–971 (2015).

74. Plesch, E. *et al.* Selective agonist of TRPML2 reveals direct role in chemokine release from innate immune cells. *Elife* **7**, e39720 (2018).

75. Gerndt, S. *et al.* Agonist-mediated switching of ion selectivity in TPC2 differentially promotes lysosomal function. *Elife* **9**, e54712 (2020).

76. Zou, J. *et al.* Reactivation of Lysosomal Ca2+ Efflux Rescues Abnormal Lysosomal Storage in FIG4-Deficient Cells. *J. Neurosci.* **35**, 6801–6812 (2015).

77. Scotto Rosato, A. *et al.* TRPML1 links lysosomal calcium to autophagosome biogenesis through the activation of the CaMKKb/VPS34 pathway. *Nat. Commun.* **10**, 5630 (2019).

78. Di Paola, S., Scotto-Rosato, A. & Medina, D. L. TRPML1: The Ca(2+)retaker of the lysosome. *Cell Calcium* **69**, 112–121 (2018).

79. Scotto-Rosato, A., Tang, R. & Grimm, C. Two-pore and TRPML cation channels: Regulators of phagocytosis, autophagy and lysosomal exocytosis. *Pharmacol. Ther.* **220**, 107713 (2021).

80. International Human Genome Sequencing Consortium. Initial sequencing and analysis of the human genome. *Nature* **409**, 860–921 (2001).

81. Terstappen, G. C., Schlüpen, C., Raggiaschi, R. & Gaviraghi, G. Target deconvolution strategies in drug discovery. *Nat. Rev. Drug Discov.* **6**, 891–903 (2007).

82. Overington, J. P., Al-Lazikani, B. & Hopkins, A. L. How many drug targets are there? *Nat. Rev. Drug Discov.* **5**, 993–996 (2006).

83. Zhang, X. *et al.* Agonist-specific voltage-dependent gating of lysosomal two-pore Na+ channels. *Elife* **8**, e51423 (2019).

84. Samie, M. *et al.* A TRP channel in the lysosome regulates large particle phagocytosis via focal exocytosis. *Dev. Cell* **26**, 511–524 (2013).

85. Zhang, X. *et al.* Rapamycin directly activates lysosomal mucolipin TRP channels independent of mTOR. *PLoS Biol.* **17**, 1–24 (2019).

86. Jaślan, D., Böck, J., Krogsaeter, E. & Grimm, C. Evolutionary aspects of TRPMLs and TPCs. *Int. J. Mol. Sci.* **21**, 4181 (2020).

87. Samie, M. A. *et al.* The tissue-specific expression of TRPML2 (MCOLN-2) gene is influenced

by the presence of TRPML1. *Pflugers Arch. Eur. J. Physiol.* **459**, 79–91 (2009).

88. Dong, X.-P. *et al.* PI(3,5)P2 controls membrane trafficking by direct activation of mucolipin Ca2+ release channels in the endolysosome. *Nat. Commun.* **1**, 38 (2010).

89. Fine, M., Schmiege, P. & Li, X. Structural basis for PtdInsP2-mediated human TRPML1 regulation. *Nat. Commun.* **9**, 4192 (2018).

90. Grimm, C., Hassan, S., Wahl-Schott, C. & Biel, M. Role of TRPML and Two-Pore Channels in Endolysosomal Cation Homeostasis. *J. Pharmacol. Exp. Ther.* **342**, 236–244 (2012).

91. Steinberg, B. E. *et al.* A cation counterflux supports lysosomal acidification. *J. Cell Biol.* **189**, 1171–1186 (2010).

92. Grimm, C. Endolysosomal Cation Channels as Therapeutic Targets - Pharmacology of TRPML Channels. *Messenger* **5**, 30–36 (2016).

93. Slaugenhaupt, S. The Molecular Basis of Mucolipidosis Type IV. *Curr. Mol. Med.* **2**, 445–450 (2002).

94. Altarescu, G. *et al.* The neurogenetics of mucolipidosis type IV. *Neurology* **59**, 306–313 (2002).

95. Bargal, R. *et al.* Mucolipidosis type IV: Novel MCOLN1 mutations in Jewish and Non-Jewish patients and the frequency of the disease in the Ashkenazi Jewish population. *Hum. Mutat.* **17**, 397–402 (2001).

96. LaPlante, J. M. *et al.* Identification and characterization of the single channel function of human mucolipin-1 implicated in mucolipidosis type IV, a disorder affecting the lysosomal pathway. *FEBS Lett.* **532**, 183–187 (2002).

97. LaPlante, J. M. *et al.* Functional links between mucolipin-1 and Ca2+-dependent membrane trafficking in mucolipidosis IV. *Biochem. Biophys. Res. Commun.* **322**, 1384–1391 (2004).

98. Dong, X. P. *et al.* Activating mutations of the TRPML1 channel revealed by proline-scanning mutagenesis. *J. Biol. Chem.* **284**, 32040–32052 (2009).

99. Dong, X.-P. *et al.* The type IV mucolipidosis-associated protein TRPML1 is an endolysosomal iron release channel. *Nat. Lett.* **455**, 992–996 (2008).

100. Settembre, C. *et al.* TFEB links autophagy to lysosomal biogenesis. *Science* **332**, 1429–1433 (2011).

101. Palmieri, M. *et al.* Characterization of the CLEAR network reveals an integrated control of cellular clearance pathways. *Hum. Mol. Genet.* **20**, 3852–3866 (2011).

102. Sardiello, M. *et al.* A Gene Network Regulating Lysosomal Biogenesis and Function. *Science* **325**, 473–478 (2009).

103. Roczniak-Ferguson, A. *et al.* The Transcription Factor TFEB Links mTORC1 Signaling to Transcriptional Control of Lysosomal Homeostasis. *Sci. Signal.* **5**, ra42 (2012).

104. Wang, W. *et al.* Up-regulation of lysosomal TRPML1 channels is essential for lysosomal adaptation to nutrient starvation. *Proc. Natl. Acad. Sci. U. S. A.* **112**, E1373–E1381 (2015).

105. Li, R. J. *et al.* Regulation of mTORC1 by lysosomal calcium and calmodulin. *Elife* **5**, e19360 (2016).

106. Sun, X. *et al.* A negative feedback regulation of MTORC1 activity by the lysosomal Ca2+ channel MCOLN1 (mucolipin 1) using a CALM (calmodulin)-dependent mechanism. *Autophagy* **14**, 38–52 (2018).

107. Onyenwoke, R. U. *et al.* The mucolipidosis IV Ca2+ channel TRPML1 (MCOLN1) is regulated by the TOR kinase. *Biochem. J.* **470**, 331–342 (2015).

108. Huang, P., Xu, M., Wu, Y., Rizvi Syeda, A. K. & Dong, X. P. Multiple facets of TRPML1 in

autophagy. *Cell Calcium* **88**, 102196 (2020).

109. LaPlante, J. M. *et al.* Lysosomal exocytosis is impaired in mucolipidosis type IV. *Mol. Genet. Metab.* **89**, 339–348 (2006).

110. Medina, D. L. *et al.* Transcriptional activation of lysosomal exocytosis promotes cellular clearance. *Dev. Cell* **21**, 421–430 (2011).

111. Li, X. *et al.* A molecular mechanism to regulate lysosome motility for lysosome positioning and tubulation. *Nat. Cell Biol.* **18**, 404–417 (2016).

112. Schiffmann, R. *et al.* Constitutive achlorhydria in mucolipidosis type IV. *Proc. Natl. Acad. Sci. U. S. A.* **95**, 1207–1212 (1998).

113. Sahoo, N. *et al.* Gastric Acid Secretion from Parietal Cells Is Mediated by a Ca2+ Efflux Channel in the Tubulovesicle. *Dev. Cell* **41**, 262–273 (2017).

114. Tsunemi, T. *et al.* Increased lysosomal exocytosis induced by lysosomal Ca2+ channel agonists protects human dopaminergic neurons from α-synuclein toxicity. *J. Neurosci.* **39**, 5760–5772 (2019).

115. Cheng, X. *et al.* The intracellular Ca2+ channel MCOLN1 is required for sarcolemma repair to prevent muscular dystrophy. *Nat. Med.* **20**, 1187–1192 (2014).

116. Yu, L. *et al.* Small-molecule activation of lysosomal TRP channels ameliorates Duchenne muscular dystrophy in mouse models. *Sci. Adv.* **6**, eaaz2736 (2020).

117. Vergarajauregui, S., Martina, J. A. & Puertollano, R. Identification of the Penta-EF-hand protein ALG-2 as a Ca2+-Dependent Interactor of Mucolipin-1. *J. Biol. Chem.* **284**, 36357–36366 (2009).

118. Song, Y., Dayalu, R., Matthews, S. A. & Scharenberg, A. M. TRPML cation channels regulate the specialized lysosomal compartment of vertebrate B-lymphocytes. *Eur. J. Cell Biol.* **85**, 1253–1264 (2006).

119. Venkatachalam, K., Hofmann, T. & Montell, C. Lysosomal localization of TRPML3 depends on TRPML2 and the mucolipidosis-associated protein TRPML1. *J. Biol. Chem.* **281**, 17517–17527 (2006).

120. Karacsonyi, C., San Miguel, A. & Puertollano, R. Mucolipin-2 Localizes to the Arf6-Associated Pathway and Regulates Recycling of GPI-APs. *Traffic* **8**, 1404–1414 (2007).

121. Lev, S. *et al.* Constitutive activity of the human TRPML2 channel induces cell degeneration. *J. Biol. Chem.* **285**, 2771–2782 (2010).

122. Sun, L., Hua, Y., Vergarajauregui, S., Diab, H. I. & Puertollano, R. Novel Role of TRPML2 in the Regulation of the Innate Immune Response. *J. Immunol.* **195**, 4922–4932 (2015).

123. Chen, C.-C. *et al.* TRPML2 is an osmo/mechanosensitive cation channel in endolysosomal organelles. *Sci. Adv.* **6**, eabb5064 (2020).

124. Grimm, C., Jörs, S., Guo, Z., Obukhov, A. G. & Heller, S. Constitutive activity of TRPML2 and TRPML3 channels versus activation by low extracellular sodium and small molecules. *J. Biol. Chem.* **287**, 22701–22708 (2012).

125. Sharif, O., Bolshakov, V. N., Raines, S., Newham, P. & Perkins, N. D. Transcriptional profiling of the LPS induced NF-κB response in macrophages. *BMC Immunol.* **8**, 1–17 (2007).

126. Mayle, K. M., Le, A. M. & Kamei, D. T. The Intracellular Trafficking Pathway of Transferrin. *Biochim. Biophys. Acta* **1820**, 264–281 (2012).

127. Spix, B., Chao, Y. K., Abrahamian, C., Chen, C. C. & Grimm, C. TRPML Cation Channels in Inflammation and Immunity. *Front. Immunol.* **11**, 225 (2020).

128. Cloudman, A. M. & Bunker Jr., L. E. The Varitint-Waddler Mouse. *J. Hered.* **36**, 259–263 (1945).

129. Lane, P. W. Two new mutations in linkage group XVI of the house mouse: Flaky tail and varitint-waddler-J. *J. Hered.* **63**, 135–140 (1972).

130. Deol, M. S. The Anomalies of the Labyrinth of the Mutants Varitint-Waddler, Shaker-2 and Jerker in the Mouse. *J. Genet.* **52**, 562–588 (1954).

131. Cable, J. & Steel, K. P. Combined cochleo-saccular and neuroepithelial abnormalities in the Varitint-waddler-J (VaJ) mouse. *Hear. Res.* **123**, 125–136 (1998).

132. Kim, H. J., Jackson, T. & Noben-Trauth, K. Genetic analyses of the mouse deafness mutations Varitint-Waddler (Va) and Jerker (Espnje). *J. Assoc. Res. Otolaryngol.* **4**, 83–90 (2002).

133. Zhou, X. *et al.* Cryo-EM structures of the human endolysosomal TRPML3 channel in three distinct states. *Nat. Struct. Mol. Biol.* **24**, 1146–1154 (2017).

134. Hirschi, M. *et al.* Cryo-electron microscopy structure of the lysosomal calcium-permeable channel TRPML3. *Nature* **550**, 411–414 (2017).

135. Martina, J. A., Lelouvier, B. & Puertollano, R. The calcium channel mucolipin-3 is a novel regulator of trafficking along the endosomal pathway. *Traffic* **10**, 1143–1156 (2009).

136. Choi, S. & Kim, H. J. The Ca2+ channel TRPML3 specifically interacts with the mammalian ATG8 homologue GATE16 to regulate autophagy. *Biochem. Biophys. Res. Commun.* **443**, 56–61 (2014).

137. Kim, S. W. *et al.* Palmitoylation controls trafficking of the intracellular Ca2+ channel MCOLN3/TRPML3 to regulate autophagy. *Autophagy* **15**, 327–340 (2019).

138. Ishibashi, K., Suzuki, M. & Imai, M. Molecular cloning of a novel form (two-repeat) protein related to voltage-gated sodium and calcium channels. *Biochem. Biophys. Res. Commun.* **270**, 370–376 (2000).

139. Brailoiu, E. *et al.* An ancestral deuterostome family of two-pore channels mediates nicotinic acid adenine dinucleotide phosphate-dependent calcium release from acidic organelles. *J. Biol. Chem.* **285**, 2897–2901 (2010).

140. Xu, H. & Ren, D. Lysosomal Physiology. *Annu. Rev. Physiol.* **77**, 57–80 (2015).

141. Hedrich, R. & Neher, E. Cytoplasmic calcium regulates voltage-dependent ion channels in plant vacuoles. *Nature* **329**, 833–836 (1987).

142. Anderson, P. A. V. & Greenberg, R. M. Phylogeny of ion channels: Clues to structure and function. *Comp. Biochem. Physiol. Part B* **129**, 17–28 (2001).

143. Peiter, E. *et al.* The vacuolar Ca2+-activated channel TPC1 regulates germination and stomatal movement. *Nature* **434**, 404–408 (2005).

144. Calcraft, P. J. *et al.* NAADP mobilizes calcium from acidic organelles through two-pore channels. *Nature* **459**, 596–600 (2009).

145. Brailoiu, E. *et al.* Essential requirement for two-pore channel 1 in NAADP-mediated calcium signaling. *J. Cell Biol.* **186**, 201–209 (2009).

146. Zong, X. *et al.* The two-pore channel TPCN2 mediates NAADP-dependent Ca2+-release from lysosomal stores. *Pflugers Arch. Eur. J. Physiol.* **458**, 891–899 (2009).

147. Ruas, M. *et al.* Expression of Ca2+-permeable two-pore channels rescues NAADP signalling in TPC-deficient cells. *EMBO J.* **34**, 1743–1758 (2015).

148. Wang, X. *et al.* TPC Proteins Are Phosphoinositide-activated Sodium-selective Ion Channels in Endosomes and Lysosomes. *Cell* **151**, 372–383 (2012).

149. Cang, C. *et al.* mTOR Regulates Lysosomal ATP-Sensitive Two-Pore Na+ Channels to Adapt to Metabolic State. *Cell* **152**, 778–790 (2013).

150. Lin-Moshier, Y. *et al.* Photoaffinity labeling of nicotinic acid adenine dinucleotide phosphate

(NAADP) targets in mammalian cells. *J. Biol. Chem.* **287**, 2296–2307 (2012).

151. Lin-Moshier, Y. *et al.* The Two-pore channel (TPC) interactome unmasks isoform-specific roles for TPCs in endolysosomal morphology and cell pigmentation. *Proc. Natl. Acad. Sci. U. S. A.* **111**, 13087–13092 (2014).

152. Gunaratne, G. S. *et al.* Essential requirement for JPT2 in NAADP-evoked Ca2+ signaling. *Sci. Signal.* **14**, eabd5605 (2021).

153. Roggenkamp, H. G. *et al.* HN1L/JPT2 : A signaling protein that connects NAADP generation to Ca2+ microdomain formation. *Sci. Signal.* **14**, eabd5647 (2021).

154. Zhang, J., Guan, X., Shah, K. & Yan, J. Lsm12 is an NAADP receptor and a two-pore channel regulatory protein required for calcium mobilization from acidic organelles. *Nat. Commun.* **21**, 4739 (2021).

155. Krogsaeter, E., Tang, R. & Grimm, C. JPT2: The missing link between intracellular Ca2+ release channels and NAADP? *Cell Calcium* **97**, 102405 (2021).

156. Gerndt, S., Krogsaeter, E., Patel, S., Bracher, F. & Grimm, C. Discovery of lipophilic two-pore channel agonists. *FEBS J.* **287**, 5284–5293 (2020).

157. Rybalchenko, V. *et al.* Membrane potential regulates Nicotinic Acid Adenine Dinucleotide Phosphate (NAADP) dependence of the pH- and Ca2+-sensitive organellar two-pore channel TPC1. *J. Biol. Chem.* **287**, 20407–20416 (2012).

158. Cang, C., Bekele, B. & Ren, D. The voltage-gated sodium channel TPC1 confers endolysosomal excitability. *Nat. Chem. Biol.* **10**, 463–469 (2014).

159. Pitt, S. J., Lam, A. K. M., Rietdorf, K., Galione, A. & Sitsapesan, R. Reconstituted Human TPC1 is a proton-permeable ion channel and is activated by NAADP or Ca2+. *Sci. Signal.* **7**, ra46 (2014).

160. Lagostena, L., Margherita, F., Pusch, M. & Carpaneto, A. The human two-pore channel 1 is modulated by cytosolic and luminal calcium. *Sci. Rep.* **7**, 43900 (2017).

161. She, J. *et al.* Structural insights into the voltage and phospholipid activation of the mammalian TPC1 channel. *Nature* **556**, 130–134 (2018).

162. She, J. *et al.* Structural mechanisms of phospholipid activation of the human TPC2 channel. *Elife* **8**, e45222 (2019).

163. Ruas, M. *et al.* TPC1 Has Two Variant Isoforms, and Their Removal Has Different Effects on Endo-Lysosomal Functions Compared to Loss of TPC2. *Mol. Cell. Biol.* **34**, 3981–3992 (2014).

164. Castonguay, J. *et al.* The two-pore channel TPC1 is required for efficient protein processing through early and recycling endosomes. *Sci. Rep.* **7**, 10038 (2017).

165. Sakurai, Y. *et al.* Two-pore channels control Ebola virus host cell entry and are drug targets for disease treatment. *Science* **347**, 995–998 (2015).

166. Gunaratne, G. S., Yang, Y., Li, F., Walseth, T. F. & Marchant, J. S. NAADP-dependent Ca2+ signaling regulates Middle East Respiratory Syndrome-Coronavirus pseudovirus translocation through the endolysosomal system. *Cell Calcium* **75**, 30–41 (2018).

167. Gunaratne, G. S., Johns, M. E., Hintz, H. M., Walseth, T. F. & Marchant, J. S. A screening campaign in sea urchin egg homogenate as a platform for discovering modulators of NAADP-dependent Ca2+ signaling in human cells. *Cell Calcium* **75**, 42–52 (2018).

168. Krogsaeter, E. K., Biel, M., Wahl-Schott, C. & Grimm, C. The protein interaction networks of mucolipins and two-pore channels. *Biochim. Biophys. Acta - Mol. Cell Res.* **1866**, 1111–1123 (2019).

169. Supattapone, S., Worley, P. F., Baraban, J. M. & Snyder, S. H. Solubilization, purification, and characterization of an inositol trisphosphate receptor. *J. Biol. Chem.* **263**, 1530–1534 (1988).

170. Galione, A., Lee, H. C. & Busa, W. B. Ca2+-induced Ca2+ release in sea urchin egg homogenates: Modulation by cyclic ADP-Ribose. *Science* **253**, 1143–1146 (1991).

171. Lee, H. C. & Aarhus, R. Functional visualization of the separate but interacting calcium stores sensitive to NAADP and cyclic ADP-ribose. *J. Cell Sci.* **113**, 4413–4420 (2000).

172. Churchill, G. C. *et al.* NAADP mobilizes Ca2+ from reserve granules, lysosome-related organelles, in sea urchin eggs. *Cell* **111**, 703–708 (2002).

173. Galione, A. NAADP, a new intracellular messenger that mobilizes Ca2+ from acidic stores. *Biochem. Soc. Trans.* **34**, 922–926 (2006).

174. Churchill, G. C. & Galione, A. NAADP induces Ca2+ oscillations via a two-pool mechanism by priming IP3- and cADPR-sensitive Ca2+ stores. *EMBO J.* **20**, 2666–2671 (2001).

175. Masgrau, R., Churchill, G. C., Morgan, A. J., Ashcroft, S. J. H. & Galione, A. NAADP: A new second messenger for glucose-induced Ca2+ responses in clonal pancreatic β cells. *Curr. Biol.* **13**, 247–251 (2003).

176. Mitchell, K. J., Lai, F. A. & Rutter, G. A. Ryanodine receptor type I and nicotinic acid adenine dinucleotide phosphate receptors mediate Ca2+ release from insulin-containing vesicles in living pancreatic β-cells (MIN6). *J. Biol. Chem.* **278**, 11057–11064 (2003).

177. Marchant, J. S. & Patel, S. Questioning Regulation of Two-Pore Channels by NAADP. *Messenger* **2**, 113–119 (2013).

178. Grimm, C. *et al.* High susceptibility to fatty liver disease in two-pore channel 2-deficient mice. *Nat. Comms* **5**, 4699–4712 (2014).

179. Chao, Y.-K. *et al.* TPC2 polymorphisms associated with a hair pigmentation phenotype in humans result in gain of channel function by independent mechanisms. *Proc. Natl. Acad. Sci.* **114**, E8595–E8602 (2017).

180. Pandey, V. *et al.* Recruitment of NAADP-sensitive acidic Ca2+ stores by glutamate. *Biochem. J.* **422**, 503–512 (2009).

181. Foster, W. J. *et al.* Hippocampal mGluR1-dependent long-term potentiation requires NAADP-mediated acidic store Ca2+ signaling. *Sci. Signal.* **11**, eaat9093 (2018).

182. Pereira, G. J. S. *et al.* Nicotinic Acid Adenine Dinucleotide Phosphate (NAADP) regulates autophagy in cultured astrocytes. *J. Biol. Chem.* **286**, 27875–27881 (2011).

183. Pereira, G. J. S. *et al.* Glutamate induces autophagy via the two-pore channels in neural cells. *Oncotarget* **8**, 12730–12740 (2017).

184. García-Rúa, V. *et al.* Endolysosomal two-pore channels regulate autophagy in cardiomyocytes. *J. Physiol.* **594**, 3061–3077 (2016).

185. Lu, Y. *et al.* Two Pore Channel 2 (TPC2) Inhibits Autophagosomal-Lysosomal Fusion by Alkalinizing Lysosomal pH. *J. Biol. Chem.* **288**, 24247–24263 (2013).

186. Lu, Y., Hao, B., Graeff, R. & Yue, J. NAADP/TPC2/Ca2+ signaling inhibits autophagy. *Commun. Integr. Biol.* **6**, e27595 (2013).

187. Sun, W. & Yue, J. TPC2 mediates autophagy progression and extracellular vesicle secretion in cancer cells. *Exp. Cell Res.* **370**, 478–489 (2018).

188. Fernández, B. *et al.* Iron overload causes endolysosomal deficits modulated by NAADP-regulated 2-pore channels and RAB7A. *Autophagy* **12**, 1487–1506 (2016).

189. Huttlin, E. L. *et al.* Architecture of the human interactome defines protein communities and disease networks. *Nature* **545**, 505–509 (2017).

190. Hay, J. C. Calcium: A fundamental regulator of intracellular membrane fusion? *EMBO Rep.* **8**, 236–240 (2007).

191. Ou, X. *et al.* Characterization of spike glycoprotein of SARS-CoV-2 on virus entry and its immune cross-reactivity with SARS-CoV. *Nat. Commun.* **11**, 1620 (2020).

192. Chao, Y.-K., Chang, S.-Y. & Grimm, C. Endo-Lysosomal Cation Channels and Infectious Diseases. in *Reviews of Physiology, Biochemistry and Pharmacology* 1–18 (Springer, 2020). doi:10.1007/112_2020_31.

193. Davis, L. C. *et al.* NAADP Activates Two-Pore Channels on T Cell Cytolytic Granules to Stimulate Exocytosis and Killing. *Curr. Biol.* **22**, 2331–2337 (2012).

194. Davis, L. C., Platt, F. M. & Galione, A. Preferential Coupling of the NAADP Pathway to Exocytosis in T-Cells. *Messenger* **4**, 53–66 (2016).

195. Hamilton, A. *et al.* Adrenaline stimulates glucagon secretion by Tpc2-Dependent Ca2+ mobilization from acidic stores in pancreatic alpha-Cells. *Diabetes* **67**, 1128–1139 (2018).

196. Arredouani, A. *et al.* An emerging role for NAADP-mediated Ca2+ signaling in the pancreatic β-cell. *Islets* **2**, 323–330 (2010).

197. Arredouani, A. *et al.* Nicotinic Acid Adenine Dinucleotide Phosphate (NAADP) and Endolysosomal Two-pore Channels Modulate Membrane Excitability and Stimulus-Secretion Coupling in Mouse Pancreatic beta-Cells. *J. Biol. Chem.* **290**, 21376–21392 (2015).

198. Cane, M. C., Parrington, J., Rorsman, P., Galione, A. & Rutter, G. A. The two pore channel TPC2 is dispensable in pancreatic beta-cells for normal Ca2+ dynamics and insulin secretion. *Cell Calcium* **59**, 32–40 (2016).

199. Hockey, L. N. *et al.* Dysregulation of lysosomal morphology by pathogenic LRRK2 is corrected by TPC2 inhibition. *J. Cell Sci.* **128**, 232–238 (2015).

200. Gómez-Suaga, P. *et al.* Leucine-rich repeat kinase 2 regulates autophagy through a calcium-dependent pathway involving NAADP. *Hum. Mol. Genet.* **21**, 511–525 (2012).

201. Rivero-Ríos, P. *et al.* Alterations in late endocytic trafficking related to the pathobiology of LRRK2-linked Parkinson's disease. *Biochem. Soc. Trans.* **43**, 390–395 (2015).

202. Auburger, G. *et al.* Primary skin fibroblasts as a model of Parkinson's disease. *Mol. Neurobiol.* **46**, 20–27 (2012).

203. Xie, C., Gong, X. M., Luo, J., Li, B. L. & Song, B. L. AAV9-NPC1 significantly ameliorates Purkinje cell death and behavioral abnormalities in mouse NPC disease. *J. Lipid Res.* **58**, 512–518 (2017).

204. Chandler, R. J. *et al.* Systemic AAV9 gene therapy improves the lifespan of mice with Niemann-Pick disease, type C1. *Hum. Mol. Genet.* **26**, 52–64 (2017).

205. Hughes, M. P. *et al.* AAV9 intracerebroventricular gene therapy improves lifespan, locomotor function and pathology in a mouse model of Niemann-Pick type C1 disease. *Hum. Mol. Genet.* **27**, 3079–3098 (2018).

206. Kurokawa, Y. *et al.* Gene Therapy in a Mouse Model of Niemann–Pick Disease Type C1. *Hum. Gene Ther.* **32**, 589–598 (2021).

207. Wakabayashi, K., Gustafson, A. M., Sidransky, E. & Goldin, E. Mucolipidosis Type IV: an Update. *Mol. Genet. Metab.* **104**, 206–213 (2011).

208. Misko, A., Wood, L., Kiselyov, K., Slaugenhaupt, S. & Grishchuk, Y. Progress in Elucidating Pathophysiology of Mucolipidosis IV. *Neurosci. Lett.* **755**, 135944 (2021).

209. Berman, E. R., Livni, N., Shapira, E., Merin, S. & Levij, I. S. Congenital corneal clouding with abnormal systemic storage bodies: A new variant of mucolipidosis. *J. Pediatr.* **84**, 519–526 (1974).

210. NCL Stiftung. Kinderdemenz NCL - Die Krankheit. https://www.ncl-stiftung.de/kinderdemenz-ncl/krankheit/ (2021).

211. Haltia, M. The Neuronal Ceroid-Lipofuscinoses. *J. Neuropathol. Exp. Neurol.* **62**, 1–13 (2003).

212. Kousi, M., Lehesjoki, A. E. & Mole, S. E. Update of the mutation spectrum and clinical correlations of over 360 mutations in eight genes that underlie the neuronal ceroid lipofuscinoses. *Hum. Mutat.* **33**, 42–63 (2012).

213. Stengel, O. C. Report about a strange illness in four siblings in the vicinity of Røros. *Eyr* **1**, 347–352 (1826).

214. Batten, F. E. Cerebral degeneration with symmetrical changes in the maculae in two members of a family. *Trans. Ophthalmol. Soc. U. K.* **23**, 386–390 (1903).

215. Vogt, H. Über familiäre amaurotische Idiotie und verwandte Krankheitsbilder. *Monatsschr. Psychiatr. Neurol.* **18**, 161–171 (1905).

216. Spielmeyer, W. Über familiäre amaurotische Idiotien. *Neurol Cbl.* **24**, 620–612 (1905).

217. Mink, J. W., Augustine, E. F., Adams, H. R., Frederick, J. & Kwon, J. M. Classification and Natural History of the Neuronal Ceroid Lipofuscinoses. *J. Child Neurol.* **28**, 1101–1105 (2013).

218. Janský, J. Dosud nepopsaný pripad familiárni amaurotické idiotie komplikované s hypoplasii mozeckovou. *Sborn Lék* **13**, 165–196 (1908).

219. Bielschowsky, M. Über spätinfantile familiäre amaurotische Idiotie mit Kleinhirnsymptonen. *Dtsch. Z. Nervenheilkd.* **50**, 7–29 (1913).

220. Kufs, H. Über eine Spätform der amaurotischen Idiotie und ihre heredofamiliären Grundlagen. *Zeitschrift für die Gesamte Neurol. und Psychiatr.* **95**, 168–188 (1925).

221. Haltia, M., Rapola, J., Santavuori, P. & Keranen, A. Infantile Type of so-called Neuronal Ceroid-Lipofuscinosis Part 2 . Morphological and Biochemical Studies. *J. Neurol. Sci.* **18**, 269–285 (1973).

222. Santavuori, P., Haltia, M., Rapola, J. & Raitta, C. Infantile Type of so-called Neuronal Ceroid-Lipofuscinosis Part 1. *J. Neurol. Sci.* **18**, 257–267 (1973).

223. Mole, S. E. & Cotman, S. L. Genetics of the neuronal ceroid lipofuscinoses (Batten disease). *Biochim. Biophys. Acta* **1852**, 2237–2241 (2015).

224. Butz, E. S., Chandrachud, U., Mole, S. E. & Cotman, S. L. Moving towards a new era of genomics in the neuronal ceroid lipofuscinoses. *BBA - Mol. Basis Dis.* **1866**, 165571 (2020).

225. Vanier, M. T. Niemann-Pick disease type C. *Orphanet J. Rare Dis.* **5**, 16 (2010).

226. The International Batten Disease Consortium. Isolation of a novel gene underlying Batten disease, CLN3. *Cell* **82**, 949–957 (1995).

227. Reske-Nielsen, E., Baandrup, U., Bjerregaard, P. & Bruun, I. Cardiac involvement in juvenile amaurotic idiocy - A specific heart muscle disorder. Histological findings in 13 autopsied patients. *Acta Pathol. Microbiol. Scand. A.* **89**, 357–365 (1981).

228. Hofman, I. L., Van der Wal, A. C., Dingemans, K. P. & Becker, A. E. Cardiac pathology in neuronal ceroid lipofuscinoses- a clinicopathologic correlation in three patients. *Eur. J. Paediatr. Neurol.* **5**, 213–217 (2001).

229. Arntsen, V., Strandheim, J., Helland, I. B., Sand, T. & Brodtkorb, E. Epileptological aspects of juvenile neuronal ceroid lipofuscinosis (CLN3 disease) through the lifespan. *Epilepsy Behav.* **94**, 59–64 (2019).

230. Rietdorf, K. *et al.* Cardiac pathology in neuronal ceroid lipofuscinoses (NCL): More than a mere co-morbidity. *BBA - Mol. Basis Dis.* **1866**, 165643 (2020).

231. Kuper, W. F. E. *et al.* A Case of Unexpected Adult-Onset Neurologic Decline in CLN3-Associated Retinal Degeneration. *JAMA Ophthalmol.* **135**, 1451–1453 (2017).

232. Wang, F. *et al.* Next generation sequencing-based molecular diagnosis of retinitis

pigmentosa: Identification of a novel genotype-phenotype correlation and clinical refinements. *Hum. Genet.* **133**, 331–345 (2014).

233. Ku, C. A. *et al.* Detailed clinical phenotype and molecular genetic findings in CLN3-associated isolated retinal degeneration. *JAMA Ophthalmol.* **135**, 749–760 (2017).

234. Licchetta, L. *et al.* A novel mutation of CLN3 associated with delayed-classic juvenile ceroid lipofuscinois and autophagic vacuolar myopathy. *Eur. J. Med. Genet.* **58**, 540–544 (2015).

235. Niemann, A. Ein unbekanntes Krankheitsbild. *Jahrb. für Kinderheilkd.* **79**, (1914).

236. Pick, L. Der Morbus Gaucher und die ihm ähnlichen Erkrankungen. *Ergeb. Inn. Med. Kinderheilkd.* **29**, 519 (1926).

237. Abt, A. F. & Bloom, W. Essential Lipoiod Histiocytosis (Type Niemann-Pick). *J. Am. Med. Assoc.* **90**, 2076–2080 (1928).

238. Bloom, W. & Kern, R. Spleens from Gaucher's Disease and Lipoid Histiocytosis: The Chemical Analysis. *Arch Int Med* **39**, 456 (1927).

239. Crocker, A. C. & Farber, S. Niemann-Pick Disease: A Review of Eighteen Patients. *Medicine (Baltimore).* **37**, 1–98 (1958).

240. Crocker, A. C. The Cerebral Defect in Tay-Sachs Disease and Niemann-Pick Disease. *J. Neurochem.* **7**, 69–80 (1961).

241. Brady, R. O., Kanfer, J. N., Mock, M. B. & Fredrickson, D. S. The Metabolism of Sphingomyelin, II. Evidence of an enzymatic deficiency in Niemann-Pick Disease. *Proc. Natl. Acad. Sci. U. S. A.* **55**, 366–369 (1966).

242. Liscum, L., Ruggiero, R. M. & Faust, J. R. The Intracellular Transport of Low Density Lipoprotein-derived Cholesterol Is Defective in Niemann-Pick Type C Fibroblasts. *J. Cell Biol.* **108**, 1625–1636 (1989).

243. Wang, M. L. *et al.* Identification of Surface Residues on Niemann-Pick C2 Essential for Hydrophobic Handoff of Cholesterol to NPC1 in Lysosomes. *Cell Metab.* **12**, 166–173 (2010).

244. Tamura, H. *et al.* Niemann-Pick type C disease: Novel NPC1 mutations and characterization of the concomitant acid sphingomyelinase deficiency. *Mol. Genet. Metab.* **87**, 113–121 (2006).

245. Sun, X. *et al.* Niemann-Pick C Variant Detection by Altered Sphingolipid Trafficking and Correlation with Mutations within a Specific Domain of NPC1. *Am. J. Hum. Genet.* **68**, 1361–1372 (2001).

246. García-Arribas, A. B., Alonso, A. & Goñi, F. M. Cholesterol interactions with ceramide and sphingomyelin. *Chem. Phys. Lipids* **199**, 26–34 (2016).

247. Lim, C. Y. *et al.* ER–lysosome contacts enable cholesterol sensing by mTORC1 and drive aberrant growth signalling in Niemann–Pick type C. *Nat. Cell Biol.* **21**, 1206–1218 (2019).

248. Isobe, Y. *et al.* PIKfyve accelerates phagosome acidification through activation of TRPML1 while arrests aberrant vacuolation independent of the Ca2+ channel. *J. Biochem.* **165**, 75–84 (2019).

249. Venkatachalam, K. *et al.* Motor Deficit in a Drosophila Model of Mucolipidosis Type IV due to Defective Clearance of Apoptotic Cells. *Cell* **135**, 838–851 (2008).

250. Zhang, X. *et al.* MCOLN1 is a ROS sensor in lysosomes that regulates autophagy. *Nat. Commun.* **7**, 12109 (2016).

251. Jennings Jr., J. J. *et al.* Mitochondrial Aberrations in Mucolipidosis Type IV. *J. Biol. Chem.* **281**, 39041–39050 (2006).

252. Curcio-Morelli, C. *et al.* Macroautophagy is defective in mucolipin-1-deficient mouse neurons. *Neurobiol. Dis.* **40**, 370–377 (2010).

253. Colletti, G. A. *et al.* Loss of lysosomal ion channel transient receptor potential channel mucolipin-1 (TRPML1) leads to cathepsin B-dependent apoptosis. *J. Biol. Chem.* **287**, 8082–8091 (2012).

254. Dayam, R. M., Saric, A., Shilliday, R. E. & Botelho, R. J. The Phosphoinositide-Gated Lysosomal Ca2+ Channel, TRPML1, Is Required for Phagosome Maturation. *Traffic* **16**, 1010–1026 (2015).

255. Chen, C.-S., Bach, G. & Pagano, R. E. Abnormal transport along the lysosomal pathway in Mucolipidosis, type IV disease. *Proc. Natl. Acad. Sci. U. S. A.* **95**, 6373–6378 (1998).

256. Bargal, R. & Bach, G. Mucolipidosis type IV: Abnormal transport of lipids to lysosomes. *J. Inherit. Metab. Dis.* **20**, 625–632 (1997).

257. Pryor, P. R., Reimann, F., Gribble, F. M. & Luzio, J. P. Mucolipin-1 is a lysosomal membrane protein required for intracellular lactosylceramide traffic. *Traffic* **7**, 1388–1398 (2006).

258. Chen, C., Krogsaeter, E. & Grimm, C. Two-pore and TRP cation channels in endolysosomal osmo-/mechanosensation and volume regulation. *Biochim. Biophys. Acta - Mol. Cell Res.* **1868**, 118921 (2021).

259. Soldati, C. *et al.* Repurposing of tamoxifen ameliorates CLN3 and CLN7 disease phenotype. *EMBO Mol. Med.* e13742 (2021) doi:10.15252/emmm.202013742.

260. Böck, J. *et al.* Human genome diversity data reveal that L564P is the predominant TPC2 variant and a prerequisite for the blond hair associated M484L gain-of-function effect. *PLOS Genet.* **17**, e1009236 (2021).

261. Nguyen, O. N. P. *et al.* Two-Pore Channel Function Is Crucial for the Migration of Invasive Cancer Cells. *Cancer Res.* **77**, 1427–1438 (2017).

262. Alharbi, A. F. & Parrington, J. Endolysosomal Ca2+ Signaling in Cancer: The Role of TPC2, From Tumorigenesis to Metastasis. *Front. Cell Dev. Biol.* **7**, 302 (2019).

263. Zhao, Z., Qin, P. & Huang, Y. W. Lysosomal ion channels involved in cellular entry and uncoating of enveloped viruses: Implications for therapeutic strategies against SARS-CoV-2. *Cell Calcium* **94**, 102360 (2021).

264. Rinkenberger, N. & Schoggins, J. W. Mucolipin-2 cation channel increases trafficking efficiency of endocytosed viruses. *MBio* **9**, e02314-17 (2018).

265. Miao, Y. *et al.* TRP Channel Senses Lysosome Neutralization by Pathogens to Trigger Their Expulsion. *Cell* **161**, 1306–1319 (2015).

266. Davis, L. C., Morgan, A. J. & Galione, A. NAADP-regulated two-pore channels drive phagocytosis through endo-lysosomal Ca2+ nanodomains, calcineurin and dynamin. *EMBO J.* **39**, e104058 (2020).

267. Ruas, M., Galione, A. & Parrington, J. Two-Pore Channels: Lessons from Mutant Mouse Models. *Messenger* **4**, 4–22 (2015).

268. Arlt, E. *et al.* TPC1 deficiency or blockade augments systemic anaphylaxis and mast cell activity. *Proc. Natl. Acad. Sci. U. S. A.* **117**, 18068–18078 (2020).

269. Marchant, J. S. & Patel, S. Two-pore channels at the intersection of endolysosomal membrane traffic. *Biochem Soc Trans* **43**, 434–441 (2015).

270. Paquet, D. *et al.* Efficient introduction of specific homozygous and heterozygous mutations using CRISPR/Cas9. *Nature* **533**, 125–129 (2016).

271. Kwart, D., Paquet, D., Teo, S. & Tessier-Lavigne, M. Precise and efficient scarless genome editing in stem cells using CORRECT. *Nat. Protoc.* **12**, 329–334 (2017).

9. CURRICULUM VITAE

Einar Kleinhans Krogsaeter

Born 26th March 1994
E-mail einar.krogsaeter@gmail.com
Phone +49-(0)15-2029-36455
Address Einsteinstrasse 13, 85521 Ottobrunn Bavaria, Germany

Professional Experience

Dr. rer. nat. (PhD) Biology (Graduate School Life Sciences Munich)

Ludwig-Maximilians-Universität München (www.en.uni-muenchen.de***)*** **August 2017 – Present**

"Known and novel members of the endolysosomal transportome/channelome as candidates to rescue loss of TRPML1 function in MLIV patients," supervised by **Prof. Christian Grimm**. *In vivo* mouse maintenance and animal experiments; *ex vivo* cell isolation, immunohistochemistry; *in vitro* cell/iPSC-culture, CRISPR/Cas9 of iPSCs + quality control, cortical neuron differentiation, subcellular trafficking assays, immunocytochemistry; *in silico* modelling/docking/molecular dynamics; molecular biology, Ca^{2+} imaging, RT-qPCR. Teaching seminars on neurodegenerative diseases, IT maintenance.

Other Research Projects

The University of Oxford (www.ox.ac.uk) **June 2016 – July 2016**

"Augmenting brain creatine kinase in the murine heart," supervised by **Prof. Craig Lygate**. *In vivo* body composition analysis, conscious electrocardiography, echocardiography; *ex vivo* tissue isolation, Langendorff perfusion, isoenzyme activity analysis, HPLC; *in vitro* cell culture, hypoxia/reoxygenation assay; FACS; WB.

The University of Edinburgh (www.ed.ac.uk) ***May 2015 – July 2015***

"Do epigenetic alterations contribute to the development of fatty liver in mice selected for obesity over 60 generations," supervised by **Prof. Nik Morton**. RT-qPCR, WB, establishing ChIP/RT-qPCR.

Selected Publications

** these authors contributed equally to this work.*

- Chen C-C*, **Krogsaeter EK**, Grimm C*: Two-pore and TRP cation channels in endolysosomal osmo-/mechanosensation and volume regulation (2021). *BBA Mol. Cell. Res.* 1868(2):118921.
- Böck J*, **Krogsaeter EK***, Passon M, Chao Y-K, Sharma S, Grallert H, Peters A, Grimm C: Human genome diversity data reveal that L564P is the predominant TPC2 variant and a prerequisite for the blond hair associated M484L gain-of-function effect (2021). *PLOS Genet.* 17(1):e1009236.
- Chen C-C*, **Krogsaeter EK***, Butz ES, Li Y, Puertollano R, Wahl-Schott C, Biel M, Grimm C: TRPML2 is an osmo/mechanosensitivie cation channel in endolysosomal organelles (2020). *Science Advances* 6(46): eabb5064.
- Gerndt S, **Krogsaeter EK**, Patel S, Bracher F, Grimm C: Discovery of lipophilic two-pore channel agonists (2020). *The FEBS Journal* 287: 5284-5293.
- Jaslan D, Böck J, **Krogsaeter EK**, Grimm C: Evolutionary Aspects of TRPMLs and TPCs (2020). *Int. J. Mol. Sci.* 21(11):4181.
- Gerndt S*, Chen C-C*, Chao YK*, Yuan Y*, Scotto-Rosato A, **Krogsaeter E**, Burgstaller S, Urban N, Jacob K, Nguyen ONP, Miller MT, Keller M, Vollmar AM, Gudermann T, Zierler S, Schredelseker J, Schaefer M, Biel M, Malli R, Wahl-Schott C, Bracher F, Patel S, Grimm, C: Agonist-mediated switching of ion selectivity in TPC2 differentially promotes lysosomal function (2020). *eLIFE* 9: e54712.
- **Krogsaeter EK**, Biel M, Wahl-Schott C, Grimm C: The protein interaction networks of mucolipins and two-pore channels (2019). *BBA Mol. Cell. Res.* 1866(7):1111-1123.
- Plesch E*, Chen C-C*, Butz E*, Scotto-Rosato A, **Krogsaeter EK**, Hua Y, Bartel K, Robaa D, Keller M, Teupser D, Holdt LM, Vollmar AM, Sippl W, Puertollano R, Medina DL, Biel M, Wahl-Schott C, Bracher F, Grimm C.: Isoform-selective agonist of TRPML2 reveals direct role in cytokine release from innate immune cells (2018). *eLIFE* 7.pii: e39720.

Education

Dr. rer. nat. (PhD) Biology (Life Sciences Munich) August 2017 – Present

Ludwig-Maximilians-Universität, München (LMU), Munich (www.lsm.bio.lmu.de)

- **Doctoral project:** "Known and novel members of the endolysosomal transportome/channelome as candidates to rescue loss of TRPML1 function in MLIV patients."
- **Doctoral supervisor:** Prof. Dr. Dr. Christian Grimm, Faculty of Medicine.

BSc (Hons) Biomedical Sciences (Pharmacology) September 2013 – July 2017

University of Edinburgh (www.ed.ac.uk)

- **Overall Classification of the Qualification**: First Class (equivalent to 4.0 GPA).
- **Honours project:** "Understanding the role of Kindlin-1 in the oxidative stress response" (A3).
- **Honours review:** "History of Kindlin-1 in cell signalling and the oxidative stress response" (A2).

Positions of Responsibility

- **LMU Munich**: Student council member of the graduate school "Life Sciences Munich". Organizer of "Life Sciences Munich" retreat 2020.
- **University of Edinburgh:** Representative for 4 courses and the College of Science and Engineering.
- **September 2016-July 2017:** Chair of the University of Edinburgh Student Pharmacological Society.
- **January 2015-July 2017:** STEM Ambassador in East Scotland.

Software

MS Office Suite | **Adobe Photoshop** | **Adobe Illustrator**
Fiji/ImageJ | **GraphPad Prism** | **ChemDraw**
PyMOL | **AutoDock Tools** | **AutoDock Vina**
R | **NAMD**

Languages

English (Native) **Norwegian (Native)** **German (Fluent)** **Spanish (Basic)**

Non-Academic Certificates and Honours

- **Cambridge International PhD Scholarship**: Awarded for a proposed PhD in Pharmacology in 2017. Declined in favour of a PhD position at the LMU.
- **Physiological Society Vacation Studentship**: Recipient of the Vacation Studentship Scheme funding by the Physiological Society for my summer project of 2016.
- **Medical Research Scotland Vacation Scholarship**: Awarded for a proposed summer project. Declined in favour of the Physiological Society Vacation Studentship.
- **The Edinburgh Award**: Received the Edinburgh Award April 2015 for my work with ProScience.

References

Prof. Dr. Dr. Christian M. Grimm

Professor of Molecular Pharmacology
Ludwig-Maximilians-Universität München
Nussbaumstraße 26
80336 Munich
Bavaria, Germany
Tel: +49-(0)89-2180-73811
E-mail: christian.grimm@med.uni-muenchen.de

Prof. Susan C. Welburn

Chair of Medical and Veterinary Epidemiology
The University of Edinburgh Medical School
1 George Square
Edinburgh, EH8 9JZ
Scotland, UK
Tel: +44-(0)131-242-6544
E-mail: sue.welburn@ed.ac.uk

10. COMPLETE LIST OF ORIGINAL PUBLICATIONS

1. **Krogsaeter EK**, Biel M, Wahl-Schott C, Grimm C. "The Protein Interaction Networks of Mucolipins and Two-Pore Channels." *BBA – Molecular Cell Research*, **2018**, 1866(7):1111-1123.
2. Plesch E*, Chen C-C*, Butz E*, Scotto Rosato A, **Krogsaeter EK**, Yinan H, Bartel K, Keller M, Robaa D, Teupser D, Holdt LM, Vollmar AM, Sippl W, Puertollano R, Medina D, Biel M, Wahl-Schott C, Bracher F, Grimm C. "Selective agonist of TRPML2 reveals direct role in chemokine release from innate immune cells." *eLife*, **2018**, 7:e39720.
3. Gerndt S*, Chen C-C*, Chao Y-K*, Yuan Y*, Burgstaller S, Scotto Rosato A, **Krogsaeter EK**, Urban N, Jacob K, Nguyen ONP, Miller MT, Keller M, Vollmar AM, Gudermann T, Zierler S, Schredelseker J, Schaefer M, Biel M, Malli R, Wahl-Schott C, Bracher F, Patel S, Grimm C. "Agonist-mediated switching of ion selectivity in TPC2 differentially promotes lysosomal function." *eLife*, **2020**, 9:e54712.
4. Gerndt S*, **Krogsaeter EK***, Patel S, Bracher F, Grimm C. "Discovery of lipophilic two-pore channel agonists." *FEBS Journal*, **2020**, 287(24):5284-5293.
5. Jaslan D, Böck J, **Krogsaeter EK**, Grimm C. "Evolutionary Aspects of TRPMLs and TPCs." *International Journal of Molecular Sciences*, **2020**, 21(11):4181.
6. Chen C-C*, **Krogsaeter EK***, Butz E, Li Y, Puertollano R, Wahl-Schott C, Biel M, Grimm C. "TRPML2 is an osmo/mechanosensitive cation channel in endolysosomal organelles." *Science* Advances, **2020**, 6(46):eabb5064.
7. Böck J*, **Krogsaeter EK***, Passon M, Chao Y-K, Sharma S, Grallert H, Peters A, Grimm C. "Human Genome Diversity Data Reveal that L564P is the Predominant TPC2 Variant and a Prerequisite for the Blond Hair Associated M484L Gain-of-Function Effect." *PLoS Genetics*, **2021**, 17(1):e10092236.
8. Chen C-C, **Krogsaeter EK**, Grimm C. "Two-pore and TRP cation channels in endolysosomal osmo-/mechanosensation and volume regulation." *BBA – Molecular Cell Research* 1868(2):118921.
9. **Krogsaeter EK**, Tang R, Grimm C. "JPT2: The missing link between intracellular Ca2+ release channels and NAADP?" *Cell Calcium*, **2021**, 97: 102405.
10. Soldati C*, Lopez-Fabuel I*, Wanderlingh LG, Garcia-Macia M, Monfregola J, Esposito A, Napolitano G, Guevara-Ferrer M, Scotto Rosato A, **Krogsaeter EK**, Paquet D, Grimm C, Montefusco S, Braulke T, Storch S, Mole SE, De Matteis MA, Ballabio A, Sampaioi JL, McKay T, Johannes L, Bolanos JP, Medina DL. "Repurposing of tamoxifen ameliorates CLN3 and CLN7 disease phenotype. *EMBO Molecular Medicine* **2021**:e13742.

**these authors contributed equally to this work*

11. ACKNOWLEDGEMENTS

"Per aspera ad astra." Very fitting words for a doctoral project marked by a lab move, funding periods being completed and grants for new projects being awarded, and at the moment that you least expect it, a pandemic hitting you straight in your face. For this reason, I would like to express my heartfelt thanks to Prof. Christian Grimm, who has throughout been a driving force for the progress of an excellent research environment. He has always provided an open ear for scientific ideas an open mouth for scientific discussions and proven a truly interactive leader for the start of my scientific career. He took me on as a really fresh scientist with little research experience beyond a couple of internships, and provided the mentorship and opportunities for me to develop myself beyond my expectations. I am humbled by your trust, and grateful for everything you've taught me.

Furthermore, I extend my sincere gratitude to Prof. Dominik Paquet, who introduced me to the world of gene editing and induced pluripotent stem cells. Prof. Paquet has throughout proven a scientist of incredible integrity, with openness for discussion and pleasure in his work that has been awe-inspiring. I also extend my thanks to Prof. Angelika Vollmar, Prof. Eric Lambie, and Prof. Christof Osman, who have formed my Thesis Advisory Committee during my doctoral studies. You have all ensured that I've stayed on track, and provided valuable input on my scientific development.

I would also like to particularly thank Dr. Elisabeth Butz, Dr. Cheng-Chang Chen, Dr. Yu-Kai Chao, and Dr. Anna Scotto Rosato. These fantastic four have provided boundless inspiration through scientific discussion and taught me everything I know today in terms of science. The dynamic duo of Dr. Cheng-Chang Chen and Dr. Yu-Kai Chao proved a crucial asset to my time here through providing electrophysiological assistance and explaining the intricacies of their work. Without their guidance, I would have felt lost in a world of IV measurements and capacitance normalization. Dr. Elisabeth Butz was particularly welcoming as I started my PhD and introduced me to cell-based assays, animal handling, and staying focused and organized. Her thoughtful attitude and company during (and long after) working hours was instrumental in myself getting a good start in the Grimm lab. Dr. Anna Scotto Rosato came in towards the end of my doctoral work and augmented my knowledge of what Dr. Elisabeth Butz had started teaching me, proving a very down-to-earth researcher with a very pragmatic approach to science. You have all enriched my stay and proven instrumental in supporting my work here.

My sincere thanks also to the rest of the past and present Lysolab members, who have all been terrific, supportive and entertaining company: Dr. Dawid Jaslan, Judith Schürmann, Barbara Spix, Marcel Passon, Alina Nakhabina, Thiemo Grüsla, Iria Trasobares Magdalena, Julia Böck, Carla Abrahamian, Rachel Tang, Zagorka Bekjarova, Veronika Kudrina, Stefan Georgiev, and Ponsawan Netcharoensirisuk. Each and every one of you have proven integral to my research and enjoyment in the lab, and I really valuable the helpful and mutually supportive work environment you all have contributed to developing.

Ancient alchemists of legend struggled fruitlessly to transmute worthless rocks into gold nuggets. Where they have failed, our collaboration partner in Prof. Franz Bracher's laboratory, Dr. Susanne Gerndt, succeeded. Susi transmuted non-selective channel agonists into the powerful tools presented herein. Beyond this, Susi has been a cheerful addition to our laboratory environment. Therefore, I extend my gratitude to Dr. Gerndt, whose contributions form a crucial asset to my work.

I am furthermore sincerely grateful to those who have contributed in making the work environment so open, inclusive, and respectful for all ideas (and my annoying questions during journal club). That includes the current and past members of Prof. Martin Biel's laboratory – Prof. Stylianos Michalakis, Prof. Christian Wahl-Schott, Dr. Elvir Becirovic, Dr. Stefanie Fenske, Dr. Verena Hammelmann, Dr. Christian Schön, Dr. Karim Le Meur, Dr. Elisa Murenu, Dr. Verena Schlüdi, Dr. Sybille Böhm, Dr. Verena Schöttle, Dr. Victoria Splith, Dr. Anna Geserich, Dr. Johanna Wagner, Dr. Marc Stieglitz, Dr. Lisa Riedmayr, Dr. Anna Panagiotopoulos, Dr. Constanze Scheel, Dr. Marina Pavlou, Dr. Yanfen Li, Manuela Brümmer, Grazia Giorgio, Konstantin Hennis, Klara Hinrichsmeyer, Jennifer Kass, Julia

Rilling, Rene Rötzer, Lena Zobel, Mariella Grüner, Katharina Hahn, Selina Scheungrab, Christopher Wolf, Berit Noack, Kerstin Skokann, Tamara Gehringer, and Johanna Weiker.

I would also like to express my endless gratitude to the past and present members of Prof. Paquet's lab, who were incredible in supporting my iPSC- and gene-editing -based work. This includes Dr. Isabel Weisheit, Julien Klimmt, Angelika Dannert, Judit Gonzalez Gallego, Liliana Pedro, Joseph Kroeger, Marvin Reich, Sophie Robinson, Carolina Goncalves, Katja Salbaum, Samantha Ho, Annika Wagener, Merle Bublitz, and Berenice Horlacher, Jennifer Yilmaz, and Andrea Stüven. Your openness and willingness to share your knowledge has really been instrumental for my work. Most of all however, I am incredibly grateful to Prof. Paquet's laboratory technician, Dennis Crusius. Dennis taught me pretty much everything that I am today able to practically do with iPSCs and CRISPR/Cas9. Beyond this however, Dennis has been a really good friend and an exceptional individual, who has trusted me with my work, supported me when needed, and been excellent company. I am truly grateful.

Huge thanks to the institutions that have supported my work – The ML4 Foundation and Care for Rare Foundation for supporting the beginning of my project on one hand, but in particular, the NCL Stiftung. The NCL Stiftung took me on as a NCL Fellow, and gave me ample opportunities beyond their material support, inviting me to conferences, meetings, and symposia to exchange ideas surrounding the devastating diseases that the lysosomal storage diseases and Batten Disease are. I am very grateful particularly to Dr. Frank Stehr and Dr. Herman van der Putten of the NCL Foundation for their support and drive to combat Batten Disease, and I truly believe that with their inspiring engagement and passion, Batten can be beaten. Thank you.

I also must extend my gratitude to the organizers and members of the Life Sciences Munich graduate school (LMU-LSM) - Francisca Rosa Mende and Nadine Hamze. You really made my study here in Germany as easy to approach as an international as it could be, and provided ample opportunities for personal development and scientific exchange. You have really made the LSM programme as good as it possibly could be, and I'm incredible grateful for all of your support.

My thanks also go out to my past teachers and supervisors, who have been colossal in inspiring me through their own fascinations for science. Particularly, I would like to thank Isabella Pareliussen (Natural Sciences, primary school), Alan Jenkins (Chemistry, high school), Prof. Tom Freeman (systems/pathway biology, university), Nik Morton, and Craig Lygate (both supervisors for summer projects during my pre-PhD studies).

Finally, I must express my most heartfelt gratitude to those who have supported me personally both before and throughout my studies. First of all, my family - My parents Mette Krogsaeter and Uwe Kleinhans always pushed me to do what I'm interested in, and I'm certain I wouldn't have had the motivation to complete a successful PhD in something I'd have been pushed into. My highly competitive younger sisters Sofie and Hanne Kleinhans Krogsaeter have always challenged me to be as good as I can, normally exceeding my own achievements when they could. My grandparents Arnfinn, Solveig, Jürgen and Liesel, for bringing creativity into my life, for their relentless support in everything I do, and really being the most compassionate people you could dream of finding. And of course, I must express my sincere gratitude to my girlfriend Lena Bergmann, who always heroically accepted my late-night experiments in the lab, yet kept me grounded, ensuring that I also spent time outside the laboratory, travelling to see new countries and gathering new experiences. You have made my Munich time a very special part of my life, and I am terribly excited for the times that are yet to come. Lots of love to you all.

12. APPENDIX OF MANUSCRIPTS

The following pages contain the reprinted **Manuscripts I-VI**:

I. **Selective agonist of TRPML2 reveals direct role in chemokine release from innate immune cells**
Eva Plesch*, Cheng-Chang Chen*, Elisabeth Butz*, Anna Scotto Rosato, **Einar K. Krogsaeter**, Hua Yinan, Karin Bartel, Marco Keller, Dina Robaa, Daniel Teupser, Lesca M. Holdt, Angelika M. Vollmar, Wolfgang Sippl, Rosa Puertollano, Diego Medina, Martin Biel, Christian Wahl-Schott, Franz Bracher, & Christian Grimm
eLIFE. 2018;7:e39720.

II. **Agonist-mediated switching of ion selectivity in TPC2 differentially promotes lysosomal function**
Susanne Gerndt*, Cheng-Chang Chen*, Yu-Kai Chao*, Yu Yuan*, Sandra Burgstaller, Anna Scotto Rosato, **Einar K. Krogsaeter**, Nicole Urban, Katharina Jacob, Ong Nam Phuong Nguyen, Meghan T. Miller, Marco Keller, Angelika M. Vollmar, Thomas Gudermann, Susanna Zierler, Johann Schredelseker, Michael Schaefer, Martin Biel, Roland Malli, Christian Wahl-Schott, Franz Bracher, Sandip Patel, & Christian Grimm.
eLIFE. 2020;9:e54712.

III. **TRPML2 is an osmo/mechanosensitive cation channel in endolysosomal organelles**
Cheng-Chang Chen*, **Einar K. Krogsaeter***, Elisabeth S. Butz, Yanfen Li, Rosa Puertollano, Christian Wahl-Schott, Martin Biel, & Christian Grimm.
Science Advances. 2020;6:eabb5064.

IV. **Human genome diversity data reveal that L564P is the predominant TPC2 variant and a prerequisite for the blond hair associated M484L gain-of-function effect**
Julia Böck*, **Einar K. Krogsaeter***, Marcel Passon, Yu-Kai Chao, Sapna Sharma, Harald Grallert, Annette Peters, & Christian Grimm
PLOS Genetics. 2021;17(1):e1009236

V. **Repurposing of tamoxifen ameliorates CLN3 and CLN7 disease phenotype**
Chiara Soldati*, Irene Lopez-Fabuel*, Luca G. Wanderlingh, Marina G. Macia, Jlenia Monfregola, Alessanddra Esposito, Gennaro Napolitano, Marta Guevara-Ferrer, Anna Scotto Rosato, **Einar K. Krogsaeter**, Dominik Paquet, Christian Grimm, Sandro Montefusco, Thomas Braulke, Stephan Storch, Sara E. Mole, Maria Antonietta De Matteis, Andrea Ballabio, Julio Lopes-Sampaio, Tristan McKay, Ludger Johannes, Juan P. Bolanos, & Diego L. Medina.
EMBO Molecular Medicine. 2021;e13742.

VI. **Targeting TPC2 rescues lysosomal storage in mucolipidosis type IV, Niemann-Pick type C1 and Batten disease**
Einar K. Krogsaeter*, **Anna Scotto Rosato***, Carla Abrahamian, Dawid Jaslan, Julia Böck, Chiara Soldati, Barbara Spix, Amanda Wyatt, Daniela Borchert, Marcel Passon, Marc Stieglitz, Guido Hermey, Sandra Markmann, Doris Gruber-Schoffnegger, Susan Cotman, Ulrich Boehm, Thorsten Marquardt, Christian Wahl-Schott, Martin Biel, Elena Polishchuk, Diego Medina, Dominik Paquet, & Christian Grimm.
Manuscript in preparation.

Manuscript I

Selective agonist of TRPML2 reveals direct role in chemokine release from innate immune cells

Eva Plesch*, Cheng-Chang Chen*, Elisabeth Butz*, Anna Scotto Rosato, **Einar K. Krogsaeter**, Hua Yinan, Karin Bartel, Marco Keller, Dina Robaa, Daniel Teupser, Lesca M. Holdt, Angelika M. Vollmar, Wolfgang Sippl, Rosa Puertollano, Diego Medina, Martin Biel, Christian Wahl-Schott, Franz Bracher, & Christian Grimm

eLIFE. 2018;7:e39720.

eLIFE elifesciences.org

RESEARCH ARTICLE

Selective agonist of TRPML2 reveals direct role in chemokine release from innate immune cells

Eva Plesch[1†], Cheng-Chang Chen[1†], Elisabeth Butz[1†], Anna Scotto Rosato[2], Einar K Krogsaeter[3], Hua Yinan[4], Karin Bartel[1], Marco Keller[1], Dina Robaa[5], Daniel Teupser[6], Lesca M Holdt[6], Angelika M Vollmar[1], Wolfgang Sippl[5], Rosa Puertollano[4], Diego Medina[2], Martin Biel[1], Christian Wahl-Schott[7]*, Franz Bracher[1]*, Christian Grimm[3]*

[1]Department of Pharmacy, Center for Drug Research and Center for Integrated Protein Science Munich, Ludwig Maximilian University of Munich, Munich, Germany; [2]Telethon Institute of Genetics and Medicine, Naples, Italy; [3]Department of Pharmacology and Toxicology, Medical Faculty, Ludwig Maximilian University of Munich, Munich, Germany; [4]Cell Biology and Physiology Center, National Heart, Lung, and Blood Institute, National Institutes of Health, Bethesda, United States; [5]Department of Pharmaceutical Chemistry, Institute of Pharmacy, Martin Luther University of Halle-Wittenberg, Halle, Germany; [6]Institute of Laboratory Medicine, University Hospital Munich, Munich, Germany; [7]Institute for Neurophysiology, Hannover Medical School, Hannover, Germany

***For correspondence:** christian.wahl@cup.uni-muenchen.de (CW-S); franz.bracher@cup.uni-muenchen.de (FB); chgrph@cup.uni-muenchen.de (CG)

[†]These authors contributed equally to this work

Competing interests: The authors declare that no competing interests exist.

Funding: See page 19

Received: 01 July 2018
Accepted: 26 October 2018
Published: 20 November 2018

Reviewing editor: Michael L Dustin, University of Oxford, United Kingdom

Abstract Cytokines and chemokines are produced and secreted by a broad range of immune cells including macrophages. Remarkably, little is known about how these inflammatory mediators are released from the various immune cells. Here, the endolysosomal cation channel TRPML2 is shown to play a direct role in chemokine trafficking and secretion from murine macrophages. To demonstrate acute and direct involvement of TRPML2 in these processes, the first isoform-selective TRPML2 channel agonist was generated, ML2-SA1. ML2-SA1 was not only found to directly stimulate release of the chemokine CCL2 from macrophages but also to stimulate macrophage migration, thus mimicking CCL2 function. Endogenous TRPML2 is expressed in early/recycling endosomes as demonstrated by endolysosomal patch-clamp experimentation and ML2-SA1 promotes trafficking through early/recycling endosomes, suggesting CCL2 being transported and secreted via this pathway. These data provide a direct link between TRPML2 activation, CCL2 release and stimulation of macrophage migration in the innate immune response.
DOI: https://doi.org/10.7554/eLife.39720.001

Introduction

Cytokines/chemokines are released from a wide range of immune cells such as macrophages, B- and T-lymphocytes, neutrophils, mast cells and dendritic cells. They are essential for intercellular communication in both innate and adaptive immunity. Remarkably, our knowledge of the function of cytokines/chemokines in immunity is much more advanced than our knowledge about how they are packaged and secreted from immune cells. Understanding how innate immune cells release cytokines/chemokines is important, as these factors are indispensable for communication between immune but also with non-immune cells to coordinate inflammatory responses (***Lacy and Stow, 2011***). Importantly, secretion pathways vary between different cell types. Macrophages for example

lack typical secretory granules (**Lacy and Stow, 2011**). Thus, macrophage cytokine/chemokine release is mediated either by direct transport to the cell surface from the trans-Golgi network (TGN) (e.g. IL-10), by transport via recycling endosomes (RE) to the cell surface (e.g. TNF-α, IL-6, IL-10) (**Manderson et al., 2007**; **Murray and Stow, 2014**), or via late endosomes/lysosomes (LE/LY), for example IL-1β (**Andrei et al., 1999**; **Lopez-Castejon and Brough, 2011**).

We show here that the endolysosomal calcium-permeable cation channel TRPML2 plays a direct role in chemokine secretion, thereby modulating the inflammatory response. Expression of TRPML2 in different immune cells and tissues has been demonstrated by several groups (**Cuajungco et al., 2016**; **Valadez and Cuajungco, 2015**; **García-Añoveros and Wiwatpanit, 2014**; **Sun et al., 2015**). On the subcellular level, TRPML2 has been shown to be expressed primarily on RE and LE/LY by immunocytochemistry experiments (**Sun et al., 2015**; **Venkatachalam et al., 2006**; **Karacsonyi et al., 2007**). However, functional expression of TRPML2 in different intracellular vesicles and organelles has not been confirmed yet by direct and selective patch-clamp analysis, that is patch-clamping of RE, EE (early endosomes), LE/LY, or other endolysosomal vesicles. Furthermore, it remains unclear whether direct and selective stimulation of TRPML2 leads to an increase in cytokine/chemokine release from macrophages, and which intracellular trafficking pathways mediate the release of these cytokines/chemokines.

One important impediment for the investigation of different endogenous TRPML-like currents and their functional impact on secretion, endolysosomal trafficking, or autophagy, is the lack of isoform-selective agonists. Development of such agonists would allow demonstration of the TRPML isoform-specific contribution towards observed phenomena, for example chemokine secretion. Currently available TRPML channel agonists belong to different chemotypes, including benzenesulfonamides (e.g. SN-1- or SF-21-type), thiophenesulfonamides (e.g. SF-22-type, including MK6-83), isoindolediones (e.g. SF-51-type, including ML-SA1), isoxazolines (e.g. SN-2-type) and others (**Grimm et al., 2010**; **Yamaguchi and Muallem, 2010**; **Grimm et al., 2012b**; **Shen et al., 2012**). Efficacy, potency and selectivity of these compounds can vary between species. Furthermore, none of the currently available TRPML agonists is selective for TRPML1 or TRPML2. ML-SA1 for example activates TRPML1 and TRPML3 in mouse, while it activates all three human isoforms (**Shen et al., 2012**; **Grimm, 2016**). MK6-83 activates TRPML1 and TRPML3 in both mouse and human (**Grimm, 2016**; **Chen et al., 2014**). The putative endogenous TRPML channel activator $PI(3,5)P_2$ activates all three TRPML channel isoforms in both species and, in addition, also activates the endolysosomal cation channels TPC1 and TPC2 (**Chen et al., 2014**; **Wang et al., 2012**; **Cang et al., 2013**; **Grimm et al., 2014**). Through systematic chemical modification of known lead structures we have now generated the first isoform-selective TRPML2 channel agonist, ML2-SA1.

We demonstrate that ML2-SA1 activates TRPML2 in EE and LE/LY as well as in Rab11+ and Tf+/TfR+ (transferrin/transferrin receptor) vesicles. In macrophages, LPS (lipopolysaccharide) exposure leads to a strong upregulation of TRPML2 expression, while TRPML1 and TRPML3 expression levels remain unaffected by LPS (**Sun et al., 2015**). Importantly, activation by ML2-SA1 was not observed in macrophages without LPS treatment which express TRPML2 only at very low levels, further confirming specificity of the compound. We also show that direct activation of TRPML2 by ML2-SA1 results in an increased release of the chemokine CCL2 from LPS-stimulated WT macrophages, while $TRPML2^{-/-}$ macrophages show no release increase, suggesting that TRPML2 channel activity is directly linked to CCL2 trafficking and secretion. We further provide evidence that CCL2 is released via the early/recycling endosomal pathway but not via LE/LY. Finally, we show that stimulation with ML2-SA1 promotes macrophage migration, one of the major physiological functions of the chemoattractant CCL2, one synonym of which is monocyte chemoattractant protein 1 (MCP-1).

Results

Development of a potent isoform-selective TRPML2 channel agonist

With the aim to further improve the characteristics of existing TRPML channel agonists, we generated more than 80 novel derivatives of recently reported lead activators of TRPML channels which had been originally identified by random screening of the MLSMR small molecule library (Scripps Research Institute Molecular Screening Center) (**Grimm et al., 2010**). Here, novel derivatives of the lead compounds SN-2 and ML-SA1, a SF-51 analogue (**Grimm et al., 2010**; **Shen et al., 2012**;

Grimm, 2016; *Chen et al., 2014*) were evaluated for their efficacy, potency, and selectivity profiles, respectively.

We first synthesized and tested >50 chemically modified versions of the TRPML3 activator SN-2 (*Figure 1*; *Figure 1—figure supplement 1*; *Supplementary file 1*). These modifications comprise systematic variations of the substitution pattern of the aryl ring, variations of the aliphatic norbornane ring system, aromatisation of the isoxazoline to an isoxazole fragment, introduction of polar substituents, as well as replacement of the isoxazol(in)e ring by other heterocycles. Crucial steps in these syntheses were Huisgen-type 1,3-dipolar cycloaddition reactions of norbornene (for the closer analogues) and other alkenes with nitrile oxides (*Jawalekar et al., 2011*; *Huisgen, 1963*) and related 1,3-dipoles. Related aromatic isoxazole analogues were prepared via cycloaddition of nitrile oxides with ketone enolates (*Vitale and Scilimati, 2013*) or enamines (*Fos et al., 1992*). General synthesis strategies for these modifications are shown in *Figure 1A*.

Derivatives of SF-51/ML-SA1 (*Figure 1—figure supplement 2*; *Figure 1—figure supplement 3*; *Supplementary file 1*) were synthesized by combining appropriate amine building blocks (partially hydrogenated quinolines and other cyclic and open-chain analogues) with *N*-acyl spacers and imide/lactam-type residues following standard procedures (*Figure 1—figure supplement 3A*).

Following synthesis, we initially tested the compounds in HEK293 cells transiently transfected with human TRPML1, TRPML2, or TRPML3 (C-terminally fused to YFP) by using the fura-2 calcium imaging technique. When expressed in HEK293 cells, TRPML2 and TRPML3 but not TRPML1 substantially localize at the plasma membrane besides endolysosomes as described previously (*Grimm et al., 2010*), enabling standard fura-2 calcium imaging experimentation. To evaluate effects on TRPML1, a plasma membrane variant with mutated lysosomal targeting sequences in the N- and C-termini (TRPML1(NC)) was used as reported previously (*Grimm et al., 2010*).

The majority of the SN-2 and SF-51/ML-SA1 derivatives were either inactive, non-selective like ML-SA1, or selective for TRPML3 like SN-2 (*Figure 1B*; *Figure 1—figure supplement 3B*). A subset of molecules however displayed a strong preference for TRPML2: ML2-SA1 (=EVP-22), a derivative of SN-2, as well as derivatives of SF-51/ML-SA1: EVP-198, EVP-207 and EVP-209. The latter three SF-51/ML-SA1 derivatives however showed lower efficacy compared to ML2-SA1 (*Figure 1B*; *Figure 1—figure supplement 3B*).

TRPML2 activity is detectable in EE, LE/LY as well as Rab11+ and TfR + organelles

In endolysosomal patch-clamp experiments using transiently transfected HEK293 cells, we investigated TRPML2 channel activity in wortmannin/latrunculin B (Wort./Lat.B)-enlarged EE (*Chen et al., 2017a*), in YM201636-enlarged LE/LY (*Chen et al., 2017a*), as well as in vacuolin-enlarged Rab11 + and TfR+ organelles (*Figure 2*; *Figure 2—figure supplement 1*). In LE/LY, both ML2-SA1 (*Figure 2B*; *Figure 2—figure supplement 1A*) and PI(3,5)P_2 (*Figure 2—figure supplement 1A*) evoked TRPML2 activation while no or very little activation was detectable for TRPML1 and TRPML3. In contrast, the latter ones were robustly activated by ML-SA1 as a positive control (*Figure 2C–E*). The time course for activation of TRPML2 in LE/LY patch-clamp experiments and the relative Ca^{2+} permeability are shown in *Figure 2G* and *Figure 2—figure supplement 1B*. In addition to LE/LY, TRPML2 channel activity was also detectable in EE after stimulation with ML2-SA1 (*Figure 2H and K*). In order to patch-clamp discrete populations of vesicles involved in early/recycling endosomal trafficking, cells were transfected with fluorophore-tagged Rab11 or TfR, and enlarged with vacuolin. ML2-SA1 elicited significant currents in Rab11+ and in TfR+ vesicles (*Figure 2I–K*).

Furthermore, the effect of luminal pH on TRPML2 channel activity was evaluated (*Figure 2—figure supplement 1A and C*). TRPML2 activity (stimulated with PI(3,5)P_2 or with ML2-SA1) increases with increasing, that is less acidic luminal pH. This differs from TRPML1 which shows maximal activity in highly acidic luminal pH (*Chen et al., 2017a*; *Dong et al., 2010*). These findings argue TRPML2 channel function is adapted to vesicles of only slightly acidic or neutral pH such as EE/RE rather than highly acidic LE/LY. The strong colocalization between TfR or Rab11 with TRPML2 confirms an important functional role of TRPML2 in RE (*Figure 2—figure supplement 2A–B*).

In summary, ML2-SA1 was found to be a potent and efficacious activator of both hTRPML2 and mTRPML2. The calculated EC_{50} values for human and mouse TRPML2 were 1.24 ± 0.12 µM and 2.38 ± 0.01 µM, respectively (*Figure 2F*; *Figure 2—figure supplement 3A*). ML2-SA1 shows high selectivity over h/mTRPML1 and h/mTRPML3 in both calcium imaging and endolysosomal patch-

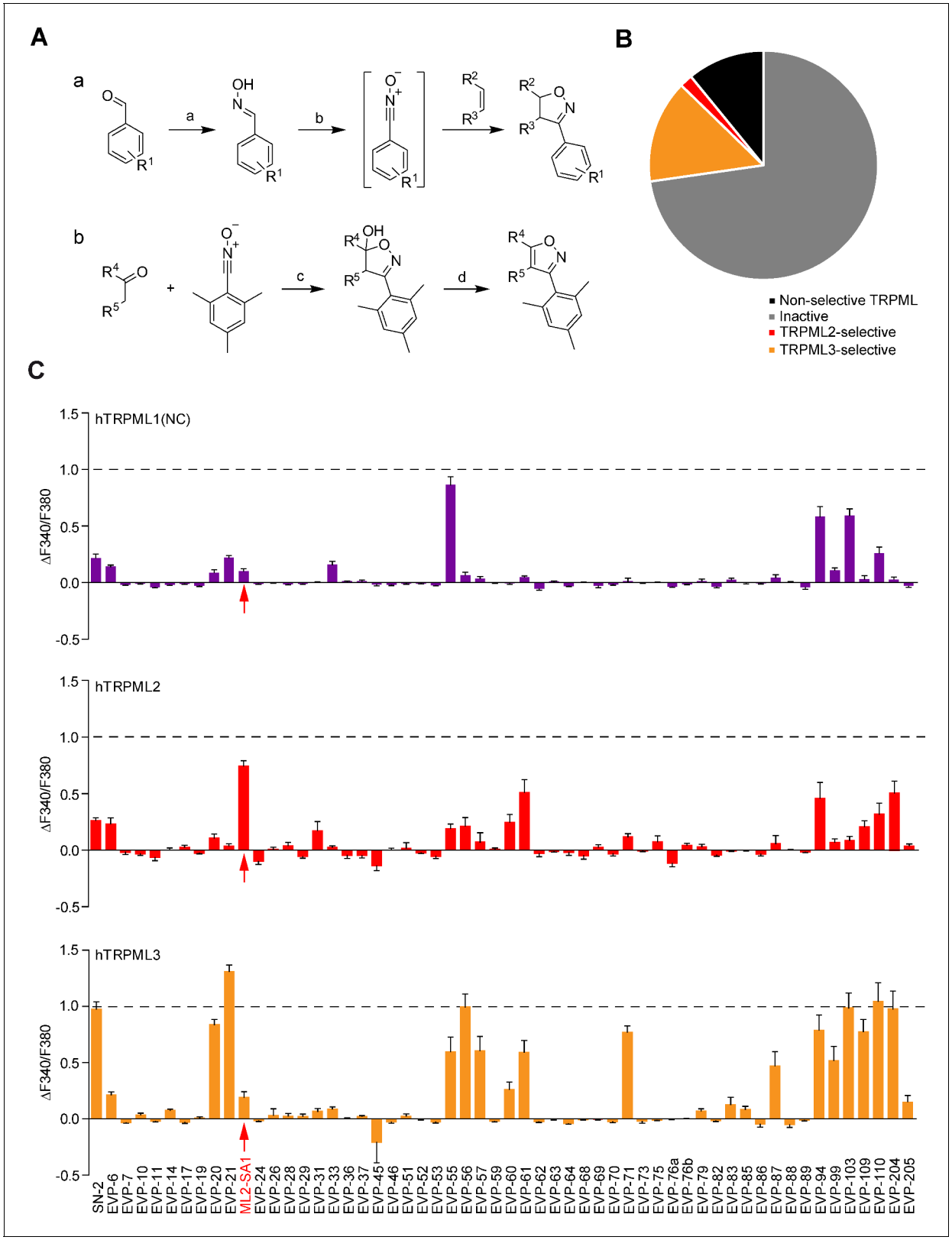

Figure 1. Chemical synthesis strategies and functional evaluation of SN-2 analogous compounds using calcium imaging. (**A**) Shown are synthesis strategies a and b used to generate most of the SN-2 analogous compounds shown in Suppl. ***Figure 1***. R^1 = alkyl/ halogen/nitro/ methoxy; R^2 / R^3 = (cyclo)alkyl/phenyl/ hydroxyalkyl; R^4 / R^5=alkyl/ phenyl / (hetero)cycles; **a**) H_2N-OH • HCl (1.5 eq.), NaOH (3 eq.), H_2O:EtOH (1:1), 0°C - rt, 18 hr; **b**) PIFA (1.2 eq.), alkene (1.5 eq.), H_2O:MeOH (1:2), rt, 1–24 hr; **c**) ketone (2 eq.), LDA (2 eq.), THF, −78°C, 2 hr, mesitonitrile oxide, −78°C - rt, 2–15 hr; **d**)

Figure 1 continued on next page

Figure 1 continued

Na_2CO_3, MeOH:H_2O (2:1), 95°C, 2 hr. (**B**) Cartoon showing schematically the fractions of inactive, non-selective TRPML activating, TRPML2-selective, and TRPML3-selective agonists (total number = 55). (**C**) Fura-2 calcium imaging results showing the effect of SN-2 and its analogues (10 μM) on hTRPML1(NC)-YFP, hTRPML2-YFP, and hTRPML3-YFP transfected HEK293 cells. Mean values normalized to basal (200 s after compound application)± SEM of up to >100 independent experiments with 3–10 cells per experiment are shown.

DOI: https://doi.org/10.7554/eLife.39720.002

The following figure supplements are available for figure 1:

Figure supplement 1. Structures of SN-2 analogues.

DOI: https://doi.org/10.7554/eLife.39720.003

Figure supplement 2. Structures of SF-51/ML-SA1 analogues.

DOI: https://doi.org/10.7554/eLife.39720.004

Figure supplement 3. Chemical synthesis strategies and functional evaluation of SF-51/ML-SA1-analogous compounds using calcium imaging.

DOI: https://doi.org/10.7554/eLife.39720.005

clamp experiments and it does not activate TPC1 nor TPC2 (***Figure 1***; ***Figure 2***; ***Figure 2—figure supplement 3B–F***).

Molecular modeling of ML2-SA1 binding

Several recent papers have provided in-depth information on the structures of TRPML1 and TRPML3 channels (***Schmiege et al., 2017***; ***Chen et al., 2017b***; ***Hirschi et al., 2017***). ***Schmiege et al., 2017*** found that a hydrophobic cavity created by I468 and F465 of PH1 (pore helix 1), F428, C429, V432 and Y436 of S5, F505 and F513 of S6, and Y499 and Y507 of S6 in the neighboring subunit, tightly accommodates ML-SA1 (***Figure 3A***). In a molecular modeling approach using these recently published structures of TRPML1 and TRPML3 as a basis, we simulated the binding of ML-SA1 as well as ML2-SA1 to hTRPML1 and hTRPML2 (***Figure 3***; ***Figure 3—figure supplement 1***). Complete 3D models of the open conformation of hTRPML1 and hTRPML2 were constructed and used for ligand docking analysis. Amino acids differing between hTRPML1 and hTRPML2 are colored green (***Figure 3B–D***). Based on this model, ML2-SA1 (both enantiomers are described, one in ***Figure 3—figure supplement 1***) is predicted to bind to the same binding pocket as ML-SA1 as observed in the cryo-EM structure of hTRPML1 (***Figure 3A–B***). Six amino acids (A422, A424, G425, A453, V460, and I498) in this pocket are unique to hTRPML2 (highlighted in green; ***Figure 3C–D***). The orientation of ML2-SA1 in the binding pocket of hTRPML2 with the highest docking score is shown in ***Figure 3C***. The dichlorophenyl ring shows favorable π-stacking interaction with F502 whereas the polar isoxazole ring is located near the side chain OH-groups of Y428 and Y496. The hydrophobic norbornane ring is interacting with G425 and Y428. Other possible orientations of ML2-SA1 binding to hTRPML2 are shown in ***Figure 3—figure supplement 1C–D***). The observed binding mode of ML2-SA1 at hTRPML1 is different and appears to be energetically less favorable compared to hTRPML2 due to the observed amino acid substitutions in the predicted binding cavity (***Figure 3D***). We subsequently replaced each of the six amino acids that are unique to the predicted hTRPML2 binding pocket with the respective amino acids of hTRPML1. We analysed these mutant isoforms first in calcium imaging experiments where we found the strongest reduction of the ML2-SA1 effect in G425A (***Figure 3E***). In the next step, we performed endolysosomal patch-clamp experiments with this mutant. Mutation of G425 to alanine was found to selectively abrogate the effect of ML2-SA1, while ML-SA1 was still able to activate G425A to a degree not significantly different from WT (***Figure 3E–F***). G425 is close to the norbornane ring of ML2-SA1 (minimum distance 3.6 Å) docked to hTRPML2 and substitution to alanine is unfavorable for this binding mode (***Figure 3C***). The experimental data corroborate binding of ML2-SA1 to the ML-SA1 binding pocket and confirm a critical role of G425 in mediating ML2-SA1 selectivity.

Effect of ML2-SA1 on endogenous TRPML2 channel activity in organelles isolated from LPS-stimulated macrophages

In macrophages significant TRPML2 channel expression is found only after stimulation with LPS, as demonstrated previously by qRT-PCR and western blot analysis (***Sun et al., 2015***). We confirmed this finding by qRT-PCR and endolysosomal patch-clamping, revealing that only after several hours of LPS treatment, robust endogenous TRPML2 channel expression and activity were detectable

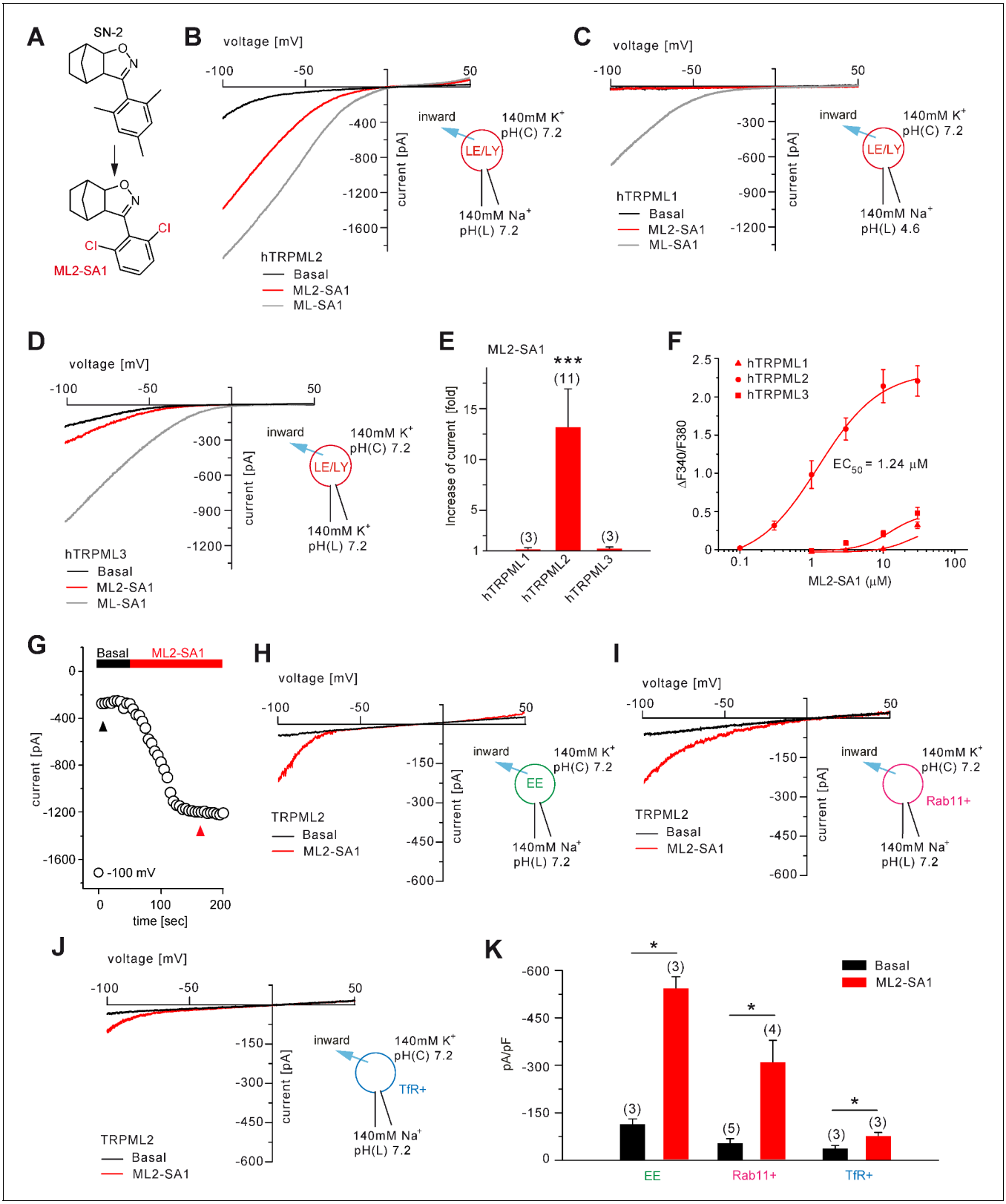

Figure 2. Effect of ML2-SA1 on TRPML channels. (**A**) Cartoon depicting chemical structures of SN-2 and ML2-SA1. (**B**) Representative ML2-SA1 or ML-SA1 (10 μM) elicited currents from YM201636-enlarged LE/LY isolated from hTRPML2 expressing HEK293 cells. (**C–D**) Representative ML2-SA1 or ML-SA1 (10 μM) elicited currents from YM201636-enlarged LE/LY isolated from hTRPML1 or hTRPML3 expressing HEK293 cells. (**E**) Statistical summary of ML2-SA1 data as shown in B-D as fold increase compared to the respective basal currents in LE/LY. Shown are mean values ± SEM at −100 mV of n

Figure 2 continued on next page

Figure 2 continued

independent experiments as indicated, each. (**F**) Dose-response curves obtained from fura-2 calcium imaging experiments with hTRPML1(NC), hTRPML2, and hTRPML3 expressed in HEK293 cells and elicited with ML2-SA1 at varying concentrations. The calculated EC_{50} value for hTRPML2 is: 1.24 ± 0.12 μM (mean ± SEM). (**G**) Time course of TRPML2 activation by ML2-SA1 taken from experiments as shown in B. Black and red arrows indicate time points for basal and ML2-SA1 induced TRPML2 activity that were used for the IV relationship. (**H–J**) Representative basal and ML2-SA1 (10 μM) elicited currents from Wort./Lat.B-enlarged EE, from vacuolin-enlarged Rab11+, or form TfR+ vesicles isolated from hTRPML2 expressing HEK293 cells. (**K**) Statistical summary of data as shown in G-I. * indicates p<0.05, ** indicates p<0.01, *** indicates p<0.001, ***Figure 2E***, one-way ANOVA test followed by Tukey's post-hoc test, ***Figure 2J***, paired t-test.

DOI: https://doi.org/10.7554/eLife.39720.006

The following figure supplements are available for figure 2:

Figure supplement 1. Effect of ML2-SA1 on TRPML2 under different pH conditions.

DOI: https://doi.org/10.7554/eLife.39720.007

Figure supplement 2. Co-transfection of HEK293 cells with fluorescently labelled TRPML2 and vesicle-specific markers of the endolysosomal system.

DOI: https://doi.org/10.7554/eLife.39720.008

Figure supplement 3. DRC of ML2-SA1 effect on mTRPML2, effects of ML2-SA1, SN2, and ML-SA1 on mTRPML channel isoforms, and cytotoxicity of ML2-SA1.

DOI: https://doi.org/10.7554/eLife.39720.009

(***Figure 4A–G***). In LPS-stimulated bone marrow-derived macrophages (BMDMΦ) ML2-SA1-induced currents were detectable in Tf-Alexa555 loaded, vacuolin-enlarged vesicles, while no significant TRPML2 channel activity could be detected in non-LPS stimulated BMDMΦ Tf+ vesicles (***Figure 4A–B***). Currents measured in BMDMΦ LE/LY with ML2-SA1 after LPS-stimulation were smaller than currents measured in Tf+ loaded vesicles (***Figure 4C–D***). In contrast, in LE/LY isolated from alveolar macrophages (AMΦ), TRPML2 currents elicited with ML2-SA1 were larger on average than in BMDMΦ (***Figure 4E–F***). These data confirm that ML2-SA1 elicits robust TRPML2 currents in endogenously expressing cells.

Effect of selective TRPML2 activation on CCL2 secretion

To evaluate effects of the novel TRPML2 channel agonist on chemokine secretion from macrophages, we performed experiments based on the results recently provided by ***Sun et al. (2015)*** (***Figure 5A***). We found that incubation with ML2-SA1 significantly increased secretion of the chemokine CCL2 from BMDMΦ, both after 4 hr and 8 hr of LPS treatment (***Figure 5A***). Importantly, ML2-SA1 did not induce CCL2 secretion in unstimulated BMDMΦ. Furthermore, CCL2 secretion was severely reduced in $TRPML2^{-/-}$ BMDMΦ and ML2-SA1 showed no further increase of CCL2 secretion in the $TRPML2^{-/-}$ BMDMΦ, corroborating the specificity of the agonist (***Figure 5A***). To characterise the pathway of ML2-SA1-induced CCL2 secretion from macrophages, we performed lysosomal exocytosis and Tf trafficking experiments to distinguish between LE/LY and EE/RE as possible secretion routes. Lysosomal exocytosis experiments revealed no significant effect of ML2-SA1 on lysosomal enzyme (beta-hexosaminidase) release (***Figure 5B***). In accordance with this, ML2-SA1 application did not result in translocation of LAMP1 to the plasma membrane (***Figure 5C***), arguing against LE/LY being involved in CCL2 secretion in BMDMΦ. These findings are supported by the LE/LY environment being less favorable for TRPML2 activity as outlined above. More favorable conditions are found in EE/RE compartments (less acid to neutral pH). In line with this, ML2-SA1 application resulted in a significant enhancement of Tf trafficking and recycling through EE/RE (***Figure 5D–E***). Taken together, these data argue for a TRPML2-dependent trafficking route of CCL2 from Golgi to EE/RE (***Figure 5F***).

ML2-SA1 promotes macrophage migration

To assess effects of ML2-SA1 on cell migration, we performed migration assays in a modified Boyden chamber setup (***Figure 6—figure supplement 1***). BMDMΦ in the presence or absence of LPS were seeded in the lower compartment of the chamber and exposed to different concentrations of ML2-SA1. LPS-stimulated, ML2-SA1 pre-treated BMDMΦ were able to significantly increase migration of untreated BMDMΦ through the transwell chamber, while LPS-stimulated BMDMΦ without ML2-SA1 pre-treatment (only DMSO) were not able to alter migration properties of untreated BMDMΦ. (***Figure 6A***). This is in accordance with the enhanced release of CCL2 by ML2-SA1, which

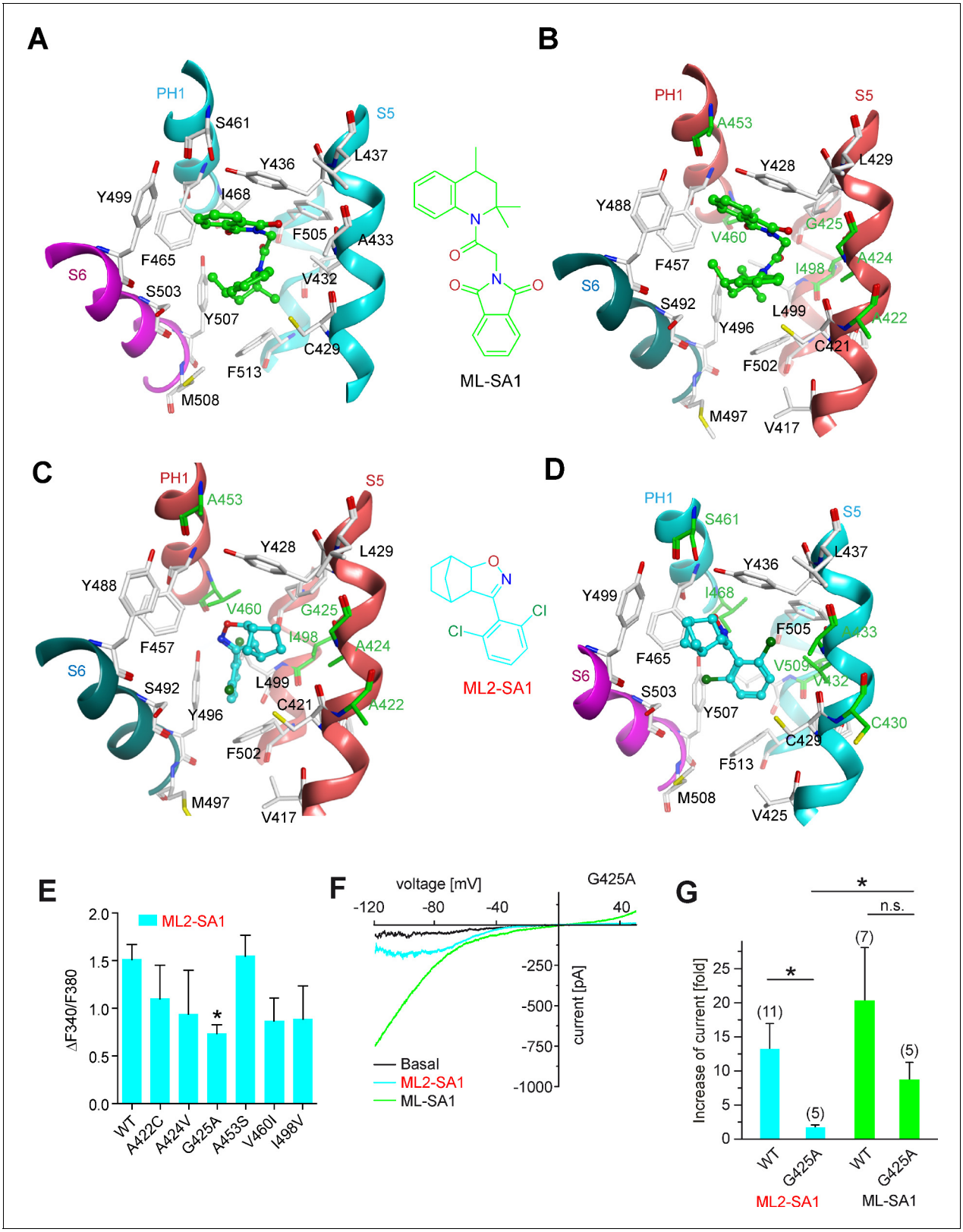

Figure 3. Molecular modeling of ML2-SA1 and ML-SA1 binding. (**A**) Binding mode of ML-SA1 (green colored carbon atoms) at hTRPML1, showing residues within 5 Å of ML-SA1, as observed in one of the four identical binding pockets of the cryo-EM structure (PDB ID: 5WJ9). The S6 helix of monomer A of hTRPML1 is colored magenta, the PH1 and S5 helices of monomer B are colored cyan. (**B**) Binding mode of ML-SA1 (green colored carbon atoms) at hTRPML2 (homology model generated with MODELLER) as predicted by the ligand docking. Only residues within 5 Å of ML-SA1 in

Figure 3 continued on next page

Figure 3 continued

one of the four identical binding pockets are displayed. The S6 helix of monomer A of hTRPML2 is colored petrol blue, the PH1 and S5 helices of monomer B are colored salmon. Amino acid residues that are different in hTRPML1 and hTRPML2 are colored green (**C**) Binding mode of one ML2-SA1 enantiomer (cyan colored carbon atoms; 3a*S*, 4*S*, 7*R*, 7a*S*) at hTRPML2 as predicted by ligand docking. Only residues within 5 Å of ML2-SA1 in one of the four identical binding pockets are displayed (same coloring and representation style as in ***Figure 3B***). Binding of the other ML2-SA1 enantiomer (3a*R*, 4*R*, 7*S*, 7a*R*) resulted in a similar binding mode that is shown in ***Figure 3—figure supplement 1B*** (**D**) Binding mode of one ML2-SA1 enantiomer (cyan colored carbon atoms; 3a*S*, 4*S*, 7*R*, 7a*S*) at hTRPML1 as predicted by ligand docking. Only residues within 5 Å of ML2-SA1 in one of the four identical binding pockets are displayed (same coloring and representation style as in ***Figure 3a***). (**E**) Fura-2 calcium imaging results showing the effect of ML2-SA1 (10 μM) on hTRPML2-YFP WT and mutant transfected HEK293 cells. Mean values normalized to basal (120 s after compound application)± SEM of at least three independent experiments, each. * indicates p<0.05, one-way ANOVA, followed by Dunnet post-hoc test. (**F**) Representative ML2-SA1 or ML-SA1 (10 μM) elicited currents from YM201636-enlarged LE/LY isolated from hTRPML2(G425A) expressing HEK293 cells. (**G**) Statistical summary of data as shown in F as fold increase compared to the respective basal currents in LE/LY. Shown are mean values ± SEM at −100 mV of at n independent experiments as indicated. * indicates p<0.05, unpaired t-test.

DOI: https://doi.org/10.7554/eLife.39720.010

The following figure supplement is available for figure 3:

Figure supplement 1. Additional molecular modeling of ML2-SA1 and ML-SA1 binding.

DOI: https://doi.org/10.7554/eLife.39720.011

serves as chemoattractant for untreated BMDMΦ. To exclude a chemotactic effect of the compounds themselves, we used a classical Boyden chamber setup without cells in the lower compartment. Yet, neither LPS nor ML2-SA1 alone were able to significantly enhance BMDMΦ migration, while supplementation of recombinant CCL2 led to a substantial increase in BMDMΦ migration (***Figure 6B***; ***Figure 6—figure supplement 2A–B***). Overall, these data suggest that ML2-SA1 is able to induce CCL2 secretion selectively in TRPML2-expressing macrophages, thus serving as chemoattractant to recruit more macrophages.

Discussion

We describe here a novel, isoform-selective activator of the TRPML2 channel and describe how TRPML2 activation enhances endosomal trafficking to induce inflammatory mediator release in LPS-stimulated macrophages. Until now, selective activators for TRPML2 had not been available. In an effort to identify such selective activators we synthesized >80 chemical compounds by systematic variation of the known lead structures SN-2 and SF-51/ML-SA1 (***Grimm et al., 2010***; ***Shen et al., 2012***), generating a library of analogues of sufficient size to deduce structure-activity relationships. In the ML-SA1 series, improved TRPML2 activation was achieved by modification of the length of the acyl spacer, but the resulting selective activators were of only intermediate efficacy and potency. By contrast, the activator ML2-SA1 from the series of norbornene-derived isoxazolines (based on SN-2) is characterized by high TRPML2 subtype selectivity as well as high efficacy and potency, rendering this new small molecule a valuable compound for future studies on this ion channel (***Supplementary file 2***). Molecular modeling data support specific binding of ML2-SA1 to the pore region of the channel, as observed for ML-SA1. The binding orientation of ML-SA1 at hTRPML2 was found to be similar to the experimentally observed binding to hTRPML1 (***Schmiege et al., 2017***) which is in agreement with nonselective activation. In contrast, the binding orientation of docked ML2-SA1 at hTRPML1 differs from that found for hTRPML2, suggesting a plausible rationale for its selectivity. In an experimental approach where we investigated the functional consequences of point mutations in hTRPML2 with the endolysosomal patch-clamp technique we found that in mutant G425A activation by ML2-SA1 is selectively lost, while activation by ML-SA1 is preserved, indicating that this amino acid is highly critical for the selective effect of ML2-SA1 on TRPML2.

Sun et al. (2015) have recently shown that the levels of TRPML2 are strongly upregulated in macrophages upon TLR4 (toll-like receptor) activation (***Supplementary file 2***). Thus, treatment with LPS was found to lead to TRPML2 upregulation in, for example microglia, peritoneal macrophages, bone marrow derived macrophages, or alveolar macrophages (***Sun et al., 2015***). The authors further found that the translation and secretion of several chemokines such as CCL2 was reduced in TRPML2$^{-/-}$ mice, and concluded that TRPML2 might play a role in the regulation of trafficking and/or

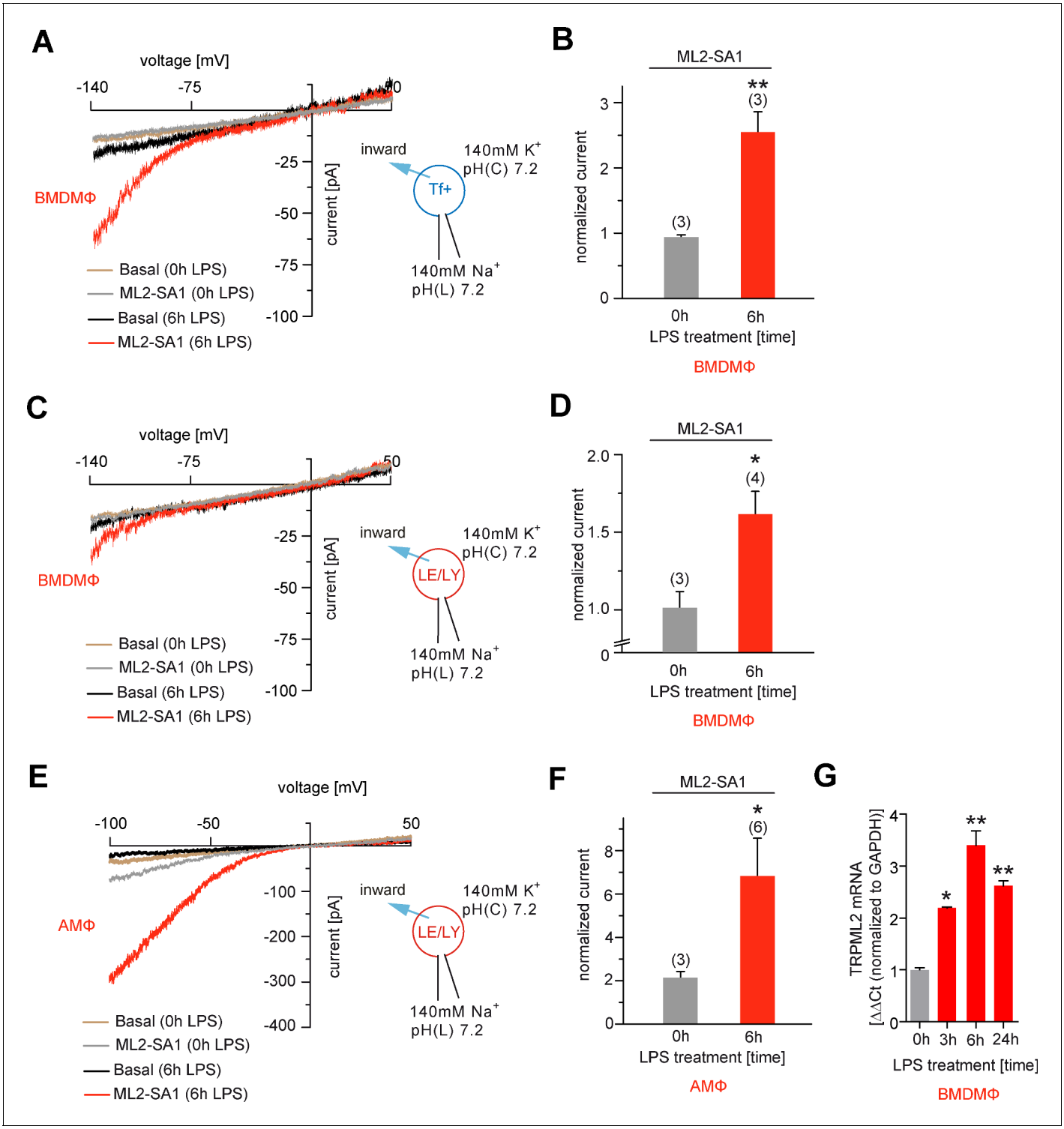

Figure 4. Effect of ML2-SA1 on channel currents in endolysosomal organelles isolated from different primary mouse macrophages. (**A**) Representative currents from vacuolin-enlarged/Tf+ vesicles isolated from murine (LPS 6 hr or LPS 0 hr) primary WT BMDMΦ, basal or elicited by an application of 10 µM ML2-SA1. All currents are normalized to basal current without ML2-SA1. (**B**) Statistical summary of data shown in A. (**C**) Representative currents from YM201636-enlarged LE/LY isolated from murine (LPS 6 hr or LPS 0 hr) primary WT bone marrow macrophages (BMDMΦ), basal or elicited by an application of 10 µM ML2-SA1. (**D**) Statistical summary of data shown in C. (**E**) Representative currents from YM201636-enlarged LE/LY isolated from murine (LPS 6 hr or LPS 0 hr) primary WT alveolar macrophages (AMΦ), basal or elicited by an application of 10 µM ML2-SA1. (**F**) Statistical summary of data shown in E. * indicates $p<0.05$, ** indicates $p<0.01$, Student's t test, unpaired. (**G**) qPCR data showing levels of TRPML2 expression after 3, 6, and 24 hr LPS treatment compared to untreated (0 hr). * indicates $p<0.05$, ** indicates $p<0.01$, one-way ANOVA test followed by Tukey's post-hoc test.

Figure 4 continued on next page

Figure 4 continued

DOI: https://doi.org/10.7554/eLife.39720.012

secretion of these chemokines. However, it remained unclear whether TRPML2 is directly involved in these processes and whether activation of TRPML2 channel activity would show increased release.

Here, we present data strongly supporting a direct involvement of TRPML2, as direct stimulation of TRPML2 with ML2-SA1 leads to an increase in CCL2 secretion from macrophages. Using the specific TRPML2 agonist and the TRPML2$^{-/-}$ knockout mouse model as control, we demonstrate a positive relationship between TRPML2 activity and CCL2 secretion. Using the endolysosomal patch-clamp technique we demonstrate that TRPML2 is present in LE/LY and EE as well as in Rab11+ and TfR+/Tf+ vesicles (***Supplementary file 2***). However, early endosomes including RE provide more favorable activation conditions for TRPML2 than LE/LY due to their less acidic/neutral luminal pH. In accordance with this, TRPML2 currents elicited with ML2-SA1 in LE/LY isolated from endogenously expressing BMDMΦ were smaller than currents in Tf+ vesicles. In addition, no evidence was found that ML2-SA1 can promote lysosomal exocytosis, while ionomycin or ML-SA1 were able to increase the release of beta-hexosaminidase as previously reported (***Samie et al., 2013***). The subcellular distribution of LAMP1 did also not change during ML2-SA1 treatment and no translocation to the PM was observed. In contrast, ML2-SA1 application was found to significantly promote Tf trafficking through the early/recycling endosomal compartment, arguing for a role of TRPML2 in CCL2 release via the early/recycling endosomal pathway (***Figure 5F***).

Loss of function mutations in the TRPML2-related channel TRPML1 result in lysosomal storage and endolysosomal trafficking defects underlying the neurodegenerative disease mucolipidosis type IV (***Bach, 2001***; ***Pryor et al., 2006***; ***Chen et al., 2014***). Mechanistically, it was postulated that loss of TRPML1 impairs lysosomal exocytosis (***LaPlante et al., 2006***). It was also suggested that TRPML1 is required for lysosomal pH regulation (***Soyombo et al., 2006***) and for vesicle fusion (***Venkatachalam et al., 2013***) while, very recently, data have been presented, supporting that TRPML1 may regulate lysosomal fission (***Chen et al., 2017a***). A further interesting finding has been presented by ***Park et al. (2016)***, suggesting that, in secretory cells, a major role for TRPML1 is to guard against unintended, pathological fusion of lysosomes with other intracellular organelles, for example secretory vesicles. TRPML1 has also been attributed to mediate lysosomal trafficking via Ca^{2+}-dependent motor protein recruitment, its activity favoring retrograde lysosomal movement (***Vergarajauregui et al., 2009***; ***Li et al., 2016***).

Like TRPML1, TRPML3 was also suggested to regulate membrane trafficking. In particular, it was found to regulate trafficking of early endosomes and to affect endocytosis (***Kim et al., 2009***). ***Lelouvier and Puertollano (2011)*** further presented data showing that TRPML3 is required for proper calcium homeostasis in the endosomal pathway and that impairment of TRPML3 function leads to defective endosomal acidification and defective membrane trafficking. Surprisingly, the authors found increased endosomal fusion after depletion of TRPML3. Recently, ***Miao et al. (2015)*** showed that TRPML3 activation, upon neutralization of lysosomal pH, mediates efflux of Ca^{2+} ions from lysosomes, which in turn induces lysosome exocytosis. TRPML3 is normally inactive in highly acidic lysosomes, in contrast to early/recycling endosomes with more neutral pH, but when the pH in the lumen of the lysosome is neutralized, TRPML3 becomes activated, releases Ca^{2+} into the cytosol, which in turn triggers spontaneous exocytosis of the lysosome and its contents.

TRPML2 has been suggested to play a role in the regulation of the Arf6-associated pathway and, more specifically, in the trafficking of GPI-APs (***Karacsonyi et al., 2007***). Arf6 has been implicated in the regulation of endocytosis as well as endocytic recycling and cytoskeleton remodeling. More recently, TRPML2 has been found to increase trafficking efficiency of endocytosed viruses (***Rinkenberger and Schoggins, 2018***). Furthermore, we are showing here that TRPML2 is, like its relatives TRPML1 and 3, Ca^{2+} permeable (***Figure 2—figure supplement 1C***).

Taken together, these findings imply that all three TRPML channels can impact intracellular trafficking processes while the mechanisms how they affect trafficking might differ. While it is likely, based on the available data, that the effect of TRPML2 knockout/activation on CCL2 trafficking and release is occurring at the level of EE/RE, it remains to be further established where along this pathway the effect takes place. Possible scenarios might be: fusion of Golgi vesicles with RE, fission from

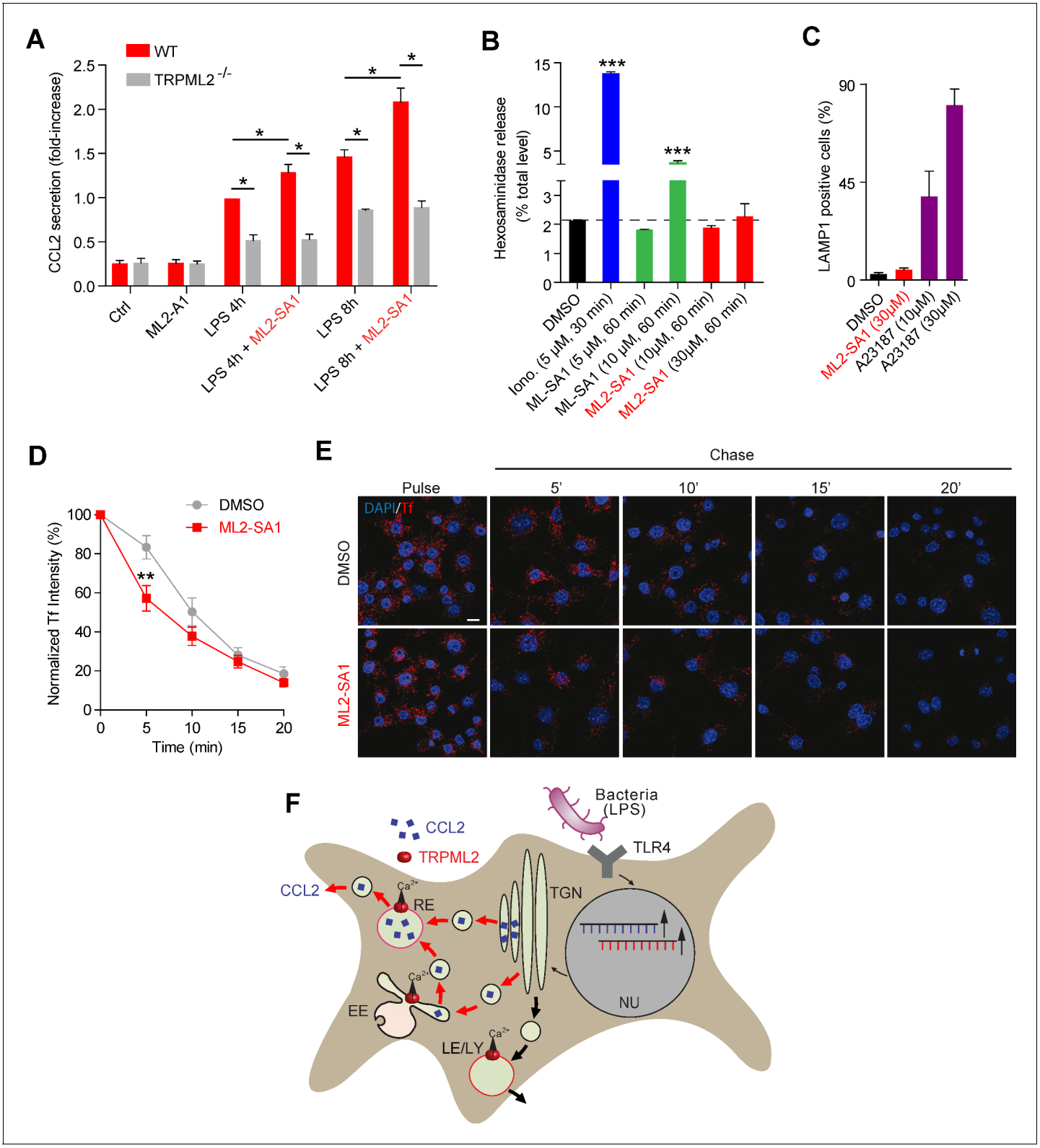

Figure 5. Effect of ML2-SA1 on chemokine release from primary mouse macrophages. (**A**) Shown are data obtained from primary WT and TRPML2$^{-/-}$ mouse bone marrow macrophages (BMDMΦ) with and without LPS treatment for 4 hr and 8 hr, respectively. The fraction treated with LPS and 10 µM ML2-SA1 showed significantly increased CCL2 secretion compared to WT controls treated with LPS only. TRPML2$^{-/-}$ cells displayed strongly reduced CCL2 secretion. Shown are normalized mean values ± SEM of 5 mice each. * indicates $p<0.05$, Student's t test, unpaired. (**B**) Lysosomal exocytosis assay showing the increase in beta-hexosaminidase release upon stimulation with either ionomycin, ML-SA1, or ML2-SA1 (conc. as indicated) from LPS (6 hr)

Figure 5 continued on next page

Figure 5 continued

stimulated BMDMΦ. *** indicates p<0.001, one-way ANOVA test followed by Tukey's post-hoc test. (**C**) Lysosomal exocytosis assay by flow cytometry showing the percentage of cells which show an increase in LAMP1 fluorescence on the plasma membrane. Cells were treated with DMSO, calcium ionophore A23187 (calcimycin), and 30 μM ML2-SA1. (**D–E**) Recycling endosome assay showing the decrease of Tf mean fluorescence in LPS stimulated RAW264.7 cells, treated with either DMSO or 30 μM ML2-SA1. Scale bar (identical for all images)=10 μm. Plot shows the normalized Tf intensity (shown is the average of 3 independent experiments, each). **p<0.01, two-way ANOVA, repeated measures, followed by Bonferroni post-hoc test. (**F**) Cartoon showing organelles with functional TRPML2 expression as confirmed by endolysosomal patch-clamp analysis (EE, RE, LE/LY). CCL2 (MCP-1) is hypothesized to be trafficked and secreted via the EE/RE pathway, based on the observation that ML2-SA1 promotes Tf trafficking in the EE/RE compartment, while no effect on lysosomal exocytosis was found. No secretory vesicles are reported to exist in macrophages.

DOI: https://doi.org/10.7554/eLife.39720.013

RE, fusion of Golgi vesicles with EE, fission from EE, fusion of EE-derived vesicles with the RE (***Figure 5F***).

Functionally, we found that ML2-SA1 promotes migration of untreated macrophages towards LPS-treated macrophages. This suggests that TRPML2-dependent CCL2 release is enhancing the inflammatory response by recruiting innate immune cells to the site of inflammation. This is in accordance with the results presented by ***Sun et al. (2015)*** who found that macrophage migration is impaired in vivo in the absence of TRPML2.

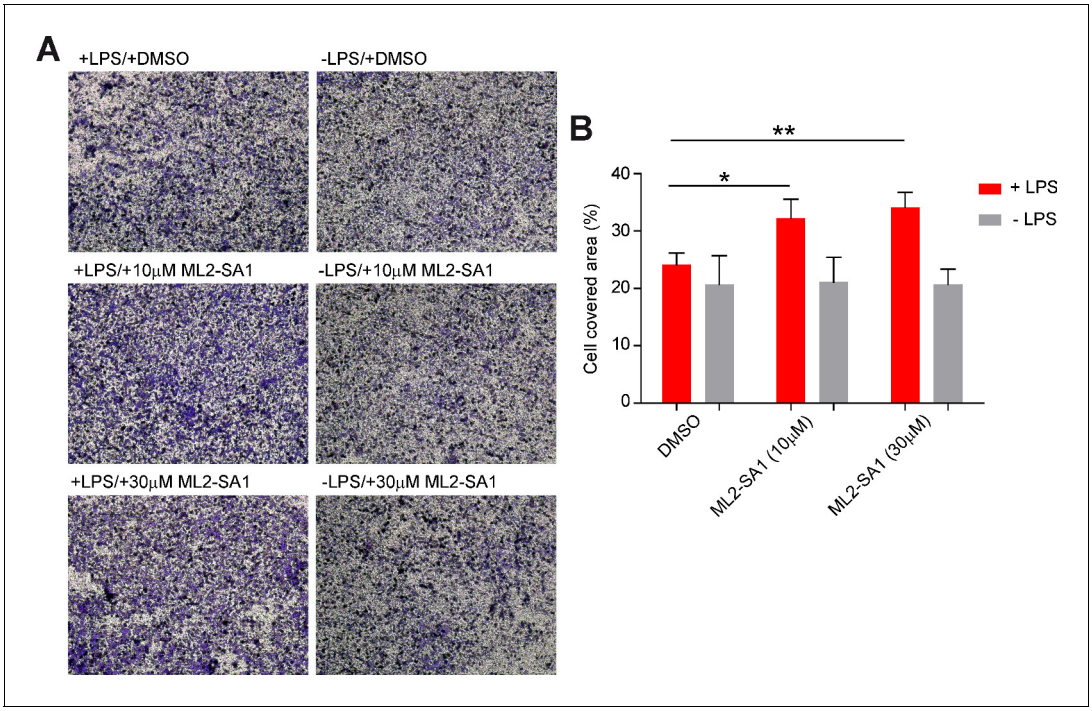

Figure 6. Effect of ML2-SA1 on macrophage migration. (**A**) Shown are representative images obtained from a modified Boyden chamber experiment. Images show fixed and crystal violet stained BMDMΦ after 3 hr migration through a transwell chamber along a chemotactic gradient created by BMDMΦ in the lower compartment. Indicated treatments refer to treatment of the cells in the lower compartment. (**B**) Quantification of migration in the modified Boyden chamber setup (**A**) shows a significant increase in migration when LPS pre-treated cells in the lower compartment were subjected to 10 or 30 μM ML2-SA1. Shown are mean values ± SEM of 4 independent experiments. * indicates p<0.05, ** indicates p<0.01, repeated measures, one-way ANOVA with Greenhouse-Geisser correction, followed by Dunnet post-hoc test.

DOI: https://doi.org/10.7554/eLife.39720.014

The following figure supplements are available for figure 6:

Figure supplement 1. Modified and classical Boyden chamber setup.

DOI: https://doi.org/10.7554/eLife.39720.015

Figure supplement 2. Migration assay without cells in the lower compartment of the classical Boyden chamber.

DOI: https://doi.org/10.7554/eLife.39720.016

CCL2 is known to be a key chemokine regulating migration and infiltration of monocytes/macrophages (**Deshmane et al., 2009**). Since CCL2 is implicated in the pathogenesis of diseases characterized by infiltrates containing macrophages like psoriasis, rheumatoid arthritis, multiple sclerosis, and atherosclerosis (**Deshmane et al., 2009**; **Xia and Sui, 2009**; **Daly and Rollins, 2003**), we postulate that TRPML2 may be an attractive novel target for the treatment of such innate immunity-related inflammatory diseases.

Materials and methods

Key resources table

Designation	Source or reference	Identifiers	Additional information
HEK293	DSMZ	ACC 305	
HEK 293 stable stably expressing TRPML3-YFP	**Grimm et al. (2010)**; PMID: 20189104		
HEK 293 stable stably expressing TRPML1-YFP	**Chen et al. (2014)**, PMID: 25119295		
TRPML1 (encoded by the *Mcoln1* gene) KO mouse; Mcoln1tm1Sasl, C57BL/6	**Venugopal et al. (2007)**; PMID: 17924347	MGI ID: 3794204	
TRPML2 (encoded by the *Mcoln2* gene) KO mouse; C57BL/6	**Sun et al. (2015)**; PMID: 26432893	MGI: 1915529	
TRPML3 (encoded by the *Mcoln3* gene) KO mouse; Mcoln3tm1.1Hels, FVB/NJ	**Jörs et al. (2010)**; PMID: 21179200	MGI ID: 5319089	
anti-LAMP-1 (1D4B) (rat monoclonal)	Santa Cruz	Cat#A-11006; RRID: AB_2134495	(1:100)
Goat anti-Rat IgG (H + L) Secondary Antibody, Alexa Fluor 488	ThermoFisher	Cat#sc-19992; RRID: AB_2534074	(1:1000)
mcherry-Transferrin Receptor 20 (plasmid)	N/A	Addgene Plasmid #55144	
DsRed-Rab11 (plasmid)	**Choudhury et al. (2002)**; PMID: 12070301	Addgene Plasmid #12679	
TRPML1-YFP (plasmid)	**Grimm et al. (2010)**, PMID: 20189104		
TRPML2-YFP (plasmid)	**Grimm et al. (2010)**, PMID: 20189104		
TRPML3-YFP (plasmid)	**Grimm et al. (2010)**, PMID: 20189104		
Quikchange primers for TRPML2:YFP A422C	this paper		forward: CTTCGGTTTTGTTGTTGTG CTGGTATGATTTATCTGGG reverse: CCCAGATAAATCATACCAGC ACAACAACAAAACCGAAG
Quikchange primers for TRPML2:YFP A424V	this paper		forward: CGGTTTTGTGCTTG TGTTGGTATGATTTATCTGGGTTACAC reverse: GTGTAACCCAGATAAATCAT ACCAACACAAGCACAAAACCG
Quikchange primers for TRPML2:YFP G425A	this paper		forward: CGGTTTTGTGCTTGT GCTGCTATGATTTATCTGGGTTACAC reverse: GTGTAACCCAGATAAATCA TAGCAGCACAAGCACAAAACCG
Quikchange primers for TRPML2:YFP A453S	this paper		forward: CTGAACACAGTTTCTG AGTGTCTGTTTTCTCTGG reverse: CCAGAGAAAACAGACA CTCAGAAACTGTGTTCAG

Continued on next page

Continued

Designation	Source or reference	Identifiers	Additional information
Quikchange primers for TRPML2:YFP V460I	this paper		forward: TGTCTGTTTTCTCTGATCA ACGGTGATGACATG reverse: CATGTCATCACCGTTGATC AGAGAAAACAGACA
Quikchange primers for TRPML2:YFP I498V	this paper		forward: CCTTCATCAGCCTTTTTATATATA TGGTTCTCAGTCTTTTTATTGC reverse: GCAATAAAAAGACTGAGAACCA TATATATAAAAAGGCTGATGAAGG
qPCR Primer for TRPML1 (NM_053177)	www.pga.mgh.harvard.edu/primerbank	PrimerBankID: 16716462 c2	forward: GCCTTGGGCCAATGGATCA reverse: CCCTTGGATCAATGTCAAAGGTA
qPCR Primer for TRPML2 (NM_026656)	this paper		forward: AATTTGGGGTCACGTCATGC reverse: AGAATCGAGAGACGCCATCG
qPCR Primer for TRPML3 (NM_134160)	this paper		forward: GAGTTACCTGGTGTGGCTGT reverse: TGCTGGTAGTGCTTAATTGTTTCG
qPCR Primer for HPRT (NM_013556)	***Hruz et al. (2011)***; PMID: 21418615	N/A	forward: GCTCGAGATGTCATGAAGGAGAT reverse: AAAGAACTTATAGCCCCCCTTGA
Lipopolysaccharides (LPS) from Escherichia coli O26:B6	Sigma-Aldrich	Cat#L2762	
Lipopolysaccharides (LPS) from Escherichia coli O111:B4	Sigma-Aldrich	Cat#L4391	
Fura-2, AM, cell permeant	ThermoFisher	Cat#F1201	
Mouse M-CSF, premium grade	Miltenyi Biotech	Cat#130-101-703	
Transferrin from human serum, Alexa FluorTM 546-conjugated	TermoFisher	Cat# T23364	
Transferrin from human serum, Alexa FluorTM 555-conjugated	Thermo Fisher	Cat#T35352	
JE/MCP-1/CCL2 from mouse, recombinant	Sigma-Aldrich	Cat# SRP4207	
YM201636	Chemdea	Cat#CD0181	
MLSA-1	Sigma-Aldrich	Cat#SML0627	
PI(3,5)P2	AG Scientific	Cat#P-1123	
Wortmannin	Sigma-Aldrich	Cat#W1628	
LatrunculinB	Sigma-Aldrich	Cat#L5288	
Vacuolin	Santa Cruz	Cat# sc-216045	
Calcium ionophore A23187	Sigma-Aldrich	Cat#C7522	
4-Methylumbelliferyl N-acetyl-b-D-glucosaminide	Sigma-Aldrich	Cat#M2133	
RNeasy Plus Mini Kit	Qiagen	Cat# 74134	
RevertAid first strand cDNA synthesis Kit	ThermoScientific	Cat# K1621	
CD11b MicroBeads, human and mouse	Miltenyi Biotech	Cat#130-049-601	
QuikChange II Site-Directed Mutagenesis Kit	Agilent	Cat#200523	
Mouse/rat CCL2/ JE/MCP-1 Quantikine ELISA Kit	BioLegend	Cat#432707	
Origin8	OriginLab		
GraphPad Prism	GraphPad Software Inc.		

Endolysosomal patch-clamp and calcium imaging experiments

Whole-LE/LY and whole-EE recordings have been described previously in detail (*Chen et al., 2017a*; *Chen et al., 2017c*). In brief, for whole-LE/LY manual patch-clamp recordings, cells were treated with YM201636 (HEK293 cells: 800 nM o/n; macrophages: 800 nM 1 hr). For whole-EE manual patch-clamp recordings, cells were treated with a combination of 200 nM wortmannin and 10 nM latrunculin B (HEK293 cells: 10–15 min). Cells were treated with compounds at 37˚C and 5% CO_2. YM201636 was obtained from Chemdea (CD0181), wortmannin and latrunculin B from Sigma (W1628 and L5288), and vacuolin from Santa Cruz (sc-216045). Compounds were washed out before patch-clamp experimentation.

For other organelle patch-clamp recordings, HEK293 cells were transfected with the markers Rab11-DsRed or TfR-mCherry, respectively, and treated with 1 µM vacuolin o/n. Since macrophages could not be transfected with standard transfection protocols or by electroporation, cells were loaded with transferrin-Alexa555 and simultaneously treated with vacuolin for 1 hr to enlarge and visualize vesicles for patch-clamp.

Isolation-micropipettes were used to open up the plasma membrane, and push the enlarged vesicle of interest out of the cell. Afterwards, electrode-micropipettes were applied to patch-clamp the isolated vesicles.

Macrophages were used for experiments within 2–10 days after isolation. Mean capacitance values for Rab11+ vesicles isolated from HEK293 cells was 0.7 ± 0.2 (n = 6), for TfR+ vesicles (n = 3) 1.4 ± 0.3 pF, for EE (n = 10) 0.4 ± 0.1 pF, and for LE/LY (n = 51) 1.0 ± 0.2 pF. For LE/LY isolated from primary macrophages it was 0.8 ± 0.1 pF (n = 41), for Tf-loaded vesicles 1.3 ± 0.5 pF (n = 8). Currents were recorded using an EPC-10 patch-clamp amplifier (HEKA, Lambrecht, Germany) and PatchMaster acquisition software (HEKA). Data were digitized at 40 kHz and filtered at 2.8 kHz. Fast and slow capacitive transients were cancelled by the compensation circuit of the EPC-10 amplifier. Recording glass pipettes were polished and had a resistance of 4–8 MΩ. For all experiments, salt-agar bridges were used to connect the reference Ag-AgCl wire to the bath solution to minimize voltage offsets. Liquid junction potential was corrected. For the application of the lipids (A.G. Scientific) or small molecule agonists (ML2-SA1, ML-SA1), cytoplasmic solution was completely exchanged by cytoplasmic solution containing agonist. Unless otherwise stated, cytoplasmic solution contained 140 mM K-MSA, 5 mM KOH, 4 mM NaCl, 0.39 mM $CaCl_2$, 1 mM EGTA and 10 mM HEPES (pH was adjusted with KOH to 7.2). Luminal solution contained 140 mM Na-MSA, 5 mM K-MSA, 2 mM Ca-MSA 2 mM, 1 mM $CaCl_2$, 10 mM HEPES and 10 mM MES (pH was adjusted with NaOH to 7.2). For optimal conditions of TRPML1, luminal pH was adjusted to 4.6 and Na-MSA was used in the luminal solution. For optimal conditions of TRPML2, luminal pH was adjusted to 7.2 and Na-MSA was used in the luminal solution. For optimal conditions of TRPML3, luminal pH was adjusted to 7.2 and K-MSA was applied to replace Na-MSA in the luminal solution. In all experiments, 500 ms voltage ramps from −100 to +100 mV were applied every 5 s, holding potential at 0 mV. The current amplitudes at −100 mV were extracted from individual ramp current recordings. All statistical analysis was done using Origin8 software.

Calcium imaging experiments were performed using fura-2 as described previously (*Grimm et al., 2012a*). Briefly, HEK293 cells were plated onto glass coverslips, grown over night and transiently transfected with the respected cDNAs using TurboFect transfection reagent (Thermo Scientific). After 24–48 h cells were loaded for 1 hr with the fluorescent indicator fura2-AM (4 µM; Invitrogen) in a standard bath solution (SBS) containing (in mM) 138 NaCl, 6 KCl, 2 $MgCl_2$, 2 $CaCl_2$, 10 HEPES, and 5.5 D-glucose (adjusted to pH 7.4 with NaOH). Cells were washed in SBS for 30 min before measurement. Calcium imaging was performed using a monochromator-based imaging system (Polychrome IV mono-chromator, TILL Photonics).

Computational methods

Analysis of electron density map. The electron density maps for the cryo-electron microscopy structures of hTRPML1 and hTRPML3 in open agonist-bound form (PDB IDs: 5WJ9 and 6AYF, respectively) were downloaded from the Protein Data Bank (PDB; ww.rcsb.org) (*Berman et al., 2000*) and visualized in PyMOL (The PyMOL Molecular Graphics System, Version 1.7.4 Schrödinger, LLC). Homology modelling of TRPML2. The amino acid sequence of hTRPML2 was retrieved from UniProt

(*The UniProt Consortium, 2017*); Accession number: Q8IZK6-1) and a Blast (*Altschul et al., 1990*) search using BLOSUM62 matrix was performed against the PDB to find the closest homologues. Subsequently, sequence alignment of hTRPML2 to the top scored template, hTRPML3 (Sequence identity 59%), was conducted in MOE2012.10 (*Molecular Operating Environment (MOE)*, 2016.08; Chemical Computing Group Inc., 1010 Sherbooke St. West, Suite #910, Montreal, QC, Canada, H3A 2R7, 2016) and the alignment file was used to generate the homology model using MODELLER 9.11 (*Webb and Sali, 2014*). Ligand-bound homology models of hTRPML2 were finally built using the agonist-bound structure of hTRPML3 (PDB ID: 6AYF) and ranked according to their DOPE score (*Shen and Sali, 2006*). Molecular docking to hTRPML1 and −2. The ligands were prepared for docking using the LigPrep tool as implemented in Schrödinger's software (*Schrödinger Release 2017–1*: LigPrep, Schrödinger, LLC, New York, NY, 2017), where the two stereoisomers of ML2-SA1 were generated and energy minimized using the OPLS force field. Conformers of the prepared ligands were calculated with ConfGen using the default settings and allowing minimization of the output conformations.

Protein preparation. The cryo-electron microscopy structure of the open conformation of hTRPML1 in complex with ML-SA1 (PDB ID: 5WJ9) and the generated hTRPML2 homology model were prepared with Schrödinger's Protein Preparation Wizard (*Schrödinger Release 2017–1*: Schrödinger Suite 2017–1 Protein Preparation Wizard; Epik, Schrödinger, LLC, New York, NY, 2016; Impact, Schrödinger, LLC, New York, NY, 2016; Prime, Schrödinger, LLC, New York, NY, 2017): Hydrogen atoms were added and the H-bond network was subsequently optimized. The protonation states at pH 7.0 were predicted using the PROPKA tool in Schrödinger. The structures were finally subjected to a restrained energy minimization step using the OPLS2005 force field (RMSD of the atom displacement for terminating the minimization was 0.3 Å).

The receptor grid preparation for the docking procedure was carried out by assigning the agonist as the centroid of the grid box. The generated ligand conformers were docked into the proteins using Glide (*Small-Molecule Drug Discovery Suite 2017–1*: Glide, Schrödinger, LLC, New York, NY, 2017) in the Standard Precision mode. A total of 100 poses per ligand conformer were included in the post-docking minimization step and a maximum of 20 docking clusters were output for each ligand. Redocking of the ligand ML-SA1 into the hTRPML1 pocket gave a docking pose with root mean square deviation of 1.22 Å for the top-ranked solution (***Figure 3—figure supplement 1A***).

Cell culture of primary macrophages isolated from knockout and WT mice

For preparation of primary alveolar macrophages (AMΦ), mice were deeply anesthetized and euthanized by exsanguination. Afterwards, the trachea was carefully exposed and cannulated by inserting a 20 gauge catheter (B. Braun, cat. no. 4252110B). AMΦ were harvested by eight consecutive lung lavages with 1 ml of DPBS each. After a centrifugation step, cells were immediately collected and cultured in RPMI 1640 medium supplemented with 10% fetal bovine serum and 1% antibiotics. AMΦ were directly seeded onto 12 mm glass cover slips and used for experiments within 5 days after preparation. Bone marrow-derived macrophages (BMDMΦ) were isolated from femur and tibias of mice. Thus, bones were isolated and bone marrow was flushed with 10 ml PBS using a sterile 25 gauge needle. Cells were obtained by centrifugation, resuspended and subsequently cultured in 10 cm petri dishes in RPMI 1640 medium supplemented with 10% fetal bovine serum and 1% penicillin/streptomycin and 40 ng/mL murine M-CSF (Miltenyi Biotech). Cells were incubated for 5 days, before they were plated onto poly-L-lysine coated cover slips for experiments. All cells were maintained at 37˚C in 5% CO_2 atmosphere. If necessary, cells were stimulated with 1 µg/mL LPS (Escherichia coli O26:B6, Sigma, L2762) prior to experiments for different time periods as stated in the text. Animals were used under approved animal protocols and University of Munich (LMU) Institutional Animal Care Guidelines.

Measurement of CCL2 content in bmdmφ culture supernatants by ELISA

Cell culture supernatants from WT or TRPML2$^{-/-}$ BMDMΦ were collected at 4 hr or 8 hr following LPS treatment in the presence or absence of TRPML2 agonist (ML2-SA1), and CCL2 was measured

using an ELISA kit (BioLegend, 432707), per the manufacturer's instructions. Cell culture supernatants were diluted ten times for the assay, and 50 µL diluted supernatant was assessed.

Transferrin trafficking assay

RAW264.7 cells were seeded overnight with 0.1 mg/mL of lipopolysaccharide (LPS) (L4391, Sigma). Then, cells were loaded for 20 min at 37°C with transferrin from human serum, Alexa Fluor 546-conjugated (T23364, ThermoFisher) at the concentration of 50 µg/mL in complete medium (DMEM 10% FBS). The analysis of recycling kinetics was performed by chasing for 5, 10, 15 and 20 min in complete media plus 50 µg/mL of unconjugated transferrin (T0665, Sigma) in the presence of either DMSO or ML2-SA1 (30 µM). Before fixation with 4% paraformaldehyde (PFA), non-internalized transferrin was acid-stripped (150 mM NaCl, 0.5% acetic acid in H_2O) for 30 s. Images were acquired using a Zeiss LSM 800 with 63x magnification.

Lysosomal exocytosis assay (FACS)

RAW264.7 cells were seeded overnight with 0.1 mg/mL of lipopolysaccharide (LPS) (L4391, Sigma). Then, cells were treated with DMSO, calcium ionophore A23187 (C7522, Sigma) or ML2-SA1 for 3 hr. After 3 h cells were collected and stained with LAMP1 antibody (SC-19992, Santa Cruz) in PBS (1% BSA) during agitation for 20 min (4°C). Cells were then collected by centrifugation and resuspended in PBS (1% BSA) with goat anti-rat, Alexa488 (A-11006 ThermoFisher) during agitation for 1 hr (4°C). Finally, cells were washed in PBS and left on ice until FACS analysis. Cells were loaded into the FACS machine using a nozzle of 100 µm and the LAMP1 fluorescence intensity was measured using a 488 nm excitation laser and a FITCH (530/30 nm) emission filter. The threshold was set using DMSO-treated samples, and 1000 events were counted for each condition.

Lysosomal exocytosis assay (Hexosaminidase)

For measurement of lysosomal hexosaminidase enzyme release, bone marrow macrophages were treated with ML2-SA1, ML-SA1 or DMSO in serum-free RPMI medium, concentrations and durations as indicated. Ionomycin was used as control. After treatment, supernatants were collected, centrifuged and incubated with natrium citrate buffer (pH 4.5) and 4-Methylumbelliferyl N-acetyl-β-D-glucosaminide (M1233, Sigma, 1 mM final concentration) for 1.5 hr. Cells were lysed with Triton-X buffer and lysates were processed in parallel. The reaction was stopped by adding glycin buffer to the samples and the turnover of hexosaminidase substrate was detected as fluorescence (Exitation: 365 nm; Emission: 450 nm) using a plate reader (Spectramax ID3, Molecular Devices). The increase in substrate turnover was analyzed as fluorescence increase in supernatants relative to lysates.

Site-directed mutagenesis

Generation of point mutant isoforms of hTRPML2 (encoded by the *MCOLN2* gene) was performed as described previously (***Grimm et al., 2010***) using the QuikChange protocol. The following primers were used to generate hTRPML2 mutant isoforms: A422C forward primer: CTTCGGTTTTGTTGTTG TGCTGGTATGATTTATCTGGG; A422C reverse primer: CCCAGATAAATCATACCAGCACAACAA-CAAAACCGAAG; A424V forward primer: CGGTTTTGTGCTTGTGTTGGTATGATTTATCTGGGTTA-CAC; A424V reverse primer: GTGTAACCCAGATAAATCATACCAACACAAGCACAAAACCG; G425A forward primer: CGGTTTTGTGCTTGTGCTGCTATGATTTATCTGGGTTACAC; G425A reverse primer: GTGTAACCCAGATAAATCATAGCAGCACAAGCACAAAACCG; A453S forward primer: CTGAACACAGTTTCTGAGTGTCTGTTTTCTCTGG; A453S reverse primer: CCAGAGAAAA-CAGACACTCAGAAACTGTGTTCAG; V460I forward primer: TGTCTGTTTTCTCTGATCAACGGTGA TGACATG; V460I reverse primer: CATGTCATCACCGTTGATCAGAGAAAACAGACA; I498V forward primer: CCTTCATCAGCCTTTTTATATATATGGTTCTCAGTCTTTTTATTGC; I498V reverse primer: GCAATAAAAAGACTGAGAACCATATATATAAAAAGGCTGATGAAGG.

Macrophage migration experiments

ML2-SA1 effects on macrophage migration were assessed by a modified Boyden chamber setup (***Figure 6—figure supplement 2***). In the modified Boyden chamber setup, BMDMΦ were plated onto poly-L-lysine coated cover slips in a twenty-four well plate (lower compartment) in the presence or absence of 1 µg/ml LPS for 6 hr. After 6 hr, media was replaced with media containing 10 or 30

μM ML2-SA1 or DMSO. 1 × 10^5 BMDMΦ were placed on top of the transwell chamber (Corning) in media without any compound. Transwell chambers were placed into the twenty-four well plate and incubated for 3 hr at 37°C in 5% CO_2 atmosphere. In the classical Boyden chamber approach a twenty-four well plate was filled with media containing either DMSO, 1 μg/ml LPS and DMSO, 1 μg/ml LPS and 30 μM ML2-SA1, or 10 ng/ml CCL2. Transwell chambers were equally prepared and incubated. Migrated cells were fixed and stained with crystal violet/methanol. The top of the transwell chamber was cleaned an images were taken. Cell covered area was determined with ImageJ (NIH, Bethesda, MD).

Acknowledgement

We thank Lars Allmendinger, Yu-Kai Chao, Berit Noack, Martina Stadler, Wolfgang Wilfert, and Christopher Wolf for technical support. This work was supported, in part, by funding of the German Research Foundation (SFB/TRR152 projects P04 to CG, P06 to CW-S., and P12 to MB. as well as SFB1123 project B1 to LMH and DT), the NCL (Neuronal Ceroid Lipofuscinosis) Foundation Award 2016 to CG, and the University of Pennsylvania Orphan Disease Center and the Mucolipidosis IV Foundation Grant MDBR-17–120 ML4 to CG.

Additional information

Funding

Funder	Grant reference number	Author
Deutsche Forschungsgemeinschaft	SFB/TRR152 P04	Christian Grimm
Mucolipidosis IV Foundation	MDBR-17-120-ML4	Christian Grimm
Deutsche Forschungsgemeinschaft	SFB/TRR152 P06	Christian Wahl-Schott
Deutsche Forschungsgemeinschaft	SFB/TRR152 P12	Martin Biel
Deutsche Forschungsgemeinschaft	SFB1123 B1	Lesca M Holdt Daniel Teupser

The funders had no role in study design, data collection and interpretation, or the decision to submit the work for publication.

Author contributions

Eva Plesch, Data curation, Formal analysis, Methodology; Cheng-Chang Chen, Conceptualization, Data curation, Formal analysis, Methodology, Writing—review and editing; Elisabeth Butz, Anna Scotto Rosato, Einar K Krogsaeter, Rosa Puertollano, Conceptualization, Data curation, Formal analysis, Methodology; Hua Yinan, Karin Bartel, Conceptualization, Data curation, Formal analysis, Investigation; Marco Keller, Supervision, Writing—review and editing; Dina Robaa, Data curation, Formal analysis; Daniel Teupser, Angelika M Vollmar, Resources, Supervision, Funding acquisition; Lesca M Holdt, Resources, Supervision, Funding acquisition, Methodology; Wolfgang Sippl, Resources, Data curation, Formal analysis, Supervision, Methodology; Diego Medina, Conceptualization, Resources, Supervision; Martin Biel, Resources, Funding acquisition; Christian Wahl-Schott, Resources, Funding acquisition, Methodology; Franz Bracher, Conceptualization, Resources, Data curation, Formal analysis, Supervision, Methodology; Christian Grimm, Conceptualization, Resources, Data curation, Formal analysis, Supervision, Funding acquisition, Validation, Investigation, Visualization, Methodology, Writing—original draft, Project administration, Writing—review and editing

Author ORCIDs

Elisabeth Butz http://orcid.org/0000-0002-5956-6434
Einar K Krogsaeter http://orcid.org/0000-0001-8232-5498

Rosa Puertollano http://orcid.org/0000-0002-1106-5489
Christian Grimm http://orcid.org/0000-0002-0177-5559

Ethics

Animal experimentation: This study was performed where applicable in strict accordance with the recommendations in the Guide for the Care and Use of Laboratory Animals of the National Institutes of Health. This study was performed where applicable in strict accordance with the recommendations of the Bavarian Government (ROB; AZ_55.2-1-54-2532-27-2015).

Decision letter and Author response

Decision letter https://doi.org/10.7554/eLife.39720.021
Author response https://doi.org/10.7554/eLife.39720.022

Additional files

Supplementary files

- Supplementary file 1. Synthesis details and analytical data

DOI: https://doi.org/10.7554/eLife.39720.017

- Supplementary file 2. Summary of characteristics of TRPML channels

DOI: https://doi.org/10.7554/eLife.39720.018

- Transparent reporting form

DOI: https://doi.org/10.7554/eLife.39720.019

All data generated or analysed during this study are included in the manuscript and supporting files.

References

Akiba K, Kashiwagi K, Ohyama Y, Yamamoto Y, Ohkata K. 1985. Ring transformation equilibrium (bond switch) in 5-(2-aminovinyl)isothiazole system via hypervalent sulfurane. synthesis, structure determination, and kinetic study. *Journal of the American Chemical Society* **107**:2721–2730. DOI: https://doi.org/10.1021/ja00295a026

Altschul SF, Gish W, Miller W, Myers EW, Lipman DJ. 1990. Basic local alignment search tool. *Journal of Molecular Biology* **215**:403–410. DOI: https://doi.org/10.1016/S0022-2836(05)80360-2, PMID: 2231712

Andrei C, Dazzi C, Lotti L, Torrisi MR, Chimini G, Rubartelli A. 1999. The secretory route of the leaderless protein interleukin 1beta involves exocytosis of endolysosome-related vesicles. *Molecular Biology of the Cell* **10**:1463–1475. DOI: https://doi.org/10.1091/mbc.10.5.1463, PMID: 10233156

Bach G. 2001. Mucolipidosis type IV. *Molecular Genetics and Metabolism* **73**:197–203. DOI: https://doi.org/10.1006/mgme.2001.3195, PMID: 11461186

Bala S, Saini M, Kamboj S, Saini V. 2012. Synthesis Of 2-[4-(Substituted Benzylidene)-5-Oxo-4,5-Dihydro-Oxazol-2-Ylmethyl]-Isoindole-1,3-Dione derivatives as novel potential antimicrobial agents. *Iranian Journal of Pharmacology and Therapeutics* **2012**:45–52.

Bansode TN, Shelke JV, Dongre VG. 2009. Synthesis and antimicrobial activity of some new N-acyl substituted phenothiazines. *European Journal of Medicinal Chemistry* **44**:5094–5098. DOI: https://doi.org/10.1016/j.ejmech.2009.07.006, PMID: 19651462

Berman HM, Westbrook J, Feng Z, Gilliland G, Bhat TN, Weissig H, Shindyalov IN, Bourne PE. 2000. The Protein Data Bank. *Nucleic Acids Research* **28**:235–242. DOI: https://doi.org/10.1093/nar/28.1.235, PMID: 10592235

Cang C, Zhou Y, Navarro B, Seo YJ, Aranda K, Shi L, Battaglia-Hsu S, Nissim I, Clapham DE, Ren D. 2013. mTOR regulates lysosomal ATP-sensitive two-pore Na(+) channels to adapt to metabolic state. *Cell* **152**:778–790. DOI: https://doi.org/10.1016/j.cell.2013.01.023, PMID: 23394946

Cerri A, De Micheli C, Gandolfi R. 1974. Dihydro-^{1},2-oxazole Derivatives. Part IX ^{1} . Stereoselective Synthesis of Tetrahydro-^{1},2-oxazoles by Sodium Borohydride Reduction of 4,5-Dihydro-^{1},2-oxazolium Tetrafluoroborates. *Synthesis* **1974**:710–712. DOI: https://doi.org/10.1055/s-1974-23410

Chen R, Yang X, Tian H, Wang X, Hagfeldt A, Sun L. 2007. Effect of tetrahydroquinoline dyes structure on the performance of organic dye-sensitized solar cells. *Chemistry of Materials* **19**:4007–4015. DOI: https://doi.org/10.1021/cm070617g

Chen CC, Keller M, Hess M, Schiffmann R, Urban N, Wolfgardt A, Schaefer M, Bracher F, Biel M, Wahl-Schott C, Grimm C. 2014. A small molecule restores function to TRPML1 mutant isoforms responsible for mucolipidosis type IV. *Nature Communications* **5**:4681. DOI: https://doi.org/10.1038/ncomms5681, PMID: 25119295

Chen CC, Butz ES, Chao YK, Grishchuk Y, Becker L, Heller S, Slaugenhaupt SA, Biel M, Wahl-Schott C, Grimm C. 2017a. Small Molecules for Early Endosome-Specific Patch Clamping. *Cell Chemical Biology* **24**:907–916. DOI: https://doi.org/10.1016/j.chembiol.2017.05.025, PMID: 28732201

Chen Q, She J, Zeng W, Guo J, Xu H, Bai XC, Jiang Y. 2017b. Structure of mammalian endolysosomal TRPML1 channel in nanodiscs. *Nature* **550**:415–418. DOI: https://doi.org/10.1038/nature24035, PMID: 29019981

Chen CC, Cang C, Fenske S, Butz E, Chao YK, Biel M, Ren D, Wahl-Schott C, Grimm C. 2017c. Patch-clamp technique to characterize ion channels in enlarged individual endolysosomes. *Nature Protocols* **12**:1639–1658. DOI: https://doi.org/10.1038/nprot.2017.036, PMID: 28726848

Choudhury A, Dominguez M, Puri V, Sharma DK, Narita K, Wheatley CL, Marks DL, Pagano RE. 2002. Rab proteins mediate Golgi transport of caveola-internalized glycosphingolipids and correct lipid trafficking in Niemann-Pick C cells. *Journal of Clinical Investigation* **109**:1541–1550. DOI: https://doi.org/10.1172/JCI0215420, PMID: 12070301

Cuajungco MP, Silva J, Habibi A, Valadez JA. 2016. The mucolipin-2 (TRPML2) ion channel: a tissue-specific protein crucial to normal cell function. *Pflügers Archiv - European Journal of Physiology* **468**:177–192. DOI: https://doi.org/10.1007/s00424-015-1732-2, PMID: 26336837

Daly C, Rollins BJ. 2003. Monocyte chemoattractant protein-1 (CCL2) in inflammatory disease and adaptive immunity: therapeutic opportunities and controversies. *Microcirculation* **10**:247–257. DOI: https://doi.org/10.1080/mic.10.3-4.247.257, PMID: 12851642

Deshmane SL, Kremlev S, Amini S, Sawaya BE. 2009. Monocyte chemoattractant protein-1 (MCP-1): an overview. *Journal of Interferon & Cytokine Research* **29**:313–326. DOI: https://doi.org/10.1089/jir.2008.0027, PMID: 19441883

Dong XP, Shen D, Wang X, Dawson T, Li X, Zhang Q, Cheng X, Zhang Y, Weisman LS, Delling M, Xu H. 2010. PI(3,5)P(2) controls membrane trafficking by direct activation of mucolipin Ca(2+) release channels in the endolysosome. *Nature Communications* **1**:1–11. DOI: https://doi.org/10.1038/ncomms1037, PMID: 20802798

Escudero MI, Kremenchuzky LD, Perillo IA, Cerecetto H, Blanco MM. 2011. Efficient Cesium Carbonate Promoted N-Alkylations of Aromatic Cyclic Imides Under Microwave Irradiation. *Synthesis* **2011**:571–576. DOI: https://doi.org/10.1055/s-0030-1258398

Fos E, Borràs L, Gasull M, Mauleón D, Carganico G. 1992. Synthesis of isomeric series of aryltetrahydrobenzisoxazoles and arylcyclopentisoxazoles. *Journal of Heterocyclic Chemistry* **29**:203–208. DOI: https://doi.org/10.1002/jhet.5570290137

García-Añoveros J, Wiwatpanit T. 2014. TRPML2 and mucolipin evolution. *Handbook of experimental pharmacology* **222**:647–658. DOI: https://doi.org/10.1007/978-3-642-54215-2_25, PMID: 24756724

Grimm C, Jörs S, Saldanha SA, Obukhov AG, Pan B, Oshima K, Cuajungco MP, Chase P, Hodder P, Heller S. 2010. Small molecule activators of TRPML3. *Chemistry & Biology* **17**:135–148. DOI: https://doi.org/10.1016/j.chembiol.2009.12.016, PMID: 20189104

Grimm C, Hassan S, Wahl-Schott C, Biel M. 2012a. Role of TRPML and two-pore channels in endolysosomal cation homeostasis. *Journal of Pharmacology and Experimental Therapeutics* **342**:236–244. DOI: https://doi.org/10.1124/jpet.112.192880, PMID: 22518024

Grimm C, Jörs S, Guo Z, Obukhov AG, Heller S. 2012b. Constitutive activity of TRPML2 and TRPML3 channels versus activation by low extracellular sodium and small molecules. *Journal of Biological Chemistry* **287**:22701–22708. DOI: https://doi.org/10.1074/jbc.M112.369876, PMID: 22753890

Grimm C, Holdt LM, Chen CC, Hassan S, Müller C, Jörs S, Cuny H, Kissing S, Schröder B, Butz E, Northoff B, Castonguay J, Luber CA, Moser M, Spahn S, Lüllmann-Rauch R, Fendel C, Klugbauer N, Griesbeck O, Haas A, et al. 2014. High susceptibility to fatty liver disease in two-pore channel 2-deficient mice. *Nature Communications* **5**:4699. DOI: https://doi.org/10.1038/ncomms5699, PMID: 25144390

Grimm C. 2016. Endolysosomal cation channels as therapeutic targets—pharmacology of TRPML channels. *Messenger* **5**:30–36. DOI: https://doi.org/10.1166/msr.2016.1061

Hirschi M, Herzik MA, Wie J, Suo Y, Borschel WF, Ren D, Lander GC, Lee SY. 2017. Cryo-electron microscopy structure of the lysosomal calcium-permeable channel TRPML3. *Nature* **550**:411–414. DOI: https://doi.org/10.1038/nature24055, PMID: 29019979

Hruz T, Wyss M, Docquier M, Pfaffl MW, Masanetz S, Borghi L, Verbrugghe P, Kalaydjieva L, Bleuler S, Laule O, Descombes P, Gruissem W, Zimmermann P. 2011. RefGenes: identification of reliable and condition specific reference genes for RT-qPCR data normalization. *BMC Genomics* **12**:156. DOI: https://doi.org/10.1186/1471-2164-12-156, PMID: 21418615

Huisgen R. 1963. 1.3-Dipolare cycloadditionen rückschau und ausblick. *Angewandte Chemie* **75**:604–637. DOI: https://doi.org/10.1002/ange.19630751304

Jawalekar AM, Reubsaet E, Rutjes FPJT, van Delft FL. 2011. Synthesis of isoxazoles by hypervalent iodine-induced cycloaddition of nitrile oxides to alkynes. *Chemical Communications* **47**:3198–3200. DOI: https://doi.org/10.1039/c0cc04646a

Jörs S, Grimm C, Becker L, Heller S. 2010. Genetic Inactivation of Trpml3 Does Not Lead to Hearing and Vestibular Impairment in Mice. *PLoS ONE* **5**:e14317. DOI: https://doi.org/10.1371/journal.pone.0014317

Karacsonyi C, Miguel AS, Puertollano R. 2007. Mucolipin-2 localizes to the Arf6-associated pathway and regulates recycling of GPI-APs. *Traffic* **8**:1404–1414. DOI: https://doi.org/10.1111/j.1600-0854.2007.00619.x, PMID: 17662026

Kim HJ, Soyombo AA, Tjon-Kon-Sang S, So I, Muallem S. 2009. The Ca(2+) channel TRPML3 regulates membrane trafficking and autophagy. *Traffic* **10**:1157–1167. DOI: https://doi.org/10.1111/j.1600-0854.2009.00924.x, PMID: 19522758

Kuehne ME, Weaver SJ, Franz P. 1964. Enamines as 1,3-Dipolarophiles1. *The Journal of Organic Chemistry* **29**:1582–1586. DOI: https://doi.org/10.1021/jo01029a075

Lacy P, Stow JL. 2011. Cytokine release from innate immune cells: association with diverse membrane trafficking pathways. *Blood* **118**:9–18. DOI: https://doi.org/10.1182/blood-2010-08-265892, PMID: 21562044

LaPlante JM, Sun M, Falardeau J, Dai D, Brown EM, Slaugenhaupt SA, Vassilev PM. 2006. Lysosomal exocytosis is impaired in mucolipidosis type IV. *Molecular Genetics and Metabolism* **89**:339–348. DOI: https://doi.org/10.1016/j.ymgme.2006.05.016, PMID: 16914343

Lelouvier B, Puertollano R. 2011. Mucolipin-3 regulates luminal calcium, acidification, and membrane fusion in the endosomal pathway. *Journal of Biological Chemistry* **286**:9826–9832. DOI: https://doi.org/10.1074/jbc.M110.169185, PMID: 21245134

Li Z, Wang W, Zhang X, Hu C, Zhang W. 2013. One-Pot Synthesis of Indolo[2,3-c]quinolin-6-ones by Sequential Photocyclizations of 3-(2-Azidophenyl)-N-phenylacrylamides. *Synlett : Accounts and Rapid Communications in Synthetic Organic Chemistry* **24**:73–78. DOI: https://doi.org/10.1055/s-0032-1317703

Li X, Rydzewski N, Hider A, Zhang X, Yang J, Wang W, Gao Q, Cheng X, Xu H. 2016. A molecular mechanism to regulate lysosome motility for lysosome positioning and tubulation. *Nature Cell Biology* **18**:404–417. DOI: https://doi.org/10.1038/ncb3324, PMID: 26950892

Li M, Zhang WK, Benvin NM, Zhou X, Su D, Li H, Wang S, Michailidis IE, Tong L, Li X, Yang J. 2017. Structural basis of dual Ca^{2+}/pH regulation of the endolysosomal TRPML1 channel. *Nature Structural & Molecular Biology* **24**:205–213. DOI: https://doi.org/10.1038/nsmb.3362, PMID: 28112729

Lopez-Castejon G, Brough D. 2011. Understanding the mechanism of IL-1β secretion. *Cytokine & Growth Factor Reviews* **22**:189–195. DOI: https://doi.org/10.1016/j.cytogfr.2011.10.001, PMID: 22019906

Manderson AP, Kay JG, Hammond LA, Brown DL, Stow JL. 2007. Subcompartments of the macrophage recycling endosome direct the differential secretion of IL-6 and TNFalpha. *The Journal of Cell Biology* **178**:57–69. DOI: https://doi.org/10.1083/jcb.200612131, PMID: 17606866

Miao Y, Li G, Zhang X, Xu H, Abraham SN. 2015. A TRP channel senses lysosome neutralization by pathogens to trigger their expulsion. *Cell* **161**:1306–1319. DOI: https://doi.org/10.1016/j.cell.2015.05.009, PMID: 26027738

Murray RZ, Stow JL. 2014. Cytokine Secretion in Macrophages: SNAREs, Rabs, and Membrane Trafficking. *Frontiers in Immunology* **5**:538. DOI: https://doi.org/10.3389/fimmu.2014.00538, PMID: 25386181

Park S, Ahuja M, Kim MS, Brailoiu GC, Jha A, Zeng M, Baydyuk M, Wu LG, Wassif CA, Porter FD, Zerfas PM, Eckhaus MA, Brailoiu E, Shin DM, Muallem S. 2016. Fusion of lysosomes with secretory organelles leads to uncontrolled exocytosis in the lysosomal storage disease mucolipidosis type IV. *EMBO reports* **17**:266–278. DOI: https://doi.org/10.15252/embr.201541542, PMID: 26682800

Pryor PR, Reimann F, Gribble FM, Luzio JP. 2006. Mucolipin-1 is a lysosomal membrane protein required for intracellular lactosylceramide traffic. *Traffic* **7**:1388–1398. DOI: https://doi.org/10.1111/j.1600-0854.2006.00475.x, PMID: 16978393

Rinkenberger N, Schoggins JW. 2018. Mucolipin-2 Cation Channel Increases Trafficking Efficiency of Endocytosed Viruses. *mBio* **9**. DOI: https://doi.org/10.1128/mBio.02314-17, PMID: 29382735

Samie M, Wang X, Zhang X, Goschka A, Li X, Cheng X, Gregg E, Azar M, Zhuo Y, Garrity AG, Gao Q, Slaugenhaupt S, Pickel J, Zolov SN, Weisman LS, Lenk GM, Titus S, Bryant-Genevier M, Southall N, Juan M, et al. 2013. A TRP channel in the lysosome regulates large particle phagocytosis via focal exocytosis. *Developmental Cell* **26**:511–524. DOI: https://doi.org/10.1016/j.devcel.2013.08.003, PMID: 23993788

Schmiege P, Fine M, Blobel G, Li X. 2017. Human TRPML1 channel structures in open and closed conformations. *Nature* **550**:366–370. DOI: https://doi.org/10.1038/nature24036, PMID: 29019983

Shen D, Wang X, Li X, Zhang X, Yao Z, Dibble S, Dong XP, Yu T, Lieberman AP, Showalter HD, Xu H. 2012. Lipid storage disorders block lysosomal trafficking by inhibiting a TRP channel and lysosomal calcium release. *Nature Communications* **3**:731. DOI: https://doi.org/10.1038/ncomms1735, PMID: 22415822

Shen MY, Sali A. 2006. Statistical potential for assessment and prediction of protein structures. *Protein Science* **15**:2507–2524. DOI: https://doi.org/10.1110/ps.062416606, PMID: 17075131

Soyombo AA, Tjon-Kon-Sang S, Rbaibi Y, Bashllari E, Bisceglia J, Muallem S, Kiselyov K. 2006. TRP-ML1 regulates lysosomal pH and acidic lysosomal lipid hydrolytic activity. *Journal of Biological Chemistry* **281**:7294–7301. DOI: https://doi.org/10.1074/jbc.M508211200, PMID: 16361256

Sun L, Hua Y, Vergarajauregui S, Diab HI, Puertollano R. 2015. Novel Role of TRPML2 in the regulation of the innate immune response. *The Journal of Immunology* **195**:4922–4932. DOI: https://doi.org/10.4049/jimmunol.1500163, PMID: 26432893

Tagle LH, Terraza CA, Tundidor-Camba A, Coll D. 2017. Silicon-containing halogenated poly(amides) derived from diacids with aminoacidic and imidic moieties in the side chain: synthesis, characterization, optical studies and thermal properties. *Polymer Bulletin* **74**:263–281.

Tan C, Wei L, Ottensmeyer FP, Goldfine I, Maddux BA, Yip CC, Batey RA, Kotra LP. 2004. Structure-based de novo design of ligands using a three-dimensional model of the insulin receptor. *Bioorganic & Medicinal Chemistry Letters* **14**:1407–1410. DOI: https://doi.org/10.1016/j.bmcl.2004.01.064, PMID: 15006372

The UniProt Consortium. 2017. UniProt: the universal protein knowledgebase. *Nucleic Acids Research* **45**:D158–D169. DOI: https://doi.org/10.1093/nar/gkw1099, PMID: 27899622

Valadez JA, Cuajungco MP. 2015. PAX5 is the transcriptional activator of mucolipin-2 (MCOLN2) gene. *Gene* **555**:194–202. DOI: https://doi.org/10.1016/j.gene.2014.11.003, PMID: 25445271

Venkatachalam K, Hofmann T, Montell C. 2006. Lysosomal localization of TRPML3 depends on TRPML2 and the mucolipidosis-associated protein TRPML1. *Journal of Biological Chemistry* **281**:17517–17527. DOI: https://doi.org/10.1074/jbc.M600807200, PMID: 16606612

Venkatachalam K, Wong CO, Montell C. 2013. Feast or famine: role of TRPML in preventing cellular amino acid starvation. *Autophagy* **9**:98–100. DOI: https://doi.org/10.4161/auto.22260, PMID: 23047439

Venturini I, Filippini L, Vazzola MS. 2010. Benzamidic compounds having fungicidal activity and relative use. *World Intellectual Property Organization*. WO2010109301A1. https://patents.google.com/patent/WO2010109301A1/enGo.

Venugopal B, Browning MF, Curcio-Morelli C, Varro A, Michaud N, Nanthakumar N, Walkley SU, Pickel J, Slaugenhaupt SA. 2007. Neurologic, gastric, and opthalmologic pathologies in a murine model of mucolipidosis type IV. *The American Journal of Human Genetics* **81**:1070–1083. DOI: https://doi.org/10.1086/521954, PMID: 17924347

Vergarajauregui S, Martina JA, Puertollano R. 2009. Identification of the penta-EF-hand protein ALG-2 as a Ca2+-dependent interactor of mucolipin-1. *Journal of Biological Chemistry* **284**:36357–36366. DOI: https://doi.org/10.1074/jbc.M109.047241, PMID: 19864416

Vitale P, Scilimati A. 2013. Functional 3-Arylisoxazoles and 3-Aryl-2-isoxazolines from Reaction of Aryl Nitrile Oxides and Enolates: Synthesis and Reactivity. *Synthesis* **45**:2940–2948. DOI: https://doi.org/10.1055/s-0033-1338540

Volkov A, Tinnis F, Adolfsson H. 2014. Catalytic reductive dehydration of tertiary amides to enamines under hydrosilylation conditions. *Organic Letters* **16**:680–683. DOI: https://doi.org/10.1021/ol403302g, PMID: 24451007

Wang X, Zhang X, Dong XP, Samie M, Li X, Cheng X, Goschka A, Shen D, Zhou Y, Harlow J, Zhu MX, Clapham DE, Ren D, Xu H. 2012. TPC proteins are phosphoinositide- activated sodium-selective ion channels in endosomes and lysosomes. *Cell* **151**:372–383. DOI: https://doi.org/10.1016/j.cell.2012.08.036, PMID: 23063126

Webb B, Sali A. 2014. Comparative protein structure modeling using MODELLER. *Current Protocols in Bioinformatics* **47**:5.6.1–5.6.5. DOI: https://doi.org/10.1002/0471250953.bi0506s47

Wulfman DS, Yousefian S, White JM. 1988. The synthesis of ahyl diazomethanes. *Synthetic Communications* **18**:2349–2352. DOI: https://doi.org/10.1080/00397918808082380

Xia M, Sui Z. 2009. Recent developments in CCR2 antagonists. *Expert Opinion on Therapeutic Patents* **19**:295–303. DOI: https://doi.org/10.1517/13543770902755129, PMID: 19441905

Yamaguchi S, Muallem S. 2010. Opening the TRPML gates. *Chemistry & Biology* **17**:209–210. DOI: https://doi.org/10.1016/j.chembiol.2010.02.009, PMID: 20338511

Zhang S, Li N, Zeng W, Gao N, Yang M. 2017. Cryo-EM structures of the mammalian endo-lysosomal TRPML1 channel elucidate the combined regulation mechanism. *Protein & Cell* **8**:834–847. DOI: https://doi.org/10.1007/s13238-017-0476-5, PMID: 28936784

Zhou X, Li M, Su D, Jia Q, Li H, Li X, Yang J. 2017. Cryo-EM structures of the human endolysosomal TRPML3 channel in three distinct states. *Nature Structural & Molecular Biology* **24**:1146–1154. DOI: https://doi.org/10.1038/nsmb.3502, PMID: 29106414

Manuscript II

Agonist-mediated switching of ion selectivity in TPC2 differentially promotes lysosomal function

Susanne Gerndt*, Cheng-Chang Chen*, Yu-Kai Chao*, Yu Yuan*, Sandra Burgstaller, Anna Scotto Rosato, **Einar K. Krogsaeter**, Nicole Urban, Katharina Jacob, Ong Nam Phuong Nguyen, Meghan T. Miller, Marco Keller, Angelika M. Vollmar, Thomas Gudermann, Susanna Zierler, Johann Schredelseker, Michael Schaefer, Martin Biel, Roland Malli, Christian Wahl-Schott, Franz Bracher, Sandip Patel, & Christian Grimm.

eLIFE. 2020;9:e54712.

RESEARCH ARTICLE

Agonist-mediated switching of ion selectivity in TPC2 differentially promotes lysosomal function

Susanne Gerndt[1,2†], Cheng-Chang Chen[1†], Yu-Kai Chao[2†], Yu Yuan[3†], Sandra Burgstaller[4], Anna Scotto Rosato[2], Einar Krogsaeter[2], Nicole Urban[5], Katharina Jacob[2], Ong Nam Phuong Nguyen[1], Meghan T Miller[1,6], Marco Keller[1], Angelika M Vollmar[1], Thomas Gudermann[2], Susanna Zierler[2], Johann Schredelseker[1,2], Michael Schaefer[1,5], Martin Biel[1], Roland Malli[4], Christian Wahl-Schott[7]*, Franz Bracher[1]*, Sandip Patel[3]*, Christian Grimm[2]*

[1]Department of Pharmacy – Center for Drug Research, Ludwig-Maximilians-Universität, Munich, Germany; [2]Walther Straub Institute of Pharmacology and Toxicology, Faculty of Medicine, Ludwig-Maximilians-Universität, Munich, Germany; [3]Department of Cell and Developmental Biology, University College London, London, United Kingdom; [4]Molecular Biology and Biochemistry, Gottfried Schatz Research Center, Medical University of Graz, Graz, Austria; [5]Rudolf-Boehm-Institute for Pharmacology and Toxicology, Universität Leipzig, Leipzig, Germany; [6]Pharma Research and Early Development (pRED), Roche Innovation Center Basel, F. Hoffmann-La Roche, Basel, Switzerland; [7]Institute for Neurophysiology, Hannover Medical School, Hannover, Germany

***For correspondence:** wahl-schott.christian@mh-hannover.de (CW-S); franz.bracher@cup.uni-muenchen.de (FB); patel.s@ucl.ac.uk (SP); Christian.Grimm@med.uni-muenchen.de (CG)

[†]These authors contributed equally to this work

Competing interests: The authors declare that no competing interests exist.

Funding: See page 59

Received: 23 December 2019
Accepted: 12 March 2020
Published: 16 March 2020

Reviewing editor: Richard S Lewis, Stanford University School of Medicine, United States

Abstract Ion selectivity is a defining feature of a given ion channel and is considered immutable. Here we show that ion selectivity of the lysosomal ion channel TPC2, which is hotly debated (Calcraft et al., 2009; Guo et al., 2017; Jha et al., 2014; Ruas et al., 2015; Wang et al., 2012), depends on the activating ligand. A high-throughput screen identified two structurally distinct TPC2 agonists. One of these evoked robust Ca^{2+}-signals and non-selective cation currents, the other weaker Ca^{2+}-signals and Na^{+}-selective currents. These properties were mirrored by the Ca^{2+}-mobilizing messenger, NAADP and the phosphoinositide, $PI(3,5)P_2$, respectively. Agonist action was differentially inhibited by mutation of a single TPC2 residue and coupled to opposing changes in lysosomal pH and exocytosis. Our findings resolve conflicting reports on the permeability and gating properties of TPC2 and they establish a new paradigm whereby a single ion channel mediates distinct, functionally-relevant ionic signatures on demand.

Introduction

When ion channels open in response to a given stimulus, they allow the flow of a specific set of ions. The textbook view is that ion selectivity for a given ion channel is a hallmark feature that cannot be changed. But evidence has accrued suggesting that this may not always be the case. P2X receptors have long been proposed to change their ion selectivity in real time upon prolonged activation (***Khakh and Lester, 1999***) albeit controversially (***Li et al., 2015***). And in TRPV channels, the selectivity filter is thought to form a second gate thereby coupling channel opening with changes in ion selectivity (***Cao et al., 2013***). Other channels such as Orai channels (***McNally et al., 2012***) and the mitochondrial uniporter MCU1 (***Kamer et al., 2018***) appear to alter their ion selectivity depending on protein partners.

Two-pore channels (TPC1-3) are ancient members of the voltage-gated ion channel superfamily (**Patel, 2015**). TPCs are expressed throughout the endo-lysosomal system where they regulate the trafficking of various cargoes (**Grimm et al., 2014**; **Ruas et al., 2010**; **Sakurai et al., 2015**). Loss- and gain-of function of TPCs is implicated in a number of diseases including NAFLD (non-alcoholic fatty liver disease) and Parkinson's (**Patel, 2015**; **Patel and Kilpatrick, 2018**). Despite their pathophysiological importance, both the ion selectivity and activating ligand(s) of TPCs are equivocal. Initial studies characterized TPCs as non-selective Ca^{2+}-permeable channels activated by NAADP (nicotinic acid adenine dinucleotide phosphate) (**Brailoiu et al., 2009**; **Brailoiu et al., 2010**; **Calcraft et al., 2009**; **Grimm et al., 2014**; **Pitt et al., 2010**; **Ruas et al., 2015**; **Schieder et al., 2010**). But other studies indicate that TPCs are highly-selective Na^+ channels that similar to endo-lysosomal TRP mucolipins (TRPMLs), are activated directly by $PI(3,5)P_2$ (phosphatidylinositol 3,5-bisphosphate), and/or by voltage (**Boccaccio et al., 2014**; **Cang et al., 2014**; **Guo et al., 2017**; **She et al., 2018**; **Wang et al., 2012**). Co-regulation of TPCs by these disparate stimuli has been noted in some instances (**Jha et al., 2014**; **Ogunbayo et al., 2018**; **Pitt et al., 2014**; **Rybalchenko et al., 2012**).

Functional characterization of TPCs is challenging due to their intracellular location. The anionic nature of NAADP and $PI(3,5)P_2$ prevents sufficient plasma membrane permeability, making them less suitable for experimental use in intact cells. On the other hand, studies of isolated lysosomes may result in loss of crucial accessory factors such as NAADP-binding proteins (**Lin-Moshier et al., 2012**). To circumvent these issues, we screened for membrane-permeable small molecule activators of TPCs. Here, we report two agonists that surprisingly switch the ion selectivity of TPC2 with different consequences for lysosomal function and integrity.

Results

Identification of novel small molecule agonists of TPC2

Mutation of the N-terminal endo-lysosomal targeting motif in human TPC2 redirects it to the plasma membrane where TPC2 reportedly mediates robust Ca^{2+} entry upon activation with NAADP (**Brailoiu et al., 2010**). We took advantage of this property to screen a cell line stably expressing $TPC2^{L11A/L12A}$ with a library of 80000 natural and synthetic small molecules using a FLIPR-based Ca^{2+} assay (**Figure 1A and B**). Two structurally independent hits were identified, termed TPC2-A1-N and TPC2-A1-P (**Figure 1C and D**), which reproducibly evoked Ca^{2+} signals. The signals evoked by the compounds showed different kinetics whereby the TPC2-A1-N response reached its plateau faster than TPC2-A1-P (**Figure 1E and F**). The structures and activities of these hits were confirmed by independent chemical syntheses and subsequent retesting. Full concentration-effect relationships for the plateau response indicated EC_{50} values of 7.8 µM and 10.5 µM, for TPC2-A1-N and TPC2-A1-P, respectively (**Figure 1G and H**). We thus identified novel small molecules that activate TPC2 and confirm its Ca^{2+}-permeability in intact cells.

TPC2 agonists differentially evoke cytosolic Ca^{2+} signals in live cells

To validate the hits further, we performed ratiometric Ca^{2+} imaging of single cells transiently transfected with $TPC2^{L11A/L12A}$ or a 'pore-dead' version ($TPC2^{L11A/L12A/L265P}$). As shown in **Figure 1I and J**, TPC2-A1-N evoked Ca^{2+} signals in cells expressing $TPC2^{L11A/L12A}$ but not $TPC2^{L11A/L12A/L265P}$. These data confirm that TPC2-A1-N evoked Ca^{2+} influx through the TPC2 pore. In accord, the responses to TPC2-A1-N were selectively blocked by the recently identified TPC2 blockers tetrandrine (Tet), raloxifene (Ral), and fluphenazine (Flu) (**Penny et al., 2019**; **Sakurai et al., 2015**; **Figure 1—figure supplement 1**) and by removal of extracellular Ca^{2+} (**Figure 1—figure supplement 2**). TPC2-A1-P also induced Ca^{2+} signals in cells expressing TPC2 in the presence (**Figure 1K and L**) but not absence (**Figure 1—figure supplement 2**) of extracellular Ca^{2+}. However, the responses were smaller and delayed compared to TPC2-A1-N (**Figure 1I and K**), consistent with the results obtained in cells stably expressing $TPC2^{L11A/L12A}$ (**Figure 1E and F**). TPC2-A1-P failed to induce Ca^{2+} signals in cells expressing 'pore-dead' $TPC2^{L11A/L12A/L265P}$ (**Figure 1K and L**). Both TPC2-A1-N and TPC2-A1-P also failed to evoke Ca^{2+} signals in cells expressing human TRPML1 re-routed to the plasma membrane ($TRPML1^{\Delta NC}$) (**Grimm et al., 2010**; **Yamaguchi et al., 2011**; **Figure 1M–N** and **Figure 1—figure supplement 1A–B**). Similar negative results were obtained with the agonists in

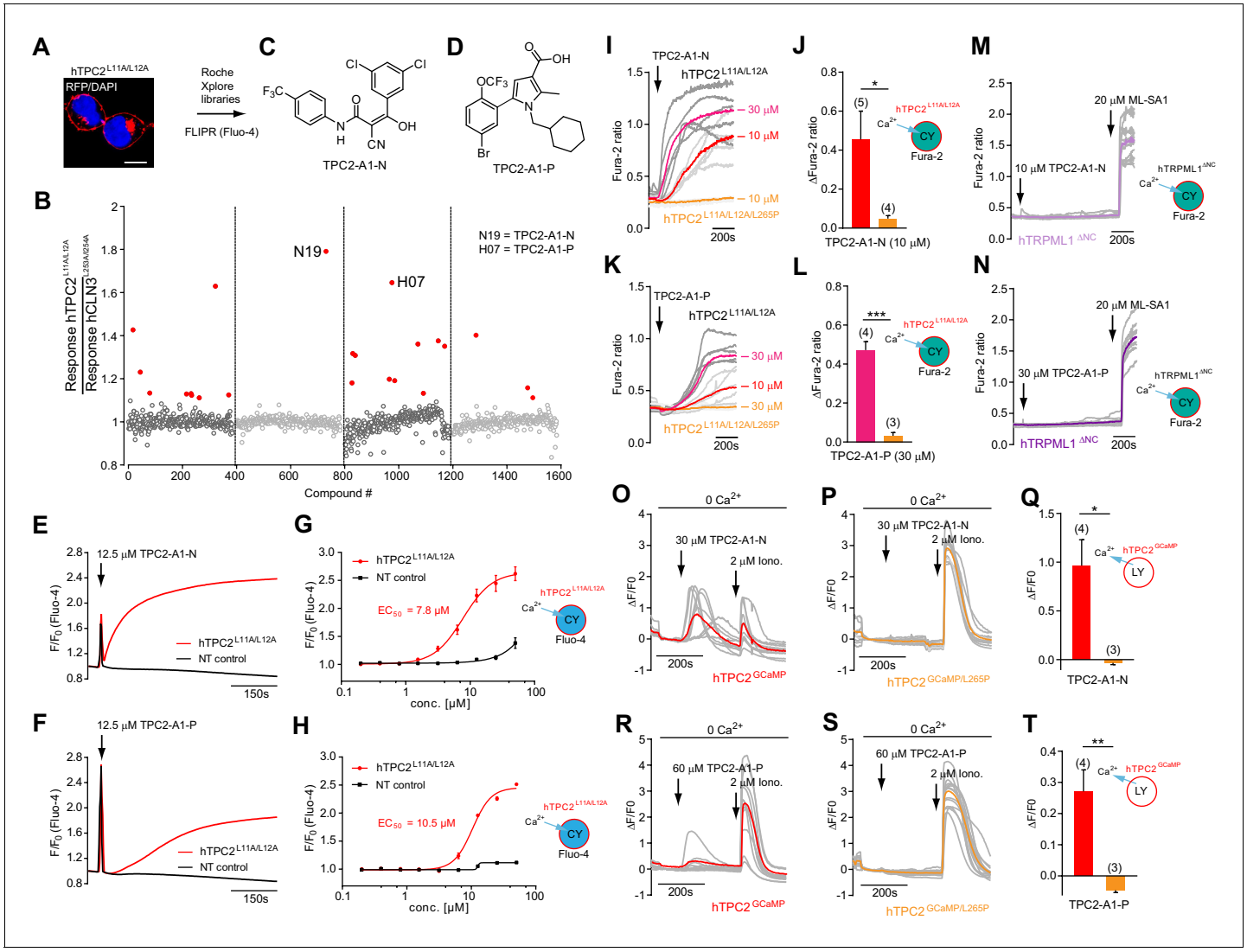

Figure 1. Identification of novel small molecule agonists of TPC2. (**A**) The chemical screening was performed using cells stably expressing human TPC2 re-routed to the plasma membrane (hTPC2$^{L11A/L12A}$) and loaded with the fluorescent Ca^{2+} indicator, Fluo-4 (CY = cytosol). For counter-screening, a stable cell line expressing cell surface human CLN3 (hCLN3$^{L253A/I254A}$) was used. (**B**) A library comprising 80.000 compounds was screened. Shown are the primary screen results of four plates (with 384 compounds, each) where the response to a given compound in cells expressing hTPC2$^{L11A/L12A}$ is expressed relative to that in cells expressing hCLN3$^{L253A/I254A}$. Primary hits are shown as red spots. Subsequent confirmatory and follow-up assays led to the identification of the two hit compounds, N19 (TPC2-A1-N) and H07 (TPC2-A1-P). (**C–D**) Figures of TPC2-A1-N and TPC2-A1-P. (**E–F**) Representative FLIPR-generated Ca^{2+} signals (Fluo-4) in TPC2$^{L11A/L12A}$–expressing cells (red lines) or non-transfected (NT) control cells (black) after addition of TPC2-A1-N (**E**) or TPC2-A1-P (**F**). (**G–H**) Concentration-effect relationships for Ca^{2+} increases (Fluo-4) in response to different concentrations of TPC2-A1-N (**G**) and TPC2-A1-P (**H**). Each concentration was tested in duplicates in two to four independent experiments, each. (**I**) Representative Ca^{2+} signals recorded from HeLa cells loaded with the ratiometric Ca^{2+} indicator, Fura-2 and stimulated with the indicated concentration of TPC2-A1-N. Cells were transiently transfected with plasma-membrane-targeted human TPC2 (hTPC2$^{L11A/L12A}$) or a pore dead mutant (TPC2$^{L11A/L12A/L265P}$). Colored lines represent the mean response from a population of cells. Traces in grey represent responses of single cells. (**J**) Statistical analysis of the maximal change in Fura-2 ratio (mean ± SEM) with the number of independent transfections in parentheses. An unpaired t-test was applied. *p<0.05. (**K–L**) Similar to I and J except that cells were stimulated with TPC2-A1-P. ***p<0.001. Traces in grey represent single cells responding to TPC2-A1-P. (**M–N**) Representative Ca^{2+} signals recorded from HeLa cells transiently transfected with human TRPML1$^{\Delta NC}$. Cells were sequentially stimulated with TPC2-A1-N (**M**) or TPC2-A1-P (**N**) and the TRPML agonist ML-SA1. (**O–T**) Ca^{2+} signals recorded from HeLa cells transiently transfected with GCaMP6(s) fused to human TPC2 (hTPC2^{GCaMP}) or a pore-dead mutant (hTPC2$^{GCaMP/L265P}$). Cells were sequentially stimulated with TPC2-A1-N (**O and P**) or TPC2-A1-P (**R and S**) and the Ca^{2+} ionophore, ionomycin in the absence of extracellular Ca^{2+}. Statistical analysis of the change in fluorescence intensity (mean ± SEM; **Q and T**). An unpaired t-test was applied. *p<0.05 and **p<0.01. CY = cytosol, LY = lysosome.

The online version of this article includes the following source data and figure supplement(s) for figure 1:

Source data 1. Identification of TPC2 hit compounds.

Figure 1 continued on next page

Figure 1 continued

Figure supplement 1. Effect of different TPC2 channel blockers on TPC2-A1-N and ML-SA1 mediated changes in intracellular calcium.
Figure supplement 1—source data 1. Effect of different TPC2 channel blockers on TPC2-A1-N and ML-SA1 mediated changes in intracellular calcium.
Figure supplement 2. TPC2-A1-N and TPC2-A1-P mediated changes in intracellular calcium in the absence of extracellular calcium.
Figure supplement 2—source data 1. TPC2-A1-N and TPC2-A1-P mediated changes in intracellular calcium in the absence of extracellular calcium.
Figure supplement 3. Effects of TPC2-A1-N and TPC2-A1-P on TRPML1, 2, and 3.
Figure supplement 3—source data 1. Effects of TPC2-A1-N and TPC2-A1-P on TRPML1, 2, and 3.
Figure supplement 4. Synthesis and functional analysis of TPC2-A1-N analogs.
Figure supplement 4—source data 1. Functional analysis of TPC2-A1-N analogs.
Figure supplement 5. Structures of **TPC2-A1-N** and analogs.
Figure supplement 6. Synthesis and functional analysis of TPC2-A1-P analogs.
Figure supplement 6—source data 1. Functional analysis of TPC2-A1-P analogs.
Figure supplement 7. Effect of TPC2-A1-N and TPC2-A1-P on TPC1.
Figure supplement 7—source data 1. Effects of TPC2-A1-N and TPC2-A1-P on TPC1 in endo-lysosomal patch-clamp experiments.

cells expressing TRPML2 or TRPML3 (***Figure 1—figure supplement 3C and D***), indicating a selective, pore-dependent action of both agonists on TPC2.

The consensus logP (octanol/water; SwissADME) values for TPC2-A1-N (4.56) and TPC2-A1-P (5.35) predict that they are cell permeable. To determine whether TPC2-A1-N and TPC2-A1-P were able to release Ca^{2+} from lysosomes, we expressed TPC2 fused to the genetically encoded Ca^{2+} indicator, GCaMP6(s) both with ($TPC2^{GCaMP}$) and without ($TPC2^{GCaMP/L265P}$) an intact pore (***Figure 1O–T***) in order to measure global Ca^{2+} signals. TPC2-A1-N and TPC2-A1-P evoked Ca^{2+} signals in cells expressing intracellular $TPC2^{GCaMP}$ but not $TPC2^{GCaMP/L265P}$. Again the responses to TPC2-A1-P were modest compared to TPC2-A1-N.

Systematic structure modifications were performed on both screening hits. Surprisingly, none of the modified versions of TPC-A1-N or TPC2-A1-P showed significantly increased efficacies (***Figure 1—figure supplements 4*** and ***5***). TPC2-A1-P analogues missing the trifluoromethoxy residue were completely inactive (***Figure 1—figure supplement 6***).

Collectively, our data show that TPC2-A1-N and TPC2-A1-P activate TPC2 with differential effects on Ca^{2+} mobilization.

TPC2 agonists differentially evoke Na^+ currents in isolated endo-lysosomes

To determine more directly whether TPC2-A1-N and TPC2-A1-P activate TPC2, endo-lysosomal patch-clamp experiments were performed (***Figure 2***). TPC2-A1-N elicited currents using Na^+ as the major permeant ion, in vacuolin-enlarged endo-lysosomes isolated from TPC2-expressing cells (***Figure 2A***). The currents were inhibited by ATP as reported previously (***Cang et al., 2013***). In contrast, no activation was found in cells expressing TPC1 (***Figure 1—figure supplement 7***). Endo-lysosomes isolated from cells expressing a gain-of-function variant of TPC2 ($TPC2^{M484L}$) (***Chao et al., 2017***) showed larger currents compared to the wild-type isoform upon application of TPC2-A1-N (***Figure 2B***). TPC2-A1-P also evoked currents in endo-lysosomes isolated from cells expressing TPC2 and $TPC2^{M484L}$ (***Figure 2C and D***). As with TPC2-A1-N, the currents were potentiated by the gain-of-function variant (***Figure 2D***). Surprisingly, the currents evoked by TPC2-A1-P were significantly larger than those evoked by TPC2-A1-N (***Figure 2E–G***) in both wild-type and gain-of-function variant. Full concentration-effect relationships for the plateau response in endo-lysosomal patch-clamp experiments indicated EC_{50} values of 0.6 μM for both TPC2-A1-N and TPC2-A1-P (***Figure 2—figure supplement 1A***).

Increased Na^+ currents in the face of reduced Ca^{2+} signals (***Figure 1***) upon TPC2-A1-P activation prompted us to examine the effects of Na^+ removal on intracellular Ca^{2+} elevation. For these experiments, we used cells stably expressing $TPC2^{L11A/L12A}$ and agonist concentrations that evoked similar responses. As shown in ***Figure 2H and J***, the amplitude of Ca^{2+} signals evoked by TPC2-A1-N were unaffected by removal of Na^+ from the extracellular solution, although the rate of rise was increased. In contrast, both the amplitude and rate of rise of the responses to TPC2-A1-P were markedly enhanced (***Figure 2I and J***). These data indicate that TPC2 is activated by TPC2-A1-N and TPC2-A1-P but that its permeability to Na^+ differs upon activation.

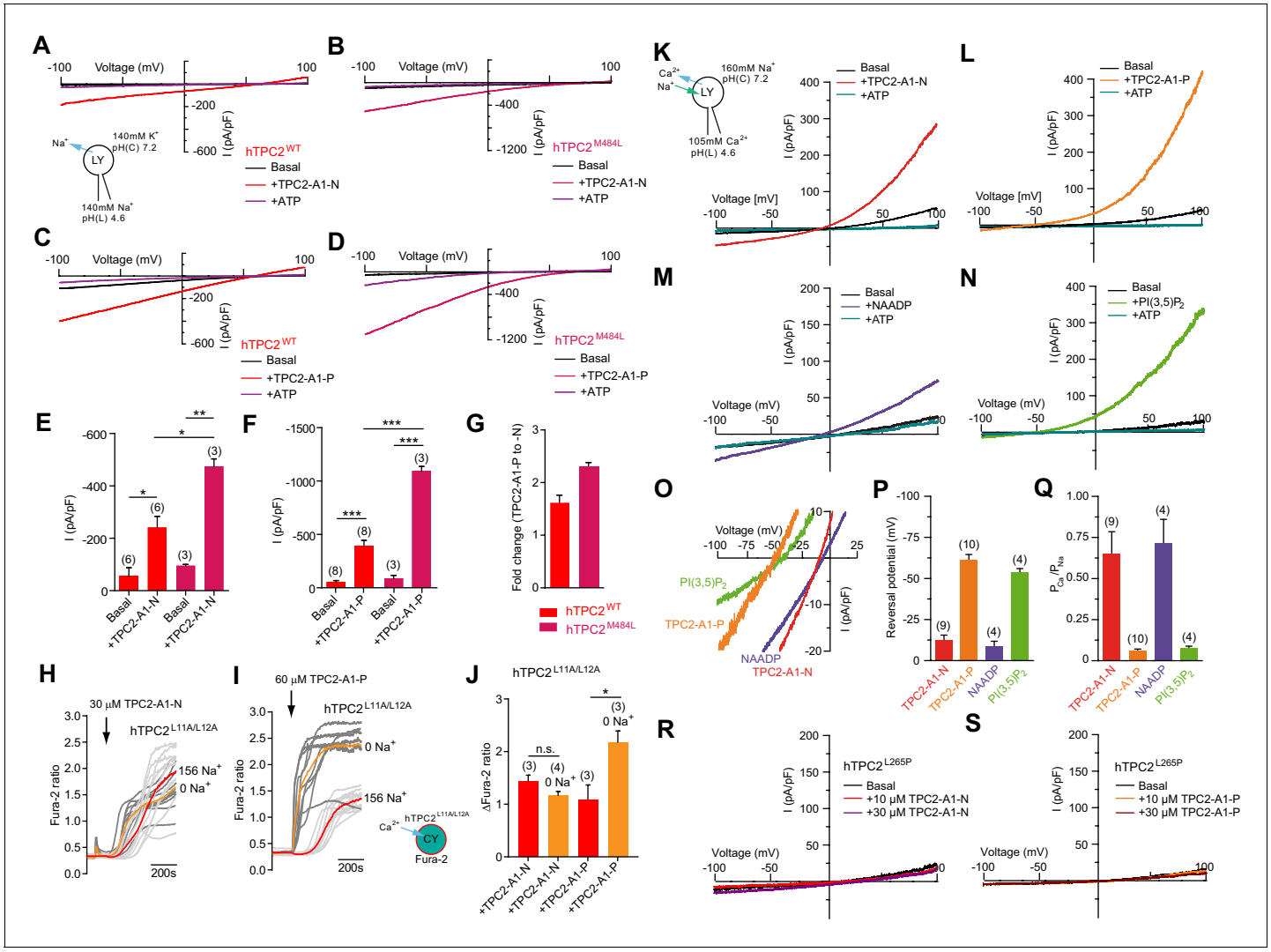

Figure 2. TPC2 agonists alter Ca^{2+}/Na^{+} permeability of TPC2. (**A–B**) Representative TPC2-A1-N-evoked currents from enlarged endo-lysosomes isolated from HEK293 cells transiently expressing human TPC2 (hTPC2) (**A**) or a gain-of-function variant, ($hTPC2^{M484L}$) (**B**). Currents were obtained before and after addition of 10 µM TPC2-A1-N in the absence or presence of 1 mM ATP. Recordings were carried out using standard bath and pipette solutions and applying ramp protocols (−100 mV to +100 mV over 500 ms) every 5 s at a holding potential of −60 mV. (**C–D**) Similar to A and B except that TPC2-A1-P (10 µM) was used. (**E–G**) Statistical analysis of current densities (mean ± SEM) recorded at −100 mV for endo-lysosomes expressing TPC2 or $TPC2^{M484L}$ for TPC2-A1-N (**E**) and TPC2-A1-P (**F**), and the fold-change in current evoked by TPC2-A1-P versus TPC2-A1-N in the two variants (**G**). Red bars are WT and maroon bars are mutant. An unpaired t-test was applied. *p<0.05, **p<0.01, and ***p<0.001 (n > 10 endo-lysosomes per condition). (**H–I**) Ca^{2+} signals evoked by TPC2-A1-N (**H**) or TPC2-A1-P (**I**) in Fura-2-loaded HEK293 cells stably expressing $hTPC2^{L11A/L12A}$. Recordings (mean responses from three to four independent experiments) were obtained in standard or Na^{+}-free extracellular solution. (**J**) Statistical analysis of the maximal change in Fura-2 ratio (mean ± SEM). An unpaired t-test was applied. *p<0.05. (**K–N**) Agonist-evoked cation currents from enlarged endo-lysosomes isolated from HEK293 cells stably expressing human TPC2 under bi-ionic conditions: 160 mM Na^{+} in the cytosol (bath) and 105 mM Ca^{2+} in the lumen (pipette). Representative current-voltage curves before and after stimulation with either 10 µM TPC2-A1-N (**K**), 10 µM TPC2-A1-P (**L**), 50 nM NAADP (4 recordings out of 8 attempts) (**M**), or 1 µM $PI(3,5)P_2$ (**N**). ATP (1 mM) was added at the end of each experiment. Recordings were carried out using ramp protocols (−100 mV to +100 mV over 500 ms) every 5 s at a holding potential of 0 mV. (**O**) Expanded views of K-N, showing the reversal potentials (E_{rev}) of currents evoked by the indicated agonist. (**P–Q**) Statistical analyses of E_{rev} (**P**) and the calculated relative cationic permeability ratios (P_{Ca}/P_{Na}) (**Q**). Shown are mean values ± SEM. (**R–S**) Representative TPC2-A1-N- (**R**) or TPC2-A1-P- (**S**) evoked currents from endo-lysosomes isolated from HEK293 cells transiently expressing $hTPC2^{L265P}$ under bi-ionic conditions.

The online version of this article includes the following source data and figure supplement(s) for figure 2:

Source data 1. TPC2 agonists alter Ca/Na permeability of TPC2.

Figure supplement 1. Dose response curves for TPC2-A1-N and TPC2-A1-P in endo-lysosomal patch-clamp experiments and endo-lysosomal patch-clamp analysis of compound effects under different conditions.

Figure 2 continued on next page

Figure 2 continued

Figure supplement 1—source data 1. Dose response curves for TPC2-A1-N and TPC2-A1-P in endo-lysosomal patch-clamp experiments and endo-lysosomal patch-clamp analysis of compound effects under different conditions.

TPC2 agonists alter Ca^{2+}/Na^{+} permeability of TPC2

The above analyses raised the intriguing possibility that the selectivity of TPC2 to Ca^{2+} and Na^{+} might not be fixed. To directly test this, we measured cation conductance evoked by the two compounds under bi-ionic conditions (luminal side: 105 mM Ca^{2+}, pH 4.6, cytosolic side: 160 mM Na^{+}, pH 7.2) (***Figure 2K and L***). For these experiments, we used cells stably expressing TPC2. Based on the reversal potential (E_{rev}), the P_{Ca}/P_{Na} permeability ratio of TPC2-A1-N-evoked currents ($I_{TPC2\text{-}A1\text{-}N}$) was 0.65 ± 0.13 (***Figure 2O–Q***). In marked contrast, E_{rev} values for TPC2-A1-P-evoked currents ($I_{TPC2\text{-}A1\text{-}P}$) were more negative such that the P_{Ca}/P_{Na} permeability ratio was 0.04 ± 0.01 (***Figure 2O–Q***) and thus Na^{+}-selective. These ratios are highly reminiscent of those obtained for endogenous NAADP-mediated currents in planar patch-clamp analyses (***Ruas et al., 2015***) and for recombinant TPC2 activated by $PI(3,5)P_2$ measured using endo-lysosomal patch-clamp experiments where the channel appeared insensitive to NAADP (***Wang et al., 2012***). We thus examined the effects of NAADP and $PI(3,5)P_2$ in parallel. NAADP (50 nM) evoked robust currents with an E_{rev} similar to TPC2-A1-N (−8.5 mV for NAADP versus −12 mV for TPC2-A1-N). The P_{Ca}/P_{Na} for NAADP (0.73 ± 0.14) was thus similar to TPC2-A1-N (***Figure 2M–Q***). In contrast, the E_{rev} for $PI(3,5)P_2$ (−53 mV) was similar to TPC2-A1-P (−61 mV) and the previously reported E_{rev} for $PI(3,5)P_2$ (−68 mV) (***Wang et al., 2012***), corresponding to a P_{Ca}/P_{Na} ratio of 0.08 ± 0.01 (***Figure 2M–Q***). No significant outward Na^{+} or inward Ca^{2+} conductances were observed in endo-lysosomes isolated from HEK293 cells expressing 'pore-dead' $TPC2^{L265P}$ in the presence of TPC2-A1-N or TPC2-A1-P (***Figure 2R–S*** and ***Figure 2—figure supplement 1B–C***). Moreover, the agonists induced similar shifts in selectivity using luminal solution containing 114 mM Na^{+} and 30 mM Ca^{2+} and a bath solution containing 160 mM Na^{+} (***Figure 2—figure supplement 1D–F***) confirming that the measured P_{Ca}/P_{Na} permeability ratio is independent of the luminal Ca^{2+} concentration. These data indicate that TPC2-A1-N and TPC2-A1-P not only differentially affect current amplitudes but also influence the P_{Ca}/P_{Na} permeability ratio (***Figure 2Q***). TPC2-A1-N-activated TPC2 shows a higher relative Ca^{2+} permeability, similar to NAADP-activated TPC2. In contrast, TPC2-A1-P-activated TPC2 shows a lower relative Ca^{2+} permeability, similar to $PI(3,5)P_2$-activated TPC2. Ion permeation through TPC2 is thus ligand-dependent providing an explanation for conflicting evidence that TPC2 is a NAADP-activated Ca^{2+} release channel (***Brailoiu et al., 2010***; ***Grimm et al., 2014***; ***Pitt et al., 2010***; ***Ruas et al., 2015***; ***Schieder et al., 2010***) or a $PI(3,5)P_2$ gated Na^{+} channel (***Boccaccio et al., 2014***; ***Guo et al., 2017***; ***Wang et al., 2012***).

TPC2 agonists activate TPC2 through distinct sites

The $PI(3,5)P_2$ binding site in TPC2 has recently been identified (***She et al., 2019***). To gain mechanistic insight into agonist action, we mutated K204 which is required for activation of TPC2 by PI(3,5)P2 (***Kirsch et al., 2018***; ***She et al., 2019***) and examined its effect on responses to TPC2-A1-N and TPC2-A1-P. Intracellular Ca^{2+} elevation mediated by TPC2-A1-N was similar in cells expressing plasma membrane targeted TPC2 with and without the K204A mutation (***Figure 3A and C***). In contrast, the responses to TPC2-A1-P were reduced approximately two-fold (***Figure 3B and C***). Similar selective inhibition was observed in GCaMP assays (***Figure 3G***). Thus, whereas responses to TPC2-A1-N were comparable for the wild-type and mutant channel, the responses to TPC2-A1-P were reduced by the mutation. Furthermore, currents evoked by TPC2-A1-N were largely unaffected by the K204A mutation (***Figure 3H and J***). In contrast, those to TPC2-A1-P were reduced (***Figure 3I and J***). Collectively, these data suggest K204 is required for activation of TPC2 by TPC2-A1-P and $PI(3,5)P_2$ but not TPC2-A1-N. Molecular determinants for agonist action in TPC2 thus differ.

TPC2 agonists differentially affect lysosomal pH

Lysosomal function and integrity critically depend on the pH in the lysosomal lumen. Previously, it has been reported that NAADP induced pH changes in the lumen of acidic Ca^{2+} stores, leading to an alkalinization (***Cosker et al., 2010***; ***Morgan and Galione, 2007***) but the role of TPC2 in

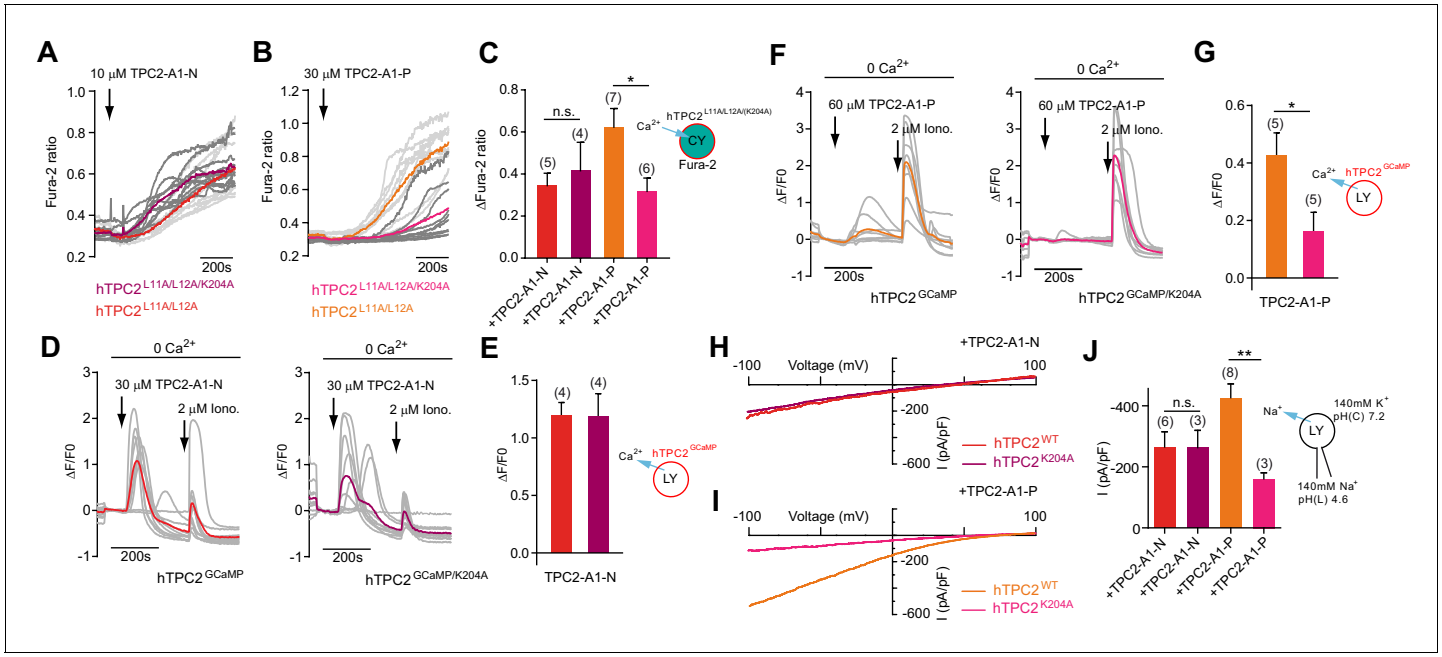

Figure 3. TPC2 agonists activate TPC2 through distinct sites. (**A–B**) Representative Ca^{2+} signals recorded from Fura-2-loaded HeLa cells (n = 10, each) stimulated with the indicated concentration of TPC2-A1-N or -P. Cells were transiently transfected with plasma membrane targeted human TPC2 ($hTPC2^{L11A/L12A}$) or the $PI(3,5)P_2$-insensitive mutant ($TPC2^{L11A/L12A/K204A}$). (**C**) Statistical analysis of the maximal change in Fura-2 ratio (mean ± SEM) with the number of independent transfections in parentheses. An unpaired t-test was applied. *p<0.05. (**D–F**) Representative Ca^{2+} signals recorded from HeLa cells (n = 10, each) transiently transfected with GCaMP6(s) fused to wild-type TPC2 ($TPC2^{GCaMP}$) or the $PI(3,5)P_2$-insensitive mutant ($TPC2^{GCaMP/K204A}$). Cells were sequentially stimulated with TPC2-A1-N or -P and the Ca^{2+} ionophore ionomycin in the absence of extracellular Ca^{2+}. (**E–G**) Statistical analysis of the change in fluorescence intensity (mean ± SEM) of experiments as shown in D and F. An unpaired t-test was applied. *p<0.05. (**H–I**) Representative TPC2-A1-N or -P-evoked currents from enlarged endo-lysosomes isolated from HEK293 cells transiently expressing human TPC2 (hTPC2) or the $PI(3,5)P_2$-insensitive mutant, ($hTPC2^{K204A}$). Currents were obtained before and after addition of 10 µM TPC2-A1-N or -P. Recordings were carried out using standard bath and pipette solutions and applying ramp protocols (−100 mV to +100 mV over 500 ms) every 5 s at a holding potential of −60 mV. (**J**) Statistical analysis of current densities (mean ± SEM) recorded at −100 mV for endo-lysosomes expressing TPC2 or $TPC2^{K204A}$ using TPC2-A1-N or TPC2-A1-P to activate, respectively. *p<0.05 and **p<0.01, using one-way ANOVA followed by Tukey's post hoc test.
The online version of this article includes the following source data for figure 3:

Source data 1. TPC2 agonists activate TPC2 through distinct sites.

regulating lysosomal pH is conflicting (***Ambrosio et al., 2016***; ***Cang et al., 2013***; ***Grimm et al., 2014***; ***Lin et al., 2015***; ***Ruas et al., 2015***). We therefore assessed the acute effects of TPC2-A1-N and TPC2-A1-P on lysosomal pH using a recently described novel lysosomal pH sensor, pH-Lemon-GPI (***Burgstaller et al., 2019***; ***Figure 4A–K*** and ***Video 1***). Results from high-resolution array confocal laser scanning microscopy revealed that TPC2-A1-N, but not TPC2-A1-P, increased pH of single vesicles in cells expressing wild-type TPC2 (***Figure 4A–B*** and ***Video 1***). In contrast, no pH changes were observed in cells expressing $TPC2^{L265P}$. Time-lapse wide-field fluorescence microscopy showed that activation of endogenous TPC2 with TPC2-A1-N modestly increased the lysosomal pH in untransfected cells in a time-dependent manner (***Figure 4C and I***). The pH response was markedly potentiated in cells expressing wild-type TPC2 but not the pore-mutant (***Figure 4D,E and I***). The response in the former was approximately half that evoked by direct alkalization with NaN_3/NH_4Cl (***Figure 4K***). Again, vesicular pH was largely unaffected by TPC2-A1-P (***Figure 4F–H and J***). Time-lapse imaging additionally revealed that vesicle motility was strongly impaired by TPC2-A1-N but not TPC2-A1-P (***Video 2***). The effect of TPC2-A1-N was reversible and appeared to temporally correlate with the increase in vesicular pH (***Video 1***). In endo-lysosomal patch-clamp experiments, we probed the proton permeability of TPC2 and found that in contrast to TPC2-A1-P, TPC2-A1-N rendered the channel proton-permeable, thus providing a direct channel-dependent mechanism leading to alkalinization (***Figure 4L–N***). Proton permeability did not substantially change our estimates of relative Ca^{2+} and Na^+ permeability as P_{Ca}/P_{Na} values were similar when proton currents were

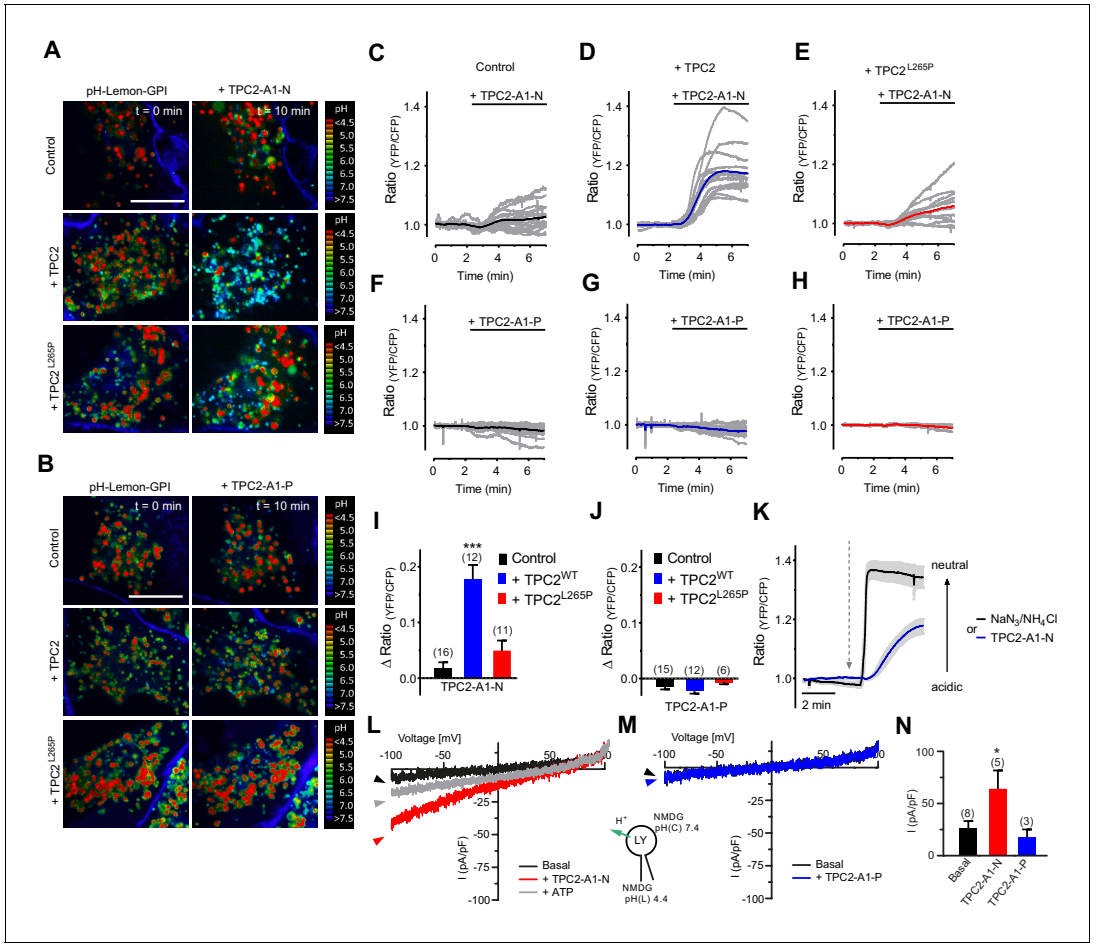

Figure 4. TPC2 agonists differentially affect lysosomal pH and proton conductance. (**A**) Representative pseudo colored ratio images (mTurquoise2/EYFP) of vesicle targeted pH-Lemon-GPI in control HeLa cells (upper panel, n = 4/141 cells), HeLa cells positive for wild-type TPC2-mCherry (middle panel, c = 3/70 cells) and HeLa cells positive for $TPC2^{L265P}$-mCherry (lower panel, n = 3/74 cells) in the absence (t = 0 min; left images) and upon treatment for 10 min with 10 µM TPC2-A1-N (t = 10 min; right images). Scale bar = 5 µm. (**B**) Representative pseudo colored ratio images (mTurquoise2/EYFP) of vesicle targeted pH-Lemon-GPI in control HeLa cells (upper panel, n = 3/121 cells), HeLa cells positive for wild-type TPC2-mCherry (middle panel, n = 3/59 cells) and HeLa cells positive for $TPC2^{L265P}$-mCherry (lower panel, n = 3/71 cells) in the absence (t = 0 min; left images) and upon treatment for 10 min with 10 µM TPC2-A1-P (t = 10 min; right images). Scale bar = 5 µm. (**C–E**) Normalized single cell responses (grey curves) and the respective average response (colored curves) of pH-Lemon-GPI upon treatment with 10 µM TPC2-A1-N in a region of high vesicle density. Shown are ratio curves of pH-Lemon-GPI expressed in control HeLa cells (n = 16 cells; **C**), in HeLa cells co-expressing wild-type TPC2-mCherry (n = 12 cells; **D**), and HeLa cells co-expressing $TPC2^{L265P}$-mCherry (n = 11 cells; **E**). (**F–H**) Experiments as in C-E for TPC2-A1-P. Shown are ratio curves of pH-Lemon-GPI expressed in control HeLa cells (n = 15 cells; **F**), in HeLa cells co-expressing wild-type TPC2-mCherry (n = 12 cells; **G**), and HeLa cells co-expressing $TPC2L^{265P}$-mCherry (n = 6 cells, (**H**). (**I–J**) Columns represent delta ratio values of pH-Lemon-GPI at min six from curves as shown in panels C-E and F-H, respectively. ***p<0.001 using unpaired student's t-test. (**K**) Average ratio signals over time of pH-Lemon-GPI in HeLa cells expressing wild-type TPC2-mCherry in response to either 0.5% NaN_3 and 50 mM NH_4Cl (black average curve ± SEM, n = 12 cells) or 10 µM TPC2-A1-N (blue average curve ± SEM, n = 12 cells). Cells were treated with compounds as indicated. (**L–M**) Representative agonist-evoked inward H^+ currents from enlarged endo-lysosomes using hTPC2-expressing HEK293 cells. Both bath and pipette solutions contained 1 mM HCl, 5 mM HEPES, 5 mM MES, 150 mM NMDG, pH as indicated, adjusted with MSA. Ramp protocol (−100 mV to +100 mV in 500 ms, holding voltage = 0 mV) was used. Currents were obtained before and after addition of 10 µM TPC2-A1-N (**L**) or TPC2-A1-P (**M**). ATP (1 mM) was added at the end of the experiment to block TPC2 (**L**). (**N**) Statistical analysis of current densities (mean ± SEM) recorded at −100 mV (inward H^+ conductance; H^+ from luminal to cytosolic site) as shown in L and M. *p<0.05, using one-way ANOVA followed by Bonferroni's post hoc test.

The online version of this article includes the following source data for figure 4:

Source data 1. Effect of TPC2-A1-N on vesicular pH.

subtracted from currents obtained under bi-ionic conditions (0.44 for TPC2-A1-N and 0.06 for TPC2-A1-P). In sum, these findings demonstrate that TPC2 activation is coupled to lysosomal pH and motility in an agonist-dependent manner.

TPC2 agonists differentially affect lysosomal exocytosis

To further probe the physiological relevance of TPC2 activation by the agonists, we assessed the effect of TPC2-A1-N and TPC2-A1-P on lysosomal exocytosis (***Figure 5***). Lysosomal exocytosis is involved in a plethora of physiological and pathophysiological processes including release of lysosomal enzymes and inflammatory mediators, clearance of lysosomal storage material and pathogens, plasma membrane repair and cancer progression (***Lopez-Castejon and Brough, 2011***; ***Machado et al., 2015***; ***Miao et al., 2015***; ***Xu and Ren, 2015***). The Ca^{2+}-dependence of this process has been mostly ascribed to activation of TRPML1 (***Xu and Ren, 2015***). Here, we used murine macrophages which express high endogenous levels of TPC2 (***Cang et al., 2013***). To assess lysosomal exocytosis, we quantified translocation of LAMP1 to the cell surface. As shown in ***Figure 5A–E***, TPC2-A1-N was without effect on lysosomal exocytosis. This was not due to lack of efficacy of TPC2-A1-N on the murine channel because Ca^{2+} measurements with mouse TPC2 fused to GCaMP6 ($MmTPC2^{GCaMP}$) confirmed that TPC2-A1-N evoked larger responses than TPC2-A1-P (***Figure 5—figure supplement 1A***) similar to the human channel (***Figure 1***). In contrast, TPC2-A1-P evoked robust lysosomal exocytosis in a time- and concentration-dependent manner (***Figure 5A–E***), providing a corollary to the effects of the agonists on lysosomal pH. To further corroborate that TPC2-A1-P triggers TPC2-dependent vesicle fusion in primary macrophages, electrophysiological measurements of membrane capacitance via the whole-cell patch-clamp technique were performed (***Figure 5F–H***). These data showed that TPC2-A1-P caused a modest increase in cell size. In the final set of experiments, we examined the effects of TPC2 knockout on agonist responses. As shown in ***Figure 5—figure supplement 1***, both TPC2-A1-N and TPC2-A1-P evoked measurable endogenous TPC2-like currents in macrophages from wild-type animals. The amplitudes of the currents were larger for TPC2-A1-P than TPC2-A1-N, again recapitulating agonist effects on human TPC2 (***Figure 2***). Importantly, currents were reduced in macrophages derived from TPC2 KO cells (***Figure 5—figure supplement 1***) and the effects of TPC2-A1-P on lysosomal exocytosis and cell size were abolished (***Figure 5A–E***). TPC2 knockout however failed to affect lysosomal exocytosis in response to ionomycin attesting to specificity (***Figure 5A–E***). Collectively, these data further identify agonist-selective effects of TPC2 on lysosomal physiology in an endogenous setting.

Discussion

We demonstrate that the ion selectivity of TPC2 is not fixed but rather agonist-dependent. To the best of our knowledge, TPC2 is a unique example of an ion channel that conducts different ions in response to different activating ligands. The novel lipophilic, membrane permeable isoform-selective small molecule agonists of TPC2 (TPC2-A1-N and TPC2-A1-P) characterized herein mimic the physiological actions of NAADP and $PI(3,5)P_2$ most likely through independent binding sites. As such, our data reconcile diametrically opposed opinion regarding activation of TPC2 by endogenous cues and the biophysical nature of the ensuing ion flux. Whether TPC1 also switches its ion selectivity remains to be established. A previous bilayer study found that $PI(3,5)P_2$ did not gate TPC1 but induced modest shifts in relative permeability to different cations when TPC1 was activated by NAADP (***Pitt et al., 2014***).

Physiologically, we demonstrate inverse effects of the agonists on key lysosomal activities. While TPC2-A1-N increases the pH in the lysosomal lumen in a TPC2-dependent manner, TPC2-A1-P has no significant effect on lysosomal pH. An alkalinizing effect of TPC2-A1-N is in accordance with effects described previously for NAADP, which likewise induces alkalinization (***Cosker et al., 2010***; ***Morgan and Galione, 2007***) and may be related to agonist-specific effects on proton permeability. The acute nature of these experiments in live cells, made possible by the lipophilicity of TPC2-A1-N, circumvents possible compensatory effects of TPC2 knockout which may have confounded steady-state analyses in previous studies (***Cang et al., 2013***; ***Grimm et al., 2014***; ***Ruas et al., 2015***). In contrast, TPC2-A1-P but not TPC2-A1-N promoted lysosomal exocytosis. The lack of effect of TPC2-A1-N is surprising given the Ca^{2+}-dependence of lysosomal exocytosis but may relate to its inhibitory effect on lysosomal motility. Boosting lysosomal exocytosis is gaining traction as a strategy to

combat disease (**Lopez-Castejon and Brough, 2011**; **Machado et al., 2015**; **Miao et al., 2015**; **Xu and Ren, 2015**). Selective activation of TPC2 in 'PI(3,5)P_2-mode' with TPC2-A1-P offers novel scope to achieve this.

In sum, TPC2 can mediate very different physiological and possibly pathophysiological effects depending on how it is activated. TPC2 therefore emerges as an integrator of adenine nucleotide- and phosphoinositide-based messengers with an intrinsic ability to signal through switchable ionic signatures.

Materials and methods

Key resources table

Reagent type (species) or resource	Designation	Source or reference	Identifiers	Additional information
Cell line (*Homo-sapiens*)	HEK 293	DSMZ	ACC 305	
Cell line (*Homo-sapiens*)	HeLa S3	ATCC	CCL-2.2	
Cell line (*Homo-sapiens*)	HeLa cells stably expressing pH-Lemon-GPI	This paper		Generated by selective antibiotic G418 disulfate salt from Sigma Aldrich (Cat#A1720). After 4 weeks of cultivation in 800 µg/mL, positive cells were selected by FACS analysis.
Cell line (*Homo-sapiens*)	HEK 293 stably expressing $TPC2^{L11A/L12A}$ -RFP	This paper		Generated by selective antibiotic neomycin from Invitrogen (Cat#10486–025) following the guideline V790-20/V795-20 (Invitrogen)
Cell line (*Homo-sapiens*)	HEK 293 stably expressing $CLN3^{L253A/I254A}$ -RFP	This paper		Generated by selective antibiotic neomycin from Invitrogen (Cat#10486–025) following the guideline V790-20/V795-20 (Invitrogen)
Recombinant DNA reagent	HsTRPML1-YFP	(**Grimm et al., 2010**) PMID:20189104		
Recombinant DNA reagent	HsTRPML2-YFP	(**Grimm et al., 2010**) PMID:20189104		
Recombinant DNA reagent	HsTRPML3-YFP	(**Grimm et al., 2010**) PMID:20189104		
Recombinant DNA reagent	HsTPC2-YFP	(**Chao et al., 2017**) PMID:28923947		
Recombinant DNA reagent	$HsTPC2^{M484L}$-YFP	(**Chao et al., 2017**) PMID:28923947		
Recombinant DNA reagent	$HsTPC2^{L11/12A}$-YFP	This paper		Generated by site-directed mutagenesis from WT plasmid published by **Chao et al. (2017)**
Recombinant DNA reagent	$HsTPC2^{L11/12A/L265P}$-YFP	This paper		Generated by site-directed mutagenesis of WT plasmid published by **Chao et al. (2017)**
Recombinant DNA reagent	$HsTPC2^{L11/12A/K204A}$-YFP	This paper		Generated by site-directed mutagenesis of WT plasmid published by **Chao et al. (2017)**
Recombinant DNA reagent	HsTPC2-GCaMP6s	This paper		Generated by subcloning (**Chao et al., 2017**) WT TPC2 construct into Addgene vector #40753
Recombinant DNA reagent	$HsTPC2^{L265P}$-GCaMP6s	This paper		Generated by site-directed mutagenesis of WT GCaMP6s plasmid

Continued on next page

Continued

Reagent type (species) or resource	Designation	Source or reference	Identifiers	Additional information
Recombinant DNA reagent	HsTPC2^{K204A}-GCaMP6s	This paper		Generated by site-directed mutagenesis of WT GCaMP6s plasmid
Recombinant DNA reagent	MmTPC2-GCaMP6s	This paper		Generated by subcloning GCaMP6s from Addgene vector #40753 into WT MmTPC2 vector
Recombinant DNA reagent	HsTPC2$^{L11/12A}$-GFP	(**Brailoiu et al., 2010**) PMID:20880839		
Recombinant DNA reagent	HsTPC2$^{L11/12A}$-RFP	(**Brailoiu et al., 2010**) PMID:20880839		
Recombinant DNA reagent	HsTPC2$^{L11/12A/L265P}$-GFP	This paper		Generated by site-directed mutagenesis of HsTPC2$^{L11/12A}$-GFP (plasmid)
Recombinant DNA reagent	TRPML1$^{\Delta NC}$-GFP	(**Yamaguchi et al., 2011**) PMID:21540176		
Recombinant DNA reagent	HsTPC2$^{L11/12A/K204A}$-GFP	(**She et al., 2019**) PMID:30860481		
Recombinant DNA reagent	MmTPC1-YFP	(**Zong et al., 2009**) PMID:19557428		Generated by subcloning into TOPO pcDNA3.1-YFP, Addgene vector (#13033)
Biological sample	Macrophages from TPC2 KO mouse	(**Grimm et al., 2014**) PMID:25144390		
Antibody	LAMP1 antibody	Santa Cruz Biotechnology	sc19992	1:200
Transfection reagent	PolyJet	SignaGen Laboratories	SL100688	
Transfection reagent	TurboFect	Thermo Fisher	R0531	
Transfection reagent	Lipofectamine 2000	Thermo Fisher	11668	
Commercial assay or kit	Fluo-4 AM, cell permeant	Thermo Fisher	F14202	
Commercial assay or kit	Fura-2 AM, cell permeant	Thermo Fisher	F1221	
Chemical compound, drug	NAADP	Tocris	3905	
Chemical compound, drug	PI(3,5)P_2	Echelon Biosciences	P-3508	
Chemical compound, drug	Ionomycin	Sigma Aldrich and Cayman Chemical	I-0634 and 11932	
Chemical compound, drug	Tetrandrine	Sigma Aldrich and Santa Cruz Biotechnology	T2695 and sc201492A	
Chemical compound, drug	Raloxifene	Cayman Chemical	10011620	
Chemical compound, drug	Fluphenazine	Sigma Aldrich	F4765	
Chemical compound, drug	ML-SA1	Merck	648493	
Chemical compound, drug	ATP	Sigma Aldrich	A9187	
Chemical compound, drug	Sodiumazide (NaN_3)	Sigma Aldrich	09718	

Continued on next page

Continued

Reagent type (species) or resource	Designation	Source or reference	Identifiers	Additional information
Chemical compound, drug	Ammoniumchloride (NH_4Cl)	Sigma Aldrich	S2002	
Software, algorithm	Origin8	OriginLab		
Software, algorithm	GraphPad Prism	GraphPad Software Inc		
Other	Glass Bottom Dish 35 mm	ibidi	81218	
Other	Perfusion Chamber PC30	Next Generation Fluorescence Imaging	PC30 (www.ngfi.eu)	Perfusion chamber used with gravity based perfusion system (NGFI, Graz, Austria)
Other	µ-Slide 8 Well	ibidi	80826	

High-throughput screening

The high-throughput screen was performed using a custom-made fluorescence imaging plate reader built into a robotic liquid handling station (Freedom Evo 150, Tecan, Männedorf, Switzerland) as previously described (***Urban et al., 2016***). HEK293 cells were used that stably expressed RFP fusion proteins of human TPC2 (C-terminally tagged) or human CLN3 (N-terminally tagged) rerouted to the plasma membrane. Targeting was achieved by mutation of the endo-lysosomal targeting motifs ($hTPC2^{L11A/L12A}$, $hCLN3^{L253A/I254A}$). Mutants were generated by site-directed mutagenesis using the QuikChange II XL protocol (Agilent), according to the manufacturer's instructions. Stable HEK293 cell lines were generated using 400 µg/mL geneticin (G418, Sigma). If G418-resistant foci were not identified after 3–4 days, the concentration of G418 was increased to 800 µg/mL. After 2–3 weeks cells were picked from G418-resistant foci and colonies were expanded in six well plates. RFP expression was assessed using confocal microscopy when cells were >50% confluent. Colonies with more than 95% RFP positive cells were selected, grown to >90% confluency, split and further expanded. For HTS experiments, cells were cultured at 37˚C with 5% of CO_2 in Dulbecco's modified Eagle medium (Thermo Fisher), supplemented with 10% fetal calf serum (Biochrom, Berlin, Germany), 2 mM L-glutamine, 100 U/mL penicillin, 0.1 mg/mL streptomycin, and 400–800 µg/mL G418. Cells were seeded on black-walled, clear-bottom 384-well plates (Greiner, Germany) and incubated with Fluo-4/AM (4 µM; Life Technologies, Eugene, OR) for 30 min at 37˚C, washed and resuspended in a HEPES-buffered solution 1 (HBS1) comprising 132 mM NaCl, 6 mM KCl, 1 mM $MgCl_2$, 1 mM $CaCl_2$, 10 mM HEPES, and 5.5 mM D-glucose (pH was adjusted to 7.4 with NaOH). For primary screening, individual compounds from Roche libraries (Xplore libraries X30 and X50, Roche, Basel, CH) were diluted in HBS1 to a working concentration of 100 µM. After recording the baseline for 30 s, compounds were injected to a final concentration of 10 µM. Recording continued for 180 s per quadrant (total 750 s). If high intensities were measured in both cell lines, the compounds were deemed false positives and excluded. Concentration-effect relationships were plotted using GraphPad Prism five and fitted to the Hill equation. The identity of the cell lines used has been authenticated by STR profiling. No mycoplasma contamination has been reported.

Ca^{2+} imaging

Single cell Ca^{2+} imaging experiments were performed using Fura-2. HeLa cells and HEK293 cells were cultured at 37˚C with 5% of CO_2 in Dulbecco's modified Eagle medium (Gibco), supplemented with 10% fetal bovine serum, 100 U/mL penicillin, and 0.1 mg/mL streptomycin. Cells were plated onto poly-L-lysine (sigma)-coated glass coverslips, grown overnight and transiently transfected for 18–24 hr with plasmids using lipofectamine 2000 (Invitrogen) or TurboFect (Thermo Fisher) according to the manufacturer's instructions. For Ca^{2+} influx experiments, cells were transfected with human TPC2 (C-terminally tagged with GFP or RFP) (***Brailoiu et al., 2010***) or TRPML1 (N-terminally-tagged with GFP (***Yamaguchi et al., 2011***) or C-terminally tagged with YFP). They were targeted to the plasma membrane by mutation/deletion of the endo-lysosomal targeting motifs. For Ca^{2+} imaging experiments with TRPML2 or TRPML3 (both C-terminally tagged with YFP ***Grimm et al., 2010***), the latter two sufficiently locating to the plasma membrane when overexpressed. A pore-dead mutant of plasma membrane, GFP-tagged TPC2 ($hTPC2^{L11A/L12A/L265P}$) was generated by site-

directed mutagenesis. Transfected cells were loaded for 1 hr at room temperature with Fura-2 AM (2.5 µM) and 0.005% (v/v) pluronic acid (both from Invitrogen) in HEPES-buffered solution 2 (HBS2) comprising 1.25 mM KH_2PO_4, 2 mM $CaCl_2$, 2 mM $MgSO_4$, 3 mM KCl, 156 mM NaCl, 10 mM D-glucose and 10 mM HEPES (adjusted to pH 7.4 with HCl). After loading, cells were washed three times in HBS2, and mounted in an imaging chamber. All recordings were performed in HBS2. Ca^{2+} imaging experiments were also performed in HEK293 cells stably expressing C-terminally RFP-tagged $hTPC2^{L11A/L12A}$ (see above). These cells were plated, loaded with Fura-2 and recorded as with HeLa cells, except for that in indicated experiments, NaCl in HBS2 was replaced with NMDG. For lysosomal Ca^{2+} release experiments, HeLa cells were transfected with human TPC2, C-terminally tagged with GCaMP6(s) ($hTPC2^{GCaMP}$). The hTPC2 sequence was amplified by PCR from the pcDNA3.1 plasmid encoding YFP-tagged hTPC2 as described previously (***Chao et al., 2017***), using a forward primer carrying a NheI restriction site followed by a Kozak sequence, and a sequence binding the first 17 base-pairs of hTPC2: TATGCTAGCGCCACCATGGCGGAACCCCAGGC. The reverse primer also contained a NheI restriction site, preceded by a GSG-linker coding sequence, and the final 20 base-pairs of hTPC2, excluding the TPC2 stop codon: ATAGCTAGCACCAGAACCCCTGCACAGCCACAGGTG. The PCR product was cloned into the GCaMP6(s) (Addgene ID 40753) vector by insertion into a NheI site, yielding plasmids encoding 6xHis tag-HsTPC2-GSG-Xpress tag-GCaMP6 fusion proteins. The ligated plasmid was sequenced by Sanger sequencing using standard CMV forward and pEGFP reverse primers, to confirm the insertion took place as desired. A pore dead mutant ($hTPC2^{GCaMP/L265P}$) was generated by site-directed mutagenesis using the QuikChange II XL protocol (Agilent), according to the manufacturer's instructions, using the forward primer sequence GAGTC TCTGACTTCCCCCCTGGTGCTGCTGAC (reverse primer reverse complement of the former). All recordings were performed in nominally Ca^{2+}-free HBS2. Images were acquired every 3 s at 20X (Fura-2) or 40X magnification using a cooled coupled device camera (TILL photonics) attached to an Olympus IX71 inverted fluorescence microscope fitted with a monochromator light source. Fura-2 was excited at 340 nm/380 nm, and GCaMP6(s) was excited at 470 nm. Emitted fluorescence was captured using 440 nm or 515 nm long-pass filters, respectively.

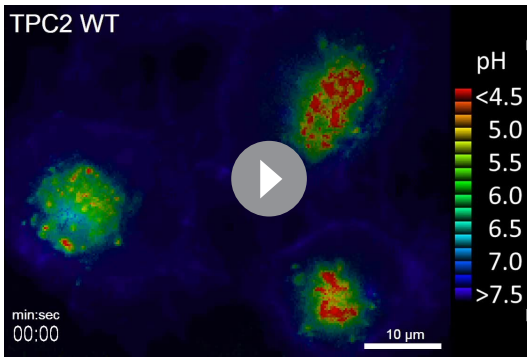

Video 1. TPC2-A1-N effectively increases vesicular pH in HeLa cells. Dynamic pseudo-colored ratio (mTurquoise2/EYFP) video of HeLa cells stably expressing pH-Lemon-GPI and co-expressing TPC2 WT upon addition of TPC2-A1-N at the time-point indicated. Pseudo-colored ratio scale with estimated pH values is shown on the right. Scale bar represents 10 µm.
https://elifesciences.org/articles/54712#video1

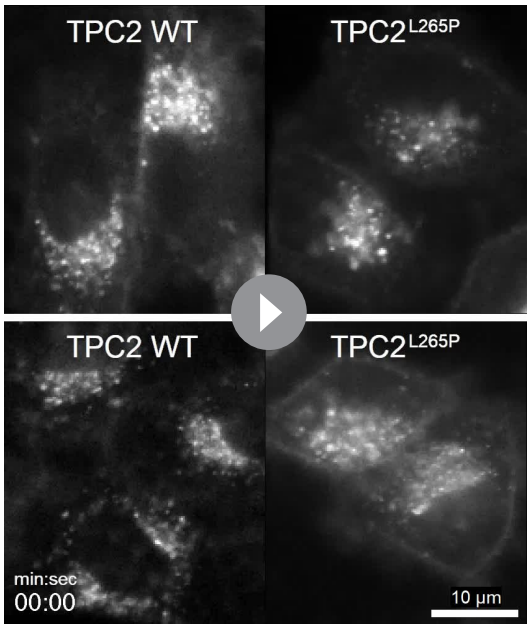

Video 2. Vesicle movement is impaired upon treatment with TPC2-A1-N, but not with TPC-A1-P. HeLa cells stably expressing pH-Lemon-GPI and co-expressing either TPC2 WT (upper left panel and lower left panel) or $TPC2^{L265P}$ (upper right panel and lower right panel) were analyzed. Shown are the mTurquoise2 fluorescence signals of pH-Lemon over time upon treatment with TPC2-A1-N (upper panels) and TPC2-A1-P (lower panels) at the time-points indicated. Time-lapse stacks were acquired using wide-field microscopy. Scale bar represents 10 µm.
https://elifesciences.org/articles/54712#video2

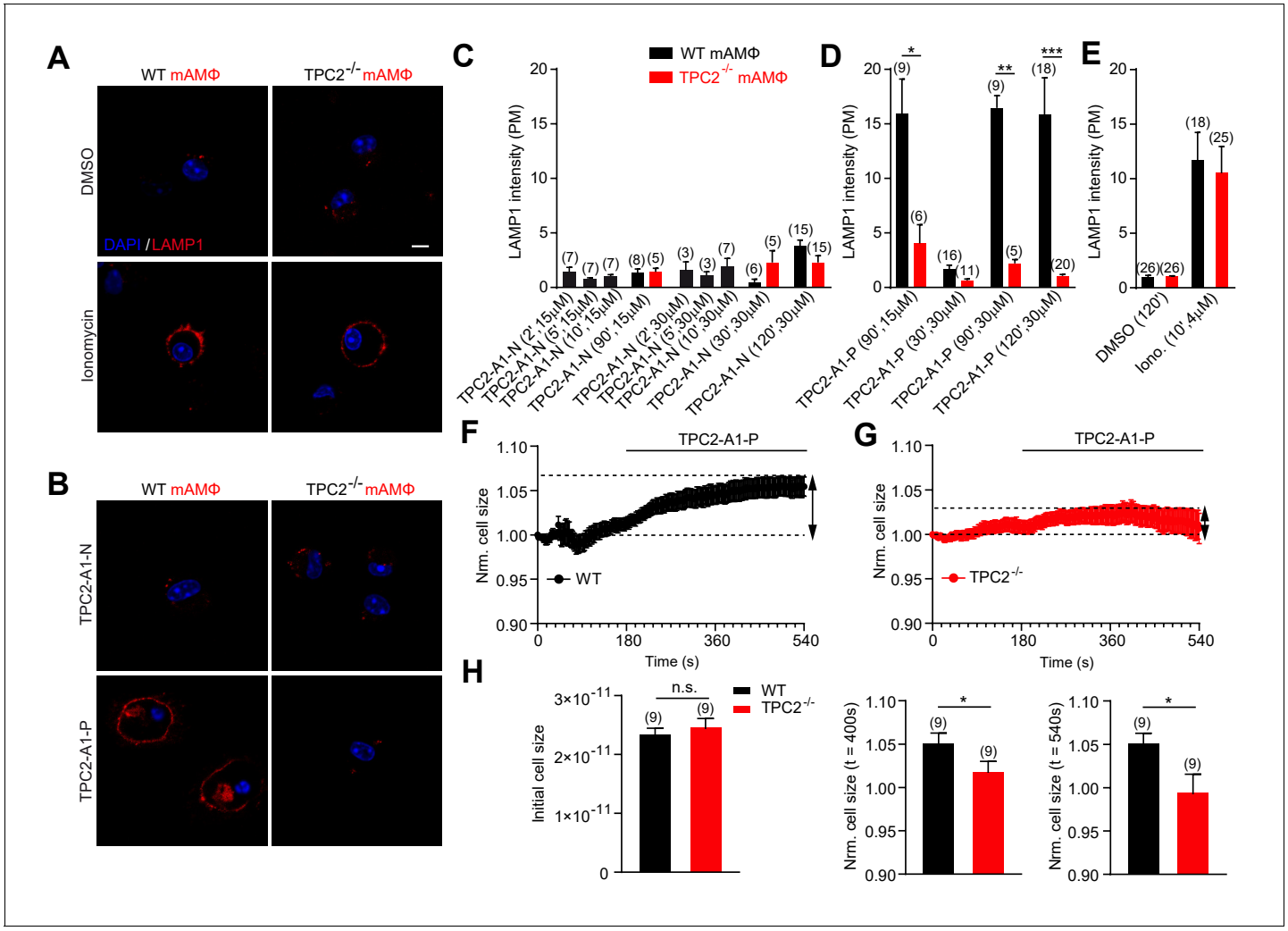

Figure 5. TPC2 agonists differentially affect lysosomal exocytosis. (**A–B**) Representative images of LAMP1 translocation assay using murine wild-type and TPC2 KO alveolar macrophages. Shown are results obtained after 120 min treatment with either DMSO, TPC2-A1-P (30 µM) or TPC2-A1-N (30 µM), or 10 min treatment with ionomycin (4 µM). (**C–E**) Statistical analysis of experiments as shown in A and B at different compound concentrations and incubation times as indicated. Shown are mean values ± SEM. **p<0.01, and ***p<0.001, using two-way ANOVA followed by Bonferroni's post hoc test. (**F–G**) Electrophysiological measurements of membrane capacitance via the whole-cell patch-clamp technique as an estimate of cell size (in picofarad [pF]) were used to record fusion of vesicles of primary alveolar macrophages isolated from WT (black, n = 9, **F**) or TPC2 KO (red, n = 9, **G**) mice. The normalized, averaged cell size was plotted versus time of the experiment. TPC2-A1-P (30 µM) was applied at 180 s until the end of the experiment indicated by the black bar. Data are shown as mean ± SEM. (**H**) Bar graphs show mean cell sizes at different time points. The initial cell size was measured immediately after whole cell break in pF and was used for normalization (left panel). Statistical analysis at 400 s (middle panel) and at 540 s (right panel). *p<0.05, unpaired student's t-test.

The online version of this article includes the following source data and figure supplement(s) for figure 5:

Source data 1. TPC2 agonists differentially affect lysosomal exocytosis.

Figure supplement 1. Effect of TPC2-A1-N and TPC2-A1-P on mouse TPC2 in overexpressing and endogenously expressing cells.

Endo-lysosomal patch-clamp experiments

Manual whole-endo-lysosomal patch-clamp recordings were performed as described previously (***Chen et al., 2017***). HEK293 cells were plated onto poly-L-lysine (Sigma)-coated glass coverslips, grown over night and transiently transfected for 17–25 hr with plasmids using TurboFect (Thermo Fisher) according to the manufacturer's instructions. Cells expressing wild-type (hTPC2) and a gain-of-function variant (hTPC2^{M484L}) of human TPC2 tagged at their C-termini with YFP were used (***Chao et al., 2017***). Cells were treated with either vacuolin or YM201636 (1 µM and 800 nM overnight, respectively) to enlarge endo-lysosomes. Currents were recorded using an EPC-10 patch-

clamp amplifier (HEKA, Lambrecht, Germany) and PatchMaster acquisition software (HEKA). Data were digitized at 40 kHz and filtered at 2.8 kHz. Fast and slow capacitive transients were cancelled by the compensation circuit of the EPC-10 amplifier. Glass pipettes for recording were polished and had a resistance of 4–8 MΩ. For all experiments, salt-agar bridges were used to connect the reference Ag-AgCl wire to the bath solution to minimize voltage offsets. Liquid junction potential was corrected as described (**Chen et al., 2017**). For the application of agonists, cytoplasmic solution was completely exchanged. Unless otherwise stated, the cytoplasmic solution comprised 140 mM K-MSA, 5 mM KOH, 4 mM NaCl, 0.39 mM $CaCl_2$, 1 mM EGTA and 10 mM HEPES (pH was adjusted with KOH to 7.2). Luminal solution comprised 140 mM Na-MSA, 5 mM K-MSA, 2 mM Ca-MSA, 1 mM $CaCl_2$, 10 mM HEPES and 10 mM MES (pH was adjusted to 4.6 with MSA). 500 ms voltage ramps from −100 to +100 mV were applied every 5 s, holding potential at 0 mV. The current amplitudes at −100 mV were extracted from individual ramp current recordings. For MmTPC1 measurements a one step protocol was applied (+140 mV over 2 s, holding potential of −70 mV) and the cytoplasmic solution contained 140 mM Na-gluconate, 5 mM NaOH, 4 mM KCl, 2 mM MgCl2, 0.39 mM CaCl2, 1 mM EGTA and mM 10 HEPES (pH 7.2). The luminal solution contained 140 mM Na-MSA, 5 mM K-MSA, 2 mM Ca-MSA, 1 mM $CaCl_2$, 10 mM HEPES and 10 mM MES (pH was adjusted to 4.6 with MSA). All statistical analyses were done using Origin8 software.

For analyses under bi-ionic conditions, HEK293 cells stably expressing hTPC2 tagged at its C-terminus with YFP were used. The cytoplasmic solution comprised 160 mM NaCl and 5 mM HEPES (pH was adjusted with NaOH to 7.2) and the luminal solution comprised 105 mM $CaCl_2$, 5 mM HEPES and 5 mM MES (pH was adjusted to 4.6 with MSA). The permeability ratio (P_{Ca}/P_{Na}) was calculated according to **Fatt and Ginsborg (1958)**:

$$\frac{P_{Ca}}{P_{Na}} = \frac{\gamma_{Na}}{\gamma_{Ca}} \cdot \frac{[Na]_i}{4[Ca]_o} \cdot exp^{\frac{E_{rev}F}{RT}} \cdot \left(exp^{\frac{E_{rev}F}{RT}} + 1\right)$$

for bi-ionic test (**Figure 2Q** and **Figure 2—figure supplement 1F**), and equation according to Eq. 13.47 from **Jackson (2006)**,

$$\frac{P_{Ca}}{P_{Na}} = \frac{\gamma_{Na}}{\gamma_{Ca}} \cdot \frac{\left([Na]_i \cdot exp^{\frac{E_{rev}F}{RT}} - [Na]_o\right)}{4[Ca]_o} \cdot \left(exp^{\frac{E_{rev}F}{RT}} + 1\right)$$

for internal and external solutions containing the same monovalent and divalent cations (**Figure 2—figure supplement 1D–F**). P_{Ca} = Ca^{2+} permeability; P_{Na} = Na^+ permeability; γ_{Ca} = Ca^{2+} activity coefficient (0.52); γ_{Na} = Na^+ activity coefficient (0.75); $[Ca]_o$ = concentration of Ca^{2+} in the lumen; $[Na]_i$ = concentration of Na^+ in the cytosol; $[Na]_o$ = concentration of Na^+ in the lumen; E_{rev} = reversal potential; F, R = standard thermodynamic constants; T = temperature.

Isolation of murine alveolar macrophages

For preparation of primary alveolar macrophages, mice were deeply anesthetized and euthanized by exsanguination. The trachea was exposed and cannulated by inserting a 20-gauge catheter (B. Braun). Cells were harvested by eight consecutive lung lavages with 1 mL of DPBS (Dulbeccos's Phosphate-Buffered Saline) and cultured in RPMI 1640 medium supplemented with 10% fetal bovine serum and 1% antibiotics. For experimentation, alveolar macrophages were directly seeded onto 12 mm glass cover slips and used within 5 days after preparation.

Lysosomal exocytosis experiments

Alveolar macrophages (3×10^4), isolated from wild-type and TPC2 KO mice (described in **Grimm et al., 2014**) were seeded on 8-well plates (Ibidi) and cultured overnight. Cells were washed once with Minimum Essential Media (MEM) supplemented with 10 mM HEPES and then treated with TPC2-A1-N or TPC2-A1-P as indicated. Ionomycin (4 µM for 10 min) was used as positive control. Following treatment, cells were incubated with an anti-LAMP1 antibody (1:200, SantaCruz) in MEM supplemented with 10 mM HEPES and 1% BSA for 20 min on ice. Cells were then fixed with 2.6% PFA (Thermo Fisher) for 20 min and incubated with Alexa Fluor 488 conjugated secondary antibody (Thermo Fisher) for 1 hr in PBS containing 1% BSA. Nuclei were stained with DAPI. Confocal images were acquired using an LSM 880 microscope (Zeiss) with 40X magnification.

Capacitance measurements

Vesicle fusion of wild-type and TPC2-deficient primary alveolar macrophages was analyzed by measuring cell membrane capacitance using the patch-clamp technique as previously described (***Zierler et al., 2016***). In brief, vesicle fusion was recorded using the automated capacitance cancellation function of the EPC-10 (HEKA, Lambrecht, Germany). Measurements were performed in a tight seal whole-cell configuration at room temperature. Membrane capacitance values directly captured after breaking the seal between the membrane and the glass pipette were used as a reference for the initial cell size. Further recorded capacitance values were normalized to this initial determined capacitance. Extracellular solution contained: 140 mM NaCl, 1 mM $CaCl_2$, 2.8 mM KCl, 2 mM $MgCl_2$, 10 mM HEPES-NaOH, 11 mM glucose (pH 7.2, 300 mosmol/L). Internal solution contained: 120 mM potassium glutamate, 8 mM NaCl, 1 mM $MgCl_2$, 10 mM HEPES-NaOH, 0.1 mM GTP (pH 7.2, 280 mosmol/L). At 180 s TPC2-A1-P (30 µM, diluted in external solution) was applied via an application pipette.

Lysosomal pH measurements

Cell culture and transfection: DMEM (Sigma Aldrich) containing 10% fetal bovine serum, 100 U/mL penicillin, 100 µg/mL streptomycin, and 2.5 µg/mL Fungizone (Thermo Fisher) was used to grow HeLa cells (all obtained from ATCC, Guernsey, UK). Transfection of cells in six-well (Greiner-Bio-One, Kremsmünster, Austria) was performed using PolyJet transfection reagent (SignaGen Laboratories, Rockville). HeLa cells stably expressing pH-Lemon-GPI (NGFI, Graz, Austria) were generated by selection with 800 µg/mL of G418 (Sigma Aldrich, St. Louis, USA) and FACS sorting for CFP (excitation at 405 nm). Wide-field fluorescence microscopy experiments were performed using an OLYMPUS IX73 inverted microscope (OLYMPUS, Vienna, Austria) using a 40X objective (UApo N 340, 40X/1.35 Oil, ∞/0.17/FN22, OLYMPUS). Illumination was performed using an OMICRON LedHUB High-Power LED Light Engine, equipped with a 455 nm and 505 nm LED light source (OMICRON electronics, Vienna, Austria), and 430 nm and 500 nm excitation filters (AHF Analysentechnik, Tübingen, Germany), respectively. Images were captured at a binning of 2 using a Retiga R1 CCD camera (TELEDYNE QIMAGING, Surrey, Canada) and emissions were separated using an optical beam splitter (DV2, Photometrics, Arizona). Array Confocal microscopy was performed using an array confocal laser scanning microscope (ACLSM) built on a fully automatic inverse microscope (Axio Observer.Z1, Zeiss, Göttingen, Germany) using a 100x objective (Plan-Apochromat 100x, 1.4 Oil M27). Excitation was performed using laser light of diode lasers (Visitron Systems): CFP of pH-lemon was excited at 445 nm and 505 nm respectively. Emitted light was acquired with emission filters ET480/40 m for CFP and ET525/50 m for EYFP (Chroma Technologies, VT). A Photometrics CCD camera (CoolSnap HQ2) was used to capture all images at a binning of 1. Device control and image acquisition was performed using VisiView image acquisition and control software (Visitron Systems, Puchheim, Germany) for both devices. Images were processed using MetaMorph analysis software (Molecular Devices, San Jose). Data and statistical analyses were done using GraphPad Prism Software.

Synthesis of the compounds

All chemicals used were of analytical grade and were obtained from abcr (Karlsruhe, Germany), Fischer Scientific (Schwerte, Germany), Sigma-Aldrich (now Merck, Darmstadt, Germany), TCI (Eschborn, Germany) or Th. Geyer (Renningen, Germany). HPLC grade and dry solvents were purchased from VWR (Darmstadt, Germany) or Sigma-Aldrich, all other solvents were purified by distillation. Hydrophobic phase separation filters (MN 617 WA, 125 mm) were purchased from Macherey Nagel (Düren, Germany). All reactions were monitored by thin-layer chromatography (TLC) using pre-coated plastic sheets POLYGRAM SIL G/UV254 from Macherey-Nagel and detected by irradiation with UV light (254 nm or 366 nm). Flash column chromatography (FCC) was performed on Merck silica gel Si 60 (0.015–0.040 mm).

NMR spectra (^1H, ^{13}C, DEPT, COSY, HSQC/HMQC, HMBC) were recorded at 23°C on an Avance III 400 MHz Bruker BioSpin or Avance III 500 MHz Bruker BioSpin instrument, unless otherwise specified. Chemical shifts δ are stated in parts per million (ppm) and are calibrated using residual protic solvents as an internal reference for proton ($CDCl_3$: δ = 7.26 ppm, $(CD_3)_2SO$: δ = 2.50 ppm) and for carbon the central carbon resonance of the solvent ($CDCl_3$: δ = 77.16 ppm, $(CD_3)_2SO$: δ = 39.52 ppm). Multiplicity is defined as s = singlet, d = doublet, t = triplet, q = quartet, sext = sextet,

m = multiplet. NMR spectra were analyzed with NMR software MestReNova, version 12.0.1–20560 (Mestrelab Research S.L.). High-resolution mass spectra were performed by the LMU Mass Spectrometry Service applying a Thermo Finnigan MAT 95 or Joel MStation Sektorfeld instrument at a core temperature of 250˚C and 70 eV for EI or a Thermo Finnigan LTQ FT Ultra Fourier Transform Ion Cyclotron Resonance device at 250˚C for ESI. IR spectra were recorded on a Perkin Elmer FT-IR Paragon 1000 instrument as neat materials. Absorption bands were reported in wave number (cm^{-1}) with ATR PRO450-S. Melting points were determined by the open tube capillary method on a Büchi melting point B-540 apparatus and are uncorrected. Microwave-assisted reactions were carried out in a Discover (S-Class Plus) SP microwave reactor (CEM GmbH, Kamp-Lintfort, Germany). HPLC purities were determined using an HP Agilent 1100 HPLC with a diode array detector and an Agilent Poroshell column (120 EC-C18; 3.0 × 100 mm; 2.7 micron) with acetonitrile/water as eluent (60:40 acetonitrile/water + 0.1% formic acid).

Preparation of the TPC2-A1-N series

General procedure A – Amide coupling

According to ***Sjogren et al. (1991)*** the appropriate aniline (1.0 eq.) and 2-cyanoacetic acid (1.0 eq.) were dissolved in DMF and cooled to 0˚C. DCC (1.0 eq.) was added portion wise. The mixture was warmed up to rt over 1 hr and subsequently diluted with hexanes/EtOAc (1:1). Precipitates were removed by filtration and the filtrate was extracted once with 1 M aq. HCl and thrice with EtOAc. The combined organic layers were washed with sat. aq. NaCl solution, dried over Na_2SO_4, filtered and concentrated *in vacuo*. Recrystallization from EtOH yielded the desired amides.

General procedure B – synthesis of *N*-aryl cyanoacetamides

According to ***Sjogren et al. (1991)*** the appropriate amides received from general procedure **A** (1.0 eq.) were dissolved in dry THF, the solution was cooled to 0˚C and NaH (dispersion in paraffin, 60%, 2.3 eq.) was added. After stirring for 15 min, the appropriate benzoyl chloride (1.1 eq.) was added. The mixture was stirred at 0˚C for 1 hr and then cautiously treated with 1 M HCl. The precipitate was collected by filtration, washed with ice water and cold EtOH and recrystallized from toluene to give the desired cyanoacetamides.

If the appropriate benzoyl chloride was not commercially available, it was prepared by refluxing the appropriate benzoic acid (1.1 eq.) in $SOCl_2$ (55 eq.) for 1 hr and concentrating *in vacuo*. The resulting acid chloride was immediately transferred to the reaction.

Preparation of the TPC2-A1-P series

General procedure C – Paal-Knorr pyrrole synthesis

Following a general procedure published by ***Kang et al. (2010)*** the appropriate β-ketoester (1.1 eq.) was dissolved in dry THF and cooled to 0˚C, before NaH (dispersion in paraffin, 60%, 1.5 eq.) was added portion wise. After the suspension was stirred for 30 min, a solution of appropriate halogenated acetophenone (1.0 eq.) and KI (1.0 eq.) in dry THF was added dropwise. The reaction mixture was allowed to warm up to rt over 2 hr, then poured on water and extracted three times with diethyl ether. The combined organic phases were washed with sat. aq. $NaHCO_3$ solution, dried over Na_2SO_4, filtered and concentrated *in vacuo*. The residue was dissolved in acetic acid and the appropriate primary amine (2.0 eq.) was added dropwise. The reaction mixture was stirred at 80˚C for 18 hr. The solvent was removed *in vacuo*, the residue disperged in water and extracted three times with diethyl ether. The collected organic phases were washed with sat. aq. $NaHCO_3$ solution, dried over Na_2SO_4 and concentrated *in vacuo*. Purification was accomplished by FCC and recrystallization from EtOH if not otherwise specified.

General procedure D – alkaline deprotection of the pyrrolecarboxylic esters

LiOH (10 eq.) was added to a solution of the appropriate ester (1.0 eq.) in dioxane/H_2O (5:1) and the reaction mixture was stirred in a closed vessel under microwave irradiation (p_{max} = 8 bar, P_{max} = 200 W, T_{max} = 180˚C) for 1–18 hr. The suspension was diluted with water to thrice original volume and aq. 2 M HCl was added dropwise under vigorous stirring until the mixture was strongly

acidic. The formed precipitate was collected by filtration, washed with water and dried. If necessary the acids were recrystallized from EtOH to yield the pure products.

Synthesis of TPC2-A1-N and analogs

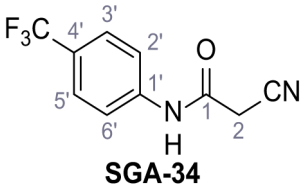

SGA-34

Chemical structure 1. 2-Cyano-*N*-(4-(trifluoromethyl)phenyl)acetamide – SGA-34.

According to general procedure **A**, 4-(trifluoromethyl)aniline (812 µL, 6.47 mmol, 1.1 eq.), 2-cyanoacetic acid (500 mg, 5.88 mmol, 1.0 eq.) and DCC (1.27 g, 6.17 mmol, 1.1 eq.) in DMF (7.0 mL) were used to yield amide **SGA-34** as colorless crystals (983 mg, 4.31 mmol, 73%). Analytical data are in accordance with literature (***Davies et al., 2009***; ***Sjogren et al., 1991***). $\mathbf{R_f}$ = 0.14 (4:1 hexanes/acetone). **m.p.:** 195˚C [(***Sjogren et al., 1991***): 191–193˚C]. **^{1}H NMR (400 MHz, $(CD_3)_2SO$)** δ/ppm = 10.65 (s, 1H, NH), 7.75 (d, *J* = 8.8 Hz, 2H, 3'-H, 5'-H), 7.70 (d, *J* = 8.8 Hz, 2H, 2'-H, 6'-H), 3.95 (s, 2H, 2 hr). **^{13}C NMR (101 MHz, $(CD_3)_2SO$)** δ/ppm = 161.9 (C-1), 141.9 (C-1'), 126.3 (q, J_{CF} = 3.7 Hz, C-3', C-5'), 124.4 (q, J_{CF} = 271.4 Hz, CF_3), 124.0 (q, J_{CF} = 32.0 Hz, C-4'), 119.2 (C-2', C-6'), 115.7 (CN), 27.0 (C-2). IR (ATR) $\tilde{V}_{max}/cm^{-1}$=3287, 3221, 3147, 1681, 1612, 1557, 1319, 1110, 1065, 849, 835. **HRMS (ESI):** calcd. for $C_{10}H_6F_3N_2O$ $(M\text{-}H)^-$ 227.04377; found 227.04371. **Purity (HPLC):**>96% (λ = 210 nm),>96% (λ = 254 nm).

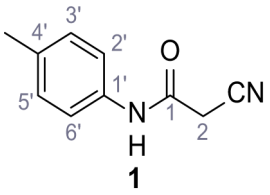

1

Chemical structure 2. 2-Cyano-*N*-(*p*-tolyl)acetamide (1).

According to general procedure **A**, *p*-toluidine (712 µL, 6.47 mmol, 1.1 eq.), 2-cyanoacetic acid (500 mg, 5.88 mmol, 1.0 eq.) and DCC (1.27 g, 6.17 mmol, 1.1 eq.) in DMF (7.0 mL) were used to yield amide one as colorless crystals (728 mg, 4.18 mmol, 71%). Analytical data are in accordance with literature (***Yuan et al., 2019***). $\mathbf{R_f}$ = 0.14 (4:1 hexanes/acetone). **m.p.:** 184˚C [(***Yuan et al., 2019***): 186˚C]. **^{1}H NMR (400 MHz, $(CD_3)_2SO$)** δ/ppm = 10.19 (s, 1H, NH), 7.47–7.36 (m, 2H, 2'-H, 6'-H), 7.13 (d, *J* = 8.2 Hz, 2H, 3'-H, 5'-H), 3.86 (s, 2H, 2 hr), 2.25 (s, 3H, CH_3). **^{13}C NMR (101 MHz, $(CD_3)_2SO$)** δ/ppm = 160.7 (CO), 135.9 (C-1'), 132.9 (C-4'), 129.3 (C-3', C-5'), 119.2 (C-2', C-6'), 116.0 (CN), 26.6 (C-2), 20.4 (CH_3). IR (ATR) $\tilde{V}_{max}/cm^{-1}$=3267, 3207, 3137, 1660, 1613, 1552, 1510, 819. **HRMS (ESI):** calcd. for $C_{10}H_9N_2O$ $(M\text{-}H)^-$ 173.07204; found 173.07194. **Purity (HPLC):** >96% (λ = 210 nm), >96% (λ = 254 nm).

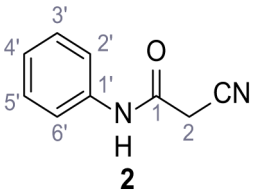

2

Chemical structure 3. 2-Cyano-*N*-phenylacetamide (2).

According to general procedure **A**, aniline (1.96 mL, 21.5 mmol, 1.0 eq.), 2-cyanoacetic acid (2.01 g, 23.6 mmol, 1.1 eq.) and DCC (4.87 g, 23.6 mmol, 1.1 eq.) in DMF (20 mL) were used to yield amide two as colorless crystals (2.60 g, 16.2 mmol, 76%). Analytical data are in accordance with

literature (*Yuan et al., 2019*). **R_f** = 0.12 (4:1 hexanes/acetone). **m.p.:** 202˚C [(*Yuan et al., 2019*): 172˚ C]. **^{1}H NMR (500 MHz, $(CD_3)_2SO$)** δ/ppm = 10.28 (s, 1H, NH), 7.54 (dt, *J* = 8.7, 1.6 Hz, 2H, 2'-H, 6'-H), 7.39–7.29 (m, 2H, 3'-H, 5'-H), 7.15–7.04 (m, 1H, 4'-H), 3.89 (s, 2H, 2 hr). **^{13}C NMR (126 MHz, $(CD_3)_2SO$)** δ/ppm = 161.0 (CO), 138.4 (C-1'), 128.9 (C-3', C-5'), 123.9 (C-4'), 119.2 (C-2', C-6'), 115.9 (CN), 26.7 (C-2). IR (ATR) $\tilde{V}_{max}$/cm^{-1}=3265, 3207, 3143, 3099, 3052, 1653, 1620, 1557, 1299, 943, 761, 696. **HRMS (ESI):** calcd. for $C_9H_7N_2O$ $(M\text{-}H)^-$ 159.05639; found 159.05628. **Purity (HPLC):**>96% (λ = 210 nm),>96% (λ = 254 nm).

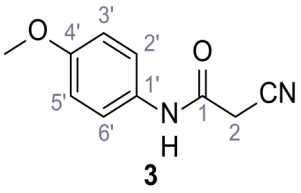

3

Chemical structure 4. 2-Cyano-*N*-(4-methoxyphenyl)acetamide (3).

According to general procedure **A**, *p*-anisidine (2.36 mL, 20.3 mmol, 1.0 eq.), 2-cyanoacetic acid (19.0 g, 22.3 mmol, 1.1 eq.) and DCC (4.61 g, 22.3 mmol, 1.1 eq.) in DMF (20 mL) were used to yield amide three as pale blue crystals (1.58 g, 8.31 mmol, 41%). Analytical data are in accordance with literature (*Yuan et al., 2019*). **R_f** = 0.10 (4:1 hexanes/acetone). **m.p.:** 137˚C [(*Yuan et al., 2019*): 176˚ C]. **^{1}H NMR (400 MHz, $(CD_3)_2SO$)** δ/ppm = 10.14 (s, 1H, NH), 7.53–7.38 (m, 2H, 2'-H, 6'-H), 7.00–6.83 (m, 2H, 3'-H, 5'-H), 3.84 (s, 2H, 2 hr), 3.72 (s, 3H, OCH_3). **^{13}C NMR (101 MHz, $(CD_3)_2SO$)** δ/ppm = 160.4 (CO), 155.6 (C-4'), 131.4 (C-1'), 120.8 (C-2', C-6'), 116.0 (CN), 114.0 (C-3', C-5'), 55.2 (OCH_3), 26.5 (C-2). IR (ATR) $\tilde{V}_{max}$/cm^{-1}=3299.3150, 1655, 1608, 1557, 1511, 1251, 1032, 828. **HRMS (ESI):** calcd. for $C_{10}H_9N_2O_2$ $(M\text{-}H)^-$ 189.06695; found 189.06688. **Purity (HPLC):**>96% (λ = 210 nm), >96% (λ = 254 nm).

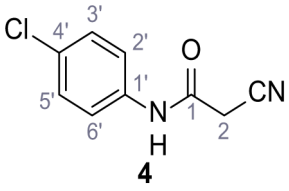

4

Chemical structure 5. N-(4-Chlorophenyl)−2-cyanoacetamide (4).

According to general procedure **A**, 4-chloroaniline (682 µL, 23.0 mmol, 1.0 eq.), 2-cyanoacetic acid (2.16 g, 25.4 mmol, 1.1 eq.) and DCC (5.23 g, 25.4 mmol, 1.1 eq.) in DMF (20 mL) were used to yield amide four as colorless crystals (3.46 g, 17.8 mmol, 77%). Analytical data are in accordance with literature (*Yuan et al., 2019*). **R_f** = 0.14 (3:2 hexanes/acetone). **m.p.:** 207˚C [(*Yuan et al., 2019*): 179˚C]. **^{1}H NMR (500 MHz, $(CD_3)_2SO$)** δ/ppm = 10.42 (s, 1H, NH), 7.62–7.51 (m, 2H, 2'-H, 6'-H), 7.50–7.27 (m, 2H, 3'-H, 5'-H), 3.91 (s, 2H, 2 hr). **^{13}C NMR (126 MHz, $(CD_3)_2SO$)** δ/ppm = 161.2 (CO), 137.3 (C-1'), 128.8 (C-3', C-5'), 127.5 (C-4'), 120.8 (C-2', C-6'), 115.8 (CN), 26.8 (C-2). IR (ATR) $\tilde{V}_{max}$/cm^{-1}=3264, 3200, 3132, 3083, 1664, 1610, 1548, 1491, 832. **HRMS (ESI):** calcd. for $C_9H_6{}^{35}ClN_2O$ $(M\text{-}H)^-$ 193.01741; found 193.01750. **Purity (HPLC):**>96% (λ = 210 nm),>96% (λ = 254 nm).

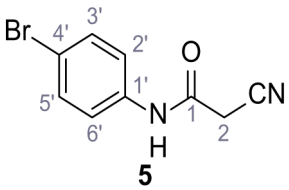

5

Chemical structure 6. N-(4-Bromophenyl)−2-cyanoacetamide (5).

According to general procedure **A**, 4-bromoaniline (2.00 mL, 17.1 mmol, 1.0 eq.), 2-cyanoacetic acid (1.60 g, 18.8 mmol, 1.1 eq.) and DCC (3.88 g, 18.8 mmol, 1.1 eq.) in DMF (20 mL) were used to

yield amide five as colorless crystals (1.62 g, 6.76 mmol, 40%). Analytical data are in accordance with literature (*Yuan et al., 2019*). R_f = 0.14 (4:1 hexanes/acetone). **m.p.:** 186˚C [(*Yuan et al., 2019*): 185˚C]. **^{1}H NMR (400 MHz, $(CD_3)_2SO$)** δ/ppm = 10.42 (s, 1H, NH), 7.52 (s, 4H, 2'-H, 3'-H, 5'-H, 6'-H), 3.90 (s, 2H, 2 hr).**^{13}C NMR (101 MHz, $(CD_3)_2SO$)** δ/ppm = 161.2 (CO), 137.7 (C-1'), 131.7 (C-2', C-6' or C-3', C-5'), 121.2 (C-2', C-6' or C-3', C-5'), 115.8 (C-4'), 115.5 (CN), 26.8 (C-2). IR (ATR) $\tilde{V}_{max}$/cm^{-1}=3322, 2927, 2849, 1608, 1547, 1245, 828. **HRMS (ESI):** calcd. for $C_9H_6{}^{79}BrN_2O$ $(M-H)^-$ 236.96690; found 236.96692. **Purity (HPLC):**>96% (λ = 210 nm),>96% (λ = 254 nm).

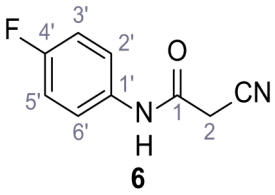

6

Chemical structure 7. 2-Cyano-*N*-(4-fluorophenyl)acetamide (6).

According to general procedure **A**, 4-fluoroaniline (2.16 mL, 22.5 mmol, 1.0 eq.), 2-cyanoacetic acid (1.91 g, 22.5 mmol, 1.0 eq.) and DCC (4.64 g, 22.5 mmol, 1.0 eq.) in DMF (20 mL) were used to yield amide six as colorless crystals (3.00 g, 16.9 mmol, 75%). Analytical data are in accordance with literature (*Ammar et al., 2006*). R_f = 0.11 (4:1 hexanes/acetone). **m.p.:** 179˚C [(*Ammar et al., 2006*): 158–160˚C]. **^{1}H NMR (400 MHz, $(CD_3)_2SO$)** δ/ppm = 10.34 (s, 1H, NH), 7.66–7.46 (m, 2H, 2'-H, 6'-H), 7.27–7.09 (m, 2H, 3'-H, 5'-H), 3.89 (s, 2H, 2 hr). **^{13}C NMR (101 MHz, $(CD_3)_2SO$)** δ/ppm = 161.0 (CO), 158.3 (d, J_{CF} = 240.5 Hz, C-4'), 134.7 (d, J_{CF} = 2.7 Hz, C-1'), 121.1 (d, J_{CF} = 7.9 Hz, C-2', C-6'), 115.9 (CN), 115.5 (d, J_{CF} = 22.3 Hz, C-3', C-5'), 26.6 (C-2). IR (ATR) $\tilde{V}_{max}$/cm^{-1}=3274, 3166, 3107, 1662, 1623, 1566, 1505, 834. **HRMS (ESI):** calcd. for $C_9H_6FN_2O$ $(M-H)^-$ 177.04696; found 177.04687. **Purity (HPLC):**>96% (λ = 210 nm),>96% (λ = 254 nm).

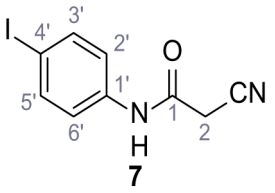

7

Chemical structure 8. 2-Cyano-*N*-(4-iodophenyl)acetamide (7).

According to general procedure **A**, 4-iodoaniline (4.50 g, 20.5 mmol, 1.0 eq.), 2-cyanoacetic acid (17.5 g, 20.5 mmol, 1.0 eq.) and DCC (4.24 g, 20.5 mmol, 1.0 eq.) in DMF (20 mL) were used to yield amide seven as pale blue crystals (4.50 g, 15.7 mmol, 77%). The compound is literature known, but no analytical data are available (*Sjogren et al., 1991*). R_f = 0.11 (4:1 hexanes/acetone). **m.p.:** 218˚C. **^{1}H NMR (400 MHz, $(CD_3)_2SO$)** δ/ppm = 10.38 (s, 1H, NH), 7.78–7.60 (m, 2H, 3'-H, 5'-H), 7.49–7.29 (m, 2H, 2'-H, 6'-H), 3.90 (s, 2H, 2 hr). **^{13}C NMR (101 MHz, $(CD_3)_2SO$)** δ/ppm = 161.2 (CO), 138.2 (C-1'), 137.6 (C-3', C-5'), 121.4 (C-2', C-6'), 115.8 (CN), 87.6 (C-4'), 26.8 (C-2). IR (ATR) $\tilde{V}_{max}$/cm^{-1}=3265, 3188, 3113, 3078, 1666, 1543, 1391, 1299, 823. **HRMS (ESI):** calcd. for $C_9H_6IN_2O$ $(M-H)^-$ 284.95303; found 284.95302. **Purity (HPLC):**>96% (λ = 210 nm),>96% (λ = 254 nm).

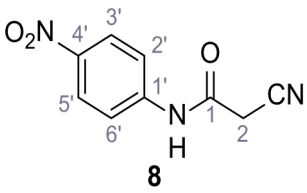

8

Chemical structure 9. 2-Cyano-*N*-(4-nitrophenyl)acetamide (8).

According to general procedure **A**, 4-nitroaniline (696 µL, 7.24 mmol, 1.0 eq.), 2-cyanoacetic acid (616 mg, 7.24 mmol, 1.0 eq.) and DCC (1.49 g, 7.24 mmol, 1.0 eq.) in DMF (20 mL) were used to

yield amide eight as yellow solid (918 mg, 4.47 mmol, 62%). Analytical data are in accordance with literature (***Sohn et al., 2017***). **R_f** = 0.11 (4:1 hexanes/acetone). **m.p.:** 218˚C [(***Sohn et al., 2017***): 220˚C]. **^{1}H NMR (400 MHz, $(CD_3)_2SO$)** δ/ppm = 10.88 (s, 1H, NH), 8.35–8.15 (m, 2H, 3'-H, 5'-H), 7.93–7.71 (m, 2H, 2'-H, 6'-H), 4.00 (s, 2H, 2 hr). **^{13}C NMR (101 MHz, $(CD_3)_2SO$)** δ/ppm = 162.2 (CO), 144.4 (C-1'), 142.7 (C-4'), 125.1 (C-3', C-5'), 119.0 (C-2', C-6'), 115.5 (CN), 27.2 (C-2). IR (ATR) $\tilde{V}_{max}$/cm^{-1}=3287, 1673, 1562, 1503, 1336, 1259, 860, 748. **HRMS (ESI):** calcd. for $C_9H_6N_3O_3$ $(M\text{-}H)^-$ 204.04146; found 204.04146. **Purity (HPLC):**>96% (λ = 210 nm),>96% (λ = 254 nm).

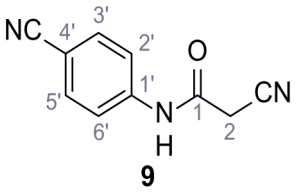

9

Chemical structure 10. 2-Cyano-*N*-(4-cyanophenyl)acetamide (9).

According to general procedure **A**, 4-aminobenzonitrile (1.00 g, 8.46 mmol, 1.0 eq.), 2-cyanoacetic acid (7.20 g, 8.46 mmol, 1.0 eq.) and DCC (1.75 g, 8.46 mmol, 1.0 eq.) in DMF (10 mL) were used to yield amide nine as yellow solid (1.22 g, 6.57 mmol, 78%). The compound is literature known, but no analytical data are available (***Sjogren et al., 1991***). **R_f** = 0.08 (4:1 hexanes/acetone). **m.p.:** 201˚C. **^{1}H NMR (500 MHz, $(CD_3)_2SO$)** δ/ppm = 10.72 (s, 1H, NH), 7.82–7.78 (m, 2H, 3'-H, 5'-H), 7.74–7.70 (m, 2H, 2'-H, 6'-H), 3.97 (s, 2H, 2 hr). **^{13}C NMR (126 MHz, $(CD_3)_2SO$)** δ/ppm = 162.0 (CO), 142.5 (C-1'), 133.5 (C-3', C-5'), 119.3 (C-2', C-6'), 118.9 (C-4'), 115.6 ($CH_2\underline{C}N$), 105.7 (CN), 27.1 (C-2). IR (ATR) $\tilde{V}_{max}$/cm^{-1}=3268, 3194, 3118, 2229, 1599, 1538, 1504, 845. **HRMS (ESI):** calcd. for $C_{10}H_6N_3O$ $(M\text{-}H)^-$ 184.05164; found 184.05161. **Purity (HPLC):**>96% (λ = 210 nm),>96% (λ = 254 nm).

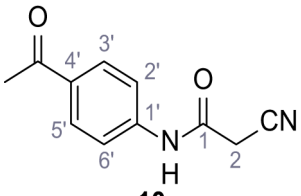

10

Chemical structure 11. N-(4-Acetylphenyl)−2-cyanoacetamide (10).

According to general procedure **A**, 4-aminoacetophenone (1.30 mL, 7.40 mmol, 1.0 eq.), 2-cyanoacetic acid (629 mg, 7.40 mmol, 1.0 eq.) and DCC (1.53 g, 7.40 mmol, 1.0 eq.) in DMF (10 mL) were used to yield amide **10** as yellow crystals (802 mg, 3.97 mmol, 54%). Analytical data are in accordance with literature (***Metwally et al., 2017***). **R_f** = 0.37 (3:2 hexanes/acetone). **m.p.:** 194˚C [(***Metwally et al., 2017***): 225˚C]. **^{1}H NMR (500 MHz, $(CD_3)_2SO$)** δ/ppm = 10.63 (s, 1H, NH), 7.99–7.91 (m, 2H, 3'-H, 5'-H), 7.74–7.62 (m, 2H, 2'-H, 6'-H), 3.96 (s, 2H, 2 hr), 2.53 (s, 3H, CH_3). **^{13}C NMR (101 MHz, $(CD_3)_2SO$)** δ/ppm = 196.5 ($\underline{C}OCH_3$), 161.7 (HNCO), 142.6 (C-1'), 132.2 (C-4'), 129.6 (C-3', C-5'), 118.5 (C-2', C-6'), 115.7 (CN), 27.0 (C-2), 26.5 (CH_3). IR (ATR) $\tilde{V}_{max}$/cm^{-1}=3286, 2250, 1695, 1651, 1599, 1536, 1279, 1249, 833, 720. **HRMS (ESI):** calcd. for $C_{11}H_9N_2O_2$ $(M\text{-}H)^-$ 201.06695; found 201.06694. **Purity (HPLC):**>96% (λ = 210 nm),>96% (λ = 254 nm).

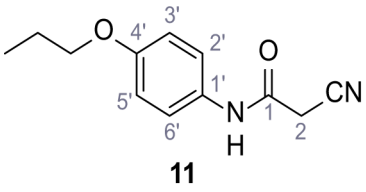

11

Chemical structure 12. 2-Cyano-*N*-(4-propoxyphenyl)acetamide (11).

According to general procedure **A**, 4-propoxyaniline (679 µL, 4.49 mmol, 1.0 eq.), 2-cyanoacetic acid (382 mg, 4.49 mmol, 1.0 eq.) and DCC (927 mg, 4.49 mmol, 1.0 eq.) in DMF (2.0 mL) were used to yield amide **11** as colorless crystals (604 mg, 2.77 mmol, 62%). **R_f** = 0.24 (95:5 CH_2Cl_2/EtOH). **m.p.:** 183˚C. **^{1}H NMR (400 MHz, $(CD_3)_2SO$)** δ/ppm = 10.13 (s, 1H, NH), 7.51–7.38 (m, 2H, 2'-H, 6'-H), 6.98–6.83 (m, 2H, 3'-H, 5'-H), 3.88 (t, *J* = 7.1 Hz, 2H, $C\underline{H}_2CH_2CH_3$), 3.84 (s, 2H, 2 hr), 1.70 (sext, *J* = 7.1 Hz, 2H, $CH_2C\underline{H}_2CH_3$), 0.96 (t, *J* = 7.1 Hz, 3H, $CH_2CH_2C\underline{H}_3$). **^{13}C NMR (101 MHz, $(CD_3)_2SO$)** δ/ppm = 160.4 (CO), 155.1 (C-4'), 131.4 (C-1'), 120.8 (C-2', C-6'), 116.0 (CN), 114.5 (C-3', C-5'), 69.0 ($\underline{C}H_2CH_2CH_3$), 26.5 (C-2), 22.0 ($CH_2\underline{C}H_2CH_3$), 10.4 ($CH_2CH_2\underline{C}H_3$). IR (ATR) $\tilde{V}_{max}$/cm^{-1}=3283, 3096, 1607, 1559, 1508, 1239, 828, 570. **HRMS (ESI):** calcd. for $C_{12}H_{13}N_2O_2$ (M-H)$^-$ 217.09825; found 217.09832. **Purity (HPLC):**>96% (λ = 210 nm),>96% (λ = 254 nm).

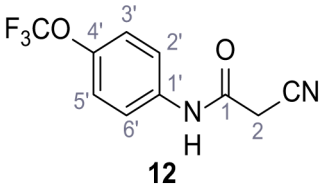

12

Chemical structure 13. 2-Cyano-*N*-(4-(trifluoromethoxy)phenyl)acetamide (12).

According to general procedure **A**, 4-(trifluoromethoxy)aniline (939 µL, 7.00 mmol, 1.0 eq.), 2-cyanoacetic acid (595 mg, 7.00 mmol, 1.0 eq.) and DCC (1.44 g, 7.00 mmol, 1.0 eq.) in DMF (10 mL) were used to yield amide **12** as colorless solid (1.23 g, 5.03 mmol, 72%). The compound is literature known, but no analytical data are available (***Sjogren et al., 1991***). **R_f** = 0.39 (95:5 CH_2Cl_2/EtOH). **m.p.:** 154˚C. **^{1}H NMR (400 MHz, $(CD_3)_2SO$)** δ/ppm = 10.49 (s, 1H, NH), 7.74–7.55 (m, 2H, 2'-H, 6'-H), 7.47–7.26 (m, 2H (3'-H, 5'-H), 3.92 (s, 2H, 2 hr). **^{13}C NMR (101 MHz, $(CD_3)_2SO$)** δ/ppm = 161.3 (CO), 144.0 (C-4'), 137.5 (C-1'), 121.8 (C-3', C-5'), 120.7 (C-2', C-6'), 120.1 (q, J_{CF} = 255.7 Hz, OCF_3), 115.8 (CN), 26.8 (C-2). IR (ATR) $\tilde{V}_{max}$/cm^{-1}=3278, 2975, 1667, 1616, 1557, 1508, 1277, 1205, 1171. **HRMS (ESI):** calcd. for $C_{10}H_6F_3N_2O_2$ (M-H)$^-$ 243.03869; found 243.03869. **Purity (HPLC):**>96% (λ = 210 nm),>96% (λ = 254 nm).

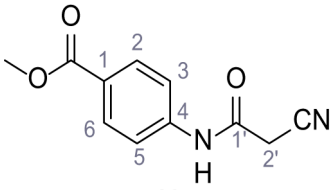

13

Chemical structure 14. Methyl 4-(2-cyanoacetamido)benzoate (13).

According to general procedure **A**, methyl 4-aminobenzoate (3.00 g, 19.5 mmol, 1.0 eq.), 2-cyanoacetic acid (1.66 g, 19.5 mmol, 1.0 eq.) and DCC (4.01 g, 19.5 mmol, 1.0 eq.) in DMF (15 mL) were used to yield amide **13** as colorless solid (2.76 g, 12.6 mmol, 65%). The compound is literature known, but no analytical data are available (***Sjogren et al., 1991***). **R_f** = 0.44 (3:2 hexanes/acetone). **m.p.:** 162˚C. **^{1}H NMR (500 MHz, $(CD_3)_2SO$)** δ/ppm = 10.63 (s, 1H, NH), 8.01–7.87 (m, 2H, 2 hr, 6 hr), 7.76–7.61 (m, 2H, 3 hr, 5 hr), 3.96 (s, 2H, 2 hr), 3.82 (s, 3H, CH_3). **^{13}C NMR (126 MHz, $(CD_3)_2SO$)** δ/ppm = 165.7 ($\underline{C}OOCH_3$), 161.7 (HNCO), 142.7 (C-4), 130.4 (C-2, C-6), 124.6 (C-1), 118.6 (C-3, C-5), 115.7 (CN), 52.0 (CH_3), 27.0 (C-2). IR (ATR) $\tilde{V}_{max}$/cm^{-1}=2809, 1722, 1608, 1558, 1507, 1431, 1274, 1110, 757. **HRMS (ESI):** calcd. for $C_{11}H_9N_2O_3$ (M-H)$^-$ 217.06187; found 217.06187. **Purity (HPLC):** >96% (λ = 210 nm),>96% (λ = 254 nm).

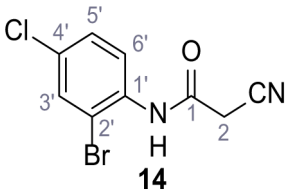

Chemical structure 15. N-(2-Bromo-4-chlorophenyl)−2-cyanoacetamide (14).

According to general procedure **A**, 2-bromo-4-chloroaniline (1.00 g, 4.84 mmol, 1.0 eq.), 2-cyanoacetic acid (412 mg, 4.84 mmol, 1.0 eq.) and DCC (999 mg, 4.84 mmol, 1.0 eq.) in DMF (10 mL) were used to yield amide **14** as colorless crystals (919 mg, 3.36 mmol, 69%). $\mathbf{R_f}$ = 0.22 (3:2 hexanes/acetone). **m.p.:** 157˚C. **^{1}H NMR (400 MHz, $(CD_3)_2SO$)** δ/ppm = 9.97 (s, 1H, NH), 7.83 (d, *J* = 2.4 Hz, 1H, 3'-H), 7.63 (d, *J* = 8.7 Hz, 1H, 6'-H), 7.49 (dd, *J* = 8.7, 2.4 Hz, 1H, 5'-H), 3.98 (s, 2H, 2 hr). **^{13}C NMR (101 MHz, $(CD_3)_2SO$)** δ/ppm = 161.8 (CO), 134.7 (C-1'), 132.0 (C-3'), 130.7 (C-4'), 128.2 (C-5'), 128.0 (C-6'), 118.5 (C-2'), 115.7 (CN), 26.1 (C-2). IR (ATR) $\tilde{V}_{max}/cm^{-1}$=3281, 2258, 1666, 1577, 1530, 1470, 1284, 822. **HRMS (ESI):** calcd. for $C_9H_5{}^{79}Br^{35}ClN_2O$ $(M\text{-}H)^-$ 270.92793; found 270.92809. **Purity (HPLC):** >93% (λ = 210 nm), >93% (λ = 254 nm).

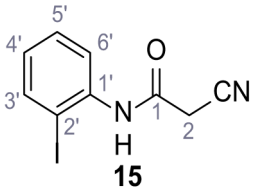

Chemical structure 16. 2-Cyano-*N*-(2-iodophenyl)acetamide (15).

According to general procedure **A**, 2-iodoaniline (1.00 g, 4.57 mmol, 1.0 eq.), 2-cyanoacetic acid (388 mg, 4.57 mmol, 1.0 eq.) and DCC (942 mg, 4.57 mmol, 1.0 eq.) in DMF (10 mL) were used to yield amide **15** as brown crystals (913 g, 3.19 mmol, 70%). $\mathbf{R_f}$ = 0.16 (4:1 hexanes/acetone). **m.p.:** 161˚C. **^{1}H NMR (400 MHz, $(CD_3)_2SO$)** δ/ppm = 9.88 (s, 1H, NH), 7.90 (d, *J* = 7.6 Hz, 1H, 3'-H), 7.46–7.38 (m, 2H, 5'-H, 6'-H), 7.03 (ddd, *J* = 8.6, 5.4, 3.6 Hz, 1H, 4'-H), 3.93 (s, 2H, 2 hr). **^{13}C NMR (101 MHz, $(CD_3)_2SO$)** δ/ppm = 161.4 (CO), 139.1 (C-3'), 138.7 (C-1'), 128.8 (C-5'), 128.3 (C-4'), 127.4 (C-6'), 115.8 (CN), 96.4 (C-2'), 26.0 (C-2). IR (ATR) $\tilde{V}_{max}/cm^{-1}$=3252, 2263, 1658, 1577, 1542, 1433, 1015, 758, 768. **HRMS (ESI):** calcd. for $C_9H_6IN_2O$ $(M\text{-}H)^-$ 284.95303; found 284.95295. **Purity (HPLC):** >96% (λ = 210 nm), >96% (λ = 254 nm).

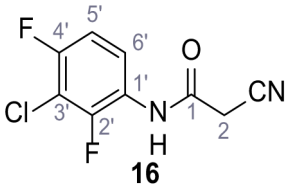

Chemical structure 17. N-(3-Chloro-2,4-difluorophenyl)−2-cyanoacetamide (16).

According to general procedure **A**, 3-chloro-2,4-difluoroaniline (1.06 g, 6.48 mmol, 1.0 eq.), 2-cyanoacetic acid (551 mg, 6.48 mmol, 1.0 eq.) and DCC (1.34 g, 6.48 mmol, 1.0 eq.) in DMF (10 mL) were used to yield amide **16** as colorless crystals (1.01 g, 4.39 mmol, 68%). $\mathbf{R_f}$ = 0.16 (4:1 hexanes/acetone). **m.p.:** 144˚C. **^{1}H NMR (400 MHz, $(CD_3)_2SO$)** δ/ppm = 10.32 (s, 1H, NH), 7.79 (td, *J* = 9.0, 5.8 Hz, 1H, 6'-H), 7.33 (td, *J* = 9.0, 2.1 Hz, 1H, 5'-H), 3.99 (s, 2H, 2 hr). **^{13}C NMR (101 MHz, $(CD_3)_2SO$)** δ/ppm = 162.0 (CO), 154.8 (dd, J_{CF} = 246.5, 2.0 Hz, C-2' or C-4'), 150.4 (dd, J_{CF} = 250.4, 3.3 Hz, C-2' or C-4'), 123.4 (dd, J_{CF} = 8.8, 2.4 Hz, C-6'), 123.0 (dd, J_{CF} = 11.8, 3.5 Hz, C-1'), 115.7 (CN), 111.9 (dd, J_{CF} = 21.4, 3.8 Hz, C-5'), 108.7 (dd, J_{CF} = 21.9, 19.7 Hz, C-3'), 26.3 (C-2). IR (ATR) $\tilde{V}_{max}/cm^{-1}$=3274.2935, 2264, 1681, 1551, 1488, 1443, 1012, 831, 628. **HRMS (ESI):** calcd. for

$C_9H_4{}^{35}ClF_2N_2O$ $(M\text{-}H)^-$ 228.99857; found 228.99850. **Purity (HPLC):**>96% (λ = 210 nm),>96% (λ = 254 nm).

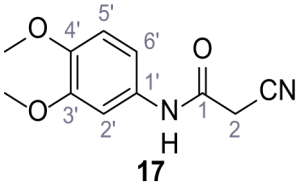

17

Chemical structure 18. 2-Cyano-*N*-(3,4-dimethoxyphenyl)acetamide (17).

According to general procedure **A**, 3,4-dimethoxyaniline (1.00 g, 6.53 mmol, 1.0 eq.), 2-cyanoacetic acid (555 mg, 6.53 mmol, 1.0 eq.) and DCC (1.35 g, 6.53 mmol, 1.0 eq.) in DMF (10 mL) were used to yield amide **17** as violet crystals (1.10 g, 4.99 mmol, 76%). The compound is literature known, but no analytical data are available (***Edraki et al., 2016***). $\mathbf{R_f}$ = 0.05 (4:1 hexanes/acetone). **m.p.:** 174˚C. **^{1}H NMR (500 MHz, $(CD_3)_2SO$)** δ/ppm = 10.15 (s, 1H, NH), 7.21 (d, *J* = 2.4 Hz, 1H, 2'-H), 7.04 (dd, *J* = 8.7, 2.4 Hz, 1H, 6'-H), 6.90 (d, *J* = 8.7 Hz, 1H, 5'-H), 3.84 (s, 2H, 2 hr), 3.79–3.66 (m, 6H, 2x OCH_3). **^{13}C NMR (126 MHz, $(CD_3)_2SO$)** δ/ppm = 160.5 (CO), 148.6 (C-3'), 145.3 (C-4'), 131.9 (C-1'), 116.0 (CN), 112.0 (C-5'), 111.2 (C-6'), 104.3 (C-2'), 55.7 (OCH_3), 55.4 (OCH_3), 26.6 (C-2). IR (ATR) $\tilde{V}_{max}/cm^{-1}$=3273, 2914, 2256, 1660, 1513, 1239, 1132, 1020, 837. **HRMS (ESI):** calcd. for $C_{11}H_{11}N_2O_3$ $(M\text{-}H)^-$ 219.07752; found 219.07751. **Purity (HPLC):** >96% (λ = 210 nm), >96% (λ = 254 nm).

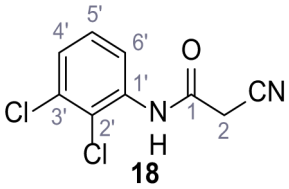

18

Chemical structure 19. 2-Cyano-*N*-(2,3-dichlorophenyl)acetamide (18).

According to general procedure **A**, 2,3-dichloroaniline (745 µL, 6.30 mmol, 1.0 eq.), 2-cyanoacetic acid (536 mg, 6.30 mmol, 1.0 eq.) and DCC (1.30 g, 6.30 mmol, 1.0 eq.) in DMF (10 mL) were used to yield amide **18** as colorless crystals (414 mg, 1.81 mmol, 29%). $\mathbf{R_f}$ = 0.21 (4:1 hexanes/acetone). **m.p.:** 176˚C. **^{1}H NMR (500 MHz, $(CD_3)_2SO$)** δ/ppm = 10.11 (s, 1H, NH), 7.69 (dd, *J* = 8.1, 1.3 Hz, 1H, 4'-H or 6'-H), 7.51 (dd, *J* = 8.1, 1.3 Hz, 1H, 4'-H or 6'-H), 7.38 (t, *J* = 8.1 Hz, 1H, 5'-H), 4.02 (s, 2H, 2 hr). **^{13}C NMR (126 MHz, $(CD_3)_2SO$)** δ/ppm = 161.9 (CO), 136.1 (C-1' or C-3'), 132.0 (C-1' or C-3'), 128.2 (C-5'), 127.3 (C-4' or C-6'), 125.3 (C-2'), 124.8 (C-4' or C-6'), 115.7 (CN), 26.3 (C-2). IR (ATR) $\tilde{V}_{max}/cm^{-1}$=3287, 2253, 1666, 1580, 1527, 1415, 1338, 1182, 953, 788. **HRMS (ESI):** calcd. for $C_9H_5{}^{35}Cl_2N_2O$ $(M\text{-}H)^-$ 226.97844; found 226.97859. **Purity (HPLC):** >96% (λ = 210 nm), >96% (λ = 254 nm).

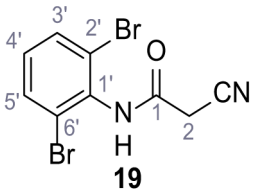

19

Chemical structure 20. 2-Cyano-*N*-(2,6-dibromophenyl)acetamide (19).

According to general procedure **A**, 2,6-dibromoaniline (1.00 g, 4.00 mmol, 1.0 eq.), 2-cyanoacetic acid (340 mg, 4.00 mmol, 1.0 eq.) and DCC (825 mg, 4.00 mmol, 1.0 eq.) in DMF (10 mL) were used to yield amide **19** as colorless crystals (514 mg, 1.62 mmol, 40%). $\mathbf{R_f}$ = 0.48 (3:2 hexanes/acetone). **m.p.:** 187˚C. **^{1}H NMR (500 MHz, $(CD_3)_2SO$)** δ/ppm = 10.37 (s, 1H, NH), 7.74 (d, *J* = 8.1 Hz, 2H, 3'-H, 5'-H), 7.22 (t, *J* = 8.1 Hz, 1H, 4'-H), 3.93 (s, 2H, 2 hr). **^{13}C NMR (126 MHz, $(CD_3)_2SO$)** δ/ppm = 161.1

(CO), 134.7 (C-1′), 132.4 (C-3′, C-5′), 130.7 (C-4′), 123.9 (C-2′, C-6′), 115.6 (CN), 25.4 (C-2). IR (ATR) $\tilde{V}_{max}/cm^{-1}$=3326, 2926, 2851, 1626, 1568, 1539, 1242, 642. **HRMS (ESI):** calcd. for $C_9H_5{}^{79}Br_2N_2O$ $(M-H)^-$ 314.87741; found 314.87761. **Purity (HPLC):**>96% (λ = 210 nm),>96% (λ = 254 nm).

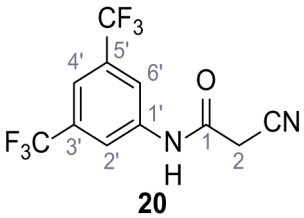

20

Chemical structure 21. N-(3,5-Bis(trifluoromethyl)phenyl)−2-cyanoacetamide (20).

According to general procedure **A**, 3,5-bis(trifluoromethyl)aniline (1.09 mL, 7.00 mmol, 1.0 eq.), 2-cyanoacetic acid (595 mg, 7.00 mmol, 1.0 eq.) and DCC (1.44 g, 7.00 mmol, 1.0 eq.) in DMF (10 mL) were used to yield amide **20** as colorless crystals (1.68 g, 5.67 mmol, 81%). The compound is literature known, but no analytical data are available (***Shah et al., 2018***). $\mathbf{R_f}$ = 0.43 (95:5 CH_2Cl_2/EtOH). **m.p.:** 141˚C. **^{1}H NMR (500 MHz, $(CD_3)_2SO$)** δ/ppm = 10.96 (s, 1H, NH), 8.28–8.12 (m, 2H, 2′-H, 6′-H), 7.90–7.77 (m, 1H, 4′-H), 4.00 (s, 2H, 2 hr). **^{13}C NMR (126 MHz, $(CD_3)_2SO$)** δ/ppm = 162.4 (CO), 140.2 (C-1′), 130.9 (q, J_{CF} = 32.9 Hz, C-3′, C-5′), 123.1 (q, J_{CF} = 272.7 Hz, CF_3), 119.2–118.7 (m, C-2′, C-6′), 116.9–116.5 (m, C-4′), 115.4 (CN), 27.1 (C-2). IR (ATR) $\tilde{V}_{max}/cm^{-1}$=3313, 1695, 1572, 1471, 1381, 1272, 1132, 889, 703, 681. **HRMS (ESI):** calcd. for $C_{11}H_5F_6N_2O$ $(M-H)^-$ 295.03116; found 295.03127. **Purity (HPLC):** >96% (λ = 210 nm), >96% (λ = 254 nm).

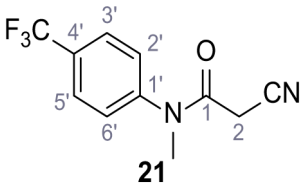

21

Chemical structure 22. 2-Cyano-*N*-methyl-*N*-(4-(trifluoromethyl)phenyl)acetamide (21).

According to general procedure **A**, *N*-methyl-4-(trifluoromethyl)aniline (403 µL, 2.85 mmol, 1.0 eq.), 2-cyanoacetic acid (243 mg, 2.85 mmol, 1.0 eq.) and DCC (589 mg, 2.85 mmol, 1.0 eq.) in DMF (10 mL) were used to yield amide **21** as colorless solid (513 mg, 2.12 mmol, 74%). Analytical data are in accordance with literature (***Kobayashi and Harayama, 2009***). $\mathbf{R_f}$ = 0.58 (95:5 CH_2Cl_2/EtOH). **m.p.:** 70˚C [(***Kobayashi and Harayama, 2009***): 66–68˚C]. **^{1}H NMR (400 MHz, $(CD_3)_2SO$)** δ/ppm = 7.77 (d, *J* = 8.6 Hz, 2H, 3′-H, 5′-H), 7.40 (d, *J* = 8.2 Hz, 2H, 2′-H, 6′-H), 3.34 (s, 3H, CH_3), 3.23 (s, 2H, 2 hr). **^{13}C NMR (101 MHz, $(CD_3)_2SO$)** δ/ppm = 161.4 (CO), 145.6 (C-1′), 131.7 (C-4′), 127.9 (C-2′, C-6′ or C-3′, C-5′), 127.8 (C-2′, C-6′ or C-3′, C-5′), 123.5 (q, *J* = 271.4 Hz, CF_3), 113.7 (CN), 38.1 (CH_3), 25.6 (C-2). IR (ATR) $\tilde{V}_{max}/cm^{-1}$=3152, 2355, 1657, 1611, 1322, 1122, 1103, 1065, 848. **HRMS (ESI):** calcd. for $C_{11}H_8F_3N_2O$ $(M-H)^-$ 241.05942; found 241.05939. **Purity (HPLC):**>96% (λ = 210 nm),>96% (λ = 254 nm).

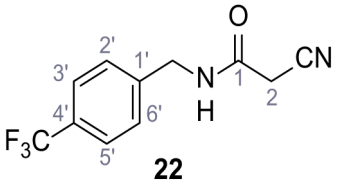

22

Chemical structure 23. 2-Cyano-*N*-(4-(trifluoromethyl)benzyl)acetamide (22).

According to general procedure **A**, 4-(trifluoromethyl)benzylamine (2.50 mL, 17.5 mmol, 1.0 eq.), 2-cyanoacetic acid (1.49 g, 17.5 mmol, 1.0 eq.) and DCC (3.62 g, 17.5 mmol, 1.0 eq.) in DMF (15 mL) were used to yield amide **22** as colorless solid (299 mg, 1.23 mmol, 7%). Analytical data are in accordance with literature (***Guo et al., 2011***). $\mathbf{R_f}$ = 0.46 (3:2 hexanes/acetone). **m.p.:** 113˚C [(***Guo et al.,***

2011): 128°C]. **^{1}H NMR (500 MHz, $(CD_3)_2SO$)** δ/ppm = 8.83 (t, J = 5.7 Hz, 1H, NH), 7.74–7.66 (m, 2H, 3'-H, 5'-H), 7.54–7.44 (m, 2H, 2'-H, 6'-H), 4.38 (d, J = 5.7 Hz, 2H, CH_2), 3.73 (s, 2H, 2 hr). **^{13}C NMR (126 MHz, $(CD_3)_2SO$)** δ/ppm = 162.5 (CO), 143.6 (C-1'), 128.0 (C-2', C-6'), 127.7 (q, J_{CF} = 31.7 Hz, C-4'), 125.2 (q, J_{CF} = 3.7 Hz, C-3', C-5'). 124.3 (q, J_{CF} = 272.1 Hz, CF_3), 116.1 (CN), 42.2 (CH_2), 25.3 (C-2). IR (ATR) $\tilde{V}_{max}$/cm^{-1}=3316, 2937, 2364, 1734, 1664, 1547, 1325, 1152, 1107, 1066. **HRMS (ESI):** calcd. for $C_{11}H_8F_3N_2O$ (M-H)$^-$ 241.05942; found 241.05949. **Purity (HPLC):** >96% (λ = 210 nm), >96% (λ = 254 nm).

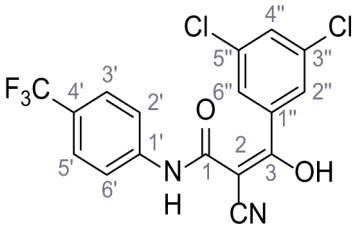

TPC2-A1-N

Chemical structure 24. 2-Cyano-3-(3,5-dichlorophenyl)−3-hydroxy-*N*-(4-(trifluoromethyl)phenyl)acrylamide – TPC2-A1-N.

According to general procedure **B**, amide **SGA-34** (228 mg, 1.00 mmol, 1.0 eq.) in dry THF (10 mL), NaH (92.0 mg, 2.30 mmol, 2.3 eq.) and 3,5-dichlorobenzoyl chloride (230 mg, 1.10 mmol, 1.1 eq.) were used to yield **TPC2-A1-N** as colorless crystals (276 mg, 0.688 mmol, 69%). **R_f** = 0.62 (4:1 hexanes/acetone). **m.p.:** 202°C [(***Sjogren et al., 1991***): 208–210°C]. **^{1}H NMR (500 MHz, $(CD_3)_2SO$)** δ/ppm = 12.36 (s, 1H, NH), 7.79–7.76 (m, 2H, 2'-H, 6'-H), 7.65 (t, J = 1.9 Hz, 1H, 4''-H), 7.62–7.60 (m, 2H, 3'-H, 5'-H), 7.59 (d, J = 1.9 Hz, 2H, 2''-H, 6''-H). **^{13}C NMR (126 MHz, $(CD_3)_2SO$)** δ/ppm = 182.7 (C-3), 166.5 (C-1), 144.9 (C-1''), 143.6 (C-1'), 133.5 (C-3'', C-5''), 128.6 (C-4''), 126.2–125.9 (m, C-3', C-5' and C-2'', C-6''), 124.6 (q, J_{CF} = 286.1 Hz, CF_3), 123.3 (C-2), 121.8 (q, J_{CF} = 31.8 Hz, C-4'), 118.7 (C-2', C-6'), 77.7 (CN). IR (ATR) $\tilde{V}_{max}$/cm^{-1}=3293, 2213, 1538, 1409, 1320, 1268, 1244, 1167, 1106, 1070, 837, 810, 660, 591. **HRMS (ESI):** calcd. for $C_{17}H_8{}^{35}Cl_2F_3N_2O_2$ (M-H)$^-$ 398.99204; found 398.99202. **Purity (HPLC):**>96% (λ = 210 nm),>96% (λ = 254 nm).

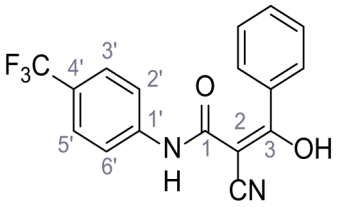

SGA-10

Chemical structure 25. 2-Cyano-3-hydroxy-3-phenyl-*N*-(4-(trifluoromethyl)phenyl)acrylamide – SGA-10.

According to general procedure **B**, amide **SGA-34** (228 mg, 1.00 mmol, 1.0 eq.) in dry THF (10 mL), NaH (92.0 mg, 2.30 mmol, 2.3 eq.) and benzoyl chloride (128 µL, 1.10 mmol, 1.1 eq.) were used to give **SGA-10** as colorless crystals (185 mg, 0.557 mmol, 56%). Analytical data are in accordance with literature (***Davies et al., 2009***). **R_f** = 0.28 (3:2 hexanes/acetone). **m.p.:** 242°C [(***Davies et al., 2009***): 245–247°C]. **^{1}H NMR (400 MHz, $(CD_3)_2SO$)** δ/ppm = 12.12 (s, 1H, NH), 7.84–7.74 (m, 2H, 2'-H, 6'-H), 7.70–7.58 (m, 4H, 3'-H, 5'-H, Ph), 7.48–7.39 (m, 3H, Ph). **^{13}C NMR (101 MHz, $(CD_3)_2SO$)** δ/ppm = 185.7 (C-3), 167.3 (C-1), 143.1 (C-1'), 139.7 (qPh), 135.0 (C-2), 130.0 (Ph), 127.8 (Ph), 127.6 (Ph), 126.0 (q, J_{CF} = 3.8 Hz, C-3', C-5'), 125.0 (d, J_{CF} = 270.6 Hz, CF_3), 122.3 (d, J_{CF} = 35.2 Hz, C-4'), 119.4 (C-2', C-6'), 77.8 (CN). IR (ATR) $\tilde{V}_{max}$/cm^{-1}=3283, 2216, 1592, 1550, 1309, 1109, 1067, 840, 694. **HRMS (ESI):** calcd. for $C_{17}H_{10}F_3N_2O_2$ (M-H)$^-$ 331.06999; found 331.06985. **Purity (HPLC):**>96% (λ = 210 nm),>96% (λ = 254 nm).

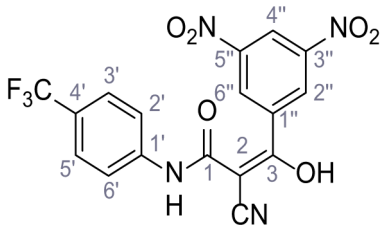

SGA-11

Chemical structure 26. 2-Cyano-3-(3,5-dinitrophenyl)−3-hydroxy-*N*-(4-(trifluoromethyl)phenyl)acrylamide – SGA-11.

According to general procedure **B**, amide **SGA-34** (228 mg, 1.00 mmol, 1.0 eq.) in dry THF (10 mL), NaH (92.0 mg, 2.30 mmol, 2.3 eq.) and 3,5-dinitrobenzoyl chloride (254 mg, 1.10 mmol, 1.1 eq.) were used to give **SGA-11** as red crystals (124 mg, 0.294 mmol, 29%). $\mathbf{R_f}$ = 0.21 (3:2 hexanes/acetone). **m.p.:** 240˚C. **^{1}H NMR (500 MHz, $(CD_3)_2SO$)** δ/ppm = 12.32 (s, 1H, NH), 10.00 (s, 1H, OH), 8.89–8.80 (m, 3H, 2''-H, 4''-H, 6''-H), 7.84–7.75 (m, 2H, 2'-H, 6'-H), 7.67–7.58 (m, 2H, 3'-H, 5'-H). **^{13}C NMR (126 MHz, $(CD_3)_2SO$)** δ/ppm = 180.5 (C-3), 166.1 (C-1), 147.6 (C-3'', C-5''), 144.4 (C-1''), 143.5 (C-1'), 127.6 (C-2'', C-6''),126.1 (q, J_{CF} = 3.5 Hz, C-3', C-5'),124.2 (q, J_{CF} = 271.0 Hz, CF_3), 123.3 (C-2), 121.8 (q, J_{CF} = 31.7 Hz, C-4'), 119.0 (C-4''), 118.6 (C-2', C-6'), 77.7 (CN). IR (ATR) $\tilde{V}_{max}$/cm^{-1}=3262, 3093, 2223, 1539, 1342, 1317, 1115, 1067, 841, 730, 703, 687. **HRMS (ESI):** calcd. for $C_{17}H_8F_3N_4O_6$ $(M\text{-}H)^-$ 421.04014; found 421.04021. **Purity (HPLC):**>96% (λ = 210 nm), >96% (λ = 254 nm).

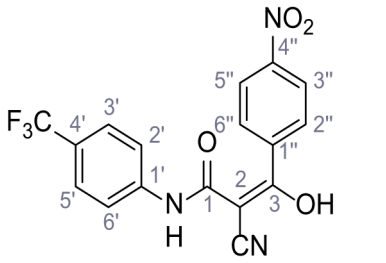

SGA-15

Chemical structure 27. 2-Cyano-3-(4-nitrophenyl)−3-hydroxy-*N*-(4-(trifluoromethyl)phenyl)acrylamide – SGA-15.

According to general procedure **B**, amide **SGA-34** (228 mg, 1.00 mmol, 1.0 eq.) in dry THF (10 mL), NaH (92.0 mg, 2.30 mmol, 2.3 eq.) and 4-nitrobenzoyl chloride (204 mg, 1.10 mmol, 1.1 eq.) were used to give **SGA-15** as yellow crystals (276 mg, 0.688 mmol, 69%). $\mathbf{R_f}$ = 0.19 (3:2 hexanes/acetone). **m.p.:** 217˚C [(***Sjogren et al., 1991***): 211–214˚C]. **^{1}H NMR (500 MHz, $(CD_3)_2SO$)** δ/ppm = 12.39 (s, 1H, NH), 8.28–8.19 (m, 2H, 3''-H, 5''-H), 7.84–7.80 (m, 2H, 2''-H, 6''-H), 7.78 (d, J = 8.6 Hz, 2H, 2'-H, 6'-H), 7.60 (d, J = 8.6 Hz, 2H, 3''-H, 5''-H). **^{13}C NMR (126 MHz, $(CD_3)_2SO$)** δ/ppm = 184.3 (C-3), 166.4 (C-1), 148.1 (C-1''), 147.5 (C-4''), 143.7 (C-1'), 128.6 (C-2'', C-6''), 126.1 (q, J_{CF} = 3.6 Hz, C-3', C-5'), 124.6 (q, J_{CF} = 270.9 Hz, CF_3), 123.2 (C-2), 123.1 (C-3'', C-5''), 121.6 (q, J_{CF} = 32.0 Hz, C-4'), 118.6 (C-2', C-6'), 77.9 (CN). IR (ATR) $\tilde{V}_{max}$/cm^{-1}=3307, 2219, 1551, 1320, 1111, 1069, 844, 750, 700. **HRMS (ESI):** calcd. for $C_{17}H_9F_3N_3O_4$ $(M\text{-}H)^-$ 376.05506; found 376.05509. **Purity (HPLC):**>96% (λ = 210 nm),>96% (λ = 254 nm).

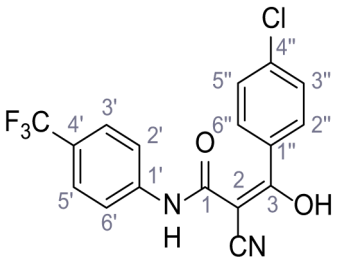

SGA-16

Chemical structure 28. 3-(4-Chlorophenyl)−2-cyano-3-hydroxy-*N*-(4-(trifluoromethyl)phenyl)acrylamide – SGA-16.

According to general procedure **B**, amide **SGA-34** (228 mg, 1.00 mmol, 1.0 eq.) in dry THF (10 mL), NaH (92.0 mg, 2.30 mmol, 2.3 eq.) and 4-chlorobenzoyl chloride (141 µL, 1.10 mmol, 1.1 eq.) were used to give **SGA-16** as colorless crystals (222 mg, 0.605 mmol, 61%). $\mathbf{R_f}$ = 0.32 (3:2 hexanes/acetone). **m.p.:** 220˚C [(***Sjogren et al., 1991***): 218–220˚C]. **^{1}H NMR (500 MHz, $(CD_3)_2SO$)** δ/ppm = 12.31 (s, 1H, NH), 7.81–7.75 (m, 2H, 2'-H, 6'-H), 7.68–7.63 (m, 2H, 2''-H, 6''-H), 7.63–7.58 (m, 2H, 3'-H, 5'-H), 7.49–7.44 (m, 2H, 3''-H, 5''-H). **^{13}C NMR (126 MHz, $(CD_3)_2SO$)** δ/ppm = 184.8 (C-3), 167.0 (C-1), 143.5 (C-1'), 139.6 (C-1''), 134.1 (C-4''), 129.4 (C-2'', C-6''), 127.8 (C-3'', C-5''), 126.0 (q, J_{CF} = 3.6 Hz, C-3', C-5'), 124.6 (q, J_{CF} = 271.0 Hz, CF_3), 123.0 (C-2), 121.8 (q, J_{CF} = 31.0 Hz, C-4'), 118.9 (C-2', C-6'), 77.5 (CN). IR (ATR) $\tilde{V}_{max}$/cm^{-1}=3282.2215, 1587, 1240, 1302, 1129, 1113, 1097, 839. **HRMS (ESI):** calcd. for $C_{17}H_9{}^{35}ClF_3N_2O_2$ $(M\text{-}H)^-$ 365.03101; found 365.03108. **Purity (HPLC):** >96% (λ = 210 nm), >96% (λ = 254 nm).

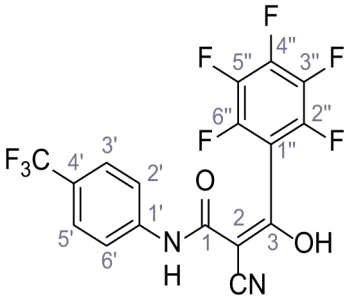

SGA-40

Chemical structure 29. 2-Cyano-3-hydroxy-3-(2,3,4,5,6-pentafluorophenyl)-*N*-(4-(trifluoromethyl)phenyl)acrylamide – SGA-40.

According to general procedure **B**, amide **SGA-34** (228 mg, 1.00 mmol, 1.0 eq.) in dry THF (10 mL), NaH (92.0 mg, 2.30 mmol, 2.3 eq.) and 2,3,4,5,6-pentafluorobenzoyl chloride (158 µL, 1.10 mmol, 1.1 eq.) were used to give **SGA-40** as colorless crystals (236 mg, 0.560 mmol, 56%). $\mathbf{R_f}$ = 0.28 (3:2 hexanes/acetone). **m.p.:** 161˚C. **^{1}H NMR (400 MHz, $(CD_3)_2SO$)** δ/ppm = 11.70 (s, 1H, NH), 7.81–7.72 (m, 2H, 2'-H, 6'-H), 7.67–7.56 (m, 2H, 3'-H, 5'-H). **^{13}C NMR (101 MHz, $(CD_3)_2SO$)** δ/ppm = 172.6 (C-3), 164.9 (C-1), 143.9–140.9 (m, C-2'', C-6'' or C-3'', C-5''), 143.3 (C-1'), 141.9–138.9 (m, C-4''), 138.5–135.1 (m, C-2'', C-6'' or C-3'', C-5''), 126.1 (q, J_{CF} = 3.6 Hz, C-3', C-5'), 124.6 (q, J_{CF} = 271.0 Hz, CF_3), 122.0 (q, J_{CF} = 31.9 Hz, C-4'), 117.5–117.0 (m, C-1''), 121.7 (C-2', C-6'), 118.7 (C-2), 81.8 (CN). IR (ATR) $\tilde{V}_{max}$/cm^{-1}=2230, 1590, 1543, 1524, 1497, 1323, 1116, 1000, 839. **HRMS (ESI):** calcd. for $C_{17}H_5F_8N_2O_2$ $(M\text{-}H)^-$ 421.02288; found 421.02337. **Purity (HPLC):**>96% (λ = 210 nm),>96% (λ = 254 nm).

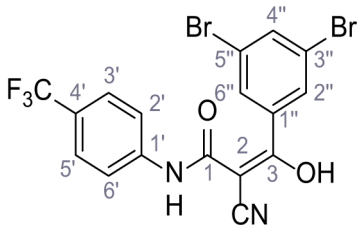

SGA-70

Chemical structure 30. 2-Cyano-3-(3,5-dibromophenyl)-3-hydroxy-*N*-(4-(trifluoromethyl)phenyl)acrylamide – SGA-70.

According to general procedure **B**, amide **SGA-34** (228 mg, 1.00 mmol, 1.0 eq.) in dry THF (10 mL), NaH (92.0 mg, 2.30 mmol, 2.3 eq.) and 3,5-dibromobenzoic acid (308 mg, 1.10 mmol, 1.1 eq.; converted into the corresponding aryl chloride) were used to give **SGA-70** as light yellow crystals (206 mg, 0.420 mmol, 42%). **R_f** = 0.32 (3:2 hexanes/acetone). **m.p.:** 211˚C. **^{1}H NMR (400 MHz, $(CD_3)_2SO$)** δ/ppm = 12.32 (s, 1H, NH), 8.96 (s, 1H, OH), 7.91–7.81 (m, 1H, 4''-H), 7.78–7.72 (m, 4H, 2'-H, 6'-H, 2''-H, 6''-H), 7.65–7.55 (m, 2H, 3'-H, 5'-H). **^{13}C NMR (101 MHz, $(CD_3)_2SO$)** δ/ppm = 182.5 (C-3), 166.4 (C-1), 145.5 (C-1''), 143.6 (C-1'), 133.7 (C-4''), 129.2 (C-2'', C-6''), 126.0 (q, J_{CF} = 3.5 Hz, C-3', C-5'), 123.9 (q, J_{CF} = 271.2 Hz, CF_3), 123.3 (C-2), 121.8 (C-3'', C-5''), 121.6 (q, J_{CF} = 31.9 Hz, C-4'), 118.5 (C-2', C-6'), 77.4 (CN). IR (ATR) $\tilde{V}_{max}$/cm^{-1}=2218, 1594, 1538, 1315, 1166, 1109, 1068, 838, 750. **HRMS (ESI):** calcd. for $C_{17}H_8{}^{79}Br_2F_3N_2O_2$ $(M\text{-}H)^-$ 486.89101; found 486.89128. **Purity (HPLC):**>96% (λ = 210 nm),>96% (λ = 254 nm).

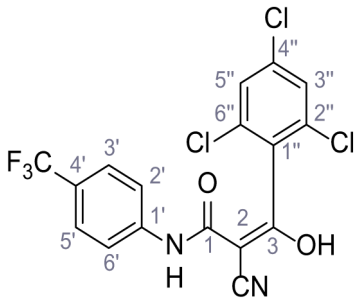

SGA-71

Chemical structure 31. 2-Cyano-3-hydroxy-3-(2,4,6-trichlorophenyl)-*N*-(4-(trifluoromethyl)phenyl)acrylamide – SGA-71.

According to general procedure **B**, amide **SGA-34** (228 mg, 1.00 mmol, 1.0 eq.) in dry THF (10 mL), NaH (92.0 mg, 2.30 mmol, 2.3 eq.) and 2,4,6-trichlorobenzoyl chloride (172 µL, 1.10 mmol, 1.1 eq.) were used to give **SGA-71** as colorless crystals (158 mg, 0.363 mmol, 36%). **R_f** = 0.14 (3:2 hexanes/acetone). **m.p.:** 220˚C. **^{1}H NMR (500 MHz, $(CD_3)_2SO$)** δ/ppm = 11.92 (s, 1H, NH), 7.79–7.74 (m, 2H, 2'-H, 6'-H), 7.66 (s, 2H, 3''-H, 5''-H), 7.63–7.58 (m, 2H, 3'-H, 5'-H). **^{13}C NMR (126 MHz, $(CD_3)_2SO$)** δ/ppm = 180.7 (C-3), 165.7 (C-1), 143.6 (C-1'), 139.5 (C-1''), 133.1 (C-4''), 132.0 (C-2'', C-6''), 127.8 (C-3'', C-5''), 126.1 (q, J_{CF} = 3.6 Hz, C-3', C-5'), 124.6 (q, J_{CF} = 271.1 Hz, CF_3), 121.9 (C-2), 121.6 (q, J_{CF} = 31.9 Hz, C-4'), 118.4 (C-2', C-6'), 79.5 (CN). IR (ATR) $\tilde{V}_{max}$/cm^{-1}=2230, 1598, 1541, 1318, 1116, 841. **HRMS (ESI):** calcd. for $C_{17}H_7{}^{35}Cl_3F_3N_2O_2$ $(M\text{-}H)^-$ 432.95307; found 432.95394. **Purity (HPLC):**>96% (λ = 210 nm),>96% (λ = 254 nm).

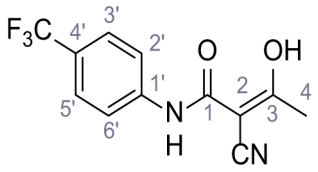

SGA-94

Chemical structure 32. 2-Cyano-3-hydroxy-*N*-(4-(trifluoromethyl)phenyl)but-2-enamide (Teriflunomide) – SGA-94.

According to general procedure **B**, amide **SGA-34** (228 mg, 1.00 mmol, 1.0 eq.) in dry THF (10 mL), NaH (92.0 mg, 2.30 mmol, 2.3 eq.) and acetyl chloride (78.5 µL, 1.10 mmol, 1.1 eq.) were used to give **SGA-94** as colorless crystals (206 mg, 0.761 mmol, 76%). Analytical data are in accordance with literature (***Métro et al., 2012***). $\mathbf{R_f}$ = 0.65 (3:2 hexanes/acetone). **m.p.:** 224˚C [(***Métro et al., 2012***): 230–232˚C]. **^{1}H NMR (400 MHz, $(CD_3)_2SO$)** δ/ppm = 12.28 (s, 1H, OH), 10.91 (s, 1H, NH), 7.81–7.72 (m, 2H, 2'-H, 6'-H), 7.70–7.61 (m, 2H, 3'-H, 5'-H), 2.25 (s, 3H, 4 hr). **^{13}C NMR (101 MHz, $(CD_3)_2SO$)** δ/ppm = 187.1 (C-3), 166.4 (C-1), 141.9 (C-1'), 125.9 (q, J_{CF} = 3.7 Hz, C-3', C-5'), 124.4 (q, J_{CF} = 271.3 Hz, CF_3), 123.5 (q, J_{CF} = 32.1 Hz, C-4'), 120.7 (C-2', C-6'), 118.9 (C-2), 80.5 (CN), 23.5 (C-4). IR (ATR) $\tilde{V}_{max}$/cm^{-1}=2335, 2214, 1551, 1319, 1154, 1113, 840, 679. **HRMS (ESI):** calcd. for $C_{12}H_8F_3N_2O_2$ $(M\text{-}H)^-$ 269.05434; found 269.05423. **Purity (HPLC):**>96% (λ = 210 nm),>96% (λ = 254 nm).

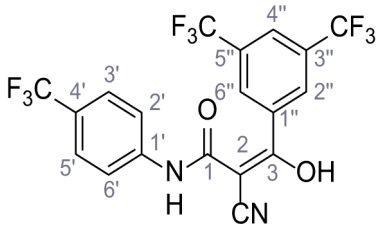

SGA-111

Chemical structure 33. 3-(3,5-Bis(trifluoromethyl)phenyl)−2-cyano-3-hydroxy-*N*-(4-(trifluoromethyl)phenyl)-acrylamide – SGA-111.

According to general procedure **B**, amide **SGA-34** (228 mg, 1.00 mmol, 1.0 eq.) in dry THF (10 mL), NaH (92.0 mg, 2.30 mmol, 2.3 eq.) and 3,5-bis(trifluoromethyl)benzoyl chloride (199 µL, 1.10 mmol, 1.1 eq.) were used to give **SGA-111** as colorless crystals (357 mg, 0.762 mmol, 76%). $\mathbf{R_f}$ = 0.43 (3:2 hexanes/acetone). **m.p.:** 230˚C. **^{1}H NMR (400 MHz, $(CD_3)_2SO$)** δ/ppm = 12.36 (s, 1H, NH), (m, 3H, 2''-H, 6''-H, 4''-H), 7.87–7.71 (m, 2H, 2'-H, 6'-H), 7.69–7.51 (m, 2H, 3'-H, 5'-H). **^{13}C NMR (101 MHz, $(CD_3)_2SO$)** δ/ppm = 182.4 (C-3), 166.3 (C-1), 144.0 (C-1''), 143.6 (C-1'), 129.8 (q, J_{CF} = 32.8 Hz, C-3'', C-5''), 128.1 (q, J_{CF} = 4.7 Hz, C-2'', C-6''), 126.1 (q, J_{CF} = 3.6 Hz, C-3', C-5'), 126.0 (q, J_{CF} = 257.2 Hz, *m*-CF_3), 123.4 (C-2), 123.3 (q, J_{CF} = 271.6 Hz, *p*-CF_3), 122.7 (q, J_{CF} = 4.0 Hz, C-4''), 121.7 (q, J_{CF} = 31.9 Hz, C-4'), 118.5 (C-2', C-6'), 77.7 (CN). IR (ATR) $\tilde{V}_{max}$/cm^{-1}=3289, 2218, 1349, 1323, 1284, 1186, 1139, 1114, 836. **HRMS (ESI):** calcd. for $C_{19}H_8F_9N_2O_2$ $(M\text{-}H)^-$ 467.04475; found 467.04496. **Purity (HPLC):**>96% (λ = 210 nm),>96% (λ = 254 nm).

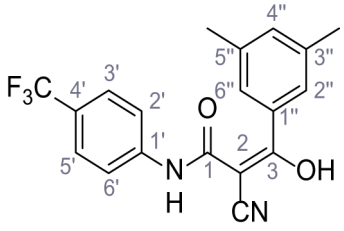

SGA-112

Chemical structure 34. 2-Cyano-3-(3,5-dimethylphenyl)−3-hydroxy-*N*-(4-(trifluoromethyl)phenyl)acrylamide – SGA-112.

According to general procedure **B**, amide **SGA-34** (228 mg, 1.00 mmol, 1.0 eq.) in dry THF (10 mL), NaH (92.0 mg, 2.30 mmol, 2.3 eq.) and 3,5-dimethylbenzoyl chloride (163 µL, 1.10 mmol, 1.1 eq.) were used to give **SGA-112** as colorless crystals (175 mg, 0.486 mmol, 49%). R_f = 0.48 (3:2 hexanes/acetone). **m.p.:** 187°C. **^{1}H NMR (500 MHz, $(CD_3)_2SO$)** δ/ppm = 12.08 (s, 1H, NH), 7.85–7.74 (m, 2H, 2'-H, 6'-H), 7.66–7.58 (m, 2H, 3'-H, 5'-H), 7.25 (s, 2H, 2''-H, 6''-H), 7.09 (s, 1H,4''-H), 2.30 (s, 6H, CH_3). **^{13}C NMR (126 MHz, $(CD_3)_2SO$)** δ/ppm = 186.5 (C-3), 167.8 (C-1), 143.6 (C-1'), 140.1 (C-1''), 137.2 (C-3'', C-5''), 131.8 (C-4''), 126.4 (q, J_{CF} = 3.8 Hz, C-3', C-5'), 125.8 (C-2'', C-6''), 125.3 (q, J_{CF} = 270.8 Hz, CF_3), 122.6 (q, J_{CF} = 31.9 Hz, C-4'), 121.8 (C-2), 119.9 (C-2', C-6'), 78.2 (CN), 21.4 (CH_3). IR (ATR) $\tilde{V}_{max}/cm^{-1}$=3270, 2218, 1526.1319, 1247, 1157, 1110, 1066, 839. **HRMS (ESI):** calcd. for $C_{19}H_{14}F_3N_2O_2$ $(M-H)^-$ 359.10129; found 359.10142. **Purity (HPLC):**>96% (λ = 210 nm),>96% (λ = 254 nm).

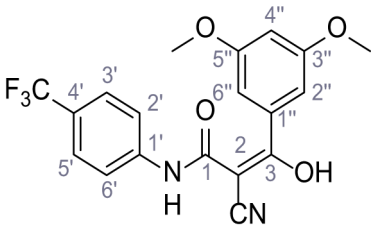

SGA-113

Chemical structure 35. 2-Cyano-3-(3,5-dimethoxyphenyl)−3-hydroxy-*N*-(4-(trifluoromethyl)phenyl)acrylamide – SGA-113.

According to general procedure **B**, amide **SGA-34** (228 mg, 1.00 mmol, 1.0 eq.) in dry THF (10 mL), NaH (92.0 mg, 2.30 mmol, 2.3 eq.) and 3,5-dimethoxybenzoyl chloride (221 mg, 1.10 mmol, 1.1 eq.) were used to give **SGA-113** as colorless crystals (309 mg, 0.789 mmol, 79%). R_f = 0.54 (3:2 hexanes/acetone). **m.p.:** 203°C. **^{1}H NMR (400 MHz, $CDCl_3$)** δ/ppm = 7.99 (s, 1H, NH), 7.73–7.63 (m, 4H, 2'-H, 6'-H, 3'-H, 5'-H), 7.12 (d, J = 2.3 Hz, 2H, 2''-H, 6''-H), 6.69 (t, J = 2.3 Hz, 1H, 4''-H), 3.85 (s, 6H, OCH_3). **^{13}C NMR (101 MHz, $CDCl_3$)** δ/ppm = 184.1 (C-3), 168.7 (C-1), 161.0 (C-3'', C-5''), 139.1 (C-1'), 133.9 (C-1''), 127.8 (q, J_{CF} = 33.2 Hz, C-4'), 126.7 (q, J_{CF} = 3.8 Hz, C-3', C-5'), 123.9 (q, J_{CF} = 270.1 Hz, CF_3), 121.0 (C-2', C-6'), 117.5 (C-2), 106.4 (C-2'', C-6''), 106.0 (C-4''), 78.5 (CN), 55.8 (OCH_3). IR (ATR) $\tilde{V}_{max}/cm^{-1}$=3297, 2215, 1550, 1324, 1208, 1156, 1095, 1067, 834. **HRMS (ESI):** calcd. for $C_{19}H_{14}F_3N_2O_4$ $(M-H)^-$ 391.09112; found 391.09140. **Purity (HPLC):**>96% (λ = 210 nm), >96% (λ = 254 nm).

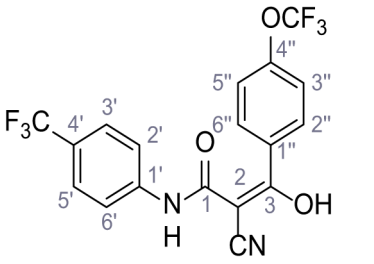

SGA-114

Chemical structure 36. 2-Cyano-3-hydroxy-3-(4-(trifluoromethoxy)phenyl)-*N*-(4-(trifluoromethyl)phenyl)-acrylamide – SGA-114.

According to general procedure **B**, amide **SGA-34** (228 mg, 1.00 mmol, 1.0 eq.) in dry THF (10 mL), NaH (92.0 mg, 2.30 mmol, 2.3 eq.) and 4-(trifluoromethoxy)benzoyl chloride (173 µL, 1.10 mmol, 1.1 eq.) were used to give **SGA-114** as colorless crystals (200 mg, 0.481 mmol, 48%). R_f = 0.58 (3:2 hexanes/acetone). **m.p.:** 198°C [(***Sjogren et al., 1991***): 188–190°C]. **^{1}H NMR (500 MHz, $CDCl_3$)** δ/ppm = 8.12–8.05 (m, 2H, 2''-H, 6''-H), 7.96 (s, 1H, NH), 7.78–7.62 (m, 4H, 2'-H, 6'-H, 3'-H, 5'-H), 7.42–7.32 (m, 2H, 3''-H, 5''-H). **^{13}C NMR (126 MHz, $CDCl_3$)** δ/ppm = 182.6 (C-3), 168.5 (C-1), 152.8 (C-4''), 139.0 (C-1'), 130.7 (C-2'', C-6''), 130.5 (C-1''), 128.0 (q, J_{CF} = 33.0 Hz, C-4'),

126.7 (q, J_{CF} = 3.7 Hz, C-3′, C-5′), 123.9 (q, J_{CF} = 271.7 Hz, CF_3), 121.0 (C-2′, C-6′), 120.8 (C-3′′, C-5′′), 120.6 (q, J_{CF} = 259.4 Hz, OCF_3), 117.3 (C-2), 78.6 (CN). IR (ATR) $\tilde{V}_{max}/cm^{-1}$=3285, 2215, 1597, 1551, 1505, 1268, 1168, 1128, 839. **HRMS (ESI):** calcd. for $C_{18}H_9F_6N_2O_3$ $(M\text{-}H)^-$ 415.05228; found 415.05225. **Purity (HPLC):**>96% (λ = 210 nm),>96% (λ = 254 nm).

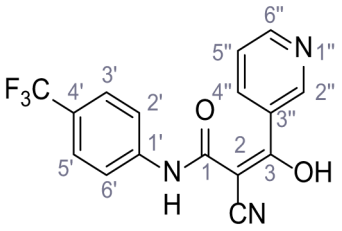

SGA-127

Chemical structure 37. 2-Cyano-3-hydroxy-3-(pyridin-3-yl)-*N*-(4-(trifluoromethyl)phenyl)acrylamide – SGA-127.

According to general procedure **B**, amide **SGA-34** (228 mg, 1.00 mmol, 1.0 eq.) in dry THF (10 mL), NaH (92.0 mg, 2.30 mmol, 2.3 eq.) and nicotinoyl chloride hydrochloride (196 mg, 1.10 mmol, 1.1 eq.) were used to give **SGA-127** as orange solid (169 mg, 0.506 mmol, 51%). $\mathbf{R_f}$ = 0.00 (3:2 hexanes/EtOAc). **m.p.:** 235˚C. **^{1}H NMR (400 MHz, $(CD_3)_2SO$)** δ/ppm = 12.22 (s, 1H, NH), 9.12 (s, 1H, 2′′-H), 8.88 (d, *J* = 5.6 Hz, 1H, 6′′-H), 8.70 (d, *J* = 8.0 Hz, 1H, 4′′-H), 8.04 (dd, *J* = 8.0, 5.6 Hz, 1H, 5′′-H), 7.83–7.72 (m, 2H, 2′-H, 6′-H), 7.67–7.56 (m, 2H, 3′-H, 5′-H). **^{13}C NMR (101 MHz, $(CD_3)_2SO$)** δ/ppm = 180.0 (C-3), 165.9 (C-1), 143.5 (C-1′), 143.3 (C-6′′), 143.0 (C-4′′), 141.9 (C-2′′), 139.9 (C-3′′), 126.2 (C-5′′), 126.1 (q, J_{CF} = 3.6 Hz, C-3′, C-5′), 124.2 (q, J_{CF} = 270.7 Hz, CF_3), 123.3 (C-2), 121.8 (q, J_{CF} = 32.0 Hz, C-4′), 118.5 (C-2′, C-6′), 78.5 (CN). IR (ATR) $\tilde{V}_{max}/cm^{-1}$=2356, 2191, 1533, 1317, 1105, 1060, 849, 698. **HRMS (ESI):** calcd. for $C_{16}H_9F_3N_3O_2$ $(M\text{-}H)^-$ 332.06523; found 332.06517. **Purity (HPLC):**>96% (λ = 210 nm),>96% (λ = 254 nm).

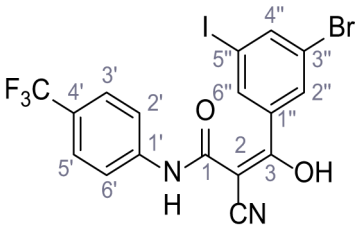

SGA-132

Chemical structure 38. 3-(3-Bromo-5-iodophenyl)−2-cyano-3-hydroxy-*N*-(4-(trifluoromethyl)phenyl)acrylamide – SGA-132.

According to general procedure **B**, amide **SGA-34** (228 mg, 1.00 mmol, 1.0 eq.) in dry THF (10 mL), NaH (92.0 mg, 2.30 mmol, 2.3 eq.) and 3-bromo-5-iodobenzoic acid (360 mg, 1.10 mmol, 1.1 eq.; converted into the corresponding aryl chloride) were used to give **SGA-132** as colorless crystals (332 mg, 0.618 mmol, 62%). $\mathbf{R_f}$ = 0.38 (3:2 hexanes/EtOAc). **m.p.:** 207˚C. **^{1}H NMR (400 MHz, $(CD_3)_2SO$)** δ/ppm = 12.31 (s, 1H, NH), 7.97 (s, 1H, 4′′-H), 7.89 (s, 1H, 2′′-H or 6′′-H), 7.78–7.72 (m, 3H, 2′-H, 6′-H and 2′′-H or 6′′-H), 7.63–7.55 (m, 2H, 3′-H, 5′-H). **^{13}C NMR (101 MHz, $(CD_3)_2SO$)** δ/ppm = 182.6 (C-3), 166.4 (C-1), 145.4 (C-1′′), 143.6 (C-1′), 139.1 (C-4′′), 135.0 (C-2′′ or C-6′′), 129.5 (C-2′′ or C-6′′), 126.0 (q, J_{CF} = 3.8 Hz, C-3′, C-5′), 123.9 (q, J_{CF} = 263.8 Hz, CF_3), 123.3 (C-2), 121.7 (q, J_{CF} = 31.6 Hz, C-4′), 121.6 (C-3′′ or C-5′′), 118.6 (C-2′, C-6′), 95.0 (C-3′′ or C-5′′), 77.4 (CN). IR (ATR) $\tilde{V}_{max}/cm^{-1}$=3276, 2213, 1532, 1318, 1163, 1112, 731. **HRMS (ESI):** calcd. for $C_{17}H_8{}^{79}BrIF_3N_2O_2$ $(M\text{-}H)^-$ 534.87714; found 534.87813. **Purity (HPLC):**>96% (λ = 210 nm),>96% (λ = 254 nm).

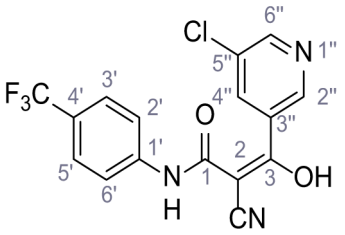

SGA-136

Chemical structure 39. 3-(5-Chloropyridin-3-yl)−2-cyano-3-hydroxy-*N*-(4-(trifluoromethyl)phenyl)acrylamide – SGA-136.

According to general procedure **B**, amide **SGA-34** (228 mg, 1.00 mmol, 1.0 eq.) in dry THF (10 mL), NaH (92.0 mg, 2.30 mmol, 2.3 eq.) and 5-chloronicotinic acid (173 mg, 1.10 mmol, 1.1 eq.; converted into the corresponding aryl chloride) were used to give **SGA-136** as light pink crystals (225 mg, 0.611 mmol, 61%). $\mathbf{R_f}$ = 0.15 (3:2 hexanes/acetone). **m.p.:** 221˚C. **^{1}H NMR (500 MHz, $(CD_3)_2SO$)** δ/ppm = 12.33 (s, 1H, NH), 8.74 (s, 1H, 2''-H or 4''-H), 8.69–8.64 (m, 1H, 6''-H), 8.11–8.05 (m, 1H, 2''-H or 4''-H), 7.81–7.73 (m, 2H, 2'-H, 6'-H), 7.64–7.55 (m, 2H, 3'-H, 5'-H). **^{13}C NMR (126 MHz, $(CD_3)_2SO$)** δ/ppm = 181.7 (C-3), 166.2 (C-1), 147.9 (C-6''), 146.1 (C-2'' or C-4''), 143.6 (C-1'), 138.8 (C-3'' or C-5''), 134.9 (C-2'' or C-4''), 130.5 (C-3'' or C-5''), 126.1 (q, J_{CF} = 3.7 Hz, C-3', C-5'), 124.6 (q, J_{CF} = 271.0 Hz, CF_3), 123.5 (C-2), 121.6 (q, J_{CF} = 31.5 Hz, C-4'), 118.5 (C-2', C-6'), 78.2 (CN). IR (ATR) $\tilde{V}_{max}/cm^{-1}$=3285, 2225, 1539, 1308, 1113, 951, 838. **HRMS (ESI):** calcd. for $C_{16}H_8{}^{35}ClF_3N_3O_2$ $(M-H)^-$ 366.02626; found 366.02652. **Purity (HPLC):**>96% (λ = 210 nm),>96% (λ = 254 nm).

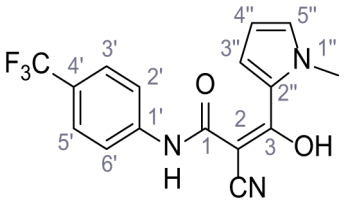

SGA-32

Chemical structure 40. 2-Cyano-3-(1-methyl-1*H*-pyrrol-2-yl)−3-hydroxy-*N*-(4-(trifluoromethyl)phenyl)acrylamide – SGA-32.

According to general procedure **B**, amide **SGA-34** (228 mg, 1.00 mmol, 1.0 eq.) in dry THF (10 mL), NaH (92.0 mg, 2.30 mmol, 2.3 eq.) and 1-methylpyrrole-2-carbonyl chloride (158 mg, 1.10 mmol, 1.1 eq.) were used to give **SGA-32** as colorless crystals (221 mg, 0.660 mmol, 66%). $\mathbf{R_f}$ = 0.57 (3:2 hexanes/acetone). **m.p.:** 203˚C. **^{1}H NMR (400 MHz, $CDCl_3$)** δ/ppm = 7.86 (s, 1H, NH), 7.69–7.61 (m, 4H, 2'-H, 6'-H, 3'-H, 5'-H), 7.57 (dd, J = 4.3, 1.6 Hz, 1H, 3''-H), 6.93–6.90 (m, 1H, 4''-H), 6.27 (dd, J = 4.3, 2.5 Hz, 1H, 5''-H), 3.93 (s, 3H, CH_3). **^{13}C NMR (101 MHz, $CDCl_3$)** δ/ppm = 175.6 (C-3), 170.2 (C-1), 139.5 (C-1'), 132.6 (C-5''), 127.4 (q, J_{CF} = 31.8 Hz, C-4'), 126.6 (q, J = 3.8 Hz, C-3', C-5'), 124.1 (C-2''), 124.0 (q, J_{CF} = 271.4 Hz, CF_3), 121.3 (C-3''), 120.7 (C-2', C-6'), 119.0 (C-2), 110.0 (C-4''), 72.6 (CN), 38.7 (CH_3). IR (ATR) $\tilde{V}_{max}/cm^{-1}$=3273, 2210, 1518, 1379, 1228, 1111, 996, 837, 745. **HRMS (ESI):** calcd. for $C_{16}H_{11}F_3N_3O_2$ $(M-H)^-$ 334.08088; found 334.08090. **Purity (HPLC):**>96% (λ = 210 nm),>96% (λ = 254 nm).

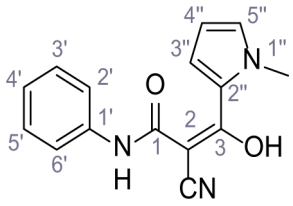

SGA-31

Chemical structure 41. 2-Cyano-3-(1-methyl-1*H*-pyrrol-2-yl)−3-hydroxy-*N*-phenylacrylamide (Prinomide) – SGA-31.

According to general procedure **B**, amide **2** (228 mg, 1.00 mmol, 1.0 eq.) in dry THF (10 mL), NaH (92.0 mg, 2.30 mmol, 2.3 eq.) and 1-methylpyrrole-2-carbonyl chloride (158 mg, 1.10 mmol, 1.1 eq.) were used to give **SGA-31** as colorless crystals (200 mg, 0.747 mmol, 75%). $\mathbf{R_f}$ = 0.65 (3:2 hexanes/acetone). **m.p.:** 171˚C [(***Walker, 1981***): 174–175˚C]. **^{1}H NMR (400 MHz, $CDCl_3$)** δ/ppm = 7.74 (s, 1H, NH), 7.54 (dd, *J* = 4.3, 1.6 Hz, 1H, 3''-H), 7.50 (d, *J* = 8.0 Hz, 2H, 2'-H, 6'-H), 7.44–7.34 (m, 2H, 3'-H, 5'-H), 7.20 (t, *J* = 7.4 Hz, 1H, 4'-H), 6.89 (t, *J* = 1.9 Hz, 1H, 5''-H), 6.25 (dd, *J* = 4.3, 2.5 Hz, 1H, 4''-H), 3.92 (s, 3H, CH_3). **^{13}C NMR (101 MHz, $CDCl_3$)** δ/ppm = 175.6 (C-3), 170.0 (C-1), 136.2 (C-1'), 132.0 (C-5''), 129.3 (C-3', C-5'), 125.7 (C-4'), 124.4 (C-2''), 121.3 (C-2', C-6'), 120.7 (C-3''), 119.1 (C-2), 109.7 (C-4''), 72.6 (CN), 38.5 (CH_3). IR (ATR) $\tilde{V}_{max}$/cm^{-1}=3293, 2210, 1526, 1382, 1231, 751, 736, 687. **HRMS (ESI):** calcd. for $C_{15}H_{12}N_3O_2$ $(M\text{-}H)^-$ 266.09350; found 266.09370. **Purity (HPLC):** >96% (λ = 210 nm),>96% (λ = 254 nm).

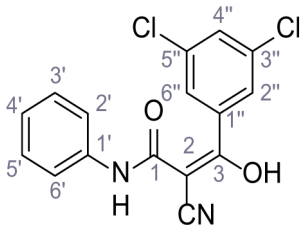

SGA-1

Chemical structure 42. 2-Cyano-3-(3,5-dichlorophenyl)−3-hydroxy-*N*-phenylacrylamide – SGA-1.

According to general procedure **B**, amide **2** (160 mg, 1.00 mmol, 1.0 eq.) in dry THF (10 mL), NaH (92.0 mg, 2.30 mmol, 2.3 eq.) and 3,5-dichlorobenzoyl chloride (230 mg, 1.10 mmol, 1.1 eq.) were used to give **SGA-1** as yellow solid (227 mg, 0.681 mmol, 68%). $\mathbf{R_f}$ = 0.67 (3:2 hexanes/acetone). **m.p.:** 200˚C. **^{1}H NMR (500 MHz, $(CD_3)_2SO$)** δ/ppm = 11.95 (s, 1H, NH), 7.61 (t, *J* = 1.9 Hz, 1H, 4''-H), 7.56 (d, *J* = 1.9 Hz, 2H, 2''-H, 6''-H), 7.53 (dd, *J* = 8.5, 1.0 Hz, 2H, 2'-H, 6'-H), 7.27–7.22 (m, 2H, 3'-H, 5'-H), 6.96–6.90 (m, 1H, 4'-H). **^{13}C NMR (126 MHz, $(CD_3)_2SO$)** δ/ppm = 182.2 (C-3), 166.1 (C-1), 145.3 (C-1''), 140.1 (C-1'), 133.4 (C-3'', C-5''), 128.7 (C-3', C-5'), 128.3 (C-4''), 126.1 (C-2'', C-6''), 123.6 (C-2), 121.7 (C-4'), 118.8 (C-2', C-6'), 77.4 (CN). IR (ATR) $\tilde{V}_{max}$/cm^{-1}=3294, 2212, 1579, 1445, 810, 748, 683. **HRMS (ESI):** calcd. for $C_{16}H_9{}^{35}Cl_2N_2O_2$ $(M\text{-}H)^-$ 331.00466; found 331.00465. **Purity (HPLC):**>96% (λ = 210 nm),>96% (λ = 254 nm).

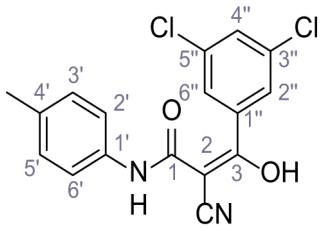

SGA-4

Chemical structure 43. 2-Cyano-3-(3,5-dichlorophenyl)−3-hydroxy-*N*-(*p*-tolyl)acrylamide – SGA-4.

According to general procedure **B**, amide **1** (174 mg, 1.00 mmol, 1.0 eq.) in dry THF (10 mL), NaH (92.0 mg, 2.30 mmol, 2.3 eq.) and 3,5-dichlorobenzoyl chloride (230 mg, 1.10 mmol, 1.1 eq.) were used to give **SGA-4** as yellow crystals (185 mg, 0.534 mmol, 53%). $\mathbf{R_f}$ = 0.28 (3:2 hexanes/acetone). **m.p.:** 214°C. **^{1}H NMR (400 MHz, $(CD_3)_2SO$)** δ/ppm = 11.82 (s, 1H, NH), 7.63 (t, *J* = 1.9 Hz, 1H, 4''-H), 7.56 (d, *J* = 1.9 Hz, 2H, 2''-H, 6''-H), 7.46–7.39 (m, 2H, 2'-H, 6'-H), 7.09–7.02 (m, 2H, 3'-H, 5'-H), 2.24 (s, 3H, CH_3). **^{13}C NMR (101 MHz, $(CD_3)_2SO$)** δ/ppm = 182.0 (C-3), 166.0 (C-1), 145.1 (C-1''), 137.4 (C-1'), 133.4 (C-3'', C-5''), 130.6 (C-4'), 129.1 (C-3', C-5'), 128.3 (C-4''), 126.1 (C-2'', C-6''), 123.5 (C-2), 119.0 (C-2', C-6'), 77.5 (CN), 20.4 (CH_3). IR (ATR) $\tilde{V}_{max}$/cm^{-1}=3299, 2212, 1543, 1518.866, 806, 654. **HRMS (ESI):** calcd. for $C_{17}H_{11}{}^{35}Cl_2N_2O_2$ $(M\text{-}H)^-$ 345.02031; found 345.02052. **Purity (HPLC):**>96% (λ = 210 nm),>96% (λ = 254 nm).

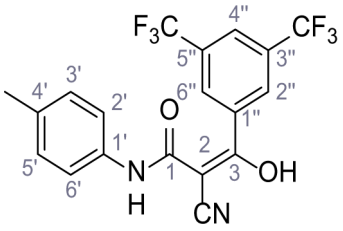

SGA-108

Chemical structure 44. 3-(3,5-Bis(trifluoromethyl)phenyl)−2-cyano-3-hydroxy-*N*-(*p*-tolyl)acrylamide – SGA-108.

According to general procedure **B**, amide **1** (174 mg, 1.00 mmol, 1.0 eq.) in dry THF (10 mL), NaH (92.0 mg, 2.30 mmol, 2.3 eq.) and 3,5-bis(trifluoromethyl)benzoyl chloride (199 µL, 1.10 mmol, 1.1 eq.) were used to give **SGA-108** as light yellow crystals (208 mg, 0.502 mmol, 50%). $\mathbf{R_f}$ = 0.28 (3:2 hexanes/acetone). **m.p.:** 183°C. **^{1}H NMR (500 MHz, $CDCl_3$)** δ/ppm = 8.45 (s, 2H, 2''-H, 6''-H), 8.10 (s, 1H, 4''-H), 7.86 (s, 1H, NH), 7.43–7.37 (m, 2H, 2'-H, 6'-H), 7.25–7.20 (m, 2H, 3'-H, 5'-H), 2.37 (s, 3H, CH_3). **^{13}C NMR (126 MHz, $CDCl_3$)** δ/ppm = 180.4 (C-3), 167.9 (C-1), 136.7 (C-4'), 134.7 (C-1''), 132.7 (C-1'), 132.6 (q, J_{CF} = 34.2 Hz, C-3'', C-5''), 130.1 (C-3', C-5'), 128.6 (q, J_{CF} = 3.1 Hz, C-2'', C-6''), 126.3 (q, J_{CF} = 3.7 Hz, C-4''), 122.8 (q, J_{CF} = 272.9 Hz, CF_3), 121.8 (C-2', C-6'), 116.5 (C-2), 79.7 (CN), 21.2 (CH_3). IR (ATR) $\tilde{V}_{max}$/cm^{-1}=3276, 2213, 1538, 1278, 1129, 811, 681. **HRMS (ESI):** calcd. for $C_{19}H_{11}F_6N_2O_2$ $(M\text{-}H)^-$ 413.07302; found 413.07301. **Purity (HPLC):**>96% (λ = 210 nm),>96% (λ = 254 nm).

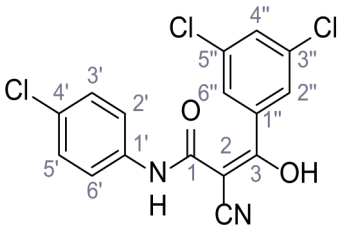

SGA-2

Chemical structure 45. N-(4-Chlorophenyl)−2-cyano-3-(3,5-dichlorophenyl)−3-hydroxyacrylamide – SGA-2.

According to general procedure **B**, amide **4** (195 mg, 1.00 mmol, 1.0 eq.) in dry THF (10 mL), NaH (92.0 mg, 2.30 mmol, 2.3 eq.) and 3,5-dichlorobenzoyl chloride (230 mg, 1.10 mmol, 1.1 eq.) were used to give **SGA-2** as yellow solid (256 mg, 0.695 mmol, 70%). $\mathbf{R_f}$ = 0.71 (3:2 hexanes/acetone). **m.p.:** 230°C. **^{1}H NMR (500 MHz, $(CD_3)_2SO$)** δ/ppm = 12.12 (s, 2H, NH), 7.62 (t, *J* = 1.9 Hz, 1H, 4''-H), 7.60–7.57 (m, 2H, 2'-H, 6'-H), 7.55 (d, *J* = 1.9 Hz, 2H, 2''-H, 6''-H), 7.30–7.26 (m, 2H, 3'-H, 5'-H). **^{13}C NMR (126 MHz, $(CD_3)_2SO$)** δ/ppm = 182.5 (C-3), 166.1 (C-1), 145.4 (C-1''), 139.1 (C-1'), 133.4 (C-3'', C-5''), 128.6 (C-3', C-5'), 128.3 (C-4''), 126.0 (C-2'', C-6''), 125.0 (C-4'), 123.6 (C-2), 120.2 (C-2', C-6'), 77.2 (CN). IR (ATR) $\tilde{V}_{max}$/cm^{-1}=3305, 2212, 1545, 1495, 1506, 1316, 1098, 809. **HRMS (ESI):** calcd. for $C_{16}H_8{}^{35}Cl_3N_2O_2$ $(M\text{-}H)^-$ 364.96568; found 364.96593. **Purity (HPLC):**>96% (λ = 210 nm),>96% (λ = 254 nm).

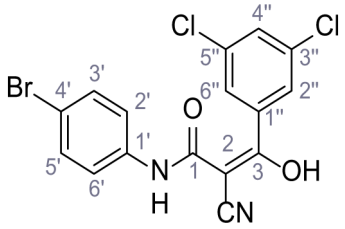

SGA-3

Chemical structure 46. N-(4-Bromophenyl)−2-cyano-3-(3,5-dichlorophenyl)−3-hydroxyacrylamide – SGA-3.

According to general procedure **B**, amide **5** (239 mg, 1.00 mmol, 1.0 eq.) in dry THF (10 mL), NaH (92.0 mg, 2.30 mmol, 2.3 eq.) and 3,5-dichlorobenzoyl chloride (230 mg, 1.10 mmol, 1.1 eq.) were used to give **SGA-3** as yellow crystals (289 mg, 0.702 mmol, 70%). $\mathbf{R_f}$ = 0.73 (3:2 hexanes/acetone). **m.p.:** 237˚C. **^{1}H NMR (400 MHz, $(CD_3)_2SO$)** δ/ppm = 12.09 (s, 1H, NH), 7.62 (t, *J* = 1.9 Hz, 1H, 4''-H), 7.58–7.51 (m, 4H, 2'-H, 6'-H, 2''-H, 6''-H), 7.44–7.38 (m, 2H, 3'-H, 5'-H).**^{13}C NMR (101 MHz, $(CD_3)_2SO$)** δ/ppm = 182.4 (C-3), 166.1 (C-1), 145.2 (C-1''), 139.4 (C-1'), 133.4 (C-3'', C-5''), 131.4 (C-3', C-5'), 128.3 (C-4''), 126.0 (C-2'', C-6''), 122.6 (C-2), 120.7 (C-2', C-6'), 112.9 (C-4'), 77.4 (CN). IR (ATR) $\tilde{V}_{max}$/cm^{-1}=3309, 2211, 1540, 1493, 1403, 1316, 1290, 1012, 809. **HRMS (ESI):** calcd. for $C_{16}H_8{}^{79}Br^{35}Cl_2N_2O_2$ $(M\text{-}H)^-$ 408.91517; found 408.91581. **Purity (HPLC):**>96% (λ = 210 nm), >96% (λ = 254 nm).

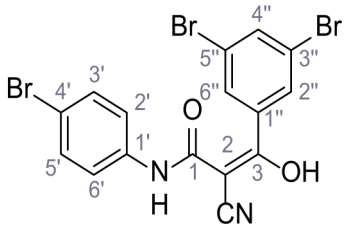

SGA-75

Chemical structure 47. N-(4-Bromophenyl)−2-cyano-3-(3,5-dibromophenyl)−3-hydroxyacrylamide – SGA-75.

According to general procedure **B**, amide **5** (239 mg, 1.00 mmol, 1.0 eq.) in dry THF (10 mL), NaH (92.0 mg, 2.30 mmol, 2.3 eq.) and 3,5-dibromobenzoic acid (308 mg, 1.10 mmol, 1.1 eq.; converted into the corresponding aryl chloride) were used to give **SGA-75** as colorless crystals (222 mg, 0.443 mmol, 44%). $\mathbf{R_f}$ = 0.20 (3:2 hexanes/acetone). **m.p.:** 233˚C. **^{1}H NMR (400 MHz, $(CD_3)_2SO$)** δ/ppm = 12.05 (s, 1H, NH), 7.86 (t, *J* = 1.8 Hz, 1H, 4'-H), 7.73 (d, *J* = 1.8 Hz, 2H, 2''-H, 6''-H), 7.57–7.50 (m, 2H, 2'-H, 6'-H), 7.46–7.37 (m, 2H, 3'-H, 5'-H). **^{13}C NMR (101 MHz, $(CD_3)_2SO$)** δ/ppm = 182.2 (C-3), 166.1 (C-1), 145.5 (C-1''), 139.4 (C-1'), 133.7 (C-4''), 131.5 (C-3', C-5'), 129.2 (C-2'', C-6''), 122.7 (C-2), 121.8 (C-3'', C-5''), 120.8 (C-2', C-6'), 113.0 (C-4'), 77.4 (CN). IR (ATR) $\tilde{V}_{max}$/cm^{-1}=3314, 2214, 1596, 1543, 865, 817, 748, 658. **HRMS (ESI):** calcd. for $C_{16}H_8{}^{79}Br_3N_2O_2$ $(M\text{-}H)^-$ 496.81414; found 496.81449. **Purity (HPLC):**>96% (λ = 210 nm),>96% (λ = 254 nm).

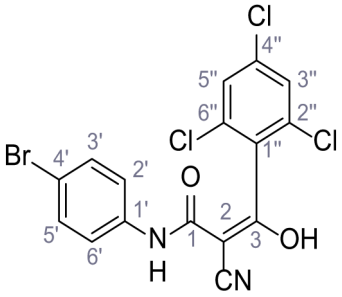

SGA-72

Chemical structure 48. N-(4-Bromophenyl)−2-cyano-3-hydroxy-3-(2,4,6-trichlorophenyl)acrylamide – SGA-72.

According to general procedure **B**, amide **5** (239 mg, 1.00 mmol, 1.0 eq.) in dry THF (10 mL), NaH (92.0 mg, 2.30 mmol, 2.3 eq.) and 2,4,6-trichlorobenzoyl chloride (172 µL, 1.10 mmol, 1.1 eq.) were used to give **SGA-72** as colorless solid (227 mg, 0.507 mmol, 51%). $\mathbf{R_f}$ = 0.14 (3:2 hexanes/acetone). **m.p.:** 191˚C. **^{1}H NMR (400 MHz, $(CD_3)_2SO$)** δ/ppm = 11.69 (s, 1H, NH), 7.65 (s, 2H, 3''-H, 5''-H), 7.58–7.52 (m, 2H, 2'-H, 6'-H), 7.44–7.38 (m, 2H, 3'-H, 5'-H). **^{13}C NMR (101 MHz, $(CD_3)_2SO$)** δ/ppm = 180.3 (C-3), 165.4 (C-1), 139.6 (C-1' or C-1''), 139.4 (C-1' or C-1''), 133.0 (C-4''), 132.0 (C-2'', C-6''), 131.5 (C-3', C-5'), 127.8 (C-3'', C-5''), 122.1 (C-2), 120.5 (C-2', C-6'), 112.9 (C-4'), 79.5 (CN). IR (ATR) $\tilde{V}_{max}$/cm^{-1}=2238, 1588, 1539, 1488, 1307, 856, 818. **HRMS (ESI):** calcd. for $C_{16}H_7{}^{79}Br^{35}Cl_3N_2O_2$ $(M\text{-}H)^-$ 442.87620; found 442.87747. **Purity (HPLC):**>96% (λ = 210 nm),>96% (λ = 254 nm).

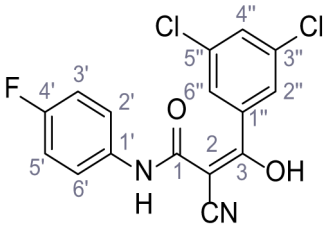

SGA-8

Chemical structure 49. Cyano-3-(3,5-dichlorophenyl)-*N*-(4-fluorophenyl)−3-hydroxyacrylamide – SGA-8.

According to general procedure **B**, amide **6** (178 mg, 1.00 mmol, 1.0 eq.) in dry THF (10 mL), NaH (92.0 mg, 2.30 mmol, 2.3 eq.) and 3,5-dichlorobenzoyl chloride (230 mg, 1.10 mmol, 1.1 eq.) were used to give **SGA-8** as white crystals (220 mg, 0.626 mmol, 63%). $\mathbf{R_f}$ = 0.69 (3:2 hexanes/acetone). **m.p.:** 225˚C. **^{1}H NMR (400 MHz, $(CD_3)_2SO$)** δ/ppm = 11.92 (s, 1H, NH), 7.63 (t, J = 1.9 Hz, 1H, 4''-H), 7.60–7.53 (m, 4H, 2'-H, 6'-H, 2''-H, 6''-H), 7.12–7.03 (m, 2H, 3'-H, 5'-H). **^{13}C NMR (101 MHz, $(CD_3)_2SO$)** δ/ppm = 182.2 (C-3), 166.1 (C-1), 157.3 (d, J_{CF} = 236.9 Hz, C-4'), 144.9 (C-1''), 136.3 (d, J_{CF} = 2.4 Hz, C-1'), 133.4 (C-3'', C-5''), 128.4 (C-4''), 126.1 (C-2'', C-6''), 123.3 (C-2), 120.5 (d, J_{CF} = 7.6 Hz, C-2', C-6'), 115.2 (d, J_{CF} = 22.0 Hz, C-3', C-5'), 77.4 (CN). IR (ATR) $\tilde{V}_{max}$/cm^{-1}=3296, 2212, 1739, 1549, 1506, 1210, 823, 809, 645. **HRMS (ESI):** calcd. for $C_{16}H_8{}^{35}Cl_2FN_2O_2$ $(M\text{-}H)^-$ 348.99523; found 348.99526. **Purity (HPLC):**>96% (λ = 210 nm),>96% (λ = 254 nm).

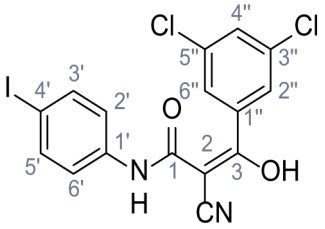

SGA-9

Chemical structure 50. 2-Cyano-3-(3,5-dichlorophenyl)-*N*-(4-iodophenyl)−3-hydroxyacrylamide – SGA-9.

According to general procedure **B**, amide **7** (286 mg, 1.00 mmol, 1.0 eq.) in dry THF (10 mL), NaH (92.0 mg, 2.30 mmol, 2.3 eq.) and 3,5-dichlorobenzoyl chloride (230 mg, 1.10 mmol, 1.1 eq.) were used to give **SGA-9** as yellow crystals (279 mg, 0.608 mmol, 61%). $\mathbf{R_f}$ = 0.71 (3:2 hexanes/acetone). **m.p.:** 238˚C. **^{1}H NMR (400 MHz, $(CD_3)_2SO$)** δ/ppm = 12.04 (s, 1H, NH), 7.63 (t, *J* = 1.9 Hz, 1H, 4''-H), 7.59–7.53 (m, 4H, 3'-H, 5'-H, 2''-H, 6''-H), 7.44–7.38 (m, 2H, 2'-H, 6'-H). **^{13}C NMR (101 MHz, $(CD_3)_2SO$)** δ/ppm = 182.4 (C-3), 166.2 (C-1), 145.1 (C-1''), 139.8 (C-1'), 137.3 (C-3', C-5' or C-2'', C-6''), 133.4 (C-3'', C-5''), 128.4 (C-4''), 126.1 (C-3', C-5' or C-2'', C-6''), 123.3 (C-2), 121.1 (C-2', C-6'), 84.5 (C-4'), 77.5 (CN). IR (ATR) $\tilde{V}_{max}$/cm^{-1}=3303, 2217, 1592, 1523, 1485, 1314, 817, 806, 658. **HRMS (ESI):** calcd. for $C_{16}H_8{}^{35}Cl_2IN_2O_2$ $(M\text{-}H)^-$ 456.90130; found 456.90014. **Purity (HPLC):** >96% (λ = 210 nm),>96% (λ = 254 nm).

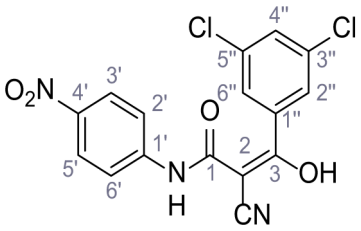

SGA-13

Chemical structure 51. 2-Cyano-3-(3,5-dichlorophenyl)-*N*-(4-nitrophenyl)−3-hydroxyacrylamide – SGA-13.

According to general procedure **B**, amide **8** (205 mg, 1.00 mmol, 1.0 eq.) in dry THF (16 mL), NaH (92.0 mg, 2.30 mmol, 2.3 eq.) and 3,5-dichlorobenzoyl chloride (230 mg, 1.10 mmol, 1.1 eq.) were used to give **SGA-13** as yellow solid (208 mg, 0.550 mmol, 55%). $\mathbf{R_f}$ = 0.82 (3:2 hexanes/acetone). **m.p.:** 246˚C. **^{1}H NMR (400 MHz, $(CD_3)_2SO$)** δ/ppm = 12.64 (s, 1H, NH), 8.19–8.13 (m, 2H, 3'-H, 5'-H), 7.82–7.77 (m, 2H, 2'-H, 6'-H), 7.64 (t, *J* = 1.9 Hz, 1H, 4''-H), 7.57 (d, *J* = 1.9 Hz, 2H, 2''-H, 6''-H). **^{13}C NMR (101 MHz, $(CD_3)_2SO$)** δ/ppm = 181.6 (C-3), 166.9 (C-1), 149.4 (C-1''), 147.0 (C-1'), 141.3 (C-4'), 133.9 (C-3'', C-5''), 129.0 (C-4''), 126.5 (C-2'', C-6''), 125.7 (C-3', C-5'), 121.8 (C-2), 118.6 (C-2', C-6'), 77.0 (CN). IR (ATR) $\tilde{V}_{max}$/cm^{-1}=3314, 2209, 1568, 1546, 1514, 1498, 1340, 1309, 847, 813, 656. **HRMS (ESI):** calcd. for $C_{16}H_8{}^{35}Cl_2N_3O_4$ $(M\text{-}H)^-$ 375.98973; found 375.98970. **Purity (HPLC):**>96% (λ = 210 nm),>96% (λ = 254 nm).

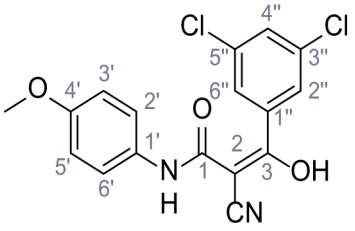

SGA-12

Chemical structure 52. 2-Cyano-3-(3,5-dichlorophenyl)-*N*-(4-methoxyphenyl)−3-hydroxyacrylamide – SGA-12.

According to general procedure **B**, amide **3** (190 mg, 1.00 mmol, 1.0 eq.) in dry THF (10 mL), NaH (92.0 mg, 2.30 mmol, 2.3 eq.) and 3,5-dichlorobenzoyl chloride (230 mg, 1.10 mmol, 1.1 eq.) were used to give **SGA-12** as yellow solid (220 mg, 0.606 mmol, 61%). $\mathbf{R_f}$ = 0.76 (3:2 hexanes/acetone). **m.p.:** 207˚C. **^{1}H NMR (400 MHz, $(CD_3)_2SO$)** δ/ppm = 11.36 (s, 1H, NH), 9.87 (s, 1H, OH), 7.71 (t, *J* = 1.8 Hz, 1H, 4'-H), 7.65 (d, *J* = 1.8 Hz, 2H, 2''-H, 6''-H), 7.49–7.41 (m, 2H, 2'-H, 6'-H), 6.90–6.85 (m, 2H, 3'-H, 5'-H), 3.72 (s, 3H, OCH_3). ^{13}C NMR (101 MHz, $(CD_3)_2SO$) δ/ppm = 181.6 (C-3), 166.4 (C-1), 155.2 (C-4'), 142.6 (C-1''), 133.7 (C-3'', C-5''), 131.9 (C-1'), 129.3 (C-4''), 126.3 (C-2'', C-6''), 121.7 (C-2', C-6'), 121.4 (C-2), 113.9 (C-3', C-5'), 78.1 (CN), 55.2 (OCH_3). IR (ATR) $\tilde{V}_{max}/cm^{-1}$=3296, 2211, 1601, 1467, 1441, 1297, 1251, 1032, 764. HRMS (ESI): calcd. for $C_{17}H_{11}{}^{35}Cl_2N_2O_3$ $(M\text{-}H)^-$ 361.01522; found 361.01516. Purity (HPLC):>96% (λ = 210 nm),>96% (λ = 254 nm).

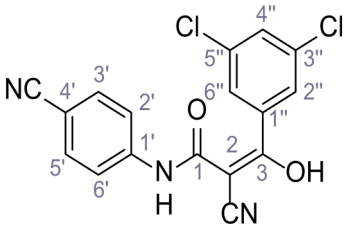

SGA-38

Chemical structure 53. 2-Cyano-*N*-(4-cyanophenyl)−3-(3,5-dichlorophenyl)−3-hydroxyacrylamide – SGA-38.

According to general procedure **B**, amide **9** (185 mg, 1.00 mmol, 1.0 eq.) in dry THF (10 mL), NaH (92.0 mg, 2.30 mmol, 2.3 eq.) and 3,5-dichlorobenzoyl chloride (230 mg, 1.10 mmol, 1.1 eq.) were used to give **SGA-38** as yellow solid (137 mg, 0.382 mmol, 38%). $\mathbf{R_f}$ = 0.12 (3:2 hexanes/acetone). **m.p.:** 236˚C. **^{1}H NMR (500 MHz, $(CD_3)_2SO$)** δ/ppm = 12.42 (s, 1H, NH), 7.75–7.72 (m, 2H, 3'-H, 5'-H), 7.71–7.67 (m, 2H, 2'-H, 6'-H), 7.64 (t, *J* = 1.9 Hz, 1H, 4''-H), 7.57 (d, *J* = 1.9 Hz, 2H, 2''-H, 6''-H). **^{13}C NMR (126 MHz, $(CD_3)_2SO$)** δ/ppm = 183.0 (C-3), 166.4 (C-1), 145.1 (C-1''), 144.3 (C-1'), 133.5 (C-3'', C-5''), 133.3 (C-3', C-5'), 128.5 (C-4''), 126.0 (C-2'', C-6''), 123.2 (C-4'), 119.4 (C-2), 118.8 (C-2', C-6'), 103.1 (4'-CN), 77.4 (2-CN). IR (ATR) $\tilde{V}_{max}/cm^{-1}$=3321, 2360, 2340, 1533, 839, 655. **HRMS (ESI):** calcd. for $C_{17}H_8{}^{35}Cl_2N_3O_2$ $(M\text{-}H)^-$ 355.99991; found 356.00057. **Purity (HPLC):**>96% (λ = 210 nm),>96% (λ = 254 nm).

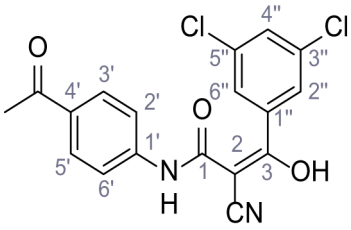

SGA-76

Chemical structure 54. N-(4-Acetylphenyl)−2-cyano-3-(3,5-dichlorophenyl)−3-hydroxyacrylamide – SGA-76.

According to general procedure **B**, amide **10** (202 mg, 1.00 mmol, 1.0 eq.) in dry THF (10 mL), NaH (92.0 mg, 2.30 mmol, 2.3 eq.) and 3,5-dichlorobenzoyl chloride (230 mg, 1.10 mmol, 1.1 eq.) were used to give **SGA-76** as off white solid (296 mg, 0.789 mmol, 79%). $\mathbf{R_f}$ = 0.08 (3:2 hexanes/acetone). **m.p.:** 209˚C. **^{1}H NMR (500 MHz, $(CD_3)_2SO$)** δ/ppm = 12.32 (s, 1H, NH), 7.91–7.86 (m, 2H, 3'-H, 5'-H), 7.71–7.66 (m, 2H, 2'-H, 6'-H), 7.64 (t, *J* = 1.9 Hz, 1H, 4''-H), 7.58 (d, *J* = 1.9 Hz, 2H, 2''-H, 6''-H), 2.51 (s, 3H, CH_3, collapses with DMSO). **^{13}C NMR (101 MHz, $(CD_3)_2SO$)** δ/ppm = 196.3 (CO), 182.8 (C-3), 166.3 (C-1), 145.1 (C-1''), 144.5 (C-1'), 133.5 (C-3'', C-5''), 130.4 (C-4'), 129.7 (C-3', C-5'), 128.5 (C-4''), 126.1 (C-2'', C-6''), 123.3 (C-2), 117.9 (C-2', C-6'), 77.6 (CN), 26.3 (CH_3). IR (ATR) $\tilde{V}_{max}/cm^{-1}$=3304, 2207, 1682, 1596, 1544, 1355, 1272, 809. **HRMS (ESI):** calcd. for $C_{18}H_{11}{}^{35}Cl_2N_2O_3$ $(M\text{-}H)^-$ 373.01522; found 373.01580. **Purity (HPLC):**>96% (λ = 210 nm),>96% (λ = 254 nm).

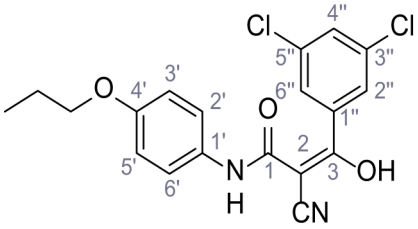

SGA-84

Chemical structure 55. 2-Cyano-3-(3,5-dichlorophenyl)−3-hydroxy-*N*-(4-propoxyphenyl)acrylamide – SGA-84.

According to general procedure **B**, amide **11** (218 mg, 1.00 mmol, 1.0 eq.) in dry THF (10 mL), NaH (92.0 mg, 2.30 mmol, 2.3 eq.) and 3,5-dichlorobenzoyl chloride (230 mg, 1.10 mmol, 1.1 eq.) were used to give **SGA-84** as yellow solid (245 mg, 0.626 mmol, 63%). $\mathbf{R_f}$ = 0.15 (3:2 hexanes/acetone + 2% TEA). **m.p.:** 184°C. **^{1}H NMR (500 MHz, $(CD_3)_2SO$)** δ/ppm = 11.36 (s, 1H, NH), 9.30 (s, 1H, OH), 7.71 (t, *J* = 1.7 Hz, 1H, 4''-H), 7.67–7.62 (m, 2H, 2''-H, 6''-H), 7.49–7.40 (m, 2H, 3'-H, 5'-H), 6.90–6.82 (m, 2H, 2'-H, 6'-H), 3.88 (t, *J* = 6.5 Hz, 2H, $C\underline{H}_2CH_2CH_3$), 1.71 (sext, *J* = 7.2 Hz, 2H, $CH_2C\underline{H}_2CH_3$), 0.97 (t, *J* = 7.4 Hz, 3H, $CH_2CH_2C\underline{H}_3$). **^{13}C NMR (126 MHz, $(CD_3)_2SO$)** δ/ppm = 181.6 (C-3), 166.4 (C-1), 154.6 (C-4'), 142.7 (C-1''), 133.7 (C-3'', C-5''), 131.9 (C-1'), 129.3 (C-4''), 126.3 (C-2'', C-6''), 121.6 (C-3', C-5'), 121.5 (C-2), 114.5 (C-2', C-6'), 78.0 (CN), 69.1 ($\underline{C}H_2CH_2CH_3$), 22.1 ($CH_2\underline{C}H_2CH_3$), 10.4 ($CH_2CH_2\underline{C}H_3$). IR (ATR) $\tilde{V}_{max}$/cm^{-1}=3304, 2208, 1601, 1550, 1511, 1249, 1235, 822, 811. **HRMS (ESI):** calcd. for $C_{19}H_{15}{}^{35}Cl_2N_2O_3$ $(M\text{-}H)^-$ 389.04652; found 389.04631. **Purity (HPLC):**>96% (λ = 210 nm),>96% (λ = 254 nm).

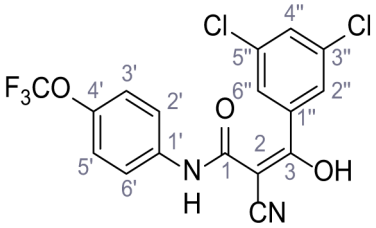

SGA-86

Chemical structure 56. 2-Cyano-3-(3,5-dichlorophenyl)−3-hydroxy-*N*-(4-(trifluoromethoxy)phenyl)acrylamide – SGA-86.

According to general procedure **B**, amide **12** (244 mg, 1.00 mmol, 1.0 eq.) in dry THF (10 mL), NaH (92.0 mg, 2.30 mmol, 2.3 eq.) and 3,5-dichlorobenzoyl chloride (230 mg, 1.10 mmol, 1.1 eq.) were used to give **SGA-86** as colorless solid (344 mg, 0.825 mmol, 83%). $\mathbf{R_f}$ = 0.53 (3:2 hexanes/acetone). **m.p.:** 195°C. **^{1}H NMR (500 MHz, $(CD_3)_2SO$)** δ/ppm = 12.02 (s, 1H, NH), 9.41 (s, 1H, OH), 7.69–7.64 (m, 3H, 2'-H, 6'-H, 4''-H), 7.59 (d, *J* = 1.9 Hz, 2H, 2''-H, 6''-H), 7.28–7.23 (m, 2H, 3'-H, 5'-H). **^{13}C NMR (126 MHz, $(CD_3)_2SO$)** δ/ppm = 182.3 (C-3), 166.3 (C-1), 144.6 (C-1''), 142.7 (C-4'), 139.1 (C-1'), 133.5 (C-3'', C-5''), 128.6 (C-4''), 126.1 (C-2'', C-6''), 123.0 (C-2), 121.6 (C-3', C-5'), 120.3 (q, J_{CF} = 255.2 Hz, OCF_3), 120.2 (C-2', C-6'), 77.6 (CN). IR (ATR) $\tilde{V}_{max}$/cm^{-1}=3304, 2218, 1614, 1536, 1506, 1262, 1208, 1164, 661. **HRMS (ESI):** calcd. for $C_{17}H_8{}^{35}Cl_2F_3N_2O_3$ $(M\text{-}H)^-$ 414.98696; found 414.98676. **Purity (HPLC):**>96% (λ = 210 nm),>96% (λ = 254 nm).

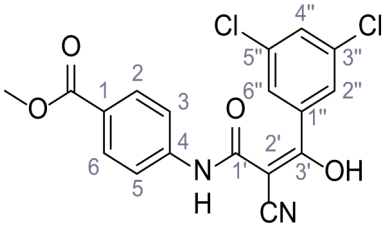

SGA-133

Chemical structure 57. Methyl 4-(2-cyano-3-(3,5-dichlorophenyl)−3-hydroxyacrylamido)benzoate – SGA-133.

According to general procedure **B**, amide **13** (218 mg, 1.00 mmol, 1.0 eq.) in dry THF (10 mL), NaH (92.0 mg, 2.30 mmol, 2.3 eq.) and 3,5-dichlorobenzoyl chloride (230 mg, 1.10 mmol, 1.1 eq.) were used. The resulting solid was washed with hexanes, EtOH and water to give **SGA-133** as colorless solid (331 mg, 0.846 mmol, 85%). $\mathbf{R_f}$ = 0.15 (3:2 hexanes/acetone). **m.p.:** 234˚C. **^{1}H NMR (400 MHz, $(CD_3)_2SO$)** δ/ppm = 12.33 (s, 1H, NH), 11.41 (s, 1H, OH), 7.90–7.83 (m, 2H, 2 hr, 6 hr), 7.71–7.66 (m, 2H, 3 hr, 5 hr), 7.64 (t, *J* = 1.9 Hz, 1H, 4''-H), 7.57 (d, *J* = 1.9 Hz, 2H, 2''-H, 6''-H), 3.81 (s, 3H, CH_3). **^{13}C NMR (101 MHz, $(CD_3)_2SO$)** δ/ppm = 182.8 (C-3'), 166.3 (C-1'), 166.0 (CO), 145.1 (C-1''), 144.6 (C-4), 133.4 (C-3'', C-5''), 130.4 (C-2, C-6), 128.5 (C-4''), 126.1 (C-2'', C-6''), 123.3 (C-2'), 122.3 (C-1), 118.1 (C-3, C-5), 77.6 (CN), 51.7 (CH_3). IR (ATR) $\tilde{V}_{max}$/cm^{-1}=3304, 3093, 2215, 1727, 1591, 1534, 1415, 1283, 1262, 1112, 810, 766. **HRMS (ESI):** calcd. for $C_{18}H_{11}{}^{35}Cl_2N_2O_4$ $(M\text{-}H)^-$ 389.01014; found 389.01077. **Purity (NMR):**>96% (λ = 210 nm),>96% (λ = 254 nm).

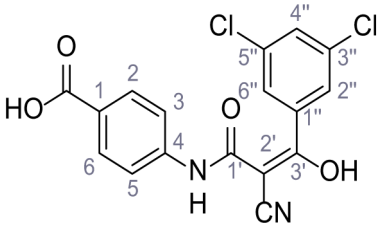

SGA-137

Chemical structure 58. 4-(2-Cyano-3-(3,5-dichlorophenyl)−3-hydroxyacrylamido)benzoic acid – SGA-137.

Ester **SGA-133** (95.0 mg, 0.243 mmol, 1.0 eq.) was dissolved in dioxane/H_2O (3:1; 4.0 mL) and LiOH (61.2 mg, 2.43 mmol, 10 eq.) was added. The mixture was stirred at rt for 3 hr, before 1 M aq. HCl (5.0 mL) was added. The precipitate was filtered off, washed with cold water and dried to give **SGA-137** as colorless solid (59.6 mg, 0.158 mmol, 65%). $\mathbf{R_f}$ = 0.00 (3:2 hexanes/acetone). **m.p.:** 244˚C. **^{1}H NMR (500 MHz, $(CD_3)_2SO$)** δ/ppm = 12.30 (s, 1H, NH), 7.87–7.81 (m, 2H, 2 hr, 6 hr), 7.68–7.64 (m, 2H, 3 hr, 5 hr), 7.63 (t, *J* = 1.9 Hz, 1H, 4''-H), 7.57 (d, *J* = 1.9 Hz, 2H, 2''-H, 6''-H). **^{13}C NMR (126 MHz, $(CD_3)_2SO$)** δ/ppm = 182.7 (C-3'), 167.1 (CO), 166.3 (C-1'), 145.2 (C-1''), 144.2 (C-4), 133.4 (C-3'', C-5''), 130.5 (C-2, C-6), 128.4 (C-4''), 126.1 (C-2'', C-6''), 123.5 (C-1), 123.4 (C-2'), 118.0 (C-3, C-5), 77.5 (CN). IR (ATR) $\tilde{V}_{max}$/cm^{-1}=3311, 2215, 1696, 1595, 1550, 1415, 1294, 855, 770. **HRMS (ESI):** calcd. for $C_{17}H_9{}^{35}Cl_2N_2O_4$ $(M\text{-}H)^-$ 374.99449; found 374.99480. **Purity (HPLC):**>96% (λ = 210 nm),>96% (λ = 254 nm).

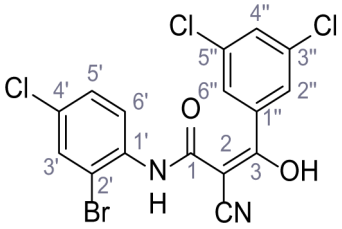

SGA-27

Chemical structure 59. N-(2-Bromo-4-chlorophenyl)−2-cyano-3-(3,5-dichlorophenyl)−3-hydroxyacrylamide – SGA-27.

According to general procedure **B**, amide **14** (274 mg, 1.00 mmol, 1.0 eq.) in dry THF (10 mL), NaH (92.0 mg, 2.30 mmol, 2.3 eq.) and 3,5-dichlorobenzoyl chloride (230 mg, 1.10 mmol, 1.1 eq.) were used to give **SGA-27** as colorless solid (330 mg, 0.738 mmol, 74%). $\mathbf{R_f}$ = 0.25 (3:2 hexanes/acetone). **m.p.:** 203°C. **^{1}H NMR (500 MHz, $(CD_3)_2SO$)** δ/ppm = 12.29 (s, 1H, NH), 8.56 (d, *J* = 9.0 Hz, 1H, 6'-H), 7.68 (d, *J* = 2.5 Hz, 1H, 3'-H), 7.63 (t, *J* = 1.9 Hz, 1H, 4''-H), 7.58 (d, *J* = 1.9 Hz, 2H, 2''-H, 6''-H), 7.36 (dd, *J* = 9.0, 2.5 Hz, 1H, 5'-H). **^{13}C NMR (126 MHz, $(CD_3)_2SO$)** δ/ppm = 182.7 (C-3), 166.4 (C-1), 145.2 (C-1''), 137.8 (C-1'), 133.4 (C-3'', C-5''), 131.4 (C-6'), 128.4 (C-4''), 127.8 (C-5'), 126.1 (C-2'', C-6''), 125.4 (C-4'), 123.5 (C-2), 122.1 (C-3'), 112.1 (C-2'), 77.3 (CN). IR (ATR) $\tilde{V}_{max}$/cm^{-1}=3366, 3087, 2208, 1556, 1521, 1469, 1360, 1292, 863, 815. **HRMS (ESI):** calcd. for $C_{16}H_7{}^{79}Br^{35}Cl_3N_2O_2$ $(M\text{-}H)^-$ 442.87620; found 442.87736. **Purity (HPLC):**>96% (λ = 210 nm),>96% (λ = 254 nm).

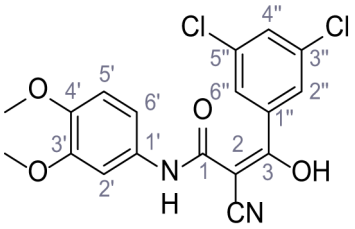

SGA-28

Chemical structure 60. 2-Cyano-3-(3,5-dichlorophenyl)-*N*-(3,4-dimethoxyphenyl)−3-hydroxyacrylamide – SGA-28.

According to general procedure **B**, amide **17** (220 mg, 1.00 mmol, 1.0 eq.) in dry THF (10 mL), NaH (92.0 mg, 2.30 mmol, 2.3 eq.) and 3,5-dichlorobenzoyl chloride (230 mg, 1.10 mmol, 1.1 eq.) were used to give **SGA-28** as yellow solid (200 mg, 0.508 mmol, 51%). $\mathbf{R_f}$ = 0.17 (3:2 hexanes/acetone). **m.p.:** 195°C. **^{1}H NMR (500 MHz, $(CD_3)_2SO$)** δ/ppm = 11.52 (s, 1H, NH), 7.68 (t, *J* = 1.8 Hz, 1H, 4''-H), 7.62 (d, *J* = 1.8 Hz, 2H, 2''-H, 6''-H), 7.30 (d, *J* = 2.2 Hz, 1H, 2'-H), 7.01 (dd, *J* = 8.7, 2.2 Hz, 1H, 6'-H), 6.86 (d, *J* = 8.7 Hz, 1H, 5'-H), 3.73 (s, 3H, OCH_3), 3.71 (s, 3H, OCH_3). **^{13}C NMR (126 MHz, $(CD_3)_2SO$)** δ/ppm = 181.7 (C-3), 166.2 (C-1), 148.6 (C-3'), 144.4 (C-4'), 143.6 (C-1''), 133.6 (C-3'', C-5''), 133.0 (C-1'), 128.9 (C-4''), 126.2 (C-2'', C-6''), 122.2 (C-2), 112.3 (C-5'), 111.5 (C-6'), 104.9 (C-2'), 77.9 (CN), 55.8 (OCH_3), 55.4 (OCH_3). IR (ATR) $\tilde{V}_{max}$/cm^{-1}=3284, 2217, 1608, 1549, 1516, 1238, 1028, 810. **HRMS (ESI):** calcd. for $C_{18}H_{13}{}^{35}Cl_2N_2O_4$ $(M\text{-}H)^-$ 391.02579; found 391.02608. **Purity (HPLC):**>96% (λ = 210 nm),>96% (λ = 254 nm).

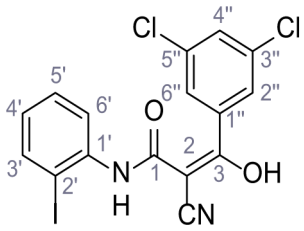

SGA-39

Chemical structure 61. 2-Cyano-3-(3,5-dichlorophenyl)−3-hydroxy-*N*-(2-iodophenyl)acrylamide – SGA-39.

According to general procedure **B**, amide **15** (286 mg, 1.00 mmol, 1.0 eq.) in dry THF (10 mL), NaH (92.0 mg, 2.30 mmol, 2.3 eq.) and 3,5-dichlorobenzoyl chloride (230 mg, 1.10 mmol, 1.1 eq.) were used to give **SGA-39** as yellow solid (237 mg, 0.515 mmol, 52%). $\mathbf{R_f}$ = 0.20 (3:2 hexanes/acetone). **m.p.:** 171˚C. **^{1}H NMR (400 MHz, $(CD_3)_2SO$)** δ/ppm = 11.87 (s, 1H, NH), 8.27 (dd, *J* = 8.3, 1.5 Hz, 1H, 6'-H), 7.80 (dd, *J* = 7.9, 1.5 Hz, 1H, 3'-H), 7.63 (t, *J* = 1.9 Hz, 1H, 4''-H), 7.59 (d, *J* = 1.9 Hz, 2H, 2''-H, 6''-H), 7.29 (ddd, *J* = 8.4, 7.3, 1.5 Hz, 1H, 5'-H), 6.80–6.67 (m, 1H, 4'-H). **^{13}C NMR (126 MHz, $(CD_3)_2SO$)** δ/ppm = 182.2 (C-3), 166.4 (C-1), 145.1 (C-1''), 141.5 (C-1'), 139.0 (C-3'), 133.4 (C-3'', C-5''), 128.4 (C-4''), 128.3 (C-5'), 126.1 (C-2'', C-6''), 124.0 (C-4'), 123.6 (C-2), 122.1 (C-6'), 89.2 (C-2'), 77.2 (CN). IR (ATR) $\tilde{V}_{max}$/cm^{-1}=3337, 2213, 1579, 1537, 1294, 742. **HRMS (ESI):** calcd. for $C_{16}H_8{}^{35}Cl_2IN_2O_2$ $(M\text{-}H)^-$ 456.90130; found 456.90095. **Purity (HPLC):**>96% (λ = 210 nm),>96% (λ = 254 nm).

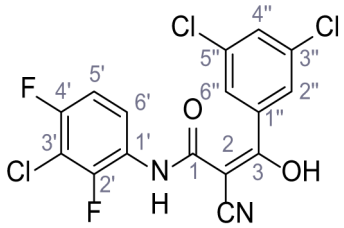

SGA-33

Chemical structure 62. N-(3-Chloro-2,4-difluorophenyl)−2-cyano-3-(3,5-dichlorophenyl)−3-hydroxyacrylamide – SGA-33.

According to general procedure **B**, amide **16** (231 mg, 1.00 mmol, 1.0 eq.) in dry THF (10 mL), NaH (92.0 mg, 2.30 mmol, 2.3 eq.) and 3,5-dichlorobenzoyl chloride (230 mg, 1.10 mmol, 1.1 eq.) were used to give **SGA-33** as colorless crystals (290 mg, 0.719 mmol, 72%). $\mathbf{R_f}$ = 0.15 (3:2 hexanes/acetone). **m.p.:** 193˚C. **^{1}H NMR (400 MHz, $(CD_3)_2SO$)** δ/ppm = 12.34 (s, 1H, NH), 8.43 (td, *J* = 9.0, 6.0 Hz, 1H, 6'-H), 7.63 (t, *J* = 1.9 Hz, 1H, 4''-H), 7.58 (d, *J* = 1.9 Hz, 2H, 2''-H, 6''-H), 7.23 (td, *J* = 9.2, 2.1 Hz, 1H, 5'-H). **^{13}C NMR (101 MHz, $(CD_3)_2SO$)** δ/ppm = 182.9 (C-3), 166.3 (C-1), 152.1 (d, J_{CF} = 242.4 Hz, C-4'), 147.7 (d, J_{CF} = 245.4 Hz, C-2'), 145.0 (C-1''), 133.4 (C-3'', C-5''), 128.5 (C-4''), 126.3 (dd, J_{CF} = 10.3, 2.6 Hz, C-1'), 126.1 (C-2'', C-6''), 123.2 (C-2), 119.1 (dd, J_{CF} = 7.8, 3.0 Hz, C-6'), 111.5 (dd, J_{CF} = 20.7, 3.6 Hz, C-5'), 107.8 (dd, J_{CF} = 22.2, 2.9 Hz, C-3'), 77.3 (CN). IR (ATR) $\tilde{V}_{max}$/cm^{-1}=3293, 2206, 1539, 1497, 1370, 1289, 1023, 803. **HRMS (ESI):** calcd. for $C_{16}H_6{}^{35}Cl_3F_2N_2O_2$ $(M\text{-}H)^-$ 400.94684; found 400.94724. **Purity (HPLC):**>96% (λ = 210 nm),>96% (λ = 254 nm).

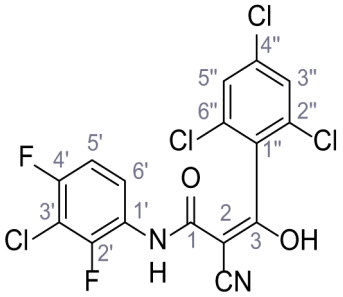

SGA-73

Chemical structure 63. N-(3-Chloro-2,4-difluorophenyl)−2-cyano-3-hydroxy-3-(2,4,6-trichlorophenyl)acrylamide – SGA-73.

According to general procedure **B**, amide **16** (231 mg, 1.00 mmol, 1.0 eq.) in dry THF (10 mL), NaH (92.0 mg, 2.30 mmol, 2.3 eq.) and 2,4,6-trichlorobenzoyl chloride (172 µL, 1.10 mmol, 1.1 eq.) were used to give **SGA-73** as colorless solid (217 mg, 0.496 mmol, 50%). $\mathbf{R_f}$ = 0.16 (1:1 hexanes/acetone). **m.p.:** 199˚C. **^{1}H NMR (500 MHz, $(CD_3)_2SO$)** δ/ppm = 11.93 (s, 1H, NH), 8.45 (td, J = 9.1, 5.9 Hz, 1H, 6'-H), 7.66 (s, 2H, 3''-H, 5''-H), 7.23 (td, J = 9.2, 2.0 Hz, 1H, 5'-H). **^{13}C NMR (126 MHz, $(CD_3)_2SO$)** δ/ppm = 180.8 (C-3), 165.6 (C-1), 152.1 (d, J_{CF} = 242.6 Hz, C-4'), 147.5 (d, J_{CF} = 245.6 Hz, C-2'), 139.4 (C-1'' or C-4''), 133.1 (C-1'' or C-4''), 132.0 (C-2'', C-6''), 127.8 (C-3'', C-5''), 126.3 (dd, J_{CF} = 10.2, 3.2 Hz, C-1'), 121.8 (C-2), 118.8 (dd, J_{CF} = 7.9, 2.9 Hz, C-6'), 111.5 (dd, J_{CF} = 20.7, 3.5 Hz, C-5'), 107.9 (dd, J_{CF} = 22.0, 19.2 Hz, C-3'), 79.4 (CN). IR (ATR) $\tilde{V}_{max}$/cm^{-1}=3279, 2222, 1626, 1590, 1519, 1484, 1445, 1359, 1275, 1017, 816, 631. **HRMS (ESI):** calcd. for $C_{16}H_5{}^{35}Cl_4F_2N_2O_2$ $(M\text{-}H)^-$ 434.90787; found 434.90791. **Purity (HPLC):**>96% (λ = 210 nm),>96% (λ = 254 nm).

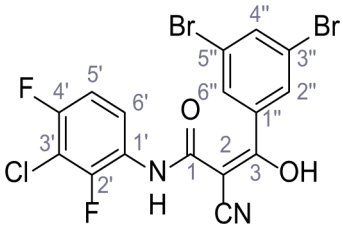

SGA-90

Chemical structure 64. N-(3-Chloro-2,4-difluorophenyl)−2-cyano-3-(3,5-dibromophenyl)−3-hydroxyacrylamide – SGA-90.

According to general procedure **B**, amide **16** (231 mg, 1.00 mmol, 1.0 eq.) in dry THF (10 mL), NaH (92.0 mg, 2.30 mmol, 2.3 eq.) and 3,5-dibromobenzoic acid (308 mg, 1.10 mmol, 1.1 eq.; converted into the corresponding aryl chloride) were used to give **SGA-90** as light yellow solid (374 mg, 0.759 mmol, 76%). $\mathbf{R_f}$ = 0.16 (1:1 hexanes/acetone). **m.p.:** 192˚C. **^{1}H NMR (400 MHz, $(CD_3)_2SO$)** δ/ppm = 12.33 (s, 1H, NH), 8.43 (td, J = 8.9, 6.0 Hz, 1H, 6'-H), 7.86 (t, J = 1.7 Hz, 1H, 4''-H), 7.74 (d, J = 1.7 Hz, 2H, 2''-H, 6''-H), 7.23 (td, J = 9.3, 2.0 Hz, 1H, 5'-H). **^{13}C NMR (101 MHz, $(CD_3)_2SO$)** δ/ppm = 182.7 (C-3), 166.3 (C-1), 152.1 (d, J_{CF} = 242.4 Hz, C-2'), 147.7 (d, J_{CF} = 242.4 Hz, C-4'), 145.4 (C-1''), 133.7 (C-4''), 129.2 (C-2'', C-6''), 126.3 (dd, J_{CF} = 10.3, 3.2 Hz, C-1'), 123.2 (C-2), 121.8 (C-3'', C-5''), 119.1 (dd, J_{CF} = 7.5, 2.9 Hz, C-6'), 111.5 (dd, J_{CF} = 20.7, 3.6 Hz, C-5'), 108.3–107.7 (m, C-3'), 77.3 (CN). IR (ATR) $\tilde{V}_{max}$/cm^{-1}=3297, 2205, 1586, 1531, 1496, 1022, 803, 750. **HRMS (ESI):** calcd. for $C_{16}H_6{}^{79}Br_2ClF_2N_2O_2$ $(M\text{-}H)^-$ 488.84581; found 488.84607. **Purity (HPLC):**>96% (λ = 210 nm),>96% (λ = 254 nm).

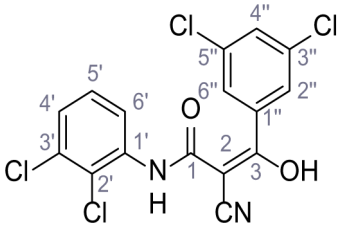

SGA-78

Chemical structure 65. 2-Cyano-*N*-(2,3-dichlorophenyl)−3-(3,5-dichlorophenyl)−3-hydroxyacrylamide – SGA-78.

According to general procedure **B**, amide **18** (229 mg, 1.00 mmol, 1.0 eq.) in dry THF (10 mL), NaH (92.0 mg, 2.30 mmol, 2.3 eq.) and 3,5-dichlorobenzoyl chloride (230 mg, 1.10 mmol, 1.1 eq.) were used to give **SGA-78** as colorless crystals (344 mg, 0.856 mmol, 86%). $\mathbf{R_f}$ = 0.17 (3:2 hexanes/acetone). **m.p.:** 211˚C. **^{1}H NMR (400 MHz, $(CD_3)_2SO$)** δ/ppm = 12.49 (s, 1H, NH), 8.58 (dd, *J* = 8.3, 1.5 Hz, 1H, 6'-H), 7.63 (t, *J* = 1.9 Hz, 1H, 4''-H), 7.59 (d, *J* = 1.9 Hz, 2H, 2''-H, 6''-H), 7.27 (t, *J* = 8.2 Hz, 1H, 5'-H), 7.20 (dd, *J* = 8.0, 1.5 Hz, 1H, 4'-H). **^{13}C NMR (126 MHz, $(CD_3)_2SO$)** δ/ppm = 182.8 (C-3), 166.4 (C-1), 145.1 (C-1''), 139.3 (C-1'), 133.4 (C-3'', C-5''), 131.4 (C-3'), 128.5 (C-4''), 128.0 (C-5'), 126.1 (C-2'', C-6''), 123.4 (C-2), 122.6 (C-4'), 119.3 (C-2'), 119.1 (C-6'), 77.5 (CN). IR (ATR) $\tilde{V}_{max}$/cm^{-1}=3355, 2203, 1649, 1584, 1539, 1453, 1415, 872, 812, 777. **HRMS (ESI):** calcd. for $C_{16}H_7{}^{35}Cl_4N_2O_2$ $(M\text{-}H)^-$ 398.92671; found 398.92789. **Purity (HPLC):**>96% (λ = 210 nm),>96% (λ = 254 nm).

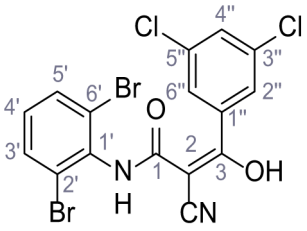

SGA-77

Chemical structure 66. 2-Cyano-*N*-(2,6-dibromophenyl)−3-(3,5-dichlorophenyl)−3-hydroxyacrylamide – SGA-77.

According to general procedure **B**, amide **19** (318 mg, 1.00 mmol, 1.0 eq.) in dry THF (10 mL), NaH (92.0 mg, 2.30 mmol, 2.3 eq.) and 3,5-dichlorobenzoyl chloride (230 mg, 1.10 mmol, 1.1 eq.) were used to give **SGA-77** as colorless crystals (66.0 mg, 0.134 mmol, 13%). $\mathbf{R_f}$ = 0.78 (3:2 hexanes/acetone). **m.p.:** 226˚C. **^{1}H NMR (400 MHz, $(CD_3)_2SO$)** δ/ppm = 10.64 (s, 1H, NH), 8.09–7.90 (m, 3H, 2''-H, 6''-H, 4''-H), 7.79 (d, *J* = 8.0 Hz, 2H, 3'-H, 5'-H), 7.26 (t, *J* = 8.0 Hz, 1H, 4'-H). **^{13}C NMR (101 MHz, $(CD_3)_2SO$)** δ/ppm = 162.4 (C-1, C-3), 136.6 (C-1''), 135.2 (C-1'), 134.6 (C-3'', C-5''), 132.3 (C-3', C-5'), 131.5 (C-4''), 130.7 (C-4'), 126.4 (C-2'', C-6''), 124.4 (C-2', C-6'), 76.4 (CN), C-2 is missing. IR (ATR) $\tilde{V}_{max}$/cm^{-1}=3206, 2215, 1650.1567, 1516, 1283, 779, 750, 723. **HRMS (ESI):** calcd. for $C_{16}H_7{}^{79}Br_2{}^{35}Cl_2N_2O_2$ $(M\text{-}H)^-$ 486.82568; found 486.82870. **Purity (HPLC):**>96% (λ = 210 nm),>96% (λ = 254 nm).

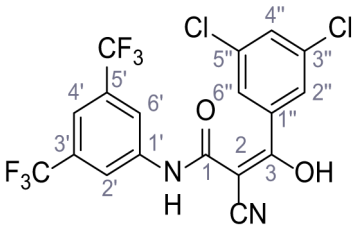

SGA-85

Chemical structure 67. N-(3,5-Bis(trifluoromethyl)phenyl)−2-cyano-3-(3,5-dichlorophenyl)−3-hydroxyacrylamide –

SGA-85.

According to general procedure **B**, amide **20** (296 mg, 1.00 mmol, 1.0 eq.) in dry THF (10 mL), NaH (92.0 mg, 2.30 mmol, 2.3 eq.) and 3,5-dichlorobenzoyl chloride (230 mg, 1.10 mmol, 1.1 eq.) were used to give **SGA-85** as colorless solid (320 mg, 0.682 mmol, 68%). $\mathbf{R_f}$ = 0.15 (3:2 hexanes/acetone). **m.p.:** 210˚C. **^{1}H NMR (400 MHz, $(CD_3)_2SO$)** δ/ppm = 12.58 (s, 1H, NH), 8.93 (s, 1H, OH), 8.25 (s, 2H, 2'-H, 6'-H), 7.65 (t, J = 1.9 Hz, 1H, 4''-H), 7.62–7.56 (m, 3H, 4'-H, 2''-H, 6''-H). **^{13}C NMR (101 MHz, $(CD_3)_2SO$)** δ/ppm = 183.5 (C-3), 167.3 (C-1), 145.4 (C-1''), 142.3 (C-1'), 134.0 (C-3'', C-5''), 131.2 (q, J_{CF} = 32.6 Hz, C-3', C-5'), 129.1 (C-4''), 126.5 (C-2'', C-6''), 123.7 (q, J_{CF} = 270.8 Hz, CF_3), 123.4 (C-2), 119.1–118.8 (m, C-2', C-6'), 114.8–114.5 (m, C-4'), 77.6 (CN). IR (ATR) $\tilde{V}_{max}$/cm^{-1}=2230, 1637, 1571, 1547, 1375, 1275, 1175, 1128, 810. **HRMS (ESI):** calcd. for $C_{18}H_7{}^{35}Cl_2F_6N_2O_2$ $(M\text{-}H)^-$ 466.97943; found 466.97933. **Purity (HPLC):**>96% (λ = 210 nm),>96% (λ = 254 nm).

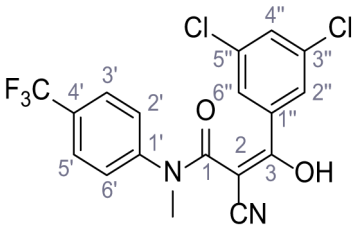

SGA-115

Chemical structure 68. 2-Cyano-3-(3,5-dichlorophenyl)−3-hydroxy-*N*-methyl-*N*-(4-(trifluoromethyl)phenyl)-acrylamide – SGA-115.

According to general procedure **B**, amide **21** (242 mg, 1.00 mmol, 1.0 eq.) in dry THF (10 mL), NaH (92.0 mg, 2.30 mmol, 2.3 eq.) and 3,5-dichlorobenzoyl chloride (230 mg, 1.10 mmol, 1.1 eq.) were used to give **SGA-115** as colorless solid (198 mg, 0.476 mmol, 48%). $\mathbf{R_f}$ = 0.67 (3:2 hexanes/acetone). **m.p.:** 147˚C. **^{1}H NMR (400 MHz, $CDCl_3$)** δ/ppm = 7.80–7.73 (m, 2H, 3'-H, 5'-H), 7.64 (d, J = 1.9 Hz, 2H, 2''-H, 6''-H), 7.49 (t, J = 1.9 Hz, 1H, 4''-H), 7.47–7.41 (m, 2H, 2'-H, 6'-H), 3.48 (s, 3H, CH_3). **^{13}C NMR (101 MHz, $CDCl_3$)** δ/ppm = 184.2 (C-3), 170.4 (C-1), 145.2 (C-1'), 135.8 (C-1''), 135.5 (C-3'', C-5''), 132.5 (C-4''), 131.4 (q, J_{CF} = 32.9 Hz, C-4'), 127.8 (C-2', C-6'), 127.5 (q, J = 3.6 Hz, C-3', C-5'), 127.2 (C-2'', C-6''), 123.7 (q, J_{CF} = 272.6 Hz, CF_3), 115.3 (C-2), 78.6 (CN), 39.9 (CH_3). IR (ATR) $\tilde{V}_{max}$/cm^{-1}=3074, 2214, 1578, 1540, 1396, 1331, 1165, 1118, 807. **HRMS (ESI):** calcd. for $C_{18}H_{10}{}^{35}Cl_2F_3N_2O_2$ $(M\text{-}H)^-$ 413.00769; found 413.00806. **Purity (HPLC):**>96% (λ = 210 nm),>96% (λ = 254 nm).

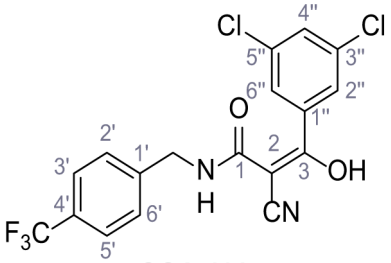

SGA-138

Chemical structure 69. 2-Cyano-3-(3,5-dichlorophenyl)−3-hydroxy-*N*-(4-(trifluoromethyl)benzyl)acrylamide – SGA-138.

According to general procedure **B**, amide **22** (242 mg, 1.00 mmol, 1.0 eq.) in dry THF (10 mL), NaH (92.0 mg, 2.30 mmol, 2.3 eq.) and 3,5-dichlorobenzoyl chloride (230 mg, 1.10 mmol, 1.1 eq.) were used to give **SGA-138** as colorless solid (228 mg, 0.549 mmol, 55%). $\mathbf{R_f}$ = 0.70 (3:2 hexanes/acetone). **m.p.:** 173˚C. **^{1}H NMR (500 MHz, $(CD_3)_2SO$)** δ/ppm = 9.57 (s, 1H, NH), 7.84 (t, J = 1.8 Hz, 1H, 4''-H), 7.77 (d, J = 1.8 Hz, 2H, 2''-H, 6''-H), 7.74–7.69 (m, 2H, 3'-H, 5'-H), 7.57–7.50 (m, 2H, 2'-H, 6'-H), 4.52 (s, 2H, CH_2). **^{13}C NMR (126 MHz, $(CD_3)_2SO$)** δ/ppm = 181.1 (C-3), 169.2 (C-1), 143.5 (C-

1'), 138.5 (C-1''), 134.2 (C-3'', C-5''), 130.8 (C-4''), 128.1 (C-2', C-6'), 127.7 (q, J_{CF} = 31.7 Hz, C-4'), 126.6 (C-2'', C-6''), 125.3 (q, J_{CF} = 3.8 Hz, C-3', C-5'), 124.3 (q, J_{CF} = 271.9 Hz, CF_3), 118.1 (C-2), 78.0 (CN), 42.4 (CH_2). IR (ATR) $\tilde{V}_{max}/cm^{-1}$=3326, 2206, 1538, 1324, 1108, 1067, 805. **HRMS (ESI):** calcd. for $C_{18}H_{10}{}^{35}Cl_2F_3N_2O_2$ $(M\text{-}H)^-$ 413.00769; found 413.00780. **Purity (HPLC):**>96% (λ = 210 nm), >96% (λ = 254 nm).

Synthesis of TPC2-A1-P and analogs

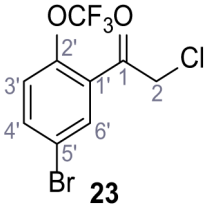

23

Chemical structure 70. 1-(5-Bromo-2-(trifluoromethoxy)phenyl)−2-chloroethan-1-one (23).

4-Bromo-2-iodo-1-(trifluoromethoxy)benzene (610 mg, 1.66 mmol, 1.0 eq.) was dissolved in dry THF (8.0 mL) and cooled to −78˚C, then *n*-BuLi (0.670 mL, 1.66 mmol, 1.0 eq.) was added dropwise. The mixture was stirred for 20 min at −78˚C and a solution of 2-chloro-*N*-methoxy-*N*-methylacetamide (700 mg, 4.99 mmol, 3.0 eq.) in dry THF (8.0 mL) was added slowly. The mixture was stirred for 1 hr at −78˚C and then poured on sat. aq. NH_4Cl solution. The mixture was extracted with pentane, the organic layer was washed with sat. aq. NaCl solution, dried using hydrophobic phase separation filter papers and filtered through a short silica column (eluent: pentane). The product was carefully concentrated under ambient pressure to yield a colorless oil (**23**, 221 mg, 0.696 mmol, 42%). R_f = 0.65 (9:1 hexanes/EtOAc). **^{1}H NMR (500 MHz, $CDCl_3$)** δ/ppm = 7.93 (d, *J* = 2.5 Hz, 1H, 6'-H), 7.71 (dd, *J* = 8.8, 2.5 Hz, 1H, 4'-H), 7.25–7.22 (m, 1H, 3'-H), 4.61 (s, 2H, 2 hr). **^{13}C NMR (126 MHz, $CDCl_3$)** δ/ppm = 190.5 (C-1), 146.2 (C-2'), 137.1 (C-4'), 134.1 (C-6'), 130.8 (C-5'), 122.2 (C-3'), 120.8 (C-1'), 120.3 (q, J_{CF} = 261 Hz, OCF_3), 49.0 (C-2). IR (ATR) $\tilde{V}_{max}/cm^{-1}$=1703, 1592, 1480, 1398, 1308, 1252, 1174, 1129, 1088, 822, 664. **HRMS (EI):** calcd. for $C_9H_5{}^{79}Br^{35}ClF_3O_2$ $(M)^+$ 315.9108; found 315.9106. **Purity (HPLC):**>96% (λ = 210 nm),>96% (λ = 254 nm).

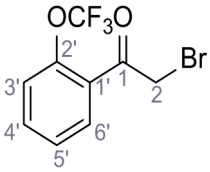

24

Chemical structure 71. 2-Bromo-1-(2-(trifluoromethoxy)phenyl)ethan-1-one (24).

2'-(Trifluoromethoxy)acetophenone (779 µL, 4.90 mmol, 1.0 eq.) was dissolved in CH_2Cl_2 (10 mL), then *p*-toluenesulfonic acid (86.1 mg, 0.490 mmol, 0.10 eq.) and *N*-bromosuccinimide (872 mg, 4.90 mmol, 1.0 eq.) were added. The mixture was stirred for 24 hr at rt, then sat. aq. NaCl (10 mL) was added. The aqueous phase was extracted with CH_2Cl_2 (3 × 10 mL), dried using a hydrophobic filter paper and concentrated *in vacuo*. Purification by FCC (pentane/EtOAc 9:1) yielded bromoketone **24** (672 mg, 2.87 mmol, 49%) as light brown liquid. Analytical data are in accordance with literature (***Saruta et al., 2015***). R_f = 0.58 (9:1 hexanes/EtOAc). **^{1}H NMR (400 MHz, $CDCl_3$)** δ/ppm = 7.81 (dd, *J* = 7.8, 1.8 Hz, 1H, 6'-H), 7.60 (ddd, *J* = 8.3, 7.6, 1.8 Hz, 1H, 4'-H), 7.41 (td, *J* = 7.6, 1.0 Hz, 1H, 5'-H), 7.37–7.32 (m, 1H, 3'-H), 4.47 (s, 2H, 2 hr). **^{13}C NMR (101 MHz, $CDCl_3$)** δ/ppm = 191.5 (C-1), 147.1 (q, *J* = 1.7 Hz, C-2'), 134.3 (C-4'), 131.6 (C-6'), 129.3 (C-1'), 127.3 (C-5'), 120.6 (C-3'), 120.5 (q, *J* = 260.1 Hz, OCF_3), 35.1 (C-2). IR (ATR) $\tilde{V}_{max}/cm^{-1}$=1698, 1603, 1450, 1295, 1248, 1200, 1160. **HRMS (EI):** calcd. for $C_9H_6{}^{79}BrF_3O_2$ $(M)^+$ 281.9498; found 281.9494. **Purity (HPLC):**>96% (λ = 210 nm),>96% (λ = 254 nm).

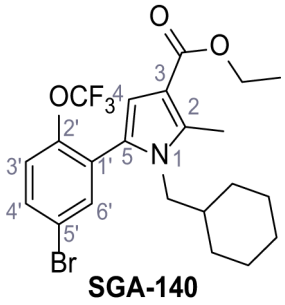

SGA-140

Chemical structure 72. Ethyl 5-(5-bromo-2-(trifluoromethoxy)phenyl)−1-(cyclohexylmethyl)−2-methyl-1*H*-pyrrole-3-carboxylate. – SGA-140.

Following general procedure **C**, ethyl acetoacetate (88.0 µL, 0.693 mmol, 1.1 eq.) in dry THF (3.0 mL), NaH (37.8 mg, 0.945 mmol, 1.5 eq.) and a solution of ketone **23** (200 mg, 0.630 mmol, 1.0 eq.) and KI (209 mg, 1.26 mmol, 2.0 eq.) in dry THF (3.0 mL) were used. Then the residue was dissolved in acetic acid (6.0 mL) and cyclohexanemethanamine (0.160 mL, 1.26 mmol, 2.0 eq.) was added. FCC (hexanes/EtOAc 99:1) yielded **SGA-140** as colorless oil (140 mg, 0.287 mmol, 46%). $\mathbf{R_f}$ = 0.30 (9:1 hexanes/EtOAc). **^{1}H NMR (400 MHz, $CDCl_3$)** δ/ppm = 7.54–7.50 (m, 2H, 4'-H, 6'-H), 7.20 (ddt, *J* = 7.6, 3.0, 1.5 Hz, 1H, 3'-H), 6.55 (s, 1H, 4 hr), 4.27 (q, *J* = 7.1 Hz, 2H, $C\underline{H}_2CH_3$), 3.59 (d, *J* = 7.1 Hz, 2H, $C\underline{H}_2$-cy), 2.59 (s, 3H, CH_3), 1.60–1.54 (m, 3H, cy), 1.38–1.32 (m, 6H, $CH_2C\underline{H}_3$, cy), 1.07–0.99 (m, 3H, cy), 0.68–0.59 (m, 2H, cy). **^{13}C NMR (121 MHz, $CDCl_3$)** δ/ppm = 165.6 (<u>C</u>OOEt), 146.3 (C-2'), 137.6 (C-3), 135.7 (C-6'), 132.4 (C-4'), 129.0 (C-5'), 126.5 (C-5), 122.1 (C-3'), 120.3 (q, J_{CF} = 260.2 Hz, OCF_3), 119.9 (C-1'), 112.6 (C-2), 112.2 (C-4), 59.6 ($\underline{C}H_2CH_3$), 50.8 ($\underline{C}H_2$-cy), 39.0 (cy), 30.6 (cy), 26.2 (cy), 25.7 (cy), 14.7 ($CH_2\underline{C}H_3$), 12.1 (CH_3). IR (ATR) $\tilde{\nu}_{max}$/cm^{-1}=2976, 2925, 2854, 1699, 1254, 1240, 1206, 1190, 1169, 1080, 1064, 774. **HRMS (ESI):** calcd. for $C_{22}H_{26}{}^{79}BrF_3NO_3$ $(M+H)^+$ 488.10427; found 488.10459. **Purity (HPLC):**>96% (λ = 210 nm),>96% (λ = 254 nm).

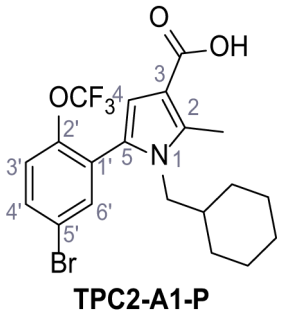

TPC2-A1-P

Chemical structure 73. 5-(5-Bromo-2-(trifluoromethoxy)phenyl)−1-(cyclohexylmethyl)−2-methyl-1*H*-pyrrole-3-carboxylic acid – TPC2-A1-P.

According to general procedure **D**, LiOH (51.6 mg, 2.05 mmol, 10 eq.) and a solution of **SGA-140** (100 mg, 0.205 mmol, 1.0 eq.) in dioxane/H_2O (3.0 mL) were used. After 2 hr the reaction was completed and recrystallization from EtOH gave **TPC2-A1-P** as a colorless solid (51.2 mg, 0.111 mmol, 54%). $\mathbf{R_f}$ = 0.14 (9:1 hexanes/EtOAc). **m.p.:** 202˚C. **^{1}H NMR (500 MHz, $CDCl_3$)** δ/ppm = 11.34 (s, 1H, COOH), 7.56–7.51 (m, 2H, 3'-H, 4'-H), 7.23–7.19 (m, 1H, 6'-H), 6.61 (s, 1H, 4 hr), 3.60 (d, *J* = 7.1 Hz, 2H, $C\underline{H}_2$-cy), 2.60 (s, 3H, CH_3), 1.62–1.56 (m, 3H, cy), 1.40–1.33 (m, 3H, cy), 1.09–1.01 (m, 3H, cy), 0.68–0.61 (m, 2H, cy). **^{13}C NMR (126 MHz, $CDCl_3$)** δ/ppm = 170.0 (COOH), 146.4 (C-2'), 138.8 (C-2), 135.7 (C-6'), 132.6 (C-4'), 128.8 (C-5'), 126.8 (C-5), 122.2 (C-3'), 120.3 (q, J_{CF} = 259.3 Hz, OCF_3), 119.9 (C-1'), 112.9 (C-4), 111.6 (C-3), 50.9 ($\underline{C}H_2$-cy), 39.0 (cy), 30.6 (cy), 26.2 (cy), 25.7 (cy), 12.3 (CH_3). IR (ATR) $\tilde{\nu}_{max}$/cm^{-1}=2961, 2924, 2875, 2853, 2359, 2342, 1667, 1266, 1243, 1212, 1198, 1171, 925, 779, 658. **HRMS (ESI):** calcd. for $C_{20}H_{20}{}^{79}BrF_3NO_3$ $(M-H)^-$ 458.05841; found 458.05889. **Purity (HPLC):**>96% (λ = 210 nm),>96% (λ = 254 nm).

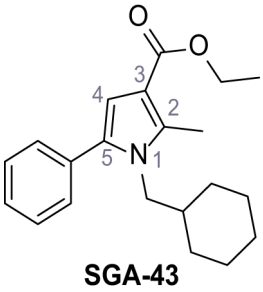

SGA-43

Chemical structure 74. Ethyl 1-(cyclohexylmethyl)−2-methyl-5-phenyl-1*H*-pyrrole-3-carboxylate – SGA-43.

Following general procedure **C**, ethyl acetoacetate (42.0 µL, 3.30 mmol, 1.1 eq.) in dry THF (12 mL), NaH (180 mg, 4.50 mmol, 1.5 eq.) and a solution of 2-bromo-1-phenylethan-1-one (405 µL, 3.00 mmol, 1.0 eq.) and KI (996 mg, 6.00 mmol, 2.0 eq.) in dry THF (10 mL) were used. Then the residue was dissolved in acetic acid (10 mL) and cyclohexanemethanamine (781 µL, 6.00 mmol, 2.0 eq.) was added. FCC (hexanes/EtOAc 9:1) yielded **SGA-43** as colorless solid (516 mg, 1.58 mmol, 53%). The compound is literature known, but no analytical data are available (***Kang et al., 2010***). $\mathbf{R_f}$ = 0.49 (9:1 hexanes/EtOAc). **m.p.:** 91˚C. **^{1}H NMR (400 MHz, $CDCl_3$)** δ/ppm = 7.42–7.36 (m, 2H, Ph), 7.35–7.29 (m, 3H, Ph), 6.53 (s, 1H, 4 hr), 4.27 (q, *J* = 7.1 Hz, 2H, $C\underline{H}_2CH_3$), 3.78 (d, *J* = 7.1 Hz, 2H, $C\underline{H}_2$-cy), 2.60 (s, 3H, CH_3), 1.58–1.49 (m, 3H, cy), 1.41–1.31 (m, 6H, cy, $CH_2C\underline{H}_3$), 1.06–0.95 (m, 3H, cy), 0.69–0.57 (m, 2H, cy). **^{13}C NMR (121 MHz, $CDCl_3$)** δ/ppm = 165.9 ($\underline{C}$OOEt), 137.0 (C-2), 134.1 (qPh), 133.7 (C-5), 129.6 (Ph), 128.5 (Ph), 127.4 (Ph), 112.0 (C-3), 110.0 (C-4), 59.4 ($\underline{C}H_2CH_3$), 50.2 ($\underline{C}H_2$-cy), 39.0 (cy), 30.6 (cy), 26.2 (cy), 25.8 (cy), 14.7 ($CH_2\underline{C}H_3$), 12.1 (CH_3). IR (ATR) $\tilde{V}_{max}/cm^{-1}$=2975, 2926, 2850, 1738, 1698, 1420, 1242, 1224, 1191, 1062, 772, 702. **HRMS (ESI):** calcd. for $C_{21}H_{28}NO_2$ $(M+H)^+$ 326.21146; found 326.21121. **Purity (HPLC):**>96% (λ = 210 nm),>96% (λ = 254 nm).

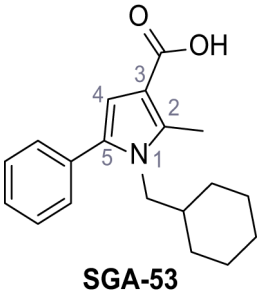

SGA-53

Chemical structure 75. 1-(Cyclohexylmethyl)−2-methyl-5-phenyl-1*H*-pyrrole-3-carboxylic acid – SGA-53.

According to general procedure **D**, LiOH (38.7 mg, 1.54 mmol, 10 eq.) and a solution of **SGA-43** (50.0 mg, 0.154 mmol, 1.0 eq.) in dioxane/H_2O (1.3 mL) were used. After 1 hr the reaction was completed and gave **SGA-53** as a colorless solid (40.4 mg, 0.136 mmol, 88%). The compound is literature known, but no analytical data are available (***Kang et al., 2010***). $\mathbf{R_f}$ = 0.18 (6:1 hexanes/EtOAc). **m.p.:** 196˚C. **^{1}H NMR (500 MHz, $CDCl_3$)** δ/ppm = 7.42–7.38 (m, 2H, Ph), 7.36–7.32 (m, 3H, Ph), 6.59 (s, 1H, 4 hr), 3.80 (d, *J* = 7.2 Hz, 2H, CH_2), 2.62 (s, 3H, CH_3), 1.59–1.52 (m, 3H, cy), 1.42–1.33 (m, 3H, cy), 1.06–0.97 (m, 3H, cy), 0.68–0.59 (m, 2H, cy). **^{13}C NMR (101 MHz, $CDCl_3$)** δ/ppm = 170.8 (COOH), 138.3 (C-2), 134.5 (C-5), 133.5 (qPh), 129.7 (Ph), 128.5 (Ph), 127.5 (Ph), 111.2 (C-3), 110.7 (C-4), 50.3 (CH_2), 39.0 (cy), 30.6 (cy), 26.2 (cy), 25.8 (cy), 12.3 (CH_3). IR (ATR) $\tilde{V}_{max}/cm^{-1}$=3030, 2971, 2921, 2848, 1738, 1660, 1533, 1435, 1364, 1267, 1227, 1205, 778, 768, 712, 703. **HRMS (ESI):** calcd. for $C_{19}H_{22}NO_2$ $(M-H)^-$ 296.16572; found 296.16560. **Purity (HPLC):**>96% (λ = 210 nm),>96% (λ = 254 nm).

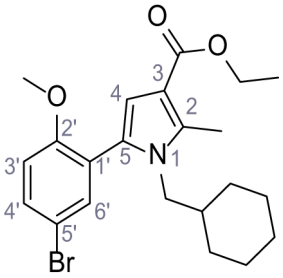

SGA-54

Chemical structure 76. Ethyl 5-(5-bromo-2-methoxyphenyl)−1-(cyclohexylmethyl)−2-methyl-1*H*-pyrrole-3-carboxylate – SGA-54.

Following general procedure **C**, ethyl acetoacetate (143 µL, 1.10 mmol, 1.1 eq.) in dry THF (5.0 mL), NaH (60.0 mg, 1.50 mmol, 1.5 eq.) and a solution of 2-bromo-1-(5-bromo-2-methoxyphenyl) ethan-1-one (308 mg, 1.00 mmol, 1.0 eq.) in dry THF (1.0 mL) were used. Then the residue was dissolved in acetic acid (5.0 mL) and cyclohexanemethanamine (0.260 mL, 2.00 mmol, 2.0 eq.) was added. FCC (hexanes/EtOAc 9:1) yielded **SGA-54** as colorless solid (411 mg, 0.947 mmol, 95%). $\mathbf{R_f}$ = 0.37 (6:1 hexanes/EtOAc). **m.p.:** 83˚C. **^{1}H NMR (400 MHz, $CDCl_3$)** δ/ppm = 7.45 (dd, *J* = 8.7, 2.5 Hz, 1H, 4'-H), 7.37 (d, *J* = 2.5 Hz, 1H, 6'-H), 6.81 (d, *J* = 8.7 Hz, 1H, 3'-H), 6.48 (s, 1H, 4 hr), 4.25 (q, *J* = 7.1 Hz, 2H, $C\underline{H}_2CH_3$), 3.76 (s, 3H, OCH_3), 3.56 (d, *J* = 7.2 Hz, 2H, $C\underline{H}_2$-cy), 2.58 (s, 3H, CH_3), 1.60–1.54 (m, 3H, cy), 1.41–1.29 (m, 6H, cy, $CH_2C\underline{H}_3$), 1.08–0.97 (m, 3H, cy), 0.68–0.57 (m, 2H, cy). **^{13}C NMR (101 MHz, $CDCl_3$)** δ/ppm = 165.7 (COOEt), 156.6 (C-2'), 136.9 (C-2), 135.2 (C-6'), 132.3 (C-4'), 128.9 (C-5), 124.8 (C-1'), 112.8 (C-5'), 112.6 (C-3'), 112.1 (C-3), 110.6 (C-4), 59.3 ($\underline{C}H_2CH_3$), 55.9 (OCH_3), 50.9 (CH_2-cy), 39.0 (cy), 30.7 (cy), 26.3 (cy), 25.8 (cy), 14.7 ($CH_2\underline{C}H_3$), 12.1 (CH_3). IR (ATR) $\tilde{V}_{max}/cm^{-1}$=2979, 2928, 2849, 1695, 1676, 1473, 1461, 1434, 1253, 1234, 1187, 1176, 1060, 1048, 1027, 774, 619. **HRMS (ESI):** calculated for $C_{22}H_{29}{}^{79}BrNO_3$ $(M+H)^+$ 434.13253; found 434.13229. **Purity (HPLC):**>96% (λ = 210 nm),>96% (λ = 254 nm).

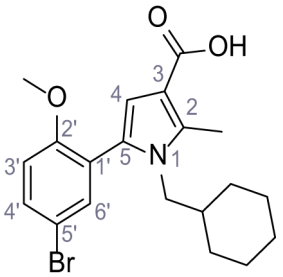

SGA-55

Chemical structure 77. 5-(5-Bromo-2-methoxyphenyl)−1-(cyclohexylmethyl)−2-methyl-1*H*-pyrrole-3-carboxylic acid – SGA-55.

According to general procedure **D**, LiOH (88.4 mg, 3.51 mmol, 10 eq.) and a solution of **SGA-54** (152 mg, 0.351 mmol, 1.0 eq.) in dioxane/H_2O (1.3 mL) were used. After 1 hr the reaction was completed and gave **SGA-55** as a colorless solid (90.0 mg, 0.222 mmol, 63%). $\mathbf{R_f}$ = 0.72 (1:1 hexanes/EtOAc). **m.p.:** 224˚C. **^{1}H NMR (400 MHz, $CDCl_3$)** δ/ppm = 7.46 (dd, *J* = 8.8, 2.5 Hz, 1H, 4'-H), 7.38 (d, *J* = 2.5 Hz, 1H, 6'-H), 6.82 (d, *J* = 8.8 Hz, 1H, 3'-H), 6.54 (s, 1H, 4 hr), 3.77 (s, 3H, OCH_3), 3.57 (d, *J* = 7.2 Hz, 2H, CH_2-cy), 2.59 (s, 3H, CH_3), 1.62–1.52 (m, 3H, cy), 1.43–1.33 (m, 3H, cy), 1.10–0.98 (m, 3H, cy), 0.69–0.58 (m, 2H, cy). **^{13}C NMR (101 MHz, $CDCl_3$)** δ/ppm = 170.4 (COOH), 156.6 (C-2'), 138.2 (C-2), 135.2 (C-6'), 132.4 (C-4'), 129.3 (C-5), 124.6 (C-1'), 112.8 (C-5'), 112.6 (C-3'), 111.4 (C-4), 111.3 (C-3), 55.9 (OCH_3), 51.0 (CH_2-cy), 39.0 (cy), 30.7 (cy), 26.3 (cy), 25.8 (cy), 12.3 (CH_3). IR (ATR) $\tilde{V}_{max}/cm^{-1}$=3027, 2969, 2926, 2850, 1739, 1658, 1476, 1462, 1442, 1362, 1274, 1244, 1205, 1018, 808, 782, 619. **HRMS (ESI):** calculated for $C_{20}H_{23}{}^{79}BrNO_3$ $(M-H)^-$ 404.08668; found 404.08697. **Purity (HPLC):**>96% (λ = 210 nm),>96% (λ = 254 nm).

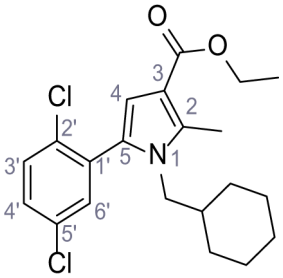

SGA-48

Chemical structure 78. Ethyl 1-(cyclohexylmethyl)−5-(2,5-dichlorophenyl)−2-methyl-1*H*-pyrrole-3-carboxylate – SGA-48.

Following general procedure **C**, ethyl acetoacetate (208 µL, 1.65 mmol, 1.1 eq.) in dry THF (5.0 mL), NaH (90.0 mg, 2.25 mmol, 1.5 eq.) and a solution of 2-bromo-1-(2,5-dichlorophenyl)ethan-1-one (402 mg, 1.50 mmol, 1.0 eq.) in dry THF (1.0 mL) were used. Then the residue was dissolved in acetic acid (5.0 mL) and cyclohexanemethanamine (390 µL, 3.00 mmol, 2.0 eq.) was added. FCC (hexanes/EtOAc 9:1), followed by recrystallization from EtOH yielded **SGA-48** as colorless solid (271 mg, 0.686 mmol, 46%). **R_f** = 0.48 (9:1 hexanes/EtOAc). **m.p.:** 98˚C. **^{1}H NMR (400 MHz, $CDCl_3$)** δ/ppm = 7.48 (d, *J* = 2.0 Hz, 1H, 6'-H), 7.29 (dd, *J* = 8.2, 2.0 Hz, 1H, 4'-H), 7.25 (d, *J* = 9.1 Hz, 1H, 3'-H, collapses with chloroform), 6.51 (s, 1H, 4 hr), 4.27 (q, *J* = 7.0 Hz, 2H, $C\underline{H}_2CH_3$), 3.55 (d, *J* = 7.0 Hz, 2H, CH_2-cy), 2.59 (s, 3H, CH_3), 1.61–1.56 (m, 3H, cy), 1.40–1.31 (m, 6H, cy, $CH_2C\underline{H}_3$), 1.08–0.99 (m, 3H, cy), 0.68–0.58 (m, 2H, cy). **^{13}C NMR (101 MHz, $CDCl_3$)** δ/ppm = 165.6 (COOEt), 137.0 (C-2), 135.9 (C-1' or C-5'), 134.8 (C-1' or C-5'), 134.0 (C-3'), 131.2 (C-2'), 129.6 (C-6'), 129.2 (C-5), 127.2 (C-4'), 112.2 (C-3), 111.1 (C-4), 59.5 ($\underline{C}H_2CH_3$), 50.8 (CH_2-cy), 39.1 (cy), 30.6 (cy), 26.2 (cy), 25.8 (cy), 14.7 ($CH_2\underline{C}H_3$), 12.1 (CH_3). IR (ATR) $\tilde{V}_{max}$/cm^{-1}=2981, 2923, 2845, 1739, 1723, 1695, 1565, 1454, 1262, 1238, 1201, 1159, 1076, 1066, 800, 771. **HRMS (ESI):** calculated for $C_{21}H_{26}{}^{35}Cl_2NO_2$ $(M+H)^+$ 394.13351; found 394.13343. **Purity (HPLC):**>96% (λ = 210 nm),>96% (λ = 254 nm).

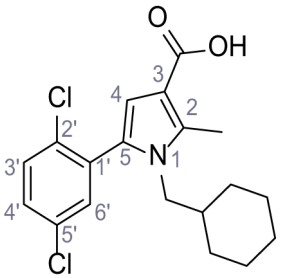

SGA-52

Chemical structure 79. 1-(Cyclohexylmethyl)−5-(2,5-dichlorophenyl)−2-methyl-1*H*-pyrrole-3-carboxylic acid – SGA-52.

According to general procedure **D**, LiOH (63.9 mg, 2.54 mmol, 10 eq.) and a solution of **SGA-48** (100 mg, 0.254 mmol, 1.0 eq.) in dioxane/H_2O (1.3 mL) were used. After 1 hr the reaction was completed and gave **SGA-52** as a colorless solid (75.7 mg, 0.207 mmol, 81%). **R_f** = 0.18 (6:1 hexanes/EtOAc). **m.p.:** 180˚C. **^{1}H NMR (500 MHz, $CDCl_3$)** δ/ppm = 7.48 (d, *J* = 2.0 Hz, 1H, 6'-H), 7.30 (dd, *J* = 8.2, 2.0 Hz, 1H, 4'-H), 7.26 (d, *J* = 8.2 Hz, 1H, 3'-H, collapses with chloroform), 6.57 (s, 1H, 4 hr), 3.57 (d, *J* = 6.4 Hz, 2H, $C\underline{H}_2$-cy), 2.60 (s, 3H, CH_3), 1.63–1.57 (m, 3H, cy), 1.42–1.36 (m, 3H, cy), 1.08–1.00 (m, 3H, cy), 0.68–0.59 (m, 2H, cy). **^{13}C NMR (126 MHz, $CDCl_3$)** δ/ppm = 170.7 (COOH), 138.3 (C-2), 136.0 (C-1' or C-5'), 135.0 (C-1' or C-5'), 134.0 (C-3'), 131.0 (C-2'), 129.7 (C-6'), 129.6 (C-5), 127.2 (C-4'), 111.8 (C-4), 111.4 (C-3), 50.9 ($\underline{C}H_2$-cy), 39.0 (cy), 30.7 (cy), 26.2 (cy), 25.8 (cy), 12.3 (CH_3). IR (ATR) $\tilde{V}_{max}$/cm^{-1}=3014, 2970, 2926, 2851, 1739, 1659, 1449, 1365, 1270, 1228, 1217, 1204, 814, 776. **HRMS (ESI):** calculated for $C_{19}H_{20}{}^{35}Cl_2NO_2$ $(M-H)^-$ 364.08766; found 364.08783. **Purity (HPLC):**>96% (λ = 210 nm),>96% (λ = 254 nm).

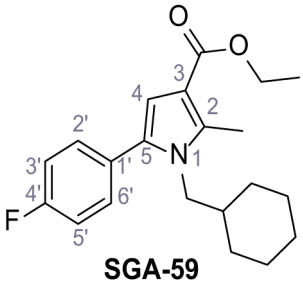

SGA-59

Chemical structure 80. Ethyl 1-(cyclohexylmethyl)−5-(4-fluorophenyl)−2-methyl-1*H*-pyrrole-3-carboxylate – SGA-59.

Following general procedure **C**, ethyl acetoacetate (208 µL, 1.65 mmol, 1.1 eq.) in dry THF (5.0 mL), NaH (90.0 mg, 2.25 mmol, 1.5 eq.) and a solution of 2-chloro-1-(4-fluorophenyl)ethan-1-one (259 mg, 1.50 mmol, 1.0 eq.) and KI (249 mg, 1.50 mmol, 1.0 eq.) in dry THF (3.0 mL) were used. Then the residue was dissolved in acetic acid (5.0 mL) and cyclohexanemethanamine (0.390 mL, 3.00 mmol, 2.0 eq.) was added. FCC (hexanes/EtOAc 9:1) yielded **SGA-59** as yellow oil (499 mg, 1.45 mmol, 97%). $\mathbf{R_f}$ = 0.43 (9:1 hexanes/EtOAc). **^{1}H NMR (500 MHz, $CDCl_3$)** δ/ppm = 7.28–7.23 (m, 2H, 2'-H, 6'-H), 7.10–7.01 (m, 2H, 3'-H, 5'-H), 6.48 (s, 1H, 4 hr), 4.25 (q, J = 7.1 Hz, 2H, $C\underline{H}_2CH_3$), 3.71 (d, J = 7.2 Hz, 2H, $C\underline{H}_2$-cy), 2.57 (s, 3H, CH_3), 1.58–1.48 (m, 3H, cy), 1.38–1.28 (m, 6H, cy, $CH_2C\underline{H}_3$), 1.06–0.89 (m, 3H, cy), 0.68–0.53 (m, 2H, cy). **^{13}C NMR (121 MHz, $CDCl_3$)** δ/ppm = 165.7 (COOH), 162.2 (d, J_{CF} = 247.0 Hz, C-4'), 136.9 (C-2), 132.8 (C-5), 131.3 (d, J_{CF} = 8.0 Hz, C-2', C-6'), 129.7 (d, J_{CF} = 3.3 Hz, C-1'), 115.4 (d, J_{CF} = 21.3 Hz, C-3', C-5'), 111.9 (C-3), 110.0 (C-4), 59.3 ($\underline{C}H_2CH_3$), 50.1 ($\underline{C}H_2$-cy), 39.0 (cy), 30.5 (cy), 26.1 (cy), 25.7 (cy), 14.6 ($CH_2\underline{C}H_3$), 12.0 (CH_3). IR (ATR) $\tilde{V}_{max}$/cm^{-1}=2977, 2925, 2853, 1693, 1242, 1227, 1218, 1195, 1152, 1062, 844, 811, 774. **HRMS (ESI):** calculated for $C_{21}H_{27}FNO_2$ $(M+H)^+$ 344.20203; found 344.20193. **Purity (HPLC):**>96% (λ = 210 nm), >96% (λ = 254 nm).

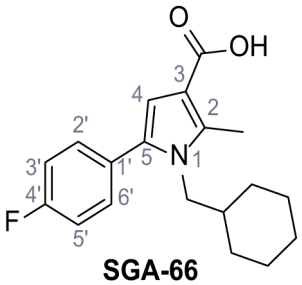

SGA-66

Chemical structure 81. 1-(Cyclohexylmethyl)−5-(4-fluorophenyl)−2-methyl-1*H*-pyrrole-3-carboxylic acid – SGA-66.

According to general procedure **D**, LiOH (169 mg, 6.71 mmol, 10 eq.) and a solution of **SGA-59** (230 mg, 0.671 mmol, 1.0 eq.) in dioxane/H_2O (3.0 mL) were used. After 2 hr the reaction was completed and gave **SGA-66** as a colorless solid (186 mg, 0.590 mmol, 88%). $\mathbf{R_f}$ = 0.24 (6:1 hexanes/EtOAc). **m.p.:** 171˚C. **^{1}H NMR (400 MHz, $CDCl_3$)** δ/ppm = 7.35–7.27 (m, 2H, 2'-H, 6'-H), 7.14–7.04 (m, 2H, 3'-H, 5'-H), 6.57 (s, 1H, 4 hr), 3.75 (d, J = 7.1 Hz, 2H, $C\underline{H}_2$-cy), 2.61 (s, 3H, CH_3), 1.63–1.51 (m, 3H, cy), 1.41–1.32 (m, 3H, cy), 1.08–0.97 (m, 3H, cy), 0.70–0.57 (m, 2H, cy). **^{13}C NMR (121 MHz, $CDCl_3$)** δ/ppm = 171.2 (COOH), 162.37 (d, J_{CF} = 247.1 Hz, C-4'), 138.3 (C-2), 133.3 (C-5), 131.42 (d, J_{CF} = 8.1 Hz, C-2', C-6'), 129.6 (d, J_{CF} = 3.4 Hz, C-1'), 115.57 (d, J_{CF} = 21.5 Hz, C-3', C-5'), 111.2 (C-3), 110.8 (C-4), 50.3 ($\underline{C}H_2$-cy), 39.0 (cy), 30.6 (cy), 26.2 (cy), 25.8 (cy), 12.3 (CH_3). IR (ATR) $\tilde{V}_{max}$/cm^{-1}=2927, 2854, 1739, 1652, 1568, 1494, 1449, 1265, 1223, 1203, 1158, 840, 776, 582. **HRMS (ESI):** calculated for $C_{19}H_{21}FNO_2$ $(M-H)^-$ 314.15618; found 314.15635. **Purity (HPLC):**>96% (λ = 210 nm),>96% (λ = 254 nm).

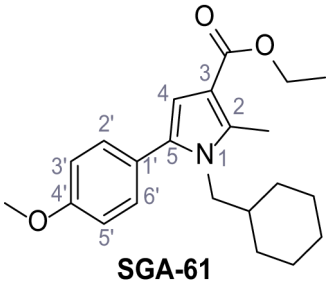

SGA-61

Chemical structure 82. Ethyl 1-(cyclohexylmethyl)−5-(4-methoxyphenyl)−2-methyl-1*H*-pyrrole-3-carboxylate – SGA-61.

Following general procedure **C**, ethyl acetoacetate (208 µL, 1.65 mmol, 1.1 eq.) in dry THF (5.0 mL), NaH (90.0 mg, 2.25 mmol, 1.5 eq.) and a solution of 2-bromo-1-(4-methoxyphenyl)ethan-1-one (344 mg, 1.50 mmol, 1.0 eq.) and KI (249 mg, 1.50 mmol, 1.0 eq.) in dry THF (3.0 mL) were used. Then the residue was dissolved in acetic acid (5.0 mL) and cyclohexanemethanamine (390 µL, 3.00 mmol, 2.0 eq.) was added. FCC (hexanes/EtOAc 9:1), followed by recrystallization from EtOH yielded **SGA-61** as colorless solid (274 mg, 0.770 mmol, 51%). $\mathbf{R_f}$ = 0.37 (9:1 hexanes/EtOAc). **m.p.:** 88˚C. **^{1}H NMR (500 MHz, $CDCl_3$)** δ/ppm = 7.25–7.21 (m, 2H, 2'-H, 6'-H), 6.95–6.89 (m, 2H, 3'-H, 5'-H), 6.47 (s, 1H, 4 hr), 4.27 (q, *J* = 7.1 Hz, 2H, $C\underline{H}_2CH_3$), 3.84 (s, 3H, OCH_3), 3.73 (d, *J* = 7.3 Hz, 2H, $C\underline{H}_2$-cy), 2.58 (s, 3H, CH_3), 1.60–1.51 (m, 3H, cy), 1.42–1.31 (m, 6H, cy, $CH_2C\underline{H}_3$), 1.07–0.96 (m, 3H, cy), 0.70–0.59 (m, 2H, cy). **^{13}C NMR (126 MHz, $CDCl_3$)** δ/ppm = 165.9 (COOH), 159.0 (C-4'), 136.6 (C-2), 133.8 (C-5), 130.9 (C-2', C-6'), 126.1 (C-1'), 113.9 (C-3', C-5'), 111.7 (C-3), 109.5 (C-4), 59.3 ($\underline{C}H_2CH_3$), 55.4 (OCH_3), 50.1 ($\underline{C}H_2$-cy), 39.0 (cy), 30.6 (cy), 26.2 (cy), 25.8 (cy), 14.7 ($CH_2\underline{C}H_3$), 12.1 (CH_3). IR (ATR) $\tilde{V}_{max}/cm^{-1}$=3016, 2970, 2928, 2847, 1739, 1693, 1568, 1532, 1496, 1443, 1424, 1373, 1243, 1226, 1195, 1175, 1064, 1031, 835, 817, 795, 774. **HRMS (ESI):** calculated for $C_{22}H_{30}NO_3$ $(M+H)^+$ 356.22202; found 356.22192. **Purity (HPLC):**>96% (λ = 210 nm),>96% (λ = 254 nm).

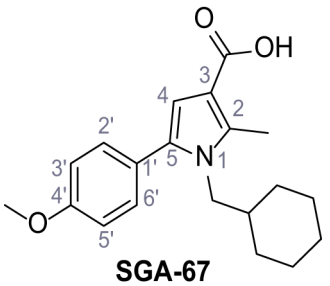

SGA-67

Chemical structure 83. 1-(Cyclohexylmethyl)−5-(4-methoxyphenyl)−2-methyl-1*H*-pyrrole-3-carboxylic acid – SGA-67.

According to general procedure **D**, LiOH (78.7 mg, 3.12 mmol, 10 eq.) and a solution of **SGA-61** (111 mg, 0.312 mmol, 1.0 eq.) in dioxane/H_2O (1.3 mL) were used. After 2 hr the reaction was completed and gave **SGA-67** as a colorless solid (95.3 mg, 0.291 mmol, 90%). $\mathbf{R_f}$ = 0.20 (6:1 hexanes/EtOAc). **m.p.:** 198˚C. **^{1}H NMR (400 MHz, $CDCl_3$)** δ/ppm = 7.27–7.23 (m, 2H, 2'-H, 6'-H), 6.95–6.91 (m, 2H, 3'-H, 5'-H), 6.54 (s, 1H, 4 hr), 3.85 (s, 3H, OCH_3), 3.75 (d, *J* = 7.2 Hz, 2H, $C\underline{H}_2$-cy), 2.60 (s, 3H, CH_3), 1.62–1.53 (m, 3H, cy), 1.43–1.33 (m, 3H, cy), 1.09–0.98 (m, 3H, cy), 0.70–0.59 (m, 2H, cy). **^{13}C NMR (101 MHz, $CDCl_3$)** δ/ppm = 171.3 (COOH), 159.0 (C-4'), 137.8 (C-2), 134.1 (C-5), 131.0 (C-2', C-6'), 125.9 (C-1'), 113.9 (C-3', C-5'), 111.0 (C-3), 110.2 (C-4), 55.3 (OCH_3), 50.2 ($\underline{C}H_2$-cy), 38.9 (cy), 30.5 (cy), 26.2 (cy), 25.8 (cy), 12.3 (CH_3). IR (ATR) $\tilde{V}_{max}/cm^{-1}$=3027, 3002, 2970, 2925, 2849, 1738, 1652, 1569, 1535, 1494, 1435, 1364, 1266, 1247, 1228, 1203, 840, 778. **HRMS (ESI):** calculated for $C_{20}H_{24}NO_3$ $(M-H)^-$ 326.17617; found 326.17633. **Purity (HPLC):** 93% (λ = 210 nm),>96% (λ = 254 nm).

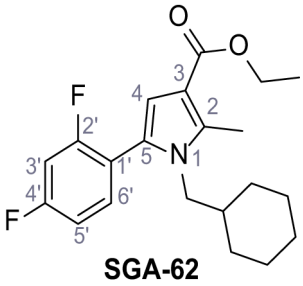

SGA-62

Chemical structure 84. Ethyl 1-(cyclohexylmethyl)−5-(2,4-difluorophenyl)−2-methyl-1*H*-pyrrole-3-carboxylate – SGA-62.

Following general procedure **C**, ethyl acetoacetate (208 µL, 1.65 mmol, 1.1 eq.) in dry THF (5.0 mL), NaH (90.0 mg, 2.25 mmol, 1.5 eq.) and a solution of 2-chloro-1-(2,4-difluorophenyl)ethan-1-one (286 mg, 1.50 mmol, 1.0 eq.) and KI (249 mg, 1.50 mmol, 1.0 eq.) in dry THF (3.0 mL) were used. Then the residue was dissolved in acetic acid (5.0 mL) and cyclohexanemethanamine (390 µL, 3.00 mmol, 2.0 eq.) was added. FCC (hexanes/EtOAc 9:1) yielded **SGA-62** as yellow solid (424 mg, 1.17 mmol, 78%). $\mathbf{R_f}$ = 0.43 (9:1 hexanes/EtOAc). **m.p.:** 94˚C. **^{1}H NMR (500 MHz, $CDCl_3$)** δ/ppm = 7.27 (td, *J* = 8.4, 6.5 Hz, 1H, 6'-H), 6.96–6.85 (m, 2H, 3'-H, 5'-H), 6.53 (s, 1H, 4 hr), 4.26 (q, *J* = 7.1 Hz, 2H, $C\underline{H}_2CH_3$), 3.60 (d, *J* = 7.1 Hz, 2H, $C\underline{H}_2$-cy), 2.58 (s, 3H, CH_3), 1.59–1.53 (m, 3H, cy), 1.38–1.30 (m, 6H, cy, $CH_2C\underline{H}_3$), 1.06–0.98 (m, 3H, cy), 0.68–0.58 (m, 2H, cy). **^{13}C NMR (121 MHz, $CDCl_3$)** δ/ppm = 165.5 (COOEt), 162.9 (dd, J_{CF} = 250.1, 11.6 Hz, C-4'), 160.2 (dd, J_{CF} = 248.9, 12.0 Hz, C-2'), 137.2 (C-2), 133.5 (dd, J_{CF} = 9.4, 4.1 Hz, C-6'), 126.2 (C-5), 117.6 (dd, J_{CF} = 15.7, 3.9 Hz, C-1'), 112.3 (C-3), 111.6 (dd, J_{CF} = 21.1, 3.7 Hz, C-5'), 111.3 (C-4), 104.20 (t, J_{CF} = 25.8 Hz, C-3'), 59.4 ($C\underline{H}_2CH_3$), 50.6 (d, J_{CF} = 3.0 Hz, $C\underline{H}_2$-cy), 39.0 (cy), 30.5 (cy), 26.1 (cy), 25.7 (cy), 14.6 ($CH_2C\underline{H}_3$), 12.0 (CH_3). IR (ATR) $\tilde{V}_{max}/cm^{-1}$=2971, 2929, 2848, 1739, 1698, 1571, 1426, 1371, 1235, 1199, 1067, 851, 834. **HRMS (ESI):** calculated for $C_{21}H_{26}F_2NO_2$ $(M+H)^+$ 362.19261; found 362.19247. **Purity (HPLC):**>96% (λ = 210 nm),>96% (λ = 254 nm).

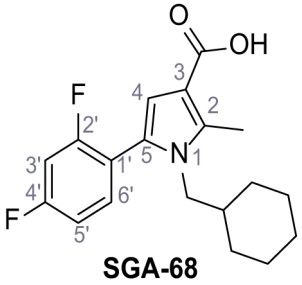

SGA-68

Chemical structure 85. 1-(Cyclohexylmethyl)−5-(2,4-difluorophenyl)−2-methyl-1*H*-pyrrole-3-carboxylic acid - SGA-68.

According to general procedure **D**, LiOH (167 mg, 6.61 mmol, 10 eq.) and a solution of **SGA-62** (239 mg, 0.661 mmol, 1.0 eq.) in dioxane/H_2O (1.3 mL) were used. After 1 hr the reaction was completed and gave **SGA-68** as a colorless solid (170 mg, 0.511 mmol, 77%). $\mathbf{R_f}$ = 0.29 (6:1 hexanes/EtOAc). **m.p.:** 168˚C. **^{1}H NMR (400 MHz, $CDCl_3$)** δ/ppm = 7.33–7.25 (m, 1H, 6'-H, collapses with chloroform), 6.98–6.86 (m, 2H, 3'-H, 5'-H), 6.60 (s, 1H, 4 hr), 3.62 (d, *J* = 7.1 Hz, 2H, $C\underline{H}_2$-cy), 2.61 (s, 3H, CH_3), 1.65–1.51 (m, 3H, cy), 1.49–1.32 (m, 3H, cy), 1.14–0.94 (m, 3H, cy), 0.72–0.56 (m, 2H, cy). **^{13}C NMR (101 MHz, $CDCl_3$)** δ/ppm = 171.0 (COOH), 163.0 (dd, J_{CF} = 250.3, 11.6 Hz, C-4'), 160.3 (dd, J_{CF} = 249.0, 12.0 Hz, C-2'), 138.5 (C-2), 133.6 (dd, J_{CF} = 9.5, 4.0 Hz, C-6'), 126.7 (C-5), 117.5 (dd, J_{CF} = 15.8, 3.8 Hz, C-1'), 112.0 (C-3), 111.7 (dd, J_{CF} = 21.3, 3.8 Hz, C-5'), 111.6 (C-4), 104.3 (t, J_{CF} = 25.9 Hz, C-3'), 50.72 (d, J_{CF} = 3.0 Hz, $C\underline{H}_2$-cy), 39.0 (cy), 30.6 (cy), 26.2 (cy), 25.7 (cy), 12.2 (CH_3). IR (ATR) $\tilde{V}_{max}/cm^{-1}$=2970, 2926, 2854, 1739, 1666, 1573, 1450, 1433, 1364, 1265, 1239, 1200, 1140, 778. **HRMS (ESI):** calculated for $C_{19}H_{20}F_2NO_2$ $(M-H)^-$ 332.14676; found 332.14697. **Purity (HPLC):**>96% (λ = 210 nm),>96% (λ = 254 nm).

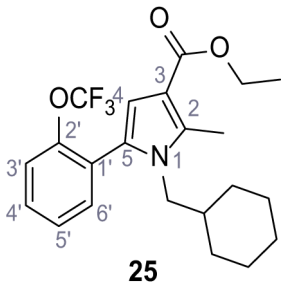

25

Chemical structure 86. Ethyl 1-(cyclohexylmethyl)−2-methyl-5-(2-(trifluoromethoxy)phenyl)−1*H*-pyrrole-3-carboxylate (25).

Following general procedure **C**, ethyl acetoacetate (123 µL, 0.972 mmol, 1.1 eq.) in dry THF (4.0 mL), NaH (53.0 mg, 1.32 mmol, 1.5 eq.) and a solution of ketone **24** (250 mg, 0.883 mmol, 1.0 eq.) and KI (147 mg, 0.883 mmol, 1.0 eq.) in dry THF (2.0 mL) were used. Then the residue was dissolved in acetic acid (5.0 mL) and cyclohexanemethanamine (230 µL, 1.77 mmol, 2.0 eq.) was added. FCC (hexanes/EtOAc 9:1) yielded ester **25** as colorless solid (345 mg, 0.845 mmol, 95%). $\mathbf{R_f}$ = 0.46 (9:1 hexanes/EtOAc). **m.p.:** 66˚C. **^{1}H NMR (100 MHz, $CDCl_3$)** δ/ppm = 7.44–7.29 (m, 4H, 3'-H, 4'-H, 5'-H, 6'-H), 6.53 (s, 1H, 4 hr), 4.27 (q, *J* = 7.1 Hz, 2H, $C\underline{H}_2CH_3$), 3.59 (d, *J* = 7.1 Hz, 2H, $C\underline{H}_2$-cy), 2.59 (s, 3H, CH_3), 1.59–1.52 (m, 3H, cy), 1.40–1.32 (m, 6H, cy, $CH_2C\underline{H}_3$), 1.06–0.94 (m, 3H, cy), 0.67–0.54 (m, 2H, cy). **^{13}C NMR (101 MHz, $CDCl_3$)** δ/ppm = 165.8 (COOEt), 147.4 (C-2'), 137.1 (C-2), 133.4 (C-4', C-5' or C-6'), 129.6 (C-4', C-5' or C-6'), 127.9 (C-5), 126.9 (C-1'), 126.7 (C-4', C-5' or C-6'), 120.5 (q, J_{CF} = 257.4 Hz, OCF_3), 120.4 (C-3'), 112.2 (C-3), 111.4 (C-4), 59.5 ($\underline{C}H_2CH_3$), 50.7 ($\underline{C}H_2$-cy), 39.0 (cy), 30.6 (cy), 26.2 (cy), 25.8 (cy), 14.7 ($CH_2\underline{C}H_3$), 12.1 (CH_3). IR (ATR) $\tilde{V}_{max}/cm^{-1}$=1934, 1692, 1447, 1422, 1242, 1192, 1155, 1059, 769. **HRMS (ESI):** calculated for $C_{22}H_{27}F_3NO_3$ $(M+H)^+$ 410.19375; found 410.19336. **Purity (HPLC):**>96% (λ = 210 nm),>96% (λ = 254 nm).

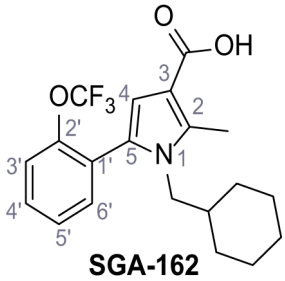

SGA-162

Chemical structure 87. 1-(Cyclohexylmethyl)−2-methyl-5-(2-(trifluoromethoxy)phenyl)−1*H*-pyrrole-3-carboxylic acid – SGA-162.

According to general procedure **D**, LiOH (142 mg, 5.62 mmol, 10 eq.) and a solution of ester **25** (230 mg, 0.562 mmol, 1.0 eq.) in dioxane/H_2O (3.0 mL) were used. After 2 hr the reaction was completed and gave **SGA-162** as a colorless solid (199 mg, 0.523 mmol, 93%). $\mathbf{R_f}$ = 0.11 (9:1 hexanes/EtOAc). **m.p.:** 170˚C. **^{1}H NMR (400 MHz, $CDCl_3$)** δ/ppm = 11.13 (s, 1H, COOH), 7.46–7.30 (m, 4H, 3'-H, 4'-H, 5'-H, 6'-H), 6.59 (s, 1H, 4 hr), 3.60 (d, *J* = 7.1 Hz, 2H, $C\underline{H}_2$-cy), 2.61 (s, 3H, CH_3), 1.61–1.52 (m, 3H, cy), 1.41–1.31 (m, 3H, cy), 1.09–0.96 (m, 3H, cy), 0.67–0.55 (m, 2H, cy). **^{13}C NMR (101 MHz, $CDCl_3$)** δ/ppm = 169.9 (COOH), 147.4 (C-2'), 138.3 (C-2), 133.4 (C-4', C-5' or C-6'), 129.8 (C-4', C-5' or C-6'), 128.3 (C-5), 126.8 (C-4', C-5' or C-6'), 126.7 (C-1'), 120.5 (q, J_{CF} = 260.2 Hz, OCF_3), 120.4 (C-4'), 112.1 (C-4), 111.2 (C-3), 50.8 ($\underline{C}H_2$-cy), 38.9 (cy), 30.6 (cy), 26.2 (cy), 25.7 (cy), 12.3 (CH_3). IR (ATR) $\tilde{V}_{max}/cm^{-1}$=2927, 1642, 1473, 1444, 1249, 1199, 1156, 776, 759. **HRMS (ESI):** calculated for $C_{20}H_{21}F_3NO_3$ $(M-H)^-$ 380.14790; found 380.14805. **Purity (HPLC):**>96% (λ = 210 nm).

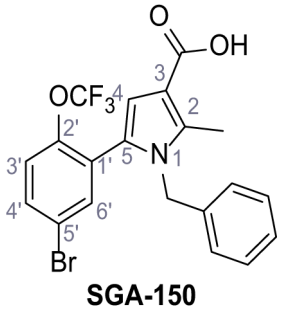

SGA-150

Chemical structure 88. 1-Benzyl-5-(5-bromo-2-(trifluoromethoxy)phenyl)−2-methyl-1*H*-pyrrole-3-carboxylic acid – SGA-150.

Following general procedure **C**, ethyl acetoacetate (104 µL, 0.821 mmol, 1.1 eq.) in dry THF (4.0 mL), NaH (44.8 mg, 1.12 mmol, 1.5 eq.) and a solution of ketone **23** (237 mg, 0.746 mmol, 1.0 eq.) and KI (124 mg, 0.746 mmol, 1.0 eq.) in dry THF (2.0 mL) were used. Then the residue was dissolved in acetic acid (5.0 mL) and benzylamine (204 µL, 1.87 mmol, 2.5 eq.) was added. FCC (hexanes/EtOAc 97:3) yielded ethyl 5-(5-bromo-2-(trifluoromethoxy)phenyl)−1-isopropyl-2-methyl-1*H*-pyrrole-3-carboxylate (**26**) as colorless oil (107 mg, 0.222 mmol). This product was used without further purification or characterization for the next step. $\mathbf{R_f}$ = 0.44 (9:1 hexanes/EtOAc). According to general procedure **D**, LiOH (55.9 mg, 2.22 mmol, 10 eq.) and a solution of ester **26** (107 mg, 0.222 mmol, 1.0 eq.) in dioxane/H_2O (3.0 mL) were used. After 16 hr the reaction was completed and gave **SGA-150** as a colorless solid (34.4 mg, 0.0757 mmol, 10% over two steps). $\mathbf{R_f}$ = 0.27 (9:1 hexanes/EtOAc). **m.p.:** 185˚C. **^{1}H NMR (400 MHz, CD_2Cl_2)** δ/ppm = 11.12 (s, 1H, COOH), 7.51 (dd, J = 8.8, 2.5 Hz, 1H, 4'-H), 7.39 (d, J = 2.5 Hz, 1H, 6'-H), 7.30–7.18 (m, 4H, 3'-H, Ph), 6.83–6.77 (m, 2H, Ph), 6.70 (s, 1H, 4 hr), 5.00 (s, 2H, CH_2), 2.49 (s, 3H, CH_3). **^{13}C NMR (121 MHz, CD_2Cl_2)** δ/ppm = 169.9 (COOH), 147.0 (C-2'), 139.6 (C-2), 137.4 (C-1'), 136.3 (C-6'), 133.4 (C-4'), 129.3 (Ph), 128.5 (qPh), 128.0 (Ph), 127.3 (C-5), 126.2 (Ph), 122.8 (C-3'), 120.8 (q, J_{CF} = 258.7 Hz, OCF_3), 120.3 (C-5'), 113.1 (C-4), 112.3 (C-3), 48.7 (CH_2), 12.2 (CH_3). IR (ATR) $\tilde{V}_{max}/cm^{-1}$=2925, 2360, 1670, 1249, 1223, 1198, 1171, 733. **HRMS (ESI):** calculated for $C_{20}H_{14}{}^{79}BrF_3NO_3$ $(M\text{-}H)^-$ 452.01146; found 452.01168. **Purity (HPLC):** >96% (λ = 210 nm),>96% (λ = 254 nm).

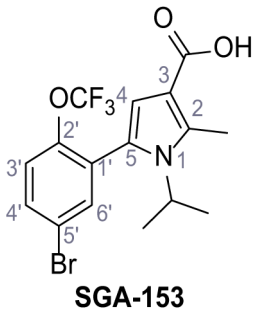

SGA-153

Chemical structure 89. 5-(5-Bromo-2-(trifluoromethoxy)phenyl)−1-isopropyl-2-methyl-1*H*-pyrrole-3-carboxylic acid – SGA-153.

Following general procedure **C**, ethyl acetoacetate (87.6 µL, 0.693 mmol, 1.1 eq.) in dry THF (4.0 mL), NaH (37.8 mg, 0.945 mmol, 1.5 eq.) and a solution of ketone **23** (200 mg, 0.630 mmol, 1.0 eq.) and KI (105 mg, 0.630 mmol, 1.0 eq.) in dry THF (2.0 mL) were used. Then the residue was dissolved in acetic acid (5.0 mL) and isopropylamine (108 µL, 1.26 mmol, 2.0 eq.) was added. FCC (hexanes/EtOAc 99:1) yielded ethyl 5-(5-bromo-2-(trifluoromethoxy)phenyl)−1-isopropyl-2-methyl-1*H*-pyrrole-3-carboxylate (**27**) as colorless oil (65.9 mg, 0.152 mmol). This product was used without further purification or characterization for the next step. $\mathbf{R_f}$ = 0.55 (9:1 hexanes/EtOAc). According to general procedure **D**, LiOH (38.3 mg, 1.52 mmol, 10 eq.) and a solution of ester **27** (65.9 mg, 0.152 mmol, 1.0 eq.) in dioxane/H_2O (3.0 mL) were used. After 18 hr the reaction was completed and gave **SGA-153** as a colorless solid (32.4 mg, 0.0798 mmol, 12% over two steps). $\mathbf{R_f}$ = 0.11 (9:1 hexanes/EtOAc). **m.p.:** 192˚C. **^{1}H NMR (400 MHz, C_3D_6O)** δ/ppm = 7.75 (dd, J = 8.8, 2.6 Hz, 1H, 4'-H), 7.65 (d,

J = 2.6 Hz, 1H, 6'-H), 7.44 (dq, *J* = 8.8, 1.5 Hz, 1H, 3'-H), 6.47 (s, 1H, 4 hr), 4.27 (p, *J* = 7.0 Hz, 1H, CH), 2.72 (s, 3H, CH_3), 1.45 (d, *J* = 7.0 Hz, 6H, $CH(C\underline{H}_3)_2$). **^{13}C NMR (101 MHz, C_3D_6O)** δ/ppm = 166.4 (COOH), 147.7 (C-2'), 137.5 (C-2), 137.0 (C-6'), 134.0 (C-4'), 130.5 (C-1'), 126.4 (C-5), 123.7 (q, *J* = 257.6 Hz, OCF_3), 123.5 (C-3'), 120.6 (C-5'), 113.9 (C-3), 113.0 (C-4), 50.2 (CH), 22.0 ($CH(\underline{C}H_3)_2$), 13.0 (CH_3). IR (ATR) $\tilde{V}_{max}$/cm^{-1}=2936, 2358, 1672, 1248, 1214, 1200, 1166. **HRMS (ESI):** calculated for $C_{16}H_{14}{}^{79}BrF_3NO_3$ $(M-H)^-$ 404.01146; found 404.01164. **Purity (HPLC):**>96% (λ = 210 nm), >96% (λ = 254 nm).

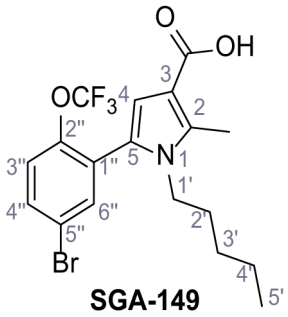

SGA-149

Chemical structure 90. 5-(5-Bromo-2-(trifluoromethoxy)phenyl)−2-methyl-1-pentyl-1*H*-pyrrole-3-carboxylic acid – SGA-149.

Following general procedure **C**, ethyl acetoacetate (87.6 µL, 0.693 mmol, 1.1 eq.) in dry THF (4.0 mL), NaH (37.8 mg, 0.945 mmol, 1.5 eq.) and a solution of ketone **23** (200 mg, 0.630 mmol, 1.0 eq.) and KI (105 mg, 0.630 mmol, 1.0 eq.) in dry THF (2.0 mL) were used. Then the residue was dissolved in acetic acid (5.0 mL) and *n*-pentylamine (146 µL, 1.26 mmol, 2.0 eq.) was added. FCC (hexanes/EtOAc 99:1) yielded ethyl 5-(5-bromo-2-(trifluoromethoxy)phenyl)−2-methyl-1-pentyl-1*H*-pyrrole-3-carboxylate (**28**) as colorless oil (81.5 mg, 0.176 mmol). The product was used without further purification or characterization for the next step. **R_f** = 0.51 (9:1 hexanes/EtOAc). According to general procedure **D**, LiOH (44.4 mg, 1.76 mmol, 10 eq.) and a solution of ester **28** (81.5 mg, 0.176 mmol, 1.0 eq.) in dioxane/H_2O (3.0 mL) were used. After 18 hr the reaction was completed and gave **SGA-149** as a colorless solid (40.5 mg, 0.0933 mmol, 15% over two steps). **R_f** = 0.06 (9:1 hexanes/EtOAc). **m.p.:** 121˚C. **^{1}H NMR (400 MHz, $CDCl_3$)** δ/ppm = 7.57–7.51 (m, 2H, 4''-H, 6''-H), 7.24–7.20 (m, 1H, 3''-H), 6.61 (s, 1H, 4 hr), 3.74–3.68 (m, 2H, 1'-H), 2.61 (s, 3H, CH_3), 1.49–1.43 (m, 2H, 2'-H), 1.19–1.06 (m, 4H, 3'-H, 4'-H), 0.80 (t, *J* = 7.2 Hz, 3H, 5'-H). **^{13}C NMR (101 MHz, $CDCl_3$)** δ/ppm = 169.4 (COOH), 146.6 (C-2''), 138.3 (C-2), 135.9 (C-6''), 132.8 (C-4''), 128.7 (C-5''), 126.1 (C-5), 122.5 (q, *J* = 279.8 Hz, OCF_3), 122.4 (C-3''), 120.0 (C-1''), 112.7 (C-4), 111.4 (C-3), 44.7 (C-1'), 30.2 (C-2'), 28.8 (C-3'), 22.1 (C-4'), 13.9 (C-5'), 11.9 (CH_3). IR (ATR) $\tilde{V}_{max}$/cm^{-1}=2929, 1663, 1471, 1436, 1247, 1212, 1194, 1160, 781. **HRMS (ESI):** calculated for $C_{18}H_{20}{}^{79}BrF_3NO_3$ $(M+H)^+$ 434.05732; found 434.05765. **Purity (HPLC):**>96% (λ = 210 nm),>96% (λ = 254 nm).

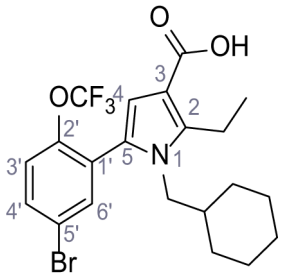

SGA-152

Chemical structure 91. 5-(5-Bromo-2-(trifluoromethoxy)phenyl)−1-(cyclohexylmethyl)−2-ethyl-1*H*-pyrrole-3-carboxylic acid – SGA-152.

Following general procedure **C**, ethyl propionylacetate (99.9 µL, 0.693 mmol, 1.1 eq.) in dry THF (4.0 mL), NaH (37.8 mg, 0.945 mmol, 1.5 eq.) and a solution of ketone **23** (200 mg, 0.630 mmol, 1.0 eq.) and KI (105 mg, 0.630 mmol, 1.0 eq.) in dry THF (2.0 mL) were used. Then the residue was

dissolved in acetic acid (5.0 mL) and cyclohexanemethanamine (164 µL, 1.26 mmol, 2.0 eq.) was added. FCC (hexanes/EtOAc 99:1) yielded ethyl 5-(5-bromo-2-(trifluoromethoxy)phenyl)−1-(cyclohexylmethyl)−2-ethyl-1*H*-pyrrole-3-carboxylate (**29**) as colorless oil (98.0 mg, 0.195 mmol). This product was used without further purification or characterization for the next step. **R_f** = 0.58 (9:1 hexanes/EtOAc). According to general procedure **D**, LiOH (49.2 mg, 1.95 mmol, 10 eq.) and a solution of ester **29** (98.0 mg, 0.195 mmol, 1.0 eq.) in dioxane/H_2O (3.0 mL) were used. After 18 hr the reaction was completed and gave **SGA-152** as yellow solid (30.8 mg, 0.0649 mmol, 9% over two steps). **R_f** = 0.24 (9:1 hexanes/EtOAc). **m.p.:** 152˚C. **^{1}H NMR (500 MHz, $CDCl_3$)** δ/ppm = 11.35 (s, 1H, COOH), 7.57–7.50 (m, 2H, 4'-H, 6'-H), 7.20 (dd, *J* = 8.6, 1.4 Hz, 1H, 3'-H), 6.61 (s, 1H, 4 hr), 3.61 (d, *J* = 7.2 Hz, 2H, C$\underline{H}_2$-cy), 3.04 (q, *J* = 7.4 Hz, 2H, C$\underline{H}_2$CH$_3$), 1.64–1.54 (m, 3H, cy), 1.39–1.31 (m, 3H, cy), 1.23 (t, *J* = 7.4 Hz, 3H, CH$_2$C$\underline{H}_3$), 1.08–0.99 (m, 3H, cy), 0.70–0.60 (m, 2H, cy). **^{13}C NMR (121 MHz, $CDCl_3$)** δ/ppm = 169.8 (COOH), 146.3 (C-2'), 145.1 (C-2), 135.5 (C-4' or C-6'), 132.5 (C-4' or C-6'), 129.1 (C-1'), 126.7 (C-5), 122.3 (C-3'), 120.3 (q, J_{CF} = 259.2 Hz, OCF_3), 120.0 (C-5'), 113.2 (C-4), 110.8 (C-3), 50.9 (C$\underline{H}_2$-cy), 39.6 (cy), 30.7 (cy), 26.2 (cy), 25.8 (cy), 19.2 (C$\underline{H}_2$CH$_3$), 14.5 (CH$_2$C$\underline{H}_3$). IR (ATR) $\tilde{V}_{max}$/cm^{-1}=2927, 2359, 1659, 1469, 1441, 1250, 1212, 1192, 1172. **HRMS (ESI):** calculated for $C_{21}H_{22}{}^{79}BrF_3NO_3$ $(M-H)^-$ 472.07406; found 472.07418. **Purity (HPLC):**>96% (λ = 210 nm),>96% (λ = 254 nm).

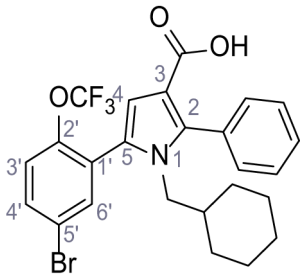

SGA-154

Chemical structure 92. 5-(5-Bromo-2-(trifluoromethoxy)phenyl)−1-(cyclohexylmethyl)−2-phenyl-1*H*-pyrrole-3-carboxylic acid – SGA-154.

Following general procedure **C**, ethyl benzoylacetate (134 µL, 0.693 mmol, 1.1 eq.) in dry THF (4.0 mL), NaH (37.8 mg, 0.945 mmol, 1.5 eq.) and a solution of ketone **23** (200 mg, 0.630 mmol, 1.0 eq.) and KI (105 mg, 0.630 mmol, 1.0 eq.) in dry THF (2.0 mL) were used. Then the residue was dissolved in acetic acid (5.0 mL) and cyclohexanemethanamine (328 µL, 2.52 mmol, 4.0 eq.) was added. FCC (hexanes/EtOAc 99:1) yielded ethyl 5-(5-bromo-2-(trifluoromethoxy)phenyl)−1-(cyclohexylmethyl)−2-phenyl-1*H*-pyrrole-3-carboxylate (**30**) as yellow solid (151 mg, 0.274 mmol). This product was used without further purification or characterization for the next step. **R_f** = 0.50 (9:1 hexanes/EtOAc). According to general procedure **D**, LiOH (69.2 mg, 2.74 mmol, 10 eq.) and a solution of ester **30** (151 mg, 0.274 mmol, 1.0 eq.) in dioxane/H_2O (3.0 mL) were used. After 18 hr the reaction was completed and gave **SGA-154** as yellow solid (91.5 mg, 0.175 mmol, 28% over two steps). **R_f** = 0.12 (9:1 hexanes/EtOAc). **m.p.:** 170˚C. **^{1}H NMR (400 MHz, $CDCl_3$)** δ/ppm = 7.61 (d, *J* = 2.5 Hz, 1H, 6'-H), 7.55 (dd, *J* = 8.7, 2.5 Hz, 1H, 4'-H), 7.47–7.41 (m, 3H, Ph), 7.39–7.35 (m, 2H, Ph), 7.23 (dq, *J* = 8.7, 1.3 Hz, 1H, 3'-H), 6.74 (s, 1H, 4 hr), 3.56 (d, *J* = 7.4 Hz, 2H, C$\underline{H}_2$-cy), 1.48–1.42 (m, 3H, cy), 1.11–1.05 (m, 2H, cy), 1.03–0.95 (m, 1H, cy), 0.90–0.82 (m, 3H, cy), 0.43–0.32 (m, 2H, cy). **^{13}C NMR (101 MHz, $CDCl_3$)** δ/ppm = 167.7 (COOH), 146.1 (C-2'), 141.7 (C-2), 135.2 (C-6'), 132.7 (C-4'), 131.7 (C-5, C-1', C-5' or qPh), 131.0 (Ph), 128.8 (C-5, C-1', C-5' or qPh), 128.7 (Ph), 128.3 (Ph), 122.4 (C-3'), 120.4 (q, J_{CF} = 266.3 Hz, OCF_3), 120.2 (C-5, C-1', C-5' or qPh), 113.8 (C-4), 112.7 (C-3), 52.0 (C$\underline{H}_2$-cy), 38.7 (cy), 30.3 (cy), 26.1 (cy), 25.6 (cy). One quaternary carbon is missing. IR (ATR) $\tilde{V}_{max}$/cm^{-1}=2915, 2335, 1667, 1487, 1248, 1208, 1169, 1127, 796, 697. **HRMS (ESI):** calculated for $C_{25}H_{22}{}^{79}BrF_3NO_3$ $(M-H)^-$ 520.07406; found 520.07418. **Purity (HPLC):**>96% (λ = 210 nm),>96% (λ = 254 nm).

Statistical analysis

All error bars are depicted as SEM. Statistical significance was determined via Student's t-test, one-way ANOVA, or two-way ANOVA followed by either Tukey's or Bonferroni's post hoc test.

Significance is denoted on figures with asterisks as outlined in the legends. All data presented are representative of three or more independent experiments.

Acknowledgements

We thank Christopher Wolf and Elisabeth Butz for their assistance with pilot studies, Dr. Youxing Jiang (University of Texas Southwestern Medical Center) for plasmid gifts, and Dr. Herman van der Putten (NCL Foundation) for valuable discussions. This work was supported, in part, by funding from the German Research Foundation, DFG (project number 239283807, SFB/TRR152 projects P04 to CG, P06 to CW-S, P12 to MB, and P14 to SZ; BR 1034/7–1 to FB; GR 4315/2–1 to CG), the University of Pennsylvania Orphan Disease Center and the Mucolipidosis IV Foundation grant MDBR-17–120 ML4 to CG, the Mucolipidosis IV Foundation grant (project number 404.510.2577) to CG, the NCL Foundation grant (project 2018-Grimm-Paquet) to CG, and the BBSRC grant (BB/N01524X/1) to SP.

Additional information

Funding

Funder	Grant reference number	Author
Mucolipidosis IV Foundation	MDBR-17-120- ML4	Christian Grimm
Deutsche Forschungsgemeinschaft	SFB/TRR152 P04	Christian Grimm
Deutsche Forschungsgemeinschaft	SFB/TRR152 P06	Christian Wahl-Schott
Deutsche Forschungsgemeinschaft	SFB/TRR152 P12	Martin Biel
Deutsche Forschungsgemeinschaft	BR 1034/7-1	Franz Bracher
Biotechnology and Biological Sciences Research Council	BB/N01524X/1	Sandip Patel
Deutsche Forschungsgemeinschaft	239283807	Christian Grimm
Deutsche Forschungsgemeinschaft	SFB/TRR152 P14	Christian Grimm
Deutsche Forschungsgemeinschaft	GR 4315/2-1	Christian Grimm
University of Pennsylvania	Orphan Disease Center	Christian Grimm
Mucolipidosis IV Foundation	404.510.2577	Christian Grimm
NCL Foundation	2018-Grimm-Paquet	Christian Grimm

The funders had no role in study design, data collection and interpretation, or the decision to submit the work for publication.

Author contributions

Susanne Gerndt, Data curation, Formal analysis, Validation, Visualization; Cheng-Chang Chen, Formal analysis, Validation, Visualization, Methodology; Yu-Kai Chao, Data curation, Formal analysis, Validation, Visualization, Methodology; Yu Yuan, Anna Scotto Rosato, Katharina Jacob, Data curation, Formal analysis, Validation, Investigation, Visualization, Methodology; Sandra Burgstaller, Conceptualization, Data curation, Formal analysis, Validation, Investigation, Visualization, Methodology; Einar Krogsaeter, Data curation, Formal analysis, Investigation, Methodology; Nicole Urban, Ong Nam Phuong Nguyen, Data curation, Formal analysis, Validation, Investigation, Methodology; Meghan T Miller, Data curation, Validation; Marco Keller, Conceptualization, Resources, Validation; Angelika M Vollmar, Resources, Funding acquisition, Project administration; Thomas Gudermann, Resources, Funding acquisition; Susanna Zierler, Conceptualization, Resources; Johann

Schredelseker, Conceptualization; Michael Schaefer, Resources, Methodology; Martin Biel, Resources; Roland Malli, Conceptualization, Resources, Validation, Methodology; Christian Wahl-Schott, Conceptualization, Resources, Methodology; Franz Bracher, Conceptualization, Resources, Data curation, Formal analysis, Supervision, Funding acquisition, Validation, Methodology; Sandip Patel, Conceptualization, Resources, Data curation, Supervision, Funding acquisition, Investigation, Methodology, Writing - original draft, Project administration, Writing - review and editing; Christian Grimm, Conceptualization, Resources, Data curation, Formal analysis, Supervision, Funding acquisition, Validation, Investigation, Visualization, Methodology, Writing - original draft, Project administration, Writing - review and editing

Author ORCIDs
Cheng-Chang Chen http://orcid.org/0000-0003-1282-4026
Yu-Kai Chao http://orcid.org/0000-0002-1202-2448
Einar Krogsaeter http://orcid.org/0000-0001-8232-5498
Susanna Zierler https://orcid.org/0000-0002-4684-0385
Johann Schredelseker http://orcid.org/0000-0002-6657-0466
Roland Malli http://orcid.org/0000-0001-6327-8729
Christian Grimm https://orcid.org/0000-0002-0177-5559

Ethics
Animal experimentation: This study was performed in strict accordance with the recommendations in the Guide for the Care and Use of Laboratory Animals of the Bavarian Government and the European Union. All of the animals were handled according to approved institutional animal care protocols of the University of Munich. The protocol was approved by the Bavarian Government (AZ55.2-1-54-2532-170-17).

Decision letter and Author response
Decision letter https://doi.org/10.7554/eLife.54712.sa1
Author response https://doi.org/10.7554/eLife.54712.sa2

Additional files
Supplementary files
- Transparent reporting form

Data availability
All data generated or analysed during this study are included in the manuscript and supporting files.

References
Ambrosio AL, Boyle JA, Aradi AE, Christian KA, Di Pietro SM. 2016. TPC2 controls pigmentation by regulating melanosome pH and size. *PNAS* **113**:5622–5627. DOI: https://doi.org/10.1073/pnas.1600108113, PMID: 27140606

Ammar YA, Ismail MMF, El-Sehrawi HM, Noaman E, Bayomi AH, Shawer TZ. 2006. Novel pirfenidone analogues: synthesis of Pyridin-2-ones for the treatment of pulmonary fibrosis. *Archiv Der Pharmazie* **339**:429–436. DOI: https://doi.org/10.1002/ardp.200600017

Boccaccio A, Scholz-Starke J, Hamamoto S, Larisch N, Festa M, Gutla PV, Costa A, Dietrich P, Uozumi N, Carpaneto A. 2014. The phosphoinositide PI(3,5)P_2 mediates activation of mammalian but not plant TPC proteins: functional expression of endolysosomal channels in yeast and plant cells. *Cellular and Molecular Life Sciences* **71**:4275–4283. DOI: https://doi.org/10.1007/s00018-014-1623-2, PMID: 24770793

Brailoiu E, Churamani D, Cai X, Schrlau MG, Brailoiu GC, Gao X, Hooper R, Boulware MJ, Dun NJ, Marchant JS, Patel S. 2009. Essential requirement for two-pore channel 1 in NAADP-mediated calcium signaling. *The Journal of Cell Biology* **186**:201–209. DOI: https://doi.org/10.1083/jcb.200904073, PMID: 19620632

Brailoiu E, Rahman T, Churamani D, Prole DL, Brailoiu GC, Hooper R, Taylor CW, Patel S. 2010. An NAADP-gated two-pore channel targeted to the plasma membrane uncouples triggering from amplifying Ca2+ signals.

Journal of Biological Chemistry **285**:38511–38516. DOI: https://doi.org/10.1074/jbc.M110.162073, PMID: 20880839

Burgstaller S, Bischof H, Gensch T, Stryeck S, Gottschalk B, Ramadani-Muja J, Eroglu E, Rost R, Balfanz S, Baumann A, Waldeck-Weiermair M, Hay JC, Madl T, Graier WF, Malli R. 2019. pH-Lemon, a fluorescent Protein-Based pH reporter for acidic compartments. *ACS Sensors* **4**:883–891. DOI: https://doi.org/10.1021/acssensors.8b01599, PMID: 30864782

Calcraft PJ, Ruas M, Pan Z, Cheng X, Arredouani A, Hao X, Tang J, Rietdorf K, Teboul L, Chuang KT, Lin P, Xiao R, Wang C, Zhu Y, Lin Y, Wyatt CN, Parrington J, Ma J, Evans AM, Galione A, et al. 2009. NAADP mobilizes calcium from acidic organelles through two-pore channels. *Nature* **459**:596–600. DOI: https://doi.org/10.1038/nature08030, PMID: 19387438

Cang C, Zhou Y, Navarro B, Seo YJ, Aranda K, Shi L, Battaglia-Hsu S, Nissim I, Clapham DE, Ren D. 2013. mTOR regulates lysosomal ATP-sensitive two-pore na(+) channels to adapt to metabolic state. *Cell* **152**:778–790. DOI: https://doi.org/10.1016/j.cell.2013.01.023, PMID: 23394946

Cang C, Bekele B, Ren D. 2014. The voltage-gated sodium channel TPC1 confers endolysosomal excitability. *Nature Chemical Biology* **10**:463–469. DOI: https://doi.org/10.1038/nchembio.1522, PMID: 24776928

Cao E, Liao M, Cheng Y, Julius D. 2013. TRPV1 structures in distinct conformations reveal activation mechanisms. *Nature* **504**:113–118. DOI: https://doi.org/10.1038/nature12823, PMID: 24305161

Chao YK, Schludi V, Chen CC, Butz E, Nguyen ONP, Müller M, Krüger J, Kammerbauer C, Ben-Johny M, Vollmar AM, Berking C, Biel M, Wahl-Schott CA, Grimm C. 2017. TPC2 polymorphisms associated with a hair pigmentation phenotype in humans result in gain of channel function by independent mechanisms. *PNAS* **114**:E8595–E8602. DOI: https://doi.org/10.1073/pnas.1705739114, PMID: 28923947

Chen CC, Cang C, Fenske S, Butz E, Chao YK, Biel M, Ren D, Wahl-Schott C, Grimm C. 2017. Patch-clamp technique to characterize ion channels in enlarged individual endolysosomes. *Nature Protocols* **12**:1639–1658. DOI: https://doi.org/10.1038/nprot.2017.036, PMID: 28726848

Cosker F, Cheviron N, Yamasaki M, Menteyne A, Lund FE, Moutin MJ, Galione A, Cancela JM. 2010. The ecto-enzyme CD38 is a nicotinic acid adenine dinucleotide phosphate (NAADP) synthase that couples receptor activation to Ca2+ mobilization from lysosomes in pancreatic acinar cells. *Journal of Biological Chemistry* **285**:38251–38259. DOI: https://doi.org/10.1074/jbc.M110.125864, PMID: 20870729

Davies M, Heikkilä T, McConkey GA, Fishwick CW, Parsons MR, Johnson AP. 2009. Structure-based design, synthesis, and characterization of inhibitors of human and *Plasmodium falciparum* dihydroorotate dehydrogenases. *Journal of Medicinal Chemistry* **52**:2683–2693. DOI: https://doi.org/10.1021/jm800963t, PMID: 19351152

Edraki N, Iraji A, Firuzi O, Fattahi Y, Mahdavi M, Foroumadi A, Khoshneviszadeh M, Shafiee A, Miri R. 2016. 2-Imino 2H-chromene and 2-(phenylimino) 2H-chromene 3-aryl carboxamide derivatives as novel cytotoxic agents: synthesis, biological assay, and molecular docking study. *Journal of the Iranian Chemical Society* **13**:2163–2171. DOI: https://doi.org/10.1007/s13738-016-0934-7

Fatt P, Ginsborg BL. 1958. The ionic requirements for the production of action potentials in crustacean muscle fibres. *The Journal of Physiology* **142**:516–543. DOI: https://doi.org/10.1113/jphysiol.1958.sp006034, PMID: 13576452

Grimm C, Jörs S, Saldanha SA, Obukhov AG, Pan B, Oshima K, Cuajungco MP, Chase P, Hodder P, Heller S. 2010. Small molecule activators of TRPML3. *Chemistry & Biology* **17**:135–148. DOI: https://doi.org/10.1016/j.chembiol.2009.12.016, PMID: 20189104

Grimm C, Holdt LM, Chen CC, Hassan S, Müller C, Jörs S, Cuny H, Kissing S, Schröder B, Butz E, Northoff B, Castonguay J, Luber CA, Moser M, Spahn S, Lüllmann-Rauch R, Fendel C, Klugbauer N, Griesbeck O, Haas A, et al. 2014. High susceptibility to fatty liver disease in two-pore channel 2-deficient mice. *Nature Communications* **5**:4699. DOI: https://doi.org/10.1038/ncomms5699, PMID: 25144390

Guo D, Chen T, Ye D, Xu J, Jiang H, Chen K, Wang H, Liu H. 2011. Cell-permeable iminocoumarine-based fluorescent dyes for mitochondria. *Organic Letters* **13**:2884–2887. DOI: https://doi.org/10.1021/ol200908r, PMID: 21548645

Guo J, Zeng W, Jiang Y. 2017. Tuning the ion selectivity of two-pore channels. *PNAS* **114**:1009–1014. DOI: https://doi.org/10.1073/pnas.1616191114, PMID: 28096396

Jackson MB. 2006. *Molecular and Cellular Biophysics*. Cambridge University Press.

Jha A, Ahuja M, Patel S, Brailoiu E, Muallem S. 2014. Convergent regulation of the lysosomal two-pore channel-2 by Mg^{2+}, NAADP, $PI(3,5)P_2$ and multiple protein kinases. *The EMBO Journal* **33**:501–511. DOI: https://doi.org/10.1002/embj.201387035, PMID: 24502975

Kamer KJ, Sancak Y, Fomina Y, Meisel JD, Chaudhuri D, Grabarek Z, Mootha VK. 2018. MICU1 imparts the mitochondrial uniporter with the ability to discriminate between Ca^{2+} and Mn^{2+}. *PNAS* **115**:E7960–E7969. DOI: https://doi.org/10.1073/pnas.1807811115, PMID: 30082385

Kang SY, Park EJ, Park WK, Kim HJ, Jeong D, Jung ME, Song KS, Lee SH, Seo HJ, Kim MJ, Lee M, Han HK, Son EJ, Pae AN, Kim J, Lee J. 2010. Arylpiperazine-containing pyrrole 3-carboxamide derivatives targeting serotonin 5-HT(2A), 5-HT(2C), and the serotonin transporter as a potential antidepressant. *Bioorganic & Medicinal Chemistry Letters* **20**:1705–1711. DOI: https://doi.org/10.1016/j.bmcl.2010.01.093, PMID: 20149649

Khakh BS, Lester HA. 1999. Dynamic selectivity filters in ion channels. *Neuron* **23**:653–658. DOI: https://doi.org/10.1016/S0896-6273(01)80025-8, PMID: 10482233

Kirsch SA, Kugemann A, Carpaneto A, Böckmann RA, Dietrich P. 2018. Phosphatidylinositol-3,5-bisphosphate lipid-binding-induced activation of the human two-pore channel 2. *Cellular and Molecular Life Sciences* **75**:3803–3815. DOI: https://doi.org/10.1007/s00018-018-2829-5, PMID: 29705952

Kobayashi Y, Harayama T. 2009. Triflic anhydride-mediated tandem formylation/cyclization of cyanoacetanilides: a concise synthesis of glycocitlone alkaloids. *Tetrahedron Letters* **50**:6665–6667. DOI: https://doi.org/10.1016/j.tetlet.2009.09.073

Li M, Toombes GE, Silberberg SD, Swartz KJ. 2015. Physical basis of apparent pore dilation of ATP-activated P2X receptor channels. *Nature Neuroscience* **18**:1577–1583. DOI: https://doi.org/10.1038/nn.4120, PMID: 26389841

Lin PH, Duann P, Komazaki S, Park KH, Li H, Sun M, Sermersheim M, Gumpper K, Parrington J, Galione A, Evans AM, Zhu MX, Ma J. 2015. Lysosomal two-pore channel subtype 2 (TPC2) regulates skeletal muscle autophagic signaling. *Journal of Biological Chemistry* **290**:3377–3389. DOI: https://doi.org/10.1074/jbc.M114.608471, PMID: 25480788

Lin-Moshier Y, Walseth TF, Churamani D, Davidson SM, Slama JT, Hooper R, Brailoiu E, Patel S, Marchant JS. 2012. Photoaffinity labeling of nicotinic acid adenine dinucleotide phosphate (NAADP) targets in mammalian cells. *Journal of Biological Chemistry* **287**:2296–2307. DOI: https://doi.org/10.1074/jbc.M111.305813, PMID: 22117075

Lopez-Castejon G, Brough D. 2011. Understanding the mechanism of IL-1β secretion. *Cytokine & Growth Factor Reviews* **22**:189–195. DOI: https://doi.org/10.1016/j.cytogfr.2011.10.001, PMID: 22019906

Machado E, White-Gilbertson S, van de Vlekkert D, Janke L, Moshiach S, Campos Y, Finkelstein D, Gomero E, Mosca R, Qiu X, Morton CL, Annunziata I, d'Azzo A. 2015. Regulated lysosomal exocytosis mediates Cancer progression. *Science Advances* **1**:e1500603. DOI: https://doi.org/10.1126/sciadv.1500603, PMID: 26824057

McNally BA, Somasundaram A, Yamashita M, Prakriya M. 2012. Gated regulation of CRAC channel ion selectivity by STIM1. *Nature* **482**:241–245. DOI: https://doi.org/10.1038/nature10752, PMID: 22278058

Métro T-X, Bonnamour J, Reidon T, Sarpoulet J, Martinez J, Lamaty F. 2012. Mechanosynthesis of amides in the total absence of organic solvent from reaction to product recovery. *Chemical Communications* **48**:11781–11783. DOI: https://doi.org/10.1039/c2cc36352f

Metwally NH, Abdelrazek FM, Eldaly SM, Metz P. 2017. 3-(3,5-Dimethyl-1 *H* -Pyrazol-1-yl)-3-Oxopropanenitrile as Precursor for Some New Mono-Heterocyclic and Bis-Heterocyclic Compounds . *Journal of Heterocyclic Chemistry* **54**:289–294. DOI: https://doi.org/10.1002/jhet.2578

Miao Y, Li G, Zhang X, Xu H, Abraham SN. 2015. A TRP channel senses lysosome neutralization by pathogens to trigger their expulsion. *Cell* **161**:1306–1319. DOI: https://doi.org/10.1016/j.cell.2015.05.009, PMID: 26027738

Morgan AJ, Galione A. 2007. NAADP induces pH changes in the lumen of acidic $^{Ca2+}$ stores. *Biochemical Journal* **402**:301–310. DOI: https://doi.org/10.1042/BJ20060759, PMID: 17117921

Ogunbayo OA, Duan J, Xiong J, Wang Q, Feng X, Ma J, Zhu MX, Evans AM. 2018. mTORC1 controls lysosomal Ca^{2+} release through the two-pore channel TPC2. *Science Signaling* **11**:eaao5775. DOI: https://doi.org/10.1126/scisignal.aao5775, PMID: 29636391

Patel S. 2015. Function and dysfunction of two-pore channels. *Science Signaling* **8**:re7. DOI: https://doi.org/10.1126/scisignal.aab3314, PMID: 26152696

Patel S, Kilpatrick BS. 2018. Two-pore channels and disease. *Biochimica Et Biophysica Acta (BBA) - Molecular Cell Research* **1865**:1678–1686. DOI: https://doi.org/10.1016/j.bbamcr.2018.05.004, PMID: 29746898

Penny CJ, Vassileva K, Jha A, Yuan Y, Chee X, Yates E, Mazzon M, Kilpatrick BS, Muallem S, Marsh M, Rahman T, Patel S. 2019. Mining of ebola virus entry inhibitors identifies approved drugs as two-pore channel pore blockers. *Biochimica Et Biophysica Acta (BBA) - Molecular Cell Research* **1866**:1151–1161. DOI: https://doi.org/10.1016/j.bbamcr.2018.10.022

Pitt SJ, Funnell TM, Sitsapesan M, Venturi E, Rietdorf K, Ruas M, Ganesan A, Gosain R, Churchill GC, Zhu MX, Parrington J, Galione A, Sitsapesan R. 2010. TPC2 is a novel NAADP-sensitive Ca2+ release channel, operating as a dual sensor of luminal pH and $^{Ca2+}$. *The Journal of Biological Chemistry* **285**:35039–35046. DOI: https://doi.org/10.1074/jbc.M110.156927, PMID: 20720007

Pitt SJ, Lam AK, Rietdorf K, Galione A, Sitsapesan R. 2014. Reconstituted human TPC1 is a proton-permeable ion channel and is activated by NAADP or Ca2+. *Science Signaling* **7**:ra46. DOI: https://doi.org/10.1126/scisignal.2004854, PMID: 24847115

Ruas M, Rietdorf K, Arredouani A, Davis LC, Lloyd-Evans E, Koegel H, Funnell TM, Morgan AJ, Ward JA, Watanabe K, Cheng X, Churchill GC, Zhu MX, Platt FM, Wessel GM, Parrington J, Galione A. 2010. Purified TPC isoforms form NAADP receptors with distinct roles for ca(2+) signaling and endolysosomal trafficking. *Current Biology* **20**:703–709. DOI: https://doi.org/10.1016/j.cub.2010.02.049, PMID: 20346675

Ruas M, Davis LC, Chen CC, Morgan AJ, Chuang KT, Walseth TF, Grimm C, Garnham C, Powell T, Platt N, Platt FM, Biel M, Wahl-Schott C, Parrington J, Galione A. 2015. Expression of Ca^{2+}-permeable two-pore channels rescues NAADP signalling in TPC-deficient cells. *The EMBO Journal* **34**:1743–1758. DOI: https://doi.org/10.15252/embj.201490009, PMID: 25872774

Rybalchenko V, Ahuja M, Coblentz J, Churamani D, Patel S, Kiselyov K, Muallem S. 2012. Membrane potential regulates nicotinic acid adenine dinucleotide phosphate (NAADP) dependence of the pH- and $^{Ca2+}$-sensitive organellar two-pore channel TPC1. *Journal of Biological Chemistry* **287**:20407–20416. DOI: https://doi.org/10.1074/jbc.M112.359612, PMID: 22500018

Sakurai Y, Kolokoltsov AA, Chen CC, Tidwell MW, Bauta WE, Klugbauer N, Grimm C, Wahl-Schott C, Biel M, Davey RA. 2015. Ebola virus. Two-pore channels control ebola virus host cell entry and are drug targets for disease treatment. *Science* **347**:995–998. DOI: https://doi.org/10.1126/science.1258758, PMID: 25722412

Saruta K, Hayashi N, Sakurai O, Sawamoto H, Oboki E. 2015. Aromatische, heterocyclische verbindung. *European Patent Office*. EP2862856A1. https://patents.google.com/patent/EP2862856A1/de.

Schieder M, Rötzer K, Brüggemann A, Biel M, Wahl-Schott CA. 2010. Characterization of two-pore channel 2 (TPCN2)-mediated Ca2+ currents in isolated lysosomes. *The Journal of Biological Chemistry* **285**:21219–21222. DOI: https://doi.org/10.1074/jbc.C110.143123, PMID: 20495006

Shah N, Patel PN, Karia DC. 2018. Synthesis characterization and biological evaluation of some novel amino pyrazole derivatives. *Asian Journal of Chemistry* **30**:2647–2651. DOI: https://doi.org/10.14233/ajchem.2018.21499

She J, Guo J, Chen Q, Zeng W, Jiang Y, Bai XC. 2018. Structural insights into the voltage and phospholipid activation of the mammalian TPC1 channel. *Nature* **556**:130–134. DOI: https://doi.org/10.1038/nature26139, PMID: 29562233

She J, Zeng W, Guo J, Chen Q, Bai XC, Jiang Y. 2019. Structural mechanisms of phospholipid activation of the human TPC2 channel. *eLife* **8**:e45222. DOI: https://doi.org/10.7554/eLife.45222, PMID: 30860481

Sjogren EB, Rider MA, Nelson PH, Bingham S, Poulton AL, Emanuel MA, Komuniecki R. 1991. Synthesis and biological activity of a series of diaryl-substituted alpha-cyano-beta-hydroxypropenamides, a new class of anthelmintic agents. *Journal of Medicinal Chemistry* **34**:3295–3301. DOI: https://doi.org/10.1021/jm00115a020, PMID: 1956049

Sohn DH, Park JI, Cho SJ, Kang J. 2017. Novel anion receptors for selective recognition of dimethyl phosphinate and carboxylate. *Tetrahedron* **73**:212–221. DOI: https://doi.org/10.1016/j.tet.2016.11.076

Urban N, Wang L, Kwiek S, Rademann J, Kuebler WM, Schaefer M. 2016. Identification and validation of larixyl acetate as a potent TRPC6 inhibitor. *Molecular Pharmacology* **89**:197–213. DOI: https://doi.org/10.1124/mol.115.100792, PMID: 26500253

Walker GN. 1981. Alphacarbamoyl-pyrrolpropionitriles. *Novartis Corp*. US4256759. https://patents.google.com/patent/US4256759.

Wang X, Zhang X, Dong XP, Samie M, Li X, Cheng X, Goschka A, Shen D, Zhou Y, Harlow J, Zhu MX, Clapham DE, Ren D, Xu H. 2012. TPC proteins are phosphoinositide- activated sodium-selective ion channels in endosomes and lysosomes. *Cell* **151**:372–383. DOI: https://doi.org/10.1016/j.cell.2012.08.036, PMID: 23063126

Xu H, Ren D. 2015. Lysosomal physiology. *Annual Review of Physiology* **77**:57–80. DOI: https://doi.org/10.1146/annurev-physiol-021014-071649, PMID: 25668017

Yamaguchi S, Jha A, Li Q, Soyombo AA, Dickinson GD, Churamani D, Brailoiu E, Patel S, Muallem S. 2011. Transient receptor potential mucolipin 1 (TRPML1) and two-pore channels are functionally independent organellar ion channels. *Journal of Biological Chemistry* **286**:22934–22942. DOI: https://doi.org/10.1074/jbc.M110.210930, PMID: 21540176

Yuan W, Chen X, Liu N, Wen Y, Yang B, Andrei G, Snoeck R, Xiang Y, Wu Y, Jiang Z, Schols D, Zhang Z, Wu Q, Liu NN, Wen YN, Wu YW, Wu QP. 2019. Synthesis, Anti-Varicella-Zoster virus and Anti-Cytomegalovirus activity of 4,5-Disubstituted 1,2,3-(1H)-Triazoles. *Medicinal Chemistry* **15**:801–812. DOI: https://doi.org/10.2174/1573406414666181109095239

Zierler S, Sumoza-Toledo A, Suzuki S, Dúill FÓ, Ryazanova LV, Penner R, Ryazanov AG, Fleig A. 2016. TRPM7 kinase activity regulates murine mast cell degranulation. *The Journal of Physiology* **594**:2957–2970. DOI: https://doi.org/10.1113/JP271564, PMID: 26660477

Zong X, Schieder M, Cuny H, Fenske S, Gruner C, Rötzer K, Griesbeck O, Harz H, Biel M, Wahl-Schott C. 2009. The two-pore channel TPCN2 mediates NAADP-dependent Ca2+-release from lysosomal stores. *Pflügers Archiv - European Journal of Physiology* **458**:891–899. DOI: https://doi.org/10.1007/s00424-009-0690-y

Manuscript III

TRPML2 is an osmo/mechanosensitive cation channel in endolysosomal organelles
Cheng-Chang Chen*, **Einar K. Krogsaeter***, Elisabeth S. Butz, Yanfen Li, Rosa Puertollano, Christian Wahl-Schott, Martin Biel, & Christian Grimm.
Science Advances. 2020;6:eabb5064.

CELL BIOLOGY

TRPML2 is an osmo/mechanosensitive cation channel in endolysosomal organelles

Cheng-Chang Chen[1]*†, Einar Krogsaeter[2†], Elisabeth S. Butz[3], Yanfen Li[1], Rosa Puertollano[4], Christian Wahl-Schott[5], Martin Biel[1]*, Christian Grimm[2]*

Endolysosomes are dynamic, intracellular compartments, regulating their surface-to-volume ratios to counteract membrane swelling or shrinkage caused by osmotic challenges upon tubulation and vesiculation events. While osmosensitivity has been extensively described on the plasma membrane, the mechanisms underlying endolysosomal surface-to-volume ratio changes and identities of involved ion channels remain elusive. Endolysosomes mediate endocytosis, exocytosis, cargo transport, and sorting of material for recycling or degradation. We demonstrate the endolysosomal cation channel TRPML2 to be hypotonicity/mechanosensitive, a feature crucial to its involvement in fast-recycling processes of immune cells. We demonstrate that the phosphoinositide binding pocket is required for TRPML2 hypotonicity-sensitivity, as substitution of L314 completely abrogates hypotonicity-sensitivity. Last, the hypotonicity-insensitive TRPML2 mutant L314R slows down the fast recycling pathway, corroborating the functional importance of hypotonicity-sensitive TRPML2. Our results highlight TRPML2 as an accelerator of endolysosomal trafficking by virtue of its hypotonicity-sensitivity, with implications in immune cell surveillance and viral trafficking.

INTRODUCTION

The endolysosomal system consists of early endosomes, late endosomes (LE), lysosomes (LY), and recycling endosomes (RE) alongside autolysosomes (AL) and phagosomes. These are quasi-spherical organelles that play essential roles in a range of physiological processes. Intracellular cargo such as receptors trafficked for recycling or degradation or inflammatory mediators such as cytokines and chemokines for immediate release are transported via endolysosomal trafficking routes. Dysfunction of endolysosomal trafficking and cargo sorting appear broadly pathogenic, manifesting in lysosomal storage disease, metabolic disorders, and infectious diseases (*1*–*4*). Intracellular compartmental trafficking is mediated by a series of tubulation and vesiculation events, dynamically altering endolysosomal surface-to-volume ratios and reducing radii of curvature (*5*). According to the Young-Laplace equation for spheres (vesiculation) $\Delta p = 2\gamma/R$ and for cylinders (tubulation) $\Delta p = \gamma/R$, the pressure difference (Δp) between the luminal side and the cytosolic side of the endolysosomal surface increases when the radii (R) of the spheres or cylinders decrease. Accordingly, an increase in Δp leads to an increase in surface tension (γ). Membrane tension may not only be generated by increasing surface-to-volume ratio during vesiculation but could also result from spontaneous bending of the lipid bilayer during tubulation (*6*–*7*).

On the cell surface, several volume-regulated and osmotically sensitive ion channels have been identified and characterized, such as TRPV4 and LRRC8 (*8*, *9*). These ion channels sense surface-to-volume ratio variations and correspondingly mediate anion and cation fluxes across the plasma membrane, regulating the cytosolic ion concentration and osmolyte-driven osmosis. Compared to whole cells, endolysosomes are much smaller, and thus, variations of organellar surface-to-volume ratios are very rapid and severe. While whole-cell diameters range from 10 to 20 μm, the diameter of spherical vacuoles ranges from 0.1 to 0.5 μm, while tubules can be much narrower (0.05 μm). However, osmolarity or surface-to-volume ratio-sensitive endolysosomal ion channels remain unidentified.

Several endolysosomal cation channel activities have been observed on endolysosomal membranes and have been suggested to play critical roles in organelle trafficking, fusion, and fission (*10*, *11*). The mucolipin [The transient receptor potential mucolipin (TRPML)] family and the two-pore channels belong to the transient receptor potential (TRP) superfamily and are often discussed in the context of Ca^{2+}/Na^{+} transport and their ability to release cations from the endolysosomal lumen, mediating organellar fusion and fission events (*11*–*13*). They play essential roles in several physiological and pathological states, including lysosomal storage disorders, metabolic diseases, (cancer) cell migration, and metastasis formation, as well as infectious diseases (*2*, *14*–*17*). These cation channels are particularly highly expressed in a variety of quasi-spherical organelles, which may contribute to the regulation of the surface-to-volume ratio of the tubules and vesicles during fission and trafficking processes. Our recent study employed a novel selective TRPML2 channel agonist, ML2-SA1, to demonstrate that TRPML2 activation in the endolysosomal system promotes the release of the chemoattractant CCL2 from lipopolysaccharide (LPS)–activated macrophages and subsequent macrophage migration (*18*). Here, we further identified that TRPML2 acts as an osmo/mechanosensitive cation channel in endolysosomes derived from innate immune cells with a predominant activation in fast recycling, Rab4A-positive vesicles, enabling rapid adaptation to osmotic changes upon tubulation and vesiculation processes.

[1]Department of Pharmacy–Center for Drug Research, Ludwig-Maximilians-Universität, Munich, Germany. [2]Walther Straub Institute of Pharmacology and Toxicology Faculty of Medicine, Ludwig-Maximilians-Universität, Munich, Germany. [3]Center for Genomic Medicine, Department of Neurology, Massachusetts General Hospital, Harvard Medical School, Boston, MA, United States. [4]Cell and Developmental Biology Center, National Heart, Lung, and Blood Institute, National Institutes of Health, Bethesda, MD, United States. [5]Institute for Neurophysiology, Hannover Medical School, Hannover, Germany.
*Corresponding author. Email: cheng-chang.chen@cup.uni-muenchen.de (C.-C.C.); mbiel@cup.uni-muenchen.de (M.B.); christian.grimm@med.uni-muenchen.de (C.G.)
†These authors contributed equally to this work.

RESULTS

Characterization of hypotonicity-sensitive TRPML2 channels in endolysosomes

To identify osmotically sensitive cation channels in the endolysosomal system, we used a whole-intracellular organelle patch-clamp approach to measure current fluxes across intact organelle membranes (*18*–*20*). Exposure to a hypotonic cytosolic solution (220 mOsm) markedly increased inwardly rectifying cation currents from endolysosomes isolated from TRPML2-transfected human embryonic kidney–293 (HEK293) cells. We initially used the LE/LY patch-clamp approach to identify hypotonicity-induced ML2-SA1–evoked currents in TRPML2-transfected HEK293 cells (Fig. 1, A and B). In contrast to TRPML2, neither the TRPML1 channel nor TRPML3 was found to be sensitive to hypotonic stimulation (Fig. 1, C and D). We further observed that pan-TRPML agonist (ML-SA1)–evoked TRPML2-like currents from human and mouse variants of TRPML2 were also increased under hypotonic conditions (fig. S1), as well as currents evoked by applying hypotonic solution alone (fig. S2). Recent studies demonstrated that TRPML2 expression and channel activity are significantly increased in endolysosomes isolated from LPS-stimulated macrophages (*18*, *21*). Endolysosomal recordings from primary alveolar macrophages (AMØ) illustrate that the endogenously expressed

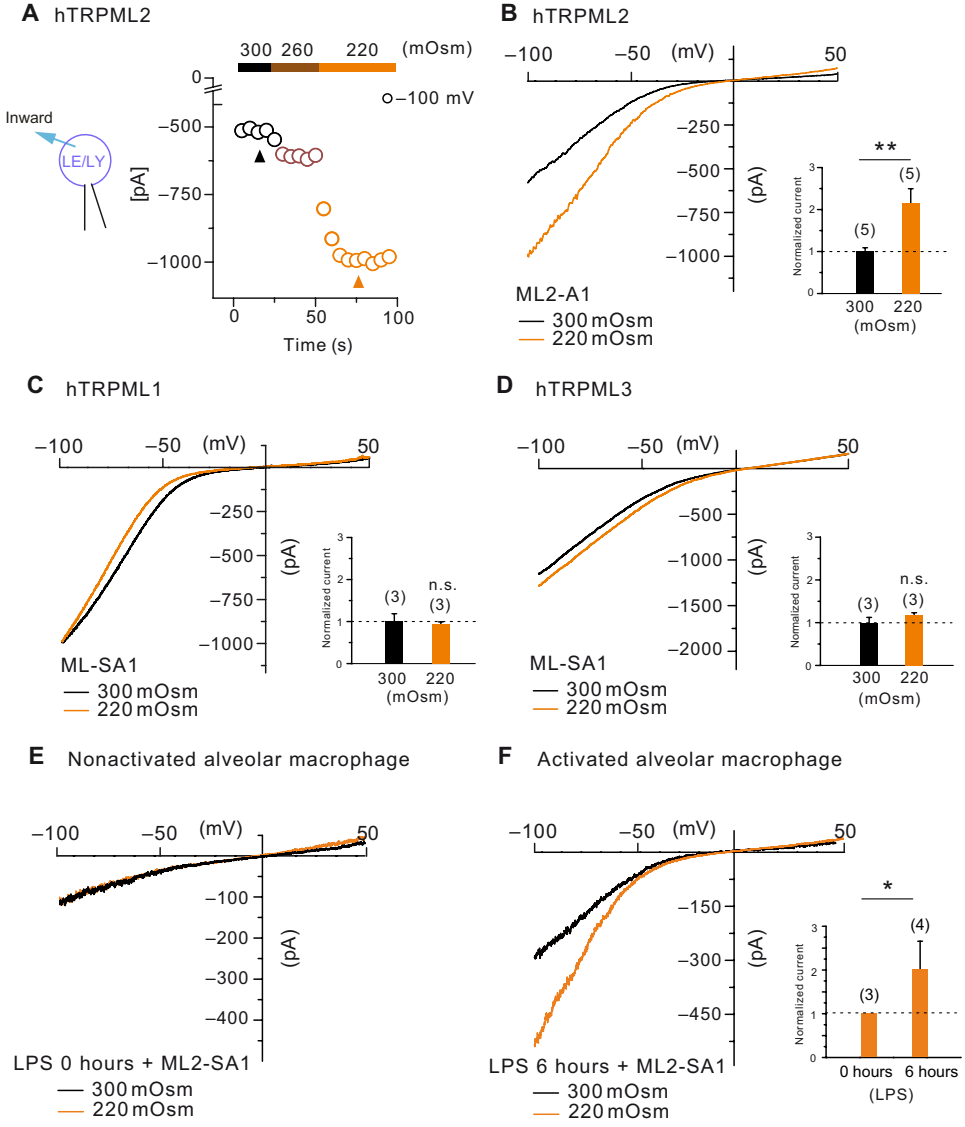

Fig. 1. Hypotonic stimulation-evoked TRPML2 currents. Whole-LE/LY patch-clamp recordings. Inward current indicates cations flowing from the vesicle lumen into the cytosol (bath). (**A**) Time course of whole LE/LY recordings with ramp protocols (every 5 s; holding potential, 0 mV). Recordings at time points (indicated) were used for the current-voltage (*I-V*) relationships in (**B**). Representative hypotonic conditions increased ML2-SA1 (10 μM)–elicited currents from LE/LY isolated from hTRPML2 expressing HEK293 cells. (**C** and **D**) Representative osmolarity-insensitive inward currents recorded from hTRPML1- or hTRPML3-expressing HEK293 cells. (**E** and **F**) Representative hypotonicity-sensitive TRPML2-like currents recorded from isolated LE/LY from nonactivated (E) and LPS-activated (F) alveolar macrophages. Statistical summary of data, as shown as fold increase compared to the respective currents under physiological osmolarity, is shown as an inset of *I-V* plots. The current amplitudes at −100 mV were extracted from individual ramp current recordings. The numbers of individual organelles are in parentheses. Data are represented as mean ± SEM. **P* < 0.05 and ***P* < 0.01; Student's *t* test, unpaired. n.s., not significant difference.

TRPML2 channel is also sensitive to hypotonic stimulation (Fig. 1, E and F). These data indicate that TRPML2 is a hypotonicity-sensitive cation channel in endolysosomes, both in an overexpression system and in endogenously expressing activated macrophages.

Phosphoinositide binding pocket involved in hypotonicity-sensitivity of TRPML2

The coupling of cellular osmolarity change to pore opening could be mediated by a mechanical stimulus and interactions of a membrane lipid with a binding pocket on the channel (*9*). The binding pockets and interacting mechanisms of phosphatidylinositol phosphates (PIPs) with TRPML1 and TRPML3 have been revealed by cryo–electron microscopy recently (*22*–*25*). Given the irresponsiveness of TRPML1 and TRPML3 to osmolarity changes and the possible involvement of phosphoinositides in connecting membrane tension with channel activity, we hypothesized that the unique osmolarity sensitivity of TRPML2 might be conferred by differences in the channel's $PI(3,5)P_2$binding pocket. Accordingly, we used the published TRPML1 and TRPML3 structures to map these (Fig. 2A). On the basis of the sequence alignment and homology modeling of the $PI(3,5)P_2$binding pocket, we found TRPML2 to share several critical residues required for $PI(3,5)P_2$ activity with TRPML1 and TRPML3 but lacking an arginine at position 314 (TRPML1 R323, TRPML2 L314, and TRPML3 R309; Fig. 2, A and B). The positive charge of arginines in the PIP pocket is likely of functional relevance, providing a charged interaction partner of the negatively charged phosphoinositide head. On the basis of the hypothesis that osmoregulation might be conferred by phosphoinositide recruitment, we reasoned that mutation of L314 into its positively charged TRPML1/3 counterpart would abolish TRPML2 osmoregulation. We subsequently analyzed mutant isoforms L314R and the neighboring, non-PIP–interacting A315G in whole-LE/LY patch-clamp experiments (Fig. 2, B to E). Both A315G and L314R remained responsive to ML-SA1 (Fig. 2, B and D) and ML2-SA1 and $PI(3,5)P_2$ (fig. S3), indicating that the mutant channel remained functional. However, the TRPML2 L314R mutation was found to abolish the effect of hypotonic stress, while its adjacent A315G mutation remained able to sense hypotonic stimulations similar to wild-type (WT) TRPML2 (Fig. 2, C and E). These data suggest that the L314R mutation specifically impairs the channels' responsiveness to changes in cytosolic osmolarity while it does not affect principal activation gating. While this experiment demonstrated that L314 within the phosphoinositide binding site is a crucial determinant of hypotonicity sensing in TRPML2, other channel domains very likely also contribute to this function. In agreement with this hypothesis, introducing leucine residues at positions corresponding to L314 in TRPML1 (R322L) or TRPML3 (R309L) was not sufficient to endow these channels with hypotonicity sensing (fig. S4).

Mechanosensitivity of TRPML2 on endolysosomes

Most mechanosensitive ion channels are regulated by osmotic stress, such as TRP vallinoid (TRPV) and canonical (TRPC) family channels (*26*). To assess whether physical forces mediate TRPML2 activation through affecting the lipid membrane tension, we applied additional pressure (+0.06 ml of a 1-ml syringe; ~+40 mm Hg) into the lumen of the isolated whole organelles with the patch pipette,

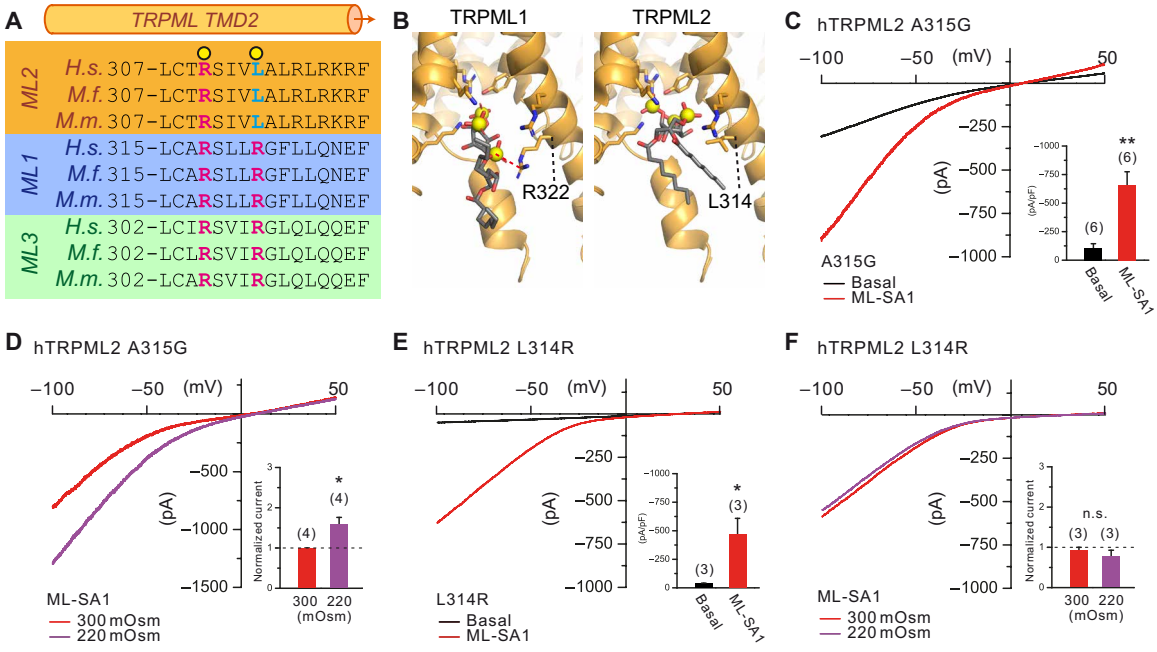

Fig. 2. PIP_2 binding pocket contributes to hypotonicity-sensitive TRPML2 activation. (**A**) Sequence alignment of the PIP_2 binding pocket transmembrane domain 2 (TMD2) of TRPML1-3 as illustrated. To highlight conserved residues, amino acid sequences for *Homo sapiens* (*H.s.*), *Macaca fascicularis* (*M.f.*), and *Mus musculus* (*M.m.*) are shown. Yellow circles mark residues suggested to be essential for $PI(3,5)P_2$ binding at TRPML1 based on the cryo-EM structure and therefore may be necessary for PIP-dependent surface-to-volume ratio sensitivity. Positive charges of $PI(3,5)P_2$-interacting arginines are denoted by pink font color, while cyan marks hydrophilic leucines conserved and present in TRPML2 only. (**B**) Comparison of the TRPML2 homology model PIP binding pocket and that experimentally resolved for TRPML1. In TRPML1, the $PI(3,5)P_2$ C1-phosphate can be seen to interact with R322, while the substitution of the arginine with a leucine in TRPML2 disfavors a similar interaction. (**C** to **F**) Whole-LE/LY recordings of ML-SA1 (10 μM) elicited TRPML2 currents under isotonic or hypotonic conditions from TRPML2 A315G (C and D) and TRPML2 L314R (E and F) expressing HEK293 cells. Data are represented as mean ± SEM. **P* < 0.05, ***P* < 0.01, Student's *t* test, paired.

mimicking the expected increased membrane tension upon hypotonic stimulation. The additional positive pressure increased mechanical membrane tension and, correspondingly, TRPML2 inward cation current amplitudes (Fig. 3). In contrast, the L314R mutant channel did lose not only the sensitivity of hypotonic stimulation but also the mechanosensitivity (Fig. 3, E and F). These data suggest that TRPML2 is activated by hypotonic stimulation and also by mechanical forces in membrane patches.

TRPML2 in recycling endosomes is sensitive to osmolarity changes

As reported recently, TRPML2 promotes trafficking and secretion of the chemokine CCL2 from murine macrophages via the apical endosomal pathway (*18*). To demonstrate the osmosensitivity of TRPML2 in apical endosomes, we cotransfected transferrin receptor (TfR) with TRPML2 and patch-clamped TfR^+ and $TRPML2^+$ RE. Similarly, as demonstrated for LE/LY, TRPML2 currents were increased in TfR^+ RE under hypotonic conditions (fig. S5, A and B). Transferrin (Tf)–loaded RE, isolated from LPS-stimulated alveolar macrophages, likewise showed an increase of TRPML2 channel activity under hypotonic conditions (fig. S5C).

Substantial TRPML2 activities in fast recycling endosomes

We have previously demonstrated that pharmacological TRPML2 activation with ML2-SA1 resulted in a significant enhancement of Tf trafficking and recycling through the apical endosomal system within the first ~5 min, corresponding to the fast recycling pathway (*18*). Rab4A and Rab11A are used to distinguish fast and slow recycling endosomes, with Rab4A mediating rapid recycling and Rab11A mediating slow recycling activities (*27*). We cotransfected TRPML2 with either Rab4A or Rab11A and measured the respective TRPML2 activities. These measurements revealed that TRPML2 channel activities were markedly higher in Rab4A-positive fast RE compared to Rab11A-positive slow RE (Fig. 4), suggesting that TRPML2 is highly active in the fast RE pathway.

The hypotonicity-insensitive TRPML2 mutant isoform L314R slows down the fast recycling pathway

To validate the effect of hypotonicity/mechanosensitivity of TRPML2 in recycling processes, hTRPML2 WT and the hypotonicity/lateral membrane tension-insensitive isoform (L314R) were expressed in HEK293 cells. The cells were pulsed with fluorescently labeled Tf and chased in the presence of unlabeled Tf and the TRPML2 agonist ML2-SA1 (30 μM). The obtained data imply that the loss-of-function (LOF) mutant isoform (hTRPML2 L314R) exhibited a significantly slower Tf recycling rate within the fast recycling time frame (initial 5 min) compared to WT TRPML2 (Fig. 5). Hypothesizing that TRPML2 might accelerate tubulation and vesiculation events in Tf-containing endosomes, we assessed the localization of TRPML2. We found TRPML2 to localize to tubules in both overexpressing

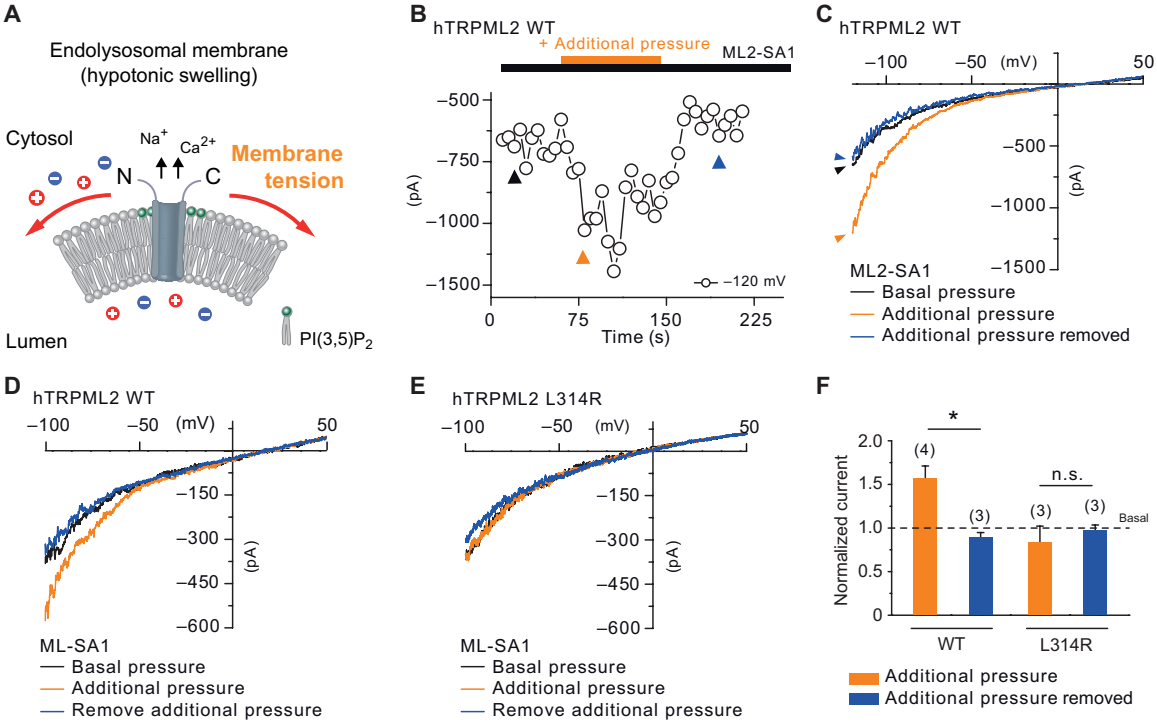

Fig. 3. Mechanical force stimulus-evoked TRPML2 currents. (**A**) Hypotonic stimulation changes the osmotic gradient, which induces swelling and directly increases lateral tension in the lipid bilayer. The hypotonicity/mechanosensitive ion channel converts mechanical stimuli into ion flux. (**B** to **E**) Whole-LY/LE currents were recorded from hTRPML2 WT and L314R mutant isoform-expressing HEK293 cells ± pressure-induced membrane physical force. Time course (B) and representative traces (C) of pressure-enhanced ML2-SA1–evoked currents from TRPML2 WT channels. Additional pressure was directly applied to the membrane patch (+0.06 ml of a 1-ml syringe) and released after 1 min. (D and E) ML-SA1–evoked TRPML2 inward cation currents were increased by additional physical force on LE/LY from TRPML2 WT-expressing HEK293 cells (D) but not from L314R expressing HEK293 cells (E). (**F**) Statistical summary of date as shown as fold increase compared to the respective currents without additional pressure. The numbers of individual organelles are in parentheses. Data are represented as mean ± SEM. *$P < 0.05$, one-way ANOVA, repeated measures, followed by Bonferroni post hoc test.

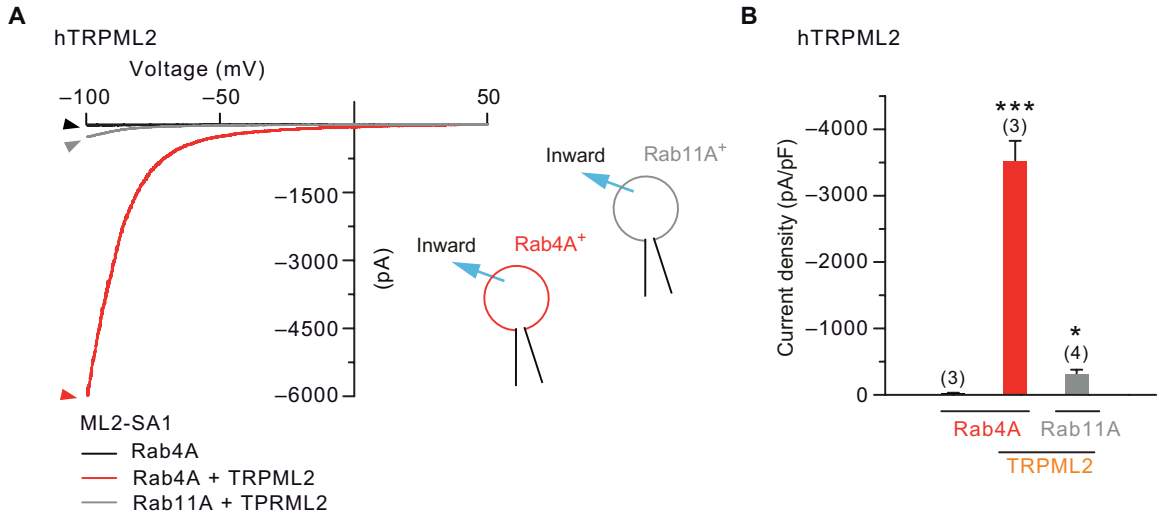

Fig. 4. Whole fast/slow recycling endosome recordings. (**A**) Representative hTRPML2 currents recorded from Rab4A-positive (red) or Rab11A-positive (gray) RE isolated from TRPML2-coexpressing HEK293 cells. (**B**) Statistical summary of data, as shown in A. Numbers of individual organelles are in parentheses. Data are represented as mean ± SEM. *$P < 0.05$ and ***$P < 0.001$; one-way ANOVA, repeated measures, followed by Bonferroni post hoc test.

HEK293 cells and endogenously expressing macrophages (Fig. 5C, fig. S6, and movies S1 to S6). Furthermore, TRPML2-expressing tubular endosomes could be loaded with fluorescent Tf, which were emptied during the chase period (Fig. 5C). Together, our findings show the hypotonicity/membrane lateral tension sensitivity of TRPML2 to be crucial for appropriately regulating TRPML2 activity within the Rab4A fast recycling pathway.

DISCUSSION

In this study, we report that TRPML2 is a hypotonicity-sensitive and mechanosensitive cation channel in intracellular organelles, isolated from either overexpressing HEK293 cells or endogenously expressing activated macrophages. Until now, osmosensitive and mechanosensitive ion channels had not been identified in intracellular compartments. We applied the whole-endolysosome patch-clamp technique to characterize TRPML2 as the only hypotonicity-sensitive ion channel of the TRPML subfamily in the endolysosomal system. Using structure-guided site-directed mutagenesis, we found the TRPML1/TRPML3-like point mutation L314R within the TRPML2 $PI(3,5)P_2$ binding pocket to abrogate TRPML2 osmo/mechanosensitivity. We mutated TRPML1 and TRPML3 at the positions equivalent to L314 in TRPML2, but this did not result in gain of osmosensitive function. Together, our results imply that TRPML2 osmo/mechanosensitivity requires L314, while TRPML1 and TRPML3 require more than a single amino acid substitution to respond to osmotic/mechanical force.

Recent studies have suggested that TRPML2 promotes recycling in innate immune cells (*18*, *21*). Fast recycling of endolysosomal compartments is accompanied by active tubulation, vesiculation, and rapid changes of surface-to-volume ratios. These dynamic changes increase membrane tension in the RE membrane surface during the fast recycling process. Here, we observed that TRPML2 colocalizes with Tf in tubular structures and observe substantial TRPML2 channel activity in Rab4A-positive fast RE compared with Rab11A-positive slow RE. We furthermore observed the LOF mutant L314R to slow down the fast recycling pathway compared to its WT counterpart, likely resulting from high TRPML2 channel activity in fast RE. These findings suggest that osmo/mechanosensitive TRPML2 plays a role in fast recycling pathways, enabling rapid recycling through enhancement of the adaptation processes following the surface-to-volume-ratio-change of tubulation and vesiculation.

On the basis of the studies of hypotonicity-sensitive ion channels in the plasma membrane, hypotonicity-sensitive mammalian TRP channels often sense mechanical stress, such as TRPV2, TRPC1, TRPP2, and TRPM3. Our whole-endolysosomal patch-clamp experiments show that both ~+40 mm Hg and 220 mOsm stimuli further enhance TRPML2 ion flux, the stimuli being close to the typical range of pressure and osmotic challenge for osmo/mechanosensitive TRP channels on the plasma membrane (*28*). Multiple mechanisms of osmo/mechanosensitivity are suggested for plasma membrane TRP channels. The first hypothesis proposes that hypotonic stimuli lead to swelling and increase in membrane tension, causing the membrane lipids to pull away from the channel protein leading to a conformational change of the channel. The second hypothesis suggests that accessory ligands between lipids and channel proteins transduce a response to mechanical forces on the membrane. The third model is an indirect pathway, suggesting that the channel is not directly sensing mechanical forces via lipid-protein interactions.

In contrast, sometimes, mechanical forces result in secondary signaling components (lipases, kinases, and heterotrimeric GTP-binding proteins) to facilitate channel activation pathways such as for TRPV4 (*29*). Mutagenesis experiments suggest that the $PI(3,5)P_2$ binding pocket impacts the mechanism of osmo/mechanosensitivity. However, the scenario underlying the osmo/mechanosensitivity of TRPML2 requires high-speed adaptation pressure (1 mmHg within 10 ms) by endolysosomal patch clamp, which allows precise observation of size changes of the organellar compartment. It remains unlikely that the TRPML2 volume-to-surface ratio sensitivity is mediated by second messengers, which require more time to exert an effect downstream of their activation. The identification of a single amino acid crucial for osmo/mechanosensitivity further supports this conclusion.

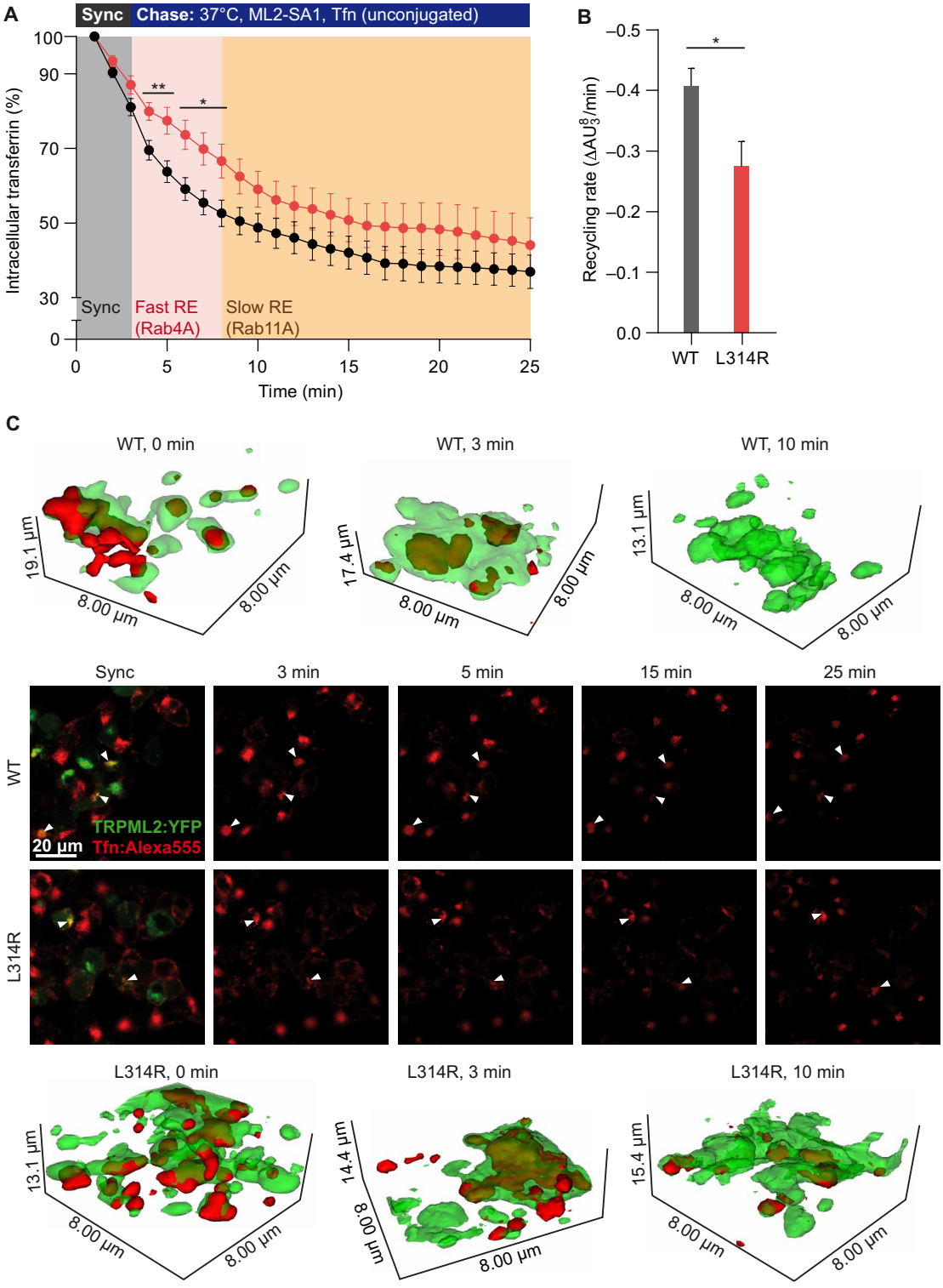

Fig. 5. Cells expressing the hypotonicity/membrane lateral tension-insensitive TRPML2 variant L314R exhibited slower Tf recycling through the fast recycling pathway. Tf trafficking experiments were performed on WT and L314R TRPML2-overexpressing HEK293 cells. (**A**) Plot of intracellular Tf normalized to initially loaded Tf over time, images taken at 1-min intervals. Significantly more Tf remained inside the L314R-mutant cells within the first 5 min of chasing compared to WT-transfected counterparts. (**B**) Calculation of the fast recycling rate (slope for the initial 5 min of recycling) showed the L314R mutant to possess a significantly slower fast recycling rate. (**C**) Two-dimensional images from representative images for data presented in (A) and (B). Arrowheads indicate Tf-positive endosomes expressing TRPML2. The average of three independent experiments is shown. Three-dimensional panels provide higher resolution of Tf (red)–containing endosomes expressing WT or L314R TRPML2 (green) at the indicated time points of chasing (0, 3, and 10 min). Corresponding videos are provided (movies S1 to S6). *$P < 0.05$, **$P < 0.01$, two-way ANOVA, followed by Bonferroni post hoc test for (A) and *t* test for (B).

On the other hand, endolysosomes are dynamic, quasi-spherical organelles in the absence of basic support by the cytoskeleton and filaments. The frequency and rate of variation of size and membrane tension considerably exceed the fluctuations observed at the plasma membrane. Endolysosomal ion channels regulate osmolyte influx and efflux across the organellar membrane and promote surface-to-volume adaptation (*5*). These changes may require a more massive and faster reaction in fast endosomal recycling compartments that rely on sustained rapid trafficking, particularly in the scavenging, surveilling, and signaling macrophages of the innate immune response. These results suggest that the osmo/mechanosensitive TRPML2 may play an essential role in fast recycling and secretion processes of activated innate immune cells.

A growing number of studies imply essential roles for TRPML2 in a number of physiological and pathophysiological processes including innate immune response, adaptive immune response, tumor progression (e.g., glioma), and virus infection (*30*–*32*). Our work reveals a novel and exciting role for TRPML2 in the response to osmo/mechanical stimuli as a way to enhance specific trafficking pathways in macrophages. It may also imply that the surface-to-volume-ratio changes of tubulation and vesiculation of endolysosomes during immune surveillance is necessary to maintain physiological functions in immune cells. In summary, TRPML2 is the first characterized osmo/mechanosensitive endolysosomal ion channel on intracellular membranes, making this channel unique among the other endolysosomal cation channels, particularly its relatives TRPML1 and TRPML3.

MATERIALS AND METHODS

Endolysosomal patch-clamp experiments

Whole-endolysosome recordings have been described previously in detail (*18*–*20*). In brief, for whole-LE/LY patch-clamp recordings, isolated intact vesicles from cells were manually isolated after YM201636 treatment (HEK293 cells, 1 μM o/n; macrophages, 800 nM, 1 hour). For whole-RE patch-clamp recordings, HEK293 cells were transfected with the markers Rab4A-mCherry (for fast-RE) or Rab11A-DsRed (for slow-RE) or TfR-mCherry (for RE), respectively, and treated with 1 μM vacuolin overnight. Human TRPML2 WT, mouse TRPML2 WT, and point mutation isoforms of human TRPML2 [C-terminally fused to yellow fluorescent protein (YFP)] were transiently transfected into HEK293 cells using TurboFect Transfection Reagent (Thermo Fisher Scientific). Preparation of primary alveolar macrophages has been described previously (*18*). Animals were used under approved animal protocols and the University of Munich (LMU) Institutional Animal Care Guidelines. Cells were treated with compounds at 37°C and 5% CO_2. YM201636 was obtained from Chemdea (CD0181), and vacuolin from Santa Cruz Biotechnology (sc-216045). Compounds were washed out before patch-clamp experimentation. Alveolar macrophages were used for experiments within 2 to 10 days after isolation. Currents were recorded using an Axonpatch 200B (Molecular Devices) and pClamp v10 software (Molecular Devices). Data were digitized at 40 kHz and filtered at 2.8 kHz. Capacitive transients were canceled by the compensation circuit of the Axonpatch 200B amplifier.

Recording glass pipettes were polished and had a resistance of 4 to 8 megaohm. Liquid junction potential was corrected. For the application of $PI(3,5)P_2$ (AG Scientific) or small-molecule agonists (ML2-SA1 and ML-SA1), the perfusion system was applied to exchange cytoplasmic solution by cytoplasmic solution containing agonist completely. Unless otherwise stated, the cytoplasmic solution (bath) contained 140 mM K-MSA (methanesulfonate), 5 mM KOH, 4 mM NaCl, 0.39 mM $CaCl_2$, 1 mM EGTA, and 10 mM Hepes (pH was adjusted with KOH to 7.2). Luminal solution (pipette) contained 140 mM Na-MSA, 5 mM K-MSA, 2 mM CaMSA, 1 mM $CaCl_2$, 5 mM Hepes, and 5 mM MES (2-(N-Morpholino)-ethane sulfonic acid) (pH was adjusted with NaOH to 7.2). For optimal recordings of TRPML1, luminal pH was adjusted to 4.6, and Na-MSA was used in the luminal solution. For optimal recordings of TRPML2, luminal pH was adjusted to 7.2, and Na-MSA was used in the luminal solution. For optimal recordings of TRPML3, luminal pH was adjusted to 7.2 and K-MSA. All statistical analysis was done using Origin software.

Tf trafficking assay

HEK293 cells were split on 18-mm glass coverslips coated with poly-L-lysine. Cells were transfected with constructs of interest [hTRPML2(WT):YFP and hTRPML2(L314R):YFP] using TurboFect Transfection Reagent (Thermo Fisher Scientific), according to the manufacturer's instructions. Transfections were left for 18 hours before the experiment.

Upon starting the live-cell Tf trafficking assay, cells were first washed once with phosphate-buffered saline (PBS) (Thermo Fisher Scientific) and starved in serum-free Dulbecco's modified Eagle's medium (DMEM) (Thermo Fisher Scientific) for 30 min at 37°C. Subsequently, cells were washed with PBS and synchronized by incubation in serum-free DMEM for 10 min at 4°C. Cells were washed once more with ice-cold PBS and pulsed with fluorescently labeled Tf-Alexa555 (20 μg/ml) in serum-free medium for 30 min at 37°C. Following the pulse, cells were washed twice with ice-cold PBS, synchronization medium for imaging was added (ice-cold phenol red–free DMEM with Hepes, Thermo Fisher Scientific) and immediately transferred to a Zeiss LSM880 confocal microscope for recording, preequilibrated at 37°C in a temperature-controlled climate chamber. Images were taken using a 63×/1.20 water-based objective/photomultiplier tube detector and a resolution of 1024 × 1024 pixels (pixel size 0.22 μm) to compromise between endosomal (spatial) and temporal resolution. The initial image was taken using the green (488 nm) and red (561 nm) channels for TRPML2:YFP and loaded Tf, respectively. Subsequently, the time lapse acquisition was started, capturing Tf intensities (562 nm) every minute over a 25-min time frame. At 3 min of imaging, the chase was commenced upon adding 37°C medium containing ML2-SA1 (30 μM) and a high-dose unconjugated Tf (200 μg/ml). The analysis was performed using the MeanROI function of ZenBlue, selecting cells expressing TRPML2:YFP for analysis. Loss of fluorescent Tf within the 5 min following the chase (i.e., between 3 and 8 min) was attributed to fast recycling activity, and fast recycling kinetics were calculated on the basis of this time window. Statistical analysis was performed using GraphPad Prism 8. Time lapse plots were analyzed as a repeated-measures analysis of variance (ANOVA) followed post hoc by a Bonferroni test, while recycling rates were analyzed by a Student's *t* test.

For high-resolution images of Tf-loaded tubules, we opted to fix the cells to avoid endosomal movement during image acquisition, which could underlie false-positive identification of endosomal tubules. The experiment was performed as described above, until the addition of synchronization medium. Instead, the cells were either immediately fixed or chased for 10 min [DMEM +30 μM ML2-SA1 and unconjugated Tf (200 mg/ml)]. Fixation was performed using

4% paraformaldehyde (PFA) at room temperature. The cells were rinsed with PBS and mounted on microscope slides. Images were acquired using a Zeiss LSM880 confocal microscope, using a 100×/1.46 oil-based objective, acquiring *z* stacks at 0.34-µm intervals covering the TRPML2-fluorescent area. *Z* stacks were deconvolved using the Fiji plugins "Diffraction PSF 3D" and "Iterative Deconvolve 3D," and regions of interest cropped to 8 µm by 8 µm. Three-dimensional (3D) surfaces were visualized using the Fiji plugin "3D Viewer," applying uniform thresholds, and setting TRPML2 transparency to 0.5.

Immunofluorescence

Preparation of primary murine bone marrow–derived macrophages (BMDMØ) has been described previously (*18*). Animals were used under approved animal protocols and the University of Munich (LMU) Institutional Animal Care Guidelines. BMDMØ were stimulated using LPS (1 µg/ml) and fixed using 2% PFA at room temperature for 30 min. Cells were blocked for 90 min at room temperature (0.5% Triton X-100 and 5% normal goat serum in PBS). The staining solution was prepared as PBS with 0.5% Triton X-100 and 1% normal goat serum. Primary antibody incubation was performed overnight at 4°C using a rabbit primary anti-TRPML2 antibody (gift from R. Puertollano; 1:100 in staining solution). Coverslips were rinsed three times and stained with secondary anti-rabbit Alexa488 for 2 hours at room temperature (1:500 in staining solution; Molecular Probes, 4412S). Coverslips were rinsed with PBS, mounted, and imaged using a Leica SP8 with a 63×/1.40 oil-based objective.

Site-directed mutagenesis

The hTRPML2(WT):YFP pcDNA3.1 construct was initially described recently used by Plesch *et al*. (*18*). Site-directed mutagenesis of hTRPML2 was performed as previously described using the QuikChange II Site-Directed Mutagenesis Kit (Agilent Technologies) according to the manufacturer's instructions. The following primers were employed to generate mutant TRPML2 isoforms: L314R (forward: ACAAGATCCATTGTTCGTGCTCTAAGGTTACGG; reverse: CCGTAACCTTAGAGCACGAACAATGGATCTTGT) and A315G: (forward: AGATCCATTGTTCTTGGTCTAAGGTTACGGAAG; reverse: CTTCCGTAACCTTAGACCAAGAACAATGGATCT).

SUPPLEMENTARY MATERIALS

Supplementary material for this article is available at http://advances.sciencemag.org/cgi/content/full/6/46/eabb5064/DC1

View/request a protocol for this paper from *Bio-protocol*.

REFERENCES AND NOTES

1. F. M. Platt, Sphingolipid lysosomal storage disorders. *Nature* **510**, 68–75 (2014).
2. C. Grimm, E. Butz, C.-C. Chen, C. Wahl-Schott, M. Biel, From mucolipidosis type IV to Ebola: TRPML and two-pore channels at the crossroads of endo-lysosomal trafficking and disease. *Cell Calcium* **67**, 148–155 (2017).
3. E. Lloyd-Evans, A. J. Morgan, X. He, D. A. Smith, E. Elliot-Smith, D. J. Sillence, G. C. Churchill, E. H. Schuchman, A. Galione, F. M. Platt, Niemann-pick disease type C1 is a sphingosine storage disease that causes deregulation of lysosomal calcium. *Nat. Med.* **14**, 1247–1255 (2008).
4. H. Xu, D. Ren, Lysosomal physiology. *Annu. Rev. Physiol.* **77**, 57–80 (2015).
5. S. A. Freeman, S. Uderhardt, A. Saric, R. F. Collins, C. M. Buckley, S. Mylvaganam, P. Boroumand, J. Plumb, R. N. Germain, D. Ren, S. Grinstein, Lipid-gated monovalent ion fluxes regulate endocytic traffic and support immune surveillance. *Science* **367**, 301–305 (2020).
6. S. A. Freeman, S. Grinstein, Resolution of macropinosomes, phagosomes and autolysosomes: Osmotically driven shrinkage enables tubulation and vesiculation. *Traffic* **19**, 965–974 (2018).
7. R. Lipowsky, Spontaneous tubulation of membranes and vesicles reveals membrane tension generated by spontaneous curvature. *Faraday Discuss.* **161**, 305–331; discussion 419–459 (2013).
8. F. K. Voss, F. Ullrich, J. Münch, K. Lazarow, D. Lutter, N. Mah, M. A. Andrade-Navarro, J. P. von Kries, T. Stauber, T. J. Jentsch, Identification of LRRC8 heteromers as an essential component of the volume-regulated anion channel VRAC. *Science* **344**, 634–638 (2014).
9. T. J. Jentsch, VRACs and other ion channels and transporters in the regulation of cell volume and beyond. *Nat. Rev. Mol. Cell Biol.* **17**, 293–307 (2016).
10. E. K. Krogsaeter, M. Biel, C. Wahl-Schott, C. Grimm, The protein interaction networks of mucolipins and two-pore channels. *Biochim. Biophys. Acta Mol. Cell Res.* **1866**, 1111–1123 (2019).
11. C. Grimm, C.-C. Chen, C. Wahl-Schott, M. Biel, Two-pore channels: Catalyzers of endolysosomal transport and function. *Front. Pharmacol.* **8**, 45 (2017).
12. X. Li, N. Rydzewski, A. Hider, X. Zhang, J. Yang, W. Wang, Q. Gao, X. Cheng, H. Xu, A molecular mechanism to regulate lysosome motility for lysosome positioning and tubulation. *Nat. Cell Biol.* **18**, 404–417 (2016).
13. M. Ruas, K. Rietdorf, A. Arredouani, L. C. Davis, E. Lloyd-Evans, H. Koegel, T. M. Funnell, A. J. Morgan, J. A. Ward, K. Watanabe, X. Cheng, G. C. Churchill, M. X. Zhu, F. M. Platt, G. M. Wessel, J. Parrington, A. Galione, Purified TPC isoforms form NAADP receptors with distinct roles for Ca^{2+} signaling and endolysosomal trafficking. *Curr. Biol.* **20**, 703–709 (2010).
14. C.-C. Chen, M. Keller, M. Hess, R. Schiffmann, N. Urban, A. Wolfgardt, M. Schaefer, F. Bracher, M. Biel, C. Wahl-Schott, C. Grimm, A small molecule restores function to TRPML1 mutant isoforms responsible for mucolipidosis type IV. *Nat. Commun.* **5**, 4681 (2014).
15. Y. Sakurai, A. A. Kolokoltsov, C.-C. Chen, M. W. Tidwell, W. E. Bauta, N. Klugbauer, C. Grimm, C. Wahl-Schott, M. Biel, R. A. Davey, Ebola virus. Two-pore channels control Ebola virus host cell entry and are drug targets for disease treatment. *Science* **347**, 995–998 (2015).
16. Y.-K. Chao, V. Schludi, C.-C. Chen, E. Butz, O. N. P. Nguyen, M. Müller, J. Krüger, C. Kammerbauer, M. Ben-Johny, A. M. Vollmar, C. Berking, M. Biel, C. A. Wahl-Schott, C. Grimm, TPC2 polymorphisms associated with a hair pigmentation phenotype in humans result in gain of channel function by independent mechanisms. *Proc. Natl. Acad. Sci. U.S.A.* **114**, E8595–E8602 (2017).
17. O. N. P. Nguyen, C. Grimm, L. S. Schneider, Y.-K. Chao, C. Atzberger, K. Bartel, A. Watermann, M. Ulrich, D. Mayr, C. Wahl-Schott, M. Biel, A. M. Vollmar, Two-pore channel function is crucial for the migration of invasive cancer cells. *Cancer Res.* **77**, 1427–1438 (2017).
18. E. Plesch, C.-C. Chen, E. Butz, A. Scotto Rosato, E. K. Krogsaeter, H. Yinan, K. Bartel, M. Keller, D. Robaa, D. Teupser, L. M. Holdt, A. M. Vollmar, W. Sippl, R. Puertollano, D. Medina, M. Biel, C. Wahl-Schott, F. Bracher, C. Grimm, Selective agonist of TRPML2 reveals direct role in chemokine release from innate immune cells. *eLife* **7**, e39720 (2018).
19. C.-C. Chen, C. Cang, S. Fenske, E. Butz, Y.-K. Chao, M. Biel, D. Ren, C. Wahl-Schott, C. Grimm, Patch-clamp technique to characterize ion channels in enlarged individual endolysosomes. *Nat. Protoc.* **12**, 1639–1658 (2017).
20. C.-C. Chen, E. S. Butz, Y.-K. Chao, Y. Grishchuk, L. Becker, S. Heller, S. A. Slaugenhaupt, M. Biel, C. Wahl-Schott, C. Grimm, Small molecules for early endosome-specific patch clamping. *Cell Chem. Biol.* **24**, 907–916.e4 (2017).
21. L. Sun, Y. Hua, S. Vergarajauregui, H. I. Diab, R. Puertollano, Novel role of TRPML2 in the regulation of the innate immune Response. *J. Immunol.* **195**, 4922–4932 (2015).
22. X. Zhou, M. Li, D. Su, Q. Jia, H. Li, X. Li, J. Yang, Cryo-EM structures of the human endolysosomal TRPML3 channel in three distinct states. *Nat. Struct. Mol. Biol.* **24**, 1146–1154 (2017).
23. M. Hirschi, M. A. Herzik Jr., J. Wie, Y. Suo, W. F. Borschel, D. Ren, G. C. Lander, S.-Y. Lee, Cryo-electron microscopy structure of the lysosomal calcium-permeable channel TRPML3. *Nature* **550**, 411–414 (2017).
24. Q. Chen, J. She, W. Zeng, J. Guo, H. Xu, X.-c. Bai, Y. Jiang, Structure of mammalian endolysosomal TRPML1 channel in nanodiscs. *Nature* **550**, 415–418 (2017).
25. M. Li, W. K. Zhang, N. M. Benvin, X. Zhou, D. Su, H. Li, S. Wang, I. E. Michailidis, L. Tong, X. Li, J. Yang, Structural basis of dual Ca^{2+}/pH regulation of the endolysosomal TRPML1 channel. *Nat. Struct. Mol. Biol.* **24**, 205–213 (2017).
26. R. Jiao, D. Cui, S. C. Wang, D. Li, Y.-F. Wang, Interactions of the mechanosensitive channels with extracellular matrix, integrins, and cytoskeletal network in osmosensation. *Front Mol. Neurosci.* **10**, 96 (2017).
27. S. Pfeffer, Membrane domains in the secretory and endocytic pathways. *Cell* **112**, 507–517 (2003).
28. M. Jin, J. Berrout, R. G. O'Neil, chap. 16: Regulation of TRP channels by osmomechanical stress, in *TRP Channels*, M. X. Zhu, Ed. (CRC Press, 2011), pp. 353–373.
29. J. Vriens, H. Watanabe, A. Janssens, G. Droogmans, T. Voets, B. Nilius, Cell swelling, heat, and chemical agonists use distinct pathways for the activation of the cation channel TRPV4. *Proc. Natl. Acad. Sci. U.S.A.* **101**, 396–401 (2004).

30. M. P. Cuajungco, J. Silva, A. Habibi, J. A. Valadez, The mucolipin-2 (TRPML2) ion channel: A tissue-specific protein crucial to normal cell function. *Pflugers Arch.* **468**, 177–192 (2016).
31. M. B. Morelli, M. Nabissi, C. Amantini, D. Tomassoni, F. Rossi, C. Cardinali, M. Santoni, A. Arcella, M. A. Oliva, A. Santoni, C. Polidori, M. P. Mariani, G. Santoni, Overexpression of transient receptor potential mucolipin-2 ion channels in gliomas: role in tumor growth and progression. *Oncotarget* **7**, 43654–43668 (2016).
32. N. Rinkenberger, J. W. Schoggins, Mucolipin-2 cation channel increases trafficking efficiency of endocytosed viruses. *mBio* **9**, e02314-17 (2018).

Acknowledgments: We acknowledge B. Spix for providing the expertise required for the Tf trafficking assay and valuable advice in adapting it for live-cell imaging. We thank B. Noack for excellent technical assistance. We appreciate the encouragement and comments from C. Schön, Y.-K. Chao, and other members of the Biel and Grimm laboratories. **Funding:** This work was supported, in part, by funding of the German Research Foundation, DFG (project number 239283807 and SFB/TRR152 projects P04 to C.G., P06 to C.W.-S., and P12 to M.B.) and the University of Pennsylvania Orphan Disease Center and the Mucolipidosis IV Foundation Grant MDBR-17-120-ML4 to C.G. **Author contributions:** C.-C.C. designed the study and performed electrophysiological experiments. C.-C.C. and E.K. wrote the manuscript. E.K. designed and performed trafficking assays and mutagenesis experiments. E.S.B., Y.L., and R.P. provided the expertise and materials required for primary cells and cell preparation. M.B. and C.G. provided resources, funding, and edited the manuscript. All of the authors discussed the results and proofread the manuscript. **Competing interests:** The authors declare that they have no competing interests. **Data and materials availability:** All data needed to evaluate the conclusions in the paper are present in the paper. Additional data related to this paper may be requested from the authors.

Submitted 28 February 2020
Accepted 24 September 2020
Published 11 November 2020
10.1126/sciadv.abb5064

Citation: C.-C. Chen, E. Krogsaeter, E. S. Butz, Y. Li, R. Puertollano, C. Wahl-Schott, M. Biel, C. Grimm, TRPML2 is an osmo/mechanosensitive cation channel in endolysosomal organelles. *Sci. Adv.* **6**, eabb5064 (2020).

Science Advances

TRPML2 is an osmo/mechanosensitive cation channel in endolysosomal organelles

Cheng-Chang Chen, Einar Krogsaeter, Elisabeth S. Butz, Yanfen Li, Rosa Puertollano, Christian Wahl-Schott, Martin Biel and Christian Grimm

Sci Adv **6** (46), eabb5064.
DOI: 10.1126/sciadv.abb5064

Manuscript IV

Human genome diversity data reveal that L564P is the predominant TPC2 variant and a prerequisite for the blond hair associated M484L gain-of-function effect
Julia Böck*, **Einar K. Krogsaeter***, Marcel Passon, Yu-Kai Chao, Sapna Sharma, Harald Grallert, Annette Peters, & Christian Grimm
PLOS Genetics. 2021;17(1):e1009236

PLOS GENETICS

RESEARCH ARTICLE

Human genome diversity data reveal that L564P is the predominant TPC2 variant and a prerequisite for the blond hair associated M484L gain-of-function effect

Julia Böck[1☯], Einar Krogsaeter[1☯], Marcel Passon[1], Yu-Kai Chao[1], Sapna Sharma[2], Harald Grallert[2], Annette Peters[2], Christian Grimm[1]*

1 Walther Straub Institute of Pharmacology and Toxicology, Faculty of Medicine, Ludwig-Maximilians-Universität, Munich, Germany, **2** Helmholtz Zentrum–Deutsches Forschungszentrum für Gesundheit und Umwelt (GmbH), Institute of Epidemiology, Neuherberg, Germany

☯ These authors contributed equally to this work.
* christian.grimm@med.uni-muenchen.de

Citation: Böck J, Krogsaeter E, Passon M, Chao Y-K, Sharma S, Grallert H, et al. (2021) Human genome diversity data reveal that L564P is the predominant TPC2 variant and a prerequisite for the blond hair associated M484L gain-of-function effect. PLoS Genet 17(1): e1009236. https://doi.org/10.1371/journal.pgen.1009236

Editor: Elena Oancea, Brown University, UNITED STATES

Received: May 6, 2020

Accepted: October 29, 2020

Published: January 19, 2021

Peer Review History: PLOS recognizes the benefits of transparency in the peer review process; therefore, we enable the publication of all of the content of peer review and author responses alongside final, published articles. The editorial history of this article is available here: https://doi.org/10.1371/journal.pgen.1009236

Data Availability Statement: All relevant data are within the manuscript and its Supporting Information files.

Abstract

The endo-lysosomal two-pore channel (TPC2) has been established as an intracellular cation channel of significant physiological and pathophysiological relevance in recent years. For example, TPC2$^{-/-}$ mice show defects in cholesterol degradation, leading to hypercholesterinemia; TPC2 absence also results in mature-onset obesity, and a role in glucagon secretion and diabetes has been proposed. Infections with bacterial toxins or viruses e.g., cholera toxin or Ebola virus result in reduced infectivity rates in the absence of TPC2 or after pharmacological blockage, and TPC2$^{-/-}$ cancer cells lose their ability to migrate and metastasize efficiently. Finally, melanin production is affected by changes in hTPC2 activity, resulting in pigmentation defects and hair color variation. Here, we analyzed several publicly available genome variation data sets and identified multiple variations in the TPC2 protein in distinct human populations. Surprisingly, one variation, L564P, was found to be the predominant TPC2 isoform on a global scale. By applying endo-lysosomal patch-clamp electrophysiology, we found that L564P is a prerequisite for the previously described M484L gain-of-function effect that is associated with blond hair. Additionally, other gain-of-function variants with distinct geographical and ethnic distribution were discovered and functionally characterized. A meta-analysis of genome-wide association studies was performed, finding the polymorphisms to be associated with both distinct and overlapping traits. In sum, we present the first systematic analysis of variations in TPC2. We functionally characterized the most common variations and assessed their association with various disease traits. With TPC2 emerging as a novel drug target for the treatment of various diseases, this study provides valuable insights into ethnic and geographical distribution of TPC2 polymorphisms and their effects on channel activity.

Funding: This work was supported, in part, by funding of the German Research Foundation DFG (SFB/TRR152 project P04 to CG and GR-4315/4-1 to CG) and by the NCL (Neuronal Ceroid Lipofuscinosis) Foundation, Hamburg, Germany. The funders had no role in study design, data collection and analysis, decision to publish, or preparation of the manuscript.

Competing interests: The authors declare that they have no conflict of interest.

Author summary

The endo-lysosomal cation channel TPC2 is implicated in numerous human diseases ranging from metabolic disease, Parkinson's disease, cancer and pigmentation defects, to infectious diseases such as Ebola, Covid-19, and bacterial infections. Here, we present a functional analysis of several polymorphisms occurring in the human TPC2 protein in distinct populations. By evaluating several human genome databases, we identified a large number of single nucleotide polymorphisms in TPC2. We electrophysiologically characterized the most common polymorphisms by applying the endo-lysosomal patch-clamp technique. We thereby identified several novel gain-of-function variants and found the TPC2 variation L564P to be a prerequisite for the previously described M484L gain-of-function effect associated with blond hair. In addition, publicly available genome-wide association study databases were assessed, and linked traits of the investigated TPC2 polymorphisms interrogated. Considering that different human populations have a different likelihood of carrying the identified gain-of-function variations, these findings appear highly relevant for further assessment of TPC2 as a pharmacological drug target.

Introduction

DNA variants are traditionally divided into DNA mutations and single nucleotide polymorphisms (SNPs), based on their occurrence in <1% and >1% of the population, respectively. Variations with a proven effect on gene function are also termed functional polymorphisms. Such functional polymorphisms may impact development of disease or response to pathogens, chemicals, vaccines or drugs. This is particularly important in the context of personalized medicine, as gene variation can affect, e.g. drug metabolism or side effects. Biomedical research is increasingly focusing on a better understanding of the functional relevance of such variations and their association with diseases and therapies. For instance, variations associated with a certain disease in one population may appear harmless or are irrelevant in other populations. One famous example is malaria resistance in people carrying certain variations in hemoglobin, which on the one hand results in sickle-cell anemia, but on the other hand is a selection advantage, at least for heterozygous carriers, in geographic regions where malaria is prevalent [1,2]. As with other genetic variations, functional variations in TPC2 may also impact health and survival under certain environmental conditions and in certain geographical areas, while in others they might not.

The two-pore cation channel (TPC2) has recently emerged as an intracellular ion channel of significant physiological and pathophysiological relevance. TPC2 has been associated with various essential functions in endo-lysosomes, such as trafficking, autophagy, exocytosis, and lysosomal cation/pH homeostasis [3–6]. Accordingly, changes to its function bear consequences for numerous diseases, e.g. infectious diseases in which viruses or bacterial toxins are trafficked through the endo-lysosomal system [7–9], metabolic diseases caused by defects in endo-lysosomal trafficking or cargo degradation[10,11], cancer [12–16], or pathologies involving lysosome-related organelles such as platelet dense granules [17], melanosomes [18,19], or cytolytic granules [20]. Recently, two variations in TPC2 associated with hair pigmentation defects were found to be gain-of-function (GOF) variants: rs35264875 (encoding M484L) results in an increased sensitivity to the endogenous TPC2 ligand $PI(3,5)P_2$, while rs3829241 (encoding G734E) results in reduced channel inhibition by ATP [21]. Given their direct functional relevance to channel activity, and the link between channel function and various diseases, we predict TPC2 polymorphisms confer traits which can be acted upon by various

selection pressures. For example, TPC2 GOF polymorphisms could represent risk factors, enhancing endosomal trafficking and predisposing carriers to infections [7–9,22]. Furthermore, since TPC2 activity has been implicated in glucose homeostasis, altered TPC2 activity may correlate with the development of diabetes mellitus [23–25].

In an attempt to assess the global distribution of TPC2 variations in humans, we analyzed several human genome datasets: the Simons Genome Diversity Project (SGDP) dataset, comprising genomes of 279 individuals from 142 indigenous populations in Africa, Europe, Asia, Australia, Oceania, and America [26], the 1000 Genome Project dataset (1000GP, 2504 genomes) [27], and the gnomAD data set (~140.000 genomes) [28]. We screened these datasets for polymorphisms in TPC2 and other endo-lysosomal cation channels, namely TPC1, TRPML1, TRPML2, and TRPML3. We found that TPC2 variations are more frequent than variations in the other channels. One variation in TPC2, L564P, occurs much more frequently on a global scale than the nominal "wild-type" TPC2 isoform. Other variations were found to occur in more geographically restricted manners. Unexpectedly, we found L564P to be a prerequisite for the blond hair-associated M484L variant to exert its GOF effect, as demonstrated by endo-lysosomal patch-clamp electrophysiology. Furthermore, additional variants were found to occur frequently in a homozygous manner with distinct ethnic or geographical distribution. While some of these variations had no apparent effect on channel activity, others showed increased sensitivity to the endogenous TPC2 ligand $PI(3,5)P_2$, akin to the previously characterized M484L polymorphism. These results reveal a functional diversity of TPC2 between distinct populations, with potential relevance in manifestation and progression of TPC2-associated diseases.

Results

L564P is the predominant TPC2 variant on a global scale

We used the data provided by SGDP, 1000GP, and gnomAD to assess the occurrence of variations in the sequence of TPC2 and its related endo-lysosomal cation channels TPC1, TRPML1, TRPML2, and TRPML3 across different populations and ethnicities. In the SGDP dataset, 22 variations were identified for TPC2, while only 7 were found for TPC1 and TRPML1 each, 10 for TRPML2, and 5 for TRPML3 (Figs 1A and 1B and S1). One of the identified variations in TPC2, L564P, was found with particularly high frequency (Figs 1A, 1C, 1D, 2E and 2G). Other homozygous variations found to occur with increased frequency in TPC2 in the SGDP data set were V219I, K376R, G387D, M484L, and G734E. The polymorphisms V219I, M484L and G734E are frequently present in European populations (Fig 2A, 2D, 2F and 2G). G387D showed a low frequency across most populations (Fig 2C and 2G), while K376R (Fig 2B and 2G) showed comparably high frequencies across all populations with the exception of Native Americans, who over all showed low TPC2 variation rates in their genomes (Fig 2G). L564P occurs at a very high frequency in a homozygous manner on a global scale except for Native Americans and some African and Asian populations. Nearly all European SGDP samples were found to be homozygous for L564P, with only one sampled Hungarian being heterozygous for L564P. Similarly, in most Asian, African, Australian and Oceanian populations, the homozygous L564P variant predominates (Fig 2G).

Analysis of the 1000GP and the gnomAD datasets confirmed the SGDP dataset findings, including the very high frequency of the L564P variation across all populations (Figs 3 and S2 and S3). Like the SGDP dataset, the 1000GP dataset revealed a higher variation frequency in TPC2 (63 SNPs) compared to TPC1 (33 SNPs), TRPML1 (34 SNPs), TRPML2 (34 SNPs), and TRPML3 (31 SNPs) (S2 Fig). Accordingly, the gnomAD dataset supported these observations, revealing higher variation frequencies for TPC2 (412 SNPs) compared to TPC1 (381),

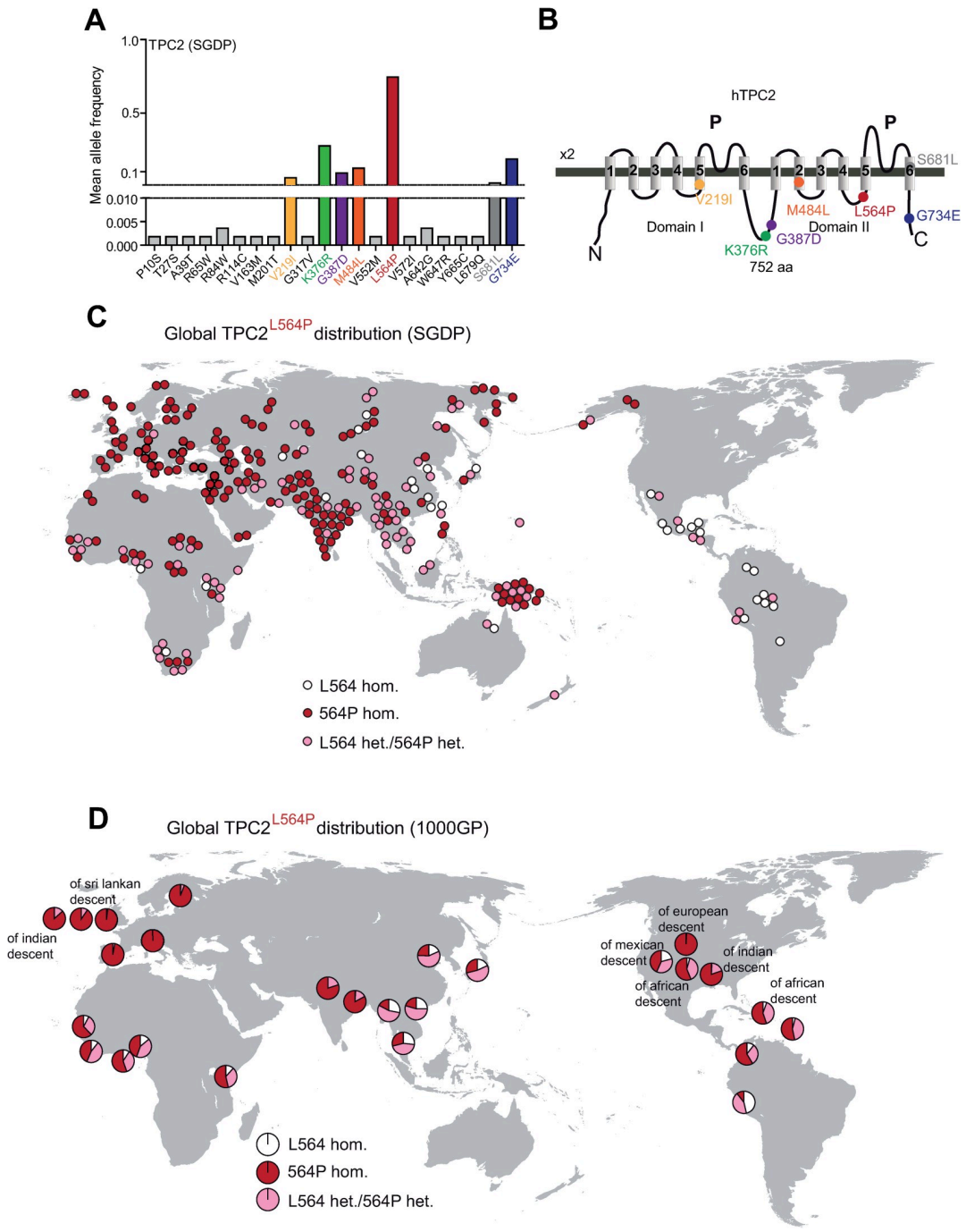

Fig 1. Analysis of the sequencing data derived from the SGDP data set and the 1000GP data set. (A) Mean allele frequency in the Simons Genome Diversity Project (SGDP) data set of all homozygous (colored) and heterozygous SNPs in the TPC2 gene leading to a missense mutation. (B) Cartoon showing the estimated positions of the polymorphisms in the human TPC2 protein. (C) Map of the worldwide distribution of $TPC2^{L564P}$ in the SGDP data set. Each circle represents one individual from an indigenous population, respectively. White circles represent individuals homozygous for $TPC2^{P564L}$, red circles represent individuals homozygous for $TPC2^{L564P}$, and pink circles represent heterozygous individuals. (D) Map of the worldwide distribution of $TPC2^{L564P}$ in the 1000GP data set. Each circle represents one of the 26 populations (indigenous or non-indigenous (other descent) as indicated). Color coding scheme corresponds to the one in (C).

https://doi.org/10.1371/journal.pgen.1009236.g001

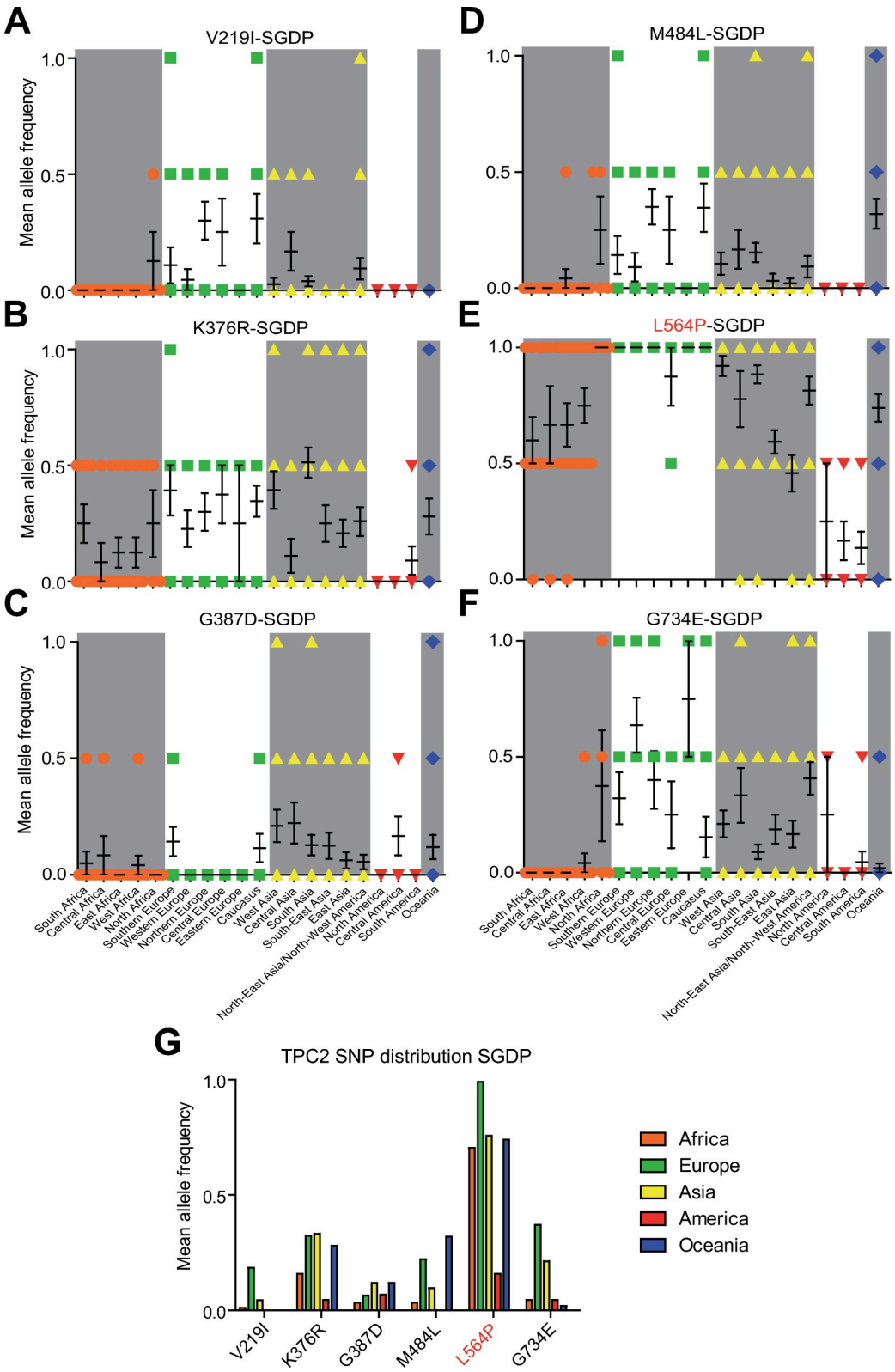

Fig 2. Geographical distribution of all homozygous TPC2 SNPs found in the SGDP data set. The 297 samples were grouped according to their geographic origin. (A-F) Mean allele frequency of each SNP (mean ± SEM) grouped by geographic region, each symbol (circle, square, triangle) represents one sample (G) Mean allele frequency of each SNP grouped by continent.

https://doi.org/10.1371/journal.pgen.1009236.g002

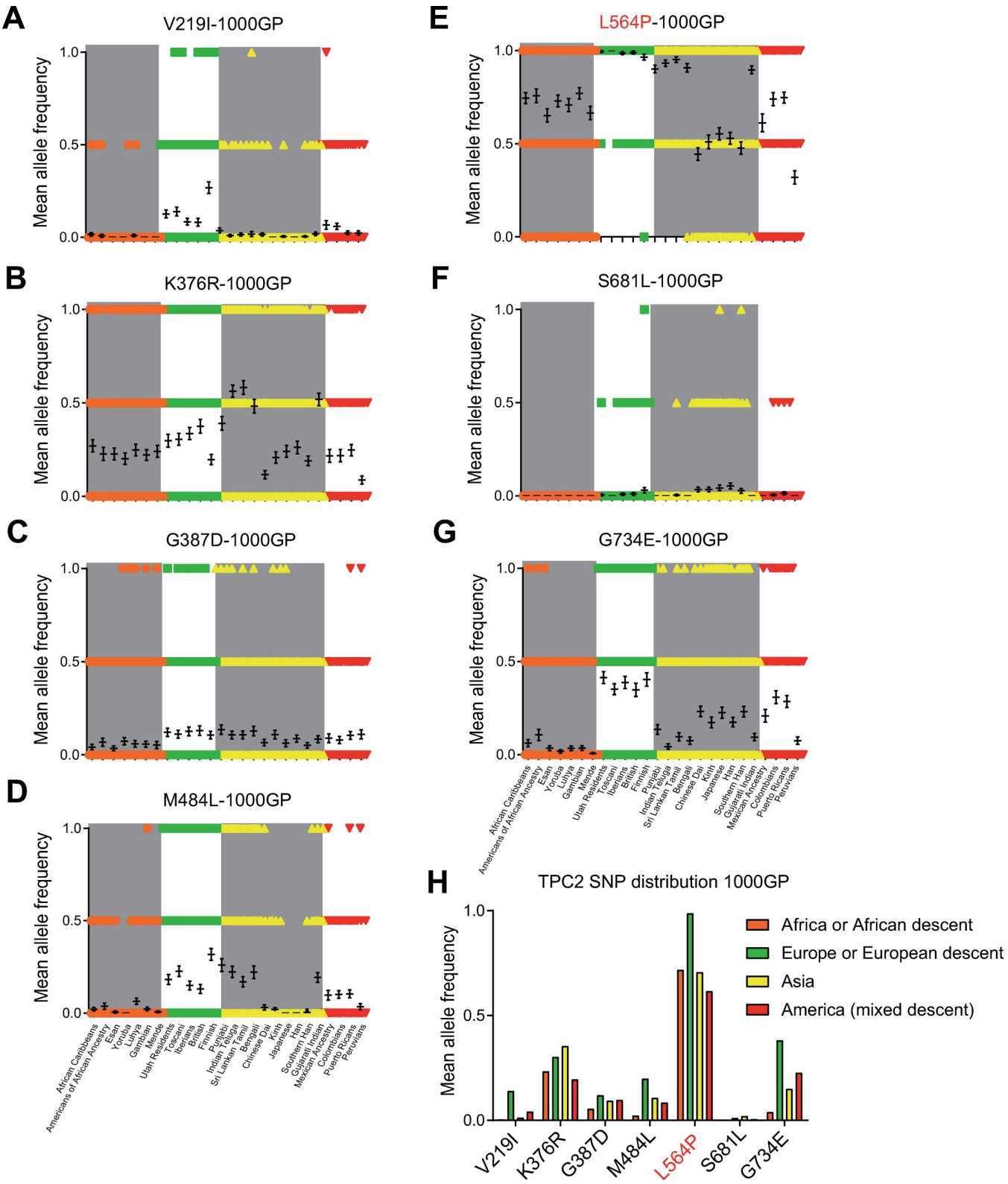

Fig 3. Geographical distribution of all homozygous TPC2 SNPs found in the 1000GP data set. The 2054 samples were grouped according to geographic origin. (A-G) Mean allele frequency of each SNP (mean ± SEM) in each population grouped by geographic region, each symbol (circle, square, triangle, rhombus) represents one sample. (H) Mean allele frequency of each SNP grouped by continent.

https://doi.org/10.1371/journal.pgen.1009236.g003

TRPML1 (272), TRPML2 (278), and TRPML3 (260) (S3 Fig). In general, variations were more frequent in TPC2 compared to the other endo-lysosomal cation channels (S1–S3 Figs). In addition to the homozygously occurring variations in TPC2 in the SGDP dataset (V219I, K376R, G387D, M484L, L564P, and G734E), another variation, S681L, was found to occur in a homozygous manner in the 1000GP and gnomAD datasets. This variation occurs mainly in Han Chinese and Japanese samples (Figs 3 and S2 and S3). Homozygously occurring variations were less frequent in other endolysosomal ion channels. In the 1000GP dataset, only one homozygously occurring variation was found in TPC1 (G803W) and three in TRPML2 (V20I, M365V, and K370Q), but none in TRPML1 and TRPML3 (S2 Fig). Only in the gnomAD dataset, homozygously occurring variations were found for TRPML1 and TRPML3 (S3 Fig). Neither of the homozygously occurring TRPML1 variations are known to cause mucolipidosis type IV, a rare neurodegenerative lysosomal storage disease caused by certain TRPML1 mutations [29,30]. For TRPML2 and TRPML3, homozygous premature stop codon variants were detected, revealing the existence of people with complete loss of either TRPML2 or TRPML3 channels.

TPC2 in ancient human genomes and in evolution

Next, we analyzed published genome sequencing data from ancient samples. In Neanderthal, Denisovan, and ancient modern humans, both L564 and 564P were present. Again, 564P occurred with higher frequency, suggesting that at least in the last 40.000 to 50.000 years, the occurrence and geographical distribution of L564 versus 564P was not very different from contemporary samples. An analysis of TPC2 variations in non-human primates revealed that all assessed primate reference genomes have the L564P variation, suggesting an evolutionary conserved high prevalence of 564P (S4 Fig).

TPC2 variations have predominantly developed on the background of L564P

The structure of the human TPC2 channel was recently described, pinpointing amino acid 564 to be present on the five-residue 2TMD4/2TMD5 (IIS4-S5) loop, which is of importance in channel gating [31]. As position 564 is located on a critical part of the protein, we assessed channel function of the $TPC2^{L564P}$ in comparison to the "wildtype" variant, $TPC2^{P564L}$ by using the endo-lysosomal patch-clamp technique. Stimulation of both variants with the endogenous TPC2 agonist, $PI(3,5)P_2$, revealed no significant difference in channel conductance (Figs 4A, 4B and 5H). However, the genomic data analysis demonstrated that individuals homozygous for 564P have an increased likelihood of carrying additional homozygous variations in TPC2 (Fig 4C–4H). Only one SNP, S681L, predominantly found in East Asian populations, appeared associated with the L564 background (Fig 4H). Taking this into consideration, we re-evaluated the human donor fibroblast samples used by Chao et al. (2017) for studying the GOF variations of TPC2. We found that all fibroblasts were homozygous for the L564P polymorphism, and that the cDNA originally isolated from HEK293 cells used by Chao et al. (2017) was likewise homozygous for L564P [21]. Therefore, the question arose whether amino acid 564 may affect the recently described GOF variation of TPC2, namely $TPC2^{M484L}$.

L564P is essential for the blond hair associated GOF effect of M484L

Surprisingly, in endo-lysosomal patch-clamp experiments we found that M484L only acts as a GOF variant on the 564P, but not on the L564, background (Fig 5A, 5B and 5H). Thus, $PI(3,5)P_2$-elicited currents in the $TPC2^{M484L/P564L}$ variant were not significantly different from $TPC2^{P564L}$ ("wild type") or $TPC2^{L564P}$, while $TPC2^{M484L/L564P}$ showed a GOF effect as reported

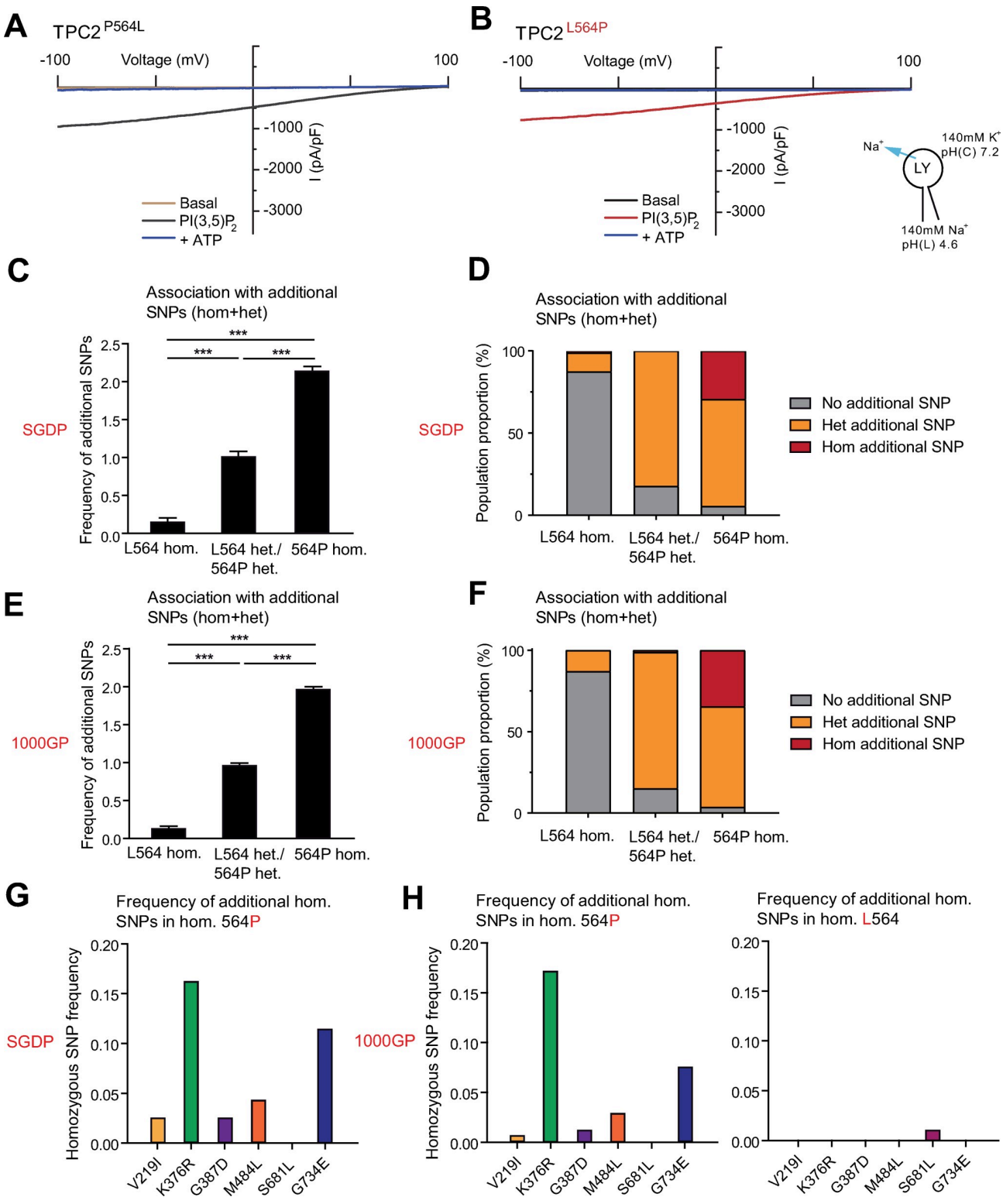

Fig 4. TPC2^{L564P} in association with other TPC2 SNPs. (A, B) Representative PI(3,5)P_2 (1 μM) activated current densities in vacuolin-enlarged lysosomal vesicles expressing TPC2^{L564P} or TPC2^{P564L} and the corresponding currents after block with ATP (1 mM). (C-F) Frequency of other homozygous and heterozygous TPC2 SNPs on either L564 or 564P background. (C, D) Results from the SGDP data set. (E, F) Results from the 1000GP data set. (G-H) Frequency of homozygous SNPs on either L564 or 564P background in the SGDP data set or the 1000GP data set.

https://doi.org/10.1371/journal.pgen.1009236.g004

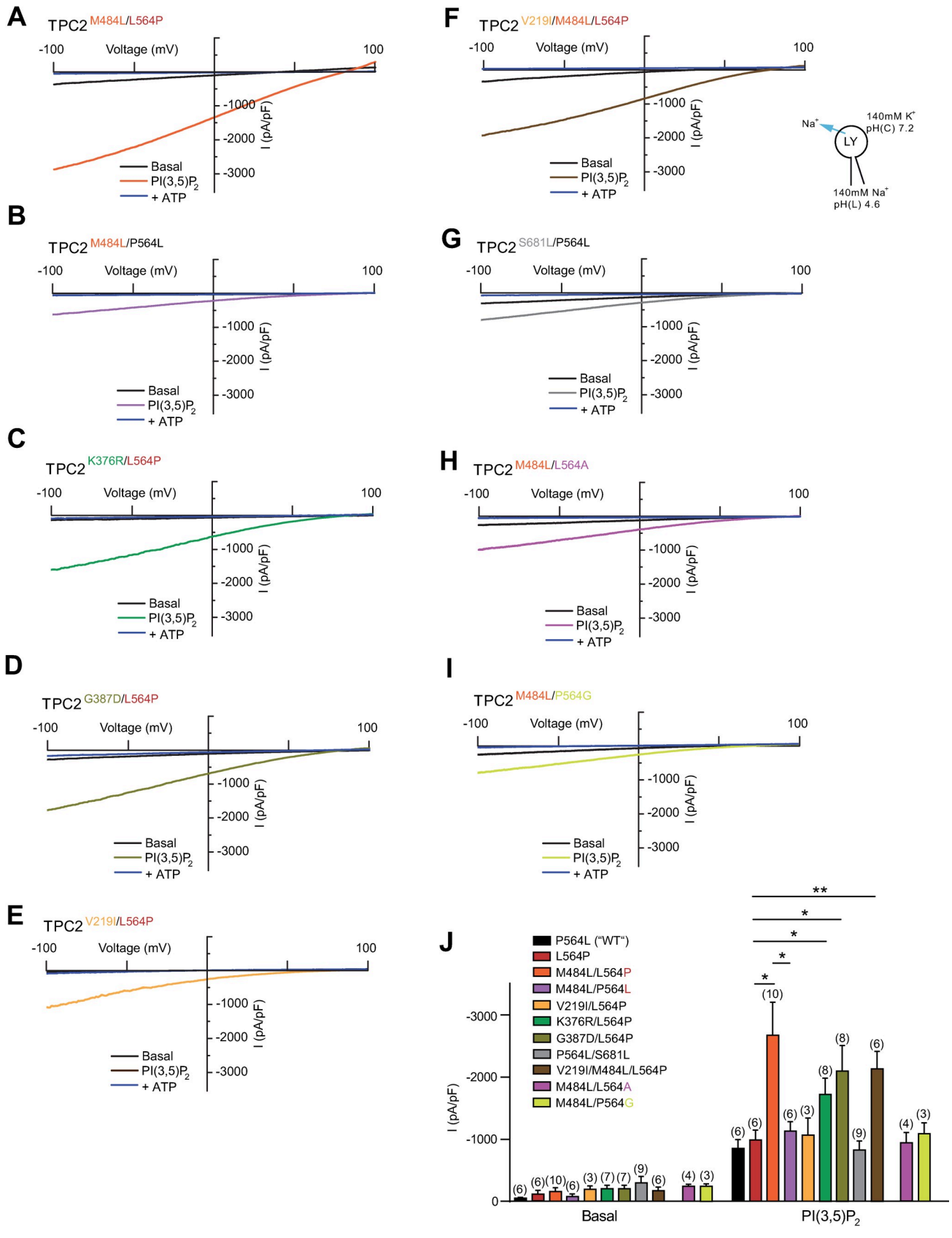
A
TPC2 M484L/L564P
B
TPC2 M484L/P564L
C
TPC2 K376R/L564P
D
TPC2 G387D/L564P
E
TPC2 V219I/L564P
F
TPC2 V219I/M484L/L564P
G
TPC2 S681L/P564L
H
TPC2 M484L/L564A
I
TPC2 M484L/P564G
-100
Voltage (mV)
100
-1000
-2000
-3000
I (pA/pF)
Basal
PI(3,5)P2
+ ATP
Na+
140mM K+
pH(C) 7.2
LY
140mM Na+
pH(L) 4.6
J
P564L ("WT")
L564P
M484L/L564P
M484L/P564L
V219I/L564P
K376R/L564P
G387D/L564P
P564L/S681L
V219I/M484L/L564P
M484L/L564A
M484L/P564G
I (pA/pF)
Basal
PI(3,5)P2

Fig 5. Effect of PI(3,5)P_2 on different variations of TPC2. (A-I) Representative PI(3,5)P_2 (1 μM) activated current densities in vacuolin-enlarged lysosomal vesicles isolated from HEK293 cells overexpressing different human TPC2 variants and the corresponding currents after block with ATP (1 mM). (J) Statistical summary of data as shown in A-I and in Fig 4A and 4B. Shown are average current densities (mean ± SEM) at -100 mV. Unpaired t-test were applied. $^{*}p < 0.05$ and $^{**}p < 0.01$.

https://doi.org/10.1371/journal.pgen.1009236.g005

previously [21]. To further elucidate the surprising finding that M484L only results in a GOF in combination with proline at position 564, we applied site-directed mutagenesis and found that introduction of prolines up- or downstream of 564, i.e., at position 563 or 565, did not result in GOF in combination with M484L (S7A and S7B Fig). Furthermore, we tested 564A and 564G in combination with M484L. As expected, alanine showed no GOF effect in combination with M484L. Also glycine, which may act as a helix breaker, albeit milder than proline, showed no GOF effect (Fig 5H–5J). These data suggest that only a strong helix breaking amino acid (P) but not A, L or G is capable of mediating the observed GOF effect in combination with 484L. Based on the recently resolved hTPC2 (M484/564P) cryo-EM structure [31] it is evident that L564P is situated directly between M484L and the channel pore. We therefore assume the M484L-associated GOF to be transduced through the L564P-encoding IIS4-S5 linker, dilating the channel pore further upon PI(3,5)P_2 activation. The IIS4-S5 linker has already been implicated in channel gating, as an extension of the IIS4-S5 linker appears necessary to provide space for pore dilation and channel opening. Substituting the helix-initiating 564P with a leucine would dramatically affect this linker helix extension. We therefore propose a model where M484L is amplifying the effect of PI(3,5)P_2 activation, requiring signal transduction through L564P to result in pore dilation. However, to confirm this, comparative cryo-EM of polymorphic channels and/or molecular dynamics simulations would be required (S7C Fig).

In addition to the GOF variant TPC2$^{M484L/P564L}$, endo-lysosomal patch-clamp experimentation revealed two further variants that showed moderately increased activation levels after stimulation with PI(3,5)P_2 compared to control: TPC2$^{K376R/L564P}$ and TPC2$^{G387D/L564P}$ (Fig 5C, 5D and 5J). Both combinations occur in several populations with similar frequency, but are the least common in African, and Native American populations (Figs 2 and 3). In contrast, the variant TPC2$^{V219I/L564P}$, mainly found in European populations, showed no significant difference compared to TPC2^{L564P}, nor did the V219I polymorphism appear to affect the GOF effect of its associated SNP M484L (Fig 5E, 5F and 5J). As noted previously, the SNP S681L was only found on the L564 background in contrast to all other homozygously occurring variations. TPC2$^{P564L/S681L}$ is predominantly found in East Asian populations. Albeit showing a trend towards increased basal activity, the activity level of the TPC2$^{P564L/S681L}$ variant upon stimulation with PI(3,5)P_2 was not significantly different from control, i.e., TPC2^{P564L} (Fig 5G and 5J). By contrast, the blond-hair associated GOF variant TPC2$^{M484L/L564P}$ is barely found among East Asians and mainly present in European, Caucasian and West Asian populations (S5 Fig). All variants showed similar subcellular localization, highly correlating with lysotracker localization. In addition, no significant expression differences in western blot analysis were found (S6 Fig).

Functional analysis of TPC2 SNPs in endogenously expressing human donor fibroblast samples

As a next step we wanted to confirm these findings in endogenously expressing cells. 136 human donor samples were genotyped [21] out of which, nine donor fibroblast samples were collected for subculture and further experimentation. All fibroblast donors were of Caucasian/European origin. In accordance with the interrogated genome databases, all donor samples

were homozygous for L564P (S8A Fig). Likewise, as expected, neither of the donors carried the East Asian variant S681L. Four donors (donor 1, 2, 5, and 8) were homozygous for M484L. All four were simultaneously either homo- or heterozygous for V219I, a SNP not significantly affecting basal or $PI(3,5)P_2$-stimulated channel activity. Of the four M484L donors, three were blond, and one brown-haired, in accordance with previously published data [21]. Another blond-haired donor reported previously [21] was homozygous for G734E (donor 6). Donors 3 and 9 were both heterozygous for K376R and G387D. Donor 4 was homozygous for K376R and donor 7 homozygous for G387D (S8A Fig). Endo-lysosomal patch-clamp experiments revealed significantly higher $PI(3,5)P_2$-stimulated TPC2 activity for all four M484L fibroblast samples compared to donor 3, which does not encode the M484L variation, nor any of the other variations in a homozygous manner (S8B and S8C Fig). Donor 4 (homozygous for K376R) and donor 7 (homozygous for G387D) both showed significantly higher $PI(3,5)P_2$-stimulated activity compared to control, but lower activity compared to the M484L samples. This mild GOF activity of both K376R and G387D is in accordance with overexpression data described above (Fig 5). In sum, these data reproduce key findings obtained from overexpressing HEK293 cells. The data further show complex TPC2 variation patterns in different individuals with several SNPs occurring at the same time. As expected, the combination of M484L and P564L was not found among the 136 samples, as it does not seem to occur naturally.

Analysis of GWAS data

Publicly available GWAS databases were assessed and their inclusion of TPC2 polymorphisms interrogated [32,33]. Analysis of the NHGRI-EBI GWAS Catalog revealed associations of V219I, K376R, M484L, and G734E variants with hair color, which is in line with previous studies on the matter (see also S1 Table) [21,34]. Our meta-analysis revealed additional associations beyond hair pigmentation, showing V219I and M484L to be associated with a decreased risk for type 2 diabetes mellitus (T2DM). Furthermore, the G734E polymorphism appeared to be associated with bone mineral density. We investigated these findings further by interrogating the Type 2 Diabetes Knowledge Portal, a publicly available web-based GWAS tool providing access to human genetic information linked to T2DM and various other traits [33]. The top 5 significant associations of 7 TPC2 SNPs with phenotypes were collected (S2 Table) and are depicted in Fig 6A–6G. The data presented were collected from different consortia, such as the UK biobank eBMD, GIANT, GoT2D, and DIAMANTE, with sample sizes ranging from 1997 to 898130. V219I, M484L, and G734E appeared most strongly associated with hair pigmentation. V219I and M484L appeared protective against T2DM, and G734E was associated with increased bone mineral density and decreased height. Of interest, we found K376R to be associated with decreased bone mineral density and increased height, contrasting the associations of G734E. It should be further noted that the associations of V219I could be confused with associations due to the M484L polymorphism, as the two polymorphisms appear to be linked (Fig 6H). This observation is also supported by the donor fibroblast genotypes (S8 Fig). Taken together, TPC2 polymorphisms appear to be associated with various phenotypes, most consistently with hair color, T2DM, and bone mineral density.

Discussion

We provide here the first in-depth analysis of variations of the endo-lysosomal cation channels TPC1, TPC2, TRPML1, TRPML2, and TRPML3, across different human populations including ancient human genomes. We analyzed genomes from three different genome datasets: The Simons genome data set, the 1000 genome project dataset, and the gnomAD dataset. All three datasets revealed higher occurrence of variations in TPC2 compared to the other endo-

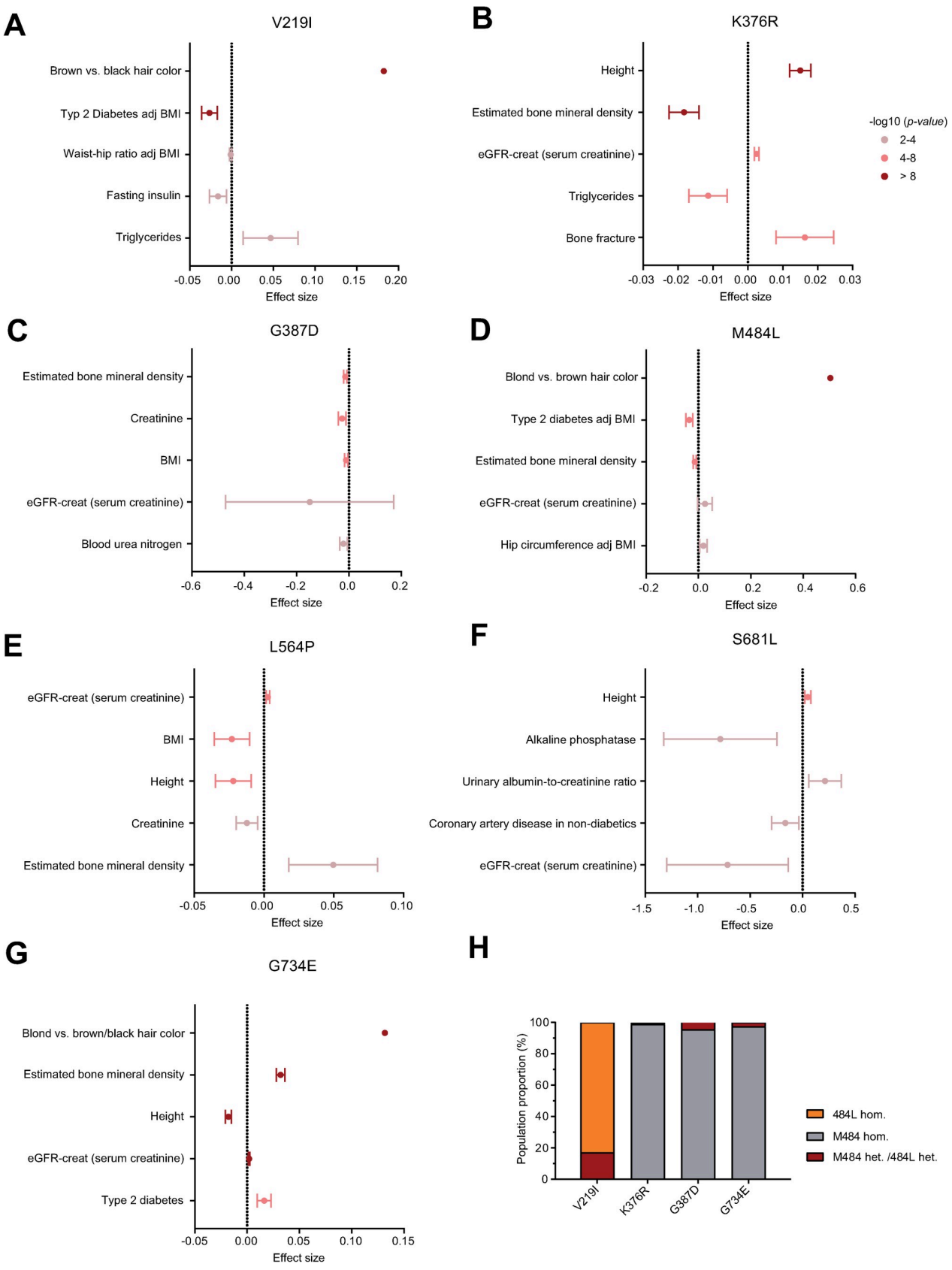
A
V219I
Brown vs. black hair color
Typ 2 Diabetes adj BMI
Waist-hip ratio adj BMI
Fasting insulin
Triglycerides
-0.05 0.00 0.05 0.10 0.15 0.20
Effect size
B
K376R
Height
Estimated bone mineral density
eGFR-creat (serum creatinine)
Triglycerides
Bone fracture
-0.03 -0.02 -0.01 0.00 0.01 0.02 0.03
Effect size
-log10 (p-value)
2-4
4-8
> 8
C
G387D
Estimated bone mineral density
Creatinine
BMI
eGFR-creat (serum creatinine)
Blood urea nitrogen
-0.6 -0.4 -0.2 0.0 0.2
Effect size
D
M484L
Blond vs. brown hair color
Type 2 diabetes adj BMI
Estimated bone mineral density
eGFR-creat (serum creatinine)
Hip circumference adj BMI
-0.2 0.0 0.2 0.4 0.6
Effect size
E
L564P
eGFR-creat (serum creatinine)
BMI
Height
Creatinine
Estimated bone mineral density
-0.05 0.00 0.05 0.10
Effect size
F
S681L
Height
Alkaline phosphatase
Urinary albumin-to-creatinine ratio
Coronary artery disease in non-diabetics
eGFR-creat (serum creatinine)
-1.5 -1.0 -0.5 0.0 0.5
Effect size
G
G734E
Blond vs. brown/black hair color
Estimated bone mineral density
Height
eGFR-creat (serum creatinine)
Type 2 diabetes
-0.05 0.00 0.05 0.10 0.15
Effect size
H
Population proportion (%)
0 20 40 60 80 100
V219I
K376R
G387D
G734E
484L hom.
M484 hom.
M484 het. /484L het.

Fig 6. GWAS analysis to assess TPC2 SNP disease association. (A-G) The Type 2 Diabetes Knowledge Portal was employed to assess phenotypes associated with high-frequency TPC2 SNPs [33]. Odds ratios were converted into effect sizes to render the data format uniform, and standard error of the mean estimated from P values, sample sizes, and effect sizes. Forest plots were subsequently plotted for the top five associated traits, centered around an effect size of 0. Decreasing effect sizes would suggest inverse associations between the trait and the SNP (such as for M484L and type 2 diabetes), while increasing effect sizes suggest direct associations (such as for G734E and bone mineral density). Colors indicate statistical significance, with dark red data-points indicating genome-wide significance ($P < 10^{-8}$). (H) We further investigated the association between V219I and other SNPs. We found V219I and M484L SNPs to be linked, with less linkage between M484L and other SNPs. Since M484L affects channel function more dramatically than V219I, we assume shared phenotypes associated with V219I to be largely attributable to the linked M484L.

https://doi.org/10.1371/journal.pgen.1009236.g006

lysosomal, non-selective cation channels TPC1, TRPML1, TRPML2, and TRPML3. Surprisingly, the TPC2 variant L564P occurs with such high frequency that the variant described hitherto as "wild-type" seems to be a rather rare variant. In addition, most other variations were found to occur on the 564P background rather than the L564 background, apart from S681L. Finally, all publicly available primate reference genomes carry proline instead of leucine at position 564. Functionally, by using endo-lysosomal patch-clamp experimentation we found that 564P has a surprising effect on the recently described M484L GOF variant of TPC2: without 564P, the M484L variation shows no GOF effect. Therefore, 564P appears to be a prerequisite for the M484L GOF effect, which is associated with a higher likelihood of light pigmentation and blond hair color, as previously reported [21,34]. The data further suggest that M484L has developed on the background of 564P, as it does not occur in combination with L564 in any of the analyzed genome samples. Furthermore, additional GOF variants of TPC2 were identified.

Given the many physiological and pathophysiological roles that TPC2 plays as outlined above, our data suggest that individuals with different TPC2 variations will likely show different susceptibilities to various diseases. Indeed, certain TPC2 polymorphisms appear to be correlated with bone mineral density (G734E, loss-of-inhibition) [35] and inversely correlate with type 2 diabetes mellitus (M484L, gain-of-function) [36], conditions previously associated with TPC2 function [23–25,37]. Beyond its association with diseases, the functional spectra of TPC2 also appear of interest pharmacologically. TPC2 was recently shown to be druggable, with two groups independently developing channel agonists either by drug repurposing [38] or drug screening for high-efficacy agonists [39]. Genetically informed drug design has been estimated to double the success rate of clinical drug development [40], for example the development of SLC30A8 antagonists as a potential therapy for type 2 diabetes [41,42]. Given the relevance of TPC2 in health and disease alongside its potential translational value, the presented findings suggest the channel to be a likely contributor to multigenic traits, with implications in basic research and pharmacogenomics. Additionally, the functional variability of TPC2 appears intriguing, and warrants further investigation into how individual TPC2 polymorphisms historically have been selected for by various selection pressures.

Materials and methods

Analysis of human genome variation data sets

The Simons Genome Project (SGDP) was accessed through the Cancer Genomics Cloud, and visualized using the Integrative Genomics Viewer through loading.BAM and.BAI URLs. Available metadata was recorded, identifying sample gender, ancestry, and continental affiliation. 1000 genome dataset and primate genomes were accessed through the ncbi.nlm.nih.gov website, the gnomAD dataset through gnomad.broadinstitute.org. All missense, nonsense or stop gained SNPs of each channel were included in the analysis. Due to their indirect affiliation with the channels, intronic variants were excluded from the analysis. Wild-type samples were assigned with the number 0, heterozygous samples with 0.5 und samples with homozygous

polymorphisms with the number 1, and mean allele frequencies (MAF) calculated. Published genomes of ancient samples were accessed as described in the respective publications [43–62]. Only genomes that had sequencing coverage of 5 or more for the amino acid 564 of TPCN2 were included.

Human donor gDNA purification and sequencing

Genomic DNA was isolated from previously described, cultured primary human fibroblasts [21]. gDNA extraction was performed using the PureLink Genomic DNA Kit (Invitrogen) according to manufacturer's instructions. Loci of interest were amplified by PCR using Q5 polymerase (NEB) according to manufacturer's instructions, and primers suitable for polymorphic site amplification. Primers for amplifying and sequencing M484L and G734E loci were previously described [21]. The following primers for amplifying and sequencing the newly described TPC2 SNPs from gDNA were used: GCCCCCAGGGTTTCATTTGT (V219I forward), GAGTCCGCACATGGGTTAGG (V219I reverse, fragment size 427 bp), GGTG AAGTCAGTTTGCGCC (K376R forward), AAGGTGAGCGCCCTCGAA (K376R reverse, fragment size 444 bp), GCCATGATGGAGGTACCCG (G387D forward), GTTCCCCAGG TGATCAAGGG (G387D reverse, fragment size 381 bp), GCCTGACAGGCTGTGTGG (L564P forward), ACTCCAGTGCATAACCCGCC (L564P reverse, fragment size 303 bp), GTGCTCTTGCTTTGCTCATC (S681L forward), CGACTCTCCCATCAAAGTTCC (S681L reverse, fragment size 246 bp). Amplified PCR products were purified by agarose gel electrophoresis, band excision, and gel extraction using the QIAquick Gel Extraction Kit (Qiagen) according to manufacturer's instructions. Subsequently, samples were sequenced using forward and reverse amplification primers to identify TPC2 genotypes.

Endo-lysosomal patch-clamp experiments

For whole-endolysosome manual patch-clamp recordings, cells were treated with vacuolin (1 μM) overnight [63]. Currents were recorded using an EPC-10 patch-clamp amplifier (HEKA, Lambrecht, Germany) and PatchMaster acquisition software (HEKA). Data were digitized at 40 kHz and filtered at 2.8 kHz. Fast and slow capacitive transients were cancelled by the compensation circuit of the EPC-10 amplifier. Recording glass pipettes were polished and had a resistance of 4–8 MΩ. Cytoplasmic solution contained 140 mM K-MSA, 5 mM KOH, 4 mM NaCl, 0.39 mM $CaCl_2$, 1 mM EGTA and 10 mM HEPES (pH was adjusted with KOH to 7.2). Luminal solution contained 140 mM Na-MSA, 5 mM K-MSA, 2 mM Ca-MSA, 1 mM $CaCl_2$, 10 mM HEPES and 10 mM MES (pH was adjusted with NaOH to 4.6). In all experiments, 500-ms voltage ramps from -100 to +100 mV were applied every 5 s, holding potential at -60 mV. The current amplitudes at -100 mV were extracted from individual ramp current recordings. All statistical analyses were performed using Origin8 software.

Cell culture and mutagenesis

HEK293 cells were maintained in DMEM supplemented with 10% FBS, 100 U penicillin/mL, and 100 μg streptomycin/mL at 37˚C and 5% CO_2. For patch clamp experiments, cells were plated on poly-L-lysine (0,1%)-coated glass coverslips 60–96 hours before experimentation, and transiently transfected with Turbofect (ThermoFisher) according to the manufacturer's protocols and used for patch clamp experiments 36 hours after transfection.

Human genomic DNA sampling and human fibroblast isolation were approved by the Ludwig-Maximilians-Universität Ethics Committee (headed by Prof. Dr. Eisenmenger; reference no. 254–16). Acquisition of human material was performed after obtaining written informed consent by the donors as described previously [21]. Primary fibroblasts were isolated by Prof.

Dr. Carola Berking and colleagues (Department of Dermatology, Ludwig-Maximilians-Universität München) from the skin of healthy adult donors. Epidermis was separated from dermis using dispase II (10 mg/mL in PBS, pH 7.2–7.4, D4693; Sigma) and dermis was digested in collagenase (1 mg/mL in DMEM, C0130; Sigma) for 22 h at room temperature. Fibroblasts were cultured in DMEM with glutamine (Life Technologies, Inc.) and 10% FBS (FBS Superior, S0615; Biochrom). Human TPC2 SNPs were generated by site-directed mutagenesis as previously described [21]. The following oligonucleotide primers were used for site-directed mutagenesis PCRs to generate newly identified TPC2 SNP variants or other mutants: V219I forward: CGGAAATGGCCAGCATCGGGCTGCTGCTGGCC; V219I reverse: GGCCAG CAGC AGCCCGATGCTGGCCATTTCCG; K376R forward: GCTGGACAGCTCCCACAG ACAGGCCATGATGGAG; K376R reverse: CTCCATCATG GCCTGTCTGTGGGAGCTGT CCAGC; G387D forward: AAGGTGCGTTCCTACGACAGTGTTCTGCTGTCAGC; G387D reverse: GCTGACAGCA GAACACTGTCGTAGGAACGCACCTT; P564L forward: GCGT ATCATCCCCAGCATGAAGCTGATGGCCGTGGTGGCC; P564L reverse: GGCCACCA CGGCCATCAGCTTCATGCTGGGGATGATACGC; S681L forward: GTGGTGGCTGGTG TTGTCTGTCATCTGGG; S681L reverse: CCCAGATGACAGACAACACCAGCCACCAC. L564A forward: ATCATCCCCAGCATGAAGGCGATGGCCGTGGTG; L564A reverse: CACCACGGCCATCGCCTTCATGCTGGGGATGAT; L564G forward: ATCATCCCCAG CATGAAGGGGATGGCCGTGGTG; L564G reverse: CACCACGGCCATCCCCTTCATG CTGGGGATGAT; M562P forward: GCGTATCATCCCCAGCCCGAAGCTGATGGCCG TG; M562P reverse: CACGGCCATCAGCTTCGGGCTGGGGATGATACGC; K563P forward: TATCATCCCCAGCATGCCGCTGATGGCCGTGGTG; K563P reverse: CACCACG GCCATCAGCGGCATGCTGGGGATGATA; M565P forward: CCAGCATGAAGCTGCCG GCCGTGGTGGCCA; M565P reverse: TGGCCACCACGGCCGGCAGCTTCATGCTGG.

TPC2 genotype-phenotype linkage analysis

The high-frequency TPC2 polymorphisms were investigated for associations with phenotypes using the following identifiers: rs72928978 (V219I), rs3750965 (K376R), rs61746574 (G387D), rs35264875 (M484L), rs2376558 (L564P), rs78034812 (S681L), and rs3829241 (G734E). GWAS results obtained from the NHGRI-EBI GWAS Catalog were compiled in S1 Table for polymorphisms showing phenotype associations (V219I, K376R, M484L, and G734E) [32]. TPC2 genotypes were next investigated in the Type 2 Diabetes Knowledge Portal, which includes numerous phenotypes beyond type 2 diabetes mellitus (T2DM) [33]. Where necessary, odds ratios were converted into effect sizes as described previously [64]. For plotting forest plots, SEM values were extracted using R version 1.2 as follows: Traits, effect sizes, sample sizes, were extracted, reformatted, and stored in R dataframes for statistical analysis. T-statistics were calculated using the qt() function, providing reported P values and degrees of freedom as inputs. SEM was subsequently calculated upon dividing effect sizes with the respective T-statistic. Forest plots of the top five associations for each polymorphism were plotted using GraphPad Prism v8, and data-points colored according to P values reported by the Type 2 Diabetes Knowledge Portal.

Western blotting

For Western blot experiments transiently transfected HEK293 cells were washed twice with 1x PBS and pellets were collected. Total cell lysates were obtained by solubilizing in TRIS HCl 10 mM pH 8.0 and 0.2% SDS supplemented with protease and phosphatase inhibitors (Sigma). Protein concentrations were quantified via Bradford assay. Proteins were separated via a 7% sodium dodecyl sulphate polyacrylamide gel electrophoresis (SDS-PAGE; BioRad) and

transferred to polyvinylidene difluoride (PVDF; BioRad) membranes. Membranes were blocked with 5% bovine serum albumin (Sigma) diluted in Tris Buffered Saline supplemented with 0.5% Tween-20 (TBS-T) for 1 h at room temperature (RT), then incubated with primary antibody at 4˚C overnight. Then, membranes were washed with TBS-T and incubated with horseradish peroxidase (HRP) conjugated anti-mouse or anti-rabbit secondary antibody at RT for 1 h. Membranes were then washed and developed by incubation with Immobilon Crescendo Western HRP substrate (Merck) and by using an Odyssey imaging system (LI-COR Biosciences). Quantification was carried out using unsaturated images on ImageJ 1.52a software. The following primary antibodies were used: Rabbit polyclonal Anti-GFP, abcam, Cat# ab6556 (1:5000 in TBS-T with 5% BSA), mouse monoclonal Anti-β-tubulin, Cell Signaling, Cat# 86298S (1:1000 in TBS-T with 5% BSA). The following secondary antibodies were used: Anti-rabbit IgG, HRP-linked, Cell Signaling, Cat# 7074S (1:5000 in TBS-T with 5% BSA) and anti-mouse IgG, HRP-linked, Cell Signaling, Cat# 7076S (1:5000 in TBS-T with 5% BSA).

Statistical analysis

Details of statistical analyses and n values are provided in the Materials and Methods or the figures or figure legends. Statistical analyses were carried out using Origin 8 and GraphPad Prism 8. All error bars are depicted as mean ± SEM. Statistical significance is denoted on figures as outlined in the legends. Statistics carried out on datasets upon obtaining three independent biological and technical replicates.

Supporting information

S1 Fig. Mean allele frequency of SNPs in other endo-lysosomal cation channels in the SGDP data set. (A-D) Shown are the mean allele frequencies of all SNPs that were found in TRPML1-3 or TPC1 upon investigating the Simons Genome Diversity Project data set [26].
(EPS)

S2 Fig. Mean allele frequency of SNPs in TPC2 and other endo-lysosomal cation channels in the 1000GP data. (A-E) Shown are the mean allele frequencies of all SNPs that were found in TRPML1-3 or TPC1 and 2 when investigating the 1000 genomes project [27]. Homozygously occurring SNPs marked in red. (F) Percentage of polymorphisms for TRPML1-3 and TPC1 and 2, relative to the coding sequence length for each gene (left: all; right: only homozygous SNPs)
(EPS)

S3 Fig. Mean allele frequency of SNPs in TPC2 and other endo-lysosomal cation channels in the gnomAD data set. (A-E) Shown are the mean allele frequencies of all homozygous SNPs that were found in TRPML1-3 and TPC1 and 2 when investigating the gnomAD data set [28]. (F) Mean allele frequency of each SNP grouped by continent.
(EPS)

S4 Fig. Analysis of ancient genome and primate samples. (A) The presented map was generated using data obtained from published ancient genome sequences [43–62]. Sequencing results of 39 fossils of modern humans with a minimum coverage of 5 were analyzed. Square indicates where the fossil was found. Filled square represents a homozygous 564P sample, empty square represents a homozygous L564 sample, and semi-filled square represents a heterozygous sample. The color scheme encodes the estimated age of each fossil. (B) Shown are the 39 samples from ancient humans (blue) and an additional three samples from homo neanderthalensis (green) and one denisovan sample (red) on a time scale. Homozygous L564 samples are shown as empty triangles, homozygous 564P samples as filled triangles, and

heterozygous L564/564P as semi-filled triangles (C) Comparison of the TPC2 protein sequence in the human reference genome with other primate reference genomes. The neighbor-joining tree was created with the software MEGA X based on the FASTA sequences from the NCBI Gene database [65].
(EPS)

S5 Fig. Maps of the worldwide distribution of $TPC2^{M484L}$ in the 1000GP and the gnomAD data set. (A) Each circle represents one of the 26 populations of the 1000GP data set (indigenous or non-indigenous (other descent) as indicated) [27,28]. White color represents the fraction of homozygous carriers for $TPC2^{M484}$, red color represents the fraction homozygous for $TPC2^{484L}$, and pink color represents the heterozygous population. (B) Each circle represents a population as indicated on the gnomAD website. Color-coding as in A.
(EPS)

S6 Fig. Analysis of expression and subcellular localization of TPC2 variants. (A) Representative confocal microscopy images (Zeiss LSM 880 Airyscan) of different TPC2 variants transiently transfected in HeLa cells. Scale bar = 10 μm. (B) Colocalization of human TPC2 variants with lysotracker deep red (DR), quantified using Manders' coefficient or Pearson correlation coefficient (PCC). (C, D) Western blot analysis of the different TPC2 variants transiently transfected in HEK293 cells. Shown are (C) average relative expression levels (normalized to β-tubulin, n = 6 independent experiments, mean ± SEM) and (D) one representative blot. One-way ANOVA followed by Tukey's post-hoc test was applied to test for statistical significance
(EPS)

S7 Fig. Analysis of TPC2 mutations in the IIS4-S5 linker region. (A) Cartoon showing the location of the mutated amino acids in the IIS4-S5 linker region and mutation M484L. (B) Representative $PI(3,5)P_2$ (1 μM) activated current densities in vacuolin-enlarged lysosomal vesicles isolated from HEK293 cells expressing TPC2 mutants K563P or M565P in combination with M484L and P564L, each. (C) Model based on the recently resolved human TPC2 (M484/564P) cryo-EM structure [31]. The IIS4-S5 linker has been implicated in channel gating, as an extension of the IIS4-S5 linker appears necessary to provide space for pore dilation and channel opening. Substituting the helix-initiating 564P with a leucine would dramatically affect this linker helix extension. Our model proposes that M484L is amplifying the effect of $PI(3,5)P_2$ activation, requiring signal transduction through L564P to result in pore dilation.
(EPS)

S8 Fig. TPC2 SNPs in human donor fibroblast samples. (A) Genotyping results of human donor fibroblast samples. (B) Representative $PI(3,5)P_2$ (10 μM) activated current densities in vacuolin-enlarged lysosomal vesicles isolated from different donor fibroblasts. (C) Statistical summary of lysosomal patch-clamp data from human donor samples. Shown are average current densities (mean ± SEM) at -100 mV. Unpaired t-tests were applied. $^{*}p < 0.05$ and $^{**}p < 0.01$
(EPS)

S1 Table. TPC2 polymorphisms reaching genome-wide significance in GWAS studies. In the GWAS catalog four TPC2 polymorphism are listed that reach significant association in genome-wide association studies. The "OR" refers to the allelic odds ratio in each study. Further details can be found in the respective publications.
(XLSX)

S2 Table. Data obtained from the GWAS Catalog and Type 2 Diabetes Knowledge Portal. For each homozygous occurring TPC2 polymorphism, traits were sorted by statistical significance (p value), and the top five traits were analyzed further. Effect sizes were used as reported or calculated from the odds ratio. Standard error of the mean was calculated using the qt() function in R. The data was subsequently used to generate genotype/phenotype-association forest plots, as illustrated in Fig 6.
(XLSX)

Author Contributions

Conceptualization: Christian Grimm.

Data curation: Julia Böck, Einar Krogsaeter, Yu-Kai Chao.

Formal analysis: Julia Böck, Einar Krogsaeter, Marcel Passon, Yu-Kai Chao.

Funding acquisition: Christian Grimm.

Methodology: Julia Böck, Einar Krogsaeter, Marcel Passon, Yu-Kai Chao, Sapna Sharma, Harald Grallert, Annette Peters.

Resources: Annette Peters, Christian Grimm.

Supervision: Christian Grimm.

Validation: Julia Böck, Einar Krogsaeter, Marcel Passon, Christian Grimm.

Visualization: Julia Böck, Einar Krogsaeter, Marcel Passon, Christian Grimm.

Writing – original draft: Christian Grimm.

Writing – review & editing: Sapna Sharma, Christian Grimm.

References

1. Malowany JI, Butany J. Pathology of sickle cell disease. Semin Diagn Pathol. 2012; 29: 49–55. https://doi.org/10.1053/j.semdp.2011.07.005 PMID: 22372205
2. Ferreira A, Marguti I, Bechmann I, Jeney V, Chora Â, Palha NR, et al. Sickle hemoglobin confers tolerance to plasmodium infection. Cell. 2011; 145: 398–409. https://doi.org/10.1016/j.cell.2011.03.049 PMID: 21529713
3. Grimm C, Butz E, Chen C, Wahl-schott C, Biel M. From mucolipidosis type IV to Ebola: TRPML and two-pore channels at the crossroads of endo-lysosomal trafficking and disease. Cell Calcium. 2017; 67: 148–155. https://doi.org/10.1016/j.ceca.2017.04.003 PMID: 28457591
4. Cang C, Zhou Y, Navarro B, Seo YJ, Aranda K, Shi L, et al. MTOR regulates lysosomal ATP-sensitive two-pore Na+channels to adapt to metabolic state. Cell. 2013; 152: 778–790. https://doi.org/10.1016/j.cell.2013.01.023 PMID: 23394946
5. Sun W, Yue J. TPC2 mediates autophagy progression and extracellular vesicle secretion in cancer cells. Exp Cell Res. 2018; 370: 478–489. https://doi.org/10.1016/j.yexcr.2018.07.013 PMID: 29990474
6. Wang X, Zhang X, Dong X, Samie M, Li X, Clapham DE, et al. TPC Proteins Are Phosphoinositide-activated Sodium-selective Ion Channels in Endosomes and Lysosomes. Cell. 2012; 151: 372–383. https://doi.org/10.1016/j.cell.2012.08.036 PMID: 23063126
7. Sakurai Y, Kolokoltsov AA, Chen C-CC, Tidwell MW, Bauta WE, Klugbauer N, et al. Two-pore channels control Ebola virus host cell entry and are drug targets for disease treatment. Science. 2015; 347: 995–998. https://doi.org/10.1126/science.1258758 PMID: 25722412
8. Gunaratne GS, Yang Y, Li F, Walseth TF, Marchant JS. NAADP-dependent Ca2+ signaling regulates Middle East Respiratory Syndrome-Coronavirus pseudovirus translocation through the endolysosomal system. Cell Calcium. 2018; 75: 30–41. https://doi.org/10.1016/j.ceca.2018.08.003 PMID: 30121440
9. Ou X, Liu Y, Lei X, Li P, Mi D, Ren L, et al. Characterization of spike glycoprotein of SARS-CoV-2 on virus entry and its immune cross-reactivity with SARS-CoV. Nat Commun. 2020; 11: 1620. https://doi.org/10.1038/s41467-020-15562-9 PMID: 32221306

10. Grimm C, Holdt LM, Chen C-C, Hassan S, Muller C, Jors S, et al. High susceptibility to fatty liver disease in two-pore channel 2-deficient mice. Nat Comms. 2014; 5: 4699–4712. https://doi.org/10.1038/ncomms5699 PMID: 25144390

11. Lear P V., González-Touceda D, Couto BP, Viaño P, Guymer V, Remzova E, et al. Absence of intracellular ion channels TPC1 and TPC2 leads to mature-onset obesity in male mice, due to impaired lipid availability for thermogenesis in brown adipose tissue. Endocrinology. 2015; 156: 975–986. https://doi.org/10.1210/en.2014-1766 PMID: 25545384

12. Favia A, Desideri M, Gambara G, D'Alessio A, Ruas M, Esposito B, et al. VEGF-induced neoangiogenesis is mediated by NAADP and two-pore channel-2-dependent Ca2+ signaling. Proc Natl Acad Sci. 2014; 111: 4706–4715. https://doi.org/10.1073/pnas.1406029111 PMID: 25331892

13. Parrington J, Lear P, Hachem A. Calcium signals regulated by NAADP and two-pore channels -their role in development, differentiation and cancer. Int J Dev Biol. 2015; 59: 327–340. https://doi.org/10.1387/ijdb.150197ml PMID: 26198142

14. Nguyen ONP, Grimm C, Schneider LS, Chao Y-K, Atzberger C, Bartel K, et al. Two-Pore Channel Function Is Crucial for the Migration of Invasive Cancer Cells. Cancer Res. 2017; 77: 1427–1438. https://doi.org/10.1158/0008-5472.CAN-16-0852 PMID: 28108508

15. Grimm C, Bartel K, Vollmar AM, Biel M. Endolysosomal cation channels and cancer—a link with great potential. Pharmaceuticals. 2018; 11: 1–8. https://doi.org/10.3390/ph11010004 PMID: 29303993

16. Alharbi AF, Parrington J. Endolysosomal Ca2+ Signaling in Cancer: The Role of TPC2, From Tumorigenesis to Metastasis. Front Cell Dev Biol. 2019; 7: 1–7. https://doi.org/10.3389/fcell.2019.00001 PMID: 30733944

17. Ambrosio AL, Boyle JA, Di Pietro SM. TPC2 mediates new mechanisms of platelet dense granule membrane dynamics through regulation of Ca2+ release. Mol Biol Cell. 2015; 26: 3263–3274. https://doi.org/10.1091/mbc.E15-01-0058 PMID: 26202466

18. Ambrosio AL, Boyle JA, Aradi AE, Christian KA, Di Pietro SM. TPC2 controls pigmentation by regulating melanosome pH and size. Proc Natl Acad Sci U S A. 2016; 113: 5622–5627. https://doi.org/10.1073/pnas.1600108113 PMID: 27140606

19. Bellono NW, Escobar IE, Oancea E. A melanosomal two-pore sodium channel regulates pigmentation. Sci Rep. 2016; 6: 1–11. https://doi.org/10.1038/s41598-016-0001-8 PMID: 28442746

20. Davis LC, Morgan AJ, Chen JL, Snead CM, Bloor-Young D, Shenderov E, et al. NAADP Activates two-pore channels on t cell cytolytic granules to stimulate exocytosis and killing. Curr Biol. 2012; 22: 2331–2337. https://doi.org/10.1016/j.cub.2012.10.035 PMID: 23177477

21. Chao Y-K, Schludi V, Chen C-C, Butz E, Nguyen ONP, Müller M, et al. TPC2 polymorphisms associated with a hair pigmentation phenotype in humans result in gain of channel function by independent mechanisms. Proc Natl Acad Sci. 2017; 114: E8595–E8602. https://doi.org/10.1073/pnas.1705739114 PMID: 28923947

22. Grimm C, Butz E, Chen CC, Wahl-Schott C, Biel M. From mucolipidosis type IV to Ebola: TRPML and two-pore channels at the crossroads of endo-lysosomal trafficking and disease. Cell Calcium. 2017; 67: 148–155. https://doi.org/10.1016/j.ceca.2017.04.003 PMID: 28457591

23. Arredouani A, Ruas M, Collins SC, Parkesh R, Clough F, Pillinger T, et al. Nicotinic Acid Adenine Dinucleotide Phosphate (NAADP) and Endolysosomal Two-pore Channels Modulate Membrane Excitability and Stimulus-Secretion Coupling in Mouse Pancreatic beta-Cells. J Biol Chem. 2015; 290: 21376–21392. https://doi.org/10.1074/jbc.M115.671248 PMID: 26152717

24. Cane MC, Parrington J, Rorsman P, Galione A, Rutter GA. Cell Calcium The two pore channel TPC2 is dispensable in pancreatic [illegible] -cells for normal Ca 2 + dynamics and insulin secretion. Cell Calcium. 2016; 59: 32–40. https://doi.org/10.1016/j.ceca.2015.12.004 PMID: 26769314

25. Hamilton A, Zhang Q, Salehi A, Willems M, Knudsen JG, Stephen S, et al. Adrenaline stimulates glucagon secretion by Tpc2-dependent Ca2+ mobilization from acidic stores in pancreatic α-cells. Diabetes. 2018; 67: 1128–1139. https://doi.org/10.2337/db17-1102 PMID: 29563152

26. Mallick S, Li H, Lipson M, Mathieson I, Gymrek M, Racimo F, et al. The Simons Genome Diversity Project: 300 genomes from 142 diverse populations. Nature. 2016/09/21. 2016; 538: 201–206. https://doi.org/10.1038/nature18964 PMID: 27654912

27. Auton A, Abecasis GR, Altshuler DM, Durbin RM, Bentley DR, Chakravarti A, et al. A global reference for human genetic variation. Nature. 2015; 526: 68–74. https://doi.org/10.1038/nature15393 PMID: 26432245

28. Karczewski KJ, Francioli LC, Tiao G, Cummings BB, Wang Q, Collins RL, et al. Variation across 141,456 human exomes and genomes reveals the spectrum of loss-of- function intolerance across human protein-coding genes. bioRxiv. https://doi.org/10.1101/531210

29. Sun M, Goldin E, Stahl S, Falardeau JL, Kennedy JC, Acierno JS, et al. Mucolipidosis type IV is caused by mutations in a gene encoding a novel transient receptor potential channel. Hum Mol Genet. 2000; 9: 2471–2478. https://doi.org/10.1093/hmg/9.17.2471 PMID: 11030752

30. Chen C-C, Keller M, Hess M, Schiffmann R, Urban N, Wolfgardt A, et al. A small molecule restores function to TRPML1 mutant isoforms responsible for mucolipidosis type IV. Nat Commun. 2014; 5: 4681–4691. https://doi.org/10.1038/ncomms5681 PMID: 25119295

31. She J, Zeng W, Guo J, Chen Q. Structural mechanisms of phospholipid activation of the human TPC2 channel. Elife. 2019; 8: e45222. https://doi.org/10.7554/eLife.45222 PMID: 30860481

32. Buniello A, Macarthur JAL, Cerezo M, Harris LW, Hayhurst J, Malangone C, et al. The NHGRI-EBI GWAS Catalog of published genome-wide association studies, targeted arrays and summary statistics 2019. Nucleic Acids Res. 2019; 47: D1005–D1012. https://doi.org/10.1093/nar/gky1120 PMID: 30445434

33. AMP-T2D Consortium. Type 2 Diabetes Knowledge Portal. [cited 18 Mar 2020]. Available: http://www.type2diabetesgenetics.org/

34. Sulem P, Gudbjartsson DF, Stacey SN, Helgason A, Rafnar T, Jakobsdottir M, et al. Two newly identified genetic determinants of pigmentation in Europeans. Nat Genet. 2008; 40: 835–837. https://doi.org/10.1038/ng.160 PMID: 18488028

35. Morris JA, Kemp JP, Youlten SE, Laurent L, Logan JG, Chai RC, et al. An atlas of genetic influences on osteoporosis in humans and mice. Nat Genet. 2019; 51: 258–266. https://doi.org/10.1038/s41588-018-0302-x PMID: 30598549

36. Mahajan A, Wessel J, Willems SM, Zhao W, Robertson NR, Chu AY, et al. Refining the accuracy of validated target identification through coding variant fine-mapping in type 2 diabetes. Nat Genet. 2018; 50: 559–571. https://doi.org/10.1038/s41588-018-0084-1 PMID: 29632382

37. Notomi T, Kuno M, Hiyama A, Nozaki T, Ohura K, Ezura Y, et al. Role of lysosomal channel protein TPC2 in osteoclast differentiation and bone remodeling under normal and low-magnesium conditions. J Biol Chem. 2017; 292: 20998–21010. https://doi.org/10.1074/jbc.M117.780072 PMID: 29084844

38. Zhang X, Chen W, Li P, Calvo R, Southall N, Hu X, et al. Agonist-specific voltage-dependent gating of lysosomal two-pore Na+ channels. Elife. 2019; 8: e51423. https://doi.org/10.7554/eLife.51423 PMID: 31825310

39. Gerndt S, Chen C-C, Chao Y-K, Yuan Y, Rosato AS, Krogsaeter E, et al. Agonist-mediated switching of ion selectivity in TPC2 differentially promotes lysosomal function. Elife. 2020; 9: e54712. https://doi.org/10.7554/eLife.54712 PMID: 32167471

40. Nelson MR, Tipney H, Painter JL, Shen J, Nicoletti P, Shen Y, et al. The support of human genetic evidence for approved drug indications. Nat Genet. 2015;47. https://doi.org/10.1038/ng.3164 PMID: 25485836

41. Flannick J, Thorleifsson G, Beer NL, Jacobs SBR, Grarup N, Burtt NP, et al. Loss-of-function mutations in SLC30A8 protect against type 2 diabetes. Nat Publ Gr. 2014; 46: 357–364. https://doi.org/10.1038/ng.2915 PMID: 24584071

42. Flannick J, Mercader JM, Fuchsberger C, Udler MS, Mahajan A, Wessel J, et al. Exome sequencing of 20,791 cases of type 2 diabetes and 24,440 controls. Nature. 2019; 570: 71–76. https://doi.org/10.1038/s41586-019-1231-2 PMID: 31118516

43. Prüfer K, De Filippo C, Grote S, Mafessoni F, Korlević P, Hajdinjak M, et al. A high-coverage Neandertal genome from Vindija Cave in Croatia. Science. 2017; 358: 655–658. https://doi.org/10.1126/science.aao1887 PMID: 28982794

44. Pääbo S. A high-quality Neandertal genome sequence.

45. Broushaki F, Thomas MG, Link V, López S, Dorp L Van, Hofmanová Z, et al. Early Neolithic genomes from the eastern Fertile Crescent. Science. 2016; 353: 499–503. https://doi.org/10.1126/science.aaf7943 PMID: 27417496

46. Gamba C, Jones ER, Teasdale MD, McLaughlin RL, Gonzalez-Fortes G, Mattiangeli V, et al. Genome flux and stasis in a five millennium transect of European prehistory. Nat Commun. 2014; 5: 1–9. https://doi.org/10.1038/ncomms6257 PMID: 25334030

47. Allentoft ME, Sikora M, Sjögren KG, Rasmussen S, Rasmussen M, Stenderup J, et al. Population genomics of Bronze Age Eurasia. Nature. 2015; 522: 167–172. https://doi.org/10.1038/nature14507 PMID: 26062507

48. Schlebusch CM, Malmström H, Günther T, Sjödin P, Coutinho A, Edlund H, et al. Southern African ancient genomes estimate modern human divergence to 350,000 to 260,000 years ago. Science. 2017; 358: 652–655. https://doi.org/10.1126/science.aao6266 PMID: 28971970

49. Moreno-Mayar JV, Potter BA, Vinner L, Steinrücken M, Rasmussen S, Terhorst J, et al. Terminal Pleistocene Alaskan genome reveals first founding population of Native Americans. Nature. 2018; 553: 203–207. https://doi.org/10.1038/nature25173 PMID: 29323294

50. Kılınç GM, Omrak A, Özer F, Günther T, Büyükkarakaya AM, Bıçakçı E, et al. The Demographic Development of the First Farmers in Anatolia. Curr Biol. 2016/08/04. 2016; 26: 2659–2666. https://doi.org/10.1016/j.cub.2016.07.057 PMID: 27498567

51. Rasmussen M, Anzick SL, Waters MR, Skoglund P, Degiorgio M, Stafford TW, et al. The genome of a Late Pleistocene human from a Clovis burial site in western Montana. Nature. 2014; 506: 225–229. https://doi.org/10.1038/nature13025 PMID: 24522598

52. Fu Q, Li H, Moorjani P, Jay F, Slepchenko SM, Bondarev AA, et al. Genome sequence of a 45,000-year-old modern human from western Siberia. Nature. 2014; 514: 445–449. https://doi.org/10.1038/nature13810 PMID: 25341783

53. Malaspinas A-S, Lao O, Schroeder H, Rasmussen M, Raghavan M, Moltke I, et al. Two ancient human genomes reveal Polynesian ancestry among the indigenous Botocudos of Brazil. Curr Biol. 2014/10/23. 2014; 24: R1035–R1037. https://doi.org/10.1016/j.cub.2014.09.078 PMID: 25455029

54. Jones ER, Gonzalez-Fortes G, Connell S, Siska V, Eriksson A, Martiniano R, et al. Upper Palaeolithic genomes reveal deep roots of modern Eurasians. Nat Commun. 2015; 6: 1–8. https://doi.org/10.1038/ncomms9912 PMID: 26567969

55. Pääbo S, Mafessoni F. High coverage Chagyrskaya Neandertal.

56. Meyer M, Kircher M, Gansauge M-T, Li H, Racimo F, Mallick S, et al. A High-Coverage Genome Sequence from an Archaic Denisovan Individual. Science. 2012; 338: 222–226. https://doi.org/10.1126/science.1224344 PMID: 22936568

57. Rasmussen M, Guo X, Wang Y, Lohmueller KE, Rasmussen S, Albrechtsen A, et al. An aboriginal Australian genome reveals separate human dispersals into Asia. Science. 2011; 334: 94–98. https://doi.org/10.1126/science.1211177 PMID: 21940856

58. Gallego Llorente M, Jones ER, Eriksson A, Siska V, Arthur KW, Arthur JW, et al. Ancient Ethiopian genome reveals extensive Eurasian admixture in Eastern Africa. Science. 2015; 350: 821–822.

59. Sikora M, Seguin-Orlando A, Sousa VC, Albrechtsen A, Korneliussen T, Ko A, et al. Ancient genomes show social and reproductive behavior of early Upper Paleolithic foragers. Science. 2017; 662: 659–662. https://doi.org/10.1126/science.aao1807 PMID: 28982795

60. Lazaridis I, Patterson N, Mittnik A, Renaud G, Mallick S, Kirsanow K, et al. Ancient human genomes suggest three ancestral populations for present-day Europeans. Nature. 2014; 513: 409–413. https://doi.org/10.1038/nature13673 PMID: 25230663

61. Olalde I, Allentoft ME, Sánchez-Quinto F, Santpere G, Chiang CWK, DeGiorgio M, et al. Derived immune and ancestral pigmentation alleles in a 7,000-year-old Mesolithic European. Nature. 2014; 507: 225–228. https://doi.org/10.1038/nature12960 PMID: 24463515

62. Hofmanová Z, Kreutzer S, Hellenthal G, Sell C, Diekmann Y, Díez-Del-Molino D, et al. Early farmers from across Europe directly descended from Neolithic Aegeans. Proc Natl Acad Sci. 2016; 113: 6886–6891. https://doi.org/10.1073/pnas.1523951113 PMID: 27274049

63. Chen C-C, Cang C, Fenske S, Butz E, Chao Y-K, Biel M, et al. Patch-clamp technique to characterize ion channels in enlarged individual endolysosomes. Nat Protoc. 2017; 12: 1639–1658. https://doi.org/10.1038/nprot.2017.036 PMID: 28726848

64. Chinn S. A simple method for converting an odds ratio to effect size for use in meta-analysis. Stat Med. 2000; 19: 3127–3131. https://doi.org/10.1002/1097-0258(20001130)19:22<3127::aid-sim784>3.0.co;2-m PMID: 11113947

65. Kumar S, Stecher G, Li M, Knyaz C, Tamura K. MEGA X: Molecular evolutionary genetics analysis across computing platforms. Mol Biol Evol. 2018; 35: 1547–1549. https://doi.org/10.1093/molbev/msy096 PMID: 29722887

Manuscript V

Repurposing of tamoxifen ameliorates CLN3 and CLN7 disease phenotype
Chiara Soldati*, Irene Lopez-Fabuel*, Luca G. Wanderlingh, Marina G. Macia, Jlenia Monfregola, Alessanddra Esposito, Gennaro Napolitano, Marta Guevara-Ferrer, Anna Scotto Rosato, **Einar K. Krogsaeter**, Dominik Paquet, Christian Grimm, Sandro Montefusco, Thomas Braulke, Stephan Storch, Sara E. Mole, Maria Antonietta De Matteis, Andrea Ballabio, Julio Lopes-Sampaio, Tristan McKay, Ludger Johannes, Juan P. Bolanos, & Diego L. Medina.
EMBO Molecular Medicine. 2021;e13742.

Article

SOURCE DATA | TRANSPARENT PROCESS | OPEN ACCESS

EMBO Molecular Medicine

Repurposing of tamoxifen ameliorates CLN3 and CLN7 disease phenotype

Chiara Soldati[1,†], Irene Lopez-Fabuel[2,3,4,†], Luca G Wanderlingh[1], Marina Garcia-Macia[2,3,4], Jlenia Monfregola[1], Alessandra Esposito[1], Gennaro Napolitano[1,5], Marta Guevara-Ferrer[6], Anna Scotto Rosato[7], Einar K Krogsaeter[7], Dominik Paquet[8,9], Christian M Grimm[7], Sandro Montefusco[1], Thomas Braulke[10], Stephan Storch[11], Sara E Mole[12], Maria A De Matteis[1,13], Andrea Ballabio[1,5,14,15], Julio L Sampaio[16], Tristan McKay[6], Ludger Johannes[16], Juan P Bolaños[2,3,4,*] & Diego L Medina[1,5,**]

Abstract

Batten diseases (BDs) are a group of lysosomal storage disorders characterized by seizure, visual loss, and cognitive and motor deterioration. We discovered increased levels of globotriaosylceramide (Gb3) in cellular and murine models of CLN3 and CLN7 diseases and used fluorescent-conjugated bacterial toxins to label Gb3 to develop a cell-based high content imaging (HCI) screening assay for the repurposing of FDA-approved compounds able to reduce this accumulation within BD cells. We found that tamoxifen reduced the lysosomal accumulation of Gb3 in CLN3 and CLN7 cell models, including neuronal progenitor cells (NPCs) from CLN7 patient-derived induced pluripotent stem cells (iPSC). Here, tamoxifen exerts its action through a mechanism that involves activation of the transcription factor EB (TFEB), a master gene of lysosomal function and autophagy. *In vivo* administration of tamoxifen to the CLN7$^{\Delta ex2}$ mouse model reduced the accumulation of Gb3 and SCMAS, decreased neuroinflammation, and improved motor coordination. These data strongly suggest that tamoxifen may be a suitable drug to treat some types of Batten disease.

Keywords CLN3; CLN7; high content imaging screening; tamoxifen; TFEB

Subject Categories Genetics, Gene Therapy & Genetic Disease; Neuroscience; Organelles

DOI 10.15252/emmm.202013742 | Received 19 November 2020 | Revised 30 July 2021 | Accepted 2 August 2021

EMBO Mol Med (2021) e13742

Introduction

The neuronal ceroid lipofuscinoses (NCL), commonly known as Batten disease (BD), are a group of recessively inherited fatal diseases of the nervous system which typically arise in childhood. Neurodegenerative disorders in children are rare, with BD the most frequent; the incidence rates of the entire group of 13 genetically distinct NCL varies between 1:14,000 and 1:67,000, (Haltia & Goebel, 2013; Kauss *et al*, 2020; Mole *et al*, 2019). Current palliative treatment can reduce some symptoms but cannot prevent progressive CNS degeneration. At the cellular level, alterations in BD cells include lysosomal accumulation of toxic metabolites, lipid trafficking impairment, perturbed signalling, disturbed calcium homeostasis in the endoplasmic reticulum, and activation of the unfolded protein response (UPR) (Boustany, 2013; Mole, 2014). Genes

1 Telethon Institute of Genetics and Medicine (TIGEM), Pozzuoli, Naples, Italy
2 Institute of Functional Biology and Genomics, CSIC, University of Salamanca, Salamanca, Spain
3 Centro de Investigación Biomédica en Red sobre Fragilidad y Envejecimiento Saludable (CIBERFES), Instituto de Salud Carlos III, Madrid, Spain
4 Institute of Biomedical Research of Salamanca, University Hospital of Salamanca, CSIC, University of Salamanca, Salamanca, Spain
5 Medical Genetics Unit, Department of Medical and Translational Science, Federico II University, Naples, Italy
6 School of Healthcare Science, Manchester Metropolitan University, Manchester, UK
7 Faculty of Medicine, Walther Straub Institute of Pharmacology and Toxicology, Ludwig-Maximilians University, Munich, Germany
8 Institute for Stroke and Dementia Research (ISD), University Hospital, LMU Munich, Munich, Germany
9 Munich Cluster for Systems Neurology (SyNergy), Munich, Germany
10 Department Osteology & Biomechanics, University Medical Center Hamburg-Eppendorf, Hamburg, Germany
11 University Children's Research@Kinder-UKE, University Medical Center Hamburg-Eppendorf, Hamburg, Germany
12 Medical Research Council Laboratory for Molecular Cell Biology and UCL Great Ormond Street Institute of Child Health, University College London, London, UK
13 Department of Molecular Medicine and Medical Biotechnology, University of Napoli Federico II, Naples, Italy
14 Baylor College of Medicine, Houston, TX, USA
15 Jan and Dan Duncan Neurological Research Institute, Texas Children's Hospital, Houston, TX, USA
16 Cellular and Chemical Biology Department, Institut Curie, U1143 INSERM, UMR3666 CNRS, PSL Research University, Paris, France
*Corresponding author. Tel: +34 667258151; E-mail: jbolanos@usal.es
**Corresponding author. Tel: +39 08119230698; E-mail: medina@tigem.it
†These authors contributed equally to this work

involved in human NCLs encode soluble lysosomal enzymes (CLN1/PPT1, CLN2/TPP1, CLN10/CTSD, CLN13/CTSF), a soluble lysosomal protein that can be secreted (CLN5), a protein in the secretory pathway (CLN11/GRN), two cytoplasmic proteins that also peripherally associate with membranes (CLN4/DNAJC5, CLN14/KCTD7), and transmembrane proteins located in the endoplasmic reticulum (CLN6), endoplasmic reticulum/*cis* Golgi (CLN8) and in lysosomes (CLN3, CLN7, CLN12) (Mole & Cotman, 2015; Huber & Mathavarajah, 2018). Despite the identification of causative genes of BD, protein functional understanding remains elusive making it challenging to target therapeutic drugs by intelligent design (Mole, 2014; Kauss *et al*, 2020). In BD, systemic administration of small-molecule therapeutics is an attractive alternative to existing protein and gene therapies, which cannot readily cross the blood-brain barrier to reach the CNS. The repurposing approach of known drugs, able to correct pathological hallmarks of BD, would represent a significant therapeutic advance in the treatment of these disorders and benefit from an acceleration of their translation to clinics.

Here, we combine cell-based phenotypic screening and repurposing of FDA drugs for the identification of correctors of lysosomal storage in CLN3 and CLN7 cellular models of BD. CLN3 disease (MIM # 204200) represents the most common form of NCL worldwide, whereas CLN7 disease (MIM # 610951) is one of the most prevalent BD in southern and Mediterranean Europe. We found a significant endogenous accumulation of the glycosphingolipid globotriaosylceramide (Gb3) (Welford *et al*, 2018) within the lysosomes of human ARPE-19 cells depleted of *CLN3* or *CLN7* genes by CRISPR genome editing. Gb3 was also found in human juvenile CLN3 patient fibroblasts, neuronal progenitor cells (NPCs) derived from CLN7 patient iPSCs, and neurons in brain tissues from both $Cln3^{\Delta ex7/8}$ and $Cln7^{\Delta ex2}$ mutant mice, suggesting that Gb3 accumulation is part of the pathological storage in these diseases. By using fluorescent-conjugated bacterial toxins to label Gb3, we developed a cell-based high content imaging (HCI) screening assay for the repurposing of FDA-approved compounds able to reduce the accumulation of Gb3 within the lysosomes of BD cells. We found that tamoxifen significantly reduces the intracellular accumulation of Gb3 in CLN3 and CLN7 cell models through a mechanism that is independent of oestrogen receptors but involves activation of the transcription factor EB (TFEB), a master gene of lysosomal function and autophagy (Sardiello *et al*, 2009). TFEB activation by tamoxifen is triggered by lysosomotropic-mediated inhibition of mTORC1. Furthermore, *in vivo* administration of tamoxifen significantly rescued $Cln7^{\Delta ex2}$ mice from brain cortex Gb3 accumulation, reducing SCMAS storage, hindlimb clasping, and motor discoordination. These data indicate that Gb3 is a novel biomarker for CLN3 and CLN7 diseases, and tamoxifen may be a suitable drug for their treatment.

Results

Pathological accumulation of Gb3 in CLN3 and CLN7 diseases

Batten disease (BD) accumulates autofluorescent material, called ceroid lipofuscin, within lysosomes (Mole *et al*, 2005). The nature of this material is heterogeneous (Katz & Robison, 2002; Double *et al*, 2008) and some might derive from oxidation of either modified protein residues or lipids, including triglycerides, free fatty acids, cholesterol, and phospholipids (Double *et al*, 2008). Additionally, various CLN3 disease models present elevation of lipids belonging to the glycosphingolipid pathway such as ceramide, LacCer, GalCer, and gangliosides (Puranam *et al*, 1999; Rusyn *et al*, 2008; Somogyi *et al*, 2018). Based on these observations, we tested different fluorescently-labelled reporters for the detection of intracellular lipids and sphingosines including; Cholera Toxin B subunit (CTB) to detect GM1 ganglioside (Rusyn *et al*, 2008); LipidTOX for neutral lipids (Somogyi *et al*, 2018); Shiga Toxin subunit B (STX) for globotriaosylceramide (Gb3) (Mallard & Johannes, 2003); and Filipin III to label Cholesterol (Namdar *et al*, 2012). We assessed these reporters in human ARPE-19 cells depleted for CLN3 (ARPE-19-CLN3-KO) cells by CRISPR genome editing. Although we observed increased levels of various lipid reporters using these cells, the strong elevation of fluorescent-labelled Shiga Toxin subunit B (STX) staining suggests a dramatic accumulation of globotriaosylceramide (Gb3) in ARPE-19-CLN3-KO cells compared to their WT counterparts (Fig 1A). Also, in comparison with the staining by the other lipid reporters, the STX labelling presents the best signal window for the development of a cell-based assay in ARPE-19-CLN3-KO cells (Figs 1A and EV1A). To confirm STX staining is selective for Gb3, we used HeLa cells lacking alpha-galactosidase A (HeLa-GLA-KO), a cell model of Anderson-Fabry disease that results from mutations in the *GLA* gene leading to Gb3 accumulation (Namdar *et al*, 2012) (Fig EV1B). Further, STX staining was negative in cells depleted for Gb3 synthase (Gb3S) or treated with the glucosylceramide synthase inhibitor d-threo-1-phenyl-2-decanoylamino-3-morpholino-propanol (PDMP) (Abe *et al*, 2000; Raa *et al*, 2009) in both HeLa-GLA-KO and ARPE-19-CLN3-KO cells (Figs 1B and EV1B). Co-staining with the lysosomal marker LAMP1 indicates that in addition to the general elevation of Gb3 in cellular membranes, most intracellular Gb3 in these knockout cells accumulates within the lysosomal compartment (Fig 1B).

We investigated whether the accumulation of Gb3 is a unique phenotypic feature of CLN3 disease or whether is present in other BDs. Thus, we performed STX staining in cells depleted of either *CLN6* or *CLN7* genes by acute silencing using specific siRNAs in two cell lines, HeLa and ARPE-19 cells (Fig EV1C). As expected, STX staining revealed that the silencing of CLN3 induces Gb3 accumulation in both HeLa and ARPE-19 cells (Fig EV1C). Interestingly, the depletion of CLN7 also induces a significant elevation of Gb3 (Fig EV1C). However, Gb3 does not accumulate in cells depleted of CLN6 (Fig EV1C). PCR analysis of the *Gb3S*, *CLN3*, *CLN6,* and *CLN7* mRNA levels confirms the efficiency of gene depletion by siRNAs (Appendix Figs S1 and S2). The selectivity of STX towards Gb3 was again confirmed in ARPE-19-CLN7-KO cells (Fig 1C). Thus, either genetic or pharmacological targeting of Gb3 synthase significantly lowers STX/Gb3 staining in ARPE-19-CLN3-KO, ARPE-19-CLN7-KO, and GLA-KO cells (Figs 1B and C, and EV1B). Moreover, the direct measurement of Gb3 content by lipidomics analysis of both ARPE-19-CLN3-KO and ARPE-19-CLN7-KO cells shows a doubling of the total Gb3 present in these subtypes of BD (Fig 1D).

Next, we investigated whether the accumulation of Gb3 observed upon CLN gene depletion *in vitro* also occurs *in vivo*. Thus, we analysed tissue samples derived from the $CLN7^{\Delta ex2}$ mouse, an animal model that well recapitulates the neurological phenotype

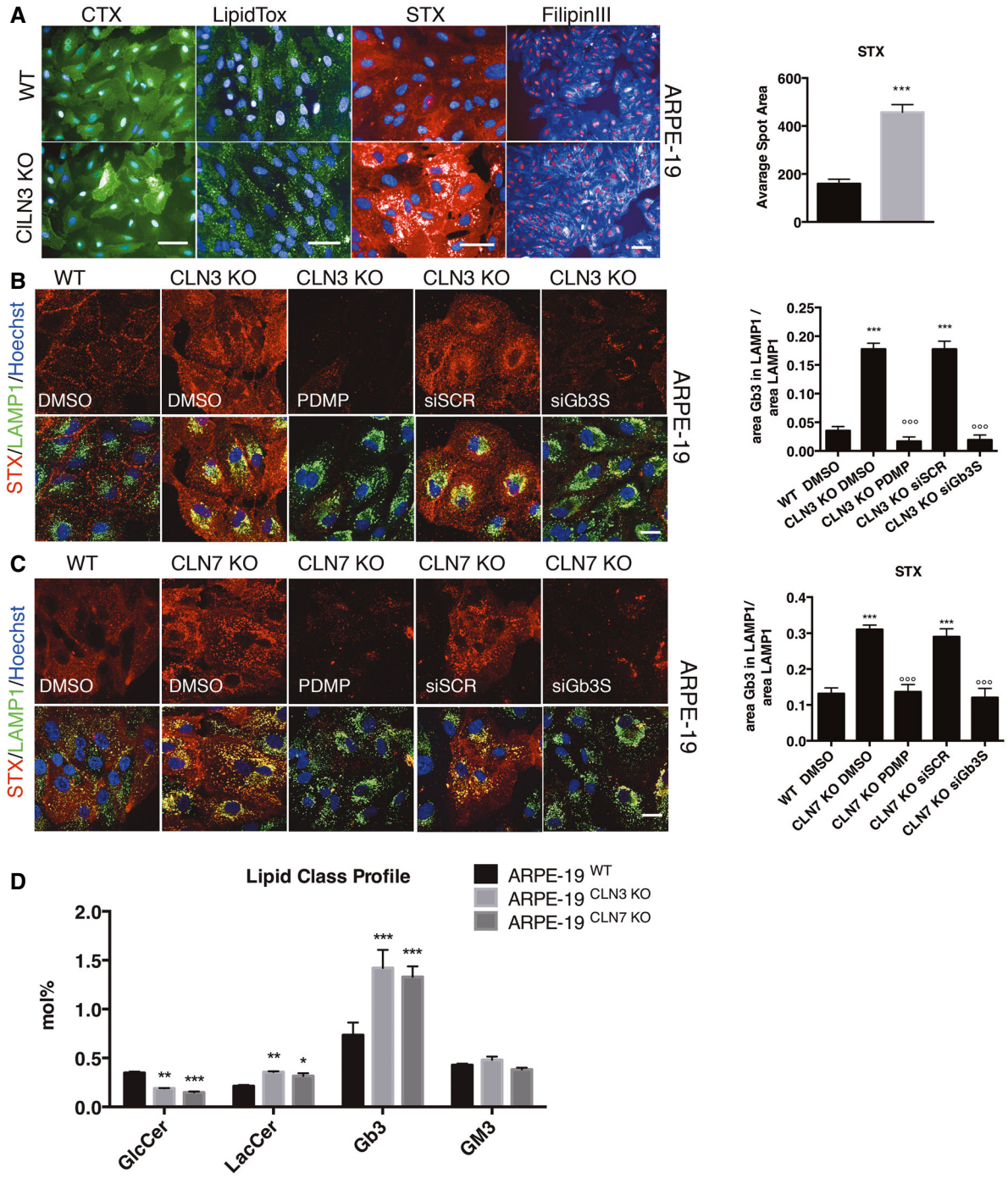

Figure 1. Accumulation of Gb3 in batten disease cellular models.

A Representative Opera images of WT and CLN3 KO ARPE 19 cell lines stained using fluorescent-conjugated cholera toxin (to detect GM1), LipidTox (to detect neutral lipids), fluorescent-conjugated Shiga toxin and is quantification (to detect Gb3) and Filipin III (to detect cholesterol). Data are presented as mean ± SD ***$P \leq 0.0001$, as determined by Student's *t*-test ($n = 3$ biological replicas in duplicate). Scale bars: 50 μm.

B, C Representative confocal images and their quantification of Gb3 accumulation within the lysosome, detected by fluorescent-conjugated Shiga toxin, from WT, CLN3-KO, and CLN7-KO ARPE-19 cells treated with PDMP or silenced for Gb3 synthase (siGb3S) (*** versus WT, °°° versus DMSO). Data are presented as mean ± SD, °°°/***$P \leq 0.0001$, as determined by ANOVA ($n = 3$ biological replicas in duplicate). Scale bars: 20 μm.

D Lipidomic analysis of ARPE-19CLN3KO and ARPE-19CLN7KO. Data are presented as mean ± SD, *$P \leq 0.01$, **$P \leq 0.001$, ***$P \leq 0.0001$, as determined by ANOVA ($n = 4$ technical replicas).

observed in the human disease (Brandenstein *et al*, 2016). By using the STX labelling of Gb3, we stained brain sections from mice at 3 and 7.5 months of age, which represent the early and late stages of disease progression (Fig 2A and B). We observed a significant accumulation of Gb3 in different brain areas such as the cortex, hippocampus, and cerebellum compared with their corresponding

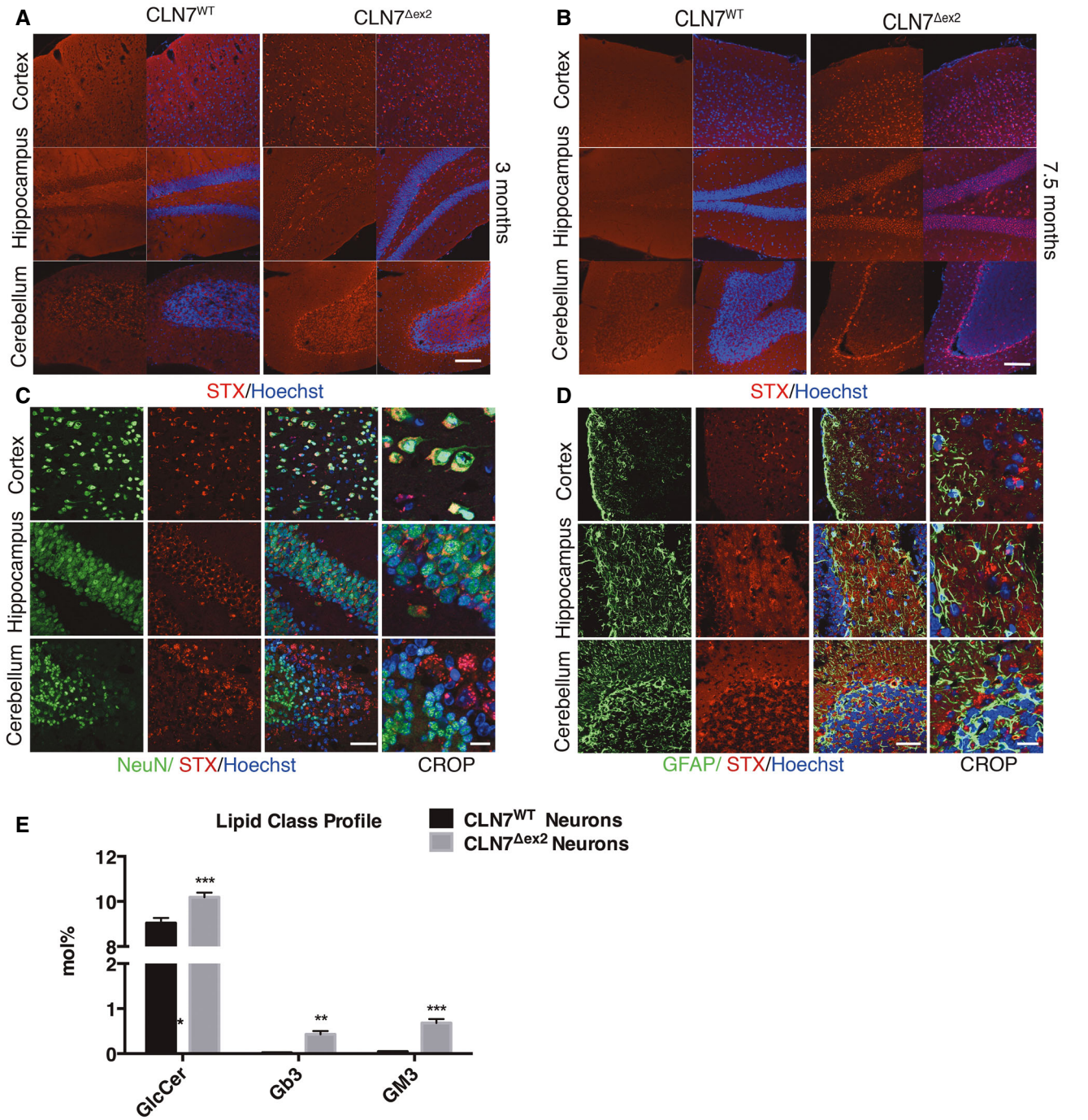

Figure 2. Neural accumulation of Gb3 in brain areas of the CLN7$^{\Delta ex2}$ mouse.

A, B Representative confocal images of Gb3 accumulation, revealed by STX staining, in brain sections from CLN7$^{\Delta ex2}$ mice at 3 and 7.5 months of age compared with CLN7 WT mice. Scale bars: 80 μm.

C, D Gb3, NeuN and GFAP distribution in brain areas of CLN7$^{\Delta ex2}$ mice at 7.5 months of age. Scale bars: 40 μm, 20 μm.

E Lipidomic analysis of neurons isolated from CLN7 WT and CLN7$^{\Delta ex2}$ mouse forebrain. Data are presented as mean ± SD, $^{**}P \leq 0.001$, $^{***}P \leq 0.0001$, as determined by ANOVA ($n = 3$ biological replicas).

healthy siblings (Fig 2A and B). The abnormal storage of Gb3 appears to be an early pathologic hallmark in the CLN7$^{\Delta ex2}$ disease since it was already present at 3 months of age (Fig 2A). Also, co-staining with neuronal nuclear antigen NeuN, but not with the astrocyte marker GFAP, indicates that Gb3 mostly accumulates in neurons and not in astrocytes (Fig 2C and D). In line with these observations, the Lipidomics analysis of immuno isolated neurons from fresh CLN7Δex2 mouse forebrain revealed a dramatic neuronal accumulation of both Gb3 and GM3, by 20- and 15-fold, respectively (Fig 2E). As expected, we also observe a similar accumulation of Gb3 in the same regions of the brain from a CLN3 mouse model at 7.5 months (Cotman *et al*, 2002; Staropoli *et al*, 2012), confirming that Gb3 storage is a signature of both BD variants (Fig EV1D).

The accumulation of Gb3 or GM3 could be a collateral effect arising from the progressive lysosomal dysfunction in the BD models tested, or in contrast, play a direct role in the pathological mechanisms of these diseases. Thus, we silenced Gb3 synthase (siGb3S) to reduce Gb3 generation using specific siRNAs and measured the accumulation of SCMAS, a characteristic component of the pathological storage of CLN3 and CLN7 disease (Palmer, 2015). We observed that acute depletion of Gb3S causes a decrease of SCMAS within the lysosomes of CLN3-depleted cells (Fig 3A). A similar result was obtained by silencing a more upstream enzyme in the glycosphingolipid synthesis pathway, LacCer synthase (siLCS), whereas silencing of the unrelated GM3 synthase (siGM3S) did not clear the accumulation of SCMAS (Fig 3A). PCR analysis of the Gb3S, LCS, and GM3S mRNA levels confirms the efficiency of the depletion of these genes by siRNAs (Appendix Fig S3). Together, these results indicate that the specific accumulation of Gb3 and not GM3 might play a role in the pathogenesis of two subtypes of Batten disease, and therefore, its targeting might ameliorate the BD phenotype.

Identification of small molecules reducing Gb3 accumulation in a cell model of Batten disease

As we found that abnormal accumulation of Gb3 appears to be pathologic in both *in vitro* and *in vivo* models of CLN3 and CLN7 diseases, we used the STX assay to identify FDA-approved compounds able to reduce the lysosomal accumulation of Gb3 by quantifying its co-localization with the lysosomal membrane protein LAMP1 in ARPE-19-CLN3-KO cells (see methods and Appendix Fig S4). The screening of 1,280 FDA drugs resulted in the identification of 9 compound hits. These include two compounds belonging to the stilbenoid class of drugs that are selective oestrogen receptor modulators (tamoxifen and toremifene), one alkaloid (apomorphine), three phenylpiperazines (itraconazole, ketoconazole, and aripiprazole), a derivative of cholesterol (pregnenolone), a diphenylmethane (benztropine) and an acetylcholinesterase inhibitor (donepezil dihydrochloride) (Fig 3B). All nine compounds were further confirmed and tested in the same STX assay in a dose–response format to determine EC50 and cell viability (Figs 3C and EV2). Tamoxifen treatment resulted in the most potent reduction of lysosomal STX accumulation with an EC50 of 0,75 μM without compromising vitality (Fig 3C). We only observed a very weak reduction in the number of nuclei at the highest concentration of tamoxifen that may suggest potential cytotoxicity at doses of > 30 μM (Fig EV2).

Tamoxifen is a readily available EMA- and FDA-approved drug used for several decades for treating breast cancer and other hormone-related disorders. Importantly, it is also safe in paediatric conditions (Gayi *et al*, 2018). Given the well-established and widespread prescription of this drug, we decided to focus on tamoxifen for further studies. We confirmed that 10μM tamoxifen promotes the clearance of lysosomal Gb3, stained with STX, in human CLN3 patient fibroblasts (Fig EV3A), ARPE-19 cells depleted of CLN7 by siRNAs (Fig EV3B), ARPE-19 CLN7-KO cells (Fig 3D), and Nestin-positive neuronal precursor cells (NPCs) derived from CLN7 patient iPSCs (Fig 3E, Appendix Fig S5). Tamoxifen was also able to reduce SCMAS levels in the same cells (Fig EV3C).

Tamoxifen is a selective oestrogen receptor modulator (SERM) and the most commonly used drug for the treatment of oestrogen receptor (ER)-positive breast cancer (Shagufta & Ahmad, 2018). Thus, we asked whether tamoxifen's ability to reduce the accumulation of Gb3 could be through targeting ERs. Surprisingly, at two concentrations, tamoxifen was able to promote Gb3 clearance in two cell lines silenced for CLN3 that do not express ERs, U2OS and HeLa cells (Kallio *et al*, 2008; Selyunin *et al*, 2019) (Figs 4A and EV3D, Appendix Fig S6A and B). These results indicate that tamoxifen induces Gb3 clearance in BD cellular models by a mechanism that is independent of the modulation of ERs. Together, we have developed a novel phenotypic screening tool for repurposing compounds able to reduce lysosomal Gb3 accumulation in BD cells and identified tamoxifen as a potential corrector of the most common subtypes of BD, CLN3 and CLN7 diseases.

Tamoxifen induces Gb3 clearance through activation of the transcription factor TFEB

The clearance activity of tamoxifen in two different types of BD through a mechanism that is ER-independent might be explained by the activation of the transcription factor TFEB. This is a master gene of lysosomal function that, upon activation, induces lysosomal clearance of pathological storage in various LSDs, including CLN3 disease (Medina *et al*, 2011). We found that tamoxifen was able to significantly induce TFEB nuclear translocation in ARPE-19-CLN3-KO cells (Fig EV4A). To determine whether TFEB activation is a requirement for tamoxifen-mediated clearance of Gb3, we tested tamoxifen in ARPE-19-CLN3-KO cells depleted of TFEB by using siRNAs (Fig 4B). While tamoxifen was effective in reducing Gb3 in ARPE-19-CLN3-KO cells treated with scrambled siRNAs (Fig 4B), it was not active in the TFEB-silenced CLN3-KO cells (Fig 4B). PCR analysis of the TFEB mRNA levels and Western blotting confirmed the efficiency of siRNA-mediated depletion of TFEB (Appendix Fig S7A and B). Consistently, viral-mediated transduction of an inducible vector expressing a nuclear-localized mutant form of TFEB was sufficient to clear Gb3 in ARPE-19-CLN3 KO cells (Fig EV4B). Indeed, tamoxifen was able to induce TFEB nuclear translocation in U2-OS cells that do not express ERs (Fig 4C), indicating that, such as tamoxifen-mediated induction of Gb3 clearance, TFEB nuclear translocation is also ER-independent. mRNA expression analysis by qPCR shows the efficiency of the CLN3 gene depletion in U2-OS cells (Appendix Fig S6).

Lysosomotropic compounds possess weak-base properties that favour their accumulation in lysosomes by ion-trapping mechanisms (Ohkuma & Poole, 1981; Pisonero-Vaquero & Medina, 2017). Recent

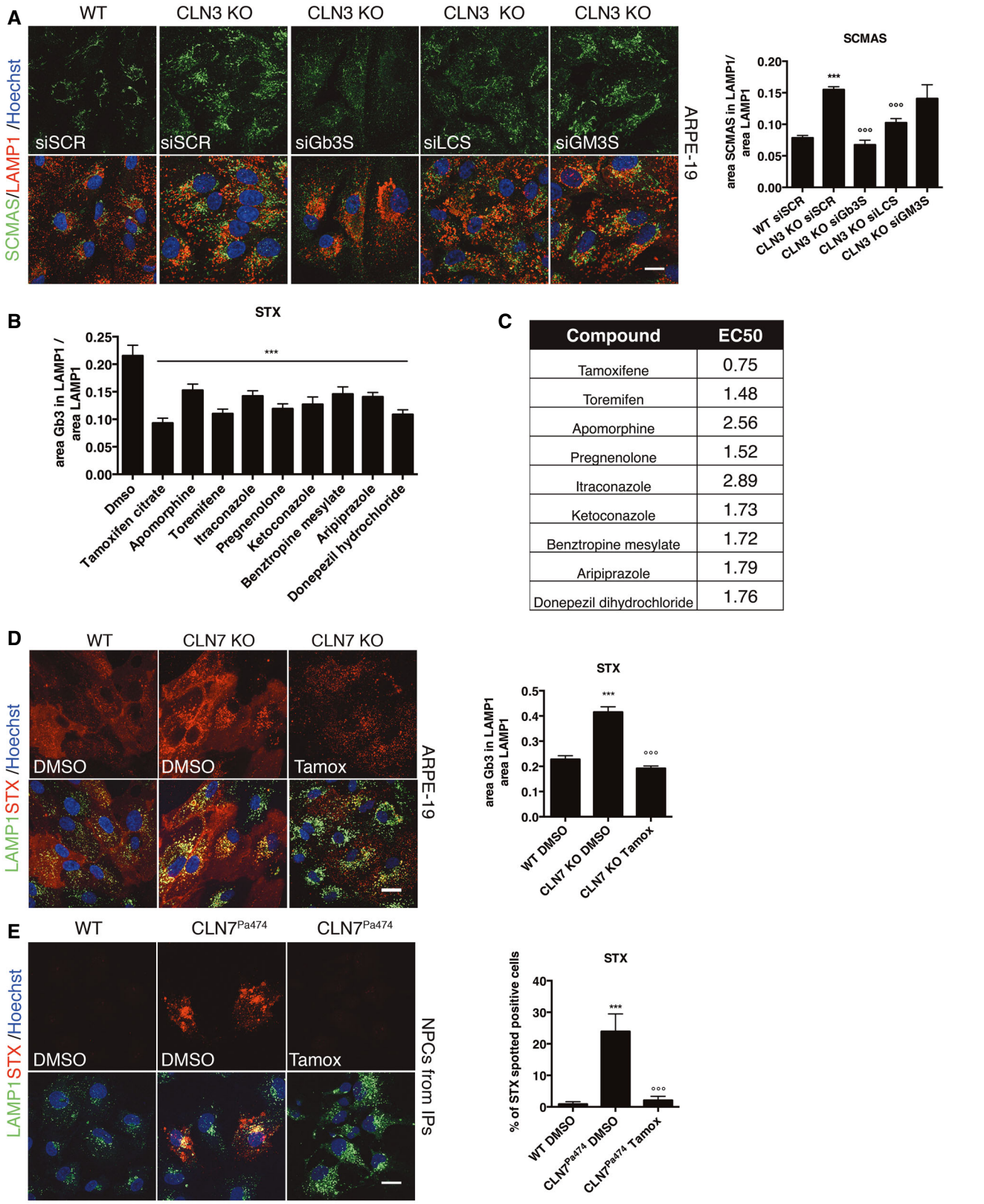

Figure 3.

Figure 3. Role of Gb3 in Batten disease and identification of correctors of Gb3 accumulation.

A Representative confocal images and quantification of SCMAS staining within the lysosome of ARPE-19 WT and CLN3 KO upon depletion of Gb3S (siGb3S), LacCer (siLCS) and GM3s (siGM3S). (***versus WT, °°° versus CLN3 KO siSCR). Data are presented as mean ± SD, °°°/***$P \leq 0.0001$, as determined by ANOVA ($n = 3$ biological replicas in duplicate). Scale bars: 20 μm.

B Identification of FDA compounds reducing Gb3 accumulation: Plot showing the ability of compound hits to reduce Gb3 within the lysosomal compartment compared with DMSO-treated mutant cells. Data are presented as mean ± SD, ***$P \leq 0.0001$, as determined by ANOVA ($n = 3$ biological replicas in duplicate).

C Table showing the EC50s (Half maximal effective concentration) from the dose–response curves of compound hits. EC50s were calculated using the Prism software.

D Representative confocal images and quantification of STX staining within the lysosome of ARPE-19 WT and CLN7 KO in DMSO or treated 48 h with Tamoxifen. (***versus WT, °°° versus CLN3 KO DMSO). Data are presented as mean ± SD, °°°/***$P \leq 0.0001$, as determined by ANOVA ($n = 3$ biological replicas in duplicate). Scale bars: 20 μm.

E Representative confocal images and quantification of STX staining within the lysosome of NPCs WT and derived from $CLN7^{Pa474}$ patient IPSCs in DMSO or treated with Tamoxifen for 48 h. (***versus WT, °°° versus $CLN7^{Pa474}$ DMSO). Data are presented as mean ± SD, °°°/***$P \leq 0.0001$, as determined by ANOVA ($n = 3$ biological replicas in duplicate). Scale bars: 20 μm.

work shows that lysosomotropic anti-cancer drugs promote lysosome-mediated cancer drug resistance by stimulating activation of TFEB and the consequent increase in lysosomal biogenesis, lysosomal exocytosis, and autophagy (Zhitomirsky *et al*, 2018). Indeed, two compound hits in our screen, tamoxifen, and toremifene, both present a tertiary amine that makes them weak-bases able to transiently modify endolysosomal pH by a mechanism that is independent of the ER (Altan *et al*, 1999; Lu *et al*, 2017; Selyunin *et al*, 2019). Consistently, tamoxifen and toremifene were able to reduce Gb3 accumulation and induce TFEB nuclear translocation (Fig EV5A). Conversely, ospemifene, which is structurally related to tamoxifen (Taras *et al*, 2001), possesses similar potency targeting ER-mediated pathways (Wurz *et al*, 2005), but has a hydroxyl group in place of the tertiary amine of tamoxifen in its side chain, was not able to induce TFEB nuclear translocation or Gb3 clearance at 10 μM (Fig EV5B). These observations suggest that the effects of tamoxifen on inducing TFEB activation and reducing intracellular Gb3 storage in BD models are due to its weak-base property. Indeed, while 10 uM tamoxifen was able to transiently alkalinize the lysosome after 3 h treatment, measured by a reduction in lysotracker staining, ospemifene was not effective at a similar concentration (Fig EV5C). Also, we confirm previous data showing that the effect of tamoxifen on lysosomal alkalinization is reversible (Fig EV5C) (Actis *et al*, 2021).

mTOR kinase is the major kinase involved in the negative regulation of TFEB (Laplante & Sabatini, 2012). Thus, we asked whether tamoxifen induces TFEB nuclear translocation by inhibiting mTORC1 activity. Interestingly, mTOR kinase activity measured by both high content imaging assays and immunoblot of its classical substrates, such as p70S6K, 4EPB and ULK1, was not affected by tamoxifen treatment (Appendix Fig S8A and B). However, and in agreement with the induction of TFEB nuclear translocation, tamoxifen reduced the phosphorylation of TFEB while ospemifene did not (Fig 5A and B). Recent work has shown that unlike other substrates of mTORC1, such as those tested above, TFEB is strictly dependent on the activation of RagC and RagD GTPases (Napolitano *et al*, 2020). Indeed, the overexpression of a constitutive active form of RagC (HA-GST-RagCS75L) was able to block tamoxifen-mediated TFEB nuclear translocation and the clearance of Gb3 (Fig 5C and D). As a negative control, we treated HelaTFEB-GFP cells with the selective mTOR kinase inhibitor torin1 that translocates TFEB even in the presence of active RagC (Napolitano *et al*, 2020) (Fig 5C). As expected, ospemifene was not effective at inducing TFEB translocation and was not affected by RagC expression (Fig 5C). Together, our results indicate that the lysosomotropic feature of tamoxifen induces TFEB nuclear translocation through the inhibition of mTORC1 via a Rag-dependent mechanism.

Tamoxifen ameliorates pathologic hallmarks of the $CLN7^{\Delta ex2}$ mouse model

To test the efficacy of tamoxifen *in vivo*, we selected the $CLN7^{\Delta ex2}$ mouse model (Brandenstein *et al*, 2016), which has a more severe phenotype than the existing CLN3 mouse models (Huber *et al*, 2020) and recapitulates the phenotype of human CLN7 patients. Thus, $CLN7^{\Delta ex2}$ mice show the accumulation of autofluorescent material and SCMAS in the central nervous system, as well as brain gliosis, clasping, hind limb paralysis and seizures (Damme *et al*, 2014; Brandenstein *et al*, 2016; Huber *et al*, 2020). We first tested the ability of tamoxifen to reduce pathologic hallmarks of disease by intraperitoneal injections of tamoxifen (40 mg/kg, twice per week) starting from 2.5 month-old mice to 7.5 months of age when the disease phenotype is well established (Brandenstein *et al*, 2016). We investigated the ability of tamoxifen to reduce Gb3 storage by using Shiga toxin staining assay. We found a significant reduction of Gb3 in the cortex and the cerebellum, but not the hippocampus, of 7.5-month-old tamoxifen-treated $CLN7^{\Delta ex2}$ mice compared with their age-matched untreated $CLN7^{\Delta ex2}$ mice (Fig 6). Then, we investigated whether other features of the disease, such as the accumulation of SCMAS and the activation of microglia, could be reversed by the treatment with tamoxifen. Similar to the reduction of Gb3, we found that tamoxifen treatment was able to significantly reduce the accumulation of SCMAS in the cortex and the cerebellum, but not the hippocampus (Fig 7). To test neuroinflammation, we first confirmed that the levels of the small calcium-binding protein IBA1, a specific marker of both resting and activated populations of microglia, were upregulated in brain sections from the $CLN7^{\Delta ex2}$ mouse (Fig 8A and B) compared to the age-matched wild-type mice. By contrast, tamoxifen-treated $CLN7^{\Delta ex2}$ mice presented a significant reduction of IBA1-positive cells in both the cortex and the cerebellum (Fig 8A and B). We found a similar trend in the hippocampus, although it was not statistically significant (Fig 8A and B). Together, these results strongly indicate that tamoxifen treatment can reduce the pathological storage of GB3 and SCMAS as well as reduce signs of neuroinflammation in the brain of $CLN7^{\Delta ex2}$ mice.

Motor deficits are one of the primary clinical features of BD (Raininko *et al*, 1990; Kovács *et al*, 2006; Mole *et al*, 2019). By 8 months of age, $Cln7^{\Delta ex2}$ mice begin to manifest signs of

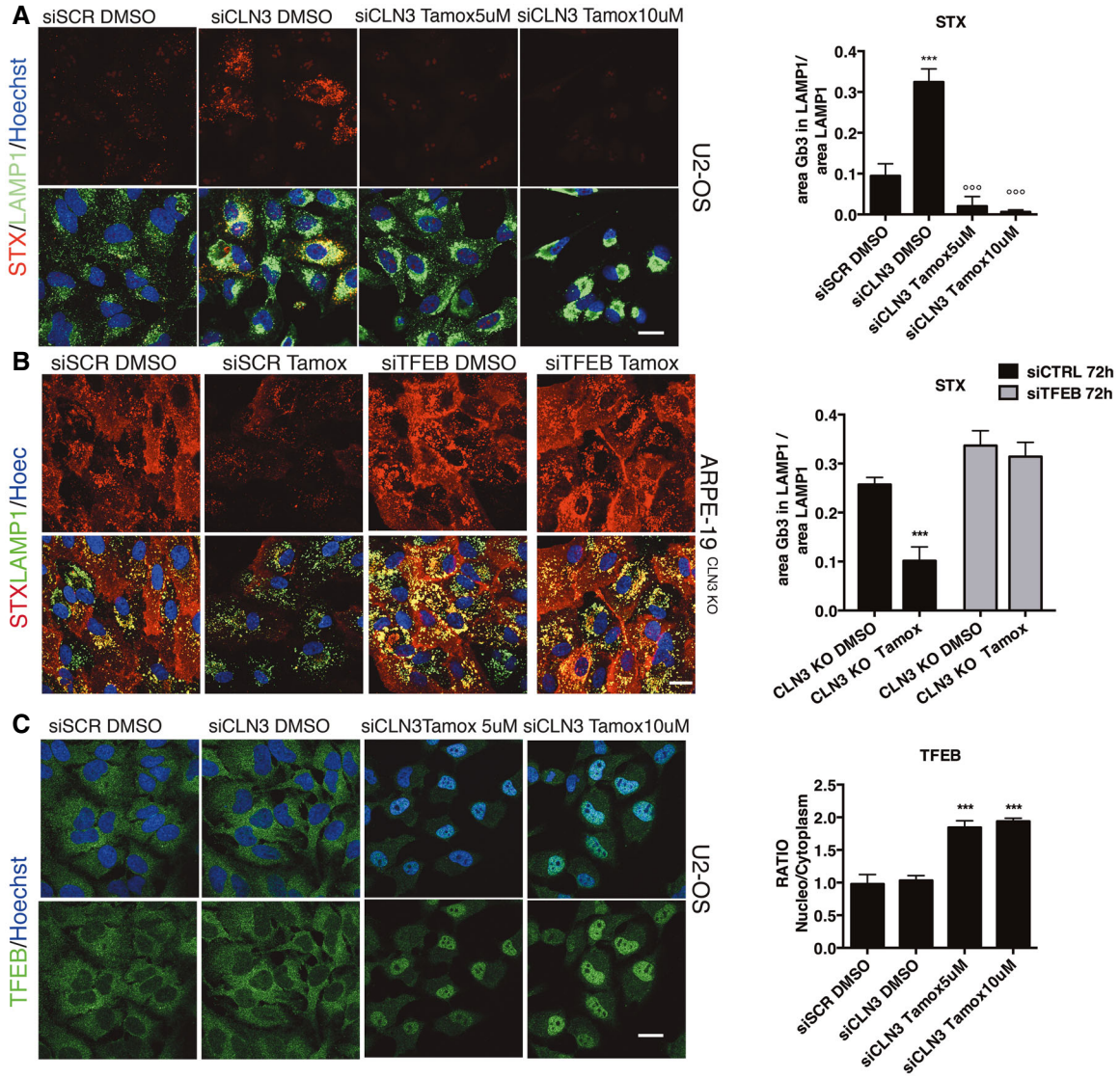

Figure 4. Tamoxifen-mediated clearance of Gb3 is ER-independent but TFEB-dependent.

A Representative confocal images and Quantification of STX within the lysosome in U2-OS and HeLa cells after acute silencing of CLN3 (siCLN3) in DMSO or treated 48 h with Tamoxifen. (***versus siSCR DMSO, °°° versus siCLN3 DMSO). Data are presented as mean ± SD, °°°/***$P \leq 0.0001$, as determined by ANOVA ($n = 3$ biological replicas in duplicate). Scale bars: 20 μm.

B Representative confocal image and quantification of Gb3 in ARPE-19 CLN3 KO cells silenced with siRNA against scramble sequence and TFEB (siTFEB) for 72 h and treated for the last 48 h with DMSO or Tamoxifen. Data are presented as mean ± SD, ***$P \leq 0.0001$, as determined by ANOVA ($n = 3$ biological replicas in duplicate). Scale bars: 20 μm.

C Representative confocal image and quantification of TFEB in U2-OS cells silenced with siRNA against scramble sequence and CLN3 (siCLN3) for 72 h and treated for the last 48 h with DMSO or Tamoxifen (5 and 10 μM). Data are presented as mean ± SD, ***$P \leq 0.0001$, as determined by ANOVA ($n = 3$ biological replicas in duplicate). Scale bars: 20 μm.

neurological deterioration attested by clasping phenotype, hind-leg paralysis, tremor and myoclonus epilepsies (Brandenstein *et al*, 2016). Motor deficits and balance are detectable by measuring the latency to fall from the rotarod and can be used as a read-out of the efficacy of potential therapeutic compounds in BD models (Finn *et al*, 2011). We performed the rotarod test (Finn *et al*, 2011) during the whole period of treatment (6 measurements in total). Interestingly, tamoxifen-treated wild-type mice improved with age. CLN7$^{\Delta ex2}$ mice exhibit a marked locomotor dysfunction in the late stages of the disease, while tamoxifen-treated CLN7$^{\Delta ex2}$ mice were less likely to fall when compared with the untreated CLN7$^{\Delta ex2}$ mice, although did not improve to the extent of wild-type mice (Fig 8C). We tested motor dysfunction by using the hindlimb clasping test (Lieu *et al*, 2013). In healthy mice, both hindlimbs remain splayed outward away from the abdomen with splayed toes. Partial retraction of one or both hindlimbs towards the body indicates a moderate phenotype. Severe motor dysfunction correlates with both hindlimbs partially retracted towards the body and touching the

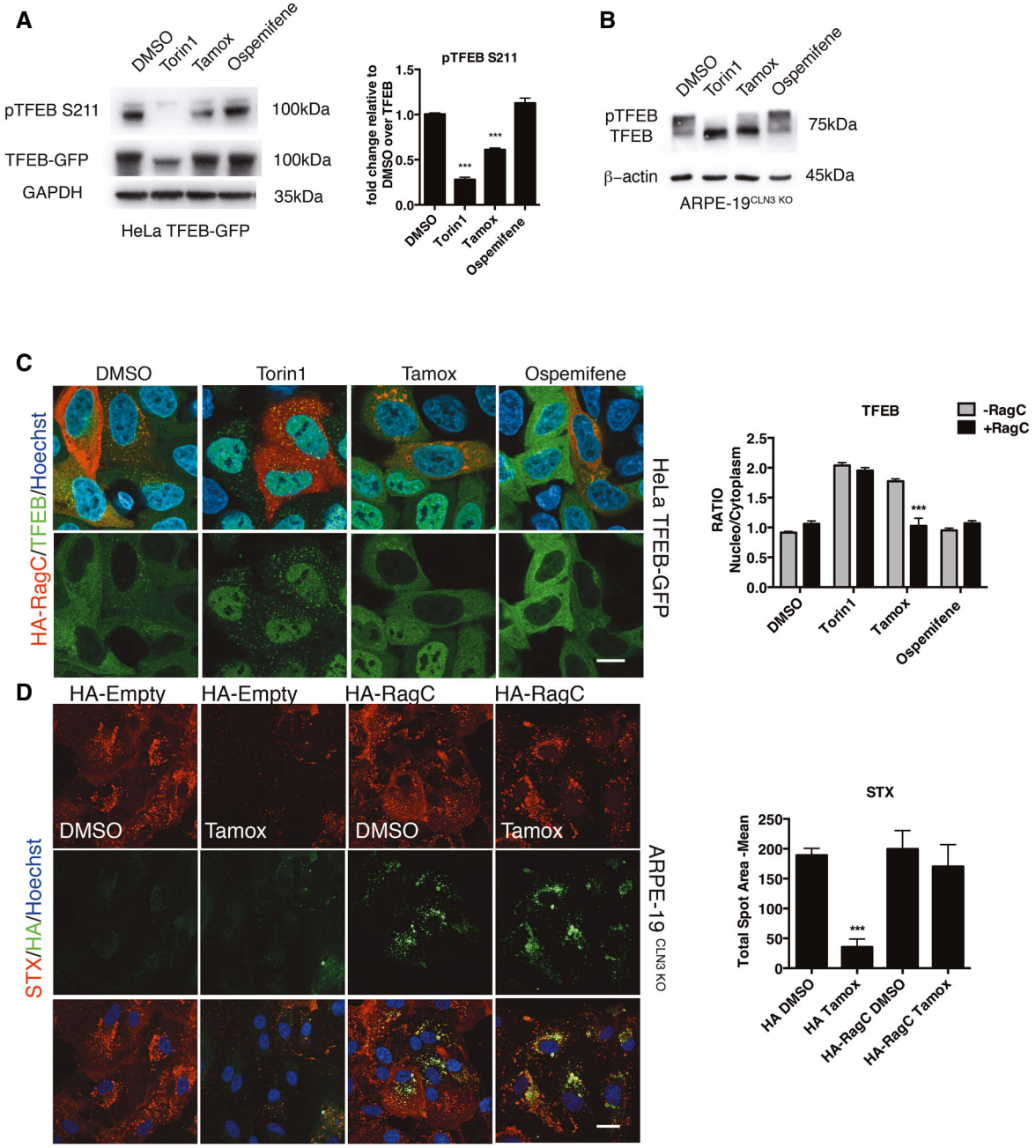

Figure 5. Tamoxifen dephosphorylates TFEB.

A Immunoblot analysis and quantification of pTFEB S211 in HeLa cells stably expressing TFEB-GFP. Data are presented as mean ± SD, ***$P \leq 0.0001$, as determined by ANOVA ($n = 3$ biological replicas). GAPDH immunoblotting was performed as a loading control.

B Immunoblot analysis of TFEB shift in ARPE-19 CLN3 KO cells. β-actin immunoblotting were performed as a loading control.

C Representative confocal image and quantification of TFEB localization in HeLa TFEB-GFP transfected with RagC for 48 h and treated for the last 3 h with DMSO, Torin1, Tamoxifen or Ospemifene. Ratios of nuclear to cytosolic TFEB localization in RagC non-expressing (RagC-) and RagC-expressing cells (RagC+) are presented as mean ± SD, ***$P \leq 0.0001$, as determined by ANOVA ($n = 3$ biological replicas in duplicate). Scale bars: 20 μm.

D Representative onfocal images and quantification of STX in ARPE-19 CLN3 KO cells transfected with empty vector or HA-RagC for 48 h and treated for 48 h with DMSO or Tamoxifen. STX average spot area presented as mean ± SD, ***$P \leq 0.0001$, as determined by ANOVA ($n = 3$ biological replicas in duplicate). Scale bars: 20 μm.

abdomen. As expected, the wild-type animals showed a normal extension reflex in the hindlimbs, while 7.5-month-old mutant mice did not. We found that hindlimb clasping improved in the tamoxifen-treated CLN7$^{\Delta ex2}$ mice (Fig 8D). Together, the results of the motor tests suggest a partial recovery of motor coordination capacity in CLN7$^{\Delta ex2}$ mice treated with tamoxifen. In conclusion,

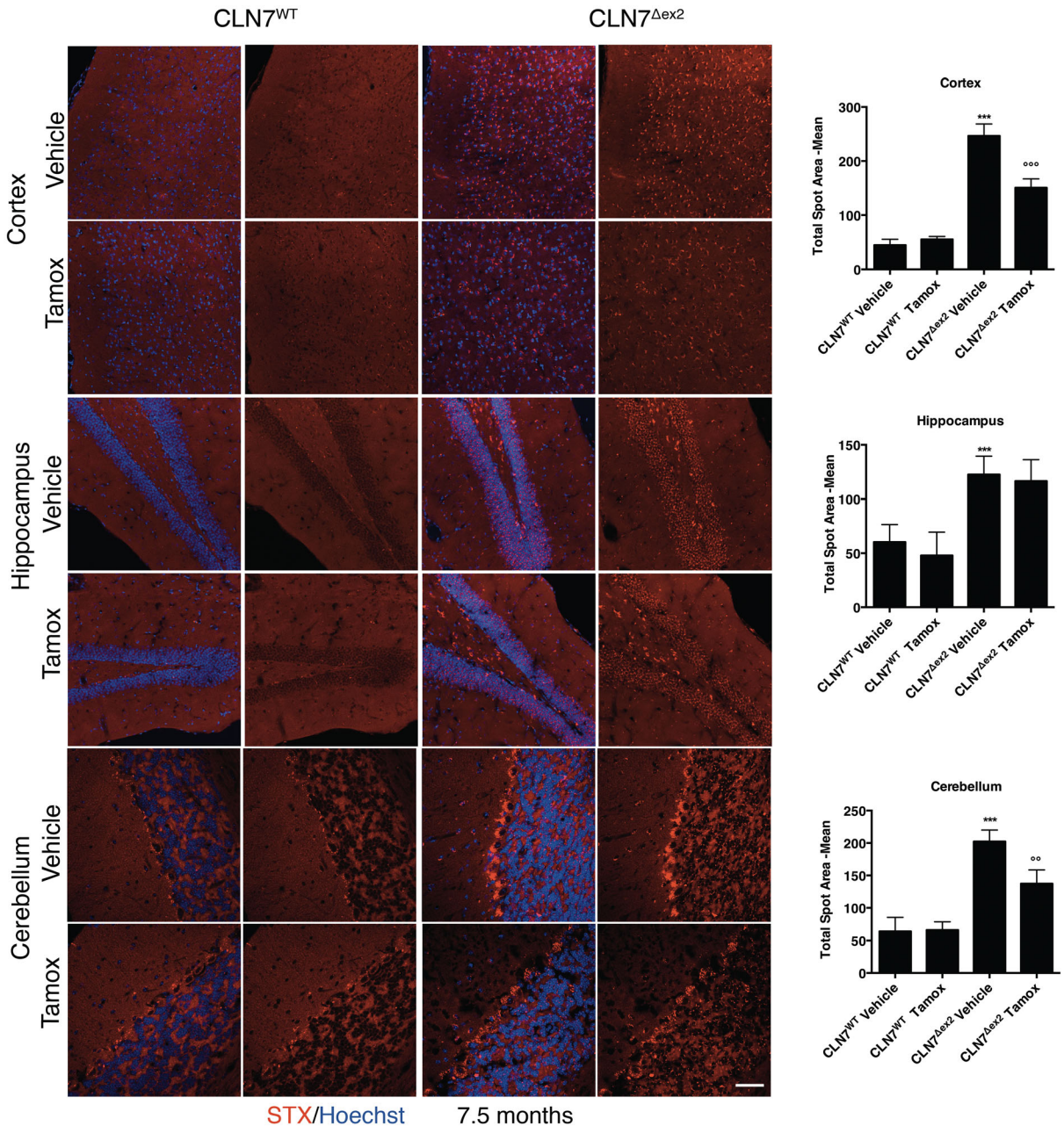

Figure 6. Tamoxifen reduce Gb3 accumulation in brain of CLN7$^{\Delta ex2}$ mice.

Representative confocal images of STX in the Cortex, Hippocampus and Cerebellum brain section derived from 7.5-month-old mouse WT or CLN7$^{\Delta ex2}$ injected with vehicle or Tamoxifen (Tamox). Quantification of confocal images, the plot shows the quantification of the STX average spot area normalized for the number of Hoechst-positive cells. (***versus WT, °°°/°° versus CLN7$^{\Delta ex2}$ Vehicle). Data are presented as mean ± SD, **/°°$P \leq 0.001$, ***/°°°:$P \leq 0.0001$, as determined by ANOVA ($N \geq 3$ biological replicas). Scale bars: 60 μm.

in vivo administration of tamoxifen improves biochemical markers and motor deficits of CLN7 disease.

Discussion

We have discovered using cellular models of CLN3 and CLN7 diseases, and NPCs generated from iPS cells derived from CLN7 patient fibroblasts that Gb3 accumulated within lysosomes as a consequence of disease. This Gb3 accumulation is even more striking in neurons of CLN3 and CLN7 mouse models. *In vitro*, silencing of Gb3 synthase leads to the reduction of Gb3 levels, and also decreases the characteristic disease storage of subunit SCMAS, indicating that the altered levels of Gb3 might be part of the neuropathological features characterizing these diseases. Previous alterations of some glycosphingolipids such as ceramide, LacCer and GM3 have

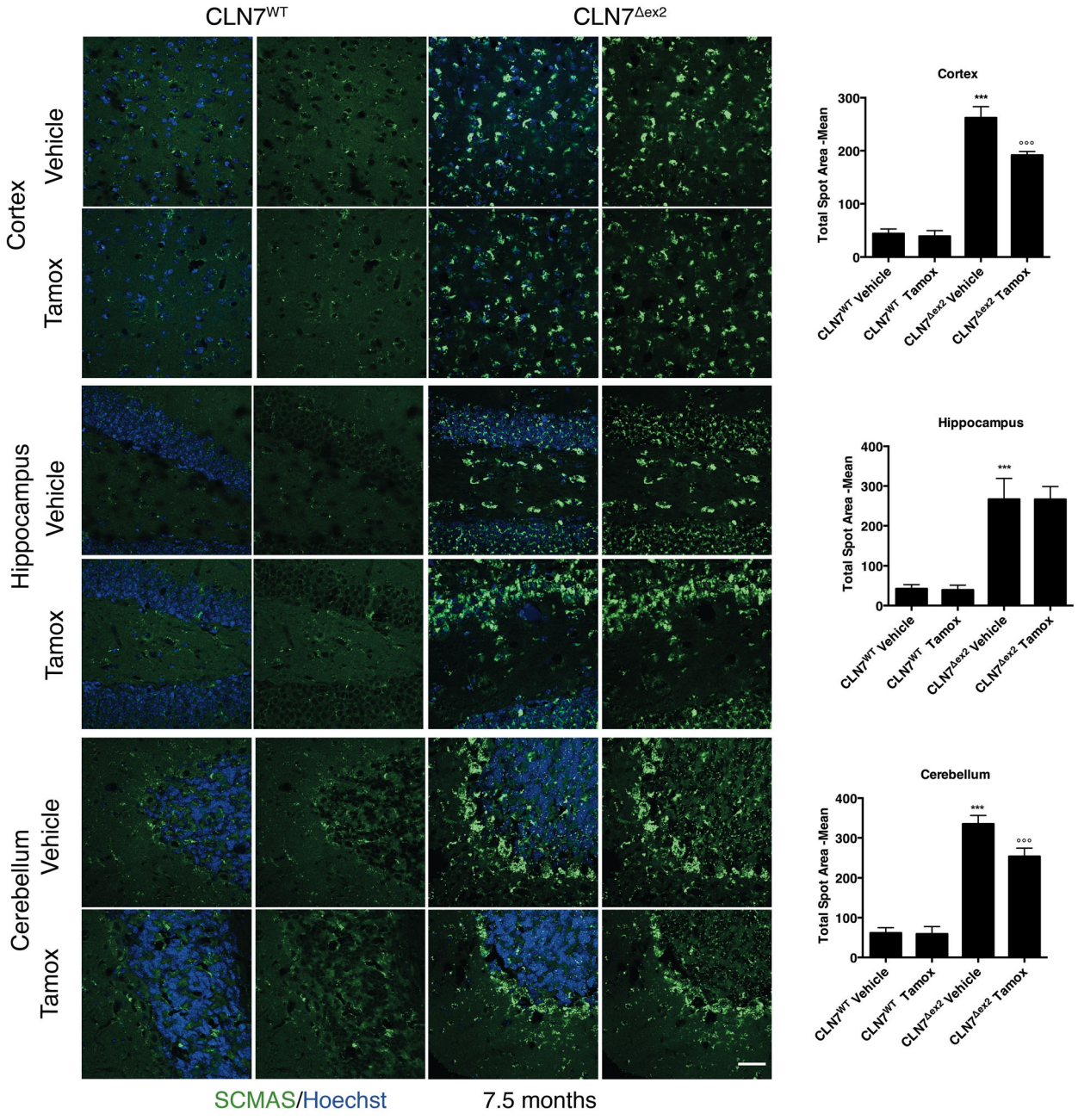

Figure 7. Tamoxifen reduces SCMAS accumulation in the brains of CLN7$^{\Delta ex2}$ mice.

Representative confocal images of SCMAS in the Cortex, Hippocampus and Cerebellum brain section derived from mouse WT or CLN7$^{\Delta ex2}$ injected with vehicle or Tamoxifen. Quantification of confocal images, the plot shows the quantification of the SCMAS average spot area normalized for the number of Hoechst-positive cells. (***versus WT, °°° versus CLN7$^{\Delta ex2}$ Vehicle). Data are presented as mean ± SD, ***$P \leq 0.0001$, as determined by ANOVA ($N \geq 3$ biological). Scale bars: 60 μm.

been described in BD models (Puranam *et al*, 1999; Rusyn *et al*, 2008; Schmidtke *et al*, 2019). Indeed, in addition to endogenous Gb3 accumulation, the lipidomic analysis of CLN3 and CLN7 KO models showed increased levels of LacCer, the common precursor of both Gb3 and GM3 synthesis. Lipidomics analysis of freshly isolated neurons from the forebrain of CLN7 mice, displays an even higher elevation of Gb3 and GM3 and their precursor GlcCer. However, we observed that while the depletion of LacCer synthase or Gb3 synthase reduced SCMAS accumulation, the silencing of the unrelated GM3 synthase did not, indicating that unbalancing the pathway involving the synthesis/degradation of Gb3 may contribute to the pathogenesis of CLN3 and CLN7 diseases. Recent SILAC-based quantitative analysis of the lysosomal proteome of MEFs from CLN7 mice showed significant differences in the expression of proteins involved in lipid trafficking and glycosphingolipid catabolism (Danyukova *et al*, 2018). Thus, these changes may be related

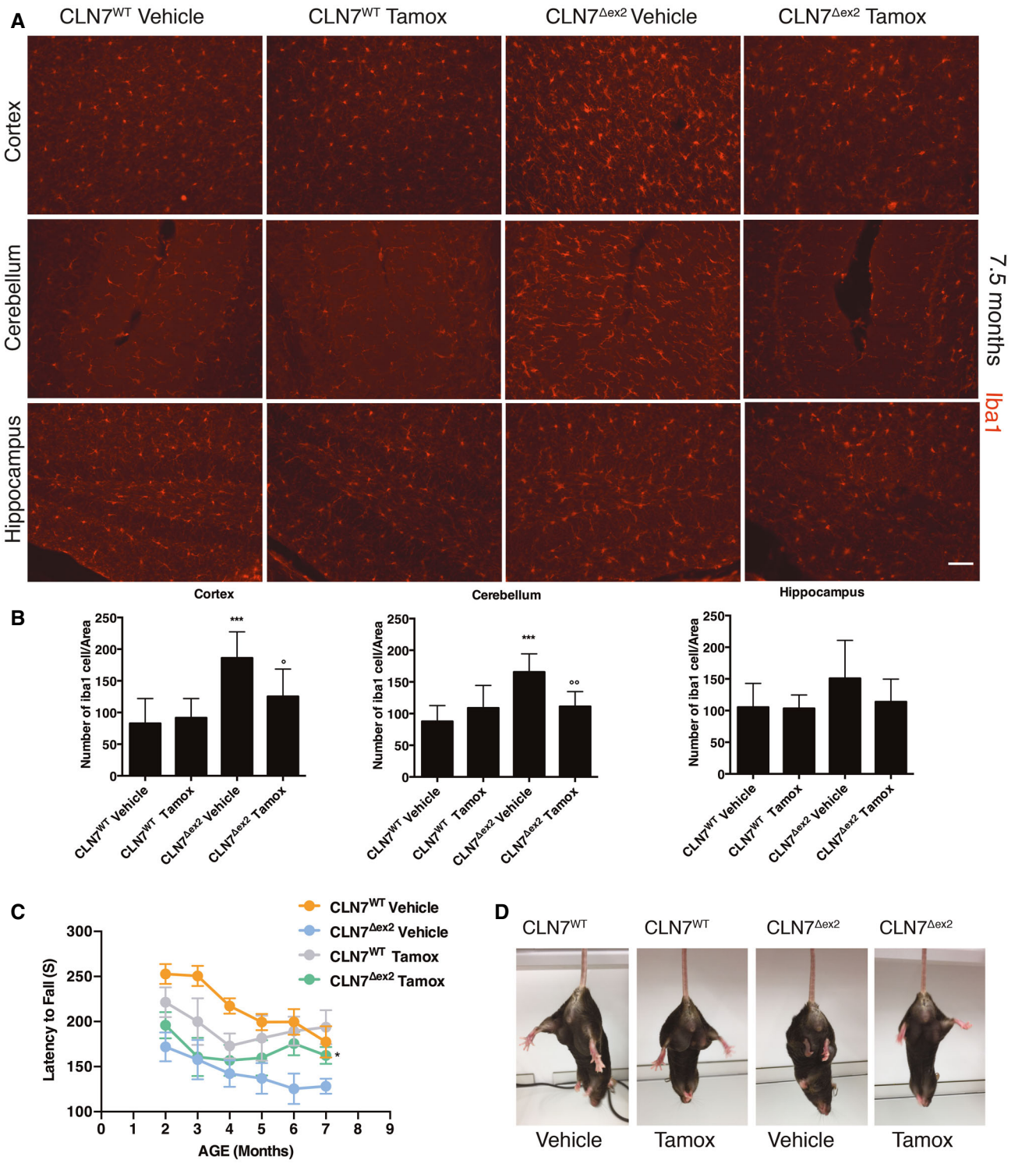

Figure 8. Tamoxifen ameliorates CLN7$^{\Delta ex2}$ phenotype.

A, B Representative confocal images and quantification of IBA-1 in the Cortex, Hippocampus and Cerebellum brain section derived from WT or CLN7$^{\Delta ex2}$ mice injected with the vehicle or Tamoxifen. (***/**/*versus WT, °°°/°°/° versus CLN7$^{\Delta ex2}$ Vehicle). Data are presented as mean ± SD, $^{*/o}P \leq 0.01$, $^{**/oo}P \leq 0.001$, $^{***}P \leq 0.0001$, as determined by ANOVA ($N \geq 3$ biological replicas). Scale bars: 50 μm.

C Plots show the quantification latency to fall from the rotarod. Data are presented as mean ± SD, $^{*}P \leq 0.01$, as determined by ANOVA ($N \geq 3$ biological replicas).

D Representative images of hindlimb clasping test in mouse WT or CLN7Δex2 injected with vehicle or Tamoxifen.

to the pathologic accumulation of Gb3 in CLN7 disease. The same study revealed that the CLN5 protein is also downregulated in CLN7 MEFs (Danyukova *et al*, 2018). CLN5 mutations present with a similar disease onset, progression and phenotypes as CLN7 disease suggesting that both genes may act in a common pathway that is disturbed in both diseases. Additionally, CLN5 can interact with CLN3 (Vesa *et al*, 2002), suggesting that CLN5 disease, together with CLN3 and CLN7, may belong to a subset of BDs accumulating Gb3. Future studies are needed to confirm this hypothesis and to determine the interaction of these three proteins in the regulation of brain Gb3 levels.

Our observations allowed us to develop a cell-based HCI for Gb3 accumulation assay to screen > 1,200 FDA compounds. Among the compound hits, we focused on the selective oestrogen receptor modulator (SERM) tamoxifen that promotes the clearance of lysosomal Gb3 in CLN3 and CLN7 cells. We found that tamoxifen activity is independent of its ER modulation but requires TFEB activation. TFEB can promote clearance of pathological storage both *in vitro* and *in vivo* in various models of LSDs (Sardiello *et al*, 2009; Spampanato *et al*, 2013; Palmer, 2015; Kauss *et al*, 2020). Indeed, we confirmed that TFEB expression was sufficient to promote Gb3 clearance in ARPE-19-CLN3-KO cells. Thus, tamoxifen-mediated clearance via TFEB activation may represent a small molecule-based strategy to treat common types of BD. Using ospemifene, an analog of tamoxifen that does not contain the tertiary amine conferring lysosomotropic properties, we determined that the activation of TFEB requires the weak-base nature of tamoxifen. Consistently, another lysosomotropic analog of tamoxifen, toremifene, also induces Gb3 clearance and TFEB activation *in vitro*. Another lysosomotropic SERM, raloxifene (Selyunin *et al*, 2019), is effective in neuroprotection and immunomodulatory effects in a mouse model of Parkinson's disease (Poirier *et al*, 2016), supporting the potential benefits of repurposing approved stilbenoids to treat LSDs and more common neurodegenerative disorders. Since most of the approved CNS-penetrant drugs are lysosomotropic, future studies are needed to elucidate whether all compounds with this feature can promote clearance of pathological storage through the activation of TFEB or other properties are involved. Also, the logP and pKa properties of five out of the nine hits identified correspond to drugs with potential lysosomotropic properties (logP > 2; pKa 6-11), supporting further studies of these compounds in BD models.

Mechanistically, we observed that tamoxifen induced TFEB nuclear translocation by specifically impairing mTORC1-mediated phosphorylation of TFEB without affecting mTORC1 activity towards canonical substrates such as S6K, 4EBP and ULK1. Giving the recent observations that RagC/D GTPase activity can mediate selective phosphorylation of mTORC1 substrates (Napolitano *et al*, 2020), we postulated that lysosomotropic properties of tamoxifen specifically affect RagC/D activity leading to the dephosphorylation of TFEB. A few reports suggest that tamoxifen can alter glycosphingolipid metabolism in cancer cells (Lavie *et al*, 1997; Morad & Cabot, 2015). Thus, future studies are needed to determine whether the reported effects of tamoxifen on glycosphingolipid regulation may contribute to Gb3 clearance and whether the activation of TFEB is involved.

We tested the efficacy of tamoxifen as a therapeutic agent by treating $CLN7^{\Delta ex2\ mice}$. Tamoxifen treatment using a therapeutic concentration of 40 mg/kg ameliorated various phenotypic hallmarks of CLN7 mouse including; (i) the accumulation of Gb3, (ii) SCMAS, (iii) microglia activation and (iv) improved motor dysfunction measured by rotarod and hindlimb clasping.

In humans, tamoxifen is used orally and crosses the blood–brain barrier. It has shown neuroprotective activity in rat and dog models of brain ischaemia and stroke, respectively (Kimelberg *et al*, 2003; Kimelberg, 2008; Boulos *et al*, 2011), and it has been used in the treatment of a variety of childhood disorders (Maddalozzo *et al*, 1993; Walter *et al*, 2000; Derman *et al*, 2003; Lawrence *et al*, 2004; Kreher *et al*, 2005). Adverse effects in these populations have been rare, and tamoxifen seems to have an excellent safety profile overall. Together with our data, therefore, we propose tamoxifen as a novel therapeutic for two types of BD, CLN3 and CLN7 diseases.

Materials and Methods

Cell culture and siRNA transfection

ARPE-19 (retinal pigment epithelium (RPE) cell line), U2-OS and HeLa cells were purchased at ATCC and cultured in DMEM F12 and DMEM, supplemented with 10% foetal bovine serum, 200 μM L-glutamine, 100 μM sodium pyruvate, 5% CO_2 at 37°C. Human ARPE-19 cells were chosen because they are diploid and non-transformed. ARPE-19 depleted of CLN3 was generated by Dr. J. Monfregola at TIGEM (Naples) and was cultured in DMEM F12 supplemented with 10% foetal bovine serum, 200 μM L-glutamine, 100 μM sodium pyruvate, 5% CO_2 at 37°C.

Human control patient fibroblasts were provided by Professor Brunetti (TIGEM), CLN3 patient fibroblasts were purchased from Coriell Institute and cultured in DMEM supplemented with 15% foetal bovine serum, 200 μM L-glutamine, 5% CO_2 at 37°C. HeLa TFEB/TFE3 KO cells were generated from Dr. R.J. Youle from the National Institutes of Health, Bethesda. U2OS was purchased at ATCC and cultured in DMEM supplemented with 10% foetal bovine serum, 200 μM L-glutamine, 5% CO_2 at 37°C.

Cells were silenced with 25 nM of siRNA against CLN3, CLN6, CLN7, Gb3S and TFEB for 72 h using Lipofectamine RNAimax (Thermo Fisher) according to the protocol from the manufacturer. All control experiments to confirm silencing efficiency (by qPCR or immunoblot) are reported.

Generation of ARPE-19 CRISPR/Cas9 CLN3 KO and CLN7 KO cell lines

ARPE-19 (ATCC CCRL-2320) cells carrying a homozygous deletion of a C were generate by using the CRISPR/Cas9 system. The gRNA sequence with low off-target score have been selected using the http://crispor.tefor.net/crispor.py tool. An "ALL in One" vector expressing Cas9, the specific gRNA and GFP was obtained from SIGMA (CAS9GFPP). The CAS9GFPP was nucleofected in ARPE19 cells using the Amaxa nucleofector kit V (Cat No VCA-1003) and transfected GFP-positive cells were FACS sorted into 96-well plates to obtain single-cell derived colonies carrying the INDEL mutations. Upon genomic DNA extraction and DNA Sanger sequencing, clones carrying the c.1055delA for CLN3 KO cells and c.103delC for CLN7 KO cells were selected and expanded.

Drugs and cellular treatments

The following drugs were used to perform the assays: Tamoxifen (10 μM, SIGMA 3–48 h), Toremifene (10 μM, SIGMA 48 h) and Ospemifene (10 μM, SIGMA 48 h).

Screening and dose-response: Cells were plated on 384-well plates (2×10^4 cells per well). After 24 h, cells were treated with 10 μM compounds or 0.1% dimethyl sulfoxide (DMSO) in complete medium. The Prestwick Library consists of 1,280 FDA-approved drugs, all off-patent, dissolved in DMSO. The drugs from the 96-well source plate were diluted and compacted in 384-well plates to a concentration of 100 μM in the DMEM medium (working plate). To study the effect of the drugs, 5 μl of the drugs at 100 μM in DMEM medium were added to plates containing 45 μl of medium (10 μM final drug concentration with 0.1% DMSO). As a positive control of Gb3 reduction, we used the glucosylceramide synthase inhibitor PDMP.

For the dose–response confirmation test, compounds were serially diluted from 10 mM stock into complete medium and added to plates starting at 30 to 0.1 μM. The final concentration of DMSO did not exceed 0.3% in the dose–response assays.

Cells were incubated together with drugs 48 h at 37°C and 5% CO_2.

Screening quality control analysis

We confirmed the robustness of the STX-assay using two different quality control scores (*Z*-score and SSMD-score) (Appendix Fig S4A). To exclude toxicity in the primary screening, we discard compounds reducing the cell viability to 40% compared to DMSO-treated controls. To ensure reproducibility, we also analyse the correlation between plate replicates (Appendix Fig S4B). As a cut-off for hit selection, we select compounds reducing the lysosomal accumulation of Gb3 greater than the mean of Gb3 in DMSO-treated CLN3 cells minus two standard deviations.

Antibodies and western blotting

The following antibodies were used: β-Actin (Santa Cruz sc-47778, 1:4,000), ULK1 (Cell signaling cat. 8054 1:1,000), Phospho-ULK1 (Ser757) (Cell signaling cat. 6888 1:1,000), p70 S6 Kinase (Cell signaling cat. 2708 1:1,000), Phospho-p70 S6 Kinase (Thr389) (Cell signaling cat. 9205 1:1,000), GAPDH (6C5) (Santa Cruz sc-32233, 1:2,000), 4EBP (Cell signaling cat. 9644 1:1,000), p4EBP (Cell signaling cat. 9456 1:1,000), TFEB (Cell signaling cat. 4240S 1:1,000) and TFEB-pS211 (custom-generated in collaboration with Bethyl Laboratories 1:1,000). For immunoblot, the total cell lysates were prepared by solubilization of cell pellets in 10mM Tris–HCl pH 8.0 and 0.2% SDS supplemented with protease and phosphatase inhibitors (SIGMA). Protein concentration was determined by the Bradford method. After SDS-PAGE and immunoblotting, the proteins recognized by the specific antibody were visualized by chemiluminescence methods (Luminata Crescendo Western HRP substrate, Millipore) using peroxidase-conjugated anti-rabbit or anti-mouse secondary antibodies (Millipore). Membranes were developed using a Chemidoc UVP imaging system (Ultra-Violet Products Ltd) and densitometric quantification was performed in unsaturated images using ImageJ (NIH).

Immunofluorescence

For immunofluorescence, the following antibodies were used: LAMP1 (Santa Cruz cat. sc-20011, 1:400), TFEB (Cell signalling cat. 4240S 1:200), Phospho-S6 Ribosomal Protein (Ser235/236) (Cell signalling cat. 9865 1:400), anti-ATP-synthase C (Abcam ab181243 1:500), HA.11 clone 16B12 (BioLegend 901501 1:500) and Nestin (Thermo Fisher MA1-110 1:200). Cells were fixed in PFA 4% for 20 min and permeabilized with blocking buffer saponin whereas for TFEB immunostaining cells were permeabilized in 0.1% (w/v) Triton X-100, 1% (w/v) horse serum, and 1% (w/v) BSA in PBS. Cells were incubated with the indicated primary antibodies for 2 h and subsequently incubated with secondary antibodies for 45 min (AlexaFluor 488 A21202, AlexaFluor 488 A11008, AlexaFluor 568, A10037, AlexaFluor 568 A10042, all Thermo Fisher 1:400). For confocal imaging, the samples were examined under a Zeiss LSM 800 confocal microscope. Optical sections were obtained under a × 63 or ×40 immersion objective at a definition of 1,024 × 1,024 pixels (average of eight or sixteen scans), adjusting the pinhole diameter to 1 Airy unit for each emission channel to have all the intensity values between 1 and 254 (linear range). For high content images, we used the OPERA high content imager from PerkinElmer.

For image analysis, we used Columbus 2.6.0.127073 (built at 03:56 on 05/02/19) released by PerkinElmer. This online platform is based on Harmony High-Content Imaging and Analysis Software which provides an easy quantification of complex cellular phenotypes.

Lipidomic analysis

For Lipidomics analysis, 200,000 cell culture lysates or 10 μg of protein of homogenized immunoisolated neuron samples were spiked with 4.28 μl of internal standard lipid mixture containing 500 pmol of Chol-d6, 100 pmol of Chol-16:0-d7, 100 pmol of DAG 17:0-17:0, 50 pmol of TAG 17:0-17:0-17:0, 100 pmol of SM 18:1;2-12:0, 30 pmol of Cer 18:1;2-12:0, 30 pmol of GalCer 18:1;2-12:0, 50 pmol of LacCer 18:1;2-12:0, 300 pmol of PC 17:0-17:0, 50 pmol of PE 17:0-17:0, 30 pmol of PI 16:0-16:0, 50 pmol of PS 17:0-17:0, 30 pmol of PG 17:0-17:0, 30 pmol of PA 17:0-17:0, 25 pmol of Gb3 18:1;2-17:0, 25 pmol of GM3 18:1;2-18:0-d5, 25 pmol of GM2 18:1;2-18:0-d9, 25 pmol of GM1 18:1;2-18:0-d5m 25 pmol of GD1a 18:1;2-17:0 and subjected to lipid extraction at 4°C, as described elsewhere (Sampaio *et al*, 2011). Briefly, the sample was dissolved in 200 μl of 155 mM ammonium bicarbonate and then extracted with 1 ml of chloroform-methanol (10:1) for 2 h. The lower organic phase was collected, and the aqueous phase was re-extracted with 1 ml of chloroform-methanol (2:1) for 1 h. The lower organic phase was collected and evaporated in a SpeedVac vacuum concentrator. Lipid extracts were dissolved in 100 μl of infusion mixture consisting of 7.5 mM ammonium acetate dissolved in propanol:chloroform:methanol [4:1:2 (vol/vol)]. Samples were analysed by direct infusion in a QExactive mass spectrometer (Thermo Fisher Scientific) equipped with a TriVersa NanoMate ion source (Advion Biosciences). 5 μl of sample was infused with gas pressure and voltage set to 1.25 psi and 0.95 kV, respectively.

HexCer was detected in the 10:1 extract, by negative ion mode FTMS as a deprotonated ion by scanning m/z = 520–1,050 Da, at

$R_{m/z\ =\ 200}$ = 280,000 with lock mass activated at a common background (m/z = 529.46262) for 30 s. Every scan is the average of 2 micro-scans, automatic gain control (AGC) was set to 1E6 and maximum ion injection time (IT) was set to 200 ms. Hex2Cer and Hex3Cer were detected in the 2:1 extract, by positive ion mode FTMS as protonated ions by scanning m/z = 800–1,600 Da, at $R_{m/z\ =\ 200}$ = 280,000 with lock mass activated at a common background (m/z = 1194.81790) for 30 s. Every scan is the average of 2 micro-scans, automatic gain control (AGC) was set to 1E6 and maximum ion injection time (IT) was set to 50ms. GM3 was detected in the 2:1 extract, by polarity switch to negative ion mode FTMS as a deprotonated ion by scanning m/z = 1,100–1,650 Da, at $R_{m/z\ =\ 200}$ = 280,000 with lock mass activated at a common background (m/z = 1175.77680) for 30 s. Every scan is the average of 2 micro-scans, automatic gain control (AGC) was set to 1E6 and maximum ion injection time (IT) was set to 50 ms. All data were acquired in centroid mode.

All data were analysed with the lipid identification software, LipidXplorer (https://doi.org/10.1186/gb-2011-12-1-r8). Tolerance for MS and identification was set to 2 ppm. Data post-processing and normalization to internal standards were done manually. For the sake of simplicity, only the pertinent data are displayed (HexCer, Hex2Cer, Hex3Cer and GM3) and normalized to the total lipid identified. Raw data are represented in Appendix Tables S1–S4.

Induced pluripotent stem cells (iPSC) and Neural Progenitor Cells (NPC) generation

CLN7 patient fibroblasts were obtained from the UCL NCL repository (https://www.ucl.ac.uk/ncl-disease/). iPSCs were generated from a cell line originally derived pre-2005 from skin biopsy fibroblasts from a CLN7 patient (UCL 474 Pa) and then characterized and differentiated to NPC as previously described (FitzPatrick *et al*, 2018). Human iPSC-derived NPCs from an age-matched control patient and patient 474 Pa harbouring a homozygous CLN7 mutation (c.1393C > T; p.R465W) were plated on Matrigel. Matrix in Nunc™ Lab-Tek™ 8-well Chamber Slides and cultured in Neural Expansion Medium (NEM) with DMEM/F12, NEAA, N-2 supplement, B-27 supplement, heparin, bFGF protein and penicillin/streptomycin.

Ethics approval

Informed consent to generate cell lines used in this research was obtained from all human subjects, and experiments conformed to the WMA Declaration of Helsinki and to the principles set out in the USA Department of Health and Human Services Belmont Report.

Fluorescent assays

Cholera toxin

Cells were cultured on 96-well plates and incubated in a serum-free medium containing 1 μg/ml AlexaFluor488-labelled cholera toxin subunit B (C22841 Thermo Fisher Scientific) for 30 min at 33°C. Subsequently, cells were washed three times with PBS and fixed in 4% (w/v) paraformaldehyde for 10 min at room temperature. Nuclei were stained with Hoechst for 10 min.

Filipin III

Cells were fixed with 4% paraformaldehyde 10 min. The paraformaldehyde was rinsed with PBS and quenched with 50 mM glycine in PBS. Cells were then incubated for 2 h at room temperature in PBS containing 50 μg/ml filipin III (from Streptomyces filipinensis SIGMA F4767). Nuclei were stained with DRQ5 1:5,000 (62254 Thermo Fisher Scientific) for 10 min.

Shiga Toxin

Cells were fixed with 4% paraformaldehyde 10 min and permeabilized in 0.1% (w/v) saponin, 0.5% (w/v) BSA and 50 mM NH_4Cl in PBS (blocking buffer saponin). STX were incubated alone or with LAMP1 antibody in blocking buffer saponin for 2 h (1:50,000) and subsequently incubated with secondary antibodies for 45 min. Nuclei were stained with Hoechst for 10 min.

Lysotracker

Cells were cultured on 96-well plates and incubated in a serum-free medium containing 1:10,000 AlexaFluor568-labelled Lysotracker Red (L7528 Thermo Fisher Scientific) for 20 min at 33°C. Subsequently, cells were washed three times with PBS and fixed in 4% (w/v) paraformaldehyde for 10 min at room temperature. Nuclei were stained with Hoechst for 10 min.

RNA extraction and quantitative PCR

Total RNA was extracted from cells using the RNeasy Plus Mini Kit (Qiagen). Reverse transcription was performed using the QuantiTect Rev Transcription Kit (Qiagen). Real-time quantitative Reverse Transcription PCR (qRT–PCR) was performed using the LightCycler® System 2.0 (Roche Applied Science). HPRT was used for qRT–PCR as a reference gene. The parameters of real-time qRT–PCR amplification were according to Roche recommendations. Primer sequences are available upon request.

Ethical use of animals

Mice were bred at the Animal Experimentation Unit of the University of Salamanca. All protocols were performed according to the European Union Directive 86/609/EEC and Recommendation 2007/526/EC, regarding the protection of animals used for experimental and other scientific purposes, enforced in Spanish legislation under the law 6/2013. All protocols were approved by the Bioethics Committee of the University of Salamanca. The $Cln3^{\Delta ex7/8}$ knock-in mice were bred in a pathogen-free animal facility at the University Medical Center Hamburg-Eppendorf according to institutional guidelines.

Mice genotyping by a polymerase chain reaction

For $Cln7^{\Delta ex2}$ genotyping, a PCR with the following primers was performed 5′-TGGTGCATTAATACAGTCCTAGAATCCAGG-3′, 5′-CTAGGGAGGTTCAGATAGTAGAACCC-3′, 5′-TTCCACCTAGAGAATGGAGCGAGATAG-3′, resulting in a 290 bp band in the case of $Cln7^{\Delta ex2}$ mice, and 400 bp for wild type (Brandenstein *et al*, 2016). In the case of $Cln3^{\Delta ex7/8}$ knock-in mice, a band with 250 bp is obtained for wild type, and a 500 bp in the case of $Cln3^{\Delta ex7/8}$ knock-in mice using the following primers: 5′- CAGCATCTCCTCAGGGCTA-3′, 5′-CCAACATAGAAAGTAGGGTGTGC-3′, 5′- GAGCTTTGTTCTGGTGCCTTC-3′, 5′- GCAGTCTCTGCCTCGTTTTCT-3′ *(19)*.

Neuronal cell isolation from the brain cortex

Adult mouse brain (from 6 months animals) tissue was dissociated with the Adult Brain Isolation Kit (Miltenyi Biotec). Neurons were separated in the dissociated cells, after removal of debris and red blood cells, and neurons were separated with the Neuron Isolation Kit (Miltenyi), according to the manufacturer's protocol. The identity of the isolated fraction was confirmed previously (Lopez-Fabuel *et al*, 2016) by Western blot against the neuronal marker microtubule-associated protein 2 (MAP2).

Tamoxifen administration

Twice per week 40 mg of tamoxifen per gram of body weight (from a stock solution of tamoxifen in 20% (vol/vol) ethanol and 80% (vol/vol) of sunflower oil) were injected intraperitoneally to male mice of 2.5 months old until they reach 7.5 months old. Body weight was evaluated before injections, as well as the general aspect of the mice (eyes, fur and behaviour) to see the influence of tamoxifen in mice. Control animals received injections with the tamoxifen vehicle (20% (vol/vol) ethanol and 80% (vol/vol) of sunflower oil). A rotarod test was done before treatment beginning, and every month during it, to all the studied animals.

Locomotor assessment (Rotarod Test)

The rotarod test (Rotarod apparatus, model 47600, Ugo Basile) was used to analyse motor balance and coordination. Male mice were previously trained during three consecutive days, 2 days before the test. The rotarod conditions were gradually accelerated from 4 to 45 r.p.m., reaching the final speed at 270 s. The latency to fall was evaluated and averaged for each animal during the 3 days of the experiment.

Mouse perfusion and immunohistochemistry

Male mice were anaesthetized by intraperitoneal injection of a mixture of xylazine hydrochloride (Rompun; Bayer) and ketamine hydrochloride/chlorbutol (Imalgene; Merial) (1:4) at 1 ml per kg body weight and then perfused intra-aortically with 0.9% NaCl followed by 5 ml per g body weight of Somogyi (Paraformaldehyde, 4% (wt/vol) and picric acid, 0.2% (vol/vol), in 0.1 MPB, pH 7.4. After perfusion, (i) brains were dissected out sagittally in two parts and post-fixed with Somogyi for 2 h at room temperature; (ii) eyes were extracted, stabbed in the lens, post-fixed overnight in 4% (wt/vol) of paraformaldehyde, and then were subjected to 5 washes of 10 min in 0.1 M of PB solution, followed by cryoprotection in 15 and 30% of sucrose (wt/vol) in 0.1 MPB sequentially at 4°C. Brain blocks were rinsed successively for 15, 30 min, 1 and 2 h with 0.1 MPB solution and cryoprotected in 10, 20, and 30% (wt/vol) sucrose in PBS sequentially, until they sank. After cryoprotection, 40-μm thick sagittal sections were obtained with a freezing-sliding cryostat (Leica; CM1950 AgProtect). The sections were collected serially in a 12-well plate in 0.1 MPB, rinsed three times for 10 min in 0.1 M PBS and used for subsequent immunohistochemistry and autofluorescence evaluation. The section-containing wells that were not used were kept in freezer mix (polyethylene glycol, 30% by volume and glycerol 30% by volume in 0.1 MPB) at −20°C. In the case of autofluorescence, sections were mounted with Fluoromount (Sigma-Aldrich) aqueous mounting medium and lamelles cover-objects (Thermo Fisher Scientific). For immunohistochemistry, sections were incubated sequentially in (i) 5 mg/ml sodium borohydride in PBS for 30 min (to remove aldehyde autofluorescence); (ii) three PBS washes of 10 min each; (iii) 1:500 anti-IBA-1 (019-19741, Wako), 1:200 anti-ATP-synthase C (ab181243 abcam), 1:500 anti-NeuN (MAB377 Millipore), 1:500 anti-GFAP (G6171, Sigma) and 1:1,000 STX in 0.02% Triton X-100 (Sigma-Aldrich) and 5% goat serum (Jackson Immuno-Research) in 0.1 MPB for 72 h at 4°C; (iv) three PB washes of 10 min each; (v) fluorophore conjugated secondary antibodies, 1:500 Cy2 goat anti-mouse or 1:500 Cy3 goat anti-rabbit (Jackson Immuno-Research) in PB for 2 h at room temperature; and (vi) 0.5 μg/ml Hoechst in PB for 10 min at room temperature. After being rinsed with PB, sections were mounted with Fluoromount.

Imaging and quantification

For confocal imaging, the sections were examined under a Zeiss LSM 800 confocal microscope. Optical sections were obtained under a × 63 or ×40 immersion objective at a definition of 1,024 × 1,024 pixels (average of eight or sixteen scans), adjusting the pinhole diameter to 1 Airy unit for each emission channel to have all the intensity values between 1 and 254 (linear range). For image analysis, we used Columbus 2.6.0.127073 (built at 03:56 on 05/02/19) released by PerkinElmer. This online platform is based on Harmony High-Content Imaging and Analysis Software.

Statistical analysis

For *in vitro* studies, we perform three or more independent experiments without data exclusion. No formal blinding was performed, but independent researchers were performing similar experiments to confirm the results.

For *in vivo* studies, we used ≥ 3 animals per group. InVivoStat software was used to determine that six animals were enough as the sample size to achieve a 20% of variation with statistical significance with a power of 100%. The presence of signs of behavioural or health problems was the criteria to exclude animals. The adscription of animals to each group was done randomly. Animals were selected arbitrarily to receive tamoxifen or vehicle injections. The analysis of animal samples was blind. The samples were identified by numbers, and the results were grouped after the analysis. For behavioural tests, the animals were tested together. Data have been analysed with the support of the Bioinformatics Core in TIGEM.

Microsoft Excel, GraphPad Prism and R software packages were used to analyse the data. Sample numbers and other information (mean or SD, number of replicates and specific statistical tests) are indicated in the main text or Figure legends.

We have first used the Shapiro–Wilk test to check the normality assumption. The *P*-value in our data is not significant, and therefore, we can assume normality.

We used Levene's test to check the homogeneity of variances. The *P*-value of Levene's test in our data is not significant. It means that there is no significant difference between variances across groups. Then, one-way or two-way ANOVA have been applied for all charts with more than two groups. Student's *t*-test was used for statistical analysis when comparing only two groups.

The paper explained

Problem
Batten disease (BD) is a group of fatal neurodegenerative rare diseases. There is neither cure nor drugs to revert the course of these diseases. Systemic administration of small-molecule therapeutics may represent an alternative to existing protein and gene therapies, which cannot readily cross the blood–brain barrier to reach the brain.

Results
We have discovered a pathological accumulation of the lipid globotriaosylceramide (Gb3) in cellular and murine models of two types of BD, CLN3, and CLN7. By using this novel disease hallmark, we developed a cell-based assay that identified the FDA-approved compound tamoxifen. *In vitro* and *in vivo* studies showed that tamoxifen ameliorates BD using human disease cells and a murine model of CLN7.

Impact
This study highlights the relevance of combining cell biology approaches with the repurposing of approved drugs to identify small-molecule therapeutics to treat rare diseases. Our data strongly suggest that the clinical compound tamoxifen may be a suitable drug to treat some types of Batten disease.

Data availability

This study includes no data deposited in external repositories.

Expanded View for this article is available online.

Acknowledgements
This work was funded by the European Union's Horizon 2020 research and innovation programme (BATCure, grant No. 666918 to DLM, JPB, SEM, TB and SS). JPB is funded by the Agencia Estatal de Investigación (PID2019-105699RB-I00/ AEI / 10.13039/501100011033 and RED2018-102576-T), Plan Nacional sobre Drogas (2020I028), Junta de Castilla y León (Escalera de Excelencia CLU-2017-03), Ayudas Equipos Investigación Biomedicina 2017 Fundación BBVA and Fundación Ramón Areces. SS was funded by a grant from the Mila's Miracle Foundation. TB was supported by German Research Council (DFG) grant FOR2625. SM benefits from MRC funding to the MRC Laboratory for Molecular Cell Biology University Unit at UCL (award code MC_U12266B) towards laboratory and office space. We acknowledge Marcella Cesana for providing the TFEB virus. Graphical abstract was created using BioRender.com.

Author contributions
DLM and CS conceived the study and produced the manuscript, which was improved by all authors. CS, IL-F, MG-M, JPB, SM, LGW, JM, JLS, AE and MG-F produced experimental data. JPB, GN, LJ, SS, SEM, TB, MADM, ASR, EKK, DP, TM, CMG and AB contributed to the interpretation of parts of the results.

Conflict of interest
The authors declare that they have no conflict of interest.

Relevant web links
https://www.tigem.it/Staff/medina
https://www.tigem.it/core-facilities/high-content-screening-facility
http://www.batcure.eu/home_page.html
https://www.bdsra.org; Batten Disease Support and Research Association (BDSRA).
http://www.beyondbatten.org; Beyond Batten Disease Foundation.
http://www.bdfa-uk.org.uk; Batten Disease Family Association.
https://www.ninds.nih.gov/Disorders/Patient-Caregiver-Education/Fact-Sheets/Batten-Disease-Fact-Sheet; Batten Disease Fact Sheet; National Institute of Neurological Disorders and Stroke, National Institutes of Health, Bethesda, MD 20892.
https://www.ucl.ac.uk/ncl-disease/mutation-and-patient-database; Mutation and Patient Database.
UniProtKB - Q13286 (CLN3_HUMAN); https://www.uniprot.org
UniProtKB - Q8NHS3 (MFSD8_HUMAN); https://www.uniprot.org

References

Abe A, Gregory S, Lee L, Killen PD, Brady RO, Kulkarni A, Shayman JA (2000) Reduction of globotriaosylceramide in Fabry disease mice by substrate deprivation. *J Clin Invest* 105: 1563 – 1571

Actis C, Muzio G, Autelli R (2021) Autophagy triggers tamoxifen resistance in human breast cancer cells by preventing drug-induced lysosomal damage. *Cancers* 13: 1252

Altan N, Chen Y, Schindler M, Simon SM (1999) Tamoxifen inhibits acidification in cells independent of the estrogen receptor. *Proc Natl Acad Sci USA* 96: 4432 – 4437

Boulos AS, Deshaies EM, Dalfino JC, Feustel PJ, Popp AJ, Drazin D (2011) Tamoxifen as an effective neuroprotectant in an endovascular canine model of stroke. *J Neurosurg* 114: 1117 – 1126

Boustany R-MN (2013) Lysosomal storage diseases–the horizon expands. *Nat Rev Neurol* 9: 583 – 598

Brandenstein L, Schweizer M, Sedlacik J, Fiehler J, Storch S (2016) Lysosomal dysfunction and impaired autophagy in a novel mouse model deficient for the lysosomal membrane protein Cln7. *Hum Mol Genet* 25: 777 – 791

Cotman SL, Vrbanac V, Lebel L-A, Lee RL, Johnson KA, Donahue L-R, Teed AM, Antonellis K, Bronson RT, Lerner TJ *et al* (2002) Cln3 Δex7/8 knock-in mice with the common JNCL mutation exhibit progressive neurologic disease that begins before birth. *Hum Mol Genet* 11: 2709 – 2721

Damme M, Brandenstein L, Fehr S, Jankowiak W, Bartsch U, Schweizer M, Hermans-Borgmeyer I, Storch S (2014) Gene disruption of Mfsd8 in mice provides the first animal model for CLN7 disease. *Neurobiol Dis* 65: 12 – 24

Danyukova T, Ariunbat K, Thelen M, Brocke-Ahmadinejad N, Mole SE, Storch S (2018) Loss of CLN7 results in depletion of soluble lysosomal proteins and impaired mTOR reactivation. *Hum Mol Genet* 27: 1711 – 1722

Derman O, Kanbur NO, Kutluk T (2003) Tamoxifen treatment for pubertal gynecomastia. *Int J Adolesc Med Health* 15: 359 – 363

Double KL, Dedov VN, Fedorow H, Kettle E, Halliday GM, Garner B, Brunk UT (2008) The comparative biology of neuromelanin and lipofuscin in the human brain. *Cell Mol Life Sci* 65: 1669 – 1682

Finn R, Kovács AD, Pearce DA (2011) Altered sensitivity of cerebellar granule cells to glutamate receptor overactivation in the Cln3(Δex7/8)-knock-in mouse model of juvenile neuronal ceroid lipofuscinosis. *Neurochem Int* 58: 648 – 655

FitzPatrick LM, Hawkins KE, Delhove JMKM, Fernandez E, Soldati C, Bullen LF, Nohturfft A, Waddington SN, Medina DL, Bolaños JP *et al* (2018) NF-κB activity initiates human ESC-derived neural progenitor cell differentiation by inducing a metabolic maturation program. *Stem Cell Rep* 10: 1766 – 1781

Gayi E, Neff LA, Massana Muñoz X, Ismail HM, Sierra M, Mercier T, Décosterd LA, Laporte J, Cowling BS, Dorchies OM *et al* (2018) Tamoxifen prolongs survival and alleviates symptoms in mice with fatal X-linked myotubular myopathy. *Nat Commun* 9: 4848

Haltia M, Goebel HH (2013) The neuronal ceroid-lipofuscinoses: a historical introduction. *Biochim Biophys Acta* 1832: 1795 – 1800

Huber RJ, Hughes SM, Liu W, Morgan A, Tuxworth RI, Russell C (2020) The contribution of multicellular model organisms to neuronal ceroid lipofuscinosis research. *Biochim Biophys Acta* 1866: 165614

Huber RJ, Mathavarajah S (2018) Secretion and function of Cln5 during the early stages of Dictyostelium development. *Biochim Biophys Acta Mol Cell Res* 1865: 1437 – 1450

Kallio A, Guo T, Lamminen E, Seppänen J, Kangas L, Väänänen HK, Härkönen P (2008) Estrogen and the selective estrogen receptor modulator (SERM) protection against cell death in estrogen receptor alpha and beta expressing U2OS cells. *Mol Cell Endocrinol* 289: 38 – 48

Katz ML, Robison WG (2002) What is lipofuscin? Defining characteristics and differentiation from other autofluorescent lysosomal storage bodies. *Arch Gerontol Geriatr* 34: 169 – 184

Kauss V, Dambrova M, Medina DL (2020) Pharmacological approaches to tackle NCLs. *Biochim Biophys Acta Mol Basis Dis* 1866: 165553

Kimelberg HK (2008) Tamoxifen as a powerful neuroprotectant in experimental stroke and implications for human stroke therapy. *Recent Pat CNS Drug Discov* 3: 104 – 108

Kimelberg HK, Jin Y, Charniga C, Feustel PJ (2003) Neuroprotective activity of tamoxifen in permanent focal ischemia. *J Neurosurg* 99: 138 – 142

Kovács AD, Weimer JM, Pearce DA (2006) Selectively increased sensitivity of cerebellar granule cells to AMPA receptor-mediated excitotoxicity in a mouse model of Batten disease. *Neurobiol Dis* 22: 575 – 585

Kreher NC, Eugster EA, Shankar RR (2005) The use of tamoxifen to improve height potential in short pubertal boys. *Pediatrics* 116: 1513 – 1515

Laplante M, Sabatini DM (2012) mTOR signaling in growth control and disease. *Cell* 149: 274 – 293

Lavie Y, Cao H-T, Volner A, Lucci A, Han T-Y, Geffen V, Giuliano AE, Cabot MC (1997) Agents that reverse multidrug resistance, tamoxifen, verapamil, and cyclosporin A, block glycosphingolipid metabolism by inhibiting ceramide glycosylation in human cancer cells. *J Biol Chem* 272: 1682 – 1687

Lawrence SE, Faught KA, Vethamuthu J, Lawson ML (2004) Beneficial effects of raloxifene and tamoxifen in the treatment of pubertal gynecomastia. *J Pediatr* 145: 71 – 76

Lieu CA, Chinta SJ, Rane A, Andersen JK (2013) Age-related behavioral phenotype of an astrocytic monoamine oxidase-B transgenic mouse model of Parkinson's disease. *PLoS One* 8: e54200

Lopez-Fabuel I, Douce JL, Logan A, James AM, Bonvento G, Murphy MP, Almeida A, Bolaños JP (2016) Complex I assembly into supercomplexes determines differential mitochondrial ROS production in neurons and astrocytes. *Proc Natl Acad Sci USA* 113: 13063 – 13068

Lu S, Sung T, Lin N, Abraham RT, Jessen BA (2017) Lysosomal adaptation: How cells respond to lysosomotropic compounds. *PLoS One* 12: e0173771

Maddalozzo J, Tenta LT, Hutchinson LR, Crawford SE, Morse DS (1993) Juvenile fibromatosis: hormonal receptors. *Int J Pediatr Otorhinolaryngol* 25: 191 – 199

Mallard F, Johannes L (2003) Shiga toxin B-subunit as a tool to study retrograde transport, In Philpott D, Ebel F (eds.), *E. coli: Shiga toxin methods and protocols* pp 209 – 220., Totowa, NJ: Humana Press

Medina D, Fraldi A, Bouche V, Annunziata F, Mansueto G, Spampanato C, Puri C, Pignata A, Martina J, Sardiello M *et al* (2011) Transcriptional activation of lysosomal exocytosis promotes cellular clearance. *Dev Cell* 21: 421 – 430

Mole SE (2014) Development of new treatments for Batten disease. *Lancet Neurol* 13: 749 – 751

Mole SE, Anderson G, Band HA, Berkovic SF, Cooper JD, Kleine Holthaus S-M, McKay TR, Medina DL, Rahim AA, Schulz A *et al* (2019) Clinical challenges and future therapeutic approaches for neuronal ceroid lipofuscinosis. *Lancet Neurol* 18: 107 – 116

Mole SE, Cotman SL (2015) Genetics of the neuronal ceroid lipofuscinoses (Batten disease). *Biochim Biophys Acta* 1852: 2237 – 2241

Mole SE, Williams RE, Goebel HH (2005) Correlations between genotype, ultrastructural morphology and clinical phenotype in the neuronal ceroid lipofuscinoses. *Neurogenetics* 6: 107 – 126

Morad SAF, Cabot MC (2015) Tamoxifen regulation of sphingolipid metabolism–therapeutic implications. *Biochim Biophys Acta* 1851, 1134 – 1145

Namdar M, Gebhard C, Studiger R, Shi Y, Mocharla P, Schmied C, Brugada P, Lüscher TF, Camici GG (2012) Globotriaosylsphingosine accumulation and not alpha-galactosidase-A deficiency causes endothelial dysfunction in Fabry disease. *PLoS One* 7: e36373

Napolitano G, Di Malta C, Esposito A, de Araujo MEG, Pece S, Bertalot G, Matarese M, Benedetti V, Zampelli A, Stasyk T *et al* (2020) A substrate-specific mTORC1 pathway underlies Birt–Hogg–Dubé syndrome. *Nature* 585: 597 – 602

Ohkuma S, Poole B (1981) Cytoplasmic vacuolation of mouse peritoneal macrophages and the uptake into lysosomes of weakly basic substances. *J Cell Biol* 90: 656 – 664

Palmer DN (2015) The relevance of the storage of subunit c of ATP synthase in different forms and models of Batten disease (NCLs). *Biochim Biophys Acta* 1852: 2287 – 2291

Pisonero-Vaquero S, Medina DL (2017) Lysosomotropic drugs: pharmacological tools to study lysosomal function. *Curr Drug Metab* 18: 1147 – 1158

Poirier A-A, Côté M, Bourque M, Morissette M, Di Paolo T, Soulet D (2016) Neuroprotective and immunomodulatory effects of raloxifene in the myenteric plexus of a mouse model of Parkinson's disease. *Neurobiol Aging* 48: 61 – 71

Puranam KL, Guo W-X, Qian W-H, Nikbakht K, Boustany R-M (1999) CLN3 defines a novel antiapoptotic pathway operative in neurodegeneration and mediated by ceramide. *Mol Genet Metab* 66: 294 – 308

Raa H, Grimmer S, Schwudke D, Bergan J, Wälchli S, Skotland T, Shevchenko A, Sandvig K (2009) Glycosphingolipid requirements for endosome-to-Golgi transport of Shiga toxin. *Traffic* 10: 868 – 882

Raininko R, Santavuori P, Heiskala H, Sainio K, Palo J (1990) CT findings in neuronal ceroid lipofuscinoses. *Neuropediatrics* 21: 95 – 101

Rusyn E, Mousallem T, Persaud-Sawin D-A, Miller S, Boustany R-MN (2008) CLN3p impacts galactosylceramide transport, raft morphology, and lipid content. *Pediatr Res* 63: 625 – 631

Sampaio JL, Gerl MJ, Klose C, Ejsing CS, Beug H, Simons K, Shevchenko A (2011) Membrane lipidome of an epithelial cell line. *Proc Natl Acad Sci USA* 108: 1903 – 1907

Sardiello M, Palmieri M, di Ronza A, Medina DL, Valenza M, Gennarino VA, Di Malta C, Donaudy F, Embrione V, Polishchuk RS *et al* (2009) A gene network regulating lysosomal biogenesis and function. *Science* 325: 473 – 477

Schmidtke C, Tiede S, Thelen M, Käkelä R, Jabs S, Makrypidi G, Sylvester M, Schweizer M, Braren I, Brocke-Ahmadinejad N *et al* (2019) Lysosomal proteome analysis reveals that CLN3-defective cells have multiple enzyme deficiencies associated with changes in intracellular trafficking. *J Biol Chem* 294: 9592 – 9604

Selyunin AS, Hutchens S, McHardy SF, Mukhopadhyay S (2019) Tamoxifen blocks retrograde trafficking of Shiga toxin 1 and 2 and protects against lethal toxicosis. *Life Sci Alliance* 2: e201900439

Shagufta & Ahmad I (2018) Tamoxifen a pioneering drug: an update on the therapeutic potential of tamoxifen derivatives. *Eur J Med Chem* 143: 515 – 531

Somogyi A, Petcherski A, Beckert B, Huebecker M, Priestman DA, Banning A, Cotman SL, Platt FM, Ruonala MO, Tikkanen R (2018) Altered expression of ganglioside metabolizing enzymes results in GM3 ganglioside accumulation in cerebellar cells of a mouse model of juvenile neuronal ceroid lipofuscinosis. *Int J Mol Sci* 19: 625

Spampanato C, Feeney E, Li L, Cardone M, Lim J-A, Annunziata F, Zare H, Polishchuk R, Puertollano R, Parenti G *et al* (2013) Transcription factor EB (TFEB) is a new therapeutic target for Pompe disease. *EMBO Mol Med* 5: 691 – 706

Staropoli JF, Haliw L, Biswas S, Garrett L, Hölter SM, Becker L, Skosyrski S, Da Silva-Buttkus P, Calzada-Wack J, Neff F *et al* (2012) Large-scale phenotyping of an accurate genetic mouse model of JNCL identifies novel early pathology outside the central nervous system. *PLoS One* 7: e38310

Taras TL, Wurz GT, DeGregorio MW (2001) *In vitro* and *in vivo* biologic effects of Ospemifene (FC-1271a) in breast cancer. *J Steroid Biochem Mol Biol* 77: 271 – 279

Vesa J, Chin MH, Oelgeschläger K, Isosomppi J, DellAngelica EC, Jalanko A, Peltonen L (2002) Neuronal ceroid lipofuscinoses are connected at molecular level: interaction of CLN5 protein with CLN2 and CLN3. *Mol Biol Cell* 13: 2410 – 2420

Walter AW, Gajjar A, Reardon DA, Thompson SJ, Langston JW, Jones-Wallace D, Kun LE, Heideman RL (2000) Tamoxifen and carboplatin for children with low-grade gliomas: a pilot study at St. Jude Children's Research Hospital. *J Pediatr Hematol Oncol* 22: 247 – 251

Welford RWD, Mühlemann A, Garzotti M, Rickert V, Groenen PMA, Morand O, Üçeyler N, Probst MR (2018) Glucosylceramide synthase inhibition with lucerastat lowers globotriaosylceramide and lysosome staining in cultured fibroblasts from Fabry patients with different mutation types. *Hum Mol Genet* 27: 3392 – 3403

Wurz GT, Read KC, Marchisano-Karpman C, Gregg JP, Beckett LA, Yu Q, Degregorio MW (2005) Ospemifene inhibits the growth of dimethylbenzanthracene-induced mammary tumors in Sencar mice. *J Steroid Biochem Mol Biol* 97: 230 – 240

Zhitomirsky B, Yunaev A, Kreiserman R, Kaplan A, Stark M, Assaraf YG (2018) Lysosomotropic drugs activate TFEB via lysosomal membrane fluidization and consequent inhibition of mTORC1 activity. *Cell Death Dis* 9: 1 – 15

Manuscript VI

Targeting TPC2 rescues lysosomal storage in mucolipidosis type IV, Niemann-Pick type C1 and Batten disease
Einar K. Krogsaeter*, **Anna Scotto Rosato***, Carla Abrahamian, Dawid Jaslan, Julia Böck, Chiara Soldati, Barbara Spix, Amanda Wyatt, Daniela Borchert, Marcel Passon, Marc Stieglitz, Guido Hermey, Sandra Markmann, Doris Gruber-Schoffnegger, Susan Cotman, Ulrich Boehm, Thorsten Marquardt, Christian Wahl-Schott, Martin Biel, Elena Polishchuk, Diego Medina, Dominik Paquet, & Christian Grimm.
Manuscript in preparation.

Targeting TPC2 rescues lysosomal storage in mucolipidosis type IV, Niemann-Pick type C1 and Batten disease

Einar Krogsaeter*[1], Anna Scotto Rosato*[1], Carla Abrahamian[1], Dawid Jaslan[1], Julia Böck[1], Chiara Soldati[2], Barbara Spix[1], Amanda Wyatt[3], Daniela Borchert[4], Marcel Passon[1], Marc Stieglitz[5], Guido Hermey[6], Sandra Markmann[4], Doris Gruber-Schoffnegger[4], Susan Cotman[7], Ulrich Boehm[3], Thorsten Marquardt[8], Christian Wahl-Schott[9], Martin Biel[5], Elena Polishchuk[2], Diego Medina[2], Dominik Paquet[10#], Christian Grimm[1#]

[1]Walther Straub Institute of Pharmacology and Toxicology, Faculty of Medicine, Ludwig-Maximilians-Universität, Munich, Germany
[2]Telethon Institute of Genetics and Medicine, Naples, Italy
[3]Saarland University, Center for Molecular Signaling (PZMS), Experimental Pharmacology
[4]Evotec AG, Hamburg, Germany
[5]Department of Pharmacy – Center for Drug Research, Ludwig-Maximilians-Universität, Munich, Germany
[6]Center for Molecular Neurobiology Hamburg (ZMNH), Institute of Molecular and Cellular Cognition, UKE Hamburg, Germany
[7]Center for Genomic Medicine, Department of Neurology, Massachusetts General Hospital, Harvard Medical School, Boston, United States
[8]Department of General Pediatrics, University of Münster, Münster, Germany
[9]Institute for Neurophysiology, Hannover Medical School, Hannover, Germany
[10]Institute for Stroke and Dementia Research (ISD), University Hospital, LMU Munich, Germany

Correspondence should be addressed to:

christian.grimm@med.uni-muenchen.de or dominik.paquet@med.uni-muenchen.de

* These authors contributed equally to this work; # Corresponding authors

Running title: Rescue of LSDs by TPC2 activation

Number of figures: 8

Number of tables: 0

Supplementary material contains:

Supplementary figures: 5

Supplementary tables: 0

Supplementary videos: 0

Keywords: TPC2, TPC1, TRPML1, TPC, lysosome, small molecule activator

Abstract

Lysosomes are cell organelles that degrade macromolecules to recycle their components. If lysosomal degradative function is impaired e.g., due to mutations in lysosomal enzymes or membrane proteins, lysosomal storage diseases (LSDs) can develop, manifesting mostly with neurological symptoms, typically starting in early childhood (childhood dementia), going along with a strongly reduced life expectancy and quality of life. We show here that small molecule activation of the endolysosomal two-pore channel 2 (TPC2) results in an amelioration of cellular phenotypes associated with LSDs such as the accumulation of cholesterol, lactosylceramide, or lipofuscin, or the formation of abnormal vacuoles seen by electron microscopy. Rescue effects of the TPC2 agonist were assessed in Batten disease, Niemann-Pick type C1, and mucolipidosis type IV (MLIV) patient fibroblasts and in neurons derived from newly generated human iPSC models for MLIV and Batten disease. Mechanistically, we found that TPC2-mediated lysosomal exocytosis contributes to the rescue effects by clearing cellular debris, thus preventing the cells from accumulating undegraded macromolecules and toxic substances in the lysosomes while TPC2-mediated autophagy induction becomes relevant only under starvation conditions. In sum, our data suggest that TPC2 is a promising novel target for the treatment of different types of LSDs.

Introduction

Release of calcium from lysosomes is of significant physiological and pathophysiological relevance. Lysosomal calcium regulates several cellular processes, e.g. autophagy (Medina *et al*, 2015; Medina & Ballabio, 2015), membrane trafficking (Dong *et al*, 2010; Pryor *et al*, 2000; Luzio *et al*, 2007; Ruas *et al*, 2010; Cao *et al*, 2015, 2017), exocytosis (Samie *et al*, 2013; Davis *et al*, 2020), nutrient adaptation (Cang *et al*, 2013), membrane repair (Cheng *et al*, 2014), and cell migration (Bretou *et al*, 2017; Plesch *et al*, 2018). Disruption of lysosomal calcium content and/or lysosomal calcium release is associated with several diseases including neurodegenerative (lysosomal storage) diseases (Kiselyov *et al*, 2010; Lloyd-Evans & Platt, 2011; Feng & Yang, 2016). The most direct link between defective lysosomal calcium release and neurodegenerative disease in humans is apparent in mucolipidosis type IV (MLIV), which is associated with loss of function of the calcium-permeable lysosomal cation channel TRPML1 (Berman *et al*, 1974; Slaugenhaupt, 2002; Feng & Yang, 2016). Disruption of TRPML1 signaling or TRPML1-mediated calcium release also manifests in other LSDs such as Niemann-Pick type C1 (NPC1) (Shen *et al*, 2012), Niemann-Pick type A (NPA) (Shen *et al*, 2012; Zhong *et al*, 2016), and Fabry disease (Zhong *et al*, 2016). Direct activation of TRPML1 with small molecules or overexpression of TRPML1 cDNA ameliorates lactosylceramide (LacCer) trafficking defects and cholesterol accumulation in NPC1 cells (Shen *et al*, 2012), while activation of the associated lysosomal big conductance Ca^{2+}-activated potassium (BK) channel was shown to correct impaired Ca^{2+} release in several LSDs in a TRPML1-dependent manner, rescuing aberrant lysosomal storage (Zhong *et al*, 2016). Furthermore, mutations in FIG4 and PYKfyve, which play critical roles in the synthesis of $PI(3,5)P_2$, an endogenous agonist of TRPMLs and the related two-pore channels (TPCs), are associated with neurological or neurodegenerative disease phenotypes (Chow *et al*, 2007; Zhang *et al*, 2007; Ferguson *et al*, 2012; Zou *et al*, 2015), and treatment of $FIG4^{-/-}$ cells with TRPML1 agonists was found to rescue lysosomal storage (Zou *et al*, 2015).

While the benefit of TRPML1 activation in neurodegenerative diseases is gaining traction, effects of activating the related two-pore channel 2 (TPC2) remain unexplored. The aim of this study was to explore activation of TPC2 as a novel therapeutic strategy to treat MLIV and other LSDs, and to directly compare effects of TPC2 and TRPML1 activation. TPC2 shares several key features with TRPML1: Both channels are non-selective cation channels,

permeable for calcium and sodium (LaPlante *et al*, 2002; Calcraft *et al*, 2009; Wang *et al*, 2012; Pitt *et al*, 2010; Ruas *et al*, 2015; Gerndt *et al*, 2020), residing predominantly in lysosomal membranes (Pryor *et al*, 2006; Kim *et al*, 2009; Calcraft *et al*, 2009; Ruas *et al*, 2010), activated by $PI(3,5)P_2$ (Dong *et al*, 2010; Wang *et al*, 2012; Gerndt *et al*, 2020); both are widely expressed including neurons and glial cells in the CNS (Bae *et al*, 2014; Pereira *et al*, 2017; Beckel *et al*, 2018; Foster *et al*, 2018; Minckley *et al*, 2019); both are leading to trafficking defects if lost or downregulated (Shen *et al*, 2012; Chen *et al*, 2014; Grimm *et al*, 2014; Dong *et al*, 2010; Nguyen *et al*, 2017; Park *et al*, 2016), both interact with mTOR/TFEB/autophagy pathways (Wang *et al*, 2015; Li *et al*, 2016; Cang *et al*, 2013; Ogunbayo *et al*, 2018; Medina & Ballabio, 2015; Medina *et al*, 2015; Scotto Rosato *et al*, 2019), and both promote lysosomal exocytosis (Samie *et al*, 2013; Gerndt *et al*, 2020).
We therefore hypothesized that activation of TPC2 might be a promising alternative strategy to modulate lysosomal calcium signaling and thus to rescue cellular phenotypes of LSDs such as MLIV, NPC1, or Batten disease (JNCL). By applying a range of methods including analysis of lactosylceramide (LacCer), cholesterol, shigatoxin (STX), or LysoTracker (LyTr) accumulation, ultrastructural abnormalities using electron microscopy, and by studying potential underlying mechanisms of rescue such as lysosomal exocytosis and autophagy in LSD patient derived fibroblasts and in newly CRISPR/Cas9-engineered isogenic LSD iPSC derived neurons, we demonstrate the potential of TPC2 activation in rescuing LSD phenotypes.

Results

TPC2 activity modulates LSD phenotypes in human patient fibroblasts. Based on the concept that disrupted endolysosomal calcium homeostasis constitutes a major pathomechanism underlying LSDs as most prominently seen in MLIV, we have assessed the effect of the recently published TPC2 agonist, TPC2-A1-P alongside TRPML1 activation on several LSD phenotypes (Gerndt *et al*, 2020). Using lactosylceramide (LacCer) trafficking as read-out, we initially assessed trafficking defects in fibroblasts isolated from different LSD patients (MLIV, NPA, NPC1, Fabry, Gaucher, GM1 gangliosidosis, and Batten disease (JNCL/CLN3$^{\Delta 1.02kb/\Delta 1.02kb}$)). LacCer is a lipid internalized from the plasma membrane by a clathrin-independent (caveolar-related) mechanism and subsequently targeted to the Golgi

apparatus in wild-type (WT) cells, whereas, in fibroblasts derived from NPC1, MLIV, GM1 gangliosidosis, Fabry, and NPA disease patients LacCer accumulates in late endosomes and lysosomes. Contrarily, no endolysosomal accumulation is described for fibroblasts from Gaucher and Batten (JNCL/CLN3$^{\Delta 1.02kb/\Delta 1.02kb}$) disease patients (Vitner *et al*, 2010). In accordance with these results, we identified consistent assay windows for NPA, NPC1, GM1, MLIV, and Fabry disease, while LacCer trafficking appeared unaffected in Gaucher and JNCL cells (Fig. 1A). Based on the above obtained assay windows (Fig. 1A), we assessed the effect of TPC2 activation in NPA, NPC1, and MLIV. TPC2 activation significantly decreased lysosomal LacCer accumulation in MLIV patient cells (Fig. 1B-C). Rescue effects were assessed in MLIV fibroblasts carrying two of the most common mutations (c.406 2A>G, also known as IVS3-2A>G or AJ major and c.511del6434, also known as Ex1-7del or AJ minor) (Bargal *et al*, 2001) in a heterozygous manner, resulting in complete loss of TRPML1 function, referred to here as MLIV. Conversely, applying TPC2 antagonists such as tetrandrine or Ned-19, or the recently published TPC2 blockers SG-005 and SG-094 (Müller *et al*, 2021) we observed exacerbation of the LacCer trafficking phenotype (Fig. 1B-C and Fig. EV1A). The TPC2-A1-P-mediated LacCer trafficking restoration was between -20% and -49% relative to untreated controls, depending on the method of analysis, while TPC2 blockers exacerbated the phenotype between +21% and >+100%. To assess maximal rescue effects, we treated MLIV patient fibroblasts in combination with TPC2 overexpression. As a positive control, we electroporated TRPML1 in combination with a commonly used TRPML agonist, ML-SA1. We also tested the effect of TPC2 activation in NPC1 and NPA patient fibroblasts (Fig. 1D-F). We observed TPC2-overexpressing NPC1 fibroblasts to respond significantly to TPC2-A1-P treatment, while ML-SA1 in TRPML1-overexpressing NPC1 cells showed only a trend towards rescuing. Trafficking defects were however not restored in NPA cells, neither by activating TRPML1 nor TPC2. To confirm calcium dependence of LacCer trafficking, we incubated WT fibroblasts with increasing concentrations of the calcium chelator BAPTA-AM and found LacCer to accumulate dose-dependently in vesicular structures instead of being transported to the Golgi (Fig. 1G). LacCer (Pryor *et al*, 2006; Vitner *et al*, 2010; Shen *et al*, 2012; Chen *et al*, 2014) trafficking from the plasma membrane is affected by intracellular cholesterol. Reduction of intracellular cholesterol restores proper LacCer trafficking to Golgi, whereas cholesterol overload redirects LacCer to endolysosomal compartments (Puri *et al*, 1999).

Next, we therefore assessed endolysosomal cholesterol accumulation (Shen *et al*, 2012; Chen *et al*, 2014; Grimm *et al*, 2014). Altered cellular cholesterol homeostasis is rather common in LSDs and can conveniently be visualized using the fluorescent cholesterol-binding polyene antibiotic filipin. The effect of TPC2 activation by TPC2-A1-P on cholesterol accumulation was assessed in MLIV, NPC1, and Batten disease (JNCL/CLN3$^{\Delta 1.02kb/\Delta 1.02kb}$) patient fibroblasts. While we could not detect cholesterol storage in JNCL/CLN3$^{\Delta 1.02kb/\Delta 1.02kb}$ cells, we observed a significant assay window for NPC1, and a smaller, yet significant assay window for MLIV (Fig. 2A-B). In both NPC1 and MLIV cells, cholesterol accumulation was strongly reduced upon treatment with TPC2-A1-P (Fig. 2C-F). In addition to the complete loss-of-function TRPML1 fibroblasts described above (MLIV; severe phenotype), rescue effects were also examined in fibroblasts carrying homo- and heterozygous MLIV-causing point or in-frame-deletion mutations, resulting in clinical and cellular phenotypes of reportedly milder severity. Thus, in patient fibroblasts with the TRPML1 mutations TRPML1$^{F408\Delta/AJ\ major}$ and TRPML1$^{T121M/T121M}$, significant TPC2-A1-P-mediated cholesterol clearance was observed. TRPML1$^{T121M/T121M}$ is a hitherto not yet functionally described homozygous mutant variant from a recently diagnosed 18-year old female patient of Yazidi origin living in Germany, representing a rare case of the same point mutation in TRPML1 being present on both alleles (Fig. EV2A-F). While TPC2-A1-P efficiently rescued the cholesterol phenotype in both mutant cell lines as well as in complete loss-of-function TRPML1 lines (MLIV lines), no rescue effects were seen with other, recently postulated TPC2 agonists of lesser potency, namely several antidepressants and riluzole (Fig. EV2G). Instead, upon administering the indicated EC_{50}s for TPC2 of these drugs, cytotoxic effects were observed (Fig. EV3), likely owing to off-target effects. Riluzole, for example, is clinically used at serum concentrations ranging between 30 nM to 4.11 µM (Grant *et al*, 2017), far below its described EC_{50} for TPC2 (181 µM), highlighting its pleiotropic activity (Zhang *et al*, 2019). In a further set of experiments, TRPML1 was overexpressed in MLIV cells to assess maximal rescue effects by restoring TRPML1 expression in combination with the TRPML1 agonist ML-SA1. This effect was mimicked by overexpression of TPC2 and treatment with TPC2-A1-P (Fig. 2E-G). When applying TPC2 blockers such as tetrandrine, SG005, or SG094, cholesterol accumulation was strongly exacerbated (Fig. EV1B-C). Finally, we applied electron microscopy (EM) to assess ultrastructural changes in lysosomes after compound treatment. It has previously been reported that changes in lysosomal morphology

can be seen by EM in MLIV and NPC1 patient fibroblasts (Garver *et al*, 2000; Vergarajauregui *et al*, 2008). We found an abundance of lysosomes with lamellar or other aberrant structures in NPC1 cells and to a lesser extent in MLIV cells, but observed no changes in lysosomal morphology in Batten disease (JNCL/CLN3$^{\Delta 1.02kb/\Delta 1.02kb}$) cells (Fig. 2H-J). Since NPC1 cells showed the most prominent abnormalities, we treated the NPC1 cells for 16 h with TPC2-A1-P, the TRPML1-activator ML-SA1, or DMSO. The strongest rescue effects were found upon TPC2-A1-P treatment (Fig. 2H-J). Batten disease patients have been shown to progressively accumulate lipofuscin in their body's tissue. The latter takes on a green-to-yellow color when viewed under an ultraviolet light microscope (Mole *et al*, 2020). By taking advantage of the cell cycle blocker mitomycin C, we exacerbated the progressive storage of lipofuscin within lysosomal compartments in human JNCL/CLN3$^{\Delta 1.02kb/\Delta 1.02kb}$ but not WT fibroblasts (Fig. 3A-C). Treatment with TPC2-A1-P or ML-SA1 fully rescued this autofluorescence, decreasing it to WT levels (Fig. 3A-C). Furthermore, by using the same experimental approach, we applied shigatoxin (STX) to visualize globotriaosylceramide (Gb3) accumulation as a further readout for JNCL/CLN3$^{\Delta 1.02kb/\Delta 1.02kb}$ as reported previously and found that both ML-SA1 and TPC2-A1-P rescued Gb3 accumulation efficiently and significantly.

Generation of human neuronal MLIV and Batten disease models using CRISPR/Cas9 and iPSCs. To extrapolate our patient fibroblast data to human neurons with corresponding isogenic controls, we used the CRISPR/Cas9 technology to generate iPSCs containing either the most common MLIV causing mutation MCOLN1$^{IVS3\text{-}2A>G/Ex1\text{-}7del}$ (Bargal *et al*, 2001) or CLN3 point mutants with varying clinical manifestations (Fig. 4A-B). To identify suitable point-mutant candidates, we performed a systematic analysis of the subcellular localization of the currently known disease-causing CLN3 point mutations, a missing point in the literature, and correlated them with their reported clinical phenotypes (Fig. EV4). Six mutants, CLN3^{S131R}, CLN3^{C134R}, CLN3^{A158P}, CLN3^{G165E}, CLN3^{L170P} and CLN3^{V330I}, appeared strongly mislocalized to the cytosol. When present in patients (usually heterozygously alongside the more prevalent CLN3$^{\Delta 1.02kb}$ variant), these disease variants reportedly result in a variety of clinical phenotypes, including classic JNCL, cone rod dystrophy, autophagic vacuolar myopathy, or retinitis pigmentosa (RP) (Munroe *et al*, 1997; Kousi *et al*, 2012; Cortese *et al*, 2014; Wang *et al*, 2014; Carss *et al*, 2017; Ku *et al*, 2017). A further six

mutants, CLN3^{L101P}, CLN3^{G189W}, CLN3^{I285V}, CLN3^{E295K}, CLN3^{R334C} and CLN3^{Q352H} showed no significant difference in colocalization with LAMP1, Rab5 or Rab11 compared to WT CLN3. For these, clinical phenotypes have either not been described, incompletely characterized, or described as protracted Batten disease or RP (Leman *et al*, 2005; Munroe *et al*, 1997; Kousi *et al*, 2012; Carss *et al*, 2017; Ku *et al*, 2017). The remaining nine mutations, CLN3^{G187A}, CLN3^{G189R}, CLN3^{G192E}, CLN3^{V290L}, CLN3^{L306H}, CLN3^{V330F}, CLN3^{R334H}, CLN3^{R405W}, and CLN3^{D416G} showed significantly reduced lysosomal localization (LAMP1), while retaining endosomal localization. CLN3^{D416G} also showed a significant decrease in Rab11 (recycling endosome) colocalization compared to WT CLN3. Rab5 (early endosome) colocalization was altered in four out of these nine mutants, including CLN3^{D416G}. Due to its consistent reduction in colocalization with all endolysosomal markers, CLN3^{D416G} was chosen as one candidate (with classic, more severe JNCL phenotype (Kousi *et al*, 2012)) while CLN3^{R405W} (less severly mislocalized, presenting with RP and retinal dystrophy only) (Wang *et al*, 2014; Mirza *et al*, 2019) was chosen as candidate with a milder phenotype. We used feeder-free human female A18944 iPSCs as template iPSCs for CRISPR/Cas9-mediated gene editing approaches following initial quality control (Weisheit *et al*, 2020). Active gRNAs were identified using TIDE (Brinkman *et al*, 2014), and encoding plasmids transiently transfected by electroporation alongside spCas9/R^{Puro} and, for knock-in editing, repair template. Since the sgRNA cut sites overlapped the introduced mutations, our approaches did not require blocking mutations to prevent re-editing, and yielded several homozygously edited clones (Paquet *et al*, 2016; Kwart *et al*, 2017). Precise introduction of desired mutations was identified by PCR and restriction fragment length polymorphism (RFLP) analysis, and confirmed by Sanger sequencing. Furthermore, undesired on-target effects and chromosome 20 triplication (conferring a growth advantage, thus being favored upon single-cell expansion) were screened for by qgPCR (Weisheit *et al*, 2020), and affected clones (60% to 75% of successfully edited cells) discarded. We also assessed puromycin sensitivity of the selected clones to ensure silencing/loss of the transfected construct. For the clones used in this study, two distinct algorithms were used to predict and sequence the five most likely off-target sites of the gRNAs, showing no off-target editing. Finally, pluripotency of edited cells was confirmed by staining for the pluripotency markers Tra1-60, Oct4, SSEA4 and NANOG (Fig. 4C).

Effect of TPC2 activation in neurons derived from human LSD iPSCs. Having generated novel LSD iPSCs, we differentiated these into disease-relevant cells. While progressive microgliosis and astrogliosis occur in the mouse models of both JNCL (Pontikis *et al*, 2004) and MLIV (Grishchuk *et al*, 2014), their clinical manifestations appear largely attributable to neuronal dysfunction. Indeed, primary neuronal dysfunction in the LSDs is evidenced by neuronal monocultures, developing pathological hallmarks such as autophagic defects, ultrastructural abnormalities, and expansion of the lysosomal compartment (Curcio-Morelli *et al*, 2010; Lojewski *et al*, 2014; Kinarivala *et al*, 2020). We therefore employed a previously described protocol (Paquet *et al*, 2016) to differentiate our WT and diseased iPSCs into cortical neurons (Paquet *et al*, 2016) (Fig. 4D), as evidenced by positive staining with neuronal markers such as TuJ and MAP2, and the cortical transcription factor CTIP2. We next assessed whether the neurons express genes relevant for disease (TRPML1 for MLIV, CLN3 for JNCL) and treatment (TRPML1 and TPC2). As a housekeeping gene, we opted for EMC7 due to consistent expression throughout neuronal differentiation (Eisenberg & Levanon, 2013; Artyukhov *et al*, 2017; Burke *et al*, 2020). As anticipated, the LSD-gene transcripts TRPML1 and CLN3 were readily detectable in the cortical neurons. TPC2, also appeared expressed at levels comparable to TRPML1, while the endolysosomal cation channels TRPML2, TRPML3, and TPC1 were hardly detectable (Fig. 4E). To further validate the neurons containing the MLIV causing mutations MCOLN1$^{IVS3\text{-}2A>G/IVS3\text{-}2A>G}$, we employed the endolysosomal patch-clamp technique (Chen *et al*, 2017) to measure TRPML1 current activities in WT and mutant neuron endolysosomes, readily recording TRPML1 currents in WT neurons, but not in MLIV neurons (Fig. 4F-G).

Aberrant lysosomal cathepsin B (CtsB) activity has been linked to cell death in MLIV (Colletti *et al*, 2012) and, conversely, decreased CtsB activity has been reported in CLN3 disease (Metcalf *et al*, 2008). We applied the fluorescence recovery after photobleaching (FRAP) method established in the latter publication, finding MLIV neurons to exhibit increased CtsB activity, while CLN3 knock-in neurons exhibited lower CtsB activity than WT controls. TPC2-A1-P pre-treatment decreased CtsB activity across the panel of iPSC-derived neurons, supporting its therapeutic relevance particularly in MLIV (Fig. 5A-B). In Western blot experiments we assessed the protein levels of intracellular CtsB and found increased levels in MLIV compared to WT neurons. The increased levels in MLIV cells were rescued by TPC2-A1-P treatment (Fig. 5C-D).

We next assessed acidic compartments as a whole by LyTr staining. We found an expansion of the lysosomal compartment in the MLIV neurons compared to WT controls that could be restored upon treatment with TPC2-A1-P (Fig. 5c-e). For CLN3 mutant neurons, positive assay windows were identified with LyTr but a significant rescue effect of TPC2-A1-P was only seen for the D416G mutant (Fig. 5c-e).

We continued with electron microscopy analyses of MLIV and CLN3 mutant neuronal rosettes to assess the ultrastructure of the LSD cells. The lysosomal inclusion bodies could be readily visualized in DMSO treated MLIV rosettes, and their number was decreased upon TPC2-A1-P treatment (Fig. 5h-i).

Next, to quantify lysosomal pH, we loaded neurons with Oregon-Green-labelled dextran overnight, facilitating its uptake into lysosomal compartments. The neurons were chased with DMSO or the H^+ pump inhibitor bafilomycin A1 (BafA1), the latter serving as a control for alkalinization. Lysosomal pH measurements were performed as previously described (Grimm *et al*, 2014). Ratiometric measurements of pH-sensitive/pH-insensitive Oregon Green spectra, followed by extrapolation to standard curves, allowing reliable quantification of lysosomal pH in neurons (Fig. EV5). The pH of WT lysosomes was determined to be 4.75, approximating previous measurements from primary hippocampal neurons (Kasper *et al*, 2005). We furthermore observed slight alkalinization of $CLN3^{R405W/R405W}$ (pH 5.24), $CLN3^{D416G/D416G}$ (pH 5.06), and $MCOLN1^{IVS3-2A>G/Ex1-7del}$ (pH 4.93) lysosomes. Our findings thus support previous studies demonstrating elevated lysosomal pH in CLN3 (Holopainen *et al*, 2001) and MLIV (Bach *et al*, 1999). However, neither ML-SA1 nor TPC2-A1-P were able to reduce the elevated pH in the diseased models (Fig. EV5). The latter finding is important in the context of pH-dependent activity of TRPML1 channels. While TRPML1 activity is strongly reduced by elevated lysosomal pH (Dong *et al*, 2008; Li *et al*, 2017; Chen *et al*, 2014), TPC2 functions largely independently of pH (Wang *et al*, 2012). TPC2 as a rescue target would thus be less affected by disease-related lysosomal pH changes.

Rescue mechanisms. We next assessed the effect of TPC2-A1-P on lysosomal exocytosis in LSD cells as potential mechanism underlying the observed rescue effects. We found that TPC2-A1-P has a strong effect on lysosomal exocytosis in WT as well as in MLIV, NPC1, and JNCL patient fibroblasts (Fig. 6A-C). This result was also confirmed in alveolar macrophages isolated from *Trpml1* knockout ($Mcoln1^{tm1Sasl}$, i.e. $Mcoln1^{\Delta Ex3-5}$) and *Cln3*

knockin ($Cln3^{tm1.1Mem}$, i.e. $Cln3^{\Delta 1.02kb}$) mice as an independent cellular model (Fig. 6D-E). As an additional potential rescue mechanism, the effect of TPC2-A1-P on autophagy was assessed. We found that TPC2-A1-P is increasing starvation-mediated autophagy in WT fibroblasts (Fig. 7A-C), and also recovers the impaired autophagic flux in both NPC1 and MLIV patient fibroblasts (Fig. 7D-I). The autophagic flux blockade in NPC1 and MLIV fibroblasts leads to P62 (SQSTM1) accumulation (Elrick *et al*, 2012; Sarkar *et al*, 2013; Vergarajauregui *et al*, 2008) (Fig. 7J-L). While starvation alone does not sufficiently clear P62 accumulation, we found co-treatment with TPC2-A1-P to ameliorate the autophagic flux blockade in both MLIV and NPC1 fibroblasts, clearing the accumulated P62 (SQSTM1) (Fig. 7J-L). In sum, these findings suggest that TPC2 can be used as a molecular target for the clearance of lysosomal storage material in MLIV, NPC1, and Batten disease cells and possibly other LSDs, as TPC2 activation promotes lysosomal exocytosis and autophagy (the latter one however only under starvation conditions). The effects seen were either comparable to effects evoked by ML-SA1 or even outperformed these effects.

TPC2 expression in human and mouse brain assessed by using a novel *Tpcn2*$^{IRES\text{-}Cre/eR26\text{-}\tau GFP}$ reporter mouse model and RT-qPCR. To demonstrate in-vivo efficacy of TPC2-A1-P, we made use of the well-established MLIV mouse model (Venugopal *et al*, 2007; Grishchuk *et al*, 2015, 2014; Walker & Montell, 2016). One essential prerequisite for TPC2 as a target for LSD treatment is expression in various cells of the CNS, as the brain constitutes the principal organ affected in most LSDs, underlying several of the most severe disease phenotypes. We engineered a novel TPC2 reporter mouse model (*Tpcn2*$^{IRES\text{-}Cre/eR26\text{-}\tau GFP}$) to assess TPC2 expression in the brain (Fig. 8A). A similar system has previously been employed to assess the expression of TRPM5, allowing determination of cell types expressing the channel of interest (Wyatt *et al*, 2017). Utilizing this novel TPC2 reporter mouse model, we first assessed regional expression throughout the 11-week-old mouse brain. We primarily focused on the hippocampus and cerebellum, appearing vulnerable regions for LSD-associated neurodegeneration (Fig. 8B) (Pontikis *et al*, 2004; Greene *et al*, 2001; Jadav *et al*, 2012; Järvelä *et al*, 1997; Grishchuk *et al*, 2014, 2015; Frei *et al*, 1998; Prasad *et al*, 2000; Walkley & Suzuki, 2004). The most striking expression pattern was witnessed in the hippocampus, where TPC2+ (GFP+) neuronal fibers extend towards the CA3 pyramidal layer. Furthermore, throughout the hippocampus (CA1 is shown), TPC2+

neurons in the pyramidal layer and their processes in the stratum radiatum were observed (Fig. 8B). Throughout the hippocampal layers, TPC2 also appeared expressed in astrocytes, microglia, and pericytes. Similarly, widespread TPC2 expression was observed in the cerebellar lobules (Fig. 8B). To quantify the extent of channel expression, we extracted mRNA from the cortex, hippocampus, cerebellum, and other brain regions of 1- and 8-week-old WT mice and analyzed channel transcript levels. Thus, we further confirmed expression of TPC2 in cortex, hippocampus, cerebellum, and other brain regions (Fig. 8C). We also quantified expression based on the immunohistochemistry data for hippocampus, cerebellum, and corpus callosum (Fig. 8D). We finally assessed the expression of TPC2 throughout the human brain by RT-qPCR and confirmed TPC2 expression in all investigated brain regions, with highest expression in the hippocampus, cerebellum, corpus callosum, nucleus accumbens, paracentral and postcentral gyrus (Fig. 8E). In conclusion, TPC2 was found to be expressed in all relevant cell types and regions of the brain to treat the here investigated lysosomal storage diseases (Fig. 8F).

Discussion

Boosting lysosomal exocytosis is emerging as a novel therapeutic strategy to improve lysosomal function in several diseases including lysosomal storage diseases (LSDs) (LaPlante *et al*, 2006; Medina *et al*, 2011; Tsunemi *et al*, 2019; Bonam *et al*, 2019; Zhong *et al*, 2016; Grimm *et al*, 2017). Here, we tested the rescue effect of the TPC2 activator TPC2-A1-P on different LSD phenotypes in human patient fibroblasts and in human CRISPR/Cas9-edited iPSC derived neurons. We provide evidence that TPC2 activation leads to a significant rescue effect on storage phenotypes in MLIV, NPC1 and JNCL cells, while blockage of TPCs exacerbates LSD phenotypes. Endolysosomal function critically depends on the activity of various channels and transporters as outlined above, hence dysfunction of these proteins is likely to affect organelle function and cause or enhance neurodegenerative disease pathology. In lysosomes, TRPML1 and TPC2 are the major cation/calcium release channels and for many neurodegenerative diseases decreased lysosomal calcium efflux has been confirmed (e.g., NPC1, MLIV, Fabry, FAD ($PSEN^{-/-}$) (Feng & Yang, 2016). TRPML1 is directly dysfunctional in MLIV (Chen *et al*, 2014), while in NPC1, TRPML1 activity is reduced by accumulating sphingomyelin (Shen *et al*, 2012).

Furthermore, luminal pH can be a limiting factor, in particular for TRPML1 activity, as increased pH reduces channel open probability (Dong *et al*, 2008; Chen *et al*, 2014). Of note in this context, TPC2 activity is independent of luminal pH (Wang *et al*, 2012). TPC2 and TRPML1 are predominantly expressed in lysosomes, both channels are activated by $PI(3,5)P_2$, and affect endolysosomal transport and trafficking as well as lysosomal exocytosis and autophagy when mutated or lost (Grimm *et al*, 2014; Bonam *et al*, 2019). Stimulation of lysosomal exocytosis with agonists of TRPML1 has recently been shown to clear α-synuclein accumulation in dopaminergic neurons derived from patients with mutations in lysosomal ATP13A2/PARK9 (Tsunemi *et al*, 2019). TPC2 activation by TPC2-A1-P likewise strongly promotes lysosomal exocytosis. Albeit elimination of pathogenic stores by lysosomal exocytosis appears to be an appealing strategy to prevent neuronal cell death (Bonam *et al*, 2019), the effect of the secretion of large amounts of toxic material into the extracellular space certainly needs to be carefully examined and further investigated (Tancini *et al*, 2019). Nevertheless, it is well established that microglia rapidly detect and dispose of not only damaged cells and germs but also all kinds of cellular debris, suggesting that exocytosis might indeed be a promising solution to the problem (Neumann *et al*, 2009; Fu *et al*, 2014; Konishi *et al*, 2020; Kreher *et al*, 2021). Taken together, our results provide incentive to further investigate the potential benefit of TRPML1 and TPC2 activation in various LSDs as well as in adult-onset neurodegenerative diseases including Parkinson's and Alzheimer's disease.

Methods

Human fibroblast cell culture

The following human fibroblast cells isolated from healthy/diseased individuals were investigated: WT (GM00969 or GM03440), MLIV (GM02048/MCOLN1$^{IVS3\text{-}2A>G/Ex1\text{-}del7}$; GM02527/MCOLN1$^{IVS3\text{-}2A>G/IVS3\text{-}2A>G}$; MCOLN1$^{F408\Delta/IVS3\text{-}2A>G}$; MCOLN1$^{T121M/T121M}$), NPC1 (NPC1$^{P237S/I1061T}$; GM03123), NPA (SMPD1$^{L302P/L302P}$; GM00112), Gangliosidosis (GLB1$^{R201C/R201C}$; GM02439), Gaucher (GBA$^{N370S/V394L}$; GM01607), Fabry (GLA$^{W162+IVS4\text{-}16A>G+IVS6\text{-}22C>T}$; GM00107) from Coriell, and JNCL fibroblasts (CLN3$^{\Delta 1.02kb/\Delta 1.02kb}$; MIN30068) provided by Prof. Dr. Susan Cotman, Harvard University, USA. The cells were grown in DMEM (supplemented with 1 g/L glucose, pyruvate, GlutaMAX, 15% FBS, and 1% P/S), and kept at 37°C with 5% CO_2. For electroporation experiments, the cells were electroporated using the Neon system (Invitrogen) with 100 µL tips according to the manufacturer's instructions, electroporating 10^6 cells at a time with 5 µg plasmid using 2x20 ms 1400 V pulses. Following electroporation, 30,000 cells were seeded for cell biological assays into ibiTreat-coated 8-well chambers (Ibidi) or onto poly-L-lysine-coated 12 mm glass cover slips.

Lactosylceramide (LacCer) trafficking assay
Human fibroblasts were cultured in ibiTreat 8-well-chambers (Ibidi) for live-cell imaging overnight prior to treatments. Cells were treated with 30 µM of the indicated agonist in DMSO (to a final DMSO concentration of 0,3%) overnight, and the lactosylceramide trafficking assay subsequently initiated: Cells were washed once with PBS, and 25 µM LacCer (BODIPY FL C5-Lactosylceramide, Invitrogen) pulsed in serum-free culture medium for 1 hour at 37°C. Cells were washed twice with PBS and chased with complete DMEM (including 15% FBS and the indicated agonists) for 2 h at 37°C. LyTr-DR (LysoTracker-Deep Red; diluted 1:10,000, Invitrogen) was added 1,5 h into the chase time to visualize acidic organelles. The cells were subsequently washed three times with PBS, before adding complete phenol-red-free medium for imaging. The cells were transferred to a pre-heated 37°C incubation chamber mounted onto a Zeiss Confocal microscope (LSM 880) and imaged using a 63X water objective at 488 nm (LacCer) and 633 nm (LyTr). mCherry was not imaged due to LyTr bleed-through into the 560 nm channel. For data quantification, the Fiji software was used alongside the JACoP plugin for colocalization quantification, calculating the Mander's coefficient for LyTr-DR overlapping LacCer. LacCer density calculations were performed using Harmony High-Content Imaging and Analysis Software (PerkinElmer).

Filipin unesterified cholesterol storage assay
Human fibroblasts were cultured in 24-well chambers on poly-L-lysine-coated cover slips overnight prior to treatments. Cells were treated with 30 µM of the indicated agonist in DMSO (to a final DMSO concentration of 0,3%) for 48-72 h, and the filipin staining initiated: Cells were washed twice with ice-cold PBS, and fixed in 4% PFA for 30 min. Fixed cells were again washed with cold PBS, and unesterified cholesterol visualized by Filipin staining (PBS with 0.05 mg/mL Filipin, Sigma-Aldrich, and 10% FBS) for 2 h at room temperature in a dark humid chamber. Cells were subsequently washed with ice-cold PBS twice, and nuclei stained using TO-PRO-3 (1:500, Invitrogen). Cells were washed twice and mounted on microscope slides overnight for imaging. Images were captured using a Zeiss Confocal microscope (LSM 880), using a 40X oil objective, at 405 nm (Filipin), 560 nm (mCherry), and 633 nm (TO-PRO-3). For data quantification we calculated average filipin intensity per cell using Harmony High-Content Imaging and Analysis Software (PerkinElmer).

Isolation and cell culture of primary macrophages from knockout and WT mice
For preparation of primary alveolar macrophages (AMΦ), mice were euthanized by a lethal dose of anesthetic, followed by exsanguination. Afterwards, the trachea was carefully exposed and cannulated by inserting a 20 G catheter (B. Braun, cat. no. 4252110B). AMΦ were harvested by 7 consecutive lung lavages with 1 ml of DPBS each. After a centrifugation step, cells were immediately collected and cultured in RPMI 1640 medium (supplemented with 10% fetal bovine serum and 1% P/S). AMΦ were directly seeded onto 8 well (Ibidi) and used for experiments within 5 days after preparation. All cells were maintained at 37 °C in 5% CO_2 atmosphere.

Mitomycin C treatment and CLN3 autofluorescence analysis
Human fibroblasts wild type and CLN3 were treated for 2h with 30µM MitomycinC (Millipore) to induce cell cycle arrest. Suddenly cells are seeded onto glass coverslip (2,5 x 10^4) overnight. After 16 h t0 is fixed with PFA 4%, the rest is treated 72h with DMSO or TPC2-A1-P or ML-SA1 (30 µM). At the end of the 72 h cells are fixed with 4%PFA. PFA is quenched for 10 min with 50mM NaCl in DPBS 1X. Cells are then blocked and permeabilized in blocking buffer (0.05% Saponin, 1%BSA, 50mM NaCl) for 20min. Immunofluorescence targeting LAMP1 protein is performed overnight (1:800, SantaCruz). Cells are then incubated with Alexa Fluor 594 conjugated secondary antibody (Thermo Fisher) for 1 h at room temperature. Nuclei are stained using To-Pro (Thermo Fisher, 1:500 in PBS1X) for 20 min. Confocal images were acquired using an LSM 880 microscope (Zeiss) with 40X magnification. Autofluorence mean intensity in the 488nm channel and 405 channel in LAMP1 area was calculated using unsaturated images on ImageJ 1.52a software.

Lysosomal exocytosis

Alveolar macrophages (3 × 10^4) isolated from wild type, MLIV and CLN3 KO mice and human fibroblasts wild type (2 x 10^4) were seeded on 8-well plates (Ibidi) and cultured overnight. Cells were washed once with Minimum Essential Media (MEM) supplemented with 10 mM HEPES and then treated with TPC2-A1-P (30 μM) or ML-SA1 (30 μM) for 90 min. Ionomycin (4 μM for 10 min) was used as positive control. Following treatment, cells were incubated with an anti-LAMP1 antibody (1:200, SantaCruz) in MEM supplemented with 10 mM HEPES and 1% BSA for 20 min on ice. Cells were then fixed with 2.6% PFA (Thermo Fisher) for 20 min and incubated with Alexa Fluor 488 conjugated secondary antibody (Thermo Fisher) for 1 h in PBS containing 1% BSA. Nuclei were stained with DAPI. Confocal images were acquired using an LSM 880 microscope (Zeiss) with 40X magnification. Plasma membrane LAMP1 mean intensity was calculated using unsaturated images on ImageJ 1.52a software.

For the flow cytometry assay human fibroblasts wild type, MLIV, NPC1 and CLN3 KO (15 x 10^4) were seeded overnight in a 6 well plate. Cells were washed once with Minimum Essential Media (MEM) supplemented with 10 mM HEPES and then treated with TPC2-A1-P (30μM) for 90 min. Ionomycin (4 μM for 10 min) was used as positive control. Following treatment, cells were collected in falcon tubes and incubated on rotation with an anti-LAMP1 antibody (1:200, SantaCruz) in MEM supplemented with 10 mM HEPES and 1% BSA for 20 min at 4°C. Cells were then fixed with 2.6% PFA (Thermo Fisher) for 20 min and incubated with Alexa Fluor 488 conjugated secondary antibody (Thermo Fisher) for 1 h in PBS containing 1% BSA. Samples were then resuspended in DPBS 1X and before FACS analysis cells were filtered with a pre-separation filter with a cut off of 20/30μm. The instrument used was BD FACS Aria III.

Autophagy assays

Human fibroblasts wild type, MLIV and NPC1 KO (5 x 10^4) were seeded in 12 well plate overnight. Treatment was performed for 180 min in complete media or HBSS 10mM Hepes (Thermo) with DMSO or TPC2-A1-P (30μM) or ML-SA1 (30μM). To determine the amplitude of the autophagic flux a co-treatment with 100nM of the vacuolar ATPase inhibitor Bafilomicyn A1 (Millipore) were performed. Samples were then prepared for western blot analysis. For western blot analysis, the following antibodies were used: β-Actin (Santa Cruz SC 47778, 1:4000), LC3 (Novus NB100-2220, 1:1000) P62/SQSMT1 (BD 610833, 1:1000), Vinculin (Cell Signaling Technology, 1:1000, cat. #4650). Total cell lysate was prepared by solubilization in TRIS HCl 10 mM pH 8.0 and 0.2% SDS supplemented with protein and phosphatases inhibitor (Sigma). Protein concentration was determined by the Bradford method (Biorad). After SDS-polyacrylamide gel electrophoresis (PAGE) and immunoblotting, the protein recognized by the specific antibody were visualized by chemiluminescence methods (Luminata Crescendo Western HRP substrate, Millipore) using peroxidase-conjugated anti-rabbit or anti-mouse secondary antibodies (Cell Signaling Technology). Membranes were developed using an Odyssey imaging system (LI-COR Biosciences). Quantification was carried out using unsaturated images on ImageJ 1.52a software.

Cell viability assay

Human patient fibroblasts were seeded at confluency of 3.000 cells per well in 96-well plates (Sarstedt). The following day, cells were treated with 1%, 10%, 30%, 50% and 100% of proposed EC_{50} for 24, 48, 72 h (Zhang *et al*, 2019). DMSO was used as vehicle control and full medium as blank. Cell viability using CellTiter-Blue reagent was used performed as described previously (Netcharoensirisuk *et al*, 2021). The compounds Amitriptyline (#PHR1384), Chlorpromazine (#C0982) Clomipramine (#C7291) and Desipramine (#D3900) were ordered from Sigma Aldrich and Riluzol (#0768) was ordered from Tocris. The analysis was performed with GraphPad Prism 9.1.

Site-directed mutagenesis and colocalization analysis using confocal microscopy

All CLN3 mutants were generated from WT cDNA templates using QuikChange Site-Directed Mutagenesis Kit (Stratagene). All mutants were verified by sequencing both strands entirely. For

site-directed mutagenesis of CLN3 mutants L101P, S131R, C134R, A158P, G165E, L170P, I285V, L306H, V330F and V330I, the KAPA HiFi Hotstart Ready Mix (Roche) was used and the already mentioned plasmid pcDNA6.2/N-EmGFP-DEST with hCLN3 as a template and (10 ng of plasmid DNA in a 25 µl reaction) and primers that had been obtained from Eurofins Genomics (see Table S2 for primer sequences). PCR was done with a Mastercycler® nexus gradient (Eppendorf) PCR conditions were set to an initial denaturing step at 95°C for 3 min, followed by 16 cycles containing of a denaturing step at 98°C for 20 sec, an annealing step at 68°C for 1 min, and an elongation step at 72°C for 7 min, followed by an additional elongation step at 72°C for 7 min. After PCR amplification, the mix was digested for 2 h at 37°C with FastDigest DpnI and 100 µl of XL1Blue E. coli cells (Agilent) were transformed with 5 µl of the digested mix by incubating them for 20 min on ice, heat-shocking them for 40 sec at 37°C, incubating them another 2 min on ice, pre-culturing them for 1 h at 37 °C in a shaker at 200 rpm after addition of 900 µl LB(+) medium, and plating 250 µl of pre-culture on an ampicillin-containing agar plate. After colony growth, colonies were cultured for 16 h at 37°C at 200 rpm in a shaker and plasmid DNA was isolated with a mini-preparation using the CompactPrep Plasmid Mini Kit. Isolated plasmid DNA was sequenced to check for successful mutagenesis. Mutants G187A, G189R, G189W, V290L, E295K, R334C, R334H, Q352H, R405W and D416G have been generated using the QuikChange Site-Directed Mutagenesis Kit (Stratagene). Sequencing of plasmid DNA was done by Eurofins Genomics. In case of successful clonation, a Midi preparation of the respective plasmid DNA was done using the CompactPrep Plasmid Midi Kit. DNA concentration was measured with a NanoDrop™ 2000c spectrophotometer. All CLN3 WT and mutant isoforms were N-terminally tagged GFP versions. For functional studies constructs were transiently expressed in $CLN3^{-/-}$ HeLa cells with the use of Turbofect (ThermoFisher) and analysed 24-48 h after transfection using a confocal microscope (Zeiss LSM 880). Colocalization analysis was done with the JACoP plugin of FiJi. For each cell, a region of interest (ROI) was selected and the channels were separated. For MCC (Mander's correlation coefficient) values, fixed thresholds were set for each transfected plasmid (GFP-CLN3: 92, LAMP1-RFP: 86, Rab5-RFP: 84, Rab11-DsRed: 77, MitoTracker-DR: 122).

Generation and quality control of lysosomal storage disease iPS cells

The protocol for generating homozygous knock-in mutations in induced pluripotent stem cells (iPSCs) has previously been extensively described (Paquet *et al*, 2016). To generate knock-in patient mutant iPS cells for JNCL ($CLN3^{R405W}$ and $CLN3^{D416G}$) and MLIV ($MCOLN1^{IVS3\text{-}2AG}$), we used CRISPOR (Concordet & Haeussler, 2018) to identify protospacer adjacent motifs (PAMs) to allow homozygous knock-in editing events, and chose suitable gRNAs to guide spCas9. gRNAs were cloned into the BsmBI cloning site of the MLM3636 vector, and their editing efficiencies assessed. gRNA-encoding plasmids were thus introduced into HEK293 cells alongside spCas9-GFP-encoding plasmids using the X-tremeGENE 9 DNA Transfection Reagent (Merck), and genomic DNA isolated using the NucleoSpin Tissue Kit (Macherey Nagel) after 48 h of culture. The edited sites were amplified by PCR and purified using the NucleoSpin Gel and PCR Clean-up Kit (Macherey Nagel) before they were sequenced by Sanger sequencing (Eurofins Genomics). Sequence traces were analyzed by sequence-trace decomposition using TIDE (Brinkman *et al*, 2014), and active gRNAs identified. Thus, we identified gRNAs suited to generate the following lysosomal storage disease iPS cells (5'→3', the edited base in bold, PAM sequence follows hyphen): $CLN3^{R405W}$ (TGGCCGCCATTGCAAACTCC-C**G**G), $CLN3^{D416G}$ (ACCTGCATCTCTG**A**CACACT-GGG), and $MLIV^{IVS3\text{-}2AG}$ cells (GCAGGCAACGCCAGGTACTG-GGG). The primers used to sequence the edited sites were (5'→3'): both $CLN3^{R405W}$ and $CLN3^{D416G}$ (AGTGCCTCAACCTGGTGTTC, CCATGGATAAAATCGGCATT), and $MLIV^{IVS3.2AG}$ (CGCAGCCTACACGCGGGAGCA, GCTCCCAACAGTGAAGCCTC). Repair templates were designed as the mutated nucleotide flanked by 50 base-pairs and ordered as Ultramer DNA Oligonucleotides (IDT). The human female episomal iPSC line A18944 (Thermo Fisher) was quality controlled for suitability for differentiations and to rule out common chromosomal abnormalities. iPS cells were maintained in Essential 8 Flex medium (Thermo Fisher) and maintained in vitronectin-coated cell culture vessels. For gene editing,

the cells were split into single cells using Accutase (Thermo Fisher) onto Geltrex (Thermo Fisher)-coated vessels, and supplemented with rock inhibitors (Y27632, Selleckchem). Two days later, the cells were dissociated into single cells, and 2 million cells electroporated by 2x20 ms, 65V pulses using the ECM830 system (BTX) with 30 µg spCas9-R^{Puro} plasmid, 5 µg gRNA-encoding plasmid, and 30 µg repair template. From each electroporation, cells were seeded onto Geltrex (Thermo Fisher)-coated 10 cm cell culture dishes and cultured in StemFlex medium (Thermo Fisher). From days 2-5, electroporated cells were selected for by Puromycin (350 ng/µL; VWR) treatment, before the cells were allowed to recuperate without Puromycin from day 5 onwards, with supplementation of rock inhibitors and RevitaCell Supplement (Thermo Fisher) depending on density and colony formation. Colonies were picked individually into 96-well plates and analyzed for presence of desired mutations. This was done by lysis and gDNA extraction, PCR amplification of the edited site, and restriction fragment length polymorphism (RFLP) analysis. $CLN3^{R405W}$ and $MLIV^{IVS3.2AG}$-edited sites were amplified with the primers previously used for sequencing the edited site, while $CLN3^{D416G}$ was screened for using primers permitting RFLP analysis of the edited site (GTGATGAGCACCGGGAGTTTACAATGGCGG, GGAGCACAGTTCATGGAGGG). RFLP analysis was next performed using BmrI to screen for $CLN3^{R405W}$ introduction, MwoI to screen for $CLN3^{D416G}$, and KpnI to screen for $MCOLN1^{IVS3.2AG}$ (all enzymes from NEB). PCR products showing presence of the desired restriction site were sequenced by Sanger sequencing using the aforementioned primer pairs, and homozygously edited clones thus selected for expansion and further quality control. The next steps of quality controls included confirming edited sequencing traces of propagated clones, assessing puromycin tolerance to ensure spCas9 vector silencing, ensuring absence of undesired on-target (Weisheit *et al*, 2020) editing events and partial chromosome 20 triplications assessed by quantitative genomic PCR (qgPCR), sequencing the top 5 predicted CFD and MIT off-target sites, staining for pluripotency markers by immunocytochemistry, and molecular karyotyping to interrogate chromosomal abnormalities. Puromycin tolerance was assessed upon performing a single-cell split of iPSCs onto Geltrex-coated 6-well wells, and treating the iPSCs with Puromycin (350 ng/µL; VWR) for 3 days. Selected clones died within the three days of Puromycin treatment. Adverse on-target editing events and chromosome 20 triplications were assessed as previously described (Amps *et al*, 2011; Weisheit *et al*, 2020). In short, genomic DNA was isolated using the NucleoSpin Tissue Kit (Macherey Nagel), and subsequently analyzed by qgPCR. The human TERT TaqMan Copy Number Reference Assay (ThermoFisher 4403316) was used as an internal control, and the BCL2L1 copy number probed using the primer set (GGTGGTTGACTTTCTCTCCTAC, TCTCCGATTCAGTCCCTTCT), and the probe 56-FAM/TGTGGAAGA/ZEN/ GAACAGGACTGAGGC/3IABkFQ for detection. To assess on-target editing effects, the same reference probe was used as for chromosome 20 qgPCR, alongside primer/probes targeting the edited site: For both $CLN3^{R405W}$ and $CLN3^{D416G}$ clones, the copy number of the edited site was assessed with the following primer set for amplification (GCATCTACCTCGTCTTCCTGA, CTCCCCAAGTGGGAGACAAT), and the probe 56-FAM/TTGCCTCTGCATGACTTCCTCTGC/ 3IABkFQ for detection. For the $MLIV^{IVS3.2AG}$ locus integrity assessment, on-target editing was not assessed by qgPCR, due to the presence of a silent, heterozygous SNP within the same sequencing trace as the edited base (rs111592394, G>T), present in the wild-type A18944 iPSCs. Presence of the heterozygous SNP alongside the edited base upon Sanger sequencing thereby indicated the presence of two edited chromosomes, ruling out larger chromosomal deletions and ensuring integrity of the edited locus. The top 5 predicted off-target sites (by CFD and MIT algorithms) were also amplified and Sanger sequenced, finding no off-target editing events in the edited cells. For staining for pluripotency markers, iPSC colonies were split onto VTN-coated glass coverslips and grown for two days. They were fixed with PFA (4% PFA in PBS, 30 min), washed three times in PBS, and blocked with blocking buffer for 1 hour (PBS with 3% donkey serum, 0.1% Triton X100, and 0.02% w/v sodium azide). The cells were next incubated in blocking buffer with primary antibodies overnight at 4°C. The following antibodies were used: Mouse anti-SSEA4 (ab16287, 1:500), rabbit anti-NANOG (D73G4, 1:500), mouse anti-Tra160 (MAB4360, 1:500), and rabbit anti-Oct4 (S090023, 1:500). The following day, cells were washed three times with PBS and stained with secondary

antibodies for 2 h at room temperature. The following secondary antibodies were used: Donkey anti-mouse Alexa488 (A32766; 1:500), goat anti-rat Alexa647 (A21247; 1:500), and donkey anti-rabbit Alexa568 (A10042; 1:500). Cells were washed once with PBS, stained with DAPI for 20 min (ThermoFisher, 1:50,000 in PBS), and washed three times with PBS before being mounted on microscope slides for confocal imaging. Images were captured using a Zeiss Confocal microscope (Zeiss LSM880) equipped with a 40X oil objective, exciting at 405 nm (DAPI), 488 nm (Alexa488-conjugated 2^{o} antibodies), and 633 nm (Alexa647-conjugated 2^{o} antibodies). Selected clones showed uniform expression of all interrogated pluripotency markers. Finally, molecular karyotyping analysis was performed by isolating genomic DNA using the NucleoSpin Tissue Kit (Macherey Nagel), and analyzing it using an Illumina BeadArray scanned with an Illumina iScan. Samples with call rates below 95% were excluded, and only SNPs with a GenTrain score above 0.7 included for analysis. The clones that were next used for differentiations and further experiments passed all of the aforementioned quality control checkpoints.

Differentiation of lysosomal storage disease iPSC-derived cortical neurons

Unless otherwise stated, reagents used for cortical neuron differentiation were obtained from Thermo Fisher. Cortical neurons were obtained as previously described (Paquet *et al*, 2016). WT and gene-edited A18944 iPSCs were expanded for neuronal inductions in Essential 8 Flex medium and split into single-cells using Accutase for 8 min at 37^{o}C. Upon dissociation, F12 medium was added to neutralize Accutase, cells were triturated, counted, and centrifuged (1000 rpm, 4 min). Cells were resuspended in neuronal induction (NI) medium, consisting of neuronal maintenance (NM) medium (50% Neurobasal, 50% DMEM/F12, 0.1 mg/mL penicillin-streptomycin, 0.5X B27 supplement, 0.5X N-2 supplement, 2 mM GlutaMAX, 0.1 mM non-essential amino acids, 5 µL insulin, 0.1 mM β-mercaptoethanol), supplemented with the self-renewal inhibitors SB431542 (10 µM; Selleckchem) and LDN193189 (250 nM; Selleckchem). Following the single-cell split, NI was furthermore supplemented with the Rock Inhibitor (RI) Y27632 (10 µM; Selleckchem). After resuspension, 1 million cells were seeded into Geltrex-coated 12-well plate wells. The day of neuronal induction was termed day in vitro 0 (DIV0) and following time-points referred to relative to this time-point. Cells were subsequently fed daily by complete NI medium exchange. At DIV8, cells were split into single cells using Accutase for 10 min at 37^{o}C before the Accutase was neutralized with F12 medium. The cells were triturated, counted, and centrifuged (1000 rpm, 4 min). Cells were resuspended in NI medium supplemented with RI at 30 million cells/mL, and 350 µL droplets seeded in crystallized poly-L-ornithine (Sigma-Aldrich)/laminin-coated 6-well plate wells. Cells were allowed to attach for 1 hour before the wells were filled with NI supplemented with RI. The subsequent day, NI+RI was replaced with NI without RI, and media replaced daily until DIV11. At DIV11, culture medium was changed to NM. At days DIV11 and DIV12, NM was supplemented with bFGF (100 ng/mL; StemCell Technologies). Two days prior to neural rosette isolation, NM was again supplemented with bFGF to boost the expansion of neural rosettes. Upon appearance of neural rosettes (around DIV23), cells were incubated for 1 hour in STEMdiff neural rosette selection reagent (NRSR; StemCell Technologies) at 37^{o}C. NRSR was replaced with NM, and rosettes manually isolated while excluding the edges of the spots, containing non-rosette cells. Rosettes were collected, triturated into smaller clumps, and centrifuged (1000 rpm, 4 min), before they were resuspended in NM supplemented with bFGF. The rosettes were seeded on fresh poly-L-ornithine/laminin-coated 6-well plates, and the medium replaced with NM+bFGF the following day. The rosettes were fed daily with NM, and at around DIV32 split with Accutase for 4 min, neutralized with NM, centrifuged (1000 rpm, 4 min), and resuspended in NM for seeding into new poly-L-ornithine/laminin-coated 6-well plates. At DIV42, neural rosettes were either frozen in NM supplemented with bFGF and 10% DMSO for long-term storage or split for terminal differentiation into mature cortical neurons. For terminal maturation, the neural rosettes were split into single-cells using Accutase for 10 min, Accutase neutralized using NM, triturated, centrifuged (1000 rpm, 4 min), resuspended in Neurobasal medium supplemented with B27, penicillin/streptomycin, and glutamine (from here on termed NB/B27), filtered through 40 µm strainers, and counted. NB/B27 medium was added to seed 400,000 cells/12 mm coverslip, or

200,000 cells/Ibidi 8-well plate well. Coverslips and Ibidi 8-well plate wells were freshly coated with poly-L-ornithine/laminin prior to neuronal seeding. NB/B27 medium was replaced as half feeds every 2-3 days. The cells were furthermore supplemented with the γ-secretase inhibitor DAPT for the first 7 days after plating to augment neuronal maturation, and with 5-fluorouracil (5-FU) for days 2-7 to prevent expansion of contaminating, proliferating cells (predominantly astrocytes). At day 7 after seeding, culture vessels were agitated to dislodge cell debris, and the medium completely replaced with NB/B27 without DAPT or 5-FU. From 7 days after plating onward, the neurons were kept in NB/B27 medium without DAPT or 5-FU until experiments were performed.

Real-time quantitative PCR analysis

In order to assess expression levels of the target channels and disease genes, we used real-time quantitative PCR (RT-qPCR) analysis to interrogate transcript levels. RNA was isolated from iPSC-derived neurons at day 10 after terminal maturation using the RNeasy Mini Kit (Qiagen), following manufacturer's instructions. RNA was immediately synthesized into cDNA and stored at -80^{o}C. cDNA was synthetized using the RevertAid First Strand cDNA Synthesis Kit (ThermoFisher), using 50 ng RNA as template for cDNA synthesis. cDNA synthesis was primed using a 1:1 combination of random hexamers and oligo(dT) primers, and cDNA synthesis initiated by a 5-minute incubation at 25^{o}C followed by a 60-minute incubationat 42^{o}C. The reaction was terminated by heating at 70^{o}C for 5 min, the cDNA diluted 1:7 with nuclease-free water, and frozen at -20^{o}C for storage. For RT-qPCR of cDNA isolated from iPSC-derived neurons, we employed the SYBR Green system (ThermoFisher) and the LightCycler 480 Instrument (Roche). Alternatively, for the prepared Human Brain cDNA Array (OriGene), we used the SYBR Green system and a CFX96 instrument (Biorad) to accommodate the pre-aliquoted cDNA plate. The primer pairs used for human samples were as follows (5'→3'): TRPML1 (TCTTCCAGCACGGAGACAAC, GCCACATGAACCCCACAAAC), TRPML2 (AACGGTGTTTCCTGTTCCGA, GCCATTGCATTTCTGACGGTTA), TRPML3 (TGCTTCTGTGGATGGATCG, GAGACCATGTTCAGAGAACG), TPC1 (TCCCAAAGCGCTGAGATTAC, TCTGGTTTGAGCTCCCTTTC), TPC2 (GTACCCCTCTTGTGTGGACG, GGCCCTGACAGTGACAACTT), CLN3 (GGTTCTCGTCAGTGGGATTT, CTGATGAGATGCTAGCGAAGAC), EMC7 (Eisenberg & Levanon, 2013; Artyukhov *et al*, 2017) (AAAGGAGGTAGTCAGGCCGT, GTTGCTTCACACGGTTTTCCA). For detecting mouse transcripts from biopsies, sample preparation and detection was performed as previously described, but transcripts detected with the following primers: TPC2 (TAAAGTACCGCTCCATCTACCA, GCAGACGTTCGAGTAATACCAG), HPRT (Hruz *et al*, 2011) (GCTCGAGATGTCATGAAGGAGAT, AAAGAACTTATAGCCCCCCTTGA).

Staining of iPSC-derived neurons

Following a week after terminal differentiation, the cortical neurons were stained for the neuronal markers β3-Tubulin/TuJ, MAP2, and CTIP2. Neurons were fixed with 4% PFA in PBS for 30 min, washed twice with PBS, and blocked for 1 hour with blocking buffer (PBS with 3% donkey serum, 0.1% Triton X100, and 0.02% w/v sodium azide). Following blocking, cells were stained overnight at 4°C with the following antibodies: chicken anti-MAP2 (ab5392; 1:1000), mouse anti-Tuj1 (MMS-435P; 1:500) and rat anti-CTIP2 (ab18465; 1:200). The following day, cells were washed three times with PBS and stained with secondary antibodies for 2 h at room temperature. The following secondary antibodies were used: Donkey anti-mouse Alexa488 (A32766; 1:500), goat anti-rat Alexa555 (A21434; 1:500), and goat anti-chicken Alexa647 (A32933; 1:500). Cells were washed once with PBS, stained with DAPI for 20 min (ThermoFisher, 1:50,000 in PBS), and washed three times with PBS before being mounted on microscope slides for confocal imaging. Images were captured using a Zeiss Confocal microscope (Zeiss LSM880) equipped with a 40X oil objective, exciting at 405 nm (DAPI), 488 nm (Alexa488-conjugated 2° antibodies), 561 nm (Alexa568-conjugated 2° antibodies), and 633 nm (Alexa647-conjugated 2° antibodies).

LysoTracker (LyTr) staining
iPSC-derived neurons were terminally matured in glass-bottom, poly-ornithine/laminin-coated 8-well chambers (ibidi) as previously described, using DAPT and 5-FU for 7 days, and kept in culture for another week before imaging. iPSC-derived neurons were treated with 0.3% DMSO or 30 µM TPC2-A1-P for 48 hours prior to live-cell imaging. Lysotracker™ Deep Red (L12492, Invitrogen) was added at a dilution factor of 1:10,000 to the culture medium 30 minutes prior to confocal microscopy. The cells were transferred to a pre-heated 37°C incubation chamber mounted onto a Zeiss Confocal microscope (LSM 880) and imaged using a 63X water objective at 633 nm (Lysotracker) capturing transmitted light. Quantification of captured images was performed using the Fiji software. A mask was generated around the neuronal cell bodies, and the mean intensity recorded.

Oregon green endolysosomal pH measurements
Assessment of lysosomal pH using Oregon green was performed as previously described. (Steinberg *et al*, 2010; Grimm *et al*, 2014) In short, iPSC-derived neurons were terminally matured for 2 weeks in glass-bottom, poly-ornithine/laminin-coated 8-well chambers (ibidi), and loaded with Oregon green conjugated to 70,000 kDa Dextran (D7173, Invitrogen) overnight. To facilitate clearance of the early endocytic pathways, the cells were next chased in culture medium without Oregon green for 1 hour, followed by 1 hour incubation with the indicated compounds. The cells were transferred to a pre-heated 37°C incubation chamber mounted onto a Zeiss Confocal microscope (LSM 880) and imaged using a 63X water objective at 458 nm (pH-insensitive reference) and 488 nm (pH-sensitive spectrum, showing H^+-dependent quenching). Images for generation of a calibration curve were afterwards captured for each cell-line, incubating the cells for 5 min with standard buffers supplemented with 10 µM valinomycin and nigericin (P35379, Invitrogen) at pH values of 3.6, 3.9, 4.1, 4.5, 4.7, 4.9, 5.1, 5.5, 6.0, 6.5, and 7.5. For data quantification, the Fiji software was used. A mask was generated for labelled endosomes using the reference channel (458 nm), and the mean intensity within each endosome measured for both channels. The 488 nm/458 nm ratio was next calculated, and the mean of the ratios converted to pH values using the standard curve. The standard curve was generated from pH-clamped images, fitting the obtained 488 nm/458 nm ratios with the Boltzmann equation.

Magic Red Cathepsin B activity measurements
Lysosomal protease activity was measured using the Magic Red Cathepsin B Kit (AbD Serotec), which utilizes a cathepsin B target sequence (RR), fused by amide bonds to the fluorophore cresyl violet and quenching its fluoresecence. Proteolytic cleavage of the quenching target sequence thus increases the cresyl violet fluorescence, which can be detected by confocal imaging. We used a fluorescence recovery after photobleaching (FRAP) approach previously utilized for assessing proteolysis upon CLN3 knock-down (Metcalf *et al*, 2008) to assess proteolysis in iPSC-derived neurons. The Magic Red Cathepsin B Kit was prepared according to manufacturer's instructions and the iPSC-derived neurons loaded for 60 min at 37°C before imaging with a Zeiss LSM880 confocal microscope, equipped with a 37°C incubation unit and a 63X water immersion objective. FRAP bleaching was performed using 514 nm, 561 nm, and 633 nm lasers targeted towards the most intensely labelled area of the neuronal soma at 100% intensity for 200 iterations (85 s). The pinhole was kept wide (4.70 AU) to image throughout several focal planes, avoiding focal plane shifts or vesicular movement in the z-direction to influence the signal. Next, fluorescence recovery was measured upon excitation with a DPSS 561 nm laser, recording images every 75 ms for 75 seconds. Fluorescence recovery within photobleached regions was finally quantified relative to the initial fluorescence after photobleaching. For compound treatment of iPSC-derived neurons, compounds were administered 48 h prior to loading Magic Red Cathepsin B.

Endolysosomal patch-clamp experiments
For whole-LE/LY manual patch-clamp recordings, cells were treated with apilimod (iPSC derived neurons: 1 µM overnight). Compounds were washed out before patch-clamp experimentation. iPSC

derived neurons were used for experiments 7-14 days after seeding on glass coverslips. Unless otherwise stated, the cytoplasmic solution contained 140 mM K-MSA, 5 mM KOH, 4 mM NaCl, 0.39 mM $CaCl_2$, 1 mM EGTA and 20 mM HEPES (pH was adjusted with KOH to 7.2) and luminal solution contained 140 mM Na-MSA, 5 mM K-MSA, 2 mM Ca-MSA, 1 mM $CaCl_2$, 10 mM HEPES and 10 mM MES (pH was adjusted with NaOH to 4.6) were used. For the application of small molecule agonists (ML-SA1, TPC2-A1P), cytoplasmic solution was completely exchanged by cytoplasmic solution containing agonist. Intact endolysosomes were manually isolated as described before (Chen *et al*, 2017). Currents were recorded using an EPC-10 patch-clamp amplifier (HEKA, Lambrecht, Germany) and PatchMaster acquisition software (HEKA). Data were digitized at 40 kHz and filtered at low-pass filter frequency of 2.9 kHz. Recording glass pipettes were polished and had a resistance in range of 8-11 MΩ. Fast and slow capacitive transients were cancelled by the compensation circuit of the EPC-10 amplifier. Mean capacitance value for LE/LY of neurons was 0.59 pF ± 0.14 (SEM; n=8). In all experiments, 500-ms voltage ramps from -100 to +100 mV were applied every 5 s, holding potential was kept at 0 mV. The current amplitudes at -100 mV were extracted from individual ramp current recordings. Obtained data were statistically analyzed with one-way ANOVA followed by Bonferroni's post-hoc comparison test. Off-line analysis was performed with the software Origin8 (OriginLab Corp., Northampton, MA, USA).

Generation and analysis of a TPC2 reporter mouse line

Mice harboring the $Tpcn2^{IRES\text{-}Cre}$ locus were bred with ROSA26-floxed-stop-τGFP mice, giving rise to mice constitutively expressing τGFP under control of the TPC2 promoter. The $Tpcn2^{IRES\text{-}Cre}$ mouse serves the purpose of expressing Cre recombinase cDNA under control of the TPC2 promoter, without affecting protein function (Mountford & Smith, 1995). The latter mouse harbors a transgene insertion on the *ROSA26* locus, consisting of a loxP-flanked (floxed) polyadenylation termination sequence followed by cDNA of the microtubule-associated protein tau (τ), conjugated to GFP. Without co-expression of Cre recombinase, the transgene is silenced by virtue of the floxed transcriptional termination signal. However, TPC2 promoter-driven Cre recombinase expression excises the termination signal, facilitating constitutive τGFP expression (Fig. 1a) (Wyatt *et al*, 2017). The fusion of GFP to τ furthermore permits GFP distribution throughout neurites, enabling identification of expressing neurons (Wen *et al*, 2011; Iwata *et al*, 2019). At 11 weeks of age, the mice were anaesthetized upon intraperitoneal injection of ketamine and xylazine, and a needle inserted into the left ventricle. A small incision was made in the right atrium for liquid to leave the body. The circulation was first flushed with PBS before 4% PFA was injected into the mouse. Organs were removed and separately post-fixated in 4% PFA for 6 h at 4°C. PFA was next aspirated, and the organs stored overnight in 18% sucrose solution at 4°C. Organs were next embedded in OCT medium, first for 4 h at room temperature, then in embedding molds in isobutane beakers surrounded by ethanol and dry ice. Frozen embedding molds were stored at -80°C until slicing. For slicing, embedding molds were thawed to -16°C, and sliced into 14 µm thick slices. Slices were stored at -80°C until further use. For immunohistochemistry, slices were thawed to room temperature for 15 min, and washed three times with PBS. The slices were next blocked for 1 hour (10% normal donkey serum, 3% bovine serum albumin, 0.3% Triton X-100), and primary antibody staining solutions added at 4°C overnight. The following primary antibodies and dilution factors in PBS were used: chicken anti-GFP (Invitrogen, A10262; 1:1000), rabbit anti-β3 tubulin (Abcam, ab18207; 1:500), rat anti-CD13 (Abcam, ab33489; 1:200), rabbit anti-Iba1 (WAKO, 019-19741; 1:100), Cy3-conjugated mouse anti-GFAP (Sigma Aldrich, C9205; 1:500), and rabbit anti-mGluR1 (Alomone, AGC-006; 1:100). Slices were washed three times with PBS, and next stained with secondary antibodies for 2 h at room temperature. The following secondary antibodies and dilution factor in PBS were used: anti-chicken Alexa488 (Invitrogen, A11039; 1:500), anti-rabbit Cy3 (Jackson Dianova, 711-165-152; 1:500), and anti-rat Cy3 (Jackson Dianova, 112-165-143; 1:500). Samples were washed once with PBS, stained with DAPI for 30 min, washed three times with PBS, and mounted for imaging using a Zeiss LSM880 confocal microscope, equipped with a 40X oil immersion objective.

Acknowledgements

We thank Dennis Crusius for supporting the gene editing and iPSC work presented herein. This work was supported, in part, by funding of the German Research Foundation (Project number 239283807; SFB/TRR152 projects P04 to C.G., P06 to C.W.-S., and P12 to M.B.), the University of Pennsylvania Orphan Disease Center and the Mucolipidosis IV Foundation Grant MDBR-17-120-ML4 to C.G and a NCL Foundation Grant to D.P. and C.G.

Author contributions

E.K., A.S.R., C.A., J.B., D.J., D.B., B.S., M.P., C.S., and S.M. collected and analyzed data. A.W. and U.B. designed and generated the TPC2 reporter mouse model (*Tpcn2*$^{IRES\text{-}Cre/eR26\text{-}\tau GFP}$). G.H. provided the HeLa CLN3$^{-/-}$ cells. C.W-S. and M.B. provided funding. S.C. provided CLN3 patient fibroblasts. S.M. and D.G.S. commented on the manuscript. E.P. and D.M. designed and funded the shigatoxin (STX) and electron microscopy studies. D.P. and C.G. designed the study, collected and analyzed data and wrote the manuscript.

All of the authors discussed the results and commented on the manuscript.

Competing financial interests

The authors declare that they have no conflict of interest.

References

Amps K, Andrews PW, Anyfantis G, Armstrong L, Avery S, Baharvand H, Baker J, Baker D, Munoz MB, Beil S, *et al* (2011) Screening ethnically diverse human embryonic stem cells identifies a chromosome 20 minimal amplicon conferring growth advantage. *Nat Biotechnol* 29: 1132–1144

Artyukhov AS, Dashinimaev EB, Tsvetkov VO, Bolshakov AP, Konovalova E V., Kolbaev SN, Vorotelyak EA & Vasiliev A V. (2017) New genes for accurate normalization of qRT-PCR results in study of iPS and iPS-derived cells. *Gene* 626: 234–240

Bach G, Chen CS & Pagano RE (1999) Elevated lysosomal pH in mucolipidosis type IV cells. *Clin Chim Acta* 280: 173–179

Bae M, Patel N, Xu H, Lee M, Tominaga-yamanaka K, Nath A, Geiger J, Gorospe M, Mattson MP & Haughey NJ (2014) Activation of TRPML1 Clears Intraneuronal A-beta in Preclinical Models of HIV Infection. *J Neurosci* 34: 11485–11503

Bargal R, Avidan N, Olender T, Asher E Ben, Zeigler M, Raas-Rothschild A, Frumkin A, Ben-Yoseph O, Friedlender Y, Lancet D, *et al* (2001) Mucolipidosis type IV: Novel MCOLN1 mutations in Jewish and Mon-Jewish patients and the frequency of the disease in the Ashkenazi Jewish population. *Hum Mutat* 17: 397–402

Beckel JM, Gómez NM, Lu W, Campagno KE, Nabe B, Albalawi F, Lim JC, Boesze-battaglia K & Mitchell CH (2018) Stimulation of TLR3 triggers release of lysosomal ATP in astrocytes and epithelial cells that requires TRPML1 channels. 1–14

Berman ER, Livni N, Shapira E, Merin S & Levij IS (1974) Congenital corneal clouding with abnormal systemic storage bodies: A new variant of mucolipidosis. *J Pediatr* 84: 519–526

Bonam SR, Wang F & Muller S (2019) Lysosomes as a therapeutic target. *Nat Rev Drug Discov* 18: 923–948

Bretou M, Sáez PJ, Sanséau D, Maurin M, Lankar D, Chabaud M, Spampanato C, Malbec O, Barbier L, Muallem S, *et al* (2017) Lysosome signaling controls the migration of dendritic cells. *Sci Immunol* 2

Brinkman EK, Chen T, Amendola M & Van Steensel B (2014) Easy quantitative assessment of genome editing by sequence trace decomposition. *Nucleic Acids Res* 42: 1–8

Burke EE, Chenoweth JG, Shin JH, Collado-Torres L, Kim SK, Micali N, Wang Y, Colantuoni C, Straub RE, Hoeppner DJ, *et al* (2020) Dissecting transcriptomic signatures of neuronal differentiation and maturation using iPSCs. *Nat Commun* 11: 1–14

Calcraft PJ, Ruas M, Pan Z, Cheng X, Arredouani A, Hao X, Tang J, Rietdorf K, Teboul L, Chuang KT, *et al* (2009) NAADP mobilizes calcium from acidic organelles through two-pore channels. *Nature* 459: 596–600

Cang C, Zhou Y, Navarro B, Seo YJ, Aranda K, Shi L, Battaglia-Hsu S, Nissim I, Clapham DE & Ren D (2013) mTOR Regulates Lysosomal ATP-Sensitive Two-Pore Na+ Channels to Adapt to Metabolic State. *Cell* 152: 778–790

Cao Q, Yang Y, Zhong XZ & Dong XP (2017) The lysosomal Ca2+release channel TRPML1 regulates lysosome size by activating calmodulin. *J Biol Chem* 292: 8424–8435

Cao Q, Zhong XZ, Zou Y, Zhang Z, Toro L & Dong X-P (2015) BK Channels Alleviate Lysosomal Storage Diseases by Providing Positive Feedback Regulation of Lysosomal Ca2+ Release. *Dev Cell* 33: 427–441

Carss K, Arno G, Erwood M, Stephens J, Sanchis-Juan A, Hull S, Megy K, Grozeva D, Dewhurst E, Malka S, *et al* (2017) Comprehensive Rare Variant Analysis via Whole-Genome Sequencing to Determine the Molecular Pathology of Inherited Retinal Disease. *Am J Hum Genet* 100: 75–90

Chen C-C, Cang C, Fenske S, Butz E, Chao Y-K, Biel M, Ren D, Wahl-Schott C & Grimm C (2017) Patch-clamp technique to characterize ion channels in enlarged individual endolysosomes. *Nat Protoc* 12: 1639–1658

Chen C-C, Keller M, Hess M, Schiffmann R, Urban N, Wolfgardt A, Schaefer M, Bracher F, Biel M, Wahl-Schott C, *et al* (2014) A small molecule restores function to TRPML1 mutant isoforms responsible for mucolipidosis type IV. *Nat Commun* 5: 4681–4691

Cheng X, Zhang X, Gao Q, Samie MA, Azar M, Tsang WL, Dong L, Sahoo N, Li X, Zhuo Y, *et al* (2014) The intracellular Ca2+ channel MCOLN1 is required for sarcolemma repair to prevent muscular dystrophy. *Nat Med* 20: 1187–1192

Chow CY, Zhang Y, Dowling JJ, Jin N, Adamska M, Shiga K, Szigeti K, Shy ME, Li J, Zhang X, *et al* (2007) Mutation of FIG4 causes neurodegeneration in the pale tremor mouse and patients with CMT4J. *Nature* 448: 68–72

Colletti GA, Miedel MT, Quinn J, Andharia N, Weisz OA & Kiselyov K (2012) Loss of lysosomal ion channel transient receptor potential channel mucolipin-1 (TRPML1) leads to cathepsin B-dependent apoptosis. *J Biol Chem* 287: 8082–8091

Concordet JP & Haeussler M (2018) CRISPOR: Intuitive guide selection for CRISPR/Cas9 genome editing experiments and screens. *Nucleic Acids Res* 46: W242–W245

Cortese A, Tucci A, Piccolo G, Galimberti CA, Fratta P, Marchioni E, Grampa G, Cereda C, Grieco G, Ricca I, *et al* (2014) Novel CLN3 mutation causing autophagic vacuolar myopathy. *Neurology* 82: 2072–2076

Curcio-Morelli C, Charles FA, Micsenyi MC, Cao Y, Venugopal B, Browning MF, Dobrenis K, Cotman SL, Walkley SU & Slaugenhaupt SA (2010) Macroautophagy is defective in mucolipin-1-deficient mouse neurons. *Neurobiol Dis* 40: 370–377

Davis LC, Morgan AJ & Galione A (2020) NAADP-regulated two-pore channels drive phagocytosis through endo-lysosomal Ca2+ nanodomains, calcineurin and dynamin. *EMBO J* 39: e104058

Dong X-P, Cheng X, Mills E, Delling M, Wang F, Kurz T & Xu H (2008) The type IV mucolipidosis-associated protein TRPML1 is an endolysosomal iron release channel. *Nat Lett* 455: 992–996

Dong X-P, Shen D, Wang X, Dawson T, Li X, Zhang Q, Cheng X, Zhang Y, Weisman LS, Delling M, *et al* (2010) PI(3,5)P2 controls membrane trafficking by direct activation of mucolipin Ca2+ release channels in the endolysosome. *Nat Commun* 1: 38–49

Eisenberg E & Levanon EY (2013) Human housekeeping genes, revisited. *Trends Genet* 29: 569–574

Elrick MJ, Yu T, Chung C & Lieberman AP (2012) Impaired proteolysis underlies autophagic dysfunction in Niemann-Pick type C disease. *Hum Mol Genet* 21: 4876–4887

Feng X & Yang J (2016) Lysosomal Calcium in Neurodegeneration. *Messenger* 5: 56–66

Ferguson CJ, Lenk GM, Jones JM, Grant AE, Winters JJ, Dowling JJ, Giger RJ & Meisler MH (2012) Neuronal expression of Fig4 is both necessary and sufficient to prevent spongiform neurodegeneration. *Hum Mol Genet* 21: 3525–3534

Foster WJ, Taylor HBC, Padamsey Z, Jeans AF, Galione A & Emptage NJ (2018) Hippocampal mGluR1-dependent long-term potentiation requires NAADP-mediated acidic store Ca2+ signaling. *Sci Signal* 11

Frei KP, Patronas NJ, Crutchfield KE, Altarescu G & Schiffmann R (1998) Mucolipidosis type IV: Characteristic MRI findings. *Neurology* 51: 565–569

Fu R, Shen Q, Xu P, Luo JJ & Tang Y (2014) Phagocytosis of microglia in the central nervous system diseases. *Mol Neurobiol* 49: 1422–1434

Garver WS, Heidenreich RA, Erickson RP, Thomas MA & Wilson JM (2000) Localization of the murine niemann-pick C1 protein to two distinct intracellular compartments. *J Lipid Res* 41: 673–687

Gerndt S, Chen C-C, Chao Y-K, Yuan Y, Rosato AS, Krogsaeter E, Urban N, Nam O, Nguyen P, Miller MT, *et al* (2020) Agonist-mediated switching of ion selectivity in TPC2 differentially promotes lysosomal function. *Elife* 9: e54712

Grant P, Farmer C, Song J, Kish T & Swedo S (2017) Riluzole Serum Concentration in Pediatric Patients Treated for Obsessive-Compulsive Disorder. *J Clin Psychopharmacol* 37: 713–716

Greene NDE, Lythgoe MF, Thomas DL, Nussbaum RL, Bernard DJ & Mitchison HM (2001) High resolution MRI reveals global changes in brains of Cln3 mutant mice. *Eur J Paediatr Neurol* 5: 103–107

Grimm C, Butz E, Chen CC, Wahl-schott C & Biel M (2017) From mucolipidosis type IV to Ebola: TRPML and two-pore channels at the crossroads of endo-lysosomal trafficking and disease. *Cell Calcium* 67: 148–155

Grimm C, Holdt LM, Chen C-C, Hassan S, Muller C, Jors S, Cuny H, Kissing S, Schroder B, Butz E, *et al* (2014) High susceptibility to fatty liver disease in two-pore channel 2-deficient mice. *Nat Comms* 5: 4699–4712

Grishchuk Y, Pena KA, Coblentz J, King VE, Humphrey DM, Wang SL, Kiselyov KI & Slaugenhaupt SA (2015) Impaired myelination and reduced brain ferric iron in the

mouse model of mucolipidosis IV. *Dis Model Mech* 8: 1591–1601

Grishchuk Y, Sri S, Rudinskiy N, Ma W, Stember KG, Cottle MW, Sapp E, Difiglia M, Muzikansky A, Betensky RA, *et al* (2014) Behavioral deficits, early gliosis, dysmyelination and synaptic dysfunction in a mouse model of mucolipidosis IV. *ACTA Neuropathol Comms* 2: 1–14

Holopainen JM, Saarikoski J, Kinnunen PKJ & Järvelä I (2001) Elevated lysosomal pH in neuronal ceroid lipofuscinoses (NCLs). *Eur J Biochem* 268: 5851–5856

Hruz T, Wyss M, Docquier M, Pfaffl MW, Masanetz S, Borghi L, Verbrugghe P, Kalaydjieva L, Bleuler S, Laule O, *et al* (2011) RefGenes: Identification of reliable and condition specific reference genes for RT-qPCR data normalization. *BMC Genomics* 12: 156

Iwata M, Watanabe S, Yamane A, Miyasaka T & Misonou H (2019) Regulatory mechanisms for the axonal localization of tau protein in neurons. *Mol Biol Cell* 30: 2441–2457

Jadav RH, Sinha S, Yasha TC, Aravinda H, Rao S, Bindu PS & Satishchandra P (2012) Magnetic resonance imaging in neuronal ceroid lipofuscinosis and its subtypes. *Neuroradiol J* 25: 755–761

Järvelä I, Autti T, Lamminranta S, Åberg L, Raininko R & Santavuori P (1997) Clinical and magnetic resonance imaging findings in Batten disease: Analysis of the major mutation (1.02-kb deletion). *Ann Neurol* 42: 799–802

Kasper D, Planells-Cases R, Fuhrmann JC, Scheel O, Zeitz O, Ruether K, Schmitt A, Poët M, Steinfeld R, Schweizer M, *et al* (2005) Loss of the chloride channel CIC-7 leads to lysosomal storage disease and neurodegeneration. *EMBO J* 24: 1079–1091

Kim HJ, Soyombo AA, Tjon-Kon-Sang S, So I & Muallem S (2009) The Ca2+ channel TRPML3 regulates membrane trafficking and autophagy. *Traffic* 10: 1157–1167

Kinarivala N, Morsy A, Patel R, Carmona A V., Sajib MS, Raut S, Mikelis CM, Al-Ahmad A & Trippier PC (2020) An iPSC-Derived Neuron Model of CLN3 Disease Facilitates Small Molecule Phenotypic Screening. *ACS Pharmacol Transl Sci* 3: 931–947

Kiselyov K, Yamaguchi S, Lyons CW & Muallem S (2010) Aberrant Ca2+ handling in lysosomal storage disorders. *Cell Calcium* 47: 103–111

Konishi H, Okamoto T, Hara Y, Komine O, Tamada H, Maeda M, Osako F, Kobayashi M, Nishiyama A, Kataoka Y, *et al* (2020) Astrocytic phagocytosis is a compensatory mechanism for microglial dysfunction. *EMBO J* 39: 1–18

Kousi M, Lehesjoki AE & Mole SE (2012) Update of the mutation spectrum and clinical correlations of over 360 mutations in eight genes that underlie the neuronal ceroid lipofuscinoses. *Hum Mutat* 33: 42–63

Kreher C, Favret J, Maulik M & Shin D (2021) Lysosomal functions in glia associated with neurodegeneration. *Biomolecules* 11: 1–17

Ku CA, Hull S, Arno G, Vincent A, Carss K, Kayton R, Weeks D, Anderson GW, Geraets R, Parker C, *et al* (2017) Detailed clinical phenotype and molecular genetic findings in CLN3-associated isolated retinal degeneration. *JAMA Ophthalmol* 135: 749–760

Kwart D, Paquet D, Teo S & Tessier-Lavigne M (2017) Precise and efficient scarless genome editing in stem cells using CORRECT. *Nat Protoc* 12: 329–334

LaPlante JM, Falardeau J, Sun M, Kanazirska M, Brown EM, Slaugenhaupt SA & Vassilev PM (2002) Identification and characterization of the single channel function of human mucolipin-1 implicated in mucolipidosis type IV , a disorder a ¡ ecting the lysosomal pathway. *FEBS Lett* 532: 183–187

LaPlante JM, Sun M, Falardeau J, Dai D, Brown EM, Slaugenhaupt SA & Vassilev PM (2006) Lysosomal exocytosis is impaired in mucolipidosis type IV. *Mol Genet Metab*

89: 339–348
Leman AR, Pearce DA & Rothberg PG (2005) Gene symbol: CLN3. Disease: Juvenile neuronal ceroid lipofuscinosis (Batten disease). *Hum Genet* 116: 544
Li M, Zhang WK, Benvin NM, Zhou X, Su D, Li H, Wang S, Michailidis IE, Tong L, Li X, *et al* (2017) Structural basis of dual Ca2+/pH regulation of the endolysosomal TRPML1 channel. *Nat Struct Mol Biol* 24: 205–213
Li RJ, Xu J, Fu C, Zhang J, Zheng YG, Jia H & Liu JO (2016) Regulation of mTORC1 by lysosomal calcium and calmodulin. *Elife* 5: 1–16
Lloyd-Evans E & Platt FM (2011) Lysosomal Ca2+ homeostasis: Role in pathogenesis of lysosomal storage diseases. *Cell Calcium* 50: 200–205
Lojewski X, Staropoli JF, Biswas-legrand S, Simas AM, Haliw L, Selig MK, Coppel SH, Goss KA, Petcherski A, Chandrachud U, *et al* (2014) Human iPSC models of neuronal ceroid lipofuscinosis capture distinct effects of TPP1 and CLN3 mutations on the endocytic pathway. *Hum Mol Genet* 23: 2005–2022
Luzio JP, Bright NA & Pryor PR (2007) The role of calcium and other ions in sorting and delivery in the late endocytic pathway. *Biochem Soc Trans* 35: 1088–1091
Medina DL & Ballabio A (2015) Lysosomal calcium regulates autophagy. *Autophagy* 11: 970–971
Medina DL, Fraldi A, Bouche V, Annunziata F, Mansueto G, Spampanato C, Puri C, Pignata A, Martina JA, Sardiello M, *et al* (2011) Transcriptional activation of lysosomal exocytosis promotes cellular clearance. *Dev Cell* 21: 421–430
Medina DL, Paola S Di, Peluso I, Armani A, Stefani D De, Venditti R, Montefusco S, Scotto-Rosato A, Prezioso C, Forrester A, *et al* (2015) Lysosomal calcium signalling regulates autophagy through calcineurin and TFEB. *Nat Cell Biol* 17: 288–299
Metcalf DJ, Calvi AA, Seaman MNJ, Mitchison HM & Cutler DF (2008) Loss of the batten disease gene CLN3 prevents exit from the TGN of the mannose 6-phosphate receptor. *Traffic* 9: 1905–1914
Minckley TF, Zhang C, Fudge DH, Dischler AM, Lejeune KD & Xu H (2019) Sub-nanomolar sensitive GZnP3 reveals TRPML1-mediated neuronal Zn2+ signals. *Nat Commun* 10: 4806
Mirza M, Vainshtein A, DiRonza A, Chandrachud U, Haslett LJ, Palmieri M, Storch S, Groh J, Dobzinski N, Napolitano G, *et al* (2019) The CLN3 gene and protein: What we know. *Mol Genet Genomic Med* 7: 1–41
Mole SE, Schulz A & Haltia M (2020) Rosenberg's Molecular and Genetic Basis of Neurological and Psychiatric Disease. In *Rosenberg's Molecular and Genetic Basis of Neurological and Psychiatric Disease*, Rosenberg RN & Pascual JM (eds) pp 53–71. Amsterdam: INC
Mountford PS & Smith AG (1995) Internal ribosome entry sites and dicistronic RNAs in mammalian transgenesis. *Trends Genet* 11: 179–184
Müller M, Gerndt S, Chao Y-K, Zisis T, Nguyen ONP, Gerwien A, Urban N, Müller C, Gegenfurtner FA, Geisslinger F, *et al* (2021) Gene editing and synthetically accessible inhibitors reveal role for TPC2 in HCC cell proliferation and tumor growth. *Cell Chem Biol*: 1–13
Munroe PB, Mitchison HM, O'Rawe AM, Anderson JW, Boustany RM, Lerner TJ, Taschner PE, de Vos N, Breuning MH, Gardiner RM, *et al* (1997) Spectrum of mutations in the Batten disease gene, CLN3. *Am J Hum Genet* 61: 310–316
Netcharoensirisuk P, Abrahamian C, Tang R, Chen CC, Rosato AS, Beyers W, Chao YK, Filippini A, Di Pietro S, Bartel K, *et al* (2021) Flavonoids increase melanin production

and reduce proliferation, migration and invasion of melanoma cells by blocking endolysosomal/melanosomal TPC2. *Sci Rep* 11: 1–14

Neumann H, Kotter MR & Franklin RJM (2009) Debris clearance by microglia: An essential link between degeneration and regeneration. *Brain* 132: 288–295

Nguyen ONP, Grimm C, Schneider LS, Chao Y-K, Atzberger C, Bartel K, Watermann A, Ulrich M, Mayr D, Wahl-Schott C, *et al* (2017) Two-Pore Channel Function Is Crucial for the Migration of Invasive Cancer Cells. *Cancer Res* 77: 1427–1438

Ogunbayo OA, Duan J, Xiong J, Wang Q, Feng X, Ma J, Zhu MX & Evans AM (2018) MTORC1 controls lysosomal Ca2+release through the two-pore channel TPC2. *Sci Signal* 11: 1–6

Paquet D, Kwart D, Chen A, Sproul A, Jacob S, Teo S, Olsen KM, Gregg A, Noggle S & Tessier-Lavigne M (2016) Efficient introduction of specific homozygous and heterozygous mutations using CRISPR/Cas9. *Nature* 533: 125–129

Park S, Ahuja M, Kim MS, Brailoiu GC, Jha A, Zeng M, Baydyuk M, Wu L-G, Wassif CA, Porter FD, *et al* (2016) Fusion of lysosomes with secretory organelles leads to uncontrolled exocytosis in the lysosomal storage disease mucolipidosis type IV. *EMBO Rep* 17: 266–278

Pereira GJS, Antonioli M, Hirata H, Ureshino RP, Nascimento AR, Bincoletto C, Vescovo T, Piacentini M, Fimia GM & Smaili SS (2017) Glutamate induces autophagy via the two-pore channels in neural cells. *Oncotarget* 8: 12730–12740

Pitt SJ, Funnell TM, Sitsapesan M, Venturi E, Rietdorf K, Ruas M, Ganesan A, Gosain R, Churchill GC, Zhu MX, *et al* (2010) TPC2 is a novel NAADP-sensitive Ca2+ release channel, operating as a dual sensor of luminal pH and Ca2+. *J Biol Chem* 285: 35039–35046

Plesch E, Chen C-C, Butz E, Scotto-Rosato A, Krogsaeter EK, Yinan H, Bartel K, Keller M, Robaa D, Teupser D, *et al* (2018) Selective agonist of TRPML2 reveals direct role in chemokine release from innate immune cells. *Elife* 7: 1–23

Pontikis CC, Cella C V, Parihar N, Lim MJ, Rezaie P, Pearce DA & Cooper JD (2004) Late onset neurodegeneration in the Cln3-/- mouse model of juvenile neuronal ceroid lipofuscinosis is preceded by low level glial activation. *Brain Res* 1023: 231–242

Prasad A, Fischer WA, Maue RA & Henderson LP (2000) Regional and developmental expression of the Npc1 mRNA in the mouse brain. *J Neurochem* 75: 1250–1257

Pryor PR, Mullock BM, Bright NA, Gray SR & Luzio JP (2000) The role of intraorganellar Ca2+ in late endosome-lysosome heterotypic fusion and in the reformation of lysosomes from hybrid organelles. *J Cell Biol* 149: 1053–1062

Pryor PR, Reimann F, Gribble FM & Luzio JP (2006) Mucolipin-1 is a lysosomal membrane protein required for intracellular lactosylceramide traffic. *Traffic* 7: 1388–1398

Puri V, Watanabe R, Dominguez M, Sun X, Wheatley CL, Marks DL & Pagano RE (1999) Cholesterol modulates membrane traffic along the endocytic pathway in sphingolipid-storage diseases. *Nat Cell Biol* 1: 386–388

Ruas M, Davis LC, Chen C-C, Morgan AJ, Chuang K-T, Walseth TF, Grimm C, Garnham C, Powell T, Platt N, *et al* (2015) Expression of Ca2+-permeable two-pore channels rescues NAADP signalling in TPC-deficient cells. *EMBO J* 34: 1743–1758

Ruas M, Rietdorf K, Arredouani A, Davis LC, Lloyd-Evans E, Koegel H, Funnell TM, Morgan AJ, Ward JA, Watanabe K, *et al* (2010) Purified TPC Isoforms Form NAADP Receptors with Distinct Roles for Ca2+ Signaling and Endolysosomal Trafficking. *Curr Biol* 20: 703–709

Samie M, Wang X, Zhang X, Goschka A, Li X, Cheng X, Gregg E, Azar M, Zhuo Y, Garrity AG, *et al* (2013) A TRP channel in the lysosome regulates large particle phagocytosis via focal exocytosis. *Dev Cell* 26: 511–524

Sarkar S, Carroll B, Buganim Y, Maetzel D, Ng AHM, Cassady J, Cohen M, Chakraborty S, Wang H, Spooner E, *et al* (2013) Impaired autophagy in the lipid storage disorder Niemann-Pick type C1 disease. *Cell Rep* 5: 1302–1315

Scotto Rosato A, Montefusco S, Soldati C, Di Paola S, Capuozzo A, Monfregola J, Polishchuk E, Amabile A, Grimm C, Lombardo A, *et al* (2019) TRPML1 links lysosomal calcium to autophagosome biogenesis through the activation of the CaMKKb/VPS34 pathway. *Nat Commun* 10: 5630

Shen D, Wang X, Li X, Zhang X, Yao Z, Dong X, Yu T, Lieberman AP, Showalter HD & Xu H (2012) Lipid Storage Disorders Block Lysosomal Trafficking By Inhibiting TRP Channel and Calcium Release. *Nat Commun* 3: 731–751

Al Shoyaib A, Archie SR & Karamyan VT (2020) Intraperitoneal Route of Drug Administration: Should it Be Used in Experimental Animal Studies? *Pharm Res* 37

Slaugenhaupt S (2002) The Molecular Basis of Mucolipidosis Type IV. *Curr Mol Med* 2: 445–450

Steinberg BE, Huynh KK, Brodovitch A, Jabs S, Stauber T, Jentsch TJ & Grinstein S (2010) A cation counterflux supports lysosomal acidification. *J Cell Biol* 189: 1171–1186

Tancini B, Buratta S, Sagini K, Costanzi E, Delo F, Urbanelli L & Emiliani C (2019) Insight into the role of extracellular vesicles in lysosomal storage disorders. *Genes (Basel)* 10: 1–21

Tsunemi T, Perez-Rosello T, Ishiguro Y, Yoroisaka A, Jeon S, Hamada K, Suresh MKV, Wong YC, Xie Z, Akamatsu W, *et al* (2019) Increased lysosomal exocytosis induced by lysosomal Ca2+ channel agonists protects human dopaminergic neurons from α-synuclein toxicity. *J Neurosci* 39: 5760–5772

Venugopal B, Browning MF, Curcio-Morelli C, Varro A, Michaud N, Nanthakumar N, Walkley SU, Pickel J & Slaugenhaupt SA (2007) Neurologic, Gastric, and Opthalmologic Pathologies in a Murine Model of Mucolipidosis Type IV. *Am J Hum Genet* 81: 1070–1083

Vergarajauregui S, Connelly PS, Daniels MP & Puertollano R (2008) Autophagic dysfunction in mucolipidosis type IV patients. *Hum Mol Genet* 17: 2723–2737

Vitner EB, Platt FM & Futerman AH (2010) Common and uncommon pathogenic cascades in lysosomal storage diseases. *J Biol Chem* 285: 20423–20427

Walker MT & Montell C (2016) Suppression of the motor deficit in a mucolipidosis type IV mouse model by bone marrow transplantation. *Hum Mol Genet* 25: 2752–2761

Walkley SU & Suzuki K (2004) Consequences of NPC1 and NPC2 loss of function in mammalian neurons. *Biochim Biophys Acta - Mol Cell Biol Lipids* 1685: 48–62

Wang F, Wang H, Tuan HF, Nguyen DH, Sun V, Keser V, Bowne SJ, Sullivan LS, Luo H, Zhao L, *et al* (2014) Next generation sequencing-based molecular diagnosis of retinitis pigmentosa: Identification of a novel genotype-phenotype correlation and clinical refinements. *Hum Genet* 133: 331–345

Wang W, Gao Q, Yang M, Zhang X, Yu L, Lawas M, Li X, Bryant-Genevier M, Southall NT, Marugan J, *et al* (2015) Up-regulation of lysosomal TRPML1 channels is essential for lysosomal adaptation to nutrient starvation. *Proc Natl Acad Sci* 112: E1373–E1381

Wang X, Zhang X, Dong X, Samie M, Li X, Clapham DE, Ren D & Xu H (2012) TPC Proteins Are Phosphoinositide-activated Sodium-selective Ion Channels in

Endosomes and Lysosomes. *Cell* 151: 372–383

Weisheit I, Kroeger JA, Malik R, Klimmt J, Crusius D, Dannert A, Dichgans M & Paquet D (2020) Detection of Deleterious On-Target Effects after HDR-Mediated CRISPR Editing. *Cell Rep* 31: 107689

Wen S, Go IN, Mai O, Schauer C, Leinders-zufall T & Boehm U (2011) Genetic Identification of GnRH Receptor Neurons : A New Model for Studying Neural Circuits Underlying Reproductive Physiology in the Mouse Brain. 152: 1515–1526

Wyatt A, Wartenberg P, Candlish M, Krasteva-christ G, Flockerzi V & Boehm U (2017) Genetic strategies to analyze primary TRP channel-expressing cells in mice. *Cell Calcium* 67: 91–104

Zhang X, Chen W, Li P, Calvo R, Southall N, Hu X, Bryant-Genevier M, Feng X, Geng Q, Gao C, *et al* (2019) Agonist-specific voltage-dependent gating of lysosomal two-pore Na+ channels. *Elife* 8: 1–18

Zhang Y, Zolov SN, Chow CY, Slutsky SG, Richardson SC, Piper RC, Yang B, Nau JJ, Westrick RJ, Morrison SJ, *et al* (2007) Loss of Vac14, a regulator of the signaling lipid phosphatidylinositol 3,5-bisphosphate, results in neurodegeneration in mice. *Proc Natl Acad Sci U S A* 104: 17518–17523

Zhong XZ, Sun X, Cao Q, Dong G, Schiffmann R & Dong XP (2016) BK channel agonist represents a potential therapeutic approach for lysosomal storage diseases. *Sci Rep* 6: 1–11

Zou J, Hu B, Arpag XS, Yan Q, Hamilton A, Zeng Y & Vanoye CG (2015) Reactivation of Lysosomal Ca2+ Efflux Rescues Abnormal Lysosomal Storage in FIG4-Deficient Cells. *J Neurosci* 35: 6801–6812

Figures

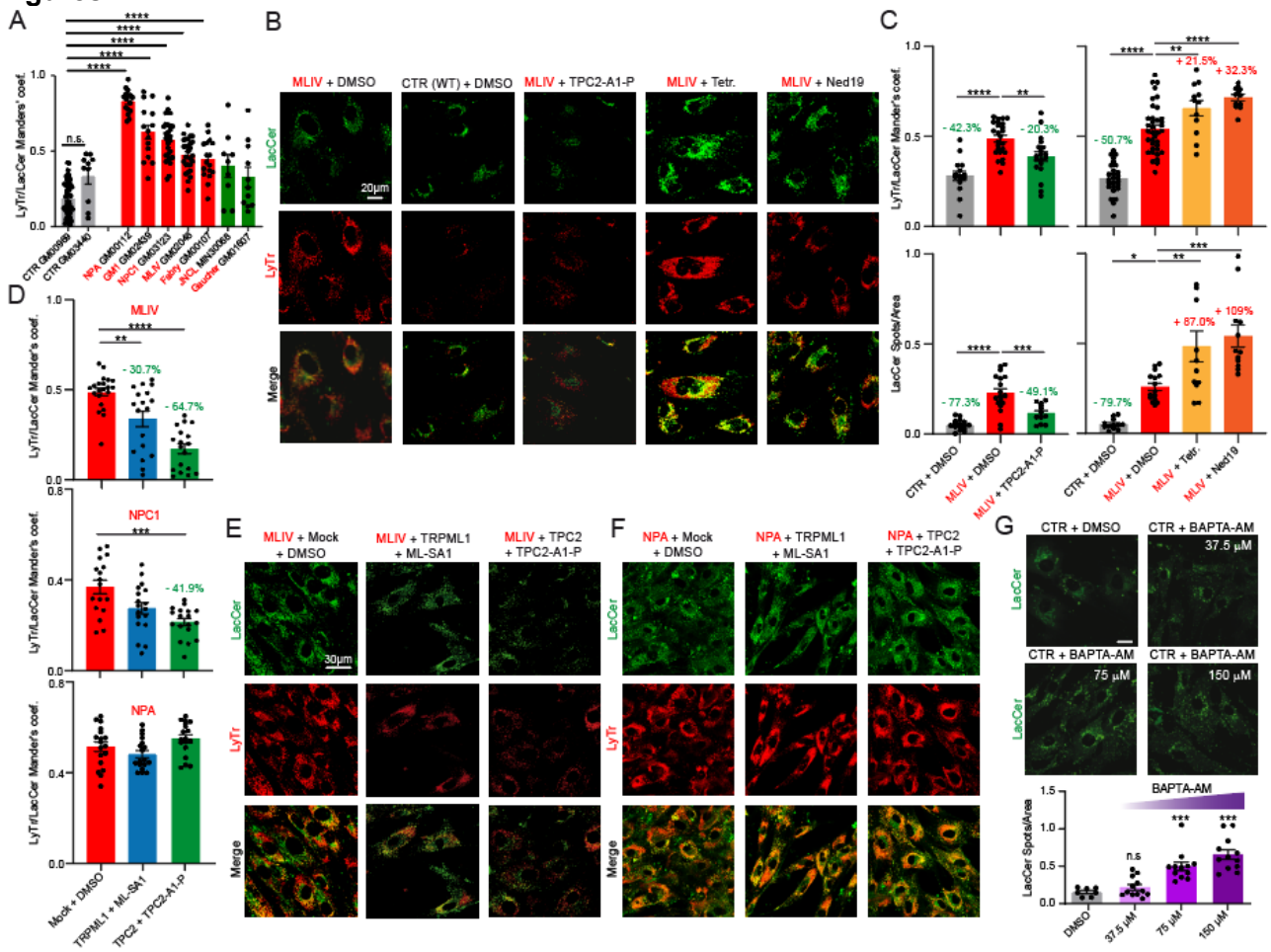

Figure 1. TPC2 agonist effect on lactosylceramide trafficking. TPC2 agonist effect on lactosylceramide trafficking. (A) Plot showing colocalization of LacCer and LysoTracker (LyTr) in human WT (CTR) and different lysosomal storage disease fibroblasts (NPA, GM1, NPC1, MLIV, Fabry, JNCL, Gaucher), and a Parkinson's disease model (LRRK2). Mander´s coefficients were calculated using the Fiji JACoP plugin. (B-C) Representative confocal images (B) and statistical analysis (C) showing colocalization of LacCer and LyTr in human WT (CTR) and MLIV fibroblasts, treated for 16 h with 30 µM of TPC2 agonist TPC2-A1-P or TPC2 blockers (1 µM tetrandrine, 100 µM Ned-19). Mander´s coefficients were calculated using the Fiji JACoP plugin. Cells were loaded with 25 µM of LacCer for 1 h and chased for 2 h with or without 30 µM TPC2 agonist TPC2-A1-P or TPC2 blocker. (D-F) Statistical analysis (D) and representative confocal images (E-F) showing colocalization of LacCer and LyTr in human WT (CTR), MLIV, NPC1, or NPA patient fibroblasts which were mock-electroporated, electroporated with mouse TRPML1:mCherry expression vector or human TPC2(M484L/ G734E):mCherry (TPC2 gain-of-function SNP containing) expression vector as indicated. Cells were treated for 16 h with 30 µM TPC2 agonist TPC2-A1-P or with the TRPML agonist ML-SA1 (30 µM). Mander´s coefficients were calculated using the Fiji JACoP plugin. Cells were loaded with 25µM of LacCer for 1 hour and chased for 2 h with or without agonist. Statistics: n>3 for each tested condition; Gaussian distribution assumed; one-way ANOVA, post hoc Bonferroni's multiple comparisons test, tests performed using GraphPad Prism 8.1.2. (G) Effect of the calcium chelator BAPTA-AM in different concentrations or DMSO as control on LacCer trafficking in human WT fibroblasts. **p-value < 0.01; ***p-value < 0.001; ****p-value < 0.0001.

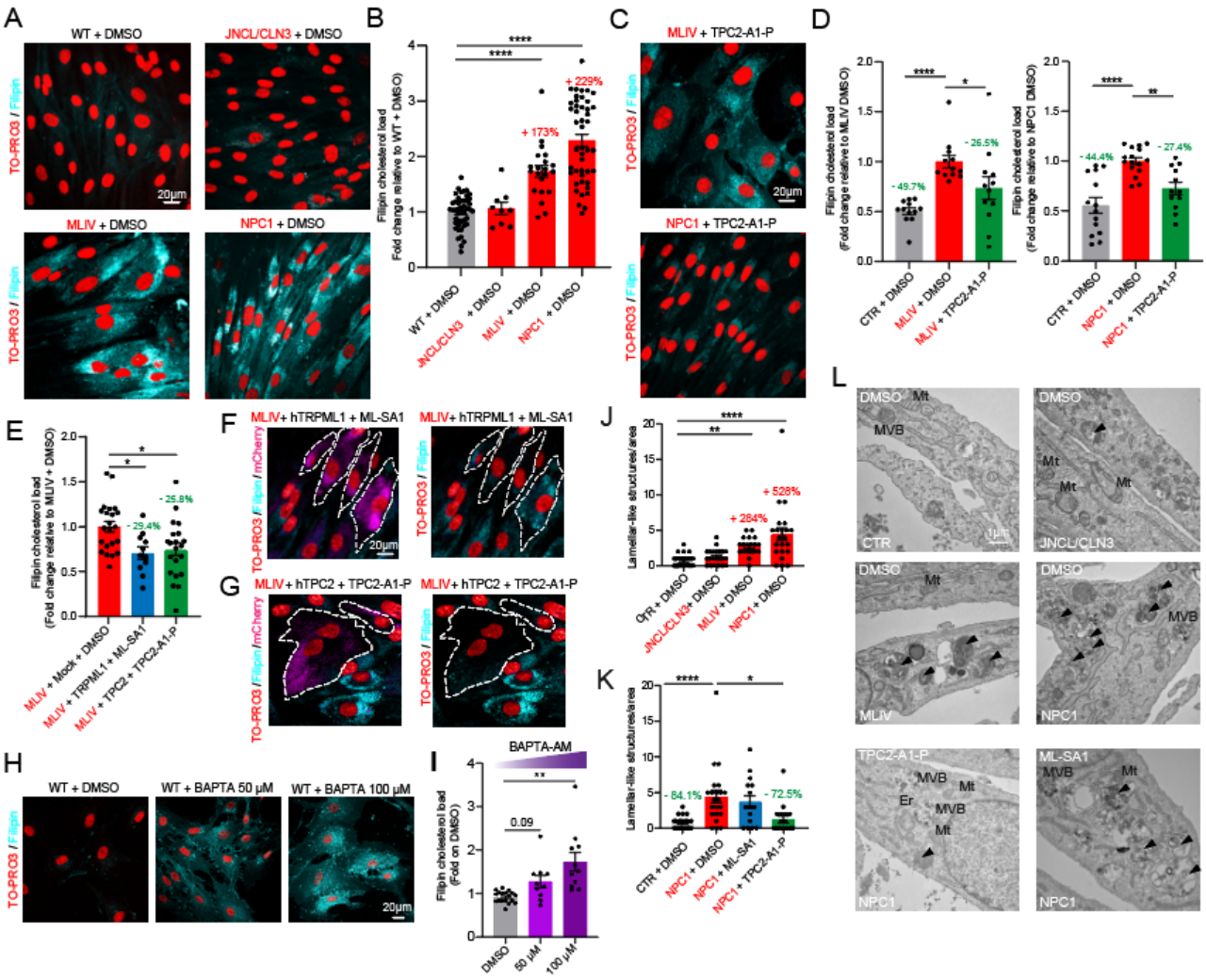

Figure 2. TPC2 agonist effect on cholesterol accumulation and ultrastructural changes. (A-B) Representative confocal images (A) and statistical analysis (B) of human WT, MLIV, JNCL/CLN3, and NPC1 fibroblasts stained with filipin to visualize cholesterol accumulation and treated with TO-PRO3 as nuclear staining. Cells were treated with DMSO as control for compound treatment as shown in C-D. A clear assay window indicative of cholesterol accumulation was evident for NPC1 and MLIV fibroblasts, but not for JNCL/CLN3 fibroblasts. (C-D) TPC2 agonist treatment significantly rescued NPC1 and MLIV cholesterol accumulation. Statistics: n > 3 for each tested condition; Gaussian distribution assumed; one-way ANOVA, post hoc Dunnett's multiple comparisons test, tests performed using GraphPad Prism 8.1.2. (E-G) MLIV patient fibroblasts were mock-electroporated, electroporated with mouse TRPML1:mCherry expression vector or human TPC2(M484L/G734E):mCherry (TPC2 gain-of-function SNP containing) expression vector as indicated. Cells were loaded with 25 µM LacCer in serum-free media for 1 hour and chased for 2 h ± 30 µM agonist as indicated. Shown are representative confocal images of MLIV patient fibroblasts ± agonist treatment. (H-I) Effect of BAPTA-AM on cholesterol accumulation in WT fibroblasts. (**J-L**) Statistics (J-K) and representative electron microscopy (EM) images (L) of human WT, MLIV, JNCL/CLN3, and NPC1 fibroblasts. In MLIV and NPC1 fibroblasts significantly increased numbers of lamellar-like structures indicative of lysosomal defect were found. Numbers were not significantly altered in JNCL/CLN3 fibroblasts. Effect of the treatment with 30 µM TRPML or TPC2 agonist was examined in NPC1 cells which showed the most significant assay window (i). Statistics: n > 3 for each tested condition; Gaussian distribution assumed; one-way ANOVA, post hoc Dunnett's multiple comparisons test, tests performed using GraphPad Prism 8.1.2. *p-value < 0.05; **p-value < 0.01; ****p-value < 0.0001.

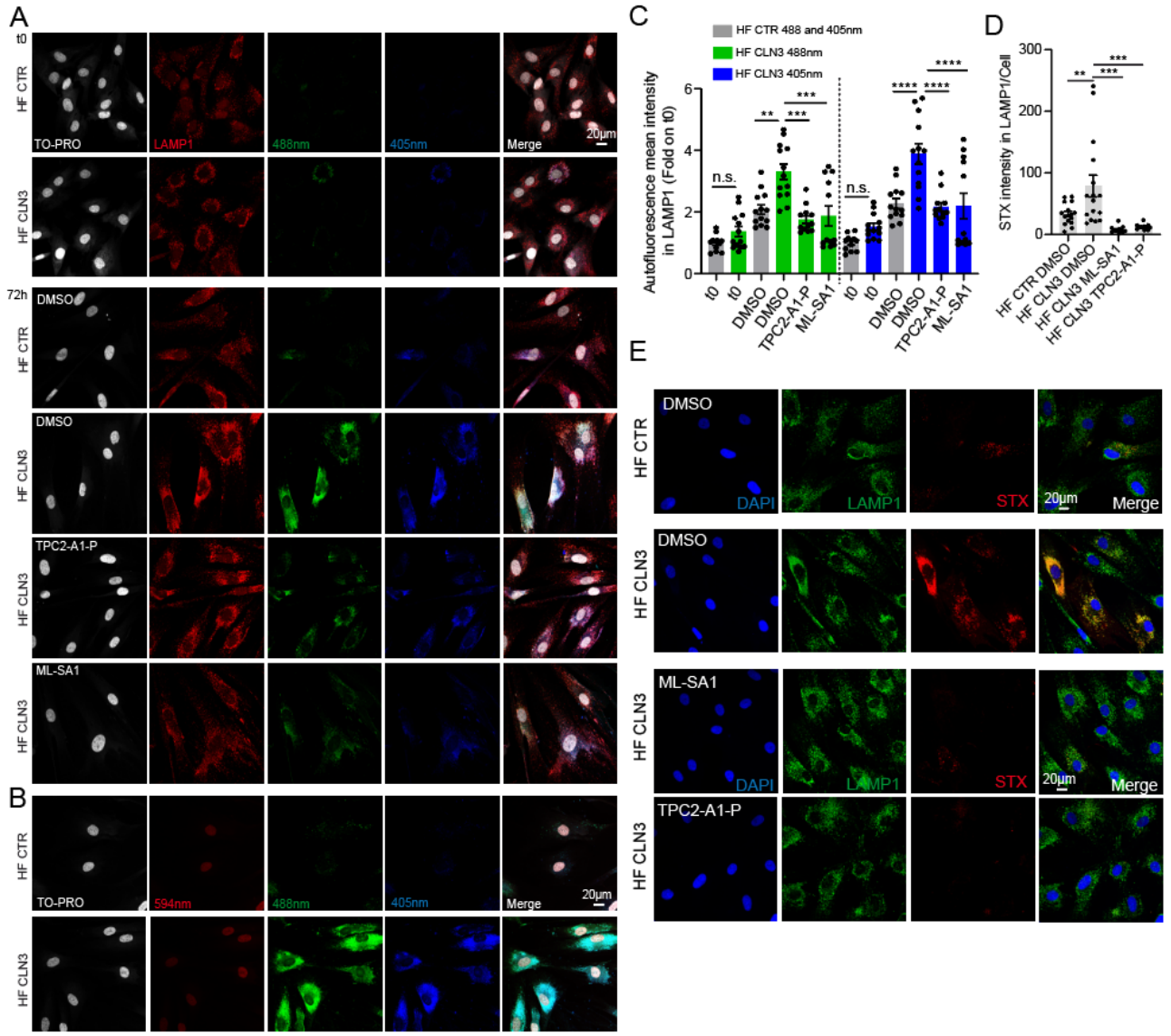

Figure 3. TPC2 agonist effect on lipofuscin and Gb3 accumulation. (A) Representative confocal images of human fibroblasts wild type (HF CTR) and CLN3 KO. Images are showing endogenous LAMP1 staining in 594nm channel and autofluorescence signal in the 488nm and 405nm channels. Cells are treated for 72h with DMSO or TPC2-A1-P or ML-SA1 after 2h of mitomycinC treatment. (B) Representative confocal images showing no autofluorescence signal in the 594nm channel. (C) Bar plot showing autofluorescence mean intensity in LAMP1 positive structure. Each dot represent the mean intensity value per cell in one field. Value are poled from 3 independent experiment. (D-E) Representative confocal images of Gb3 staining using shigatoxin (STX) in human fibroblasts wild type (HF CTR) and CLN3 KO. Cells are treated for 72h with DMSO or TPC2-A1-P or ML-SA1 after 2h of mitomycinC treatment. P-values calculated by one-way ANOVA and Dunnett's multiple comparisons test. *p-value < 0.05; **p-value < 0.01; ***p-value < 0.001.

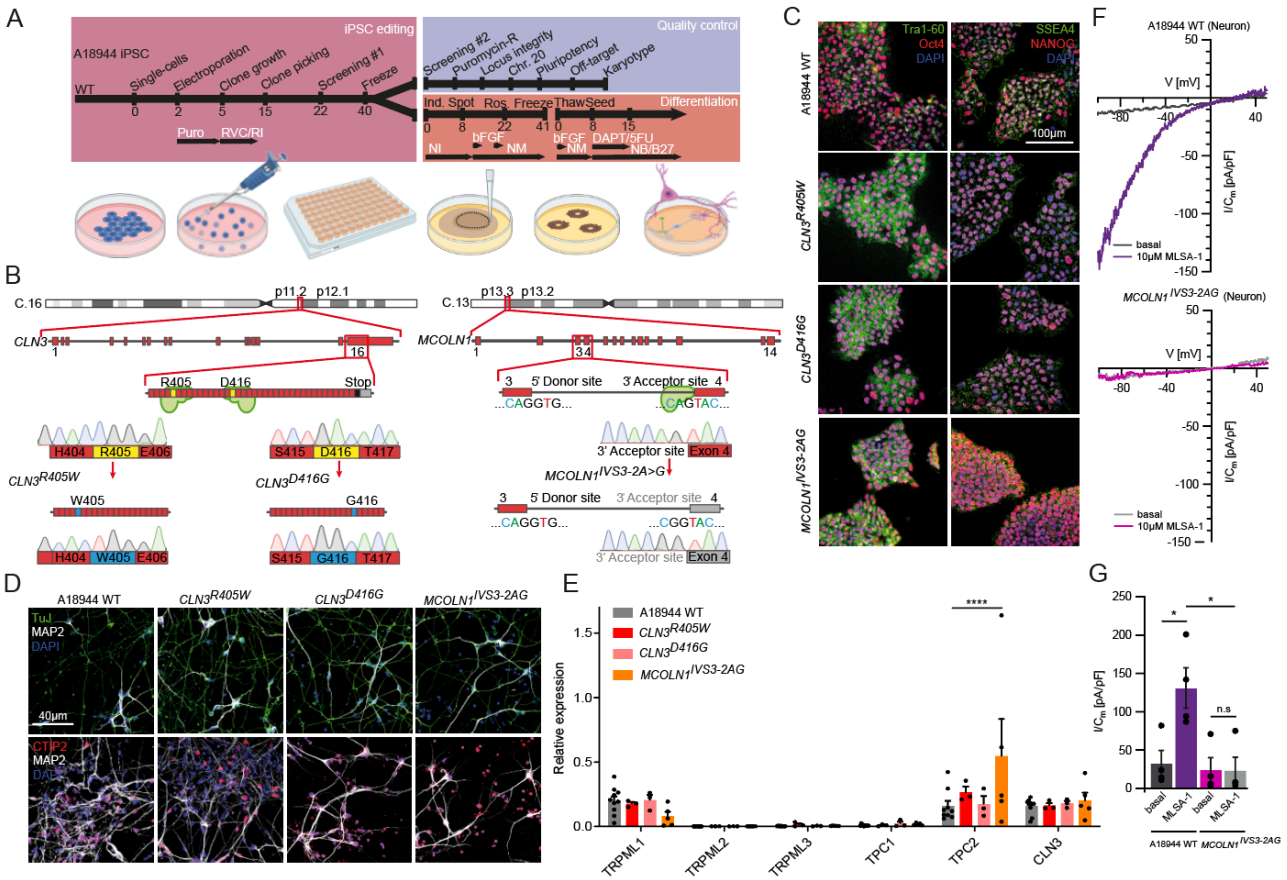

Figure 4. Generation, differentiation, and characterization of lysosomal storage disease iPSCs. (A) Timeline of the gene editing, quality control, and differentiation protocols. The A18944 iPSC line was used this WT line for gene editing. Using CRISPR/Cas9 technology, cells were electroporated with plasmid carrying spCas9, target gRNAs, and repair oligonucleotides. Detailed strategies are shown in (B). Transfected clones were selected using puromycin and expanded for analysis. Homozygously edited clones were identified by sequencing, expanded, and quality controlled. (C) Representative immunofluorescence images of pluripotency markers Tra1-60, Oct4, SSEA4, and NANOG are shown, demonstrating pluripotency of WT and gene-edited iPSCs. (D) Successfully edited, quality-controlled iPSC lines were differentiated into cortical neurons, expressing the neuronal markers TuJ and MAP2, and the cortical neuron transcription factor CTIP2. (E) Using RT-qPCR, we assessed the expression of lysosomal storage disease genes (TRPML1 for MLIV and CLN3 for JNCL) and potential endolysosomal drug targets (TRPMLs and TPCs). The most highly expressed endolysosomal channels were the strictly lysosomal channels TRPML1 and TPC2. While expression levels appeared constant across the different gene-edited iPSC-derived neurons, MLIV cells (MCOLN1IVS3-2AG) and CLN3 KO cells (CLN3ΔEx4-7) showed moderate decreases in the gene-edited transcripts. Conversely, TPC2 expression appeared robustly increased in MLIV iPSC-derived neurons. (F) iPSC-derived neurons were treated overnight with 1 µM Apilimod to selectively enlarge lysosomes, and TRPML1 responsiveness was assessed. TRPML1 currents elicited by ML-SA1 were observed on WT lysosomes, which could not be elicited in MLIV neurons, indicative of abrogated TRPML1 function. *P < 0.05, ** P < 0.01.

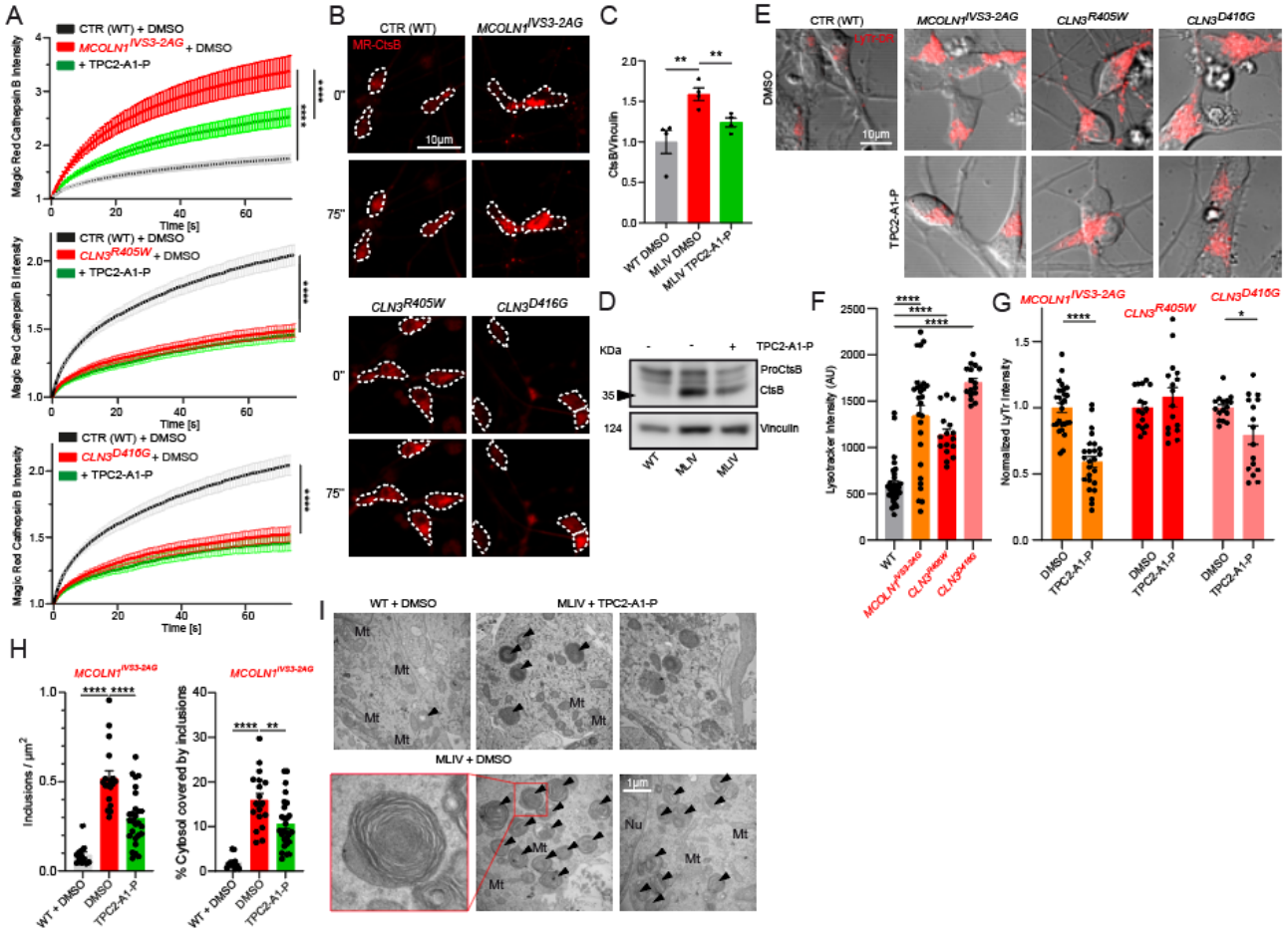

Figure 5. Effect of TPC2-A1-P on human neuronal LSD phenotypes. Cortical neurons were differentiated from the gene-edited A18944 iPSCs, generating lysosomal storage disease neurons with isogenic WT controls. (A-B) Lysosomal proteolysis in iPSC-derived neurons was measured upon 48h pre-treatment with DMSO/TPC2-A1-P (30 µM), loading neurons with magic red-cathepsin B, and performing confocal FRAP experiments to assess the rate of substrate cleavage. MCOLN1$^{IVS3-2AG}$ (MLIV) neurons showed vastly increased cathepsin B activity, while CLN3 mutant neurons exhibited lower cathepsin B activity. n > 3 for each tested condition; Gaussian distribution assumed; one-way ANOVA, post hoc Dunnett's multiple comparisons test, tests performed using GraphPad Prism 8.1.2. **P < 0.01, ***P < 0.0001. (C-D) Western blot analysis of cathepsin B (CtsB) levels in WT and MLIV cortical neurons treated with TPC2-A1-P (30 µM) or DMSO for 72 h. (E-G) Cortical neurons were treated with compounds for 48 h and loaded with LyTr to visualize the lysosomal compartment. Lysosomal expansion was observed in MCOLN1$^{IVS3-2AG}$ (MLIV) neurons, which was ameliorated by TPC2-A1-P treatment. n > 3 for each tested condition; Gaussian distribution assumed; one-way ANOVA, post hoc Dunnett's multiple comparisons test, tests performed using GraphPad Prism 8.1.2. (H-K) Electron microscopy (EM) analysis of neuronal rosettes treated for 1 week with 30 µM of the indicated compound or DMSO equivalent, and fixed with glutaraldehyde for ultrastructural analysis. TPC2-A1-P treatment significantly decreased the number of inclusion bodies. Gaussian distribution assumed; one-way ANOVA, post hoc Dunnett's multiple comparisons test, tests performed using GraphPad Prism 8.1.2. **P < 0.01, ****P < 0.0001.

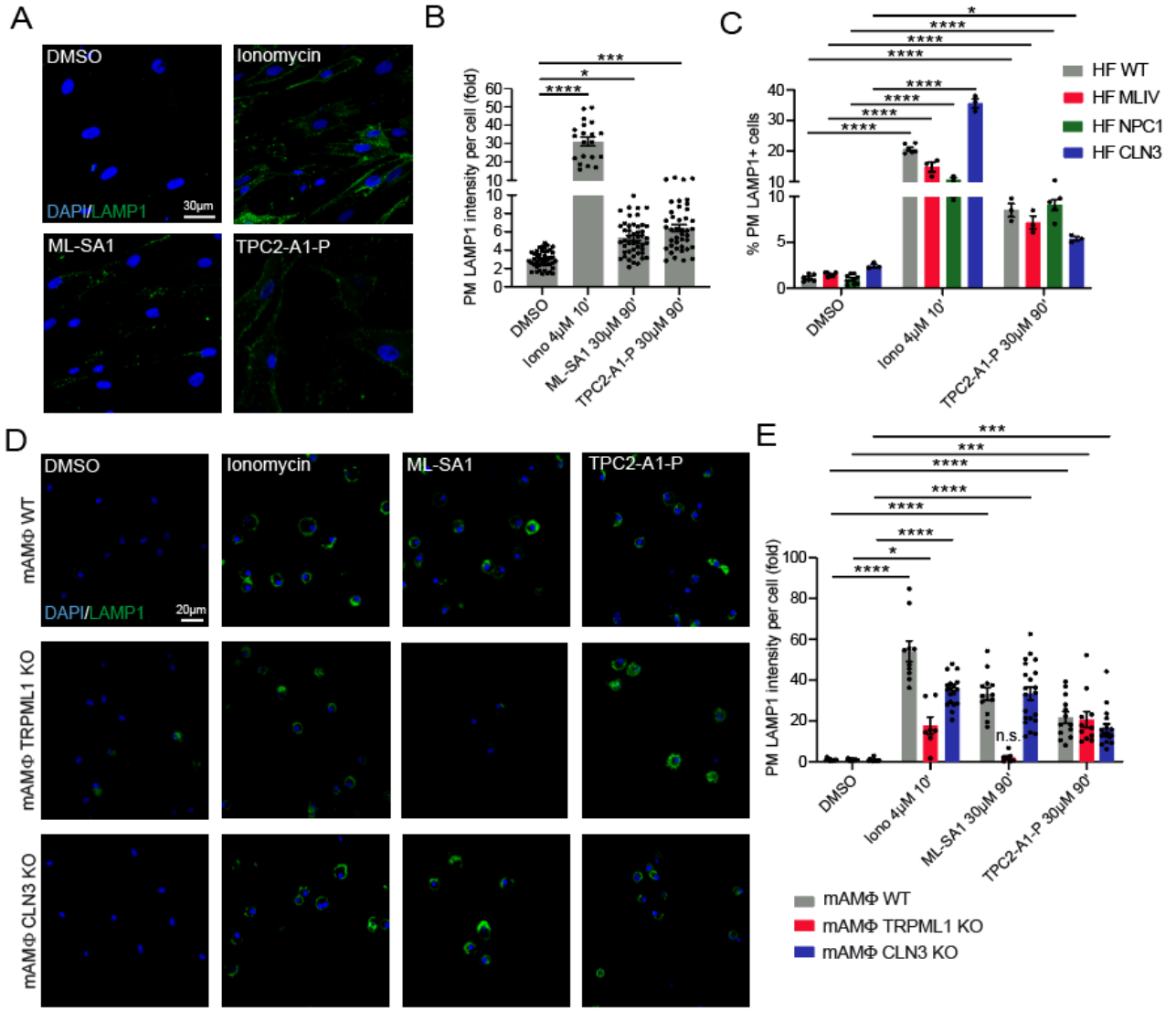

Figure 6. Effect of TPC2-A1-P on lysosomal exocytosis. (A) Lysosomal exocytosis in human fibroblasts wild type (HF WT), MLIV, NPC1 and CLN3 KO. The bar plot shows the mean intensity value of LAMP1 intensity on the plasma membrane measured by flow cytometry, expressed as % of WT DMSO-treated cells. Values are the means of at least 3 independent experiments. (B-C) Representative confocal images of endogenous plasma membrane LAMP1 immunofluorescence in WT human fibroblasts. Bar plot shows LAMP1 plasma membrane fluorescence mean intensities expressed as fold changes compared to DMSO-treated cells, values being pooled from 3 independent experiments. (D-E) Representative confocal images of endogenous plasma membrane LAMP1 immunofluorescence in mouse alveolar macrophages (AMΦ) isolated from WT, MLIV and CLN3 KO mice. Bar plot shows LAMP1 plasma membrane fluorescence mean intensity expressed as fold changes compared to DMSO-treated cells, values are pooled from 3 independent experiments. P-values calculated by 2-way ANOVA and post hoc Bonferroni's multiple comparisons test. *p-value < 0.05; **p-value < 0.01; ***p-value < 0.001.

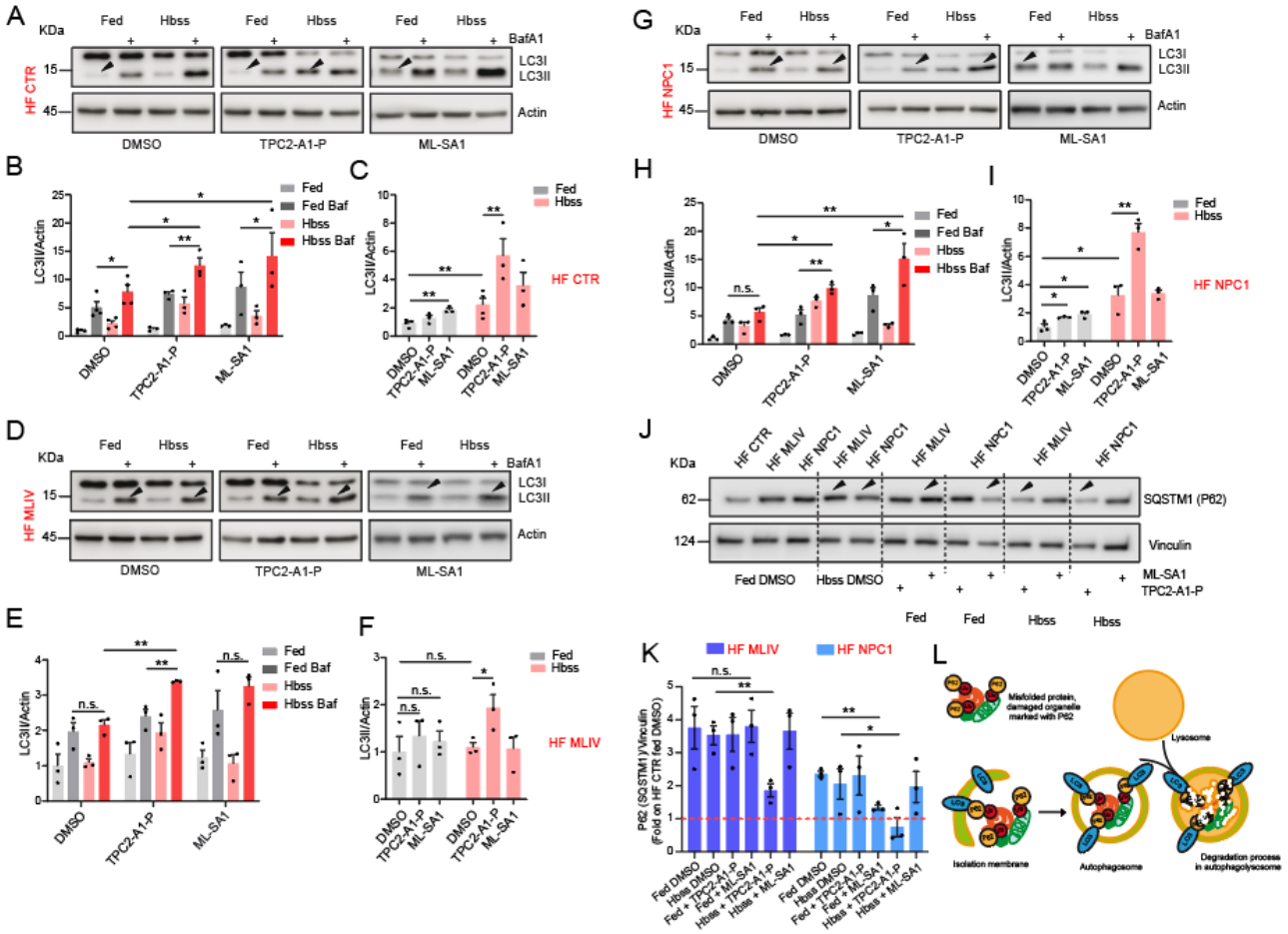

Figure 7. Effect of TPC2-A1-P on autophagy. (A-F) Representative image of immunoblot analysis of endogenous LC3 (LC3I-II) upon TPC2-A1-P and ML-SA1 treatment alone or in the presence of BafA1, in fed (complete media) and starvation (Hbss) in human fibroblasts wild type (HF CTR), MLIV and NPC1 KO. Black arrows highlight LC3II band. Plot shows the densitometry of LC3II band normalized to Actin. The data in the graphs on the right are mean values ± SD, n = 3 lysates per condition pooled from 3 independent experiments. (G-K) Representative image of immunoblot analysis of endogenous SQSTM1 (P62) upon TPC2-A1-P and ML-SA1 in fed (complete media) and starvation (Hbss), in human fibroblasts wild type (HF CTR), MLIV and NPC1 KO. The data in the graphs on the right are mean values ± SD, n = 3 lysates per condition pooled from 3 independent experiments. (L) Cartoon describing P62 role within autophagy pathway. The data in the graphs are mean values ± SD, n = 3 samples per condition. P-values calculated by two-tailed Student's t-test. *p-value < 0.05; **p-value < 0.01; ***p-value < 0.001.

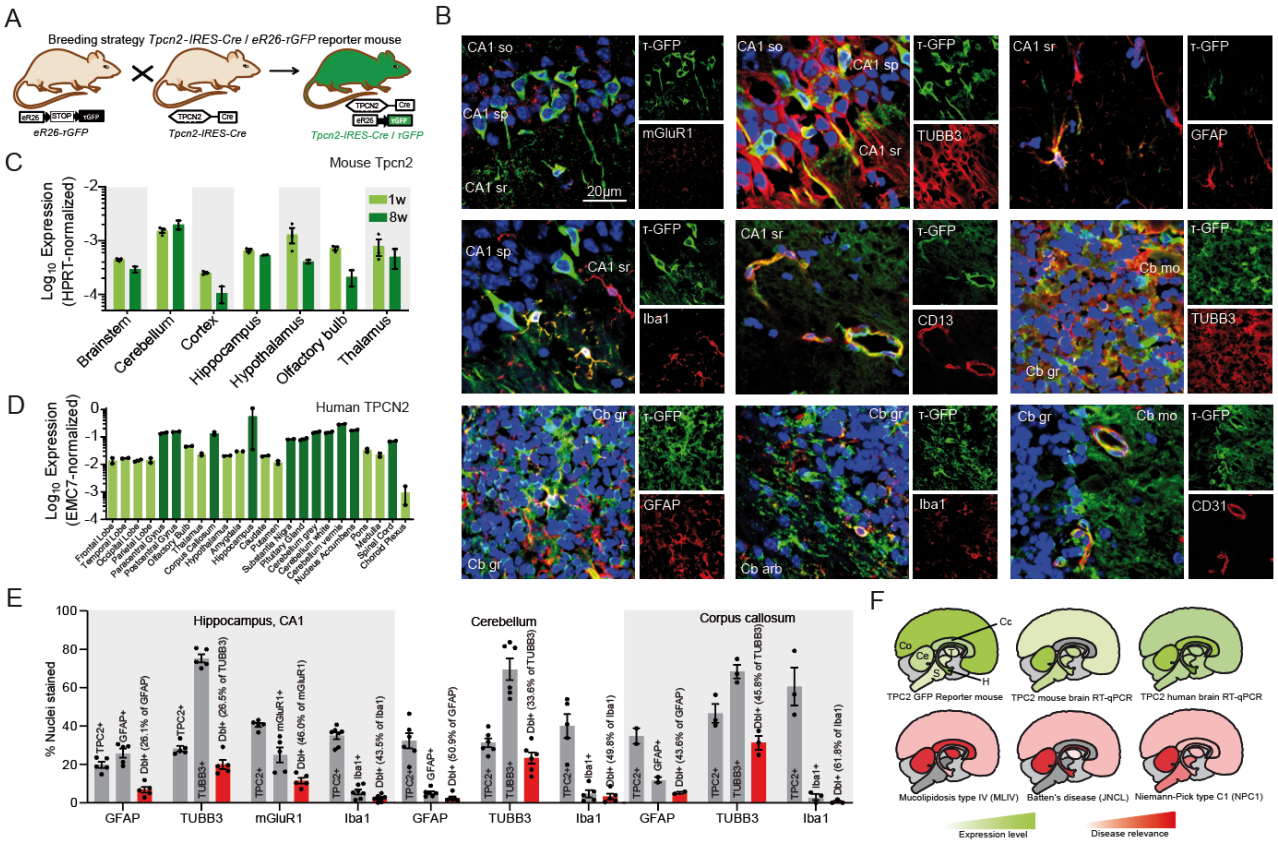

Figure 8. Expression of TPC2 in human and mouse brain. The TPC2 reporter mouse *Tpcn2*$^{\text{IRES-Cre/eR26-τGFP}}$ was generated as previously described (Wen *et al*, 2011; Wyatt *et al*, 2017) (see also Methods section). TPC2 reporter mice aged 11 weeks were sacrificed and perfused with PFA. Brains were isolated, sliced and immunohistochemistry carried out, staining for τGFP expressed under the TPC2 promoter, neuronal/glial markers, and nuclei. Both neurons and glia were found to express TPC2 in the corpus callosum, the hippocampus, and the cerebellum (A-B and E). Furthermore, certain subpopulations of astrocytes (GFAP) and microglia (Iba1) express TPC2 (E). Brains from mice aged 1 week (1w) or 8 weeks (8w) were dissected, and expression of TPC2 in different brain regions mapped using RT-qPCR. The highest expression at both ages was observed in the cerebellum, with stable expression also appearing in the hippocampus. Mild decreases in TPC2 transcript levels were observed upon ageing in the cortex, hypothalamus, and olfactory bulb (C). The TissueScan Human Brain cDNA array was employed to assess TPC2 expression in the human brain, finding TPC2 transcripts to be the highest in the cerebellum, para-/postcentral gyri, corpus callosum, and hippocampus. TPC2 transcript levels were the lowest in the choroid plexus (D). The TPC2 expression observed in the TPC2 reporter mouse (immunofluorescence), mouse brain (RT-qPCR), and human brain (RT-qPCR) is summarized as cartoons, finding the highest expression in the cerebellum and hippocampus (top panels). Moderate TPC2 levels are observed in the corpus callosum, with less expression being observed in the brain stem and thalamus. The affected brain regions in the lysosomal storage diseases MLIV, JNCL, and NPC1 based on patient and mouse data are similarly colour-coded (bottom panels). We observe high expression of TPC2 in frequently disease-relevant brain regions, namely the cerebellum, hippocampus and corpus callosum (F).

Expanded view figures

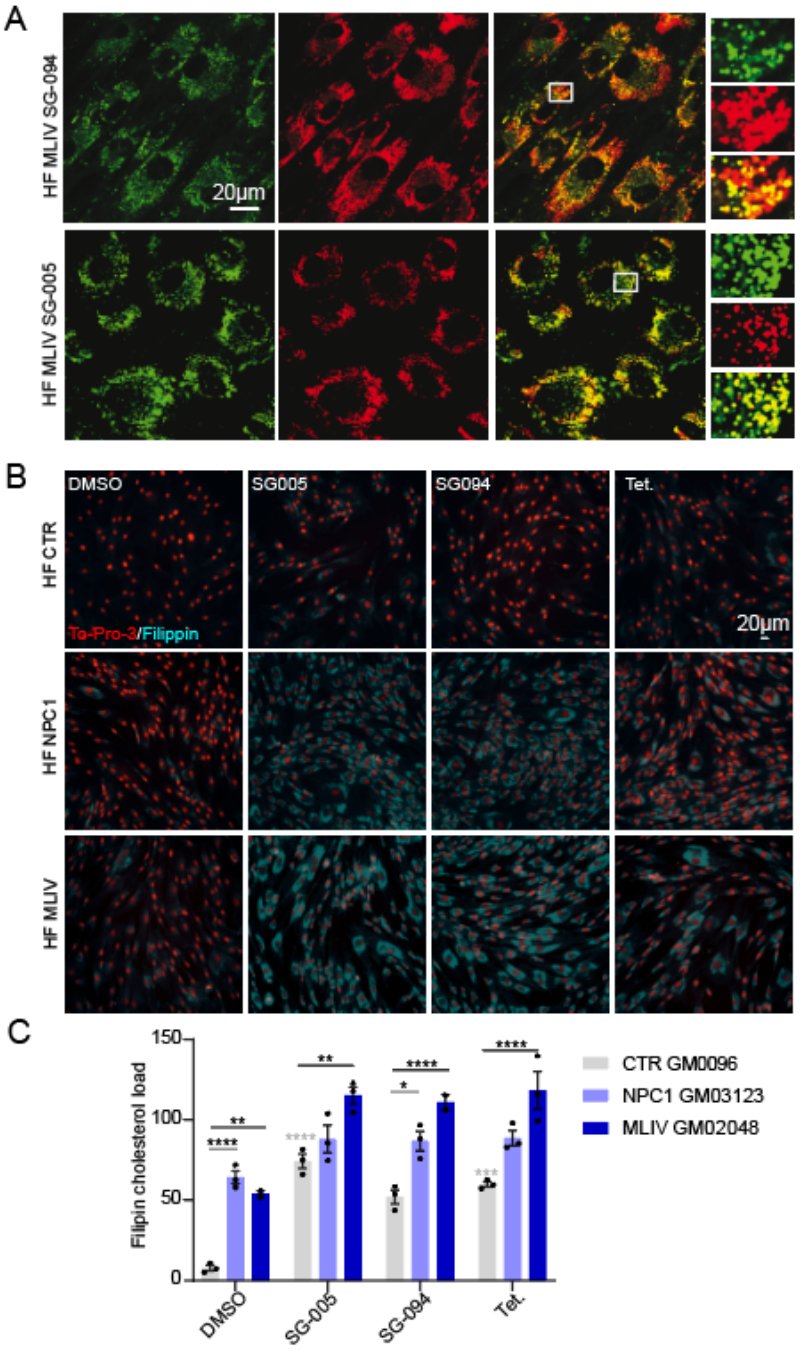

Figure EV1. TPC2 antagonist effects on lactosylceramide trafficking and cholesterol accumulation. (A) TPC2 antagonist effects (1 µM SG-005 and 1 µM SG-094) on lactosylceramide trafficking in human MLIV patient fibroblasts. Shown are representative confocal images. (b-c) Representative confocal images (B) and statistical analysis (C) of human WT, MLIV and NPC1 fibroblasts stained with filipin to visualize cholesterol accumulation and treated with TO-PRO3 as nuclear staining. Cells were treated with DMSO as control for blocker treatments (SG-005, SG-94, and 2 µM tetrandrine). Statistics: n > 3 for each tested condition; Gaussian distribution assumed; one-way ANOVA, post hoc Tukey's multiple comparisons test, tests performed using GraphPad Prism 8.1.2. *p-value < 0.05; **p-value < 0.01; ***p-value < 0.001; ****p-value < 0.0001.

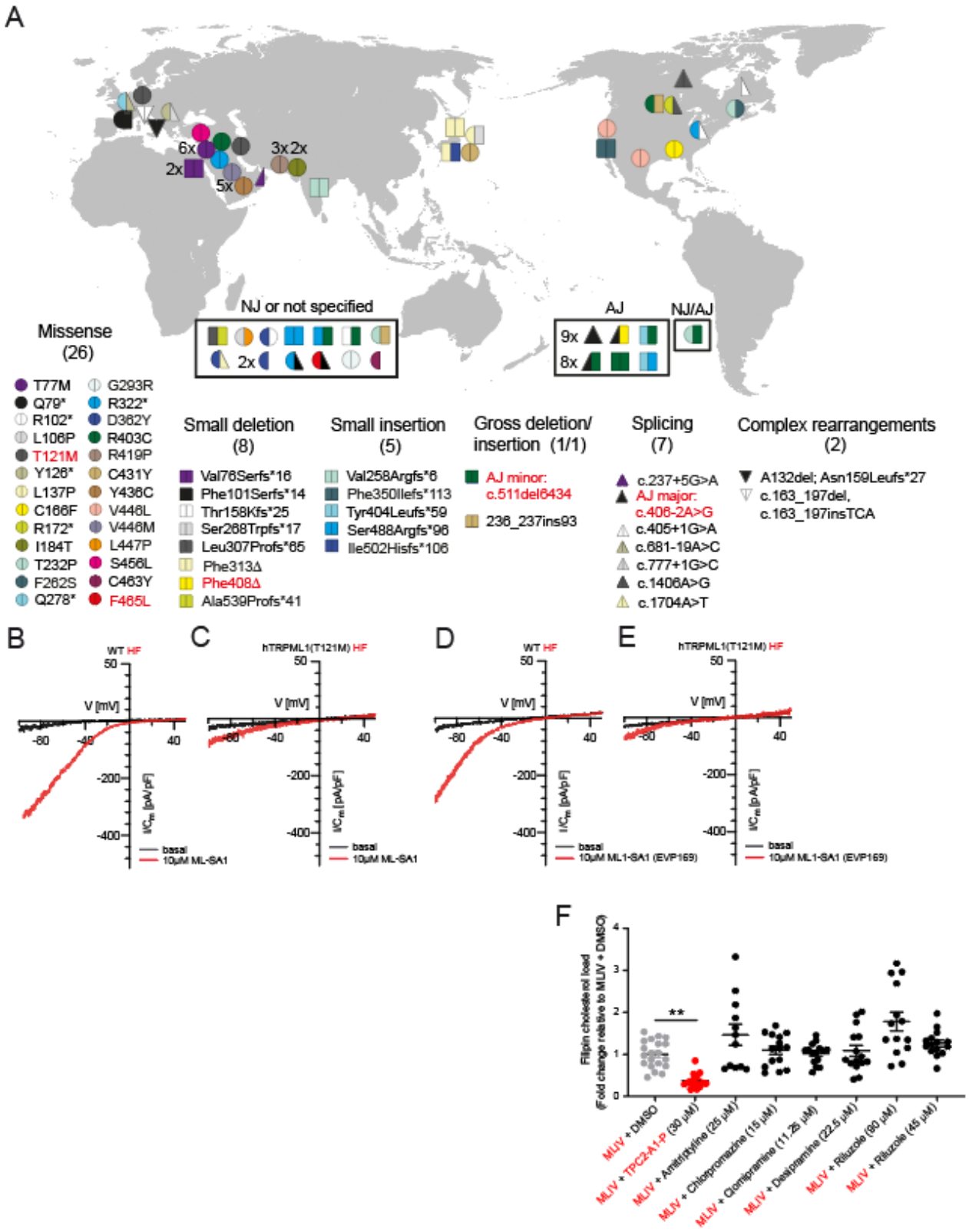

Figure EV2. Summary of known TRPML1 mutations causing MLIV in humans, electrophysiological characterization of a novel patient mutation (TRPML1$^{T121M/T121M}$) and effect of TPC2-A1-P and ther postulated TPC2 agonists on cholesterol accumulation in selected patient fibroblasts. (A) Overview of the currently known MLIV causing TRPML1 (MCOLN1) mutations in humans. Marked in red are mutations further investigated here. HGMD

Professional Database and ClinVar database were screened for TRPML1 mutations. Each symbol represents an individual (described in the literature or listed in databases), matched to its location of origin on the map. Two identical shapes on each side of the symbols represent a homozygous patient, different shapes on each side represent heterozygous individuals. Symbols with a shape only on one side represent patients which were diagnosed with MLIV while no information about the other allele is available. Ashkenazi Jewish (AJ) cases were collected seperately and individuals without information regarding origin were classified as Non-Jewish (NJ)/not specified. The two Ashkenazi founder mutations are labeled as AJ minor and AJ major. TRPML1$^{T121M/T121M}$ is a new variant found to be homozygously expressed in a patient from a Yazidi family not described in the literature yet. The patient, an 18-year old woman showed a comparably mild clinical phenotype (ability to walk and talk, delayed development with retinal degeneration (risk of blindness), reduced iron (39 µg/dl (60-140)) and ferritin (6 µg/l (16-92)) levels, reduced Hb, HCT, MCV and MCHC (iron deficiency anemia), slightly deranged liver function (ASAT: 56 U/l (<30) and ALAT: 42 U/l (<30)). Electrophysiology revealed some residual channel activity (see B-C). (B-C) Representative currents (I-V traces) from vacuolin-enlarged LE/LY, isolated from HEK293 cells overexpressing WT TRPML1 or the novel patient mutation TRPML1$^{T121M/T121M}$, activated by PI(3,5)P_2 (b) or ML-SA1 (c). (D-E) Representative currents (I-V traces) from vacuolin-enlarged LE/LY, isolated from WT TRPML1 or TRPML1^{T121M} patient fibroblasts, activated by ML1-SA1 (EVP169) (b) or ML-SA1 (c). (F) Effect of TPC2-A1-P on cholesterol accumulation in WT, MLIV and selected patient fibroblasts carrying point mutations as indicated, visualized by filipin. (G) Effect of TPC2-A1-P, amitriptyline, chlorpromazine, clomipramine, desipramine, and rilozole on cholesterol accumulation in MLIV cells, visualized by filipin. P-values calculated by 2-way ANOVA and *post-hoc* Bonferroni's multiple comparisons test. *p-value < 0.05; **p-value < 0.01; ***p-value < 0.001.

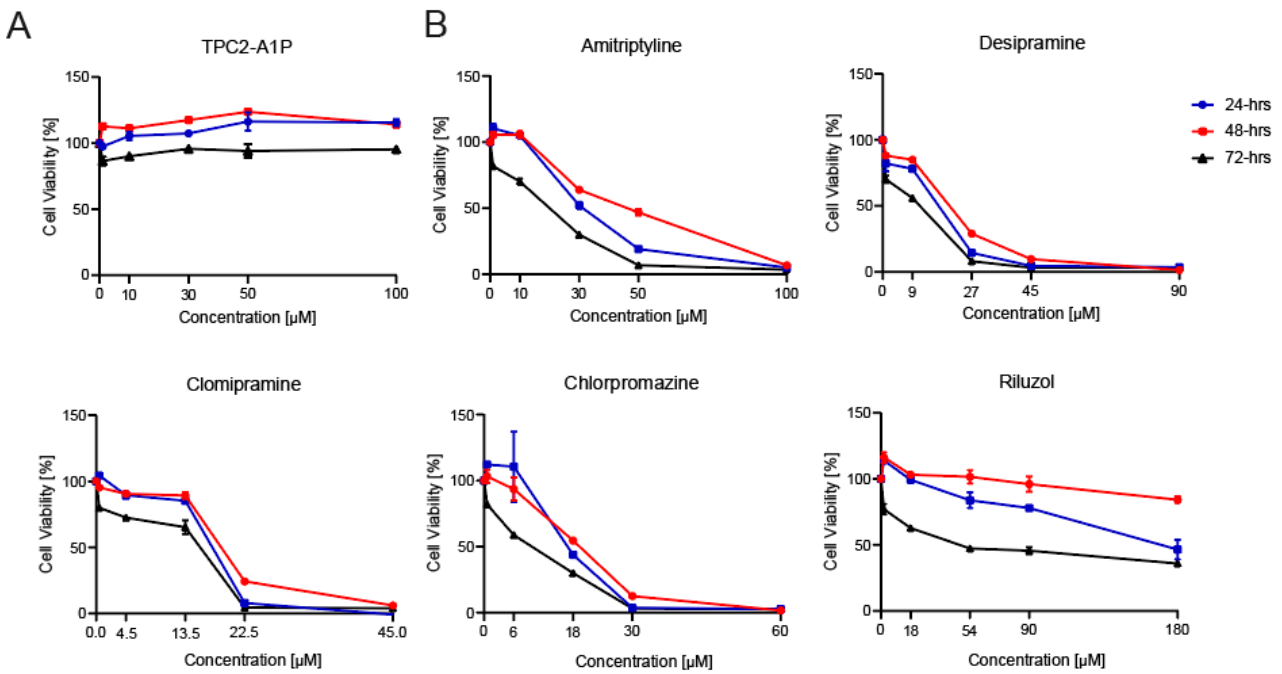

Figure EV3. Effect of various drugs and TPC2-A1-P on cell viability. (A-B) Cell viability assay for compounds on human patient fibroblasts. Cells were incubated for 24h, 48h and 72h with increasing concentrations and cell viability was assessed with CellTiter-Blue. The maximum concentrations were based on the proposed EC_{50}s of each compound.

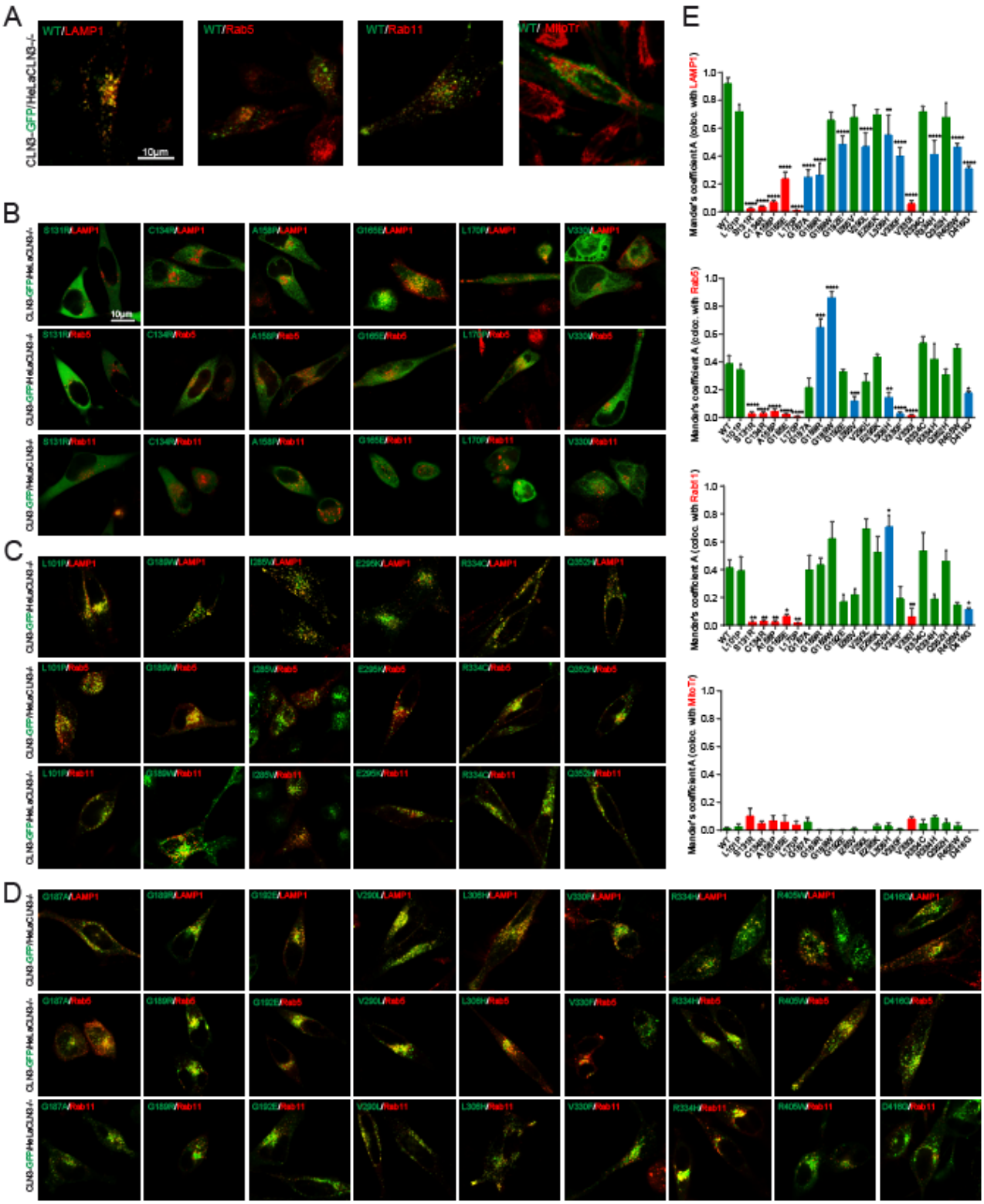

Figure EV4. Colocalization of GFP-CLN3 WT and Batten disease causing missense mutants with endolysosomal markers (LAMP1 for LE/LY, Rab5 for EE and Rab11 for RE) and MitoTracker-DR. (A-D) Representative confocal images of CLN3 KO HeLa cells co-transfected with either GFP-CLN3 (WT) or GFP-CLN3 missense mutant variants (as indicated) and endolysosomal markers: LAMP1-RFP, Rab5-RFP, or Rab11-DsRed. (E) Quantification of experiments as shown in a-d. Shown are the respective Mander's correlation coefficients (MCC) for automated colocalization

analysis (JACoP/Fiji) of GFP-CLN3 WT and missense mutants with LAMP1-RFP, Rab5-RFP, Rab11-DsRed, or MitoTracker-DR (negative control). Data are presented as mean ± SD. * P < 0.1, ** P < 0.01, *** P < 0.001, ****, P < 0.0001. Statistical significance was determined by one-way ANOVA Dunnett's multiple comparisons test.

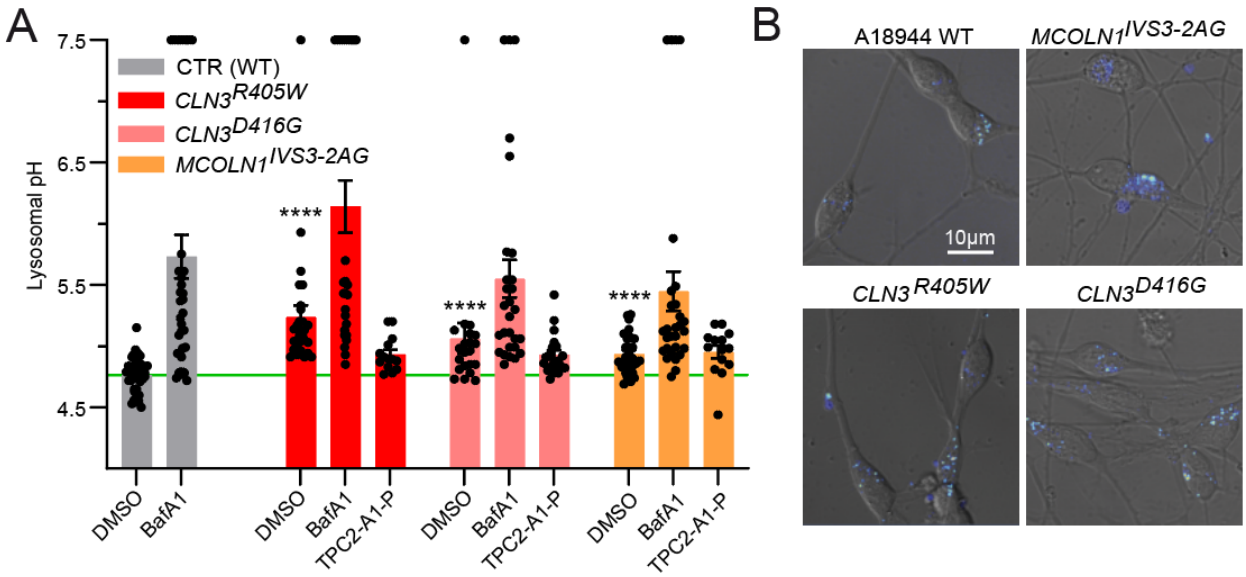

Figure EV5. Lysosomal pH in WT, MLIV and CLN3 mutant neurons. (A-B) Cortical neurons were differentiated from the gene-edited A18944 iPSCs, generating lysosomal storage disease neurons with isogenic wild-type controls. Cortical neurons were loaded with Oregon Green-labelled 70,000 Da dextran overnight to label lysosomes. Ratiometric measurement of the pH-sensitive/pH-insensitive Oregon Green spectra, followed by generation of a standard-curve upon adding ionophores plus pH standard buffers, allowed determination of lysosomal acidity. All neurons showed mild lysosomal alkalinization. As a positive control, neurons were incubated with the proton pump inhibitor bafilomycin A1 (200 nM), resulting in endosomal alkalinization. Representative images in the pH-sensitive range (488 nm).